Inorganic Glasses for Photonics

Wiley Series in Materials for Electronic and Optoelectronic Applications

www.wiley.com/go/meoa

Series Editors
Professor Arthur Willoughby, *University of Southampton, Southampton, UK*
Dr Peter Capper, formerly of *SELEX Galileo Infrared Ltd, Southampton, UK*
Professor Safa Kasap, *University of Saskatchewan, Saskatoon, Canada*

Published Titles

Bulk Crystal Growth of Electronic, Optical and Optoelectronic Materials, Edited by P. Capper
Properties of Group-IV, III–V and II–VI Semiconductors, S. Adachi
Charge Transport in Disordered Solids with Applications in Electronics, Edited by S. Baranovski
Optical Properties of Condensed Matter and Applications, Edited by J. Singh
Thin Film Solar Cells: Fabrication, Characterization, and Applications, Edited by J. Poortmans and V. Arkhipov
Dielectric Films for Advanced Microelectronics, Edited by M. R. Baklanov, M. Green, and K. Maex
Liquid Phase Epitaxy of Electronic, Optical and Optoelectronic Materials, Edited by P. Capper and M. Mauk
Molecular Electronics: From Principles to Practice, M. Petty
CVD Diamond for Electronic Devices and Sensors, Edited by R. S. Sussmann
Properties of Semiconductor Alloys: Group-IV, III–V, and II–VI Semiconductors, S. Adachi
Mercury Cadmium Telluride, Edited by P. Capper and J. Garland
Zinc Oxide Materials for Electronic and Optoelectronic Device Applications, Edited by C. Litton, D. C. Reynolds, and T. C. Collins
Lead-Free Solders: Materials Reliability for Electronics, Edited by K. N. Subramanian
Silicon Photonics: Fundamentals and Devices, M. Jamal Deen and P. K. Basu
Nanostructured and Subwavelength Waveguides: Fundamentals and Applications, M. Skorobogatiy
Photovoltaic Materials: From Crystalline Silicon to Third-Generation Approaches, G. Conibeer and A. Willoughby
Glancing Angle Deposition of Thin Films: Engineering the Nanoscale, Matthew M. Hawkeye, Michael T. Taschuk, and Michael J. Brett
Spintronics for Next Generation Innovative Devices, Edited by Katsuaki Sato and Eiji Saitoh
Physical Properties of High-Temperature Superconductors, Rainer Wesche

Inorganic Glasses for Photonics

Fundamentals, Engineering and Applications

ANIMESH JHA
Institute for Materials Research, University of Leeds, UK

WILEY

This edition first published 2016
© 2016 John Wiley & Sons, Ltd

Registered office
John Wiley & Sons Ltd, The Atrium, Southern Gate, Chichester, West Sussex, PO19 8SQ, United Kingdom

For details of our global editorial offices, for customer services and for information about how to apply for permission to reuse the copyright material in this book please see our website at www.wiley.com.

The right of the author to be identified as the author of this work has been asserted in accordance with the Copyright, Designs and Patents Act 1988.

All rights reserved. No part of this publication may be reproduced, stored in a retrieval system, or transmitted, in any form or by any means, electronic, mechanical, photocopying, recording or otherwise, except as permitted by the UK Copyright, Designs and Patents Act 1988, without the prior permission of the publisher.

Wiley also publishes its books in a variety of electronic formats. Some content that appears in print may not be available in electronic books.

Designations used by companies to distinguish their products are often claimed as trademarks. All brand names and product names used in this book are trade names, service marks, trademarks or registered trademarks of their respective owners. The publisher is not associated with any product or vendor mentioned in this book.

Limit of Liability/Disclaimer of Warranty: While the publisher and author have used their best efforts in preparing this book, they make no representations or warranties with respect to the accuracy or completeness of the contents of this book and specifically disclaim any implied warranties of merchantability or fitness for a particular purpose. It is sold on the understanding that the publisher is not engaged in rendering professional services and neither the publisher nor the author shall be liable for damages arising herefrom. If professional advice or other expert assistance is required, the services of a competent professional should be sought

Library of Congress Cataloging-in-Publication Data

Names: Jha, Animesh, author.
Title: Inorganic glasses for photonics : fundamentals, engineering, and applications / Animesh Jha.
Other titles: Wiley series in materials for electronic and optoelectronic applications.
Description: Hoboken, New Jersey : John Wiley & Sons, Inc., [2016] | Series: Wiley series in materials for electronic and optoelectronic applications | Includes bibliographical references and index.
Identifiers: LCCN 2016008930 (print) | LCCN 2016012366 (ebook) | ISBN 9780470741702 (cloth) | ISBN 0470741708 (cloth) | ISBN 9781118696101 (pdf) | ISBN 9781118696095 (epub)
Subjects: LCSH: Glass--Optical properties. | Photonics--Materials.
Classification: LCC QC375 .J43 2016 (print) | LCC QC375 (ebook) | DDC 621.36/50284--dc23
LC record available at http://lccn.loc.gov/2016008930

A catalogue record for this book is available from the British Library.

ISBN: 9780470741702

Cover description: Plumes of plasma generated from the surface of inorganic glass targets during pulsed laser deposition

Set in 10/12pt TimesLTStd-Roman by Thomson Digital, Noida, India

1 2016

To my beloved parents for enthusing me to pursue science and engineering!

My parents' family for supporting the journey to fulfil my ambitions
in my early career pursued in engineering in India!

To my friends and peers for supporting me in my academic career!

To my work place at the University of Leeds where I exchange knowledge!

To my wife, Aparna and children, Prashant and Govind,
for building a home in Leeds and inspiration for life!

Contents

Series Preface **xiii**
Preface **xv**

1. Introduction **1**
1.1 Definition of Glassy States 1
1.2 The Glassy State and Glass Transition Temperature (T_g) 1
1.3 Kauzmann Paradox and Negative Change in Entropy 4
1.4 Glass-Forming Characteristics and Thermodynamic Properties 5
1.5 Glass Formation and Co-ordination Number of Cations 14
1.6 Ionicity of Bonds of Oxide Constituents in Glass-Forming Systems 20
1.7 Definitions of Glass Network Formers, Intermediates and Modifiers and Glass-Forming Systems 23
1.7.1 Constituents of Inorganic Glass-Forming Systems 24
1.7.2 Strongly Covalent Inorganic Glass-Forming Networks 26
1.7.3 Conditional Glass Formers Based on Heavy-Metal Oxide Glasses 29
1.7.4 Fluoride and Halide Network Forming and Conditional Glass-Forming Systems 31
1.7.5 Silicon Oxynitride Conditional Glass-Forming Systems 36
1.7.6 Chalcogenide Glass-Forming Systems 37
1.7.7 Chalcohalide Glasses 45
1.8 Conclusions 46
Selected Biography 46
References 46

2. Glass Structure, Properties and Characterization **51**
2.1 Introduction 51
2.1.1 Kinetic Theory of Glass Formation and Prediction of Critical Cooling Rates 51
2.1.2 Classical Nucleation Theory 52
2.1.3 Non-Steady State Nucleation 54
2.1.4 Heterogeneous Nucleation 55
2.1.5 Nucleation Studies in Fluoride Glasses 56
2.1.6 Growth Rate 58
2.1.7 Combined Growth and Nucleation Rates, Phase Transformation and Critical Cooling Rate 59

- 2.2 Thermal Characterization using Differential Scanning Calorimetry (DSC) and Differential Thermal Analysis (DTA) Techniques 62
  - 2.2.1 General Features of a Thermal Characterization 62
  - 2.2.2 Methods of Characterization 63
  - 2.2.3 Determining the Characteristic Temperatures 64
  - 2.2.4 Determination of Apparent Activation Energy of Devitrification 66
- 2.3 Coefficients of Thermal Expansion of Inorganic Glasses 68
- 2.4 Viscosity Behaviour in the near-T_g, above T_g and in the Liquidus Temperature Ranges 71
- 2.5 Density of Inorganic Glasses 75
- 2.6 Specific Heat and its Temperature Dependence in the Glassy State 76
- 2.7 Conclusion 77
- References 77

3. Bulk Glass Fabrication and Properties 79

- 3.1 Introduction 79
- 3.2 Fabrication Steps for Bulk Glasses 80
  - 3.2.1 Chemical Vapour Technique for Oxide Glasses 80
  - 3.2.2 Batch Preparation for Melting Glasses 81
  - 3.2.3 Chemical Treatment Before and During Melting 81
- 3.3 Chemical Purification Methods for Heavier Oxide (GeO_2 and TeO_2) Glasses 84
- 3.4 Drying, Fusion and Melting Techniques for Fluoride Glasses 87
  - 3.4.1 Raw Materials 88
  - 3.4.2 Control of Hydroxyl Ions during Drying and Melting of Fluorides 88
- 3.5 Chemistry of Purification and Melting Reactions for Chalcogenide Materials 91
- 3.6 Need for Annealing Glass after Casting 96
- 3.7 Fabrication of Transparent Glass Ceramics 97
- 3.8 Sol–Gel Technique for Glass Formation 99
  - 3.8.1 Background Theory 99
  - 3.8.2 Examples of Materials Chemistry and Sol–Gel Forming Techniques 103
- 3.9 Conclusions 105
- References 105

4. Optical Fibre Design, Engineering, Fabrication and Characterization 109

- 4.1 Introduction to Geometrical Optics of Fibres: Geometrical Optics of Fibres and Waveguides (Propagation, Critical and Acceptance Angles, Numerical Aperture) 109
- 4.2 Solutions for Dielectric Waveguides using Maxwell's Equation 114
  - 4.2.1 Analysis of Mode Field Diameter in Single Mode Fibres 115
- 4.3 Materials Properties Affecting Degradation of Signal in Optical Waveguides 117
  - 4.3.1 Total Intrinsic Loss 117

- 4.3.2 Electronic Absorption 118
- 4.3.3 Experimental Aspects of Determining the Short Wavelength Absorption 121
- 4.3.4 Scattering 121
- 4.3.5 Infrared Absorption 124
- 4.3.6 Characterization of Vibrational Structures using Raman and IR Spectroscopy 126
- 4.3.7 Experimental Aspects of Raman Spectroscopic Technique 127
- 4.3.8 Fourier Transform Infrared (FTIR) spectroscopy 128
- 4.3.9 Examples of the Analysis of Raman and IR spectra 130

4.4 Fabrication of Core–Clad Structures of Glass Preforms and Fibres and their Properties 141
  - 4.4.1 Comparison of Fabrication Techniques for Silica Optical Fibres with Non-silica Optical Fibres 143
  - 4.4.2 Fibre Fabrication using Non-silica Glass Core–Clad Structures 151
  - 4.4.3 Loss Characterization of Fibres 153

4.5 Refractive Indices and Dispersion Characteristics of Inorganic Glasses 158
  - 4.5.1 Experimental Procedure for Measuring Refractive Index of a Glass or Thin Film 163
  - 4.5.2 Dependence of Density on Temperature and Relationship with Refractive Index 166
  - 4.5.3 Effect of Residual Stress on Refractive Index of a Medium and its Effect 169

4.6 Conclusion 170

References 170

5. Thin-film Fabrication and Characterization 178

5.1 Introduction 178

5.2 Physical Techniques for Thick and Thin Film Deposition 179

5.3 Evaporation 179
  - 5.3.1 General Description 179
  - 5.3.2 Technique, Materials and Process Control 179

5.4 Sputtering 181
  - 5.4.1 Principle of Sputtering 181

5.5 Pulsed Laser Deposition 183
  - 5.5.1 Introduction and Principle 183
  - 5.5.2 Process 184
  - 5.5.3 Key Features of PLD process 186
  - 5.5.4 Controlling Parameters and Materials Investigated 187
  - 5.5.5 Fabrication of Thin Film Structures using PLD and Molecular Beam Epitaxy 188

5.6 Ion Implantation 192
  - 5.6.1 Introduction 192
  - 5.6.2 Technique and Structural Changes 192
  - 5.6.3 Governing Parameters for Ion Implantation 193
  - 5.6.4 Materials Systems Investigated 194

5.7 Chemical Techniques 194
    5.7.1 Characteristics of Chemical Vapour Deposition Processes 195
    5.7.2 Materials System Studied and Applications 196
    5.7.3 Molecular Beam Epitaxy (MBE) 196
5.8 Ion-Exchange Technique 197
5.9 Chemical Solution or Sol–Gel Deposition (CSD) 200
    5.9.1 Introduction 200
    5.9.2 CSD Technique and Materials Deposited 202
5.10 Conclusion 203
References 203

6. Spectroscopic Properties of Lanthanide (Ln^{3+}) and Transition Metal (M^{3+})-Ion Doped Glasses 209
6.1 Introduction 209
6.2 Theory of Radiative Transition 209
6.3 Classical Model for Dipoles and Decay Process 212
6.4 Factors Influencing the Line Shape Broadening of Optical Transitions 214
6.5 Characteristics of Dipole and Multi-Poles and Selection Rules for Optical Transitions: 218
    6.5.1 Analysis of Dipole Transitions Based on Fermi's Golden Rule 219
    6.5.2 Electronic Structure and Some Important Properties of Lanthanides 221
    6.5.3 Laporte Selection Rules for Rare-Earth and Transition Metal Ions 224
6.6 Comparison of Oscillator Strength Parameters, Optical Transition Probabilities and Overall Lifetimes of Excited States 227
    6.6.1 Radiative and Non-Radiative Rate Equation 231
    6.6.2 Energy Transfer and Related Non-Radiative Processes 233
    6.6.3 Upconversion Process 237
6.7 Selected Examples of Spectroscopic Processes in Rare-Earth Ion Doped Glasses 238
    6.7.1 Spectroscopic Properties of Trivalent Lanthanide (Ln^{3+})-Doped Inorganic Glasses 239
    6.7.2 Brief Comparison of Spectroscopic Properties of Er^{3+}-Doped Glasses 241
    6.7.3 Spectroscopic Properties of Tm^{3+}-Doped Inorganic Glasses 247
6.8 Conclusions 257
References 257

7. Applications of Inorganic Photonic Glasses 261
7.1 Introduction 261
7.2 Dispersion in Optical Fibres and its Control and Management 261
    7.2.1 Intramodal Dispersion 262
    7.2.2 Intermodal Distortion 265
    7.2.3 Polarization Mode Dispersion (PMD) 266
    7.2.4 Methods of Controlling and Managing Dispersion in Fibres 267

7.3 Unconventional Fibre Structures 269
7.3.1 Fibres with Periodic Defects and Bandgap 269
7.3.2 TIR and Endlessly Single Mode Propagation in PCF with Positive Core–Cladding Difference 272
7.3.3 Negative Core–Cladding Refractive Index Difference 272
7.3.4 Control of Group Velocity Dispersion (GVD) 273
7.3.5 Birefringence in Microstructured Optical Fibres 274
7.4 Optical Nonlinearity in Glasses, Glass-Ceramics and Optical Fibres 275
7.4.1 Theory of Harmonic Generation 275
7.4.2 Nonlinear Materials for Harmonic Generations and Parametric Processes 279
7.4.3 Fibre Based Kerr Media and its Application 285
7.4.4 Resonant Nonlinearity in Doped Glassy Hosts 287
7.4.5 Second Harmonic Generation in Inorganic Glasses 288
7.4.6 Electric-Field Poling and Poled Glass 289
7.4.7 Raman Gain Medium 291
7.4.8 Photo-induced Bragg and Long-Period Gratings in Fibres 292
7.5 Applications of Selected Rare-earth ion and Bi-ion Doped Amplifying Devices 294
7.5.1 Introduction 294
7.5.2 Examples of Three-Level or Pseudo-Three-Level Transitions 296
7.5.3 Examples of Four-Level Laser Systems 300
7.6 Emerging Opportunities for the Future 302
7.7 Conclusions 303
References 304

Supplementary References **311**
Symbols and Notations Used **315**
Index **317**

Series Preface

Wiley Series in Materials for Electronic and Optoelectronic Applications

This book series is devoted to the rapidly developing class of materials used for electronic and optoelectronic applications. It is designed to provide much-needed information on the fundamental scientific principles of these materials, together with how these are employed in technological applications. The books are aimed at (postgraduate) students, researchers, and technologists, engaged in research, development, and the study of materials in electronics and photonics, and industrial scientists developing new materials, devices, and circuits for the electronic, optoelectronic, and communications industries.

The development of new electronic and optoelectronic materials depends not only on materials engineering at a practical level, but also on a clear understanding of the properties of materials, and the fundamental science behind these properties. It is the properties of a material that eventually determine its usefulness in an application. The series therefore also includes such titles as electrical conduction in solids, optical properties, thermal properties, and so on, all with applications and examples of materials in electronics and optoelectronics.

The characterization of materials is also covered within the series in as much as it is impossible to develop new materials without the proper characterization of their structure and properties. Structure–property relationships have always been fundamentally and intrinsically important to materials science and engineering.

Materials science is well known for being one of the most interdisciplinary sciences. It is the interdisciplinary aspect of materials science that has led to many exciting discoveries, new materials, and new applications. It is not unusual to find scientists with a chemical engineering background working on materials projects with applications in electronics. In selecting titles for the series, we have tried to maintain the interdisciplinary aspect of the field, and hence its excitement to researchers in this field.

Arthur Willoughby
Peter Capper
Safa Kasap

Preface

The pleasure of scientific and philosophical expression or communication prompts deeper thinking, which, as human beings, we share for promoting knowledge. Sharing and dissemination of knowledge is the second greatest charity, after saving and protecting life and the environment – that is what my parents taught me! Without this beacon of knowledge in human beings, civilization will remain trapped in the labyrinth of darkness. Can we imagine human civilization without any epic of knowledge – where we would be today as a civilization? These are very powerful statements and as an academic I sincerely believe in the true pursuit of knowledge and, for me, this pursuance became a reality when I completed this book.

Several years ago some of my distinguished colleagues asked me whether I would be willing to write a book on "Inorganic Glasses for Photonics", to fill a gap in this important area of physical and materials science. Perhaps it is appropriate to state at this point the importance of the subject area without emphasizing it too much. *No engineering discipline can grow without materials science and vice versa*. We chose the title *Inorganic Glasses for Photonics* because it bears two key aspects of materials science, the *structure* of the glassy state and its suitability for *functionalizing properties for photonic applications*. The study of structure–property relationships is an intrinsic part of understanding materials science, and in this book I have attempted to bring out this feature in every chapter in a concise and contextual manner, and wherever possible with examples.

During the course of writing this book, as expected, I faced many challenges and, in most cases, I turned these challenges into opportunities for learning new experiences, which helped me in forming my thoughts to adopt a different style of expression. This may become apparent to those who seek to understand the structure–property relationship of materials. Before writing a complex section, I often felt that my thoughts were in a whirlwind of thermal and configurational entropy, and that the energy requirement for achieving a coherence of thoughts, as in the manner of a laser cavity, was too high. Consequently the "slope efficiency" for writing each chapter was not the same. Exemplifying the structure–property relationship was not easy, which becomes apparent in some sections of the book, and I am sure this feature will continue to evolve in future. For this, if the readers feel there are omissions I apologize in advance. However, I have purposely kept away from incorporating chapters and sections that are well covered in other established text books in the related subject areas.

Not realizing at the outset of writing this textbook that the year 2015 would be declared by the United Nations as the *Year of Light*, in which year I would be able to finish this textbook, the conclusion of this project brought a personal sense of achievement. One hundred years ago in 1915, Albert Einstein rose to world fame by explaining new properties of light in the context of general relativity. Einstein also discovered two other important aspects of light and matter – the discovery of Brownian motion helped in confirming the value of Avogadro's number independently. Einstein's Nobel Prize winning work on the photoelectric effect is at the genesis of quantum theory. A chance to celebrate the great achievements of Einstein in the form of a book on "Inorganic Glasses for Photonics" is an infinitesimal contribution to the world community of scientists and engineers.

In this book there are seven chapters, which in future may grow into much fuller shape by incorporating emerging aspects of nonlinear optics, nano-photonics and plasmonics using inorganic glass as a medium for controlling and manipulating light. Although I have written a significant section on nonlinear optics in Chapter 7, the aspects of nano-photonics and plasmonics are not discussed because I feel these two areas have not yet reached maturity in terms of using glass as a medium for wider device applications. I hope that you would agree!

In Chapter 1, the main focus is on the glass science and structures of inorganic glasses that are commonly used for photonic devices. A range of inorganic glasses are discussed in this chapter, with examples of oxide, fluoride, chalcogenide and mixed anion glasses. I have also attempted to explain the thermodynamics of glass-forming liquids in the vicinity of deep eutectic liquid, which is often the composition range for stable glass formation. The theory of co-ordination number is also discussed in the context of phonon structure.

For photonic device applications, a chosen glass composition must be engineered using the thermal, physical and viscosity properties of a glass. These properties are discussed in Chapter 2 by emphasizing the roles of nucleation and crystal growth, e.g. for fibre drawing.

Having discussed the important thermal, viscosity and physical properties of glasses in Chapter 2, in Chapter 3 the fabrication of bulk inorganic glasses using melting and casting is discussed for a majority of known inorganic glasses. In this chapter the fabrication principles of glass-ceramic materials are also discussed. The theory of sol–gel formation and sol–gel based glass fabrication are also discussed briefly in this chapter.

In Chapter 4, I have introduced the standard geometrical optics for fibre optics and briefly discussed the Maxwell's equation for modal analysis and its importance in fibre and waveguide optics. In this chapter I have also brought together the signal degradation mechanism in waveguides and discussed them in some detail, by making comparisons. In this approach I have also attempted to bring together the properties of various glasses for fibre and waveguide fabrication. This chapter concludes with a detailed discussion on refractive index and its dependence on compositions, density, temperature and stress. The relationship of these properties in controlling bulk optical properties is especially emphasized.

In Chapter 5, the main emphasis is on the methods of thin-film fabrication using physical and chemical vapour deposition and pulsed laser deposition including ion implantation techniques. The pros and cons of each technique are discussed with some examples.

I have adopted a different style of presentation in Chapter 6, starting with an introduction to classical radiative transition theory based on dipole models, and have then explained the concept of dipoles and electron–phonon coupling in the text. By emphasizing various quantum mechanical rules, I have then attempted to discuss the radiative, non-radiative, energy transfer and upconversion processes. In view of a wealth of information on rare-earth doped glass based lasers and amplifiers, my focus has been on exemplifying the significance of a set of optical transitions for specific rare-earth ions in selected glass based devices for explaining the structure–property relationships.

The final chapter 7 is on the photonic device applications of inorganic glasses, fibres and waveguides. In this context I have discussed the importance of dispersion and dispersion control in optical fibres, unconventional fibres, namely, microstructured fibres, optical nonlinearity and finally concluding with examples of three- and four-level lasers and their applications. The book concludes with a short discussion on the emerging opportunities for inorganic glasses.

To help readers, there is an extensive list of references and supplementary references for further reading and in-depth comprehension of topical areas.

Earlier this year, in January 2015, Dr Charles Townes, who discovered masers, passed away 6 months before reaching his 100th birthday, and in this context the Optical Society of America's OPN monthly journal (May 2015 issue, pp. 44–51) published a feature article on the late Dr Townes. In the inset of this article the "Family Matters" of the Townes–Schawlow were also printed. Here is an excerpt that is quite a profound metaphor, and it goes like this: *"Tiny rabbit and beaver were looking up at the Hoover Dam. The beaver is saying to the rabbit*, '*No I didn't build it, but it was based on an idea of mine*". Since the discovery of masers in 1953 and then of lasers in 1960, today we are in the era of ultrafast femto- and atto-second lasers. The beavers have long gone, but the Hoover Dam continues to pour out knowledge. For me, it will be truly sensational to produce the most coherent and the purest form of light. Today, glass-based fibre lasers have been commoditized for manufacturing and materials processing. I hope that this book might help burgeoning minds to discover new sources of light, perhaps using novel glasses that are not yet discovered. Such engineered materials might make a significant impact in future.

Animesh Jha
July 2015, University of Leeds, Leeds (UK)

1

Introduction

1.1 Definition of Glassy States

A “glassy or vitreous” state is classified as a state of condensed matter in which there is a clear absence of a three-dimensional periodic structure. The periodicity is defined by the repetition of point groups (e.g. atoms or ions) occupying sites in the structure, following a crystallographic symmetry, namely, the mirror, inversion and rotation. A glass is a condensed matter exhibiting elasticity below a phase transition temperature, known as the glass transition temperature, which is designated in this text as (T_g). By comparison, an “amorphous” state, as in the “vitreous” state, has an all-pervasive lack of three-dimensional periodicity; it is more comparable with a liquid rather than a solid. An amorphous structure lacks elasticity and has a propensity to flow under its own weight more readily than a solid-like vitreous state does below T_g. *An amorphous inorganic film also has a glass transition temperature and elastic behaviour, which varies with that of the corresponding vitreous state of the same material.* The recognition of apparent differences in the properties of “vitreous” and “amorphous” structures, will be discussed in subsequent chapters on fabrication and processing and such comparative characterizations are essential in developing a deeper understanding of a structure–optical and spectroscopic properties of transparent “inorganic glasses as photonic materials” for guiding photons and their interactions with the medium. Such differences in structural and thermal properties between a glassy or amorphous and a crystalline state explain why the disordered materials demonstrate unique physical, thermo-mechanical, optical and spectroscopic properties, facilitating light confinement and propagation for long-haul distances better than any other condensed matter.

1.2 The Glassy State and Glass Transition Temperature (T_g)

The liquid-to-solid phase transition at the melting point (T_f) of a solid, for example, is characterized as a thermodynamically reversible or an equilibrium transition point, at which both the liquid and solid phases co-exist. Since at the melting point both phases are in equilibrium, the resulting Gibbs energy change (ΔG^f), as shown in Equation 1.1, of the phase

---

Inorganic Glasses for Photonics – Fundamentals, Engineering and Applications, First Edition. Animesh Jha.
© 2016 John Wiley & Sons, Ltd. Published 2016 by John Wiley & Sons, Ltd.

transition is zero, which then helps in defining the net entropy change associated with the phase change at T_f:

$$\Delta G^f = \Delta H^f - T_f \Delta S^f = 0 \tag{1.1}$$

In Equation 1.1, ΔH^f and ΔS^f are the enthalpy and entropy changes at the melting point. Since ΔG^f equates to a zero value at T_f, from Equation 1.1, the entropy change at T_f consequently is equal to:

$$\Delta S^f = \frac{\Delta H^f}{T_f} \tag{1.2a}$$

From Equation 1.2a, for pure solids the magnitude of entropic disorder can thus be determined at the melting point by measuring the enthalpy of fusion. This characteristic of a solid–liquid transition will become quite relevant in the examination of glass-formation in multicomponent systems. In Figure 1.1, the liquid-to-crystal and liquid-to-glass transitions are shown by identifying the T_f and a range of transition temperatures, T_g^1, T_g^2 and T_g^3, respectively. These glass transition temperatures are dependent on the quenching paths AA_1E, AA_2F and AA_3G, which differ from the equilibrium route ABCD for liquid-crystal transition at T_f.

In Figure 1.1, the glass experiencing the fastest quenching rate (Q_3) has the corresponding transition temperature at T_g^3, whereas the quenching rates Q_2 and Q_1 yield glasses having transition temperature at T_g^2 and T_g^1, respectively. The end entropic points thus relate to the thermal history of each glass. The slowest cooling rate yields the lowest temperature, as the supercooled liquid state below T_f attains a metastable thermodynamic state, which is

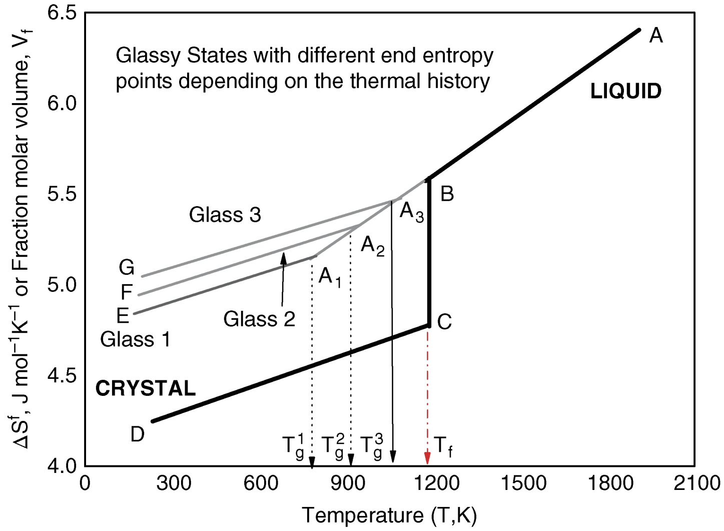

Figure 1.1 *Plot of the entropy change (ΔS^f in J mol^{-1} K^{-1}) in a solid–liquid and liquid-glassy state transitions, shown schematically to illustrate the respective apparent change in the value of entropy end point, as a result of various quench rates applied, which are designated by the paths AA_1E, AA_2F, and AA_3G.*

still higher in Gibbs energy than the equilibrium crystalline state designated by line CD in Figure 1.1. When the fastest quenching rate path, AA_3G, is followed the liquid has little time to achieve the thermodynamic equilibrium, as reflected by the transition temperature T_g^3, which is closest to the melting point.

The annealing of the fastest quenched glass in Figure 1.1, having a transition temperature at T_g^3, provides the driving force for structural relaxation to lower energy states progressively. With a prolonged isothermal annealing, the end point entropy state might eventually reach much closer to the equilibrium crystalline state (line CD in Figure 1.1). As the annealing allows the quenched glass to dissipate most of the energy in a metastable quenched state, the end point entropy never approaches the line CD, which is consistent with the theory proposed by Boltzmann in the context of the second law of thermodynamics. This condition mathematically limits the value of viscosity approaching infinity, an impossible value. Considering the thermodynamic state properties, e.g. the molar volume (V) and entropy (S), and their dependence on pressure (P) and temperature (T), any change in the entropy of a state corresponds to a proportional change in the molar volume, which follows from the differentials in Equations 1.2b–d, shown below. It is for this reason that in Figure 1.1 the discontinuity in fractional change in molar free volume (v_f), which is dependent on V, is shown along with the entropy change:

$$dG = -SdT + VdP \tag{1.2b}$$

$$\left[\frac{\partial G}{\partial T}\right]_P = -S \tag{1.2c}$$

$$\left[\frac{\partial G}{\partial P}\right]_T = +V \tag{1.2d}$$

The implication of thermodynamic state analysis in Equations 1.2b–d is that the discontinuities in glassy states are also observed when their state properties, such as the enthalpy (H), specific heats at constant pressure (C_p) and volume (C_v), thermal expansion coefficient (α_V) and isothermal compressibility (β_T), are plotted against temperature. Discontinuities in the thermodynamic state properties for several glass-forming liquids are compared and discussed by Paul [1] and Wong and Angell [2] in publications that readers may find helpful.

From Figure 1.1, the glass transition temperature is represented by the presence of a discontinuity, which is dependent on the quenching rate (Q_i), and the points representing T_gs are not sharp or abrupt, as shown in the liquid-to-crystal transition. The range of T_gs in Figure 1.1 is characterized as the "*fictive glass temperature*" and their position is dependent on the quenching history. Several text books designate the fictive temperature as T_f, and readers should cautiously interpret this temperature along with the quench rate and associated thermal history, because unlike T_f, the T_gs are not fixed phase transition points. A major discrepancy in the property characterization might arise if experiments are not carefully designed to study the sub-T_g and above-T_g structural relaxation phenomena, which are discussed in great detail by Varsheneya [3a] in his text book. Elliott [4] explains the exponential relationship between quenching rate and T_g in Equation 1.3, showing that the corresponding relaxation time (which is the inverse of the quenching rate) is likely to be imperceptibly long, since a glass is annealed to achieve a new metastable equilibrium state above a crystalline phase, corresponding to line CD in Figure 1.1:

$$Q_i = Q_o \exp\left[-B\left\{\frac{1}{T_g} - \frac{1}{T_f}\right\}\right] \tag{1.3}$$

In Equation 1.3, the value of Q_o for different glasses differs, as observed by Owen [5], and was found to be of the order of 10^{23} and $10^4\,\mathrm{K\,s^{-1}}$ between Se and As_2S_3 glasses. The constant B was found to be of the order of 3×10^{-5} K. An analysis of quenching rate and glass transition temperature implies that near T_g, there is an Arrhenius type activation energy barrier, which is path dependent and can be reached in numerous ways by following different thermal histories, which is discussed extensively by Varsheneya [3b]. Based on path dependence analysis and the associated changes in the first order thermodynamic properties, namely the enthalpy of glass transition, the phase transition is a "first-order" transition and, unlike the Curie temperature in a magnetic metallic glass, the glass transition is not a second-order transition. The Curie temperature is a fixed point, dependent upon the electronic-spin relaxation, the time-scale for which is of the order of 10^{-15} (femto to sub-femto) seconds, which is six orders of magnitude faster than the molecular relaxation characterized by an Arrhenius type of energy barrier. From reaction rate theory, the pre-exponential in the rate equation is equal to k_BT/h, where k_B and h are the Boltzmann constant and Planck's constant, respectively and T is the absolute temperature. Applying the reaction rate theory for quenching of a glass, the minimum and maximum values therefore may vary between 10^{-7} and 10^{-9} s, which leads to an interesting discussion on the interaction of ultrafast lasers (pico- and femtosecond) with a glass and consequential structural changes. It is therefore not unreasonable to expect a dramatic change in the relaxation properties of glassy thin films formed in a femtosecond quenching regime when compared with the same composition glass produced via splat ($10^6\,\mathrm{K\,s^{-1}}$) and air quenching ($10^2\,\mathrm{K\,s^{-1}}$) techniques. Such a large difference in the magnitude of quenching glass is likely to yield structural variations (molar volume, expansion coefficients, refractive index, electronic edge), which may then be manifested in the corresponding relaxation rate, in accordance with Equation 1.3

1.3 Kauzmann Paradox and Negative Change in Entropy

There has been continued debate on the Kauzmann paradox in the glass literature, in relation to the path dependence of quenching of glass-forming liquids and the attainment of an overall entropy state that is lower than that of the crystalline state (line CD in Figure 1.1), which implies that the glass attains a negative entropic state. Based on the entropy change in supercooled glycerol, reported earlier by Jäckle [6] in Figure 1.2, Kauzmann's data [7] were critically analysed by Varsheneya [3b], who explained that the laws of thermodynamics are not exempt within the concept of the "Kauzmann paradox".

In supercooled liquids the structural arrangements are so rapid that the resultant changes cannot be depicted on the time-scale of measurements. There is, though, a further argument that continues to support the nature of thermodynamic laws that the entropy change in a "system" may be negative. However, the "total or universe" entropic change is a sum of the entropies of a "system" and its "surrounding". Two examples are characterized herein to make an important point on the negative nature of entropy. The solidification point of quartz is

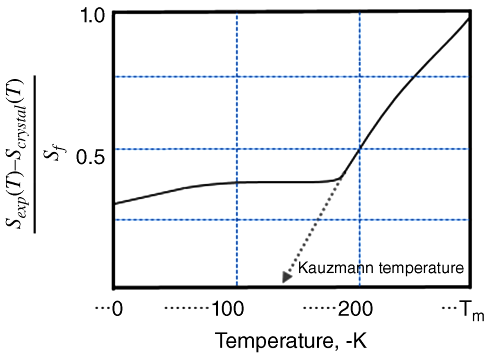

Figure 1.2 Entropy change with respect to the melting point entropy against temperature, extrapolated to determine the Kauzmann temperature (T_k) after Jäckle [6]. Source: J. Jackel 1986. Reproduced with permission from Elsevier.

2273 K, and the entropy of fusion $(\Delta S^f)_{\text{System}}$, from Equation 1.2a, is $-4.52\,\text{J mol}^{-1}\,\text{K}^{-1}$, yielding an enthalpy (ΔH^f) of solidification that is equal to $-10278\,\text{J mol}^{-1}$. Since there is only a small difference in the entropies of crystalline quartz, liquid silica and the glassy states, with a comparable value of around $4.52\,\text{J mol}^{-1}\,\text{K}^{-1}$, during quenching as the liquid is solidifying to a lower volume state the sign of entropy “changes to a negative” value below the melting point, indicating more structural order than in the liquid state above its melting point, which is consistent with Equation 1.1. The enthalpy released into the surrounding at 300 K, which is absorbing the heat (δQ), is $+10278\,\text{J mol}^{-1}$ and therefore the corresponding entropy change in the surrounding $(\Delta S)_{\text{Surrounding}}$, from the second law of thermodynamics, is equal to:

$$\frac{\delta Q}{T_{\text{Surrounding}}} = \frac{+10278}{300} = +34.26\,\text{J mol}^{-1}\,\text{K}^{-1}$$

which yields a net change in entropy of the universe that is equal to $+29.74\,\text{J mol}^{-1}\,\text{K}^{-1}$. The formation of a layer of amorphous alumina via the reaction:

$$2\text{Al(solid)} + \tfrac{3}{2}\text{O}_2\text{(gas)} = \text{Al}_2\text{O}_3\text{(solid)}$$

over the surface of aluminium follows an identical argument because of the exothermic nature of the enthalpy of formation of alumina, which is $-1.8046\times10^6\,\text{J mol}^{-1}$ of alumina and the corresponding negative value of entropy change is nearly $-132\,\text{J mol}^{-1}\,\text{K}^{-1}$. For an endothermic reaction, the signs will reverse and the argument still holds, implying that the “exemption from the universal thermodynamic laws” is “impossible” in a physical phenomenon. The irreversible and path-dependent nature of metastable glassy states beautifully follows the laws of thermodynamics, irrespective of the route by which a glass or an amorphous state is achieved, namely via the quenching, sol–gel, pulsed laser deposition and mechanical grinding techniques.

1.4 Glass-Forming Characteristics and Thermodynamic Properties

In Table 1.1 we compare the enthalpy, entropy, melting and glass transition points for several glass-forming unary compounds. This comparative exercise of melting, glass-transition and thermodynamic properties at T_f will help us in identifying an important structural feature,

Table 1.1 *Comparison of the thermodynamic state properties, enthalpy (ΔH^f, J mol^{-1}), lattice energy (ΔH_{lat} kJ mol^{-1}) and entropy (ΔS^f, in eu), and melting points (T_f, K) of glass-forming compounds and their glass transition temperatures (T_g, K) [4,8,9].*

Unary compound	T_f (K)	ΔH^f (J mol^{-1})	ΔS^f (eu)	T_g (K)	Ratio T_g/T_f	ΔH_{lat} (kJ)
Silica (SiO_2)	1996	7700–10 880	1.08–1.30	1453	0.73	−911
Beryllium fluoride (BeF_2)	825	4750	1.37	598	0.73	−1028
Germanium oxide (GeO_2)	1388	8140	1.4	853	0.61	−580
Boric oxide (B_2O_3)	723	22 180–24 060	7.33–7.95	530	0.73	−1272
Zinc chloride ($ZnCl_2$)	591	10250	4.14	380	0.64	−415
Sulfur (S)	388	1720	4.14	246	0.63	—
Selenium (Se)	494	5860	2.83	318	0.64	—
Arsenic trisulfide (As_2S_3)	585	28675	11.71	478	0.82	−168
Arsenic triselenide (As_2Se_3)	633	40815	15.0	468	0.74	−102
Arsenic tritelluride (As_2Te_3)	633	46883	17.28	379	0.60	−38
Germanium disulfide (GeS_2)	1113			765	0.69	−157
Germanium selenide ($GeSe_2$)	1013			695	0.69	−113
Si	1685	50570	7.17			—
ZrF_4	1205	Sublimes at 1177 K		—	—	−1909
BaF_2	1563	28.5	4.35			−1210
NaF	1269	33.5	6.30			−574
ZrF_4-BaF_2 equimolar glass	823			543		
$CdCl_2$	842	30.1	8.55			−392
$BaCl_2$	1195	17.2	2.06			−858
$CdCl_2$-$BaCl_2$ equimolar glass	583			425		

which will aid our understanding of the structure–property relationship. In this process of a comparative analysis of thermodynamic properties, we represent the entropy of melting in Equation 1.2a, which is divided by a factor 4.187, the conversion factor for 1 calorie unit into a joule unit. The ratio in Equation 1.2a, therefore, is redefined in terms of an "entropy unit (eu)" in Equation 1.4 as a measure of disorder:

$$\Delta S_\mathrm{f} = \frac{\Delta H^\mathrm{f}}{4.187 T_\mathrm{f}} (\mathrm{eu}) \qquad (1.4).$$

From this expression, an eu is a measure of disorder at the melting point, which shifts the entropy of a corresponding liquid at T_f along the line BC in Figure 1.1. In Table 1.1, the last but one column gives the ratio T_g over T_f, which is often used to define the glass-forming tendency of a liquid, and is known to vary between 0.60 and 0.80 for most glass formers. We also point out to the reader that the literature frequently uses terminologies such the "glass-forming ability" and "glass-forming tendency" which carry analogous meaning. However, neither of these two terminologies should be confused with the "metastable stability" of a glassy state, which can only be quantified by the kinetics of glass formation. Several glass-stability parameters have also been used in the literature, some of which are explained in the context of the kinetics of glass formation and the classical theory of crystal nucleation and growth.

A comparison of the values of eu for various unary glass formers in Table 1.1 demonstrates that there are unary compounds, namely SiO_2, BeF_2 and GeO_2, which have a relatively lower value of eu ($\sim$1.1 to 1.4) on melting, suggesting that the extent of structural disorder as a result of melting at T_f, is comparatively much smaller than any other groups of compounds in this table. The values of eu for arsenic based chalcogenides (As_2S_3, As_2Se_3 and As_2Te_3) are naturally the largest, due to their high vapour pressures at the melting points. Unfortunately, a similar comparison for germanium based chalcogenides cannot be carried out, due to the lack of relevant thermodynamic data in the literature. In Table 1.1 we also find that the values of the ratio of T_g to T_f, for glass-formers such as SiO_2, GeO_2, BeF_2, $ZnCl_2$, S and Se are predominantly in the range 0.65–0.72, which falls in a "*critical undercooling range*" of roughly ⅔ of the corresponding melting point of the unary glass-forming compound. Table 1.1 thus shows two important features: (i) there is an entropic disorder associated with the glass formation in unary compounds and (ii) each glass-former requires undercooling, with respect to melting point. Discussion of the aspects of undercooling and entropic changes associated with glass formation will be resumed later in this chapter and in Chapter 2, to help in explaining the thermal properties and viscosity of various types of glasses.

In Table 1.1 we also compare the lattice energies of commonly known glass-forming compounds and constituent components of multi-constituent glassy phases. The importance of the lattice energies of constituents is explained below in the context of eutectic compositions, at which a vast majority of liquids, when quenched, transform into a glassy phase. The lattice energy of various compounds are best quantified by their heats of formation, which yield the resulting bonds, e.g. in SiO_2 the Si—O bond, as explained by the Born–Haber cycle. In Table 1.1, the values of lattice energies (or the heats of formation) of pure glass-forming elements, namely Si, Se and S, are zero [8]. To estimate the differences in lattice energies of multi-constituent glasses, say, for example, the equimolar compositions for AgI-CsI, the lattice energy difference can be estimated by simply subtracting the value of CsI from that of AgI and dividing it by 2.

A vast majority of practical inorganic glasses used for engineering applications are constituted of more than one component. This means that the thermodynamic properties of liquid mixtures are relevant in the discussion of glass-forming liquids, which may be characterized using the concepts of classical thermodynamics. Comprehensive essays on the properties of liquid mixtures with examples of metallic and inorganic oxides are cited in a number of text books on this subject by the pioneers of applied thermodynamics, Darken and Gurry [10], Swalin [11], Richardson [12], Lupis [13], Turkdogan [9b], and also in classical ceramic and halide salt references [14,15]. The properties of liquid mixtures and the use of phase diagrams for the determination of partial molar quantities of component end members in a binary mixture are especially discussed in References 9b–13. In a binary liquid, for example, in which more than one component is required for glass formation, the overall change in the entropy of a mixture differs significantly. Thermodynamically a binary mixture, for example with X_A and X_B fractions of constituents A and B, respectively, is more stable than the pure constituents, A and B. This becomes apparent when we consider the depression in the melting point of a pure constituent, with respect to a liquidus temperature $(T^l)_i$ at a given mole fraction, X_i, which is analogous to Equation 1.2a:

$$\left(T^{l}\right)_i = \frac{\Delta H^{f} + \overline{\Delta H_i}}{\Delta S^{f} + \overline{\Delta S_i}} \tag{1.5}$$

where $\overline{\Delta H_i}$ and $\overline{\Delta S_i}$ are the partial molar enthalpy and entropy of mixing of a binary mixture. The value of $\overline{\Delta H_i}$ can be assumed to be zero for ideal mixtures. For non-ideal mixtures with negative enthalpy of mixing, the partial enthalpies are also negative in the numerator of Equation 1.5. The denominator, however, has a partial entropy of mixing $\overline{\Delta S_i}$ term, which is always positive, and for a simple ideal mixture it is equal to $-R \ln X_i$. Substituting $-R \ln X_i$ in Equation 1.5 yields Equation 1.6, in which the liquidus temperature, $(T^l)_I$ can be expressed in terms of composition (X_i) and the melting point and entropy of an end member in a binary mixture. Here R is the universal gas constant, with a value 8.314 J mol^{-1} K^{-1} in SI units:

$$\left(T^{l}\right)_i = \frac{\Delta H^{f}}{\Delta S^{f} - R \ln X_i} = \frac{T_f}{\left[1 - \dfrac{R}{\Delta S^{f}}(\ln X_i)\right]} \tag{1.6}$$

From this simple equation we find that for a given value of X_i in a binary or multicomponent liquid the drop in the liquidus temperatures, $(T^l)_I$ is large when the value of ΔS^f is small. In addition, if we consider a non-ideal glass-forming liquid in which the value of $\overline{\Delta H_i}$ is negative, the corresponding reduction in the value of predicted $(T^l)_I$ is expected to be much larger than when a liquid mixture behaves as an ideal mixture. We can, thereby, critically examine examples of glass formation in inorganic glass-forming liquids. Based on such comparisons, the corresponding drop in the liquidus leading to formation of eutectic mixtures is discussed in the context of the partial molar properties of the two binary mixtures. The first glass-forming system is a monovalent mixture of AgI-CsI, followed by the CdF_2-$BaCl_2$ system, and finally a series of tetravalent–monovalent and tetravalent–divalent fluoride liquid mixtures, especially in the ZrF_4-NaF and ZrF_4-BaF_2 systems. These liquids are classed as predominantly "ionic liquids", in which the diffusion of cations and anions is at least 2–3 orders of magnitude larger than in covalent liquids of, say, meta silicates, phosphates and borates. The importance of such a discussion on glass-formation in ionic liquids will become

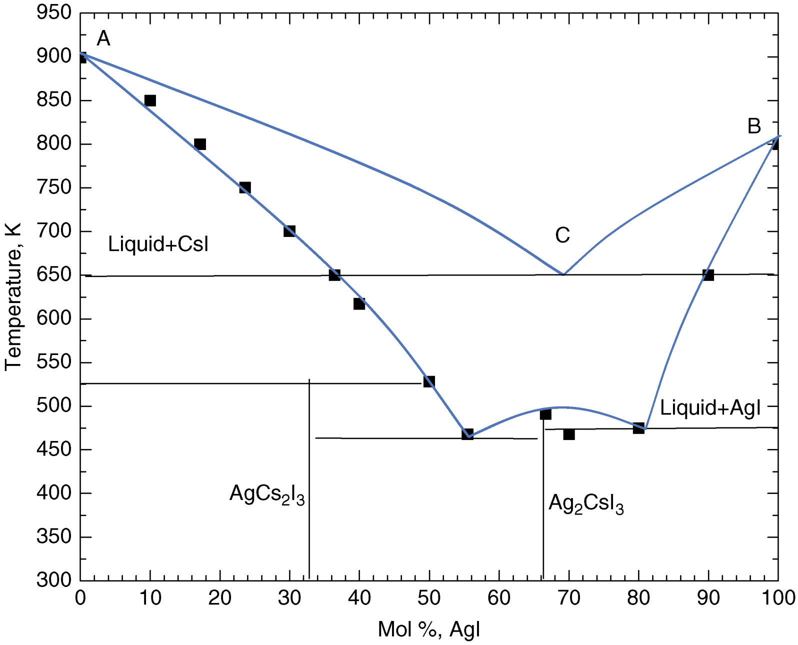

Figure 1.3 *Calculated liquidus lines, AC and BC, are compared with the experimentally determined data [16]. The experimental data also show the presence of complexes,* Ag_2CsI_3 *and* Cs_2AgI_3*, and two deeper eutectic temperatures in the vicinity of 450–470 K. Source: Hulme 1989. Adapted with permission from Society of Glass Technology, Sheffield.*

apparent when the tendency for polymerization and evolution of glass-forming networks is discussed by emphasizing the predominance of complex ordering of structures in liquids, as often seen in the properties of silicate, phosphate, germanate, and borate glasses. The nature of such ordering is then manifested through the shape and slopes of liquidus curves in the resulting phase diagrams.

Glass-formation in chloride, bromide and iodide systems, e.g. in the AgI-CsI binary, were first reported by Ding and co-workers [14]. The diffusion coefficient of Ag^+ ions in the AgI-CsI liquids is of the order of 10^{-1} to $10^{-2}\,cm^2\,s^{-1}$ below 100 °C [15]. Hulme and co-workers [16] analysed the phase constitution in AgI-CsI, including the shape of liquidus curve, leading to the formation of eutectic points. The calculated liquidus lines using Equation 1.6 and the empirically determined phase equilibrium boundaries are compared in Figure 1.3, in which it is apparent that the ideal solution model, based on Raoult's law, predicts a eutectic temperature that is ~180 K higher than the actual temperature in the vicinity of 470 K in the binary AgI-CsI system [16]. Evidently, in the AgI-CsI mixture there is a significant departure from ideal behaviour, which can be measured with respect to the value of partial molar enthalpy, $\overline{\Delta H_i}$, in Equation 1.5. A detailed analysis of the partial enthalpy of mixing in the binary halide system may be made using the Hildebrand's Regular solution and Guggenheim models both of which are well cited in the literature.

At the eutectic points the liquid solution freezes and yield solids, as shown in Figure 1.3, two of which are based on silver iodide polyanionic complexes $[Ag_2I_3]^-$ and $[AgI_3]^{2-}$, as shown in Figure 1.4, and form $AgCs_2I_3$ and Ag_2CsI_3 crystals, respectively. As explained by Brink and

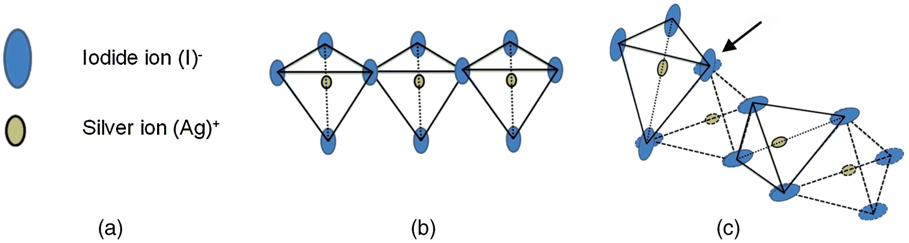

Figure 1.4 *Structures of polyanionic* $[MX_3]^{2-}$ *and* $[M_2X_3]^-$ *are shown in (b) and (c), respectively, where (a) large grey and small grey circles represent iodine and silver ions, respectively. (b) Corner shared AgI chains are prevalent in the* $AgCs_2I_3$ *complex, (c) whereas double edge-shared AgI chains dominate the* Ag_2CsI_3 *structures. The dotted pyramids in (c) represent the backplane of the paper, which is why along a shared edge four-iodine ions are shown, (see arrow) and is not required in the building of this structure. At other shared edges in (c) this is not apparent [16–18]. Source: Hulme 1989. Reproduced with permission from The Society of Glass Technology, Sheffield.*

co-workers [17], the $[M_2X_3]^-$ and $[MX_3]^{2-}$ form via edge-sharing and corner-sharing, which has been further explained by Wells [18] in his treatise on structural chemistry. The cationic radii of Ag^+ and Cs^+ are 0.127 and 0.168 nm, respectively, and the corresponding values of electronegativity are 1.9 and 0.7, which imply that in the $[M_2X_3]^-$ and $[MX_3]^{2-}$ complexes the Ag^+ cations, due to their smaller size and larger electronegativity than the Cs^+ ions, are responsible for the formation of $[M_2X_3]^-$ and $[MX_3]^2$ polyanionic species (Figure 1.4).

The second example of polymerization in ionic liquids is illustrated by the examples of glass formation in CdF_2-$BaCl_2$, which was reported by Poulain and Matecki [19]. An essential aspect of structural analysis in the divalent mixture is the Gibbs energy of mixing, which is a means of identifying how far a glass-forming solution departs from an ideal Raoult's law, as explained above in Equations 1.5 and 1.6. The determination of non-ideality in CdF_2-$BaCl_2$ can be explained by introducing a thermodynamic term, which will help later on in establishing the relationship between the viscosity and glass structure, IR absorption and spectroscopic properties.

The departure from non-ideal Raoult behaviour of a reciprocal salt mixture, CdF_2-$BaCl_2$, can be defined by calculating the entropy of mixture. When a solid mixture of CdF_2-$BaCl_2$ is heated above the melting points of it constituents, the following ionic exchange reaction occurs:

$$CdF_2(l) + BaCl_2(l) = CdCl_2(l) + BaF_2(l) \tag{1.7a}$$

$$\Delta G_{1.7a} = -38650 - 18.3T \text{ J mol}^{-1} \tag{1.7b}$$

In Equation 1.7a we observe that as a result of ionic exchange $CdCl_2$ and BaF_2 are produced. However, if the solution were an ideal one, the difference in the entropies of unmixed solid states before melting (S_{unmix}) and after melting (S_{mix}), $\Delta S_{\text{mixture}}$, is equal to zero. This means that there is no preferential structural association by forming a polyanionic complex in liquids. In reality such ideal behaviour is much rarer than the non-ideal, and as a result of mixing in CdF_2 and $BaCl_2$, the large difference in their lattice energies (enthalpy of compound formation), the heat or enthalpy of mixing is not zero (see Equation 1.6). This means that in Equation 1.5 the partial thermodynamic quantities in the numerator and denominator become non-zero, and consequently the preferential structural association for complex formation is likely to increase. Thus the "ideal configurational entropy", which can be expressed by $-R \ln X_i$ in Equation 1.6, is no longer sufficient but will require an additional component, called the thermal component (S_{th}). The thermal component of entropy of a salt mixture was introduced by Richardson [12b]; for reciprocal salt mixtures, the change in thermal entropy (ΔS_{th}) is expressed in terms of enthalpy change (ΔH) in Reaction 1.7a and is equal to equilibrium constant ($K_{1.7\mathrm{a}}$):

$$K_{1.7a} = \exp\left[-\frac{\Delta G_{\mathrm{th}}}{RT}\right] = \exp\left[-\frac{\Delta H\left(1-\dfrac{T}{12500}\right)}{ZRT}\right] \qquad (1.8).$$

Here Z, R and T are the cation co-ordination number in the polyanion structure, universal gas constant and absolute temperature, respectively. Richardson explained that the thermal contribution to entropy of a reciprocal mixture can be estimated by the change in the lattice energies or enthalpy (ΔH) and is equal to (ΔH)/12500, which is shown in Equation 1.8. The Gibbs energy change (ΔG_{th}) for reaction, given in Equation 1.7b [20], yields a value of (ΔS_{th}) of −3.07, suggesting that the overall change in the entropy should shift towards a more preferential association for a $CdCl_2$-BaF_2 distribution than a CdF_2-$BaCl_2$ type association. From Equation 1.8 the non-ideality yields a value of $K_{1.7}$ equal to 1.735 at 973 K, which from Equation 1.7b yields a value of 36.75% for the preponderance of $CdCl_2$-BaF_2. This value of preponderance is measured with respect to an ideal state having random association. Therefore, based on the differences in the lattice energies of $BaCl_2$, BaF_2, CdF_2 and $CdCl_2$, the following polyanionic species are likely to make the 36.75% excess of preferential association for Cd—Cl bonds, compared to Cd—F bonds as shown in reactions 1.9a to 1.9c:

$$CdCl_2(l) + BaCl_2(l) = [CdCl_4]^{2-}(l) + Ba^{2+}(l) \qquad (1.9a)$$

$$CdCl_2(l) + BaF_2(l) = \left[Cd(Cl_{0.5}, F_{0.5})_4\right]^{2-}(l) + Ba^{2+}(l) \qquad (1.9b)$$

$$CdF_2(l) + BaF_2(l) = [CdF_4]^{2-}(l) + Ba^{2+}(l) \qquad (1.9c)$$

$$CdCl_2(l) + KCl(l) = [CdCl_3]^{1-}(\ell) + K^{1+}(l) \qquad (1.9d)$$

The polyanionic species $[CdCl_4]^{2-}$ is analogous in chemical character to $[ZnCl_4]^{2-}$ in $ZnCl_2$-based glass-forming liquids. Matecki and Poulain [19] also reported that in the CdF_2-$BaCl_2$ glass forming liquid the incorporation of alkali fluorides and chlorides aids the glass formation. The presence of KCl, for example, promotes formation of $[CdCl_3]^-$ via the reaction shown in Equation 1.9d.

So far, it is apparent from the thermodynamic analysis that the reciprocal salt mixtures, namely $CdCl_2$-BaF_2, promote glass formation due to the presence of polyanionic species, such as $(CdCl_4)^{2-}$ and $(CdCl_3)^-$, which are stabilized in the presence of cations with a large coordination field ($z = 8$), e.g. Ba^{2+} and K^+. The preponderance of polyanions arises due to a large difference in the lattice energies of constituents of a glass-forming liquid.

The final example of the dominance of polyanionic species near glass-forming compositions is taken from the ZrF_4-BaF_2-NaF system, in which the lattice energies of ZrF_4, BaF_2 and NaF are vastly different from each other, since none of the two fluorides have comparable crystal structures. The barium fluorozirconate liquids, when mixed with NaF, form a range of glasses that were first reported by Poulain and co-workers [21]. The thermodynamic properties of barium fluorozirconate and sodium fluorozirconate liquids were analysed by Grande and co-workers [22,23] and Hatem and co-workers [24]. Grande *et al.* adopted the non-ideal solution model for determining the molar heats of mixing for ZrF_4-NaF and ZrF_4-BaF_2, showing the minima at around 40 mol.% ZrF_4, where the glass-forming tendency is maximized. The corresponding binary diagrams can be seen in Figure 1.5a and b, respectively.

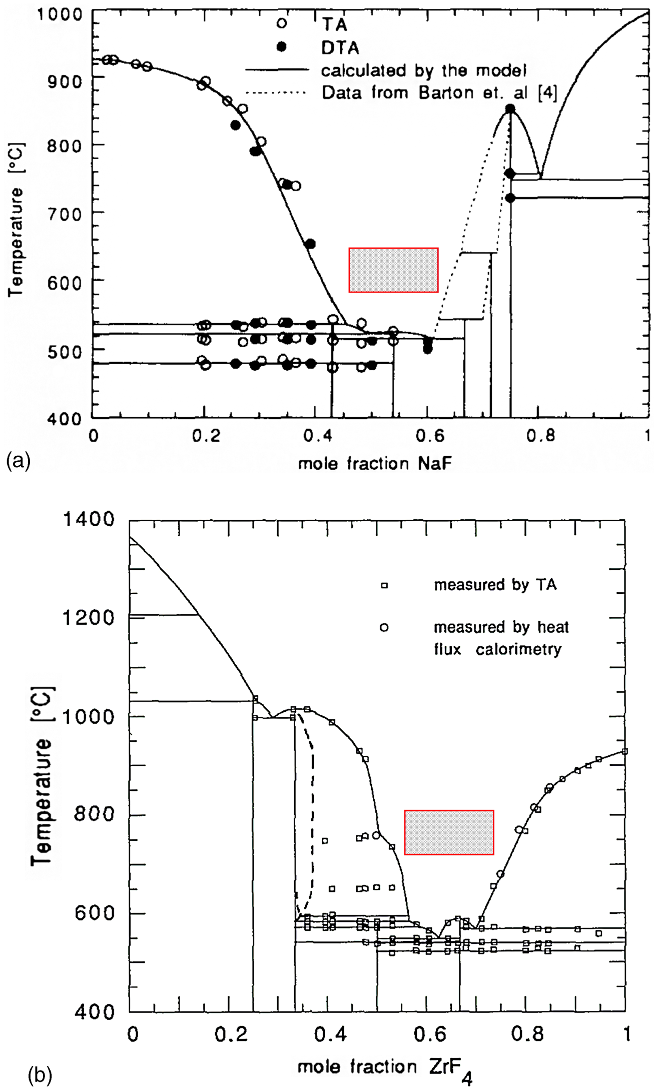

Figure 1.5 *(a) Phase-equilibrium boundaries in the NaF-ZrF_4 system, determined by Grande and co-workers by using the experimental data and a thermodynamic model [22,23]. The shaded area near equimolar NaF:ZrF_4 shows the regions of glass formation, when mixed with BaF_2. Adapted from the original in References 22,23. (b) Comparison of the experimentally determined phase-equilibrium boundaries in the BaF_2-ZrF_4 system, determined by Grande and co-workers [22,23]. The shaded area near equimolar BaF_2:ZrF_4 is the composition range of enhanced glass formation, when mixed with NaF. Adapted from the original in References 22 and 23. Source: T. Grande 1992. Reproduced with permission from Elsevier limited.*

Two major reviews by Poulain [25] and Parker [26] have explained that the ZrF_4-BaF_2 is a conditional glass former, and the incorporation of a third constituent, namely NaF or AlF_3, enhances the glass formation tendency by increasing the Coulombic asymmetry or the asymmetry in the lattice energies. The magnitude of asymmetry in the lattice energy of constituents, resulting in the formation of a non-ideal glass-forming liquid in ZrF_4-NaF-BaF_2, was characterized by Grande and co-workers [21,22] by plotting the enthalpy of mixing energies of the binary constituents and the dominance of the complex fluorides in the intermediate composition range in the ZrF_4-BaF_2-NaF (Figure 1.6a and b). Such profound experimental evidence reinforces the point made earlier in this section with reference to Equation 1.5 that the tendency for complex or compound formation in a binary and ternary phase diagram lowers the melting point (cf. Equation 1.5), as also shown in Figures 1.3, Figures 1.5a and 1.5b, and therefore promotes the glass formation.

From the examples above on molten salts, it is apparent that a strong tendency for complex formation in binary and pseudo-binary phase diagrams coincides with the glass-forming compositions. The glass-forming liquids are strongly non-ideal solutions, as depicted by the dominance of complex formation in examples of AgI-CsI, $CdCl_2$ and ZrF_4 based compositions, e.g. in Figure 1.6b. Finally, as the magnitude of Coulombic charge difference among

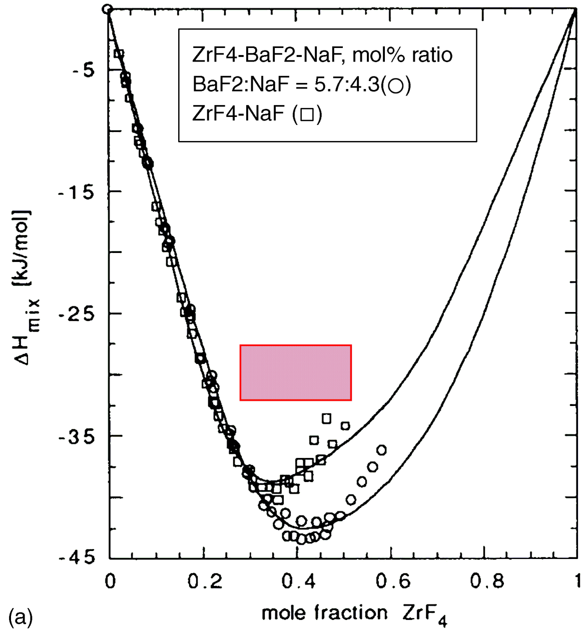

Figure 1.6 *(a) Asymmetric parabolic shape of heat of mixing (ΔH_{mix}, kJ mol^{-1}) for the ZrF_4-BaF_2-NaF and ZrF_4-NaF mixtures are plotted against the mole fraction (X_i) of ZrF_4 as a constituent of the mixture. The position of the minimum designates the likelihood of formation of complexes, which are shown (b) [22,23] and coincides with the stable glass-forming range, designated by the shaded area. Source: T Grande 1993. Reproduced with permission from Elsevier limited. (b) Plot of the number of moles of complexes, as an example, which form in the binary ZrF_4-NaF mixture, as a function of the mole fraction (X_i) of ZrF_4 which is based on the thermodynamic model for solutions [22]. Source: T Grande 1993. Reproduced with permission from Elsevier.*

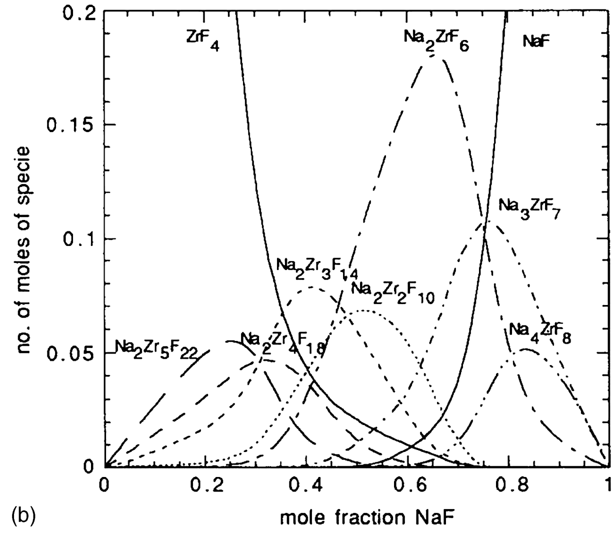

Figure 1.6 (Continued)

the cations involved in defining a glass-forming composition increases, the magnitude of partial molar quantities also tends to depart further from the idealized behaviour.

Having analysed the thermodynamic properties of glass-forming liquids in binary and pseudo-binary phase diagrams, it is possible to draw general conclusions that for complex polyanions to exist a central cation charge (e.g. Ag^+, Cd^{2+}, Zr^{4+}) needs a strong polyhedron cage, to support the structure through bonding with large anions (F^-, Cl^-, and I^-). The experimental proofs for such a polyanionic structure in glass-forming liquids appears to have a similarity with Zachariasen's random network model for covalent glasses and Goldschmidt's cation-to-anion ratio. In AgI-CsI, the complexes $[AgI_3]^{2-}$ and $[Ag_2I_3]^-$ tetrahedra and polyhedral structures may be compared as the building blocks with the random polyanion networks of $[SiO_4]^{4-}$, $[PO_4]^{3-}$ etc. in a covalent glass. The polyanions of $(Cd\{FCl\}_4)^{2-}$ in CdF_2-$BaCl_2$ and $[ZrF_6]^{2-}$ in ZrF_4-BaF_2-NaF glass-forming systems are essential for supporting the three-dimensional random networks.

For the analysis of structures in inorganic glasses, the cationic radii (R_C in nm) and Pauling's electronegativity for a cation–anion pair ($\Psi_{C\text{-}A}$), average co-ordination number (Z_c), and their effect on lattice energy (ΔH_{lat}) for representative glass-forming compounds are discussed.

1.5 Glass Formation and Co-ordination Number of Cations

Before discussing the details of glass structure, it is essential that we introduce the concept of electronegativity and co-ordination number of cations for several inorganic glass-forming compounds. The electronegativity is the tendency of an atom to attract another electron to complete a pair state of electrons in the outermost orbit of the valence band. In the periodic table, the elements are more electropositive on the left-hand side than the elements on the right-hand side, e.g. the group VII halogen elements, namely F, Cl, Br and I, which are electronegative. The elements in the middle of periodic table are neither strongly electropositive nor electronegative, and therefore tend to form bonds with both types of elements. This tendency for combining with another element determines the residual electronegativity of a bond, which in turn determines the magnitude of enthalpy of mixing in a complex glass-forming liquid. From Equation 1.5, therefore, a change in the slope of liquidus curve will be expected, depending upon the magnitude of the partial molar enthalpy of a mixture.

Among the structural models for glass formation, the Zachariasen rules [27] is the first one considered here. The original rule has been strictly developed for covalent oxide glass-formers which depict a three-dimensional continuous network of cation–anion pairs of bonds. This rule adapted the solid-state chemical structural evidence of crystalline materials to postulate the structural chemistry of covalently bonded glass networks. The interatomic forces are comparably similar in a glass and its parent crystal, which then implies naturally that the chemical bonds and the nearest neighbour cation–anion co-ordination in glass and crystals are likely to be similar. Since a glass is derived by quenching a liquid it must be at a higher energy state than the corresponding equilibrium solid, as depicted in Figure 1.1.

By defining the above postulations, Zachariasen specifically defined the model for silica glass which was subsequently found to be consistent with the X-ray diffraction data of Mozzi and Warren [28]. From the Zachariasen model applied to silica, each Si^{4+} cation must be connected to at least one O^{2-}, if not more, resulting in an average co-ordination of between 3 and 4, based on the $[SiO_4]^{4-}$ crystal model where each silicon (Si^{4+}) is surrounded by four oxygen (O^{2-}). The resulting tetrahedron must share at least one corner with a neighbour with the maximum number of shared corners being four. According to this rule, the edge and face sharing of polyhedron may not be possible. The co-ordination with a neighbouring polyhedron may be continuous, yielding a three-dimensional continuous random network. The continuous network model then further specifies the nature of oxygen as the bridging oxygen atoms between two silicons (≡Si—O—Si≡) and the non-bridging oxygen atoms (≡Si—) in which one of the oxygen sites is unoccupied. In this representation the ≡ symbol represents three other oxygen-bridged sites around silicon. In view of the covalent nature of groups IVB (Si, Ge), VB (P) and III (B), the Zachariasen model seems to work reasonably well and has been found to be consistent with the large number of experimental data on silica, silicates, phosphates, germanium oxides and borate glasses. However, for large cationic co-ordination system the rules seem to break down.

Pauling's electronegativity for a cation (C) and anion (A) pair ($\Psi_{\text{C-A}}$) is given by Equation 1.10 in which the unit of dissociation energies, E_d, of the A—C, A—A and C—C bonds are in electron volts; a factor $(\text{eV})^{-0.5}$ is then included for a dimensionless $\Psi_{\text{C-A}}$: [29]

$$\psi_{\text{C-A}} = \left(\sqrt{(E_{\text{C-A}}) - \left[\frac{E_{\text{AA}} + E_{\text{CC}}}{2}\right]}\right) x(\text{eV})^{-0.5} \tag{1.10}$$

Based on Pauling's model in Equation 1.10, the difference in Pauling's electronegativity between silicon and oxygen is 2.59, which is derived from the value of enthalpy of formation of SiO_2 at 298 K as a reference state. Since the enthalpy of formation, which corresponds to the Si—O bond, is 9.40 eV the value of ($\Psi_{\text{C-A}}$) can be derived, using the electronegativity data for oxygen and Si, which are 3.44 and 1.90 eV, respectively from the *Wikipedia* reference [29] above in Equation 1.10. For such comparisons it is easier to consider the readily available

Table 1.2 *Comparison of Pauling's electronegativity data with the entropy of fusion (ΔS^f, eu) for several glass-forming compounds for which cationic co-ordinations are also included. Py: pyramid, Ch: chain, BPy: bipyramid, Tr: tetrahedron, Oct: octahedron, C: cube.*

Compounds	Z_c	$\Psi_{C\text{-}A}$	R (Å)	ΔS_f, (eu)	Structure	R_C/R_A	Remarks
B_2O_3	3, 4	3.16, 1.68	1.55	7.33	Py, Tr	0.17	
As_2O_3	2, 3	1.11		7.2	Ch, Tr	0.43	Sublimes
SiO_2	4	2.59	1.74	1.08–1.30	Tr	0.31	
BeF_2	4	2.39	1.68	1.37	Tr	0.26	
GeO_2	4, 6	1.8, 1.08	1.85	1.4	Tr, Oct	0.40	
P_2O_5	4	3.68	1.67	13.6	Tr	0.26	Sublimes
V_2O_5	4	3.53	1.91	16.54	Tr	0.44	sublimes
GeS_2	4	0.81	2.37	5.74?	Tr	0.29	
$ZnCl_2$	4	1.32	2.55	4.14	Tr	0.41	
TeO_2	4, 6	0.76	2.02	6.91	BPy, PyPy	0.53, 0.42	
WO_3	4	2.39	1.94	10.06			
Al_2O_3	4–6	3.87	1.83	11.06	Oct, BPy, Tr	0.38	
Bi_2O_3	6	1.373	2.28	13.03	Oct	0.72	
Ga_2S_3	4, 6	2.29	2.46	?	Oct, Tr	0.33	Data unknown
ZrF_4	6	4.15	2.12	?	Oct	0.59	Sublimes
La_2O_3	6	4.03	2.71	?	Oct, 7- & C	0.77	Data unknown
La_2S_3	6	3.49	3.23	?	Oct, 7- and C	0.55	Data unknown
S	2	2.58	1.84	1.02	Ch		
Se	2	2.55	1.91	2.84			
As_2S_3	4	−0.8	2.42	11.7	Ch,	0.25	
AgI	4	−1.286	3.46	2.7	Tr	0.57	
CsI	8	1.32	3.87	6.4	C	0.76	

data for the enthalpy of formation of a compound at 298K than to hunt for the bond-pair energy which is not listed for the complex glass-forming compounds. In Table 1.2, the computed values of ($\Psi_{C\text{-}A}$) for glass-forming compounds are compared with ΔS^f, discussed above in Table 1.1. The data in Table 1.2 are also compared with the average co-ordination number of cations in the crystalline state. The bond lengths (R, Å) in Table 1.2 are represented by the sum of cationic and anionic radii, assuming that each cationic sphere is in physical contact with Z anionic spheres. The data in Table 1.2 have been plotted to show a trend in glass-forming behaviour in Figure 1.7. In Figure 1.7 the values of ($\Psi_{C\text{-}A}$), representing the bond pair of network forming compounds, are plotted against their entropy of fusion, ΔS^f.

For example, the values of electronegativity for glass-forming compounds with $Z = 4$, namely, SiO_2, BeF_2, GeO_2, $ZnCl_2$ and TeO_2, exhibit a trend in which the electronegativity of glass-forming compounds decreases with increasing entropy of fusion (in eu). This trend in Figure 1.7 also implies, from Equation 1.6, that the depth of a eutectic point with respect to the melting point increases when constituting liquidus regions are in equilibrium with solids having such low values of entropy of compounds. The deep eutectic condition favours the formation of glass on quenching such liquids. Other glass-forming materials, such as S and Se, also follow this dependence on the entropy of fusion. However, for all other Z values except $Z = 2$ and 4, the relationship shown in Figure 1.7 does not apply universally, due to the absence of the known glass-forming systems, e.g. in the family of $Z = 3$, 5 and 6. Especially

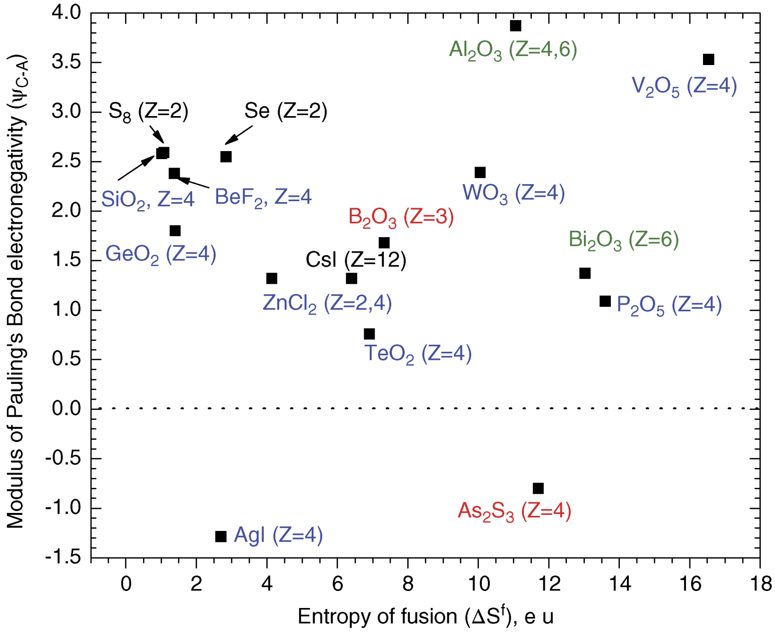

Figure 1.7 *Plot of Pauling's bond electronegativity ($\Psi_{C\text{-}A}$) against entropy of fusion (ΔS^f) of the glass-forming compounds listed in Table 1.2.*

for $Z = 6$ there is no apparent relationship between Al_2O_3, Bi_2O_3, and vanadate, niobate and tantalite family of glass forming networks. In addition, B_2O_3 cannot be compared with any other compound with $Z = 3$ in this figure, because it is neither isochemical nor isostructural with other glass-forming compounds in Figure 1.7. By contrast, we also find that the value for As_2O_3 differs from P_2O_5. Note also that the values of $(\Psi_{C\text{-}A})^2$ for As_2S_3 and AgI are negative because the enthalpy of formation, which yields the value of first term within the square root equation in Equation 1.10, is too small and as a result the whole term within the root becomes negative, which mathematically has little meaning in the context of electronegativity. Compounds such as WO_3, V_2O_5 and Al_2O_3 are conditional glass-formers, as is TeO_2, and each require another compound to be present in the liquid for glass formation.

Figure 1.7 is a plot of two structure sensitive properties ($\Psi_{C\text{-}A}$) for the analysis of strong, intermediate and weak tendencies for glass formation, which we may also be amenable to comparison with Sun's single bond [30] and Rawson's bond-strength-freezing point [31] models. The details of the Rawson's models have been discussed in detail by Varsheneya [3b], which may be useful supplementary reading on the bond energy data for glass forming, intermediates and modifier oxides. By comparison, the E_b (kJ mol^{-1}) values fall into three different types of oxides playing a different role in the glass formation. According to Sun's model glass-forming compounds (B_2O_3, SiO_2, GeO_2, P_2O_5, and BeF_2) have E_b values larger than ~360 kJ mol^{-1}. By comparison the modifying oxides (Na_2O, K_2O and CaO) have E_b values lower than ~220 kJ mol^{-1}. Between the two extreme limits of glass-formers and modifiers fall the E_b values of intermediate compounds. Unlike the rigorous thermodynamic approach discussed above, neither Sun's model nor the electronegativity model is able to explain the negative values of $(\Psi_{C\text{-}A})^2$ for As_2S_3 and AgI (Figure 1.7). As will be explained in subsequent chapters, a rigorous approach based on thermodynamic and kinetic models is the best approach in the analysis of glass-formation that must be adopted for engineering of a glass composition and its stability.

Many of the compounds in Table 1.2 manifest multiple co-ordination numbers, especially when they are present in a glassy matrix in which the three-dimensional lattice constrains are significantly reduced. Classical examples of multiple co-ordination shells are in tetrahedron co-ordination (fourfold) in $[AlO_4]^{5-}$, bipyramid (fivefold) co-ordination in $[AlO_5]^{4-}$, and octahedron (sixfold) co-ordination in $[AlO_3]^{3-}$, as well as prismatic B in $(BO_3)^{3-}$, tetrahedral co-ordination in $(BO_4)^{5-}$, bipyramid Te in $(TeO_4)^{4-}$, prismatic Te in $(TeO_3)^{2-}$ and polyhedron Te in $TeO_{3+\delta}$. Since the co-ordination shell structures determine the band gap energy, any change therein is likely to influence the UV-visible and vibrational spectroscopic, thermal and viscosity properties of a glass. The argument for co-ordination polyhedra in glass-forming systems is consistent with the Zachariasen model which is based on the parent crystalline solid, in which cation and anion pair is comparable with that of crystalline solids. Amongst various oxides, Al^{3+} as a cation has a complex co-ordination shell that is observed in both the oxide and fluoride glasses, in which the ion may be present as network former, intermediate and modifier in a composition range. Simmons and co-authors [32] have explained in detail the importance of co-ordination polyhedra for cations in the context of fluoride glass structure in which the authors have used the cation-to-anion radius (R_c/R_A) ratio as a good approximation for the description of a co-ordination polyhedron. For this reason, the Ag^+ ion in Figure 1.4 is surrounded by four iodine ions in tetrahedron symmetry because of the size difference, which is pointed out in Table 1.2.

Recently several methods for quantifying the ionicity of a bond pair have been reported using both the empirical [33] and theoretical approaches, including first principle [34] and density functional theory [35], for many ionic and semiconductor compounds. Based on reasonable comparison of data between the empirical [33] and theoretical [34,35] approaches, Al-Douri compared the data for a range of semiconductors and found reasonable agreement between his computed data and that reported by Phillips [36]. This method may be found useful for chalcogenide glasses, based on the elements belonging to groups IV, III–V, and II–VI. Furthermore, the ionicity model for chalcogenides may also be supplemented by the estimation of co-ordination number using the Mott's 8–*N* (also known as the octet) rule and Phillip's "bond-stretching and bond-bending" model. The latter appears to be specifically relevant in the context of glass formation in Ge-Se system.

Besides Pauling's electronegativity discussed above, another model was proposed by Sanderson, which adopts a different representation by considering the molecular bond electronegativity as a geometric mean of a formula unit, C_mA_n, where C and A, as explained above, designate a cation and an anion, respectively [37]. The geometrical mean of the Sanderson electronegativity $(\psi_{\mathrm{C\text{-}A}})^S$ then equals:

$$(\psi_{\mathrm{C-A}})^S = \sqrt[m+n]{(\psi_C)^m \cdot (\psi_A)^n} \tag{1.11}$$

which for alumina (Al_2O_3), $(\psi_{\mathrm{C\text{-}A}})^S$, is equal to:

$$(\psi_{\mathrm{Al-}}\mathrm{O})^S = \sqrt[5]{(\psi_{\mathrm{Al}})^2 \cdot (\psi_{\mathrm{O}})^3} = \sqrt[5]{(2.22)^2 \cdot (5.21)^3} = 3.703$$

compared to 3.87 computed from Equation 1.10 in Table 1.2 using Pauling's model. Values of Sanderson electronegativity have been compiled by West [37], where the values of partial charge on oxygen for a cation–anion pair ($-\delta_{\mathrm{O}}$) are also reported. Note that the partial charge

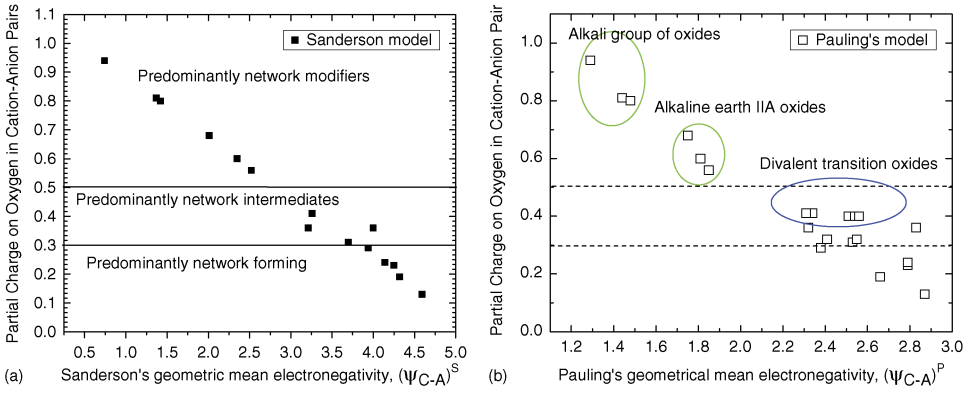

Figure 1.8 *(a) Plot of partial charge on oxygen in cation–anion bonds against the values of Sanderson electronegativity* $(\psi_{C\text{-}A})^S$*. (b) Pauling's geometric mean values plotted against the partial charge on oxygen on cation–anion pairs.*

on an anion is a negative quantity. By plotting the values of partial charge on oxygen in cation–anion pairs in oxides in Table 1.2 against the values of Sanderson electronegativity, a reasonable trend between the glass network formers, contributors and modifiers is observed (Figure 1.8a), and is characteristically absent in Figure 1.7. The corresponding data for various oxides used in Figures 1.8a and 1.8b are shown in Table 1.3, from which the

Table 1.3 *Partial charge on anions* $(-\delta_A)$ *for oxides and chlorides [37]. Source: A. R. West 1988. Reproduced with permission from John Wiley & Sons.*

Compounds **Monovalent**	$(-\delta_O)$	Compounds **Divalent**	$(-\delta_O)$	Compounds **Trivalent**	$(-\delta_O)$	Compounds **Tetravalent**	$(-\delta_O)$
Cu_2O	0.41	HgO	0.27	Ga_2O_3	0.19	CO_2	0.11
Ag_2O	0.41	ZnO	0.29	Tl_2O_3	0.21	GeO_2	0.13
Li_2O	0.8	CdO	0.32	In_2O_3	0.23	SnO_2	0.17
Na_2O	0.81	CuO	0.32	B_2O_3	0.24	PbO_2	0.18
K_2O	0.89	PbO	0.36	Al_2O_3	0.31	SiO_2	0.23
Rb_2O	0.92	SnO	0.37	Fe_2O_3	0.33	MnO_2	0.29
Cs_2O	0.94	FeO	0.40	Cr_2O_3	0.37	TiO_2	0.39
		CoO	0.40	Sc_2O_3	0.47	ZrO_2	0.44
		NiO	0.40	Y_2O_3	0.52	HfO_2	0.45
		MnO	0.41	La_2O_3	0.56		
		BeO	0.36				
		MgO	0.50				
		CaO	0.56				
		SrO	0.60				
		BaO	0.68				
Chloride compounds							
CuCl	0.29	RbCl	0.78	$CdCl_2$	0.21	$BaCl_2$	0.49
AgCl	0.30	CsCl	0.81	$BeCl_2$	0.28		
LiCl	0.65			$MgCl_2$	0.34		
NaCl	0.67			$CaCl_2$	0.40		
KCl	0.76			$SrCl_2$	0.43		

chemical character of glass network formers, contributors or intermediates and modifiers may be identified.The graphical relationships shown in Figures 1.8a and 1.8b are similar, except that in Figure 1.8b we have also included the data for divalent transition metal oxides (MnO, FeO, NiO, CoO and CuO) and for BeO, MgO and ZnO. All five divalent transition metals fall between network intermediates and divalent alkaline earth oxides.

In figure 1.8a, the network glass-formers are at the bottom right-hand corner, above which the network contributors cluster together with the transition metal oxides. The network modifiers of alkali and alkaline earth oxides lie at and above a partial charge on oxide of 0.5.

Continuing with the partial charge on the anion (e.g. oxygen for oxides), on comparing the values of partial charge on oxygen on different types of oxides in Table 1.3 with the values of entropy of fusion for oxides in Table 1.2 it is qualitatively apparent that the entropy of fusion scales with the partial charge on oxygen and with Pauling's and Sanderson's electronegativity. The glass-forming network compounds have smaller values of δ_O and entropy of fusion, in general. This trend seems to apply satisfactorily to all glass-forming networks for which the values of δ_O are known, which helps in understanding the chemical character of various compounds that partake in the constitution of a glass.

Table 1.3 also includes data for chlorides, for which a comparable trend amongst network formers, contributors and modifiers is apparent, especially when comparing the residual charge on chloride ions in $BeCl_2$ and $CdCl_2$.

A summary of the analysis of electronegativity therefore clearly demonstrates that it is the residual charge ($-\delta_A$) on anions in a compound that may be responsible for determining the structural role in glass-forming liquids and glasses. There is also a qualitative relationship between the entropy of fusion, δ_A, and $\psi_{C\text{-}A}$ (Pauling and Sanderson). Based on the concepts of electronegativity, we now introduce the ionicity of a bond and discuss it in the context of a glass network.

1.6 Ionicity of Bonds of Oxide Constituents in Glass-Forming Systems

There are several models used in the calculations of ionicity of atoms, simple and complex bond pairs. This is especially relevant in the analysis of the ionic character of bond termination sites, which may be at the surface and in the bulk. For bond termination sites, which are known as the non-bridging sites, the analysis of ionicity is important for determining not only the energetics of the cation environment but also its likely co-ordination field. In other words the ionicity is an important factor that is essential in the characterization of cationic co-ordination in crystals and glass hosts.

By considering the lattice energy and electronegativity models, proposed by Liu and co-workers [38] and Zhuralev [39], respectively it is possible to explain the two main contributing factors of a bond, namely, the ionic (U_{ion}) and covalent (U_{covalent}) parts of the lattice energy, as shown in Equation 1.12:

$$U_{\text{total}} = U_{\text{ion}} + U_{\text{covalent}} \tag{1.12}$$

Considering the bonding in crystals as a first approximation of a corresponding glassy structure, we may be able to use the Kapustinskii equation [40] shown in Equation 1.13, to describe the ionic part of the total lattice energy. We also assume that not all the bonds are alike in complex crystals:

$$U_{\text{ion}}\left(\text{kJ mol}^{-1}\right) = \left[\frac{1270(m+n)Z_C Z_A}{d}\right]\left(1-\frac{0.4}{d}\right)f_i \tag{1.13a}$$

$$U_{\text{covalent}}\left(\text{kJ mol}^{-1}\right) = \left[\frac{2100m(Z_C)^{1.64}}{d^{0.75}}\right]f_i \tag{1.13b}$$

Here d is the bond length, Z_A and Z_C are the valencies of cations and anions, respectively, and m and n are the corresponding stoichiometric indexes in the compound A_mO_n. From these two equations and the values of average band gap energy (E_g), which is composed of homopolar (E_{homo}) and heteropolar (E_{hetero}) parts of the overall bonding, such that the $\left(E_g\right)^2 = (E_{\text{homo}})^2 + (E_{\text{hetero}})^2$ [41]. Based on the approach discussed above, the derived values of ionicity of bonds are summarized in Table 1.4.

Zhuralev on the other hand, using the electronegativity model, has given the calculated values of ionicity of elements with varying co-ordination number for the cation–oxygen bridge. Table 1.5 shows the values of ionicity for MO_6 and AO_4 co-ordination polyhedron. The values for $L = 1.5$ co-ordination in MO_6 and $L = 1.4$ co-ordination in AO_4 are compared

Table 1.4 *Bond lengths (d in Å), bond Ionicity (fi), and calculated values of* $U_{covalent}$, U_{ionic}, *and* U_{Total} *(all in kJ mol*$^{-1}$*) of some simple crystals with only one type of bond. The values of* f_i *are taken from Reference [39]. Source: V. D. Zhuralev 2007. Reproduced with permission from Springer.*

Crystals	d	f_i	f_i (*Experiment*)	U_{covalent}	U_{ionic}	U_{Total}	$U_{\text{reference}}$	$U_{\text{experimental}}$
LiF	2.01	0.914		107	925.2	1032	1028	1036
NaCl	2.82	0.936		62	723	785	805	786
KI	3.53	0.948		42	605	647	656	649
RbCl	3.29	0.956		38	648	686	690	689
CsBr	3.62	0.965		28	602	630	625	631
CuCl	2.34	0.882		131	794	925	921	996
$SrCl_2$	2.99	0.968		92	2137	2229	2127	2156
MgF_2	1.992	0.911		347	2785	3132	2913	2957
CaO	2.405	0.916	0.74 ± 0.26	295	3215	3510	3414	3401
MnO	2.22	0.887		406	3325	3731	3724	3745
CoO	2.13	0.858	0.70	527	3324	3851	3837	3910
BaO			0.76 ± 0.23					
MgO			0.66 ± 0.16					
ZnO			0.60 []					
GeO_2	1.88	0.730		3430	9317	12748	12828	
SnO_2	2.054	0.784		2735	9201	11936	11807	
SiO_2			0.25					
LaN	2.65	0.759		1477	5559	7036	6876	6793
NbN	2.35	0.720		1877	5812	7689	7939	8022
SrS	3.01	0.917		238	2684	2922	3006	2848
BeS	2.105	0.611		1457	2389	3846	3927	3910
MgTe	2.77	0.589		1253	1848	3101	2878	3081
BaTe	3.179	0.897		283	2506	2789	2721	2843

Table 1.5 *Ionicity values for elements in MO_6 and AO_4 polyhedral units with co-ordination L = 1.5, and L = 1.4, respectively.*

M	Ionicity (δ) for MO_6 co-ordination polyhedral where the magnitude of *L* designates the number of M—O bridges				
	L = 1	*L* = 2	*L* = 3	*L* = 4	*L* = 5
Li	0.84	0.84	0.84	0.84	0.83
Na	0.85	0.85	0.84	0.84	0.84
K	0.86	0.86	0.86	0.85	0.85
Cs	0.87	0.87	0.87	0.86	0.86
Cu	0.79	0.78	0.78	0.78	0.77
Be	0.7	0.69	0.69	0.68	0.67
Mg	0.73	0.73	0.72	0.72	0.71
Ca	0.75	0.74	0.74	0.74	0.73
Sr	0.75	0.75	0.74	0.74	0.73
Zn	0.7	0.69	0.69	0.68	0.67
Cd	0.7	0.7	0.69	0.68	0.67
Pb	0.74	0.74	0.73	0.72	0.71
Ni	0.74	0.73	0.72	0.71	0.7
B	0.62	0.61	0.59	0.57	0.54
Al	0.68	0.67	0.66	0.64	0.62
Ga	0.65	0.64	0.63	0.61	0.59
In	0.68	0.67	0.66	0.64	0.62
Tl	0.67	0.65	0.64	0.62	0.6
Sc	0.68	0.68	0.66	0.65	0.63
La	0.7	0.69	0.68	0.67	0.65
Bi	0.67	0.66	0.65	0.63	0.61
Mn	0.66	0.65	0.64	0.62	0.6

	L = 1	*L* = 2	*L* = 3	*L* = 4		*L* = 1	*L* = 2	*L* = 3		*L* = 1	*L* = 2
M	A(4+)				M	A(5+)			Mo	A(6+)	
	0.38	0.33	0.25	0.13	N	0.23	0.16	0.05	S	0.21	0.13
Si	0.5	0.46	0.4	0.31	P	0.37	0.31	0.23	Se	0.25	0.18
Ge	0.48	0.44	0.38	0.29	As	0.39	0.33	0.25	Te	0.33	0.26
Sn	0.52	0.48	0.43	0.35	Sb	0.43	0.38	0.31	Cr	0.27	0.2
Zr	0.54	0.51	0.46	0.38	Bi	0.44	0.39	0.32	Mo	0.29	0.22
Hf	0.54	0.5	0.45	0.37	V	0.39	0.33	0.25	W	0.29	0.22
					Nb	0.39	0.34	0.26			
					Ta	0.4	0.35	0.27			

for different elements. Evidently, for all fourfold coordination, the values of ionicity are the lowest and amongst these Si, Ge, C, P, As, Sb and Sn, which either form or contribute to a glass-forming network, have the lowest values of ionicity compared with those for the alkali metals in a sixfold co-ordination. In summary, a larger the value of ionicity of an element defines the localization of valence band electrons in a bonding.

The discussion on co-ordination shell and ionicity is relevant for engineering inorganic photonic glasses, especially those doped with either rare-earth or transition metal ions, in terms of explaining the short-wavelength absorption and cut-off, vibrational spectroscopy and the contributions thereof for optical transitions.

1.7 Definitions of Glass Network Formers, Intermediates and Modifiers and Glass-Forming Systems

In Figures 1.8a above a set of terminologies for oxides, namely the network forming, intermediates and modifiers, were introduced to help in identifying the roles of the oxides of metals and sub-metals that are often constituent parts of a glass structure. The discussions based on the partial charge on anions (Cl^-, O^{2-}) and ionicity of bonds and elements in Tables 1.3–1.5 explain the delocalization of valence electrons, which are essential in determining the "glass structure continuum and mechanical stability". On this basis, energetically the network formers are preferably those elements that have the lowest ionicity. In other words when such elements combine with oxygen atoms or halogens, a partial charge on the anion is left that is another manifestation of delocalization of valence electrons, defining their wave functions and overlap integrals with another like bond pair, e.g. O—Si—O, or O—Si—O—Na^+. It is immediately apparent how the delocalization of electrons on a Si—O pair would be affected, depending on the chemical nature of its environment. It is important to emphasize at this stage that a model based on electronegativity or ionicity has similarity with Philips's topological hypothesis [42] for chalcogenide glasses, which has been extensively discussed by Varsheneya [3]. The floppiness and deformability of chemical bonds in chalcogenide systems have been described by distinguishing the dominance of chemical and mechanical stabilities across the composition. The preponderance of "bond deformability and floppiness" has been ascribed as the glassy structure, and the lack of such continuum has been identified as "amorphous" state. Indeed, the deformability of a chemical bond is an intrinsic manifestation of "valence band electron delocalization" in a chemical bond.

Before explaining the types of glass-forming systems it is also important to consider the co-ordination shell for cations. Strictly speaking, since no cations form purely covalent or purely ionic bonds, analysis of the co-ordination shell in the realm of ionicity of cations or partial charge on anions becomes even more compelling. In brief this is summarized in Table 1.6 [32]. In this table, the valence band hybridization, e.g. sp, dp, sp^2, dp^2 etc., is shown leading to a specific topological description, with the smallest R_c/R_A yielding structures such as trigonal pyramid, tetrahedron, square planar and bipyramid. For example, in a silicon–oxygen bond pair, the electronic structures of silicon and oxygen are $[Ne]3s^2 3p^2$ and $[He]2s^2 2p^4$, respectively; as a result, we expect that (p_x^2, p_y^1, p_z^1) electron wave functions from oxygen will interact with the (p_x^1, p_y^1) wave functions from silicon. The process of hybridization is comparable with what happens in a diamond or a methane structure. The silicon hybrid forms by donation of one electron from the $3s^2$ level of silicon to an empty p_z state, which then creates four unpaired states $3s^1 3(p_x^1, p_y^1, p_z^1)$. Once this metastable transition occurs only then can the four electrons in 2p level from oxygen combine and yield an sp^3-type hybridization in SiO_2. The sp^3 hybridization is an intrinsic characteristic of group IVB elements; consequently, strong covalent bonds form with tetrahedron symmetry, having bond angles close to 109.5°. The above hybridization is the basis for the $(SiO_4)^{4-}$ structure in

Table 1.6 *Co-ordination number, minimum radius ratio, orbitals and geometrical structures [32]. Source: J. H. Simonns 1991. Reproduced with permission from Academic Press, San Diego.*

Co-ordination number	Minimum radius ratio (R_C/R_A)	Orbital hybridization	Resulting geometrical structures
2		sp, dp	Linear chain
3	0.155	sp^2, ds^2	Trigonal planar
		p^3, d^2p	Trigonal pyramid
4	0.225	sp^2d, p^2d^2	Square planar
		sp^3, d^3s	Tetrahedral
		d^4	Tetragonal pyramid
5	0.155	sp^3d, d^3sp	Trigonal bipyramid
6	0.414	d^2sp^3	Octahedron
		d^4sp	Trigonal prism
7	0.592		1 atom above the face of an octahedron
8	0.645	d^4sp^3	Dodecahedral square
	0.732		Antiprism, cube
9	0.732		Right triangular prism
12	1.00		Cube, octahedron

silica and silicate glasses. Similarly, in case of phosphate $(PO_4)^{3-}$, which also has a tetrahedron structure, is a part of hypervalent molecular structure. A hypervalent structure "is a molecule that contains one or more main group of elements, formally bearing more than eight electrons in their valence shells". In this case the hybridization of wave functions is sp^3d, which is why one of the phosphorus oxygen bonds is a double-bond, resulting in a (PO_4) structure. On the other hand, boron–oxygen bonding is predominantly sp^2 (co-planar) following carbon's graphite-like arrangement in a $(BO_3)^{3-}$ trigonal pyramid, whereas in the $(BO_4)^{5-}$ tetrahedron structure the hybridization is more complex than the plain sp^3 hybridization in an $[SiO_4]^{4-}$ structure.

Examples of electronic hybridizations resulting in specific topologies are shown in Figure 1.9. Complex hybridizations, namely d^4sp^3 etc., resulting in larger co-ordination numbers yield more complex shapes than octahedron, for example. Antiprisms and dodecahedra are such examples, which are often manifested by strong electropositive cations and tri- and divalent lanthanides.

1.7.1 Constituents of Inorganic Glass-Forming Systems

In this section our main aim is to classify different types of inorganic glass-forming systems by identifying the co-ordination chemistry of the main constituent that contributes to the network formation. The method of classification based on co-ordination number of central atom bonded with anions in a structural unit allows us to visualize the pervasiveness of the three-dimensionality of a specific network former. On this basis it is easier to identify the glass-forming systems into the following categories:

(a) Glass-forming networks based on cations of B, Si, P and Ge and oxide ion as anion (O^{2-}). These are *strongly covalent* glasses, as is apparent from the electronegativity, partial

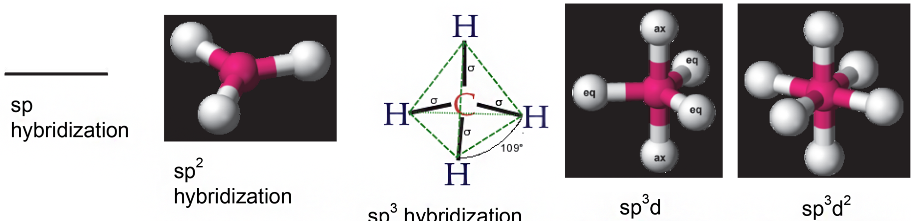

sp hybridization

sp^2 hybridization

sp^3 hybridization

sp^3d hybridization

sp^3d^2 hybridization

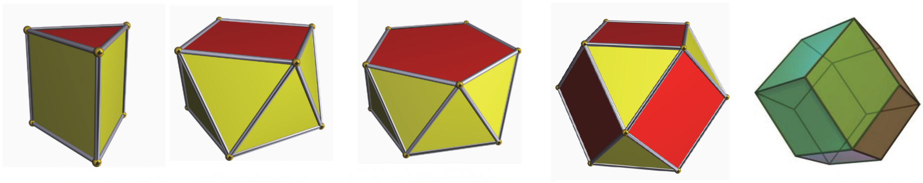

Prism

Square anti prism

Pentagonal anti prism

Cuboctahedron

Rhombo dodecahedron

Figure 1.9 *Illustrations of common electronic hybridizations (sp, sp^2, sp^3, sp^3d, sp^3d^2) and higher orders of hybridization resulting in energetically favoured geometrical shapes, e.g. prism, antiprisms, cube octahedron and rhombo-dodecahedron [43]. (See colour plate section.)*

charge of oxide ion and ionicity of bonds, discussed in Tables 1.2, 1.4 and 1.5, respectively.

(b) Glass-forming systems based on heavy-metal oxides that have significant ionic character but are not as ionic as the electropositive elements of groups IA and IIA in the periodic table. These are glasses based on the oxides of aluminium, gallium, tellurium, vanadium, niobium, tantalum and tungsten, and are also known as the *conditional glass-formers*, which means that the liquids of pure compounds require either another network modifying oxide or another network-forming component oxide for the stabilization of glass structure.

(c) As the oxygen and fluorine atoms are comparable in size and in their values of electronegativity there is also a group of fluorides that forms glass. They are based on the fluorides of Be, Zn, Cd, Al, Zr, Hf and Th. A vast majority of pure fluorides of these elements, except that of Be, are also conditional glass-formers and need either another fluoride or oxide to stabilize the glass-forming liquids, as exemplified above in Section 1.4 in Figures 1.5 and 1.6. Amongst fluoride glass-forming systems, there are also mixtures of fluorides with oxides in which a limited range of composition forms a glass. Typical examples are mixtures of silicates and aluminium phosphates with the fluorides of group IA, IIA, IIB, IIIA and lanthanide elements. In contrast, the chlorides and bromides do not mix well with oxides, and therefore do not contribute to glass formation. However, several mixtures of chlorides, bromides and iodides are known in the literature for glass formation.

(d) Since the atoms of carbon, nitrogen and oxygen have comparable atomic size, these elements, with silicon and aluminium especially, form glass when precursor compounds such as Si_3N_4, SiO_2, Al_2O_3, AlN and SiC are mixed and melted above 1700 °C in an atmosphere of argon or nitrogen. The combination of oxides and nitrides of silicon and aluminium forms a tough glass and glass ceramic called SiAlON, an acronym derived from the elements involved in its constitution [44,45]. On the other hand, mixtures of oxides and carbides are known to yield an oxycarbonitride glass [46], which might be a mixture of phase separated regions of the sp^3 hybridization of Si—C, Si—N and Si—O bonds, yielding a dark grey glass. The quality of such glasses is often quite poor due to rapid evolution of carbon dioxide and carbon monoxide gases during melting under the atmosphere of nitrogen or argon gas. The oxycarbide compositions, as a result, are not well studied.

(e) The final group of inorganic elements, where glass formation is commonly observed, is the chalcogenide elements, namely S, Se, Te and their compounds, especially with the group elements IIIA, IVB and VB. Extensive ranges of glass formation have been reported in the literature along with their optical, electronic and mechanical properties. In selected chalcogenide glass-forming systems, partial substitution of chalcogenide elements with halogens such as the chlorine, bromine and iodine have also been reported, leading to compositions called “chalcohalides”, a new hybrid name coined to represent the chemical composition.

1.7.2 Strongly Covalent Inorganic Glass-Forming Networks

As explained above, the glass-forming networks in this family of compositions are the oxides of silicon, boron, phosphorus and germanium. Silica based glasses are derived either from melting or sol–gel processing of precursors of silica with modifying and intermediate oxide materials. Since the starting material is silica, it is important to compare the structure of crystalline silica and silicates with the corresponding glass compositions, especially when other network forming oxides, intermediates and modifiers are mixed to form a glass by melting the starting crystalline materials.

The quartz crystal is the commonest form of crystalline silica, which also occurs in nature. In the crystalline form, a Si^{4+} cation is in a tetrahedron co-ordination with four oxygen (O^{2-}) ions, which is represented as a $[SiO_4]^{4-}$ tetrahedron. In crystalline form the $[SiO_4]^{4-}$ structure repeats itself over an infinitely long three-dimensional space with each fourfold co-ordinated silicon surrounded by two O^{2-}ions on either side, which is how the entire network of $[SiO_4]^{4-}$ tetrahedron repeats itself. The O—Si—O bonding is called the “bridging oxygen” and only on the surface of crystals is the bridge broken, which is identified as the “non-bridging oxygen”. In liquid and glassy silica, the first major difference is the absence of a three-dimensional periodic structure (Figure 1.10a). Figure 1.10b shows the $[SiO_4]^{4-}$ tetrahedron with the corresponding Si—O and O—O distances, which depend on crystalline, glassy and liquid forms of silica. By comparison, Figure 1.10c shows an example of α-tridymite, one of the polymorphic forms of crystalline silica; it represents the three-dimensional periodicity for which the two-dimensional representation is also compared in Figure 1.10a. Figure 1.10d shows a 2D representation of a 3D-dimensional network of glass structure that is random, which implies that with respect to a point of reference the space groups do not repeat periodically in any direction. However, a regular pattern of a hexagonal ring structure in Figure 1.10a has changed to polygonal rings in a corresponding glassy structure in Figure 1.10d. In this figure a significant number of non-bridging oxygen sites around the structure of silica glass is shown to have terminated at the edge of structure. In Figure 1.10e the structure of silica glass is further modified by the presence of monovalent sodium ions (Na^{+}) in the structure. As explained above in the context of electronegativity and

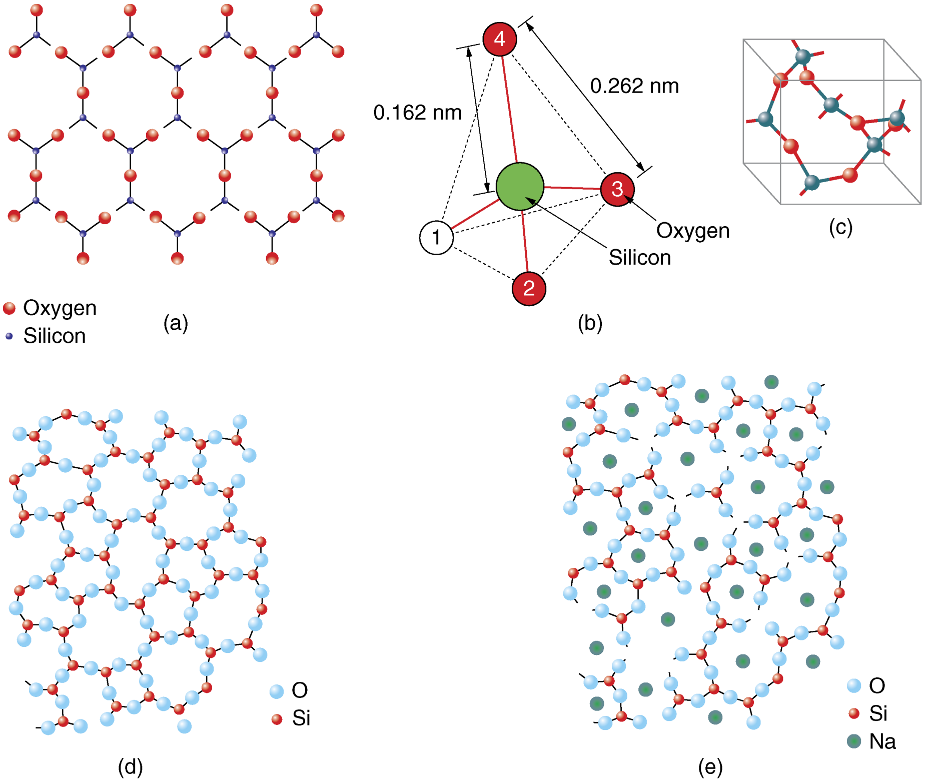

Figure 1.10 *Schematic representations of (a) a coplanar representation of the 3D-periodic array of sp^3 hybridized Si—O bonds, in which the fourth oxygen ion (O^{2-}) is perpendicular to the plane of the paper, as shown in (b); (b) a tetrahedron $(SiO_4)^{4-}$ structure of silica, which is the main building block in both the crystalline and amorphous (glassy) states; (c) the crystalline tridymite structure of SiO_2, which forms a 3D periodic continuum; (d) a 3D continuous aperiodic structure of silica glass showing bridging oxygens between two silicon atoms and the non-bridging oxygen anions at the edges which have only one silicon; (e) a sodium ion (Na^+) modified silica glass network in which Na^+ creates a more open structure by producing more non-bridging oxygen compared with the structure of pure silica glass in (d). (See colour plate section.)*

ionicity factors affecting an inorganic structure, monovalent cations tend to have a large co-ordination environment, which suggests that in order to incorporate an alkali ion the neighbouring bridging bonds between Si and O will have to terminate internally to create surfaces, as shown in Figure 1.10e. The incorporation of alkali ions in a silica matrix creates non-bridging bonds via the reaction shown in Equation 1.14, which can be adopted for other types of network formers:

$$y\left[\vdots\mathrm{Si}\text{—O—}\mathrm{Si}\vdots\right] + \mathrm{M}_x\mathrm{O}_y = y\left[\vdots\mathrm{Si}\text{—}\mathrm{O}^-\right] + x\mathrm{M}^{y+} \qquad (1.14)$$

In this equation, “$\vdots$” designates the three electrons on silicon in the formula unit that also form Si—O bonds in a tetrahedron shown in Figure 1.10b. Evidently, a modifying oxide breaks y

number of Si—O bridging bonds, and therefore creates the non-bridging bond sites in Figure 1.10e. Such internal bond cleavage has major consequences for the spectroscopic, mechanical and physical properties of most covalently bonded glass networks.

With this brief introduction to silica and silicate glass structure, our focus in the rest of this chapter will be to discuss various compositions of silicate, phosphate, borate and germanate glasses. We will then return to the structural analysis of each type of glass in Chapter 2.

Table 1.7 shows the composition ranges for glass formation in borates, silicates, germanates and phosphates. The experimental conditions adopted for determining the glass forming compositions are stated briefly.

Table 1.7 *A list of glass-forming composition range, (m) identifies the presence of miscibility gaps in silicates [1,47]. Data from [1] and [47].*

Metal oxides that modify or contribute to a glass network	Covalently bonded network oxides			
	B_2O_3 [a]	SiO_2 [b]	GeO_2 [c]	P_2O_5 [c]
Monovalent oxides				
Li_2O	100.0–57.3	100.0–64.5	100.0–76.2	100.0–40.0
Na_2O	100.0–62.0 33.5–28.5	100.0–42.2	100.0–62.0	100.0–40.0
K_2O	100.0–62.3	100.0–45.5	100.0–40.5	100.0–53.0
Tl_2O	100.0–55.5	—	100.0–52.5	100.0–50.0
Divalent oxides				
MgO	57.0–55.8	100.0–57.5 (m)	Unknown	100.0–40.0
CaO	72.9–58.9	100.0–43.3 (m)	84.5–64.5	100.0–40.0
SrO	75.8–57.0	100.0–60.0 (m)	86.0–61.0	100.0–46.0
BaO	83.0–60.2	100.0–60.0 (m)	100.0–90.0 82.5–70.4	100.0–42.0
ZnO	56.0–36.4	~2	100.0–52.0	100.0–36.0
CdO	60.9–45.0	Unknown	Unknown	100.0–43.0
PbO	80.0–23.5	0–60	100.0–43.0	100.0–38.0
Trivalent oxides				
Bi_2O_3	78.0–37.0	Up to 60	100.0–66.0	95.0–70.0
Al_2O_3	Not known	0–10	100.0–95.0	75.0–68.0
Tetravalent oxides				
TiO_2	Not known	Not known	Not known	60.0–35.0
TeO_2	20.0–40.0	limited	Up to 90.0	100.0–1.0
Pentavalent oxides				
V_2O_5	90.0–10.0	<5	Not known	Wide range
Nb_2O_5	90.0–10.0	<5	Not known	>95.0
Ta_2O_5	80.0–70.0	<5	Not known	—

[a] All boric oxide based precursor materials were batched between 1 and 3 g in size. The mixture was melted in a platinum crucible and after homogenization it was allowed to cool naturally in air.

[b] Each silicate batch size was between 1 and 2 g in size, and was melted in air and cooled naturally to room temperature, as described in footnote *a*.

[c] For germanium oxide and phosphate glasses, the batch size was between 1 and 3 g, and was melted and quenched as above in footnotes *a* and *b*.

In the binary composition, the composition range for the main component is cited. For example, with Li_2O as a second constituent in four glass forming networks, the composition of Li_2O varies between 0 and 47.7 mol.% in B_2O_3, 0 and 35.5 mol.% in silica, 0 and 23.8 mol.% in GeO_2 and 0 and 60 mol.% in phosphate liquid. In the table, the composition ranges of miscibility gaps are identified by (m), which are prevalent in silicates. Briefly, the miscibility gap is a region of composition where the constituent phases tend to physically separate in the frozen state. These may be the sub-liquidus and sub-solidus miscibility. Alternatively, the regions of immiscibility may exist in the liquid state, too, the principles of which explained by examples in subsequent chapters with reference to the properties of glass ceramics used for photonic devices.

In Table 1.7, a large number of oxides in the first column are listed that are known to dissolve in the matrix of network formers, and yield binary compositions. What is apparent from the list is that, as the cationic charge on solute oxides increases, such oxides become structurally and energetically incompatible in the network forming matrices, and promote phase separation and crystallization.

1.7.3 Conditional Glass Formers Based on Heavy-Metal Oxide Glasses

Amongst the oxide compounds, such as Al_2O_3, Ga_2O_3, TeO_2, V_2O_5, Nb_2O_5, Ta_2O_5, MO_3 and WO_3, that cannot form glass on its own and rely on the presence of other constituent oxides or similar compounds, the tellurium oxide compositions have been most extensively studied. Since these glasses rely on other constituent oxides to be present in the liquid for glass stability, these oxides glasses are the so-called "conditional" glass-formers. Among the trivalent Al_2O_3 and Ga_2O_3 glass-forming networks are the pseudo-ternary compositions that have been reported by Mazurin and co-workers [47]: Al_2O_3-$(Na,K)_2O$-TiO_2, Al_2O_3-$(Na,K,Cs)_2O$-$(Ta,Nb)_2O_5$, Al_2O_3-$(Cd,Pb)O$-Bi_2O_3, Al_2O_3-La_2O_3-CaO and Al_2O_3-BaO-TiO_2. These aluminate compositions were melted in a platinum crucible at 1500 °C in air for 30 min, and the liquid was quenched onto a stainless steel surface. The glass-forming compositions in gallium oxide are: Ga_2O_3-$(Na,K,Cs)_2O$-Ta_2O_5, Ga_2O_3-$(K,Cs)_2O$-Nb_2O_5, (Ga_2O_3:La_2O_3-CaO = 40 : 40 : 20 by wt%) and Ga_2O_3:Bi_2O_3-(Ca,Sr)O, which can be melted in the temperature range 1250–1400 °C. The glass-forming range is often limited in these ternary compositions and requires an extensive cooling rate. By comparison, when alkaline earth metal oxides are replaced by CdO, PbO and ZnO, the melting temperature for glass fabrication drops to 1000 °C, as reported by Dumbaugh [48]. It is claimed in the reference that the bismuth-lead-gallium oxide glasses can be melted at 1000 °C in air for more than 20 min and up to 200 g batches were cast using this method of melting. As an example, we show a ternary section to represent the composition map for glass formation in the $GaO_{1.5}$-$BiO_{1.5}$-PbO ternary in Figure 1.11. The aspects of co-ordination number of Al^{3+} and Ga^{3+} and their structures will be discussed in Chapter 4.

Tellurium oxide (TeO_2) falls in the category of a conditional glass-former, as it was first identified by Stanworth [49] in 1952. The tellurite family of glasses has been widely reported by many authors and amongst the earliest works by Imaoka and Yamazaki [50], Dimitriev and co-workers [51,52], and Vogel and co-workers [53]. Besides Vogel, who examined especially binary compositions listed in Table 1.8, a vast majority of previous results on the physical and chemical properties of ternary tellurite glasses were based on the mixtures of alkali, alkaline earth, sesquioxides and other higher valency oxides. Among the inorganic

Table 1.8 *List of binary composition ranges in the tellurite family of glasses [47,51]. Data from [47,51].*

Metal oxide	Composition range (mol.%)	Metal oxide	Composition range (mol.%)	Metal oxide	Composition range (mol.%)	Metal oxide	Composition range (mol.%)
Univalent oxides		**Divalent oxide**		**Trivalent oxides**		**Higher valency oxides**	
Li_2O	12.2–34.9	BeO	15.0–27.0	Al_2O_3	7.6–16.8	TiO_2	6.2–18.9
Na_2O	5.5–37.8	MgO	11.0–35.0	La_2O_3	4.5–9.5	ThO_2	5.2–11.0
K_2O	6.5–19.5	CaO	<10.0	Ga_2O_3	0.0–20.0	P_2O_5	0–50.0
Rb_2O	5.6–21.0	SrO	9.2–13.1	Bi_2O_3	0.0–5.0?	V_2O_5	0–50.0
Tl_2O	13.0–38.4	BaO	8.0–35.7	In_2O_3	<5.0	Nb_2O_5	2.2–24.0
Cs_2O	0–10.0	ZnO	17.3–37.2	Sc_2O_3	<5.0	Ta_2O_5	1.4–15.3
Ag_2O	30–50.0 wt%	PbO	12.8–22.6	Y_2O_3	<5.0	WO_3	8.5–44.0
		CuO	12.0–36.0	Gd_2O_3	~3.0		
		CdO	0.0–5.0	As_2O_3	~3.0		
				B_2O_3	0–15.0		

glasses known today, the tellurite family of glasses are unique in structure, as they are based on three different types of structural polyhedrons of Te^{4+} ions [51], namely the trigonal bipyramid $[TeO_4]^{4-}$, trigonal pyramid $[TeO_3]^{4-}$ and polyhedron $[TeO_{3+x}]^{4-x}$. Each structural unit has a lone pair electron site, which contributes to the unique spectroscopic properties of these glasses – a subject area for discussion in Chapters 4 and 6. In the tellurite

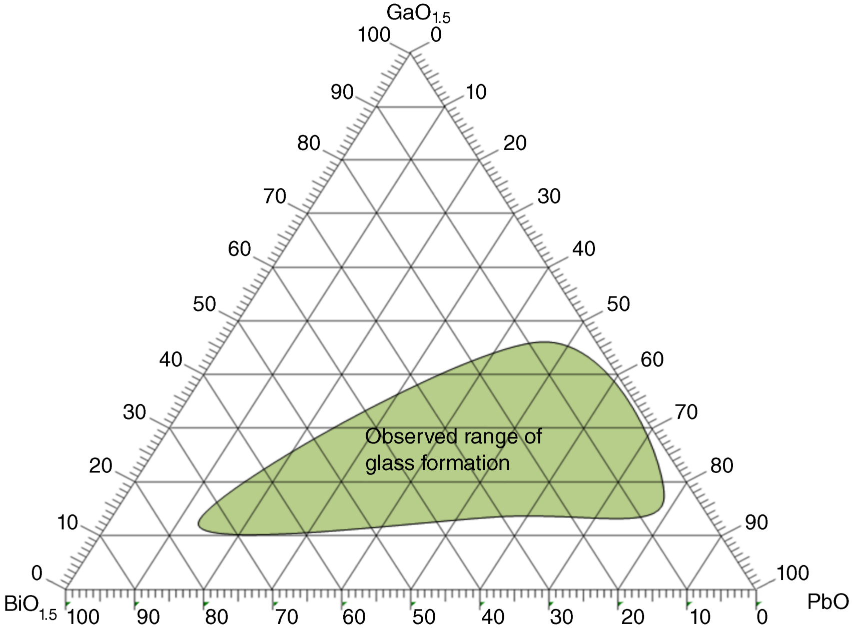

Figure 1.11 *Composition mapping of glass formation in the Ga_2O_3-Bi_2O_3-PbO system, which is represented as a $GaO_{1.5}$-$BiO_{1.5}$-PbO section. Source: W. H. Dumbaugh 1986. Adapted with permission from Society of Glass Technology.*

family of glasses one property that is frequently manifested is the mixing properties with another glass forming networks such as the borates, phosphates, silicates, germanates, niobates, tantalates, molybdates and tungstates. A binary tellurite can also mix with another chalcogenide oxide, such as the $(SO_4)^{2-}$ and $(SeO_4)^{2-}$ complexes. The compositions stated in Table 1.8 have been compiled from different sources and represent a reasonable selection of binary oxides.

Several scores of ternary tellurite composition maps with their physical and chemical properties have been compiled by Mazurin and co-authors [47]; they have formed the basis for applications of the reported compositions for device engineering.

Two different ternary composition maps are shown in Figure 1.12a and b, which define the TeO_2-Li_2O-R(Zn,Ba,Pb)O and TeO_2-Al_2O_3-$R(Li,Na,K)_2O$ sections. These ternary compositions are one of the glass-forming systems investigated in detail for fibre and planar glass based device engineering.

1.7.4 Fluoride and Halide Network Forming and Conditional Glass-Forming Systems

The BeF_2 based glasses were the very first type of fluoride glasses, which were studied in the context of using the fluoroberyllate liquid as coolants for the fuel core in nuclear power plants. Beryllium fluoride has a similar structure to that of the $[SiO_4]^{4-}$ tetrahedron because the ratio of Be^{2+} and F^- ions is too small for the stabilization of structures, namely bipyramids and octahedral. Although the constituent anion F^- is ionic, the $[BeF_4]^{2-}$ structure is known to have strong covalent bond like features and is the only fluoride liquid that can form glass without the presence of a second constituent. Like silicate networks, the $[BeF_4]^{2-}$ network can also be modified by alkali fluorides, e.g. LiF, NaF etc., and can transform into a structure consisting of bridging and non-bridging F^- ion sites (Figure 1.10e). Zachariasen [27] first adopted his model for BeF_2 based glassed by describing the 3D-continuous random network. Baldwin and Mackenzie [54] developed a model for fluoride glass formation, based on Sun's bond model for fluorides and commented that

> "the essence of the relation of the single bond strength to glass formation is the assumption that the stronger-bonded constituent cations in a glass melt are less likely to have their bonds ruptured on cooling. A preponderance of strongly bonded cations will be less likely to undergo reordering as a prerequisite to crystallization and hence glass formation will be favoured."

Close examination of the Baldwin–Mackenzie model in the light of Sun's bond energy model points out that this model, like the electronegativity model, is fundamentally based on energetics and considers the preponderance of entropy of broken bonds leading to a glassy state, which we have discussed in Section 1.5.

For halide glass formation the anions from group VII are the main building blocks, as explained in Figures 1.3–1.6. These glasses can only be synthesized by chemical processes, e.g. melting, and are popularly known as the "halide family of glasses". Among these halide glass compositions, BeF_2 and $ZnCl_2$ are of no practical interest because of their hygroscopic nature, which renders them unsuitable for engineering applications. BeF_2 is also a carcinogenic material, however, it has some attractive optical properties, e.g. for a composition (weight percent) containing 26.0 BeF_2–18.0 AlF_3–27.2 CaF_2–29.7 NaF, the values of n_D and the Verdet constant are 1.3741 and 105, respectively, implying its low dispersion. It also has

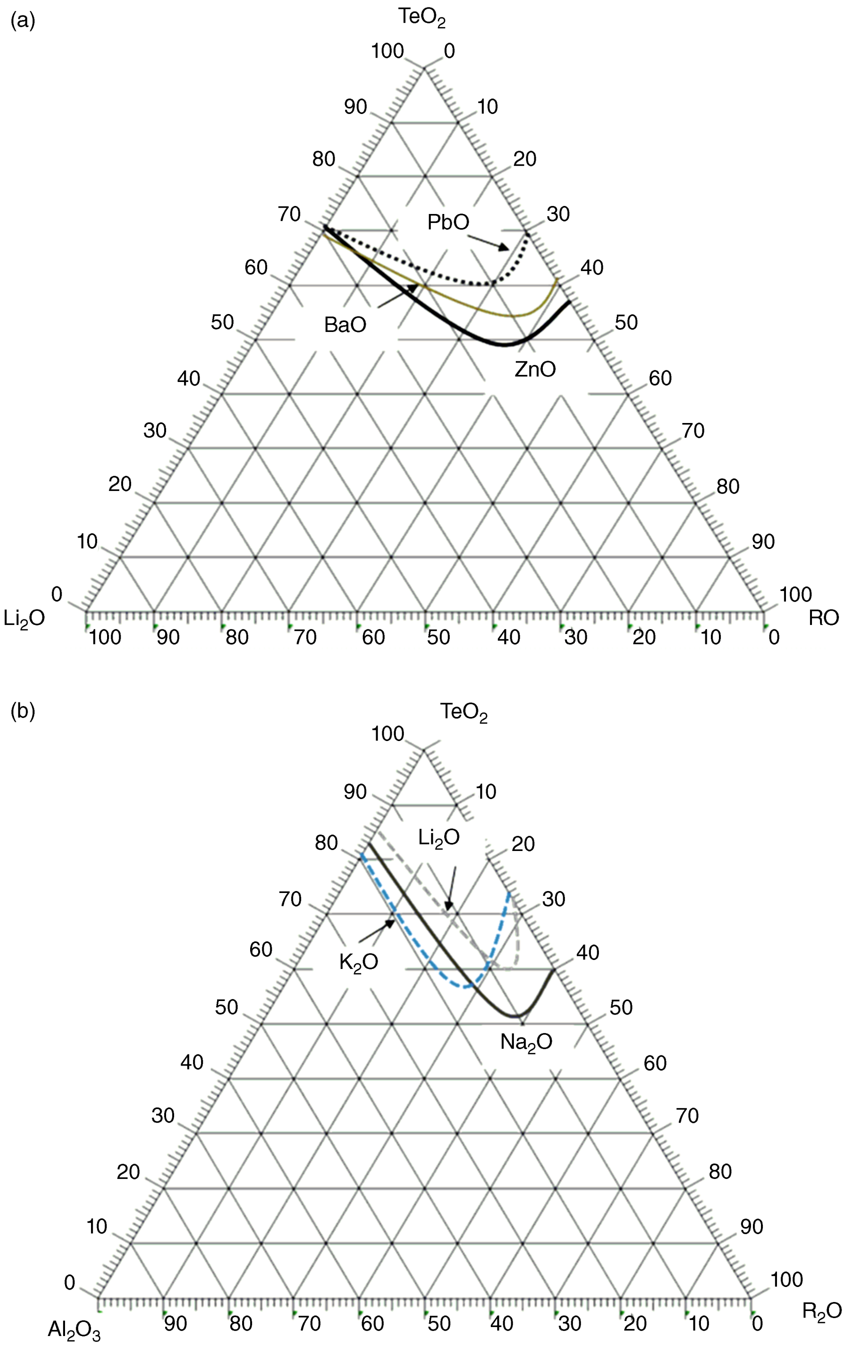

Figure 1.12 (a) TeO_2-Li_2O-R(Zn,Ba,Pb)O and (b) TeO_2-Al_2O_3-$R(Li,Na,K)_2O$. These compositions were melted in gold-palladium crucibles at 800 °C in air [47]. Source: O. V. Mazurin 1991. Adapted with permission from Elsevier.

low-loss window (<0.1 dB km^{-1}) that is at a longer wavelength that in silica. The BeF_2 glass has a low thermal expansion that is comparable with that of silica.

Besides the network formation in fluoroberyllate $(BeF_4)^{2-}$, zinc chloride and zinc iodide form glass networks based on the $[ZnX_4]^{2-}$ tetrahedron, which as in the liquid BeF_2 structure can be modified with the addition of alkali chlorides and iodides [55]. However, notably, these fluoroberyllate and zinc halide glasses are fundamentally hygroscopic, and extreme care is essential in reducing the incorporation of OH^- groups in the structure.

Trivalent and tetravalent fluoride glasses do not follow the Zachariasen model, as became apparent when they were serendipitously discovered by the Poulain brothers (Marcel and Michele Poulain) in 1975 [56], during their attempts to synthesize a sodium-barium fluorozirconate host for laser applications. The precursor powder when heat treated above 900 °C in air to synthesize the ternary crystalline compound yielded a glass instead (Figure 1.13).

A vast majority of these glasses are the "conditional glass formers" in the inorganic fluoride systems. In this section a series of conditional glass formers in halide systems are discussed along with their compositional maps. The most stable fluoride glass compositions were identified in a five-component mixture, having a nominal composition (mol.%) of $ZrF_4(55-x)$-$BaF_2(20-y)$-NaF(20)-$LaF_3(x)$-$AlF_3(y)$. These compositions have been studied extensively for device engineering, especially for fibre laser and amplifier engineering, which are also discussed in subsequent chapters. Table 1.9 reports significant compositions in the ZrF_4 based glass-forming systems. Following the serendipitous discovery of zirconium-based fluoride glasses, the University of Rennes I group in France further explored the analogues of fluorozirconate by partially and fully replacing zirconium with hafnium and studied their properties. The composition range of the thorium fluoride (ThF_4) family of glasses is much narrower than that in ZrF_4 and HfF_4 families of glasses. Besides the narrow range of stable composition of ThF_4 [57], for some compositions, e.g. ThF_4-BaF_2-LnF_3 [58], the quenching rate required is much higher than that in ZrF_4 and HfF_4 glasses. Here Ln represents the lanthanide elements in the periodic table. However, in barium-lithium thorium fluoride glasses (ThF_4-BaF_2-LiF) [59] and (ThF_4-BaF_2-LnF_3-AlF_3) [60] glasses much larger glass samples of several millimetre to centimetre sizes were cast for laser applications. Interestingly, the ThF_4 based compositions were reported to demonstrate much extended IR transmission than either ZrF_4 or HfF_4 [56]. However, the use of such glasses for engineering applications has been limited due to the radioactive nature of thorium.

Although several dozen fluoride and halide glasses have been explored and reported in the literature, very few have found their way to engineering applications and been drawn into fibres. Amongst them are the AlF_3-PbF_2-SrF_2-MgF_2 based glasses, originally reported by Sun in 1946 [61], which were further developed with and without the presence of phosphate in the form of sodium metaphosphate (Na_3PO_4). Videau *et al.* [62,63] systematically studied the ternary AlF_3-BaF_2-CaF_2 system, which were then stabilized by the addition of trivalent pre-lanthanide and rare-earth fluorides (YF_3, LnF_3) and drawn into optical fibres [64]. The compositions with phosphate group are especially interesting as it enhances the crystallization resistance and reduces the phase separation tendency. These fluoride glasses were also referred as the "Hoya" (a well-known Japanese Company) [65] glasses, which exhibit a lower refractive index than the standard silicates [66]. The combination of fluoride and phosphate in the glass network yields a unique feature of covalent and ionic bonding of $[AlF_n]$ polyhedral

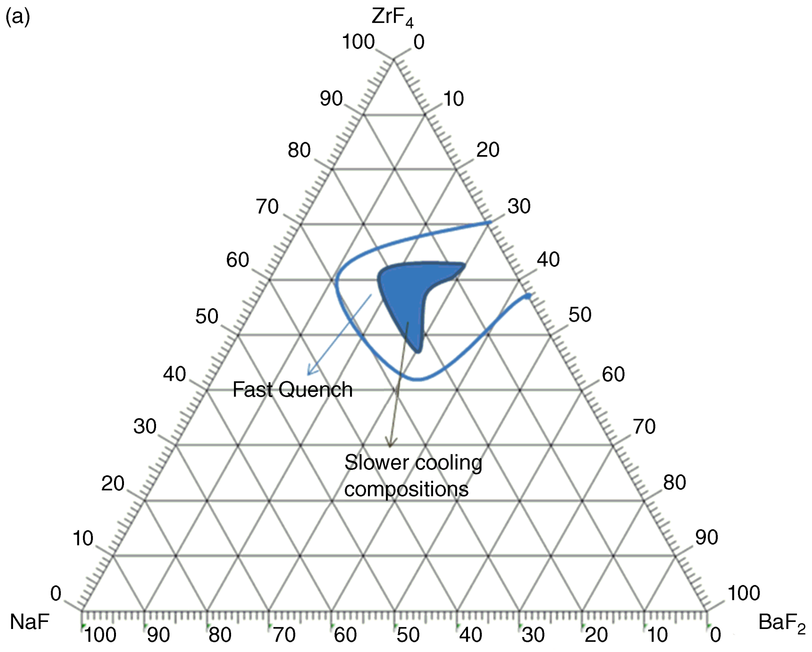

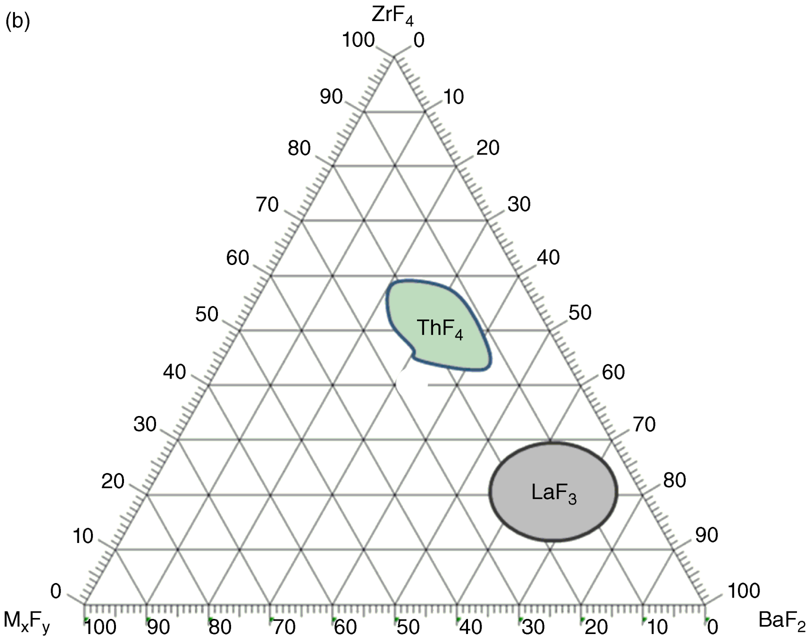

Figure 1.13 Ternary composition maps for (a) ZrF_4-BaF_2-NaF and (b) ZrF_4-BaF_2-M_xF_y where M_xF_y designates the glass-forming composition range with LaF_3 and ThF_4. These compositions require quenching in air. The fluoride mixtures were heated in an atmosphere of dry air inside a platinum crucible at 850°C [25] before melting. Source: M. Poulain 1991. Adapted with permission from Academic Press, San Diego.

Table 1.9 List of compositions of tetravalent fluoride glasses with other minor fluorides [25].

Acronym	Composition (mol.%)								
	HfF_4	ZrF_4	BaF_2	LaF_3	ThF_4	NaF	LiF	MFn	AlF_3
ZB		64	36						
HB	66		34						
ZS		70						$30SrF_2$	
HT	43				57				
ZP		70						$30PbF_2$	
ZBL		62	30	8					
ZBT		57	34		9				
ZBNa									
ZBN		60	34					$6NdF_3$	
ZBG		63	33					$4GdF_3$	
HBL	62		30	8					
HBT	60		33		7				
ZBNT		50	20		7.5	20			
ZBNT		50	20		7.5	22.5			
ZBLN		58	15	6		21			
ZBTLN		47.5	12.5	7	8	25			
ZTL		60		10	30				
ZTL		60		7	33				
ZTA		50			43				7
ZBLA		57	36	3					4
HBLA	58		33	5					4
ZBCA		60	32					$4CaF_2$	4
ZBYA		45	36					$11YF_3$	4
ZBNdA		60		28				$8NdF_3$	4
ZBGA		60.5	31.7					$3.8GdF_3$	4
ZBTA		57	29		10				4
ZBTLN		47.5	12.5	7	8	25			
ZBNA		52	24			20			4
ZBLiA		52	26				18		4
ZBLiLA		52	21	5			19		3
ZBLAN		57	18	3		17			5
ZBLAK		56	14	6				20KF	4
ZBLANK		56	14	6		10		10KF	4
ZBLANI		53	20	4		15		$4InF_3$	4

(tetrahedral, bipyramid and octahedron) and $Al(PO)_4$ tetrahedra, giving a preponderance of $[AlF_n]$ polyhedral that are dependent on the presence of alkali, alkaline-earth and trivalent pre- and post-lanthanide fluorides [67]. Such structural features increase the crystallization resistance [68].

Analogues of AlF_3-based glasses and fibres are reported in the literature; they are based on GaF_3 and InF_3. Often these compositions were found to have large concentrations of oxygen in the form of oxides of In_2O_3 and Ga_2O_3. As evident from the Table 1.10 [25], these fluoride glasses often have combinations of one or more polyhedral structural units, as in AlF_n, which

Table 1.10 *List of compositions (defined in mol.%) of trivalent and divalent halide glasses [25,57]. Source: M. Poulain 1991.*

III A Fluoride	Pre-lanthanide fluoride	IV A Fluorides	IIA Fluorides	IIB Fluorides	IA Fluorides
40 AlF_3	16 YF_3	—	22 CaF_2, 12 BaF_2, 10 SrF_2	—	—
40 AlF_3	20 YF_3	—	20 BaF_2 and 20 CaF_2	—	—
30 AlF_3	20 YF_3	20 ThF_4	30 BaF_2	—	—
50 InF_3	—	—	20 BaF_2	30 PbF_2	—
40 InF_3	17 YF_3	—	32 BaF_2	11 PbF_2	—
45 GaF_3	—	—	_	25 PbF_2	30 KF
20 AlF_3	—	20 ThF_4	20 BaF_2	40 ZnF_2	—
—	—	—	30 BaF_2	40,30 $Cd(F, Cl)_2$	—
—	—	—	11 BaF_2	42,11 $Cd(F, Cl)_2$	36 NaCl

are essential for thermal stability. The lack of covalent structure in such glasses limits their thermal stability for optical fibre and waveguide engineering, which is why incorporating the $(PO_4)^{3-}$ units to balance the positive charge against $(Ga, In, Al)^{3+}$ provides thermal stability.

Some of these compositions will be discussed in detail in the context of glass preform and fibre fabrication and loss characterization.

1.7.5 Silicon Oxynitride Conditional Glass-Forming Systems

The oxynitride glasses are predominantly based on the co-ordination chemistry of Si and its interaction with oxygen and nitrogen. Silicon forms a stable nitride, called silicon nitride (Si_3N_4), and an oxynitride (Si_2N_2O). In both compounds the silicon atom is sp^3 hybridized with N and O giving an $[SiN_4]$ and an $[SiN_{4-x}O_x]$ tetrahedron structure, respectively. The oxynitride tetrahedron is also designated as an $Si(O,N)_4$ unit. Notably, however, Si_3N_4 on its own does not form a bulk glass and yet amorphous silicon nitride films are well known for their wide use in the microelectronics industry. It is for this reason that the family of oxynitride compositions are classed as “conditional glass formers”. The propensity for glass formation, as expected from the knowledge in silicate systems, increases in the SiO_2-Si_3N_4 binary mixture when the network formers and contributors (B_2O_3, Al_2O_3) and modifiers (CaO, MgO, etc.) are added. The presence of such oxides not only lowers the glass formation but also expands the composition field, as has been explained in reviews on this subject [69,70].

Since the main components of glass-forming system are the oxides and nitrides of silicon and aluminium, these compositions are often used for engineering, e.g. a Y_2O_3 based yttrium-aluminium garnet oxide and nitride glass ceramic material (Figure 1.14). The example of a yttrium oxide based oxynitride glass is important in the context of investigating the solubility of rare-earth oxides in such a matrix. In addition, as the glass network is constituted from strongly covalent compounds, the ionic resistivity of O^{2-} ions is extremely large in these matrices, typically of the order of 10^{12} Ω cm, which makes oxynitrides an interesting material for electrical poling in order to modify the refractive index.

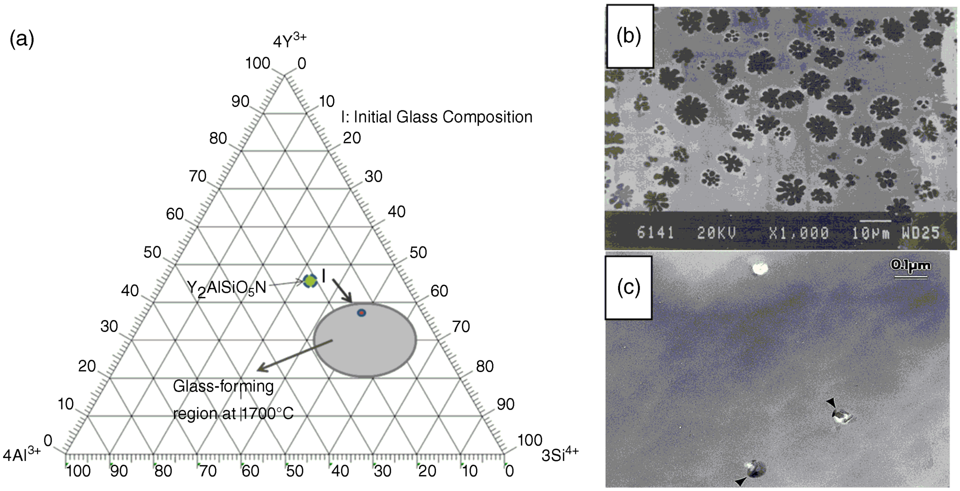
(a)
4Y^{3+}
I: Initial Glass Composition
Y_2AlSiO_5N
I
Glass-forming region at 1700°C
4Al^{3+}
3Si^{4+}
100
90
80
70
60
50
40
30
20
10
0
(b)
6141 20KV X1,000 10μm WD25
(c)
0.1μm

Figure 1.14 (a) Y_2O_3 containing SiAlON glass compositions. The ternary composition shows the range of glass formation, which is designated by the large grey circle. The small dot inside the circle identifies the initial composition of the glass, with respect to the Y_2AlSiO_5N crystalline phase composition. (b) and (c) Transmission electron microstructures of crystallized SiO_2 [71] and silica-rich phase in the matrix of a Y-SiAlON glass [72], respectively. (b) Source: S. Hampshire 1994. Reproduced with permission from Elsevier. (c) Source: W. T. Young 2000. Reproduced with permission from Elsevier.

1.7.6 Chalcogenide Glass-Forming Systems

The chalcogenide glass-forming systems are perhaps the most diverse with unique chemical, physical and spectroscopic characteristics. The unique and diverse characteristics are underpinned by the electronic configuration of chalcogenide elements which are the main constituent of this family of glasses. A chalcogenide glass-forming system *must* consist of one the elements from group VIB of the periodic table, excluding oxygen, which defines the oxide glass formers, discussed above. The main chalcogen elements are S, Se and Te. Individually when, for example, sulfur or selenium is melted and cooled rapidly, the element produces a glass. Sulfur also forms amorphous sulfur, which is not yellow but white in colour. Although the heaviest element polonium is also a chalcogen it is highly radioactive, which limits its use in engineering and technology. Selenium glassy materials were used in the old Xerox machines. The chalcogen elements also combine amongst themselves, e.g. Te and sulfur can be mixed together to form a glass.

One reason for their unique characteristics arises from the presence of a lone pair of electrons in the valence band orbital of a chalcogenide. As a result, a unique set of chemical characteristics is observed in the chalcogenide family of glasses, especially when the glasses are derived from the mixing of more than one chalcogen elements. Outside group VIB, chemical mixing via melting or other means with the elements of II(A,B), III(A,B), IV(A,B) and V(A,B) commonly yields a range of binary glasses, which are further stabilized when, for example, in a binary mixture of IIIB–VIB a third element from group IVB is mixed to make a ternary composition. Larger multicomponent compositions of chalcogenides can also be formulated. Such chemical combinations of chalcogenides predominantly form strong covalent bonds in the glass structure, although there are examples of less covalent structures such as those based on Ga_2S_3, which also form glasses on rapid quenching, especially when mixed with La_2S_3 and GeS_2. These ionic bond dominated sulfide structures are conditional glass formers.

A vast majority of chalcogenide glasses follow the $(8 - N)$ or "octet" rule, originally proposed by Professor Sir Neville Mott, who was rewarded with a shared Nobel Prize in Physics with Dr Phillip Warren Anderson at Bell Laboratories and Professor John Hasbrouck van Vleck at Harvard University for "their fundamental theoretical investigations of the electronic structure of magnetic and disordered systems". This groundbreaking discovery has since revolutionized microelectronics and now has an impact on nano-scale electronics, which can be found in Mott's Nobel lecture on "Electrons in Glass" [73]. This citation together with the classic papers authored by Ovshinsky [74,75] has opened up many applications of chalcogenide glasses. However, except for those compositions in thin film applications, many others have not yet reached fruition despite many years of research. Nonetheless a multitude of opportunities for utilizing these glasses for engineering applications lie ahead, which if achieved will bring about a new revolution in the entire field of photonics and optoelectronics. In this chapter the unique structural features are described for device applications of chalcogenide glasses.

Before describing the physical and spectroscopic properties of chalcogenide glasses, it is essential to identify the building blocks of glass-forming networks. This building block is very much dependent on the electronic structure of the elements which are briefly described below and is referenced from the original text book authored by Z U Borisova [76]. According to Borisova, the unary, binary and ternary glass forming structures are formed on the basis of the maximum allowable number of neighbours, which is determined by the valence bonds, which are as follows:

(a) Chains of selenium in a structural formula unit $SeSe_{2/2}$ are expected to exist in glassy Se structures, where $Se_{2/2}$ represents a bridging selenium with a neighbouring selenium in Figure 1.15a.

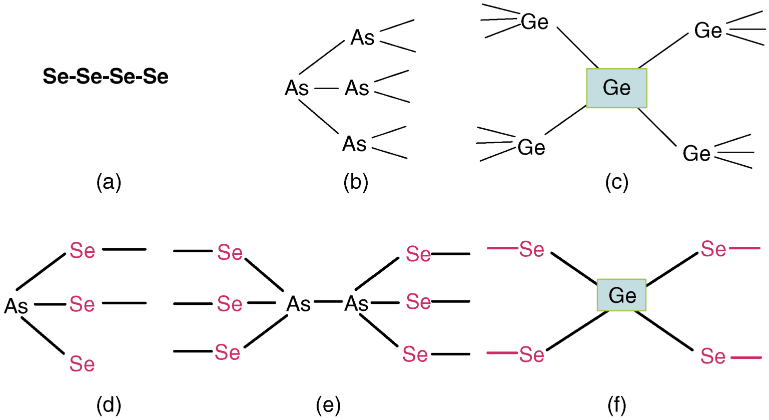

Figure 1.15 Bonding in chalcogenide elemental and compound systems based on the valency: (a) Se-Se zig-zag linear chain; (b) trivalent chain in arsenic; (c) tetrahedron structure in sp^3 hybridized Ge atoms; (d) As-based trivalent chain in As-Se (e); and (f) tetrahedron $(GeSe_4)^{4-}$ structure [76]. Source: Z. U. Borisova 1981. Adapted with permission from Plenum Press.

(b) In arsenic tri-chalcogenide systems the topographic distribution of bonds is as follows with the As $As_{3/3}$ network in Figure 1.15b.

(c) The valency of four in germanium determines the tetrahedron co-ordination (Figure 1.15c), with the spatial distribution of the units showing the Ge-$Ge_{4/4}$ network

The binary glass-forming systems with strong network formation can be designated by the hybridization of the group IVB and group VIB valence band electrons and are schematically shown as an example for selected selenium glass-forming systems. Both sulfides and tellurides can also be represented in a similar manner to the selenides shown in Figure 1.15d–f (respectively, As_2Se_3, AsSe and $GeSe_2$).

The schematic representations of chalcogenide glass-forming networks are consistent with structural analyses based on the electronegativity theory, discussed above. Many of these chalcogenide glasses exihibit strong covalency, especially when sulfur and selenium elements are involved in the glass-forming network. However, the covalency begins to diminish in such glasses as sulfur or selenium is replaced by tellurium.

Amongst the chalcogenide glass structures, described schematically in Figures 1.15a–f, there is a further opportunity to modify the glass structure by incorporating monovalent cations that occupy the sites around divalent selenium, for example, and form a network terminating site, as do the alkali ions in an oxide matrix. One of the divalent bonds at selenium at the edge of the structure preferentially becomes more negative and allows monovalent cations, such thallium, caesium, potassium and rubidium to occupy sites and terminate the network (Figure 1.16a). The incorporation of smaller cations such as sodium and lithium in selenide and telluride glass networks is more difficult due to their respective ionic sizes than in the sulfide glasses. A corollary of the structural modification using monovalent cations is the incorporation of monovalent anions such as iodide in the form of iodine. Since the chalcogenide elements are divalent, the iodine can share one of the divalent bonds and terminate the network (Figure 1.16b).

Selected examples of the ternary chalcogenide systems are shown in Figures 1.17a–f, in each of which the composition range for stable glass formation is mapped for comparative purpose. The details of complementary compositions can be found elsewhere in the literature [74]. Each of these compositions, however, represents the type of structural modifications we have discussed above in Figures 1.15 and 1.16.

The homopolar character of Ge, As, S and Se elements predominantly determines the magnitude of glass-formation regions in the Ge-As-(S,Se) systems shown in Figure 1.17a. The extended region of glass formation dramatically reduces when Se or S in the above

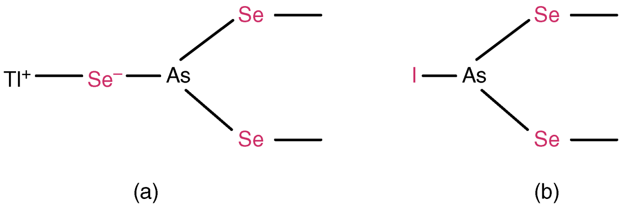

Figure 1.16 *Pictorial representation of structural modifications of an As-Se glass with monovalent ions: (a) thallium (Tl^+) and (b) iodine (I^-) anion [76] Source: Z. U. Borisova 1981. Adapted with permission from Plenum Press.*

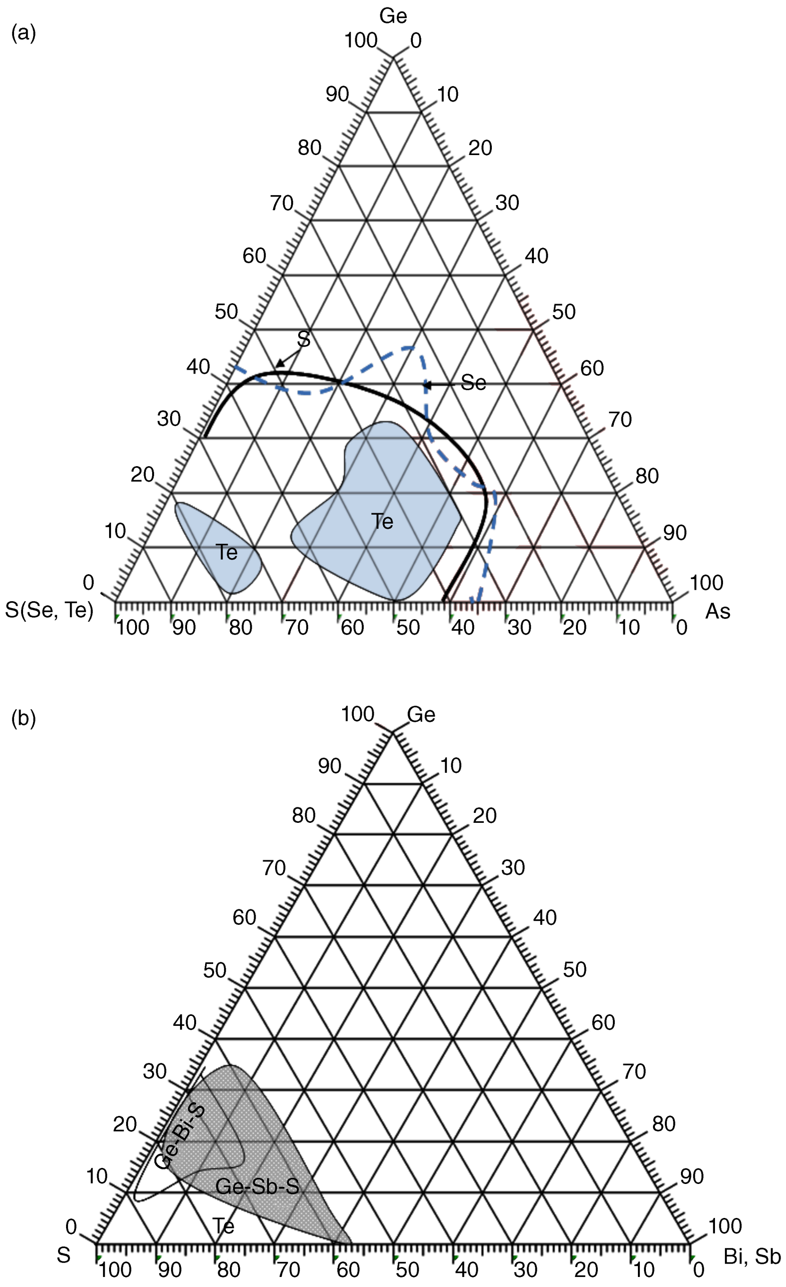

Figure 1.17 Glass-forming composition maps: (a) Ge-S-As represented by the black solid line; Ge-Se-As by the broken light grey line; and Ge-As-Te by the two shaded regions. (b) Ge-S-Bi is depicted by solid continuous line; Ge-Sb-S as the shaded area [76]. (c) Glass formation in Ge-(Ga,In)Se. (d) Ge-(Sn,Pb)-Se-As glass forming systems. (e) Glass formation in (SiGe)-(Se)-I showing different regions of stabilities. (f) Ge-(As,Pb)-Tl-Se-As glass forming systems with different regions of glassy phase [76]. Source: Z. U. Borisova 1981. Adapted with permission from Plenum Press.

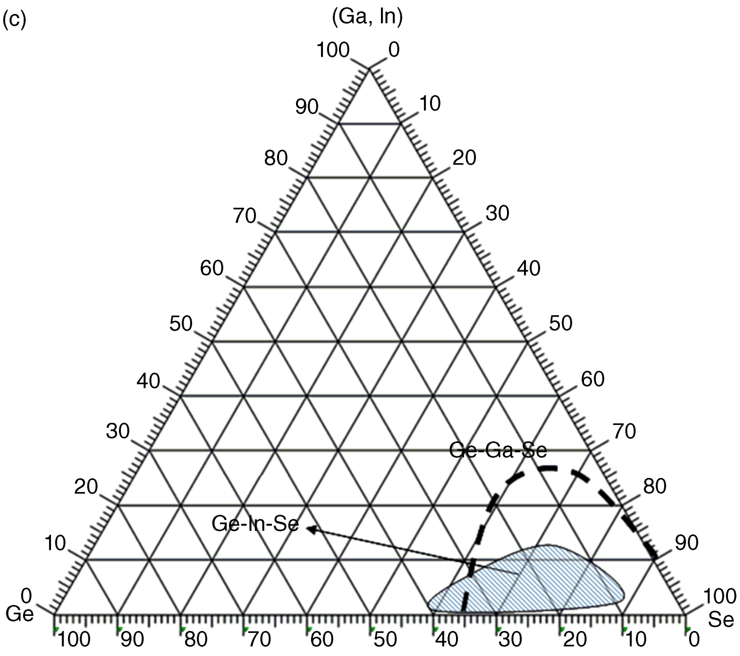

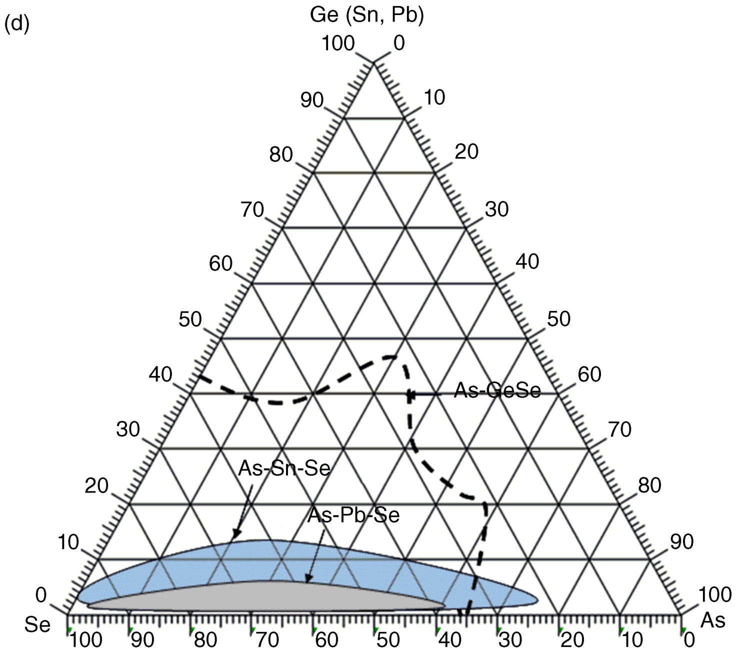

Figure 1.17 *(Continued)*

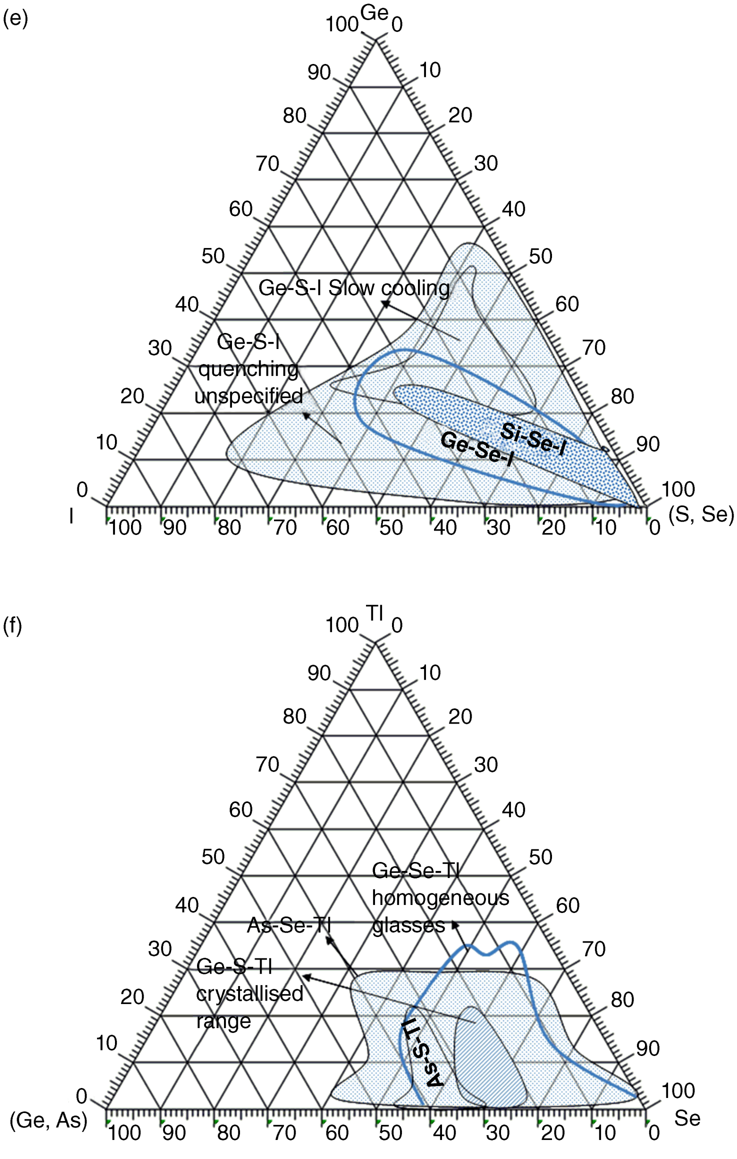

Figure 1.17 (Continued)

composition is wholly or partially replaced by Te, which is why in the Ge-As-Te system the region of glass-formation splits into two composition ranges. By contrast, in Figure 1.17b we see the influence of the lack of homopolar character of Bi and Sb on the glass-formation range in the (Bi,Sb-Ge-S) ternary, when As is replaced by Bi and Sb. The range of glass formation further reduces when Bi replaces Sb in the ternary, which may be attributed to the difference in the ionic or atomic radii of Bi and Sb.

The incorporation of gallium and indium as a third element in the Ge-Se binary, as shown in Figure 1.17c, introduces more ionic character, as opposed to homopolar bonding. The increase in ionicity is the consequence of a lack of sp^3 and sp^2 types of hybridization, which in the Ge-(Ga,In)-Se system can be increased by incorporating a proportionate amount of a group VB elements, namely P, As and Sb, so that the combination of III–V electronic hybridization yields an average of four electrons per sub-metallic element. Through this process of compositional modification, the sp^3 electronic hybridization may be enhanced in the glass structure.

As indicated in Figures 1.16a and b, the glass network sites in the chalcogenide structure encounter disruption when monovalent cations such as Tl^+ are incorporated into the glass-forming networks. Anions such as I^-, when they replace e.g. Se^{2-} in a chalcogenide structure, terminate the network sites. There is significant evidence from the composition map in Figure 1.17a that in the Ge-S-I ternary, although glass formation is more extensive than in either Ge-Se-I or Si-Se-I, the stable compositions requiring slow cooling are confined to a limited composition range. By contrast in Figure 1.17b, we see the influence of the lack of homopolar character of Bi and Sb on the glass-formation range in the (Bi, Sb-Ge-S) ternary, especially when Bi or Sb is replaced by As in Figure 1.17c. The range of glass formation further reduces when Bi replaces Sb in the ternary, which may be attributed to the difference in the ionic or atomic radii of Bi and Sb. The incorporation of gallium and indium as a third element in the Ge-Se binary, as shown in Figure 1.17d, introduces more ionic character, as opposed to the homopolar bonding. In Ge-Se-Tl the range of phase separation is quite apparent.

Although, potentially, several compositions might form glass by splat quenching in the chalcogenide systems, amongst the conditional glass-forming compositions the Ga_2S_3-La_2S_3 binary [77] (Figure 1.18) is the best known, especially due to the presence of La_2S_3,

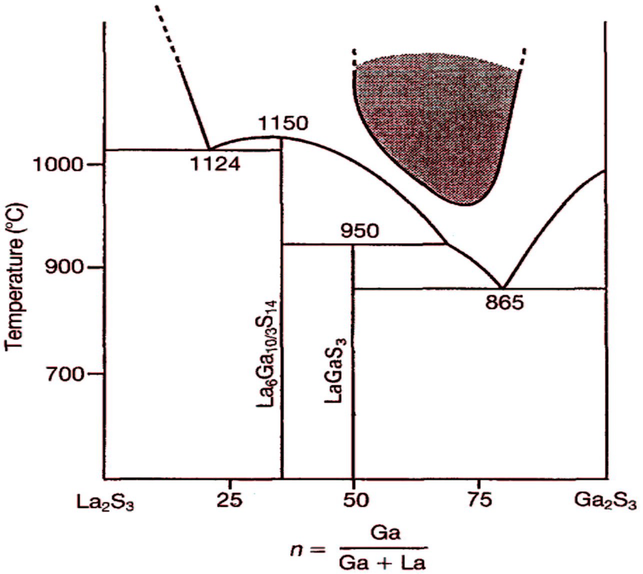

Figure 1.18 *Phase equilibrium boundaries and the glass-forming composition range in the Ga_2S_3-La_2S_3 binary system [77]. Source: Kumta, 1994. Reproduced with permission from Springer.*

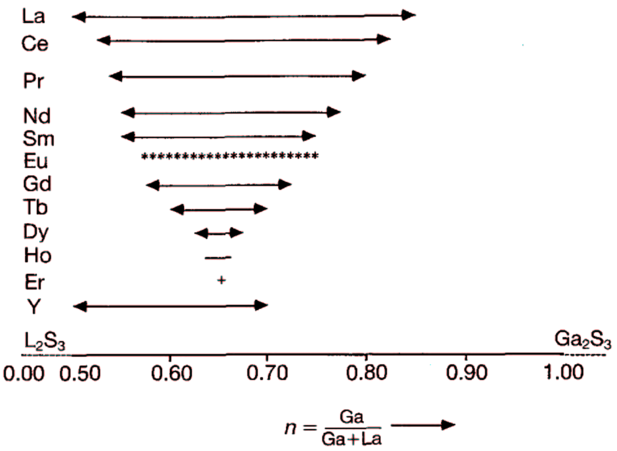

Figure 1.19 *Diagrammatic comparison of solubility limits of various lanthanides and yttrium (Y^{3+}) ions in the Ga_2S_3-La_2S_3 systems. Table 1.11 compares the ionic radii and atomic masses of various lanthanide elements [77]. Source: P. N. Kumta 1994. Reproduced with permission from Springer.*

which may be potentially substituted for other optically active rare-earth sulfides, as determined by the range of lanthanide sulfides investigated [78,79]. From these investigations, the trend in the solubility of rare-earth sulfides in the Ga_2S_3-La_2S_3 liquid seems to be quite size dependent, as shown in Figure 1.19, where we find that as the lanthanide ionic radius decreases with increasing atomic number the solubility range of rare-earth sulfide for glass formation also reduces. This decrease in solubility may be due to multiple co-ordination

Table 1.11 *Comparison of the ionic radii and atomic masses of lanthanide ions, indicating the contraction in ionic radius with increasing mass [80].*

Ionic radius (pm)	Atomic mass
$La^{3+} = 103.2$	138.905
$Ce^{3+} = 102$	140.116
$Pr^{3+} = 99$	140.907
$Nd^{3+} = 98.3$	144.242
$Sm^{3+} = 95.8$	150.360
$Eu^{3+} = 94.7$	151.964
$Gd^{3+} = 93.8$	157.250
$Tb^{3+} = 92.3$	158.925
$Dy^{3+} = 91.2$	162.500
$Ho^{3+} = 90.1$	164.930
$Er^{3+} = 89$	167.259
$Tm^{3+} = 88$	168.934
$Yb^{3+} = 86.8$	173.054
$Y^{3+} = 90$	83.905

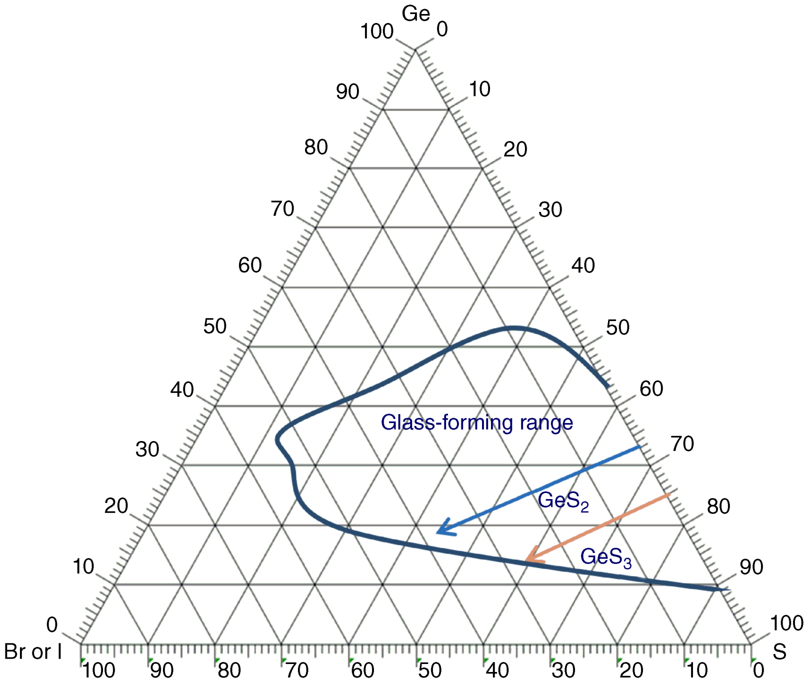

Figure 1.20 *Glass formation in the Ge-S-(Br,I) system, which falls between the GeS_2-GeS_3 binary Ge-S edge and extends towards the iodine anion (I^-) [82]. Source: S. A. Dembovskii 1971. Reproduced with permission from Springer.*

numbers (6–8) of higher lanthanides sulfides, compared with that of lower ones which have preferentially $z = 6$.

The multiplicity of co-ordination numbers in heavier lanthanides is reported by Wells [18b], where we find that the type C lanthanides (Er, Tm, Yb) may dwell in a large co-ordination field of up to eight by distorting the polyhedron. Since the gallium sulfide based structures are more ionic than the traditional sulfide, such distortions of co-ordination polyhedra might not be permissible due to geometrical constrains, which is why the heavier lanthanides tend to exhibit lower solubility in the gallium–lanthanum sulfide systems.

1.7.7 Chalcohalide Glasses

As discussed above from Borisova [74], the substitution of sulfur with iodine in a GeS_2 glass yields a non-bridging site where the iodide or bromide ions (I^- or Br^-) acts as bond terminators. Based on this model, Heo and Mackenzie [81] systematically examined the glass formation from an earlier investigation by Dembovskii *et al.* [82]. The S : I and S : Br ratio in the GeS_{2+X} (where $X = 0$ or 1) compositions were analysed and the resulting composition map is shown in Figure 1.20, in which the arrows depict the lines of constant Ge : S ratio, which vary between 2 and 3, corresponding to 66.7 and 75 at.% of S.

Many different types of chalcohalide glasses have been reported in the literature. A major review of compositions, properties and applications has been published by Sanghera and co-workers [83].

1.8 Conclusions

In this chapter the structural and thermodynamic background for the theory of glass formation is discussed along with examples that include both the covalent and ionic glasses. The compositions are discussed especially with reference to the known glass-forming range, which may be helpful for readers. Based on this background, in the following chapters the properties, fabrication and applications are discussed.

Selected Bibliography

1. A Paul, *Chemistry of Glasses*, 2nd edition (1990), Chapman and Hall (London).
2. S.R. Elliott (1984) *Physics of Amorphous Materials*, Longman.
3. A K Varsheneya, *Fundamentals of Inorganic Glasses*, 2nd edition, Society of Glass Technology (2006), Sheffield.
4. Z U Borisova, *Glassy Semiconductors* (Translated from Russian by J George Adhasko), Plenum Press (1981) New York.
5. R H Doremus, *Glass Science*, Wiley-Interscience, 1973 (1st Edition).

References

1. A. Paul (1982) *Chemistry of Glasses*, 2nd edn. Chapman & Hall, London, pp. 1–13.
2. J. Wong and C.A. Angell (1976) *Glass Structure by Spectroscopy*, 1st edn, Marcel Dekker, New York, ch. 1, pp. 1–51.
3. A.K. Varsheneya (2006) *Fundamentals of Inorganic Glasses*, 2nd edn, Society of Glass Technology, Sheffield, (a) pp. 281–283; (b) pp. 296–315.
4. S.R. Elliott (1984) *Physics of Amorphous Materials*, Longman.
5. A.E. Owen (1970) Semiconducting Glasses: Part-II on Properties and interpretations, *Contemporary Physics*, **11**, 257–286.
6. J. Jäckle (1986) Model of glass transition, *Reports on Progress in Physics*, **49**, 171–231.
7. W. Kauzmann (1948) The nature of glassy state and the behaviour of liquid at low temperatures, *Chemical Review*, **43**, 219–256.
8. O. Kubaschewski and C.B. Alcock (1979) *Metallurgical Thermochemistry*, 5th edn (Revised and enlarged), Pergamon Press, Oxford, pp. 268–339.
9. E.T. Turkdogan (1980) *Physical Chemistry of High-Temperature Technology*, Academic Press, London, (a) ch 1, pp. 5–25; (b) ch 2, pp. 26–35.
10. L.S. Darken and R.W. Gurry (1953) *Physical Chemistry of Metals*, McGraw Hill, New York.
11. R.A. Swalin (1972) *Thermodynamics of Solids*, Wiley-Interscience, New York.
12. F.D. Richardson (1974) *Physical Chemistry of Melts in Metallurgy*, Academic Press, London. (a) pp. 133–139; (b) pp. 205–213.
13. C.H.P. Lupis (1983) *Chemical Thermodynamics of Materials*, Elsevier Science Publishing Company.
14. M.F. Ding, J. Lau, and J.D. Mackenzie (1986) Halide glasses based on chloride, bromide and iodides, *Journal of Non-Crystalline Solids*, **80**, 538–542.

15. W.D. Kingery, H.K. Bowen and D.R. Uhlmann (1976) *Introduction to Ceramics*, 2nd edn, John Wiley & Sons, New York.
16. J. Hulme, A. Jha, J.M. Parker, and A. Whitehouse (1989) Formation of far-IR transmitting AgI-CsI glasses, *Physics and Chemistry of Glasses*, **30**, 254–259.
17. C. Brink, N.F. Binnendijk, and J. Van de Linde (1954) The crystal structures of $CsCu_2Cl_3$ and $CsAg_2I_3$, *Acta Crystallographica*, **7**, 176–180.
18. A. Wells (1962) *Structural Inorganic Chemistry*, 3rd edn, Clarendon Press, Oxford, pp. 863–865.
19. M. Matecki and M. Poulain (1988) Cadmium and lead fluoride glasses, *Materials Science Forum*, **32–33**, 167–172.
20. A. Jha and J.M. Parker (1990) Formation of CdF_2 mixed halide glasses, *Physics and Chemistry of Glasses*.
21. M. Poulain, M. Poulain, J. Lucas, and P. Brun (1975) Halide glasses, *Materials Research Bulletin*, **10**, 243–245.
22. T. Grande, S. Aasland, and S. Julsrud (1992) Phase equilibria in the ZrF_4-BaF_2 glass-Forming system, *Journal of Non-Crystalline Solids*, **140**, 73–76.
23. T. Grande, S. Aasland, and S. Julsrud (1993) Thermodynamics of ZrF_4-BaF_2-NaF glass-forming system, *Journal of Non-Crystalline Solids*, **161**, 86–90.
24. G. Hatem, M. Gaune-Escard, and M. Hoch (1993) Experimental thermodynamics and phase equilibria estimation in Zr-fluoride glasses, *Journal of Non-Crystalline Solids* **161**, 91–97.
25. M. Poulain (1991) Fluoride glass composition and processing, in *Fluoride Glass Fibre Optics* (eds I.D. Aggarwal and G. Lu), Academic Press, San Diego, ch 1, pp. 1–33.
26. J.M. Parker (1990) Properties of fluoride glasses, in *Fluoride Glass Optical Fibres*, Blackie, Glasgow and London, ch 2, pp. 32–37.
27. W.H. Zachariasen (1932) *Journal of the American Chemical Society*, **54**, 3841.
28. R.L. Mozzi and B.E. Warren (1969) The structure of vitreous silica, *Journal of Applied Crystallography*, **2**, 164–172.
29. Wikipedia (2015) Pauling electronegativity, http://en.wikipedia.org/wiki/Electronegativity#Pauling_electronegativity.
30. K.H. Sun (1947) *Journal of the American Ceramic Society*, **30**, 277.
31. H. Rawson (1967) *Inorganic Glass-forming Systems*, Academic Press, London, ch 1.
32. J.H. Simmons, C.A. Simmons and R. Ochoa (1991) Fluoride glass structure in *Fluoride Glass Fibre Optics* (eds I.D. Aggarwal and G. Lu), Academic Press, London, ch 2, pp. 1–33.
33. Y. Al-Douri, H. Abid, and H. Aourag (2000) Some empirical formulas for calculating the ionicity character in semiconductors. *Materials Chemistry and Physics*, **65**, 117–119.
34. R.E. Cohen and co-workers (June 1988) *Physica C: Superconductivity*, **153–155**, Part 1, pp. 202–203.
35. C. Quintanar and co-workers (2003) *International Journal of Quantum Chemistry*, **96**, 483–491.
36. J.C. Phillips (1974) *Bonds and Bands in Semiconductors*, Academic Press, San Diego.
37. A.R. West (1988) *Basic Solid State Chemistry*, John Wiley & Sons Ltd, Chichester, pp. 86–92.

38. D. Liu, S. Zhang, and Z. Wu (2003) Lattice energy estimation for inorganic ionic crystals. *Inorganic Chemistry*, **42**, 2465–2469.
39. V.D. Zhuralev (2007) Calculation of the bond ionicity in complex oxides. *Bullettin of the Russian Academy of Sciences, Physics*, **71** (No. 5), 681–685.
40. A.F. Kapustinskii (1956) *Quarterly Review of Chemical Society*, **10**, 283.
41. Z.J. Wu and S.Y. Zhang (1999) Semiempirical method for the evaluation of bond covalency in complex crystals. *Journal of Physical Chemistry A*, **103**, 4270–4274.
42. J.C. Phillips (1979) Topology of covalent non-crystalline solids I: Short-range order in chalcogenide alloys. *Journal of Non-Crystalline Solids*, **34**, 153–181; J.C. Phillips (1981) Topology of covalent non-crystalline solids II: Medium-range order in chalcogenide alloys and amorphous Si (Ge). *Journal of Non-Crystalline Solids*, **43**, 37–77.
43. Wikipedia (2015) http://en.wikipedia.org/wiki/Orbital_hybridisation.
44. S. Hampshire (2008) Oxynitride glasses. *Journal of the European Ceramic Society*, **28**, 1475–1483.
45. K. Liddell, H. Mandal, D.P. Thompson (1997) X-ray data for new Y-Si-Al-O-N glass ceramics. *Journal of the European Ceramic Society*, **17**, 781–787.
46. M.M. Imon and S.H. Risbud (1986) Oxycarbonitride glass formation by melt solidification. *Journal of Materials Science Letters*, **5**, 397–398.
47. O.V. Mazurin, M.V. Streltsina, and T.P. Shvaiko-Shvaikovskaya (1991) *Handbook of Glass Data Part D*, Physical Sciences Data 15, Elsevier Science Publishers B. V., Amsterdam.
48. W.H. Dumbaugh (1986) Heavy metal oxide glasses containing Bi_2O_3. *Physics and Chemistry of Glasses*, **27**, 119–123.
49. J.E. Stanworth (1952) *Tellurite glasses*, **Nature**, **169**, 581–582
50. M. Imaoka and T. Yamazaki (1975) Reports from Institute of Industrial Science, *University of Tokyo*, **24** (2), 80. M Imaoka and T Yamazaki (1976) Reports from Institute of Industrial Science, *University of Tokyo*, **26** (1), 4.
51. Y. Dimitriev, V. Dimitrov and M. Arnaudov (1979) Infrared spectra of related ceramic phases and glasses in the TeO_2-V_2O_5-Me_2O system. *Journal of Materials Science*, **14**, 723–727.
52. Y. Dimitriev, I. Ivanova, and E. Gatev (1981) Glass-formation in binary vanadate systems. *Journal of Non-Crystalline Solids*, **45**, 297–300.
53. W. Vogel, H. Buerger, G. Zerge, W. Mueller, and K. Forkel (1974) *Silicattech*. **26** (6) 205.
54. C.M. Baldwin and J.D. Mackenzie (1979) Fundamental condition for glass formation in fluoride systems. *J American Ceramic Society*, **62**, 537–538.
55. C.A. Angell and J. Wong (1970) Structure and glass transition thermodynamics of liquid zinc chloride from far-infrared, Raman, and probe ion electronic and vibrational spectra. *Journal of Chemical Physics*, **53**, 2053–2066.
56. M. Poulain (1981) Glass formation in Ionic systems. *Nature*, **293**, 279–280.
57. M. Poulain, M. Poulain, and G. Maze (1980) *French Patent* 80.06088.
58. J. Lucas, H. Slim, and G. Fonteneau (1981) New fluoride glasses based on 4f and 5f elements. *Journal of Non-Crystalline Solids*, **44**, 31–35.
59. M. Poulain (1983) Halide glasses. *Journal of Non-Crystalline Solids*, **56**, 1–14.

60. M. Poulain, M. Poulain, and M. Matecki (1982) Rare earths in fluoride glasses: The LnF_3-AlF_3-ThF_4-BaF_2 systems and related glasses. *Journal of Non-Crystalline Solids*, **51**, 201–215.
61. K.H. Sun (1949) Fluoride glasses. *US Pat.* 2,466,509 (5-4-49).
62. J.J. Videau, J. Portier, and B. Piriou (1979) Sur de nouveaux verres aluminofluorés, *Revue de Chimie Minerale*, **16**, 393–399.
63. J.J. Videau, B. Dubois, and J. Portier (1983) Indium fluoride based glasses. *Competes Rendus de l'Academie des Sciences Paris*, **297**, 483–485.
64. T. Kanamori and S. Sakaguchi (1986) Preparation of elevated NA Fluoride optical fibers. *Japanese Journal of Applied Physics*, **25**, L468–470.
65. T. Izumitani and M. Tsutome (1977) *US Patent application US* 05/819,440.
66. A. Mazuki (2003) PhD Thesis on Neodymium-doped AlF_3 based Glasses for Waveguide Engineering, University of Leeds.
67. L. Santos, L.F. Santos, R.M. Almeida, V.K. Tikhomirov, and A. Jha (2001) Raman spectra and structure of fluoroaluminophosphate glasses. *Journal of Non-Crystalline Solids*, **284** (1–3), 43–48.
68. A. Mazuki and A. Jha (2007) Effect of Pb-ions on the kinetics of devitrification and viscosities of AlF_3-based glasses for waveguide fabrication. *Journal of Non-Crystalline Solids*, **353**, 1283–1286.
69. K.H. Jack (1976) Sialons and related nitrogen ceramics. *Journal of Materials Science*, **11**, 1135–1158.
70. G. Leng-Ward and M.H. Lewis (1989) Oxynitride glasses and their glass-ceramic derivatives, in *Glass and Glass Ceramics* (ed M. H. Lewis), 1st edn, Chapman & Hall, London, ch 4, pp. 106–153.
71. S. Hampshire, E. Nestor, R. Flynn, J.-L. Besson, T. Rouxel, L. Mercier, P. Goursat, M. Sebai, D.P. Thompson, and K. Liddell (1994) Yttrium oxynitride glasses: properties and potential for crystallisation to glass-ceramics oxynitride glasses. *Journal of the European Ceramic Society*, **14**, 261–273.
72. W.T. Young, L.K.L. Falk, H. Lemercier, V. Peltier-Baron, Y. Menke, and S. Hampshire (2000) The crystallization of the yttrium-sialon glass: $Y_{15.2}Si_{14.7}Al_{8.7}O_{54.1}N_{7.4}$. *Journal of Non-Crystalline Solids*, **270**, 6–19.
73. N.F. Mott (1977) Electrons in glass. *Contemporary Physics*, **18**, 225–245.
74. S.R. Ovshinsky (1968) Reversible electrical switching phenomena in disordered structures. *Physical Review Letters*, **21** (Issue 20), 1450–1453.
75. J. deNeufville, S.C. Moss, and S.R. Ovshinsky (1971) Rapid reversible light-induced crystallization of amorphous semiconductors. *Applied Physics Letters*, **18**, 254–257.
76. Z.U. Borisova (1981) *Glassy Semiconductors*, Plenum Press, New York, pp. 1–35.
77. P.N. Kumta and S.H. Risbud (1994) Rare-earth chalcogenides – an emerging class of optical materials. *Journal of Materials Science*, **29**, 1135–1158.
78. L. Cervinka and A. Hruby (1982) Structure of amorphous and glassy Sb_2S_3 and its connection with the structure of As_2X_3 arsenic chalcogenide glasses. *Journal of Non-Crystalline Solids*, **48**, 231–264.
79. A.M. Loireau-Lozac'h, M. Guittard, and J. Flahaut (1977) L_2S_3-Ga_2S_3 systems (L= La, Ce, Dy, Er and Y). *Materials Research Bulletin*, **12**, 881.

80. A. Wells (1962) *Structural Inorganic Chemistry*, 3rd edn, Clarendon Press, Oxford, pp. 464–467.
81. J. Heo and J.D. Mackenzie (1989) Chalcohalide glasses: synthesis and properties of Ge-S-Br and Ge-S-I glasses. *Journal of Non-Crystalline Solids*, **111**, 29–35.
82. S.A. Dembovskii, V.V. Kirilenko and Yu.A. Buslaev (1971) Vitrification in Ge-S-I system, *Izvestiya Akademii Nauk SSSR, Neorg, Materialy*, **7**, 328.
83. J.S. Sanghera, J. Heo, and J.D. Mackenzie (1988) Chalcohalide glasses, *Journal of Non-Crystalline Solids*, **103**, 155.

2

Glass Structure, Properties and Characterization

2.1 Introduction

As discussed in Chapter 1 there is not yet a single theory that is able to predict the glass formation in materials under specified thermal or chemical conditions. In Chapter 1 we discussed (i) the structural theory of glass formation, proposed by W.H. Zachariasen [1] in 1932; (ii) the thermodynamic approach for glass formation using the partial molar properties of solutions and solids involved in constituting a solution; and (iii) the electronegativity and co-ordination theory, which also formed the basis for the bond strength criterion of K.H. Sun [2] published in 1947. In our discussion we explained, however, that amongst various theories of glass formation the kinetic theory of glass formation, originally proposed by Turnbull and Cohen [3] in 1960 and further expanded by Uhlmann [4] for determining the critical cooling rate remains the most widely adopted approach for predicting glass formation. The kinetic theory is also relevant in the engineering of thin films by vapour phase quenching and in glass-ceramic engineering.

2.1.1 Kinetic Theory of Glass Formation and Prediction of Critical Cooling Rates

Glass formation is intrinsically a kinetic phenomenon, in the sense that any liquid will yield a non-crystalline solid (NCS) if quenched quickly enough. The basic postulate of the kinetic theory is that in principle any material can be made from the melt into a glass, if the melt is cooled to a temperature below T_g so quickly that crystallization is almost prevented or bypassed kinetically. For example, through a eutectic composition as shown in Figures 1.3 and 1.5a,b, until a temperature below T_g is reached so quickly that crystallization is prevented or bypassed to reach any of the higher energy states A_1, A_2 and A_3, as shown in Figure 1.1. The process of vitrification is therefore kinetically controlled. To analyse the kinetic path permitting glass formation, *a minimum cooling rate* is required, which energetically allows the liquid–crystalline phase transformation to be bypassed. For this transformation bypass to happen, it is essential to consider two most

---

Inorganic Glasses for Photonics – Fundamentals, Engineering and Applications, First Edition. Animesh Jha.
© 2016 John Wiley & Sons, Ltd. Published 2016 by John Wiley & Sons, Ltd.

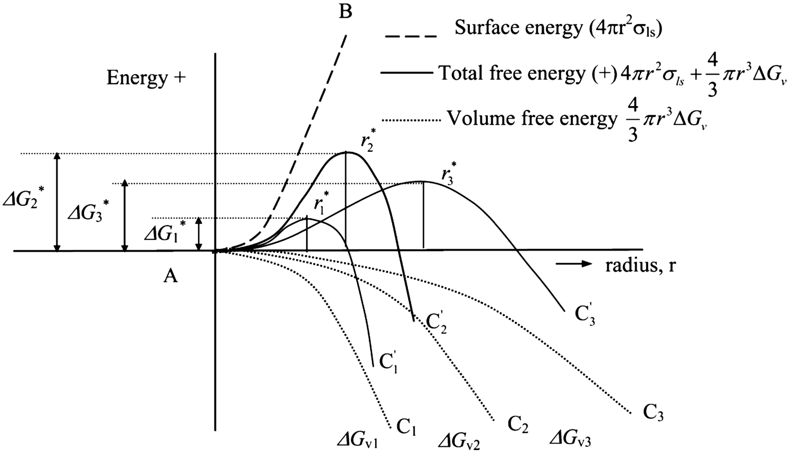

Figure 2.1 *Plots of volume ΔG_V, surface σ_{ls} and the sum ΔG^* of free energies as a function of the radius of nuclei in a super or undercooled liquid or in an amorphous matrix. Three different variations of the ΔG_V yield corresponding critical radii for a given σ_{ls}. The value of r_3^* is the largest for a slowly increasing ΔG_V curve, C_3 [6]. Source: X. Liu 2005. Reproduced with permission from Materials Research Society, Cambridge University Press.*

important factors that lead to the formation of metastable and thermodynamically stable crystalline phases. These factors are the *nucleation* of nano-scale crystallites at the liquid–crystal phase boundary which then subsequently *grow three dimensionally at a uniform rate*. The mass transport across the liquid–solid interface is determined by mass diffusivity which is defined by viscosity of the liquid at the interface, assuming the Stoke–Einstein model. Determination of the overall rate of liquid to crystal phase transformation using the rates of nucleation and crystallization from the melt will lead to an estimate of a *critical cooling rate* necessary for glass formation.

2.1.2 Classical Nucleation Theory

Using the classical nucleation theory (CNT) [5], when a liquid matrix/crystal nucleus interface is formed, with interfacial energy σ_{ls}, for spherical nuclei with a radius r, the corresponding change in the total Gibbs (ΔG_T) energy of the liquid–crystalline system is given by:

$$\Delta G_T = 4\pi r^2\sigma_{ls} + \tfrac{4}{3}\left(\pi r^3 \Delta G_V\right) \tag{2.1}$$

where ΔG_v represents the volumetric Gibbs energy change, which is always a negative quantity for a phase transformation reaction in which the equilibrium is shifted in the forward direction of lower energy than the starting state. By creating nuclei, new surfaces form by compensating against the positive term in Equation 2.1. Figure 2.1 [6] summarizes the variation of total Gibbs energy (ΔG_T) as a function of radius of a nucleus, which has a maximum value at $r = r^*$, where the energy is maximum with a value:

$$\Delta G^* = \frac{16}{3}\left[\frac{\pi\sigma_{ls}{}^3}{(\Delta G_v)^2}\right] \tag{2.2}$$

For a degree of *supercooling* $\Delta T_m = T_f - T$, it can be shown from Equation 2.2 that the Gibbs energy for a critical nucleus at r^* is:

$$\Delta G^* = \frac{16}{3}\left[\frac{\pi\sigma_{ls}^3(T_f)^2}{(\Delta H_f \Delta T_f)^2}\right] \tag{2.3}$$

where ΔH_f is the enthalpy of fusion of a congruent compound with a melting point T_m.

From Figure 2.1 further qualitative insight can be gained for glass formation, especially for the sol–gel method in which the surface energy (σ_{ls}) plays an important role by raising the barrier for nucleation (ΔG^*). The high surface energy stored in the sol–gel glass becomes apparent when it starts annealing at a much lower temperature than its high-temperature melt quenched counterpart. The value of the Gibbs energy barrier (ΔG^*) begins to decrease towards more negative values beyond $r = r^*$, suggesting that the supercritical nuclei with $r \geq r^*$ are likely to grow by lowering the overall energy of system.

The rate of *homogeneous* nucleation (I_v) (or the number of supercritical nuclei formed per unit volume and per unit time) is a product of two probability factors: thermodynamic and kinetic barriers. The thermodynamic barrier is defined by the magnitude of (ΔG^*) whereas the kinetic barrier has an activation energy (ΔG_D), which is a measure of the energy barrier against the flow of atoms or molecules present at the liquid–solid interface, and then:

$$I_V = A_o \exp\left[-\frac{(\Delta G^* + \Delta G_D)}{\kappa_B T}\right]^* \tag{2.4}$$

where:

$$A_o \exp\left(-\frac{\Delta G_D}{\kappa_B T}\right)$$

represents the kinetic barrier for nucleation at the liquid–solid interface experiencing an activation energy barrier of the magnitude $\exp(-\Delta G_D/RT)$. The kinetic barrier can be approximated by the Stoke–Einstein equation, which then replaces the $A_o\exp(-\Delta G_D/\kappa_B T)$term with the diffusivity (D), which is inverse of the viscosity (η):

$$D = \frac{\kappa_B T}{3\pi\lambda\eta}$$

for a spherical object.

The main assumption here is that we consider a steady state nucleation rate in which A_0 is a pre-exponential term, expressed in terms of temperature (T), Boltzmann (κ_B) and Planck (h) constants, interfacial surface concentration (n_s, number per unit volume) and the liquid–crystal interfacial energy (σ_{ls}) per unit area and molar volume (V): $A_o = \frac{2n_s(V)^{\frac{1}{3}}(\sigma_{ls}k_B T)^{0.5}}{h} \approx \frac{n_s\kappa_B T}{h}$

Therefore, by rearranging Equation 2.4 the rate of homogeneous nucleation is:

$$I_v = \frac{n_s\kappa T}{3\pi\lambda^3\eta}\exp\left[-\frac{\Delta G^*}{RT}\right] \tag{2.5}$$

or:

$$I_V \cong \frac{B_o}{\eta}\exp\left[-\frac{\Delta G^*}{RT}\right] \tag{2.6}$$

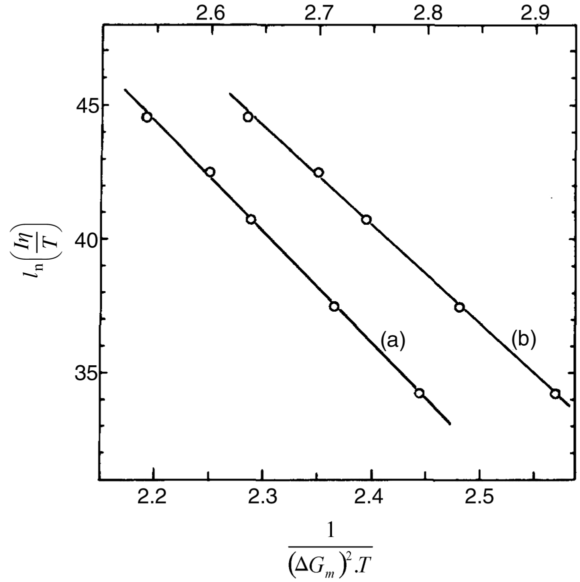

Figure 2.2 Plot of nucleation rate parameters, shown in Equation 2.6, for determining the barrier for homogeneous nucleation in a lithium silicate glass [7]. Source: E. D. Zanotto 1985. Reproduced with permission from Elsevier Limited.

where I_v is expressed in terms of number per unit volume per second (m^{-3} s^{-1}). If the experimental data for I_v, η and ΔG_m are available, then a plot of ln $(I\eta/T)$ against $1/(\Delta G_m)^2T$ should be a straight line, as shown in Figure 2.2, with a slope and an intercept that, respectively, yield the values of σ_{ls} and B_o. It turns out that this theoretical value of B_o is often many orders of magnitude higher than the theoretical limit. So far, the reason for this discrepancy in the value of the pre-exponential term in Equation 2.6 remains unresolved! [7]

A vast majority of known glass-forming systems do not follow the CNT and depict far more complex behaviour than explained above. The departure from CNT arises for two main reasons, the *first* of which is a *non-steady state nucleation* in which the equilibrium size distribution of embryonic nuclei in the supercooled liquid is not achieved immediately at a given annealing temperature for a nucleation experiment. Consequently, there is an induction period before reaching the steady state distribution of nuclei. The duration of the induction time decreases with annealing temperature and vice versa. The overlap of induction period with the glass transformation range makes the situation far more complex; the only way to solve this overlap is to anneal a quenched glass for long enough. For reliable analysis of nucleation rate, the separation of nucleation from the thermodynamic transients of glass transition temperature is essential, for the definition of Gibbs energy (ΔG_m), which is dependent on the standard state.

2.1.3 Non-Steady State Nucleation

In a treatise on "volume nucleation in silicate glasses" authored by James [8] the analytical treatment for non-steady state nucleation I' at time t, modelled by Kashchiev [9], is explained in terms of an infinite series:

$$\frac{I'}{I} = 1 + 2\sum_{n=1}^{\infty}(-1)^n \exp\left(-\frac{n^2 t}{\tau}\right) \tag{2.7}$$

where τ defines the incubation or induction time and n is an integer. The time dependent number of nuclei $N(t)$ at time t is then expressed by Equation 2.8:

$$\frac{N(t)}{I\tau} = \frac{t}{\tau} - \frac{\pi^2}{6} - 2\sum_{n=1}^{\infty}\left[\frac{(-1)^n}{n^2}\right]\exp\left(-\frac{n^2 t}{\tau}\right) \tag{2.8}$$

For $t > 5\tau$ Equation 2.8 reduces to a simple linear relationship for $N(t)$ and τ:

$$\begin{aligned} N(t) &= I\left[t - \frac{\pi^2\tau}{6}\right] \\ \tau &= \frac{48\sigma_{\mathrm{sl}}(\lambda)^5\eta}{\pi V^2(\Delta G_{\mathrm{v}})^2} \end{aligned} \tag{2.9}$$

From Equation 2.9 it is apparent that the incubation period before the steady state nucleation is proportional to the viscosity of supercooled liquid, which also explains the importance of annealing to avoid overshot of the glass transition temperature with the steady state nucleation rate. This overlap is commonly seen in metallic and alloy glasses that are specially produced via rapid quenching. Notably, despite the complex nature of the mathematical treatment for the transient nucleation, the dependence of τ on viscosity is not so straightforward, as noted by James [8].

2.1.4 Heterogeneous Nucleation

The *second* complexity in nucleation may arise from preferential surface nucleation due to the lowering of interfacial energy (σ_{sl}) of the liquid–solid interface due to a favourable wetting condition, which lowers the wetting angle for nucleation on a substrate. As a result the barrier for nucleation, $(\Delta G^*)_{\mathrm{het}}$ decreases dramatically with respect to (ΔG^*) by a factor of:

$$f(\theta) = \frac{(2 - 3\cos\ \theta - \cos{}^3\theta)}{4}$$

Here θ is the contact angle between the crystalline nucleus and the substrate, which for $0 \leq \theta \leq \pi = 180°$ yields $f(\theta) < 1$. In addition, further complexity in the interfacial energy arises due to the shape factor (convex and concave), which may increase or decrease, respectively, the value of $(\Delta G^*)_{\mathrm{het}}$, as was identified by Fletcher [10].

Whether the process of nucleation is controlled by homogeneous or heterogeneous means, it will have a maximum, at which the rate peaks, as shown in Figures 2.3 for two different types of silicate glasses, in which the volume nucleation rates near their peak temperatures differ by three orders of magnitude between lithium and barium disilicates. The temperature at which the maximum occurs in a large number of glass-forming silicates is summarized in Table 2.1.

The detailed characteristic temperatures for the disilicates discussed above are summarized in Table 2.1.

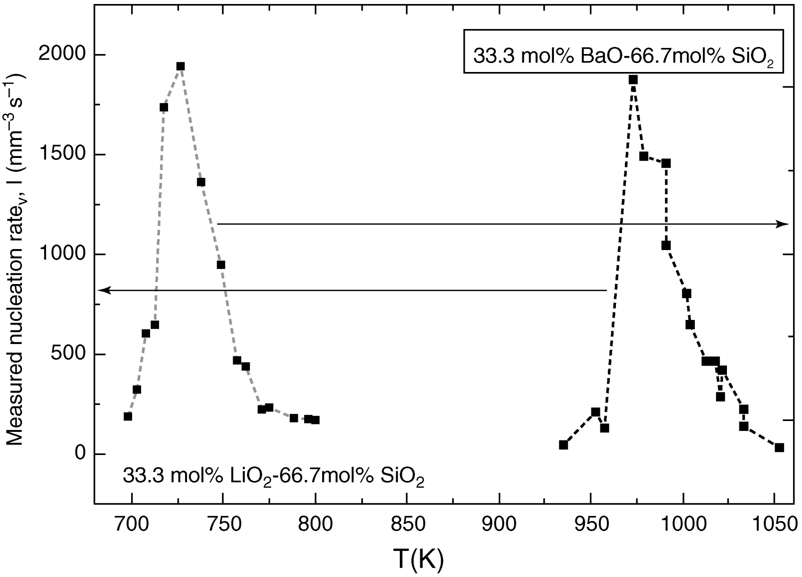

Figure 2.3 *Plot of measured nucleation rates in silicate glasses: (a) 33.3 mol.% BaO–66.7 mol. Source: E. D. Zanotto 1985. Reproduced with permission from Elsevier Limited. % SiO_2, (b) 33.3 mol.% Li_2O–66.7 mol.% SiO_2 [7,11]. Source: P. F. James 1974. Reproduced with permission from Taylor & Francis.*

2.1.5 Nucleation Studies in Fluoride Glasses

A limited amount of measurements on the nucleation kinetics in ZrF_4-based glasses were carried out by Drehman [12], Lu *et al.* [13] and Schneider and Staudt [14], which were analysed theoretically [15] and then compared with the standard classical model without utilizing knowledge of the thermodynamic parameters for the liquid and crystalline solids. The temperature range of nucleation rates in a ZrF_4 based glass is shown in Figure 2.4, where the predicted values are offset from the measured rates, because of the assumptions made in the value of ΔG_m. A set of measured data are also compared in Reference [16] which largely agree with the theoretical analysis presented in Figure 2.4, showing that the nucleation in ZBLAN begins at a much lower temperature than theoretically feasible, suggesting that the measured data might be influenced by heterogeneous nucleation process.

The conclusions made from the analysis were found to be similar to what has been classically observed in numerous silicate glasses. The following common features have been found from the nucleation studies in silicates and in a limited number of fluorides [7,8,12–14]:

(a) The values of pre-exponential (B_o) in Equation 2.6 derived from the experimental data in a large majority of glass-forming systems were found to be many orders of magnitude larger than that predicted from the theory.

(b) The temperature maxima in measured nucleation rates in oxide and fluoride glasses were found to be in the region of 0.5–0.6 of the melting point (T_m).

Table 2.1 *List of significant characteristic temperatures of network forming glasses and their reduced glass (T_g/T_f) and reduced maximum (T_{max}/T_f) temperatures for estimating the volume nucleation temperature range [8].*

Compositions of glass (mol.%)	T_g (K)	T_f (K)	T_{max} (K)	T_g/T_f	T_{max}/T_f
(a) Volume and surface nucleation					
$33.3Li_2O$-$66.7SiO_2$	727	1298	727	0.56	0.56
$40Li_2O$-$60SiO_2$	716	1403	748	0.51	0.53
$45Li_2O$-$55SiO_2$	711	1451	—	0.49	—
$48Li_2O$-$52SiO_2$	706	1470	—	0.48	—
$33.3BaO$-$66.7SiO_2$	962	1687	973	0.57	0.58
$37.5BaO$-$62.5SiO_2$	963	1720	983	0.56	0.57
$16.7Na_2O$-$33.3CaO$-$50SiO_2$	838	1552	868	0.54	0.56
$33.3Na_2O$-$16.7CaO$-$50SiO_2$	743	1457	778	0.51	0.53
$50Na_2O$-$50SiO_2$	683	1366	733	0.5	0.54
$50CaO$-$50SiO_2$	1030	1807	1053	0.57	0.58
$50SrO$-$50SiO_2$	1024	1862	—	0.55	—
$33.3Li_2O$-$66.7B_2O_3$	758	1184	—	0.64	—
(b)Surface nucleation only					
$33.3Na_2O$-$66.7SiO_2$	726	1134	—	0.64	—
$33.3K_2O$-$66.7SiO_2$	760	1310	—	0.58	—
$25CaO$-$25Al_2O_3$-$50SiO_2$	1110	1820	—	0.61	—
$25CaO$-$25MgO$-$50SiO_2$	1022	1675	—	0.61	—
$16.7BaO$-$33.3CaO$-$50SiO_2$	1015	1611	—	0.63	—
$50BaO$-$50B_2O_3$	833	1366	—	0.61	—
$50Li_2O$–$50B_2O_3$	695	1139	—	0.61	—
$50CaO$–$50P_2O_5$	769	1261	—	0.61	—
$50BaO$-$50P_2O_5$	742	1142	—	0.65	—

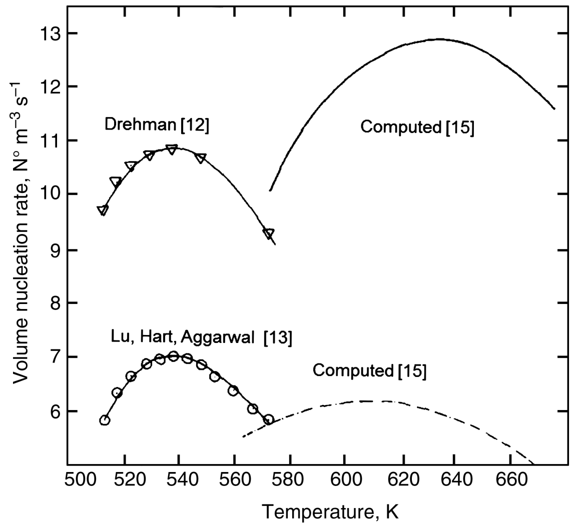

Figure 2.4 *Comparison of measured and computed nucleation rates in a zirconium fluoride (ZBLAN) glass [12–15]. Source: A. J. Drehman 1987. Reproduced with permission from Elsevier.*

(c) Within the limits of experimental error in nucleation rate and in the measured viscosity, the derived values of thermodynamic barrier vary in the region of 25–32$\kappa_B T$. The limited amount of data in fluoride glasses also fall in this regime.
(d) In the context of temperature dependence of surface energy, it is rather difficult to ascertain the contribution of heterogeneous nucleation in an overall nucleation process. However, the CNT model can be largely employed for estimating and comparing the nucleation rates.

It is evident from the literature that there is little information on the nucleation rates in any other types of glasses, which makes overall analysis harder to apply for all kinds of photonic glasses. Indeed the analytical tools discussed above form the basis for engineering transparent glass ceramics for a range of optical and photonic applications.

2.1.6 Growth Rate

Once the nuclei have formed during crystallization, growth occurs above the glass transition temperature until the melting begins. From the classical growth model [17], the growth rate (U_c) of crystals may be expressed by a general form of Equation 2.10, using the Stoke–Einstein model for diffusion growth of a spherical solid with diameter a_o submerged in a viscous medium with an apparent viscosity of η. The number of atoms crossing the liquid–crystal phase boundary is ν, which then may be defined by Equation 2.11. In Equation 2.10, f is the fraction of sites occupied at the crystal–liquid interface by the atoms from the undercooled liquid, ΔG is the Gibbs energy change for liquid–crystal phase transformation, and is dependent on the entropy of fusion, ΔS^{f}. The terms T and k_B are the temperature on the absolute scale and the Boltzmann constant:

$$U_C = f\nu a_o \left[1 - \exp\left(-\frac{\Delta G}{k_B T}\right)\right] \tag{2.10}$$

$$\nu = \frac{k_B T}{3\pi (a_o)^3 \eta} \tag{2.11}$$

The growth rate of nuclei may also depend upon the nature of the interface, i.e. whether the crystal/liquid phase boundary is rough or smooth. For a rough interface, the growth velocity is higher because $f \rightarrow 1$; in the case of a facetted interface, i.e. one which is assisted by the presence of screw dislocations [17], the value of f cannot be considered equal to 1, but it is approximated as shown in Equation 2.12:

$$f \approx \frac{\Delta T}{2\pi T_f} \tag{2.12}$$

Considering a Taylor series expansion of Equation 2.10 and ignoring higher order terms other than the first order ($\Delta G \ll k_B T$), and substituting Equations 2.11 and 2.12 in the resultant form, we find that:

$$U_C \approx f\nu a_o \left[\left(\frac{\Delta G}{k_B T}\right)\right] \tag{2.13}$$

By substituting the value of $\Delta G = \Delta S_f (T_f - T)$, we find that the growth velocity for the facetted interface is proportional to $(\Delta T)^2$ whereas for a rough interface growth the dependence is proportional to ΔT only. On the other hand, for large undercooling ($\Delta G \gg k_B T$), the growth velocity (U_c) tends to be equal to:

$$U_c \to \frac{k_B T}{3\pi(a_o)^2} \frac{1}{\eta} \tag{2.14}$$

These mathematical considerations are relevant in the engineering of micro- and nanocrystalline phases in a glass matrix, for engineering a transparent medium with minimum light scattering. Importantly, facetted crystal growth is invariably associated with the peritectic reaction in a phase constitution diagram, which involves a solid phase reacting with a liquid in equilibrium, resulting in the formation of a new solid phase. A classic example is the formation of mullite ($3Al_2O_3.2SiO_2$) rod-like crystals via a peritectic reaction from aluminium silicate liquid containing 40 mol.% Al_2O_3 and solid alumina. There are many examples in the glass and ceramic literature, which may be exploited in engineering glass ceramic materials for waveguiding [18,19] and fibre engineering applications [20]. The aspects of controlling nucleation and growth [18,19] in situ in glass-ceramic fibres for light amplification are discussed later in this book, to show the differences between the spectroscopic properties of the host glass and the glass-ceramics for active optics applications.

2.1.7 Combined Growth and Nucleation Rates, Phase Transformation and Critical Cooling Rate

Figure 2.5 shows the temperature range over which the crystal growth and nucleation dominate. It is apparent from this figure that the crystal growth rate, like nucleation, goes through a maximum and becomes negligible for large undercooling, at which point the nucleation rate begins to dominate. In Figure 2.5 a schematic representation of the

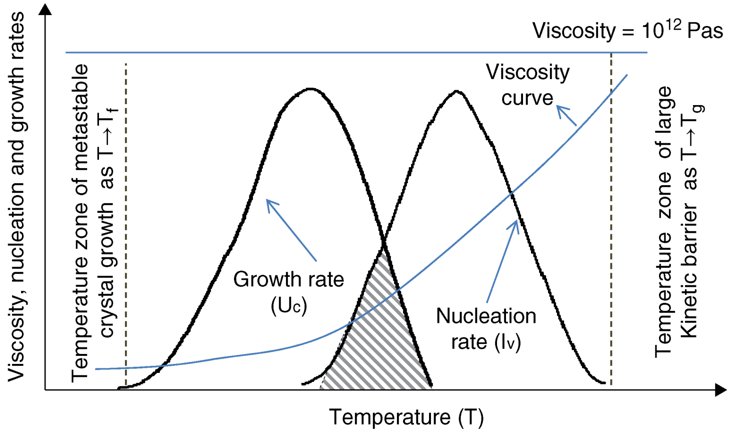

Figure 2.5 Schematic plot of the temperature dependence of the growth (U_c) and nucleation (I_v) rates in a glass-forming liquid between the melting point (T_f) and glass transition (T_g). The shaded triangle in the middle between I_v and U_c is the region where both the nucleation and growth rates dominate. The viscosity of a glass forming liquid is superimposed onto this graph, depicting the region of structural change where there is a change in the slope of the viscosity-temperature curve.

temperature dependence of viscosity is also superimposed for those liquids, which may be classed as a "fragile liquid", in which there is a strong temperature dependence of viscosity that cannot be described by a single exponential (Arrhenius type) relationship. The shaded region in Figure 2.5 shows the temperature range where both the nucleation and growth dominate, and it is this temperature range where, roughly, the vast majority of interesting "non-silicate" glass-forming liquids encounter crystallization during engineering of wave-guide and fibre based materials. It is for this reason that a critical analysis of the rates of crystal nucleation and their subsequent growth rate must be analysed a priori, to minimize the loss of guided light through scattering from crystals present in glass and glass-ceramic media.

The volume fraction (V) of crystals formed during a thermal annealing or a quenching process above the glass transition temperature can be quantified using the Johnson–Mehl–Avrami [21] equation, which is based on the assumption that there are pre-existing nuclei growing uniformly in all three dimensions. The model also assumes that the growing nuclei do not impinge on each other, which suggests that spatially two growing nuclei are far apart and, therefore, they grow unhindered. Using this model the minimum critical cooling rate (CCR) for a given volume fraction of crystals can be estimated from the following equation:

$$V = 1 - \exp\left[-\frac{\pi}{3}\left(I_{\mathrm{v}} U_{\mathrm{c}}^{3}\right) t^{4}\right] \approx \frac{\pi}{3} I_{\mathrm{v}} U_{\mathrm{c}}^{3} t^{4} \tag{2.15}$$

The quenching path defining the CCR is tangential to the nose of a time–temperature–transformation (t-t-t) curve, shown schematically in Figure 2.6 for a volume fraction of crystals, which is typically 10^{-6} for a glass-forming condition.

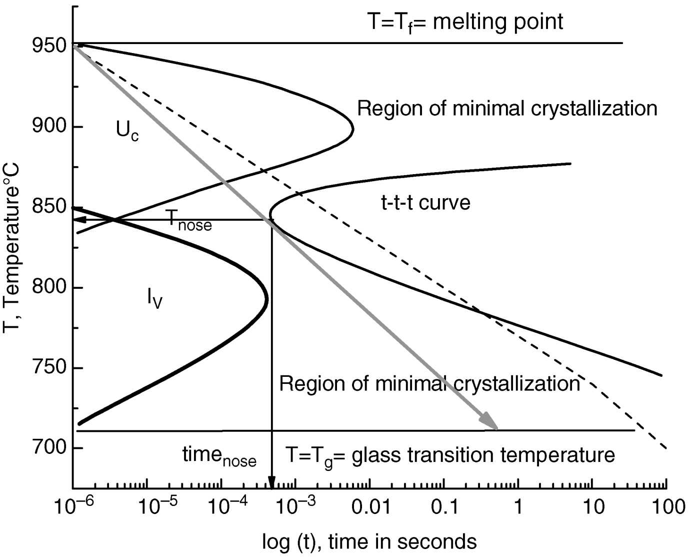

Figure 2.6 Comparison of the nucleation (I_V) and growth (U_C) rates with the time–temperature–transformation (t-t-t) curve for a glass-forming liquid. Above and below the t-t-t curve are the regions of minimal crystallization due to the limitations of crystal growth and nucleation, respectively. The nose of the t-t-t curve defines the minimum cooling rate along the tangent, required to form a specified volume fraction of crystals within the glass-forming liquid. The dotted curve cuts through the t-t-t curve and represents another rate that is much slower cooling rate than CCR.

In Figure 2.6, the CCR is defined by the tangent at the nose (T_{nose}, t_{nose}) of the t-t-t curve, which is determined by $(dT/dt)_c$ as the *slope* of the line drawn between T_m and T_{nose}:

$$\mathrm{CCR} = \left(\frac{\mathrm{d}T}{\mathrm{d}t}\right)_{\mathrm{C}} \approx \frac{\Delta T_{\mathrm{nose}}}{t_{\mathrm{nose}}} = \frac{T_{\mathrm{f}} - T_{\mathrm{nose}}}{t_{\mathrm{nose}}} \tag{2.16}$$

which means that, when the melt reaches T_n after a cooling time t_n, the crystallized fraction will not exceed the chosen value of V. The continuous cooling condition, however, corresponds to lower values of V than the calculated CCR and easier vitrification. In practice, the "melting" temperature, T_f, may actually be well over T_L, thus increasing the estimated CCR value.

Note that in Figures 2.5 and 2.6 the change in the viscosity of glass-forming liquid and the critical range in liquid-to-crystal formation, shown by shaded triangle in Figure 2.5, approximately coincide with the nose of the t-t-t curve. The temperature ratio of T_f and T_{nose} often varies between 0.7 and 0.8 for a large number of inorganic glass-forming liquids. In general, glass formation will be favoured by its resistance to overall crystallization, implying that the following features may be considered for optical materials engineering:

(i) a cooling rate that is at least equal to CCR;
(ii) minimal nucleation and growth in the critical temperature range, which may be possible by engineering compositions that depict a high viscosity in the T_{nose} region;
(iii) the absence of heterogeneous nucleation sites;
(iv) a large liquid–crystal interfacial energy, σ_{sl};
(v) in multicomponent systems, the existence of a deep eutectic liquid may help in bypassing both the nucleation and growth and lead to glass-formation by following a critical cooling path.

In Table 2.2 the known values of CCRs are compared for various glass-forming liquids.

Table 2.2 *Summary of measured and estimated critical cooling rates for different inorganic glass-forming compounds [17,22–25]. Source: W. D. Kingery 1976. Adapted with permission from John Wiley & Sons.*

Glass composition (mol.%)	Measured		Estimated	
	Homogeneous nucleation, CCR (°C s^{-1})	Heterogeneous nucleation at contact angle θ, CCR (°C s^{-1})	Homogeneous nucleation, CCR (°C s^{-1})	Heterogeneous nucleation at contact angle θ, CCR (°C s^{-1})
100 SiO_2	9×10^{-6}	10^{-5} at 100°	7×10^{-4}	6×10^{-3} at 80°
100 GeO_2	3×10^{-3}	3×10^{3}	1.2	4.3 at 80°
33.3Na_2O-66.7 SiO_2	6×10^{-3}	8×10^{-3}	4.8	46 at 80°
GeS_2	0.06	—	—	—
90GeS_2-10Ga_2S_3	0.7	—	3.0–4.0	—
80GeS_2-15Ga_2S_3-5CsI	0.03–0.1	—	—	—
ZBLAN	—	0.1–1.0	—	—
TeO_2 based glasses	0.05–0.15	—	—	—
100% H_2O	—	—	1×10^{7}	3×10^{7}

In the discussion of the crystallization process involving nucleation and growth, described above, the influence of heterogeneous nucleation could not be analysed quantitatively in detail due to the lack of data; heterogeneous nucleation reduces the surface energy by decreasing the wetting angle, θ (see the function $f(\theta)$). By reducing the surface energy, the nucleation rate is likely to increase by several orders of magnitude, and therefore increase the critical cooling rate required by shifting the nose of the t-t-t curve to the left.

The glass formation by sol–gel technique, discussed later in this book, involves formation of a gel from a sol. In a gel, unlike the heterogeneous nucleation condition, the surface energy is much larger in terms of allowing nucleation of crystals than in a standard hydrolysis reaction, although the thermodynamic driving force for the nucleation of crystals for the chemical reaction(s) remains intrinsically large and negative. It is for this reason that such materials differ classically in apparent crystallization behaviour from that of a standard liquid quenched glass.

2.2 Thermal Characterization using Differential Scanning Calorimetry (DSC) and Differential Thermal Analysis (DTA) Techniques

2.2.1 General Features of a Thermal Characterization

Photonic devices based on glass undergo several thermal processing steps involving melting, solidification and annealing in bulk glass form, evaporation and quenching for making films, during which the kinetics of glass formation plays an important role. In describing the kinetics of glass formation several characteristic temperatures are essential for defining the nucleation, crystal growth and viscosity, as explained within the Johnson–Mehl–Avrami formalism [17,26] in Equation 2.15. More importantly since the presence of critical size of crystals in glass and glass-ceramic media enhances the light scattering, the determination of characteristic temperatures—namely the glass transition (T_g), onset (T_o) and peak (T_p) of crystallization, onset (T_f) and end (T_l) of melting—is important in estimating the thermal stability of a glass and its susceptibility to temperature induced changes.

During the fabrication of bulk glass or thin films, if the crystals formed have similar refractive index, the light scattering is minimized. However, this method of control of light scattering in transparent glass ceramic, besides the difference in refractive indices of glass and crystallites, is also dependent on the crystallite size and size distribution, which is controlled by the, temperature of glass annealing above T_g in the critical temperature range and, therefore, the viscosity and crystal nucleation and growth therein, as explained in Figure 2.6. Based on this figure, it is therefore essential to characterize these temperatures using either a differential scanning calorimeter (DSC) or a differential thermal analyser (DTA), which are commercially available (Figure 2.7).

There is a significant difference in the operation of a DSC and DTA, since a DSC is a calorimeter, which implies that the machine quantifies the energy exchange directly when a sample is heated, as explained below. A schematic representation of the measurement head of a commercial DSC is shown in Figure 2.8, with a supplementary schematic diagram that helps in explaining the origin of energy and temperature differentials between the sample and the reference materials.

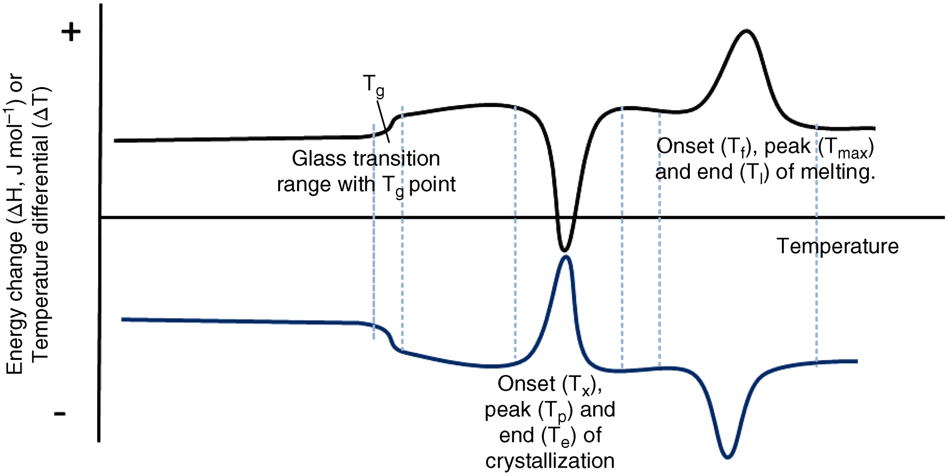

Figure 2.7 Schematic representation of a DSC (dark grey) and a DTA (light grey) scan for a glass sample, showing the glass transition (T_g), crystallization (T_x) and melting (T_f) events when heating at a constant heating rate (*β*, K or °C s^{-1}).

2.2.2 Methods of Characterization

In a DSC, the sample holder and the reference are heated via power compensation to maintain a zero temperature differential between them. As a result of the power compensation the energy needed to maintain a zero temperature differential between the sample and the reference is the value of the enthalpy (ΔH). On the other hand, in a DTA, a constant power is supplied to both sides during heating, which then yields a temperature differential (ΔT). Since $\Delta H = \int \Delta C_\mathrm{p}\,\mathrm{d}T$ the main advantage of a DSC as a technique is that it allows characterization of specific heat (ΔC_p) at constant temperature for a thermal change, which cannot be ascertained directly in a DTA operation. The operational difference between a DSC and DTA, explained above, produces the thermal scan which in a DTA appears flipped with respect to a DSC curve. Simultaneous enthalpy and temperature calibrations are essential using several samples in a DTA operation so that the machine software can then estimate the integrated area for a thermal event in order to estimate C_p.

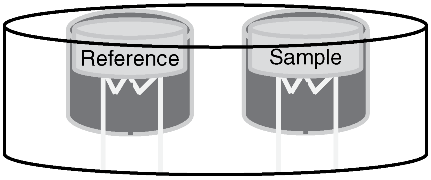

Figure 2.8 Schematic cross-section of a thermal analyser head showing the sample (right-hand side) and the reference (left-hand side) holders with heaters and thermocouples and a control system for analysing power compensation.

From Figure 2.7 it is apparent that when a glassy material is heated at a constant heating rate (β, K min^{-1}) thermal events occur as the temperature rise. The first event is the glass transition, which is a phase transition temperature above which there is a significant change in the physical state of a glass as it starts flowing. The mass transport processes (e.g. diffusion/viscous flow) within the material increases with temperature, allowing the metastable state to approach the nearest equilibrium by undergoing crystallization, for which the onset, peak and end temperatures are identified in Figure 2.7. After the crystallization terminates at (T_e), melting starts at T_f and ends at T_l, commonly known as the liquidus temperature. The integrated area under a thermal event is the total apparent enthalpy of the process. Any shift in the baseline characterizes the specific heat change (ΔC_p). Note that in Figure 2.7 the characteristic temperatures are defined with the help of dotted lines by identifying the temperature inflexion points where the event begins and ends, at which the slope of the curve changes.

2.2.3 Determining the Characteristic Temperatures

A differential thermal analyser or a differential scanning calorimeter is often used to determine the characteristic temperatures of a glass, as explained in Figure 2.7. Before analysis it is important ascertain the reactivity of sample material at a particular temperature; otherwise, the quality of data may be compromised by the heat contributed or temperature differentials from a sample–crucible chemical reaction. For example, when using a chalcogenide glass it is recommended that the test material is sealed inside a silica micro-ampoule. This is to exclude the contamination of sample and reference crucibles from sulfur-bearing gases, e.g. in a germanium sulfide glass [6,27]. To prevent contamination it is also essential to optimize the sample size to less than 20 mg in a DTA/DSC cell. If a DTA cell is used it is important that a sealed ampoule containing, say, sulfide glass should be then packed with alumina powder in the centre of the DTA cell so that the temperature gradient around the sample is minimized. An empty silica ampoule of comparable dimension must be placed in the reference head in the DTA cell, so that during measurement the temperature differential is compensated for the silica sample holder. By comparison, in a DSC cell the oxide glass sample is crimped inside a gold pan, and an empty crimped gold pan is placed in the reference head. Sulfide glasses are not ideal for running in a DSC cell due to the high vapour pressure of sulfur at test temperatures higher than 573 K.

Before any measurement is undertaken, the instrument must be calibrated for baseline correction using the standards between the low and high temperature limits of measurements. For example, in a GeS_2 based glass the temperature range of calibration is 500–1150 K, which may be achieved by using the melting and phase transformation points of four different pure metals (99.99 wt% analytical grade), namely tin (Sn) at 505 K, zinc (Zn) at 692 K and aluminium (Al) at 933 K to limit measurement errors to below ±2 K in state-of-the-art DTA equipment. For calibration above 950 K, 99.99% pure electrolytic-grade iron (sealed inside a silica tube) has been used to record the magnetic transition ($\alpha \rightarrow \beta$) and the $\beta \rightarrow \gamma$ transitions at 1043 and 1185 K, respectively. By combining the calibrations for baselines with the lowest and highest heating rates a priori, the machine software can be effectively applied for each scan. In Table 2.3, the measured characteristic temperatures for a range of glasses are summarized. These temperatures are then used for determining the resistance against devitrification of glass-forming compositions, using the following equations for thermal

Table 2.3 *Comparison of glass transition (T_g), onset and/or peak of crystallization, and melting temperatures for a range of inorganic glasses used for photonic applications. For silicate compositions in this table, the values of T_x were taken as the onset of detectable nucleation of crystals, which are reported in the literature, and the values of T_p were considered to be comparable with the maximum in nucleation [8,17,28]. Source: P. F. James 1989. Adapted with permission from Springer.*

Glass compositions (mol.%)	Characteristic temperatures (K) and heating rate (β, K s^{-1}).					References
	T_g	T_x	T_p	T_f	β	
Silicate glasses						
33.3 Li_2O, 66.7 SiO_2 ($Li_2O.2SiO_2$)	727	808	—	1307	—	[7,8]
16.67 Na_2O, 33.33 CaO, 50SiO_2	838	1003	868	1562	—	[7,8]
33.3 BaO, 66.7 SiO_2	962	973	1119	1693	—	[7,8]
33.3 Na_2O, 16.67 CaO, 50SiO_2	743	—	778	1448	—	[7,8]
50 Na_2O, 50SiO_2	683	—	733	1362	—	[7,8]
50 CaO, 50SiO_2	1030	—	1063	1817	—	[7,8]
37.5 BaO, 62.5 SiO_2	963	973	998	1706	—	[7,8]
Binary and ternary phosphate laser glasses						
30 P_2O_5-20Nb_2O_5-50V_2O_5	741	—	—	—	—	[29]
30 P_2O_5-50Nb_2O_5-20V_2O_5	888	—	—	—	—	[29]
20 P_2O_5-40Nb_2O_5-40V_2O_5	793	—	—	—	—	[29]
80 $Ba(PO_3)_2$-20 V_2O_5	733	—	—	—	—	[29]
Fluoride glasses						
62ZrF_4, 33BaF_2, 5LaF_3	588	662	—	820	10	[28,30]
52ZrF_4, 24BaF_2, 20NaF, 4AlF_3	531	617	—	723	10	[28,30]
57ZrF_4, 34BaF_2, 5LaF_3, 4AlF_3	593	665	—	786	10	[28,30]
52ZrF_4, 20BaF_2, 4LaF_3, 20NaF, 4AlF_3	535	625	—	728	10	[28,30]
40YF_3, 20AlF_3, 20BaF_2, 20CaF_2	703	808	—	983	10	[28,30]
Heavy metal oxide glasses						
90TeO_2-10ZnO	570	681	708	—	10	[25,31,32]
89.5TeO_2-10Na_2O-0.5Er_2O_3	572	680	705	—	10	[25,31,32]
80TeO_2-10ZnO-10Na_2O	557	659	—	—	10	[25,31,32]
70TeO_2-10Na_2O-10P_2O_5-10ZnO	623	723	778	903	10	[25,31,32]
70TeO_2-20La_2O_3-10WO_3	708	860	905	975	10	[25,31,32]
80TeO_2-10B_2O_3-10ZnO+5000ppm Er_2O_3	608	712	728	—	10	[25,31,32]
60 GeO_2–30PbO–6Na_2O–4Ga_2O_3	694	873	—	—	10	[33,34]
55GeO_2–30PbO–15Na_2O	641	869	—	—	10	[33,34]
Selected chalcogenide glasses						
100GeS_2	725	947	978	1090	10	[6,24,27]
80GeS_2-20Ga_2S_3	678	850	860	1008	10	[6,24,27]
75GeS_2-15Ga_2S_3-6CsI	669	855	988	1008	10	[6,24,27]
77GeS_2-15Ga_2S_3-4CsI-4Sb_2S_3	653	786	798	943	10	[6,24,27]

stability parameters:

$$\Delta T_{\mathrm{x}}(K) = \left(T_{\mathrm{x}} - T_{\mathrm{g}}\right) \tag{2.17a}$$

$$\Delta T_{\mathrm{p}}(K) = \left(T_{\mathrm{p}} - T_{\mathrm{x}}\right) \tag{2.17b}$$

$$S(K) = \frac{\Delta T_{\mathrm{x}} \Delta T_{\mathrm{p}}}{T_{\mathrm{g}}} \tag{2.17c}$$

$$H_{\mathrm{R}} = \frac{(\Delta T_{\mathrm{x}})}{(\Delta T_{\mathrm{f}})} \tag{2.17d}$$

In Equation 2.17d, $\Delta T_{\mathrm{f}} = T_{\mathrm{f}} - T_{\mathrm{x}}$, which defines the temperature differential between the onset of melting and nucleation, as defined in Equation 2.13 by the term $(\Delta T)^2$ in the classical growth model. The first stability parameter explains the barrier to crystal nucleation by the magnitude of the $(T_{\mathrm{x}} - T_{\mathrm{g}})$ differential, increasing exponentially in accordance with the classical nucleation model, discussed above. Equation 2.17b is more relevant to the thermal stability in the phase transformation regime above T_{x}, when both the nucleation and growth might become dominant. The larger the temperature width of this differential, the slower the resulting phase transformation, which is why it is not possible to see apparent crystallization in silicate and other strongly covalent glasses. The S parameter combines the features of both nucleation and growth rates by including the two temperature differentials defined in Equations 2.17a and 2.17b. For characterization of a range of inorganic glasses for photonic applications, the data in Table 2.3 may be relevant for comparing the thermal stabilities of different types of inorganic glasses.

2.2.4 Determination of Apparent Activation Energy of Devitrification

Determination of resistance against crystallization is also possible by measuring the devitrification rates for several types of oxide and non-oxide glasses, as reported elsewhere using DTA or DSC by adopting isothermal and non-isothermal DTA techniques [6]. These materials for fibre, bulk, thin film and planar optics applications were analysed by determining the apparent activation energy (Q_{x}, kJ mol^{-1}), which determines the rate of crystallization or devitrification of a glass when heated above T_{g}. The most common technique for the characterization of activation energy is the Kissinger method [35], which has been widely used for the kinetics of chemical reactions, decomposition, melting and crystallization. By rewriting the Johnson–Mehl–Avrami equation (Equation 2.15) in a form that subsumes the growth and nucleation rates into a single kinetic parameter (k), as shown in Equation 2.18, the volume fraction (V) of the crystallized fraction is then expressed as an exponent of time (t):

$$X = 1 - \exp\,(-kt)^n \tag{2.18}$$

where k is the rate factor affecting devitrification or crystallization, t is the time in seconds and n is an exponent. As the quantity k is a rate factor it can also be expressed as the standard Arrhenius equation (Equation 2.19), which may be used for temperature shifts observed under non-isothermal heating condition in the specified temperature range:

$$k = k_0 \exp\left(-\frac{Q_{\mathrm{x}}}{RT}\right) \tag{2.19}$$

where k_o is a frequency factor, Q_x is the apparent activation energy and R is the universal gas constant (8.314 J mol^{-1} K^{-1}). In the realm of the Avrami model [21] and the Chen equation [36], Equation 2.20 may also be employed for the characterization of k_o and Q_x by measuring the shifts in the melting temperatures with various heating rates over which the devitrification may occur:

$$\ln\left(\frac{T_p}{\beta}\right) = \frac{Q_x}{RT_p} + \left(\frac{1}{n}\right)\ln\left[-\ln\left(1 - X\right)\right)] - \ln\left(\frac{k_o}{2}\right) \qquad (2.20)$$

From Equation 2.20, a plot of $\ln(T_p/\beta)$ against the reciprocal of T_p, as shown in Figure 2.9a, yields a straight line with gradient equal to Q_x/R for each heating–cooling cycle. In a complex devitrification process, there may be more than one straight line, and in this case each value of the slope is used to derive the apparent activation energy for a given temperature range of devitrification. Once the value of Q_x is determined, the value of exponent n may be

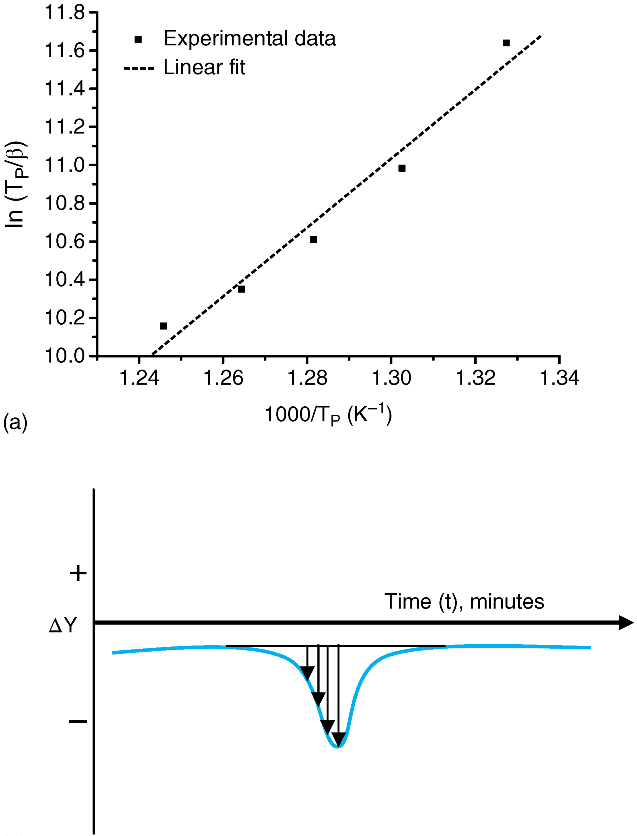

Figure 2.9 *(a) Plot of log(T_p/β) against 1/T_p for determining the apparent activation energy (Q_x); (b) a Piloyan plot for determining the exponent* n *using* Δy *against temperature, scaled against the heating rate on the* x*-axis.*

Table 2.4 *Comparison of the apparent activation energy for devitrification of a range of inorganic glasses.*

Glass composition (mol.%)	Apparent activation energy (Q_x, kJ mol^{-1})	Avrami exponent (n_{avg})	References
$80TeO_2$-$10ZnO$-$10Na_2O$	190–220	2.5	[32]
$75TeO_2$-$15BaO$-$10Bi_2O_3$	295	1.6	[25]
$75TeO_2$-$15BaO$-$10Ga_2O_3$	205	1.7	[25]
ZBLAN	195	2.9	[28,30]
Chalcogenide glasses	150, 210	1.4–1.9, 1.6	[6,27]

determined using either the Piloyan [37] (Equation 2.21) or the Augis–Bennett relationship [38]:

$$\frac{nE_m}{R} = \left[\frac{d \ln (\Delta y)}{d\left(\frac{1}{T}\right)} \right] \tag{2.21}$$

where Δy is the displacement of the non-isothermal DSC trace from the base line. Plotting ln (Δy) against $1/T$ yields a straight line with a slope of nE_m/R, from which the value of n may be derived (Figure 2.9b). Bansal *et al.* [39] have described the characterization of the apparent activation energy (Q_x) of fluoride glasses, using an isothermal method, data from which may be compared with the non-isothermal technique.

In Table 2.4 the derived values of apparent activation energy for devitrification of inorganic glasses are compared using the non-isothermal method described above.

2.3 Coefficients of Thermal Expansion of Inorganic Glasses

Glass, as a condensed state of matter, expands with increasing temperature and this expansion behaviour is consistent with the lattice vibration and cohesive energy models of solids. Based on this approach, the volume expansion coefficient (α_V) of a solid at a given temperature (T, °C) under isobaric (P, atm) conditions may be written as [22]:

$$\alpha_V = \frac{1}{V}\left(\frac{\partial V}{\partial T}\right)_P \tag{2.22}$$

which in total differential form may be rewritten as the mean expansion coefficient:

$$\alpha_V = \frac{1}{V_{RT}} \frac{\left(V_{T_g^o} - V_{RT}\right)}{\left(T_g^O - T_{RT}\right)} \tag{2.23}$$

In Equation 2.23, V_{RT} and $V^{\circ}_{T\,g}$, T_{RT} and T_g^O are the values of measured volume of a glass at room temperature (T_{RT}) and onset of glass transition temperature (T_g^O), respectively.

The thermal expansion coefficients of glasses are usually measured using a dilatometer [40] or a differential mechanical analyser; the latter is specifically suitable for the measurements of viscosity, mechanical strength and moduli of elastic constants. Selected examples of

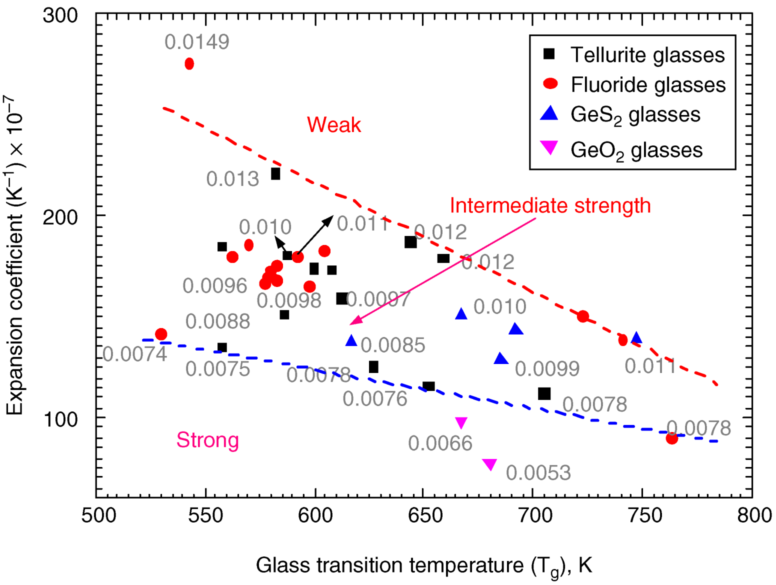

Figure 2.10 *Plot of the coefficient of thermal expansion against* T_g *for four different families of inorganic photonic glasses, showing weak, intermediate and strong network behaviour, which was estimated based on the* ($\alpha.T_g$) *product. This product is a direct measure of configurational molar free volume in a glass at a given temperature.*

coefficients of thermal expansion of tellurite, zirconium and hafnium fluoride, germanium sulfide and oxide glasses are compared in Figure 2.10. In Table 2.5, the thermal expansion coefficients of a range of oxide, fluoride and chalcogenide glasses are cited along with the corresponding values of reported glass transition temperatures (T_g). The table shows examples of the composition dependence of thermal expansion coefficients and the glass transition temperatures in a range of inorganic glasses. By comparing these values in Table 2.5 and Figure 2.10 with the strong network forming silicates, it is clear that the silica and silicate glasses have expansion coefficients nearly 10–100 times smaller than the values for heavier metal oxide, fluoride and sulfide glasses. A comparative analysis of the dilatometric properties is essential for engineering the light waveguides, optical fibres and other complex structures in which matching the thermal expansion coefficients is essential in achieving physically stable structures. The dilatometric measurements are also essential for analysis of the dimensional and refractive index changes in laser devices, in which one of their properties is often characterized by the slope of the refractive index against temperature.

By reviewing the relationship plotted in Figure 2.10, it is apparent that the ($\alpha.T_g$) product, defined by the coefficient of thermal expansion and glass transition temperature in this figure, yields data that is related to the apparent molar volume change in a glass up to the onset of glass transition, assuming that the values of α vary linearly from room temperature to this temperature (as in Equation 2.23). The values of these products in Figure 2.10 for most non-silicate, ZrF_4 and HfF_4 fluoride and chalcogenide glasses are compared, showing three different regimes—the weak regime with the values of product at or above 0.01, followed by the intermediate regime with values in the range 0.01–0.0078 and then the strong regime in

Table 2.5 Compositional dependence of the coefficient of thermal expansion and glass transition temperatures in inorganic photonic glasses [22,29,41]. All compositions are in mol.%. $B=3\alpha T_g$. Data from [22, 29, 41].

TeO_2	BaO	Bi_2O_3	PbO	WO_3	MoO_3	V_2O_5	As_2O_5	Nb_2O_5	Er_2O_3	B_2O_3	Na_2O	ZnO	α ($K^{-1} \times 10^{-7}$)	T_g (K)	$B=3\alpha T_g$
68.13	—	—	16.24	15.63	—	—	—	—	—	—	—	—	151.2	586	0.027
58.92	—	—	14.04	27.04	—	—	—	—	—	—	—	—	125	627	0.024
50.03	—	—	16.62	33.35	—	—	—	—	—	—	—	—	127	—	—
63.5	—	—	22.2	—	14.3	—	—	—	—	—	—	—	180	588	0.011
31.4	15.0	—	—	—	—	53.61	—	—	—	—	—	—	135	558	0.008
33.41	—	—	16.65	—	—	49.94	—	—	—	—	—	—	140	—	—
69.27	23.05	—	—	—	—	—	7.68	—	—	—	—	—	145	—	—
66.64	—	—	16.68	—	—	—	—	16.68	—	—	—	—	115	—	—
80	15	5	—	—	—	—	—	—	—	—	—	—	—	617	—
80	10	10	—	—	—	—	—	—	—	—	—	—	173.9	600	0.031
75	20	5	—	—	—	—	—	—	—	—	—	—	—	622	—
75	15	10	—	—	—	—	—	—	—	—	—	—	159	613	0.029
70	25	5	—	—	—	—	—	—	—	—	—	—	—	630	—
70	20	10	—	—	—	—	—	—	—	—	—	—	100	621	0.019
65	30	5	—	—	—	—	—	—	—	—	—	—	—	639	—
65	25	10	—	—	—	—	—	—	—	—	—	—	187	644	0.036
60	30	10	—	—	—	—	—	—	—	—	—	—	179	659	0.035
80	—	—	—	—	—	—	—	—	—	—	10	10	185	558	0.031
73.07	—	—	—	16.76	—	—	—	—	10.17	—	—	—	112	705	0.024
65	—	—	—	—	—	—	—	—		15	20	—	221	582	0.039
80	—	—	—	—	—	—	—	—		10	—	10	173	608	0.031
CORNING 7940 fused silica (0–573K) [22]													5.5	1473	
CORNING 7913 borosilicate [22]													7.5		
50BaO-50Ba$(PO_3)_2$ [29]													140		
50SrO-50Ba$(PO_3)_2$ [29]													139		
50CaO-50Ba$(PO_3)_2$ [29]													135		
50MgO-50Ba$(PO_3)_2$ [29]													133		
$56GeO_2$-31PbO-$9Na_2O$-$4Ga_2O_3$ [33]													109.1	660	
$55GeO_2$-30PbO-$11Na_2O$-$4Ga_2O_3$ [33]													108.4	662	
ZBLA [28]													168	593	
ZBLAN [28]													200	535	
$75GeS_2$-$15Ga_2S_3$-6CsI [6,27]													151	669	
$77GeS_2$-$15Ga_2S_3$-4CsI-$4Sb_2S_3$ [6,27]													134	653	

which the values are lower than 0.0078. Except for GeS_2 based chalcogenide, some oxide and fluoride glasses appear to have much lower $(\alpha.T_g)$ products, which is an important parameter for determining the residual thermal stress in materials. By comparison, the values of $(\alpha.T_g)$ products in pure silica and 96 mol.% silica in Table 2.5 are of the order of 8.1×10^{-4} and 1.1×10^{-3}, respectively, which when compared with the data in Figure 2.10 falls well below the 0.0078 line into the strong glass network regime. Such a manifestation of dilatometric behaviour over temperature is consistent with the cohesiveness (strength) of chemical bonds, which is further expanded on in the section below on viscosity.

2.4 Viscosity Behaviour in the near-T_g, above T_g and in the Liquidus Temperature Ranges

The viscous flow behaviour of a glass strongly depends on temperature, which determines the structural changes, namely the molar volume of a glass. Using the Arrhenius model, the temperature dependence of viscosity (η, Pa.s) of a glass may be explained as follows:

$$\eta = \eta_o \exp\left[\frac{B_{\mathrm{vis}}}{f_{\mathrm{T}}}\right], \text{ or } \eta = \eta_o \exp\left[\frac{B'}{\Delta S_{\mathrm{T}}^{\mathrm{f}}}\right] \tag{2.24}$$

Here η_o is the pre-exponential determining the frequency factor for configurational rearrangement of free volume, f_{T}. Since the free volume is a state dependent property, it may also be analogously represented by the temperature dependence of total apparent change in configurational entropy ($\Delta S_{\mathrm{T}}^{\mathrm{f}}$, J mol^{-1} K^{-1}) of molar volume. The net change in the specific heat ($\Delta C_{\mathrm{p}}^{\mathrm{g}}$, J mol^{-1} K^{-1}) associated with the apparent change in configurational entropy is then represented by the corresponding thermodynamic states between the temperature range, e.g. across the glass transition between the onset ($T_{\mathrm{g}}^{\mathrm{s}}$) and end ($T_{\mathrm{g}}^{\mathrm{e}}$) of the transition (Figure 2.11):

$$\Delta S_{\mathrm{T}}^{\mathrm{f}} = \int_{T_{\mathrm{g}}^{\mathrm{s}}}^{T_{\mathrm{g}}^{\mathrm{e}}} \Delta C_{\mathrm{p}}^{\mathrm{g}} \frac{\mathrm{d}T}{T} \tag{2.25}$$

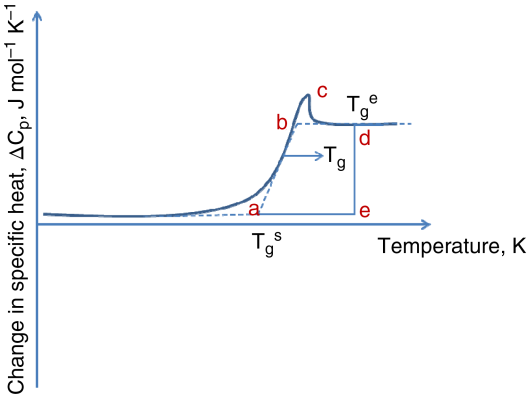
Change in specific heat, ΔC_p, J mol^{-1} K^{-1}
c
T_g^e
b
d
T_g
a
e
T_g^s
Temperature, K

Figure 2.11 *Schematic representation of the onset (T_g^s) and end (T_g^e) of a glass, when thermally scanned in a calorimeter. The area "abcde" is the measure of relaxation energy near the glass transition temperature.*

Equations 2.24 and 2.25 represent the Adam–Gibbs model [42] for viscous flow. From these two equations, it is apparent that the molar free volume also has a strong temperature dependence via entropy and specific heat relationships. The magnitude of configurational specific heat change depends upon the structure of the glass, for which Brawer [43] demonstrated that amongst the inorganic glasses silica has the smallest change in the magnitude of ΔC_p^g, followed by BeF_2 and $ZnCl_2$. The apparent change in each glass is consistent with the change in entropy data for liquids and glasses (compared in Chapter 1 in Table 1.1).

In representing the molar free volume (f_T) in forms that relate with the strength of the network structure of a glass, the following forms of equations may be considered:

$$f_T = b_1 T \tag{2.26a}$$

$$f_T = b_2(T - T_o) \tag{2.26b}$$

and:

$$f_T = b_3 \exp\left[-\frac{E_{f_T}}{\kappa_B T}\right] \tag{2.26c}$$

$$f_T = \left\{(T - T_o) + \left[a_1 T + c_1 (T - T_o)^2\right]^{0.5}\right\} \tag{2.26d}$$

which combined with Equation 2.24 yield the Arrhenius [42], Vogel–Fulcher–Tammann [44] and Eyring [45] models for describing the viscosity of a range of glass-forming liquid. In these equations the terms b_i are the parameters of the free volume equation. There is an additional model for molar free volume, in which f_T assumes a quadratic dependence on temperature ($T - T_o$) and is modelled on the percolation thresholds of different configurational rearrangements, aiding the bulk shear flow with increasing temperature. This model is known as the Cohen–Grest model [46] (Equation 2.26d) and was compared with Eyring's model for fluoride glasses [47]. The comparison yielded a satisfactory result for describing the viscosity over a temperature range. In Figure 2.12, using the above model Equations 2.26a–2.26d, the temperature dependence of viscosity ($\log_{10}\eta$, Pa.s) of glass-forming liquids is plotted on a reduced temperature scale (T_g/T), between T_g and above their melting points,

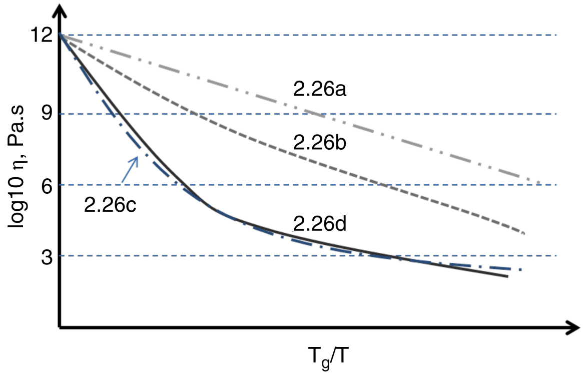

Figure 2.12 Schematic plot of viscosity of four different types of glass-forming liquids in which the molar free volume changes follow Equation 2.26a for silica, Equation 2.26b for silicates, phosphates and germinates, and Equations 2.26c and 2.26d for fluoride and halide liquids.

Table 2.6 *Summary of techniques used to measure the viscosities of glasses in different flow regimes [22]. Source: A. K. Varsheneya 2006. Reproduced with permission from Society of Glass Technology, Sheffield.*

Temperature range	Method	Viscosity (Pa.s)
Melting	Stokes' falling sphere or bubble rise	$<10^4$
	Margules rotating cylinder	$<10^{6.5}$
Softening	Penetration viscometry	$10^6<\eta<10^{11}$
	Parallel plate	$10^5<\eta<10^9$
	Fibre elongation	$10^5<\eta<10^{15.5}$
Annealing	Beam bending	$10^7<\eta<10^{12}$
	Disappearance of stress	$10^{11}<\eta<10^{15.5}$

from which it is apparent that certain glass formers undergo rapid change in their structure when the temperature is raised above T_g.

The temperature dependence of viscosity is an important property of photonic glasses for engineering a range of fibres, planar waveguides and bulk glass applications. Using the graphical representation in Figure 2.12, it is possible to characterize the following temperature ranges, which then determine the required viscosity of a glass undergoing a corresponding structural change, measured by the energy for shear flow, $E=n\kappa_B T$ term. Varsheneya [22] identified these temperatures as the "iso-viscosity reference points", as shown in Table 2.6, and the corresponding relaxation temperature points are:

(a) Strain point temperature, corresponding to a viscosity of $10^{13.5}$ Pa.s at which the residual quenched state stress is relieved slowly. The strain point annealing is relevant for glasses used in making lenses, waveguides and astronomical telescope mirrors. Telescope mirrors are often annealed for days and slowly cooled to room temperature before they are used. The strain point is also characterized as a sub-T_g relaxation of glass.

(b) At the annealing point the viscosity is nominally referred to as 10^{12} Pa.s, which is usually at the T_g. When a glass-forming liquid is quenched it is usually annealed at this temperature to relieve most of the "as-quenched stress".

(c) The softening point corresponds to a viscous regime of $10^{6.65}$ Pa.s, at which a majority of glass begins to flow under load, which is called the creep flow.

(d) The viscosity regime of 10^3 Pa.s is usually defined as the working point at which shape formation becomes feasible. The rate of drop of viscosity from $10^{6.5}$ to 10^3 Pa.s is critical in determining the shape forming properties of a glass. In strongly covalent glasses, namely in silicates, the drop in viscosity from $10^{6.5}$ to 10^3 Pa.s is extended over a much larger temperature range than in fluoride and other non-silicate glasses.

Measurements of viscosities higher than 10^{10} Pa.s require a long time, which may be ascertained by the simple formula $3\eta/G$, where G is the shear modulus. This condition implies that the value of shear modulus is 30 GPa. Various techniques for measuring viscosity across the temperature range are explained in detail by Varsheneya (Table 2.6) [22]. The measured viscosities of several glasses used in photonics and laser optics are summarized in Table 2.7. Wherever possible the viscosity data are also compared with the reported value of activation energy for shear flow at the temperature $T_g<T<T_f$.

Table 2.7 Comparison of measured viscosities of oxide, fluoride and chalcogenide glasses.

Composition (mol.%)	Log(viscosity), log η (Pa.s) at T (K)				Remarks with references
	13	***10***	***6***	***3***	
SiO_2	1313	1515	1725	2667	[22]
GeO_2	882	1075	1259	1653	
Modified commercial silicate glasses					
	Log(viscosity),logη Pa.s at T(K)				Most modified silicates follow the Vogel–Fulcher equation for the temperature dependence of viscosity, which has high activation energy at low temperature and low activation at high temperatures [22,48].
	12	***10***	***6.65***	***3***	
EZ1 Aluminosilicate	998	1085	1190	1473	
KG33 Borosilicate	855	923	1090	1528	
KG1 Alkali-lead silicate	726	778	890	1265	
Zirconium fluoride based glasses					
ZBLAN					For ZBLAN, the activation barriers are 870 and 1400 kJ mol^{-1} in the 10^{10} and 10^{13} Pa.s regimes, respectively [23]
ZBLA	573	595	628	654	
Tellurium oxide based glasses					
$80TeO_2$-$10ZnO$-$10Na_2O$	540	568	602	658	Both tellurite glasses follow the Vogel–Fulcher model [25,49]
$75TeO_2$-$15BaO$-$10Bi_2O_3$	—	606	627	662	
Modified and fluorinated germanium oxide glasses					
$55GeO_2$-$30PbO$-$11Na_2O$-$4Ga_2O_3$	678	688	743	843	Vogel–Fulcher equation for the temperature range [34].
$56GeO_2$-$22PbO$-$9Na_2O$-$4Ga_2O_3$-$9PbF_2$	640	675	733	838	
Chalcogenide glasses					
$75GeS_2$-$15Ga_2S_3$-6CsI-4SnS	665	686	744	—	Vogel–Fulcher equation for the temperature range [27]
$77GeS_2$-$15Ga_2S_3$-6CsI-$2Sb_2S_3$	643	688	777	—	
$77GeS_2$-$13Ga_2S_3$-8CsI-$2As_2S_3$	623	663	753	—	

In Figure 2.13 the viscosities of several heavy metal oxide glasses are compared with GeS_2 based chalcogenide glasses. In this figure the glass working range falls below $\log_{10}\eta = 5.5$ Pa.s, from which it is apparent that using the GeO_2 based glasses affords the smallest temperature coefficient of viscosity. This implies that such glasses may deform over a broader range of temperature than, for example, a tellurium oxide based glass, shown therein. These measured data may also be compared with the Moynihan [50] model, which was originally derived for the

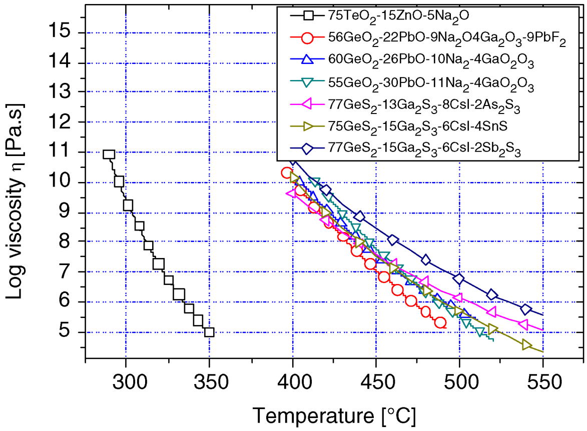

Figure 2.13 *Plot of log(viscosity) (η, Pa.s) against temperature* T *(°C) for a range of tellurite, GeO$_2$ and sulfide glasses. (See colour plate section.)*

silicate, phosphate, borates and germanium oxide glasses using the empirical data. According to this model, the viscosity (η) in the transformation range is expressed as in Equation 2.27:

$$\log_{10}\eta = -5 + \frac{14.2}{\left[0.147\left(T - T_g{}^{e}\right)/T_g{}^{e\,2}\left(1/T_g^{s} - 1/T_g^{e}\right)\right] + 1} \tag{2.27}$$

which distinguishes strong network forming glasses from weaker ones, as proposed by Angell [51]. Here T_g^s and T_g^e are the start and end of the glass transition, shown in Figure 2.11, and T is an arbitrary temperature between these two extremes. This important distinction is depicted by determining the slope of the curvature of the viscosity against the reduced temperature (T_g/T) curves. Based on the findings in Figure 2.13, it is likely that the apparent viscosities may also be fitted to Equation 2.27, yielding all the parameters.

2.5 Density of Inorganic Glasses

Amongst various physical and thermal properties of materials, the density is a direct measure of the structure of materials which then relates to the volume of one gram mole of a glass. It is characterized by the Archimedes principle using either specific gravity measurements or by mercury pycnometry. Since the structure of a glass lacks continuity of three-dimensional periodicity in the atomic arrangements, there is an excess volume arising from the disorder reflecting the configurational rearrangement. This is often characterized by the difference between the molar volumes of a glass and its corresponding crystalline structure, e.g. the difference in the density of crystalline and glassy silica at a particular temperature. Since the density is dependent on the molar volume, which is a thermodynamic state property, it depends both on temperature and pressure. It is therefore essential to define density or molar volume at constant temperature and pressure.

Table 2.8 summarizes the measured densities of selected inorganic glasses; this data will be used for the characterization of spectroscopic, optical and mechanical properties in subsequent chapters.

Table 2.8 *Room temperature density data of selected photonic glasses.*

Glass composition (mol.%)	Density (kg m^{-3})	References
Silica (100%)	2200	[29]
50BaO-50Ba(PO$_3$)	3828	[29]
50CaO-50Ba(PO$_3$)	2720	[29]
50MgO-50Ba(PO$_3$)	2416	[29]
Germanium oxide (100%)	3628	[29]
Modified binary and ternary germanium oxide glasses	3790 (25 mol.% Na$_2$O, 4369 10 mol.% Na$_2$O-10 mol.% K$_2$O)	[29]
53ZrF$_4$-20BaF$_2$-4LaF$_3$-3AlF$_3$-20NaF	4350	[28]
40AlF$_3$-20BaF$_2$-20CaF$_2$-20YF$_3$	4000	[28]
Tellurium oxide glasses (100–x)TeO$_2$ (x = 10–46)	5406–4516	[25,29]
Germanium sulfide glasses (Ge$_{25}$S$_{75}$)	2500	[27]
Arsenic triselenide glasses (As$_{40}$Se$_{60}$)	4600	

2.6 Specific Heat and its Temperature Dependence in the Glassy State

The specific heat is a thermodynamic state property that determines the enthalpy and entropy of the state under consideration in accordance with the first and second law of thermodynamics, respectively. As explained in Chapter 1, during quenching the undercooled liquid undergoes a phase transition at a quench rate (Q^*, K s^{-1}), the state property changes from liquid to glass, at which point both the enthalpy and entropy also change, and these two thermodynamic properties may be characterized by the following two equations for the glass transition range in Figure 2.11, represented by the area "abcde":

$$\Delta H = \oint \Delta \mathrm{C}_{\mathrm{p}} \mathrm{d}T \tag{2.28a}$$

and:

$$\Delta S = \oint \Delta C_{\mathrm{p}} \frac{\mathrm{d}T}{T} \tag{2.28b}$$

The temperature limiting range in this case is defined by $T_{\mathrm{g}}^{\mathrm{s}}$ and $T_{\mathrm{g}}^{\mathrm{e}}$.

The temperature dependence of heat capacity is complex and depends on several structure related factors (e.g. electronic structure, molecular or atomic vibration, allotropic transformation). As the temperature tends towards zero, the value of ΔC_{p} approaches zero, but may not necessarily be equal to zero, suggesting that electronic and nuclear spin states may still have some energy at this temperature. As the temperature increases the value of the specific heat increases and reaches the Dulong–Petit value of $3R$ for each gram atom or mole of materials. Here R is the universal gas constant (8.314 J mol^{-1} K^{-1}). At the glass transition temperature beyond T_{g}°, the value of T_{g} changes discontinuously, as shown in Figure 2.11. For ZBLAN [28], the ΔC_{p} change is equal to 0.53 J g^{-1} K^{-1}. For other glasses, the data may be found in Reference [29].

2.7 Conclusion

In this chapter the kinetic theory of glass formation is discussed in the context of liquid-to-glass formation. Based on the phase transformation theory, the construction of time–temperature–transformation (t-t-t) curves is discussed and compared with the temperature dependence of viscosity, nucleation and growth rates. Experimental methods for the characterization of phase transformation in glass during heating is summarized and discussed in the context of empirical approaches. Other thermal and thermo-mechanical properties are discussed for their role in determining the fabrication routes for light waveguides and optical fibres, and their consequential optical and spectroscopic properties.

References

1. W.H. Zachariasen (1932) *Journal of American Chemical Society*, **54**, 11.
2. K.H. Sun (1947) *Journal of American Ceramic Society*, **30**, 277.
3. D. Turnbull and M.H. Cohen (1960) in *Modern Aspects of Vitreous State; Vol 1* (ed. J. D. Mackenzie) Butterworths, London.
4. D.R. Uhlmann (1971) *Advances in Nucleation and Crystallization in Glass*, (eds L.L. Hench and S.W. Freeman) American Ceramic Society, Columbus, Ohio, p. 155.
5. J.W. Christian (1975) *The Theory of Transformations in Metals and Alloys*, Pergamon Press, London.
6. X. Liu, S. Shen, and A. Jha (2005) *Jounal of Materials Research*, **20**, 856.
7. E.D. Zanotto and P.F. James (1985) *Journal of Non-Crystalline Solids*, **74**, 373.
8. P.F. James (1989) in *Glasses and Glass-Ceramics* (ed M.H. Lewis), Chapman & Hall, London, p. 59.
9. D. Kashchiev (1969) *Surface Science*, **14**, 209.
10. N. Fletcher (1960) *Australian Journal of Physics*, **45**, 408.
11. P.F. James and S.R. Keown (1974) *Philosophical Magazine*, **30**, 789.
12. A.J. Drehman (1987) *Materials Science Forum*, **19–20**, 483.
13. G. Lu, P. Hart, and I.D. Aggarwal (1990) *Physics and Chemistry of Glasses*, **31**, 789.
14. H.W. Schneider and A. Staudt (1989) in *Influence of Various Techniques on Optical Losses in Fluoride Glass Fibres*, Clausthal-Zellerfeld, Germany, p. 57.
15. A. Jha (1991) *Journal of Non-Crystalline Solids*, **134**, 157.
16. K. Fujiura, T. Kanamori, and S. Sudo (1997) Fibre materials and fabrication, in *Optical Fiber Amplifiers: Materials, Devices, and Applications*, 1st edn, Artech House, Inc., Boston, ch 4.
17. W.D. Kingery, H.K. Bowen, and D.R. Uhlmann (1976) *Introduction to Ceramics*, John Wiley & Sons, Inc., New York.
18. R.R. Gonçalves, G. Carturan, M. Montagna, M. Ferrari, L. Zampedri, S. Pelli, G.C. Righini, S.J.L. Ribeiro, and Y. Messaddeq (2002) *Optical Materials*, **25**, 131.
19. V. Tikhomirov, D. Furniss, A. Seddon, I. Reaney, M. Beggiora, M. Ferrari, M. Montagna, and R. Rolli (2002) *Applied Physics Letters*, **81**, 1937.
20. M.C. Paul, S.W. Harun, N.A.D. Huri, A. Hamzah, S. Das, M. Pal, S.K. Bhadra, H. Ahmad, S. Yoo, M.P. Kalita, A.J. Boyland, and J.K. Sahu (2010) *Optics Letters*, **35**, 2882.

21. M. Avrami (1941) *Journal of Chemical Physics*, **9**, 9.
22. A.K. Varsheneya (2006) *Fundamentals of Inorganic Glasses*, The Society of Glass Technology, Sheffield chap. 9, pp. 213–243.
23. C.T. Moynihan, R. Mossadegh, M.G. Drexhage, and P.K. Gupta (1985) *Materials Science Forum*, **6**, 655.
24. D. Marchese, G. Kakarantzas, and A. Jha (1996) *Journal of Non-Crystalline Solids* **196**, 314.
25. A. Jha, B.D.O. Richards, G. Jose, T.T. Fernandez, C.J. Hill, J. Lousteau, and P. Joshi (2012) *International Materials Reviews*, **57**, 357.
26. D.R. Uhlmann (1972) *Journal of Non-Crystalline Solids*, **7**, 337.
27. C.J. Hill, L.H. Huang, and A. Jha (2009) *Journal of Materials Science: Materials in Electronics*, **20**, 202.
28. M. Poulain (1991) in *Fluoride Glass Fibre Optics*, 1st edn (eds I.D. Aggarwal and G. Lu), Academic Press, San Diego, p. 1.
29. O.V. Mazurin, M.V. Streltsina, and T.P. Shavio-Shavaikovskaya (1991) *Handbook of Glass Data*, Elsevier.
30. W.G. Jordan and A. Jha (1994) *Journal of Thermal Analysis*, **42**, 759.
31. A. Jha, P. Joshi, and S. Shen (2008) *Optics Express*, **16**, 13526.
32. P. Joshi, S. Shen, and A. Jha (2008) *Journal of Applied Physics*, **103**, 083543.
33. X. Jiang, J. Lousteau, B. Richards, and A. Jha (2009) *Optical Materials*, **31**, 1701.
34. X. Jiang, J. Lousteau, and A. Jha (2010) *Journal of the American Ceramic Society*, **93**, 3259.
35. H.E. Kissinger (1957) *Analytical Chemistry*, **29**, 1702.
36. H.S. Chen (1978) *Journal of Non-Crystalline Solids* **27**, 257–263.
37. G.O. Piloyan, I.D. Rybachikov, and O.S. Novikova (1966) *Nature*, **212**, 1229.
38. J.A. Augis and J.E. Bennett (1978) *Journal of Thermal Analysis*, **13**, 282.
39. N.P. Bansal, A.J. Bruce, R.H. Doremus, and C.T. Moynihan (1985) *Journal of Non-Crystalline Solids*, **70**, 379.
40. A.G. Clare and J.M. Parker (1989) *Physics Chemistry Glasses*, **30**, 205.
41. A.G. Clare and J.M. Parker (1989) *Physics Chemistry Glasses*, **30**, 205.
42. G. Adam and J.H. Gibbs (1965) *Journal of Chemical Physics*, **43**, 139.
43. S.A. Brawer (1985) *Relaxation in Viscous Liquids and Glasses: Review of Phenomenolgy, Molecular Dynamics Simulations, and Theoretical Treatments*, American Ceramic Society.
44. G.S. Fulcher (1925) *Journal of the American Ceramic Society*, **8**, 339.
45. S. Glasstone, K.J. Laidler, and H. Eyring (1941) *The Theory of Rate Processes*, McGraw Hill, New York.
46. M.H. Cohen and G.S. Grest (1979) *Physical Review B*, **20**, 1077.
47. A. Jha and J.M. Parker (1989) *Physics and Chemistry of Glasses*, **30**, 220.
48. A. Paul (1991) *Chemistry of Glasses*, Chapman & Hall, London.
49. J. Lousteau, G. Jose, D. Furniss, A.B. Seddon, T.M. Benson, and A. Jha (2009) *Journal of Non-Crystalline Solids*, **355**, 1973.
50. C.T. Moynihan (1993) *Journal American Ceramic Society*, **76**, 1081.
51. C.A. Angell (1991) *Journal of Non-Crystalline Solids*, **131**, 13.

3

Bulk Glass Fabrication and Properties

3.1 Introduction

Fabrication and processing of inorganic glasses are largely dependent on the chemical and physical properties, which are determined by the electronic structure and chemical bonding. For example, the processing of oxide and fluoride glasses for photonic device applications is carried out largely under oxidizing conditions, whereas by contrast the chalcogenide, elemental semiconductor and metallic glasses are processed under control atmosphere, either in vacuum tubes or under inert gas atmospheric pressure. In this chapter we discuss different processing aspects of glass melting, by focussing on the physical chemistry and mass transport processes. Besides glass fabrication by the application of heat, in this chapter we will also include sol–gel processing and look at specific examples of bulk glass fabrication.

For optical, spectroscopic and photonic device applications, the most important requirement is that the total propagation loss of light must be minimized at the operating wavelengths. Since the total loss of propagating signals, discussed in Chapter 4, is limited within the range of intrinsic and extrinsic losses at the operating wavelength, the materials processing and fabrication steps must ensure that the extrinsic factors are as small as possible. In considering fabrication of a photonic device, the impurities in the raw materials may contribute to the total loss, and they are characterized as the extrinsic factors that must be controlled during bulk glass, preform, fibre and waveguide fabrication, since strongly absorbing impurities and scattering centres may impair the transparency of the medium. The presence of molecular absorption species—namely OH^-, NO_3^-, SO_4^{2-} and CO_3^{2-}, which are present in the inorganic materials as impurities—may impair device performance and, therefore, such undesirable species must be either removed completely or minimized to reduce the overall propagation loss. In this chapter we mainly focus by reviewing examples of processes developed for a range of oxide, fluoride and chalcogenide glasses. For each glass forming system, wherever the data for transition metal ions are available, these will be compared and relevant citations will be provided for general reading.

Inorganic Glasses for Photonics – Fundamentals, Engineering and Applications, First Edition. Animesh Jha.
© 2016 John Wiley & Sons, Ltd. Published 2016 by John Wiley & Sons, Ltd.

3.2 Fabrication Steps for Bulk Glasses

The fabrication of bulk inorganic glasses is possible via the following techniques:

(a) The first technique is through chemical vapour formation and deposition of main glass-forming constituents. The method has been widely adopted for the formation of silica optical fibres.
(b) In the second approach, the chemical compounds as raw materials are weighed, and mixed as specified by composition requirement. The weighed and batched materials are then melted and homogenized by forming the liquid at an elevated temperature, from where the liquid is quenched into a preheated mould for making glass. The cast glass is then annealed.
(c) The third and final type of bulk glass formation is via the sol–gel technique, in which the chemical mixing of constituents is carried out through a chemical reaction at room temperature using solution precursors.

3.2.1 Chemical Vapour Technique for Oxide Glasses

All-optical communication networks, high-power near-IR lasers and large area near-IR sensor networks use silica glass optical fibres. For optical quality silica glass, ultrahigh purity silicon tetrachloride ($SiCl_4$) liquid [1] is required. The $SiCl_4$ liquid is derived from selective separation of chlorinated products from a fractional distillation column, in which the feedstock is impure SiO_2, carbon and chlorine gas, heated above 1000 °C. To make ultrahigh purity (99.9999%) material, known as the 6 nine purity (6N) purity, the fractional distillation column temperatures are maintained for separating the higher boiling point transition metal chlorides ($FeCl_2$, $FeCl_3$) and aluminium chlorides (AlCl, $AlCl_3$) from lower boiling point (25 °C) $SiCl_4$ liquid. Repeated cycles of evaporation and condensation in columns yield 6N to 7N purity $SiCl_4$, necessary for exceptionally low loss fibres. The 6N to 7N liquid is then reoxidized for making silica inside a cladding SiO_2 glass tube, also made from identical purity material, as shown schematically in Figure 3.1.

As silica deposits as soot on the inner walls of the cladding tube, either at the end of deposition or during deposition, the soot must be dried in a chlorine atmosphere to minimize the residual surface adsorption of OH^- ions. After drying, the cladding tube with silica soot is further sintered to achieve a high density, so as to minimize the scattering centres, followed by a collapse process at 2000 °C to make a uniform core–clad structure with a desired refractive index profile. The main conclusion from the above chemical process description is that the use of chlorine as drying halogen gas plays an important role in the processing of optical quality silica materials. In Chapter 4, the residual impurities present in various types of fibres will be compared alongside the OH^- absorption impurities.

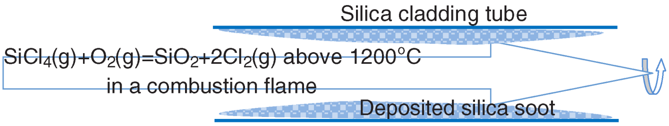

Figure 3.1 *Schematic diagram illustrating the flame oxidation of $SiCl_4$ gas in oxygen for the formation of silica soot on the walls of the cladding silica glass, rotated at a fixed rpm to obtain a uniform deposition of the silica soot for subsequent collapse to make a core–clad glass structure. (See colour plate section.)*

3.2.2 Batch Preparation for Melting Glasses

The success of silica fibres in optical communication systems [1] paved the way to the development of a range of applications in fibre lasers [2], sensors [3], and photonic crystal, band gap [4] and anti-resonant fibres [5], each of which contributed further expansion of the field. Although silica glass set the precedence for the development other types of oxide, fluoride and chalcogenide glasses, not all types of glasses are amenable to fabrication by chemical vapour deposition. A large number of inorganic oxide glasses are multicomponent in nature, the constituents of which constrain their adaptability with the CVD technique. Consequently, such glasses can only be formed by the melting technique. For example, in oxide glass-forming systems (SiO_2, P_2O_5, B_2O_3, GeO_2, and TeO_2) the ingredients are often mixed with the modifier oxides (alkali and alkaline earth), glass network intermediates (Al_2O_3, Ga_2O_3, WO_3 etc.) and refining agents. When a composition is specified in weight (wt) or mole percent (mol.%), the batch of raw materials must be weighed accurately to represent the composition needed for a specified device application.

In this section we consider a specific example of a rare-earth ion doped phosphate glass for laser cavity engineering, for which the general procedure for batch preparation, melting, refining and casting is explained. Note that phosphate glasses are widely used for laser cavity engineering. The main phosphate bearing compounds for glass melting are ammonium hydrogen phosphate crystals [$(NH_4)_2(HPO_4)$] and sodium hexametaphosphate [6,7]. If the intended phosphate glass composition does not contain any alkali, then the ammonium hydrogen phosphate is the only choice for precursor material. Crystalline phosphoric acid might also be used; however, it might not melt as it rapidly evaporates and corrodes crucible and furnace lining.

When using $(NH_4)_2(HPO_4)$, the mass calculation of P_2O_5 in the glass may be based on the molecular weight of ammonium salt, because at elevated temperatures the salt decomposes readily to ammonia, oxygen, steam and P_2O_5 (Equation 3.1). It should also be noted that above 325 °C P_2O_5 volatilizes, which means that to maintain the glass composition the heating rate must be controlled, so as to minimize the loss. The following chemical reactions summarize these two steps:

$$2\left[(NH_4)_2PO_4\right] \xrightarrow{<300°C} P_2O_5 + 4NH_3(g) + 2H_2O(g) + \tfrac{1}{2}O_2(g) \qquad (3.1)$$

$$P_2O_5(s) \xrightarrow{>325°C} P_2O_5(g) \qquad (3.2)$$

The batch calculations, therefore, must account for potential loss of materials via the reaction steps 3.1 and 3.2. The equilibrium for each reaction shifts in the forward direction because of the net positive molar volume change. The batch calculation for a phosphate glass with a composition 65 mol% P_2O_5, 12 mol% B_2O_3, 7 mol% Al_2O_3, 7 mol% Yb_2O_3, 9 mol% Li_2O is shown in the Table 3.1. The steps for calculating the mass of each constituent from molar concentrations are exemplified below in the bottom half of Table 3.1. The materials are weighed inside a dry glove box and transferred into a silica crucible or tray for drying inside a muffle furnace where the atmosphere may be controlled.

3.2.3 Chemical Treatment Before and During Melting

A phosphate glass-forming composition, such as described above, for laser cavity engineering requires significant control over the residual concentrations of OH^- ions

Table 3.1 *Conversion of weight percent (wt%) into molar percent (mol.%) and vice versa.*

Compounds	Mol.%	Molecular weight (M_{wt})	Calculated weight (= mol.% × M_{wt})	Weight percent (wt%)
P_2O_5	65	141.94	9226.1	66.84
B_2O_3	12	69.62	835.4	6.05
Al_2O_3	7	101.96	713.7	5.18
Yb_2O_3	7	394.1	2758.7	19.98
Li_2O	9	29.88	268.9	1.95
Total	100		13802.8	100
	Weight %	Molar weight	Mass fractions	Mol.%
P_2O_5	66.84	141.94	0.471	65
B_2O_3	6.05	69.62	0.087	12
Al_2O_3	5.18	101.96	0.051	7
Yb_2O_3	19.98	394.1	0.051	7
Li_2O	1.95	29.88	0.065	9
Total	100		0.725	100

in the glass. The presence of OH^- ions reduces the slope efficiency and increases the threshold power required. For controlling OH^- ions in phosphate glass-forming liquids, the following chemical equilibrium based approaches have been investigated, which are summarized in the form of chemical reactions in Table 3.2. Notably, the drying and pretreatment steps are carried out in a controlled oxidizing atmosphere. In the table, the equilibrium with respect to OH^- ions is represented as H_2O (g), corresponding to a reference thermodynamic state, which determines the dissociation of $H_2O(g) = OH^- + H^+$ in the presence of the compound under consideration. By choosing this approach, the values of equilibrium partial pressures of H_2O may be accurately determined from the dissociation reaction and then used to calculate the mass flow rate inside the reactor. In Table 3.2, for each drying reaction, the value of equilibrium constant K_{eq} is given. For example, for the chemical reaction 1 (in Table 3.2) with Cl_2 gas the equilibrium temperature is 600 °C, above which the equilibrium constant has values larger than 1. By comparison, for reactions 2 and 3, the equilibrium constants at 25 °C are several orders of magnitude larger than 1, predicting that these reactions are thermodynamically spontaneous even at room temperature; however, kinetic limitations may demand a temperature higher than room temperature. For example, for reaction 1 in Table 3.2 the values of equilibrium constant K_{eq} may then be used together with

Table 3.2 *Values of equilibrium constants for three different drying conditions, considering that the OH^- ions in the raw materials are represented by a molar equivalence of H_2O, by maintaining equilibrium via the chemical reaction* $H_2O(g) = OH^- + H^+$.

Chemical reactions	Values of $\log_{10}(K_{eq})$ at a given temperature (°C) demonstrating its magnitude above T_{eq}
1. $H_2O(g) + Cl_2(g) = 2HCl(g) + 0.5O_2(g)$	Log $K_{eq} = 0$ at 600 °C
2. $2H_2O(g) + CCl_4(g) = 4HCl(g) + CO_2(g)$	At 25 °C, $\log_{10} K = 46.46$
3. $H_2O(g) + SOCl_2(g) = 2HCl(g) + SO_2(g)$	At 25 °C, $\log_{10} K = 11.4$

the volume fractions (or the partial pressure) of each gas present in the drying gas mixture to determine the residual partial pressure ratio of H_2O and HCl:

1. Determine the partial pressure of H_2O (p_{H_2O}) from the $H_2O(g) = OH^- + H^+$ reaction.
2. Use

$$K_{eq} = \exp\left(-\frac{\Delta G^o}{RT}\right) = \frac{(p_{HCl})^2 (p_{O_2})^{0.5}}{(p_{H_2O}) p_{Cl_2}}$$

   to determine the value of K_{eq} from the Gibbs energy at a given temperature, e.g. at the equilibrium temperature where K_{eq} is unity. Using the equilibrium constant equation, fix the values of the partial pressure of H_2O, Cl_2 and O_2 gases from step 1, and insert the input ratio of O_2 and Cl_2 mixture, e.g. 9 : 1, 8 : 2 etc., to compute the partial pressure of HCl gas for each type of hydroxyl ion present in the oxide mixture, e.g. H_3PO_4, $Ca(OH)_2$, $Al(OH)_3$ etc. The lowest value of equilibrium partial pressure of HCl must be maintained for shifting the equilibrium in the forward direction when dealing with the mixtures of hydroxides.
3. Finally, check the sum of the partials pressure for Cl_2, O_2, H_2O and HCl against the total pressure P_{total}, $P_{\text{Total}}(\text{atm}) = \sum_{i=4} p$. For a drying reaction to progress, it is essential that the chemical equilibrium constant is greater than unity.

After drying, the dried mixture for a phosphate glass is melted inside a silica crucible above 1200 °C, rapidly over a short period of time. This is necessary to minimize the corrosion reaction between the liquid phosphate and the silica crucible. After first stage of melting in the silica crucible, the liquid is transferred into a platinum crucible for further melting and homogenization. In the second stage of melting, inside a platinum crucible, the liquid must be continuously stirred to achieve homogenization. The reactive gas, e.g. chlorine, may also be bubbled through the phosphate liquid to reduce the OH^- ion. Other reactive gases suitable for drying phosphate glass-forming liquid are NF_3, CCl_4 [8] and $SOCl_2$. In the context of a gaseous phase reaction with phosphate liquid above 1200 °C, the equilibrium condition may depend on the glass composition and the pretreatment temperature. Notably, the drying step must be chosen below the sublimation temperature of P_2O_5 in air to avoid the loss of phosphate materials before melting.

After dissolution of a residual precursor and ceramic phases inside the silica and platinum crucibles, further stirring and homogenization and bubbling of phosphate glass-forming liquid with pure O_2 may be necessary, to minimize subsequent ingress and recapture of residual OH during the last stage of melting (Figure 3.2). At the end of oxygen bubbling, the liquid is allowed to settle before all the trapped gases are released. Depending upon the composition of phosphate glass melted, the temperature of the liquid is lowered (somewhere below 1000 °C) before casting into a slab. The cast slab is then annealed for at least 48 h below 500 °C. Optical homogeneity of cast materials, which is critical for laser cavity engineering, is therefore dependent on melting and homogenization conditions in the platinum crucible, refining after homogenization, casting and annealing.

The above methodology is also suitable for melting multicomponent borate and silicate glasses [9]. For borate the melting temperature is much lower than 1200 °C. For a complex silicate the temperature required may be much higher than 1400 °C. For silicate glass-forming liquids, the control of OH^- may be possible by either using fluorine or chlorine gas or a reactive fluoride at the melting temperature. For example, if in a glass composition one of the components is CaO or Na_2O, the use of a small fraction (<2 wt%) of CaF_2 or NaF will reduce the OH^- via

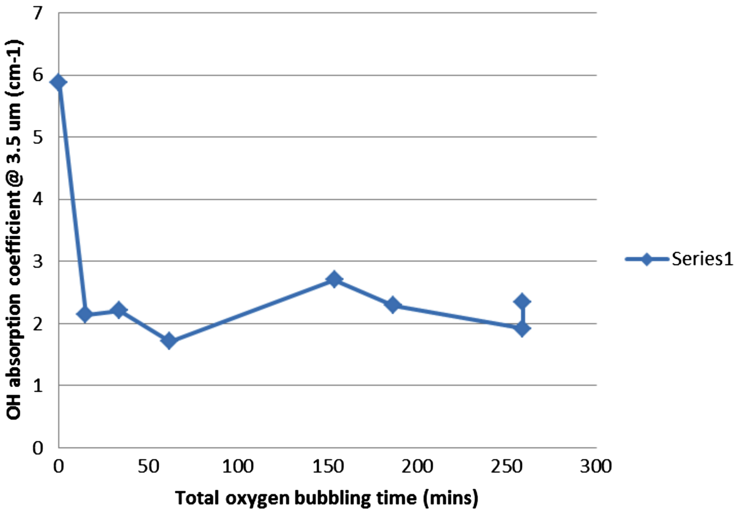

Figure 3.2 *Plot of the rate of reduction in OH⁻ ion absorption in phosphate glass (composition), melted and then purged under oxygen bubbling to reduce OH⁻ ion absorption.*

reaction with F^- ions available from CaF_2 or NaF. An example of OH^- absorption in Er_2O_3 and Yb_2O_3 doped phosphate glass as a function of processing condition is given in Figure 3.2.

Notably, phosphate glass-forming liquids, in general, form at much lower temperatures than the silicates. As discussed in the viscosity properties in Chapter 2, the silicates have strong covalent bonding and as a result exhibit much higher viscosity than any other network forming family of glasses, e.g. phosphate. Consequently, the process of homogenization of silicate glass-forming liquids takes much longer at significantly higher temperatures than 1200 °C. The chemical reactions for melting conditions for some silicate glasses are exemplified elsewhere [10].

3.3 Chemical Purification Methods for Heavier Oxide (GeO_2 and TeO_2) Glasses

Having explained the principles of reactive atmosphere melting of phosphate, silicates and borate glasses, the methodologies for heavier oxide glasses, namely germanium and tellurium oxides, are quite similar and are explained elsewhere [11,12].

Figure 3.3 is an example of the reactive atmosphere melting condition for a specified tellurium oxide glass, for which the logarithmic values of the computed equilibrium constants for dominant chemical reactions 3.3–3.7 are plotted against the temperature (°C). For each reaction the computed values are normalized for a half-mole of O_2 gas evolved via reactions 3.3–3.7. The equilibrium phase combinations for the formation of chloride and oxide phases are plotted against temperature when a chlorine gas-rich atmosphere is maintained. Notably, although the equilibrium temperatures for the formation of ZnO and TeO_2 are close to 400 °C, the reactions occur at 350 °C, which is below the equilibrium temperature. This is possible because the oxygen generated is removed

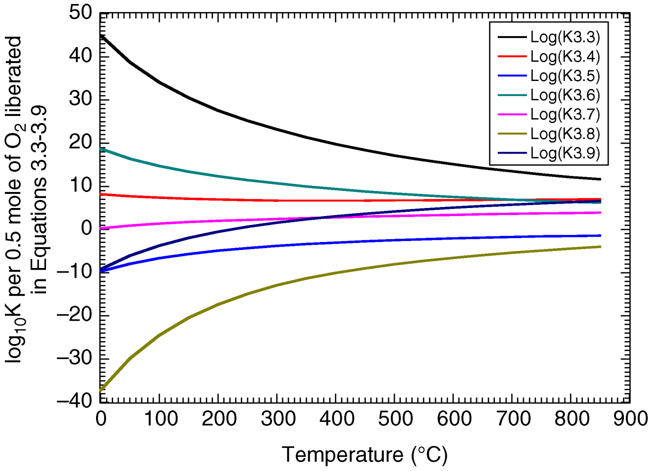

Figure 3.3 *Comparison of computed values of log*$_{10}$ K *for the reactions shown in Equations 3.3–3.9 against temperature. (See colour plate section.)*

continuously as it is an open system in which the product gas is displaced from the reaction chamber by the incoming reactant gas. Consequently, the equilibrium is shifted in the forward direction. The chloride formation reactions for NaCl and $ZnCl_2$ have much larger equilibrium constants than that for $TeCl_4$. The computed thermodynamic equilibria suggest that the chlorination reaction must be controlled in order to avoid the formation of hygroscopic compounds, such as NaCl and $ZnCl_2$.

For melting a tellurite glass composition, for example 80 mol.% TeO_2, 10 mol.% Na_2O mixed with 10 mol.% ZnO and a gas mixture of 90 vol.% O_2 and 10 vol.% Cl_2 was required. The flow rate of oxygen–chlorine was maintained at $2\,\mathrm{l\,min}^{-1}$. Clearly the as-received raw materials show a strong OH^- band absorption in Figure 3.4, compared to that pretreated above room temperature at 350 °C and 450 °C in an oxygen–chlorine mixture. In addition, note that in this figure the OH^- absorption cross-section in tellurite liquid is comparatively larger at 450 °C than at 350 °C. This is due to the over-chlorination of Na_2CO_3 and ZnO to their respective chlorides (Equations 3.3 and 3.7). Both NaCl and $ZnCl_2$ sensitize the glass-forming liquid for moisture absorption from the surrounding melting atmosphere [13]:

$$\mathrm{2NaOH(s,l) + Cl_2(g) = 2NaCl(s,l) + H_2O(g) + \tfrac{1}{2}O_2(g)} \tag{3.3}$$

$$\mathrm{Zn(OH)_2(s,l) + Cl_2(g) = ZnCl_2(s,l) + H_2O(g) + \tfrac{1}{2}O_2(g)} \tag{3.4}$$

$$\mathrm{TeO_2(s,l) + 2Cl_2(g) = TeCl_4(g) + O_2(g)} \tag{3.5}$$

$$\mathrm{NaOH(s,l) + Cl_2(g) = NaCl + HCl(g) + \tfrac{1}{2}O_2(g)} \tag{3.6}$$

$$\mathrm{Zn(OH)_2(s,l) + 2Cl_2(g) = ZnCl_2(s,l) + 2HCl(g) + O_2(g)} \tag{3.7}$$

$$\mathrm{2NaOH(s,l) + Cl_2(g) = Na_2O + 2HCl(g) + \tfrac{1}{2}O_2(g)} \tag{3.8}$$

$$\mathrm{Zn(OH)_2(s,l) + 2Cl_2(g) = ZnO(s,g) + 2HCl(g) + \tfrac{1}{2}O_2(g)} \tag{3.9}$$

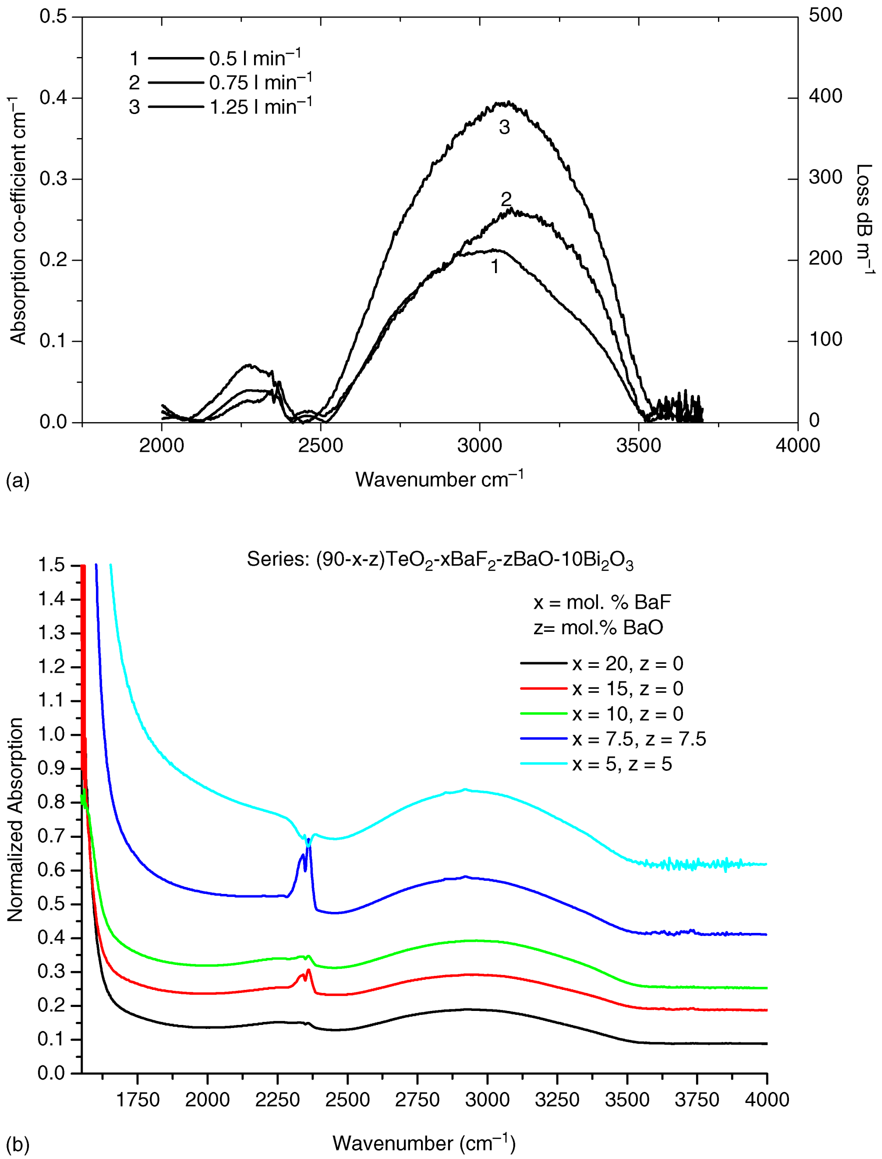

Figure 3.4 *Comparison of OH$^-$ absorption bands in (a) 80 mol.% TeO$_2$-10 mol.% ZnO-10 mol.% Na$_2$O. (b) Infrared spectra for glass compositions (mol.%) in the series (90 – x – z)TeO$_2$-xBaF$_2$-zBaO. (See colour plate section.)*

Besides chlorination, precursor materials may also be processed in a reactive atmosphere using vacuum drying above ambient temperature. However, when using any drying technique for heavy metal oxides, such as TeO$_2$, it is critically important to examine the physical chemistry of decomposition of tellurium oxides and the sublimation temperature of ZnO. Figure 3.4a shows a comparison of the OH$^-$ ion absorption as a function of the volume

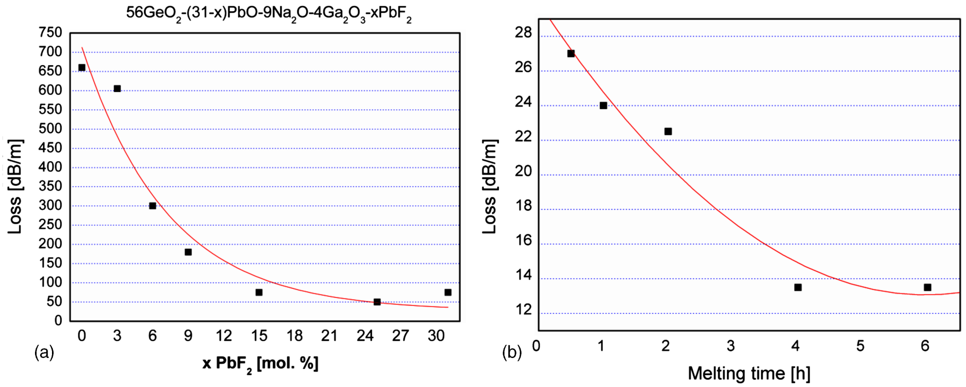

Figure 3.5 *(a) Influence of PbF_2 on the peak of OH^- absorption at 3100 nm (3225 cm^{-1}) measured in dB m^{-1}. (b) Kinetics of OH^- reduction in a glass composition (mol.%) 56GeO_2, 22PbO, 9PbF_2, 9Na_2O, 4Ga_2O_3 melted under dry oxygen.*

flow rate of reactive chlorine (10 vol.%) and oxygen (90 vol.%) gas mixture, from which it is apparent that as the overall volume of chlorine in the reaction chamber increases the OH^- absorption intensifies due to the formation of NaCl and $ZnCl_2$ via chemical Reactions 3.6 and 3.7, respectively.

In a second example of the control of OH^- ion absorption—for a binary tellurium oxide with $(100 - x - z)$ mol.% TeO_2 glass with z mol.% substitution of BaF_2 for x mol.% BaO—the influence of composition on OH^- related absorption is shown in Figure 3.4b. The method exemplifies *in situ* fluorination, which is also cited in examples in the literature. For numerous heavy metal oxide glasses, the technique based on *in situ* fluorination and chlorination may also be adopted, provided the product of reaction is less sensitive to OH^- ion absorption than the starting materials; for example, ZnO is less sensitive to hydrolysis than $ZnCl_2$. Jiang and co-workers [14] and O'Donnell *et al.* [15] demonstrated the approach for GeO_2 and TeO_2 glasses, using PbF_2 and ZnF_2, respectively. In a glass with 56 mol.% GeO_2, $(31 - x)$ mol.% PbO, 9 mol.% Na_2O, 4Ga_2O_3, $x$$PbF_2$, the influence of time and PbF_2 concentrations were investigated, and are summarized in Figure 3.5a and3.5b, respectively. Figure 3.5b compares the effect of time on the reduction in OH^- peak in the GeO_2 glass composition with 31 mol.% of PbF_2. It was also reported that as a result of the addition of PbF_2 there was little or no change in the IR cut-off edge of the glass for mid-IR application.

In summarizing this section, the most important consideration for designing a purification process is the analysis of the thermochemistry, followed by reaction engineering for maintaining the required atmosphere. This is a significant area of materials research, involving the analysis of processing chemistry and, therefore, warrants in-depth review in its entirety, which has been reported for fluoride glass-forming compounds elsewhere [1,8].

3.4 Drying, Fusion and Melting Techniques for Fluoride Glasses

As stated in Chapter 1, the fluoride and halide glass-forming liquids based ZrF_4, AlF_3, CdF_2 and AgI when quenched form glass. However, as with oxide glasses, the drying and removal of impurities, which contribute to the overall absorption in the near- and mid-IR, are essential steps. Several types of raw material purification, chemical characterization after purification and processing are explained extensively by Sudo *et al.* [1], Mimura and Nakai [8] and France [16]. Depending upon the thermodynamic stability of fluorides, the extent of hydrolysis determines the number of cation–fluoride ion bonds being replaced via a generalized equilibrium reaction:

$$M_nF_y(s,l) + H_2O(g) = M_nF_{y-2} + 2HF(g) \tag{3.10}$$

By nature halide salts are hygroscopic, which is why such materials must be stored and batched inside a dry glove box, inside which the atmosphere is maintained via periodical regeneration. The glove box atmosphere must be maintained by removing moisture and carbon dioxide, which are likely to contaminate the surface of fluoride chemicals.

3.4.1 Raw Materials

Like the conditions for handling raw materials for oxide glass fabrication, the starting fluoride precursors for fluoride glass fabrication must meet the purity requirements. Fluorides of high purity are available commercially, especially monovalent and divalent ones, but for applications where ultrahigh purity in parts per million to billion is required, further purification becomes mandatory. For volatile compounds such as ZrF_4, sublimation is one of the preferred techniques. In chemical vapour purification, the zirconium metal is converted into zirconium tetrachloride ($ZrCl_4$) via reaction with Cl_2 gas. The vapour of zirconium chloride is then fluorinated in the presence of SF_6 or HF to give ZrF_4. This vapour phase reaction was demonstrated to be quite successful in reducing the overall transition metal impurities. Another possibility is to use less expensive metallic oxides which are converted into fluorides, before or during melting, usually with the ammonium bifluoride $NH_4F.HF$, following the reactions:

$$2ZrO_{2(s)} + 7NH_4F.HF_{(s)} \leftrightarrow 2(NH_4)_3ZrF_{7(s)} + NH_{3(s)} + 4H_2O_{(g)} \tag{3.11}$$

$$(NH_4)_3ZrF_{7(s)} \leftrightarrow ZrF_{4(s)} + 3NH_4F_g \tag{3.12}$$

which may be carried out to completion in a crucible near 400 °C before melting in the presence of excess ammonium bifluoride. These reactions release large concentrations of ammonia and water, as evident from Reaction 3.11, which may contaminate the preparation procedure, including the melt and the glass prepared afterwards. In addition, the highly corrosive nature of NH_3 gas prevents the reactions being carried out under a clean environment such as a glove box. Besides the above disadvantages, during the preparation of ultrapure heavy metal fluoride glasses (HMFG), it is common practice to use small quantities of NH_4FHF in a premelting step, in order to completely fluorinate any residual oxides present in a given anhydrous batch of fluoride mixture.

3.4.2 Control of Hydroxyl Ions during Drying and Melting of Fluorides

Fluoride glasses may also contain a small amount of anionic oxygen, which may be a source of oxide inhomogeneity in the glass-forming liquid. On cooling, such liquids may form oxide crystals, acting as scattering centres in the glass. Anionic impurities, such as nitrates, carbonates and sulfates may be chemically active by being soluble in the liquid, and therefore

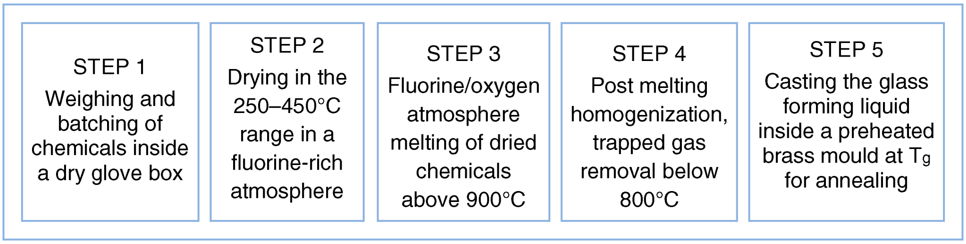
STEP 1
Weighing and batching of chemicals inside a dry glove box
STEP 2
Drying in the 250–450°C range in a fluorine-rich atmosphere
STEP 3
Fluorine/oxygen atmosphere melting of dried chemicals above 900°C
STEP 4
Post melting homogenization, trapped gas removal below 800°C
STEP 5
Casting the glass forming liquid inside a preheated brass mould at Tg for annealing

Figure 3.6 *Schematic representation of drying, melting and casting of a fluoride glass; ZBLAN glass composition in (mol.%):* ZrF_4 *(50–60),* BaF_2 *(10–20),* LaF_3 *(0–5),* AlF_3 *(0–5) and NaF (0–30) for which the melting is typically carried out at around 900 °C in an oxidizing atmosphere.*

contribute to absorption bands at long wavelengths in the mid-IR between 4000 and 8000 nm. By comparison, the chloride ions present are less problematic in terms of maintaining the IR absorption, accept that the larger atomic mass and electronic structure does affect the electronic absorption in the ultraviolet region of the overall transmission, as discussed in Chapter 2. Since fluoride anions have the largest electronegativity, the process of batching, processing and melting are described and summarized schematically, as listed below and in Figure 3.6, for a ZrF_4 based heavy metal fluoride glass.

Step 1) Weigh and batch materials inside a dry glove box, which is regenerated periodically by removing water and CO_2 molecules. The crucible for HMFG is usually made of platinum; the batched fluoride is transferred inside the crucible.

Step 2) Any fluorination step should be carefully designed by first analysing the starting raw materials using X-ray powder diffraction and quantitative chemical analysis. The data from phase and composition analysis may then be used for quantifying the addition of ammonium bifluoride. Alternatively, the reactive gases NF_3 or SF_6 may also be used for removing trace and oxide related impurities before melting.

Step 3) The pretreated fluoride precursors inside the platinum crucible may then be transferred into a suitable melting furnace, where it is essential to maintain oxidizing conditions. The presence of ultra-dry air or oxygen in the melting chamber may serve such a purpose. This is important for maintaining the stoichiometry of constituent fluorides [7,12], especially when multivalent Zr^{4+} ions are present as they tend to reduce in an inert and reducing atmosphere by losing fluorine, e.g. via Reaction 3.13:

$$ZrF_4(s) = ZrF_{4-x}(s) + \tfrac{x}{2}F_2(g) \tag{3.13}$$

Table 3.3 below gives the equilibrium conditions for removing oxygen and maintaining the 4+ valence state of ZrF_4. Selected Gibbs energy and computed partial pressure data for the sub- and oxy-fluorides of tetravalent fluorides are listed in the table, from which the equilibrium partial pressures of product gases may be computed at a temperature so as to select the atmosphere during drying and melting. The equilibrium temperatures (T_{eq}, K) are also computed, wherever possible. From this table it is apparent that the melting of ZrF_4 in oxygen gas or in air does not result in the formation of ZrO_2 crystals under drying and melting conditions, since the equilibrium pressure of fluorine formed is extremely small for both ZrO_2 and $ZrOF_2$ as condensed phases. The thermodynamic conditions for the formation of

Table 3.3 *Selected thermodynamic data for tetravalent fluorides used for heavy metal fluoride glasses [17–19]. The Gibbs energy of formation of $ZrOF_2$ were estimated from $ThOF_2$ by applying the same differences in the enthalpy and entropy values as were for ThF_4 and $ThOF_2$.*

Chemical reactions with Gibbs energy ($\Delta G°$, J mol^{-1}) or vapour pressure (atm) equation	$\Delta G°$ (J mol^{-1}) at T (K) and T_{eq} (K)			P_i (atm) at 1150 K
	T_{eq}	673	1150	
$ZrF_4(liq) + O_2(g) = ZrO_2(solid) + 2F_2(g)$ $\Delta G° = 910681 - 175.85T$	5178	792333	708453	$P(F_2) \approx 4.5 \times 10^{-17}$ atm.@ $P(O_2) = 0.21$ atm
$ZrF_4(liq) + \frac{1}{2}O_2(g) = ZrOF_2(solid) + F_2(g)$ $\Delta G° = 433360 - 59.40T$	7295	393383	365050	$P(F_2) \approx 4.4 \times 10^{-9}$ atm.@ $P(O_2) = 0.21$ atm
$ZrF_4(liq) + 2H_2O(g) = ZrO_2(solid) + 4HF(g)$ $\Delta G° = 307911 - 273.7T$	1124	123710	−6844	$P(HF) \approx 0.12$ atm. @ $P(H_2O) = 0.01$ atm
$ZrF_4(liq) + H_2O(g) = ZrOF_2(solid) + 2HF(g)$ $\Delta G° = 130154 - 194.5T$	669	−745	−93521	$P(HF) \approx 0.31$ atm. @ $P(H_2O) = 0.01$ atm
$ZrF_4(solid) = ZrF_3(solid) + 0.5F_2(g)$ ZrF_4 sublimes at 1181 K	>1673	450740	406577	$P(ZrF_4) = 1$ atm at 1181 K (908 °C)

oxide and oxyfluoride change dramatically, as shown in Table 3.3, when the partial pressure of H_2O (steam) in the gaseous atmosphere inside the fluorinating reactor increases to 0.01 atm, the resulting partial pressure of HF for oxide and oxyfluoride reactions are 0.12 and 0.31 atm, respectively. The H_2O partial pressure might change when using O_2 or air, since the reduction in the total gas pressure inside the cylinder increases the vapour pressure of water. At high pressure the water vapour condenses. It is therefore essential to pay attention to the process chemistry, when synthesizing a fluoride glass.

Finally, it is also evident from Table 3.3 that the zirconium tetrafluoride (ZrF_4) sublimes at 908 °C, and if the process of drying and melting is not maintained in an oxidizing condition the tetrafluoride phase will decompose above the sublimation point. The kinetics of decomposition, however, will depend on the reducing condition maintained inside the reactor. A characteristic feature of partially reduced tetrafluoride may be identified by the dark grey superficial discoloration of powder material. During melting above 850 °C, it may be easier to maintain a positive pressure of one of the reactive gases: SF_6, NF_3, $SOCl_2$ or O_2 mixed with CCl_4. When handling CCl_4 as a reactive gas, precaution must be taken to avoid the formation of $COCl_2$ gas (phosgene) as it is chemically hazardous and causes fatal injury on exposure. The presence of high concentrations of CCl_4 may result in the formation chloride-rich species in glass-forming liquid, which may affect both the physical and chemical properties of fluoride glasses. The problem of high chlorine solubility when using CCl_4 may be aggravated when a vitreous carbon crucible is used. For this reason, most HMFG glass is melted in a platinum crucible:

Step 4) During homogenization, the glass-forming liquid is allowed to form a single phase without the presence of any insoluble crystals, left after melting. Once the fluoride glass forming material melts, the gases evolved during melting must be allowed to escape from the liquid phase. The melt temperature is usually reduced, e.g. to 800 °C from 900 °C in step 4 in Figure 3.6, which then decreases the solubility of dissolved gases. At this stage any residual gas bubbles that may have formed as a result of one or more chemical reactions, described in Equations 3.10–3.12, are released by stirring with platinum wire. At this point there is usually little evidence for visible bubbles on the inner walls of the crucible. After stirring the melt is allowed to settle before the casting is carried out in a preheated brass mould.

Step 5) Once the liquid appears visibly free from gas bubbles, it is poured into a preheated brass mould, and then transferred into an annealing furnace. Preheating of the mould is necessary to avoid thermal induced cracking, which may adversely affect the quality of a bulk glass. Thermal gradients in a cold mould induce microscopic inhomogeneities that may compromise the optical transparency of the glass due to a stress induced refractive index, known as the birefringence. The control of birefringence is essential for fluoride bulk glass imaging lens for night-time and deep space mid-IR imaging. Annealing of cast glass is especially important for bulk optics in imaging and astronomical telescopes where the image quality may depend on the microscopic density gradient set by the thermal diffusion gradient near T_g in a glass. Annealing is essential for relieving the quenched thermal stress.

Readers may also wish to refer to the extensive reviews in references [1,8,12,16], where more details on processes for purifications and analysis of purified oxide and fluoride materials are described.

3.5 Chemistry of Purification and Melting Reactions for Chalcogenide Materials

Amongst the chalcogenide series of glass compositions discussed in Chapter 1, two main categories are the glasses with only chalcogenide (S, Se, Te) compounds [20,21] of metals, semi-metals and semiconductors, and the second category is where the chalcogenide elements are mixed with halogens (Cl, Br and I) to make chalcohalide compositions [22]. Because the anionic radii of larger halides (Cl^-, Br^-, I^-) are comparable with those of S^{2-}, Se^{2-} and Te^{2-}, these halide ions mix well due to minimization of the Gibbs energy of the resulting glass-forming liquid mixture. Due to the large electronegativity (see Chapter 1) and small ionic radium of fluoride (1.3 Å) ions, they are coulombically more compatible with the oxide matrix than the chalcogenide. As a result of the size and electronegativity differences in fluorine, phase immiscibility may arise, leading to an inhomogeneous glass.

It is important to analyse the incorporation of halide ions in the context of chalcogenide and chalcohalide glass-forming systems in the light of the following chemical reactions in order to control the overall concentrations of OH^- and oxide constituents in the resulting glass. Let us consider that an overstoichiometric composition of germanium disulfide (GeS_{2+X}), in which X represents the overstoichiometry, is mixed with 5 mol.% of ultra-dry caesium iodide (CsI) to make a binary 95 mol.% GeS_{2+X}–5 mol.% CsI glass [23,24]. Any residual OH^- ions will then react with the iodide or iodine present and form hydrogen iodide (HI) via the following reactions:

$$GeS_{2+x} + 2xCsI + [xH_2O]_{OH}(g) = Ge(S_2O_x) + 2xHI(g) + xCs_2S \tag{3.14}$$

$$GeS_{2+x} + xI_2 + [xH_2O]_{OH}(g) = Ge(S_2O_x) + 2xHI(g) + \tfrac{x}{2}S_2(g) \tag{3.15}$$

Table 3.4 *Comparison of characteristic transition temperatures and the vapour pressures of various elements and atomic and molecular chalcogenide species [18,19,26].*

Compound	Characteristic temperatures (°C)		Vapour pressure equation: $\log_{10}P = AT^{-1} + B\log T + CT + D$ (mmHg)			
	T_f	T_b	A	B	C	D
(S_2 liquid)	119		−6975	−1.53	−1.0	16.22
(Se liquid)	220	695 (Se_6)	−4990	—	—	8.09
Te_2 solid	?		−9175	−2.71	—	19.68
(Te_2) liquid	?	998	−7830	−4.27	—	22.29
(I_2 liquid)	114	183	−3205	−5.18	—	23.65
CsI (liquid)	621	1280	−9678	−3.52	—	20.35
GeS (solid)		760	−8350	—	—	10.78
As_2S_3 (solid)		459	−5100	—	—	4.67
Solid compound = vapour phase		T_m (°C)	Values of equilibrium constant ($\log_{10}K$) at T (°C)			
			0	400	800	1000
GeS_2(s)		840	−36.90	−9.74	−2.972	−1.325
$GeSe_2$		740	−37.55	−10.24	−3.32	−1.81
GeTe		725	−35.38	−9.44	−3.26	−1.96
As_2S_3		312	−15.02	−2.17	−0.46	−0.23
$As_2Se_3 = 2AsSe(g)+Se(g)$		260	−110.3	−30.67	−11.72	−7.07
$As_2Te_3 = 2AsTe(g)+Te(g)$		375	−100.74	−26.80	−10.05	−5.79
$Ga_2S_3 = Ga_2S(g)+S_2(g)$		1090	−107.7	−32.37	−13.58	−8.72
$La_2S_3 = 2LaS(g)+0.5S_2(g)$		2110	−273.98	−17.53	−53.05	−41.38
Sb_2S_3		550	−50.19	−13.16	−5.45	−3.62
$Sb_2Se_3 = 2SbSe(g)+Se(g)$		615	−126.05	−36.76	−15.05	−9.74
$Sb_2Te_3 = 2SbTe(g)+Te(g)$		619	−104.01	−28.45	−10.86	−6.98

In Equation 3.14 the iodide exchange with sulfide in the presence of OH^- (represented as H_2O) will yield Cs_2S and partially substitute oxide ions at the overstoichiometric sulfur sites in GeS_2. By contrast, in Equation 3.15 the presence of excess iodine will yield a positive pressure of S_2 gas, which may contribute to S–H vibrations in the mid-IR, as discussed below.

For the melting of chalcogenide and chalcohalide glasses, an additional feature to note is the high vapour pressure of most chalcogens, except for divalent and trivalent sulfides, at elevated temperatures. Although the high vapour pressure characteristics of chalcogenide is beneficial in the purification of some types of sulfide (e.g. arsenic trisulfides) it is, however, also a limitation for drying and melting these materials in an open system, because of the risk of loss of glass-forming constituents.

In Table 3.4 we have tabulated the characteristic temperatures (melting point, T_f) and boiling point, (T_b)) and thermodynamic properties of the main constituents of chalcogenide glasses, before going into the details of melting by taking specific examples. In this section three different examples are cited. For each glass-forming system the drying, purification and melting processes are explained.

The first example explains the process chemistry of arsenic trisulfide (As_2S_3), which invariably contains oxide impurities. For purification and melting of As_2S_3, the methods known and practiced are vacuum distillation under controlled temperature, so that the oxide constituents are retained. To minimize the oxide impurities, often either calcium metal with

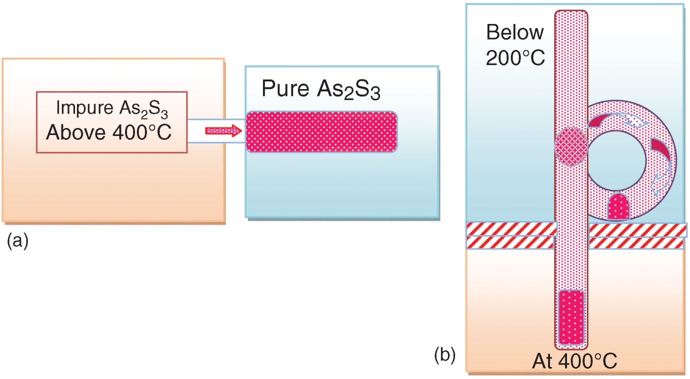

Figure 3.7 (a) A horizontal and (b) vertical set up for the purification of arsenic trisulfide in a two-temperature zone muffle furnace. Source: Adapted from [25]. (See colour plate section.)

elemental sulfur or calcium oxide is placed inside the distillation reactor (Figure 3.7a and b) [25]. In the presence of calcium and elemental sulfur, the arsenic oxide (As_2O_3) reacts with metallic calcium and forms CaO, rendering arsenic oxide into a reactive submetallic state that then combines with sulfur via Reaction 3.16 at elevated temperature and forms ultrahigh-purity vapours of As_2S_3. By comparison, the reaction in Equation 3.17 between As_2O_3 and CaO forms calcium arsenite ($CaAs_2O_4$) which has much higher sublimation and boiling points than those of either As_2O_3 or As_2S_3. This differential in vapour pressure is essential for achieving high purity As_2S_3 compounds:

$$3Ca(s) + As_2O_3(g) + 1.5S_2(g) = 3CaO + As_2S(g) \tag{3.16}$$

$$CaO(s) + As_2O_3(g) = CaO.As_2O(s) \tag{3.17}$$

The pure gaseous species of As_2S_3 condenses away from calcium arsenite or CaO via effective vapour phase separation of As_2S_3, facilitated via a temperature gradient furnace design (Figure 3.7a and b). In the high temperature part of the furnace, volatilization of chalcogen and arsenic species begins and the natural convection facilitates the separation of chalcogen compound from the residual impurities. Since arsenic bearing chemicals are poisonous, material purification is carried out either inside a sealed glove box or inside a fume hood.

For melting, the distilled As_2S_3 is retained inside the silica ampoule, shown in Figure 3.7a and b, by using an oxyacetylene flame, which seals the high-purity materials. For chalcogenide and chalcohalide glass preparation, the impurity removal (e.g. OH^- ion) is integrated with melting, which is why certain essential precautionary measures are taken to minimize the reintroduction of ^-OH ions into the liquid. Before melting a sulfide glass inside the silica ampoule, it is important to etch the inside surface of the ampoule with hydrofluoric acid (HF), which removes the superficial layer of OH-rich silica. After HF etching the ampoule is baked above 1000 °C for several hours in air, before being cooled rapidly to room temperature. After ampoule cleansing (without water) and etching, the chalcogenide chemicals for purification are batched and placed inside. The process steps for batching, drying and melting are shown as a block diagram in Figure 3.8.

The second example of fabrication of chalcogenide glass is a multicomponent mixture containing GeS_2-Ga_2S_3-CsI-Sb_2S_3 or SnS [30,31]. As shown in Table 3.4, a major difference

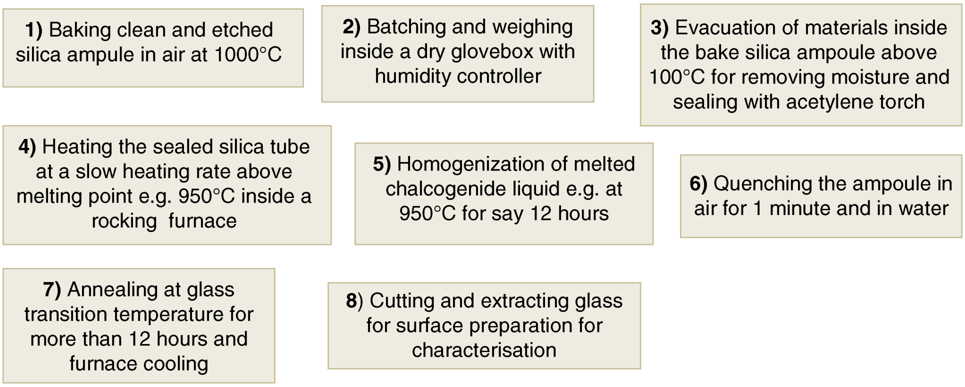

1) Baking clean and etched silica ampule in air at 1000°C

2) Batching and weighing inside a dry glovebox with humidity controller

3) Evacuation of materials inside the bake silica ampoule above 100°C for removing moisture and sealing with acetylene torch

4) Heating the sealed silica tube at a slow heating rate above melting point e.g. 950°C inside a rocking furnace

5) Homogenization of melted chalcogenide liquid e.g. at 950°C for say 12 hours

6) Quenching the ampoule in air for 1 minute and in water

7) Annealing at glass transition temperature for more than 12 hours and furnace cooling

8) Cutting and extracting glass for surface preparation for characterisation

Figure 3.8 *Steps involved in the fabrication of a chalcogenide bulk glass. The processing temperature shown represents the condition for melting GeS_2 based chalcogenide glass [27–29].*

in the melting conditions of As_2S_3 and GeS_2 glasses is in the characteristic melting, sublimation and boiling temperatures, which are much higher in GeS_2 based glasses than for most As_2S_3 compositions. From Figure 3.9 [20] the glass-forming region in the binary Ge-S system lies between GeS and GeS_{2+X} composition, which means melting the glass at more than 615 °C.

However, when designing a multicomponent GeS_2 glass with a mixture of compounds with a wide range of temperatures, it is essential to maintain the homogeneity of liquid. For example, for melting a mixture of GeS_2, Ga_2S_3, CsI and Sb_2S_3, the ampoule is heated slowly to more than 900 °C using a continuous stirring rocking furnace (Figure 3.10).

At elevated temperatures, chemical reactions occur that are described in detail in Reference [27]. One of the main products of the overall chemical reaction is the evolution of sulfur-bearing compounds, as predicted from the thermodynamic calculations in Reference [19], shown in Figure 3.11a, and evidenced in Figure 3.11b.

Besides the main difference between the characteristic temperatures of GeS_2 and As_2S_3, the GeS_2 based compositions are more amenable to structural changes, including the incorporation of rare-earth sulfides, using iodide and other sulfides than the As_2S_3 glasses. Aspects of rare-earth ion solubility in GeS_2 based glasses were analysed [24], following the earlier reports by Simons *et al.* [23]. As a result of structural changes, several thousand parts per million of Pr_2S_3 were dissolved in GeS_2 based glasses. The melted glass composition was homogenized at 950 °C before quenching and annealing (Figure 3.8).

The third example of chalcogenide glass melting is the gallium-lanthanum-sulfide (GLS) [33] family of glasses, which differ significantly in chemical properties from those of GeS_2 and As_2S_3 based glasses. As stated in Table 3.4, the sulfides of lanthanum and gallium have refractory like melting temperatures, which then precludes purification and synthesis via vapour phase. On the other hand, the halides of gallium and lanthanum form liquids at much lower temperatures; however, the vapour pressures of chlorides are insufficient for transporting them into the gaseous phase. From the literature no information is available on the direct synthesis or purification of GLS glass-forming compositions using S_2Cl_2 and hydrogen gas, which is thermodynamically feasible.

A major concern during melting a GLS composition is the presence of oxide impurities, which are prevalent in such refractory like materials due to strong chemical affinity of gallium and lanthanum. These materials also form oxysulfides, which is feasible due to predominant

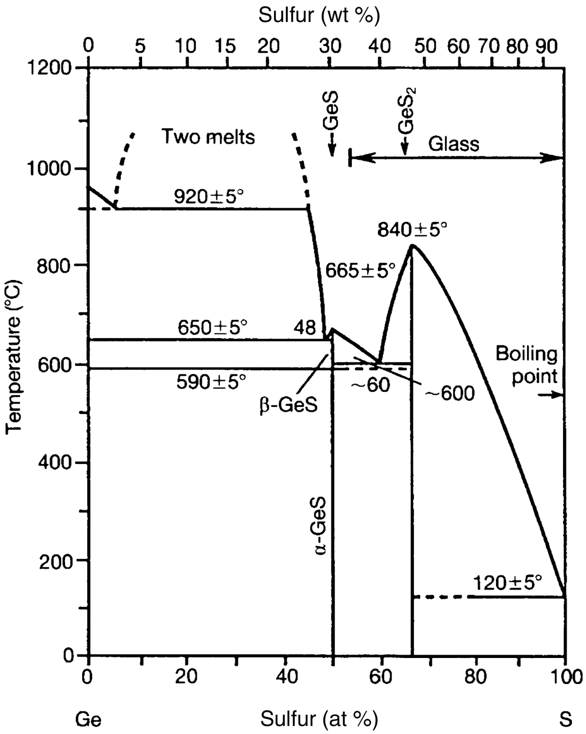

Figure 3.9 *A Ge-S phase constitution diagram, showing stabilities of various phases as a function of composition. The glass-forming region falls between GeS and* GeS_{2+X}*, where X is the overstoichiometric sulfur, representing compositions beyond 66.67 at% sulfur [21]. Source: Kumta 1994. Reproduced with permission from Springer.*

octahedron co-ordination of trivalent Ga and La ions, which allows sulfide and oxide anion exchange. From glass melting trials it was discovered that the presence of oxides and oxysulfides stabilizes the GLS glass [34].

One of the most stable compositions of GLS glass contains 70 mol.% Ga_2S_3 and 30 mol.% La_2S_3, as shown in Figure 1.18 in Chapter 1; this composition can be melted in a vitreous

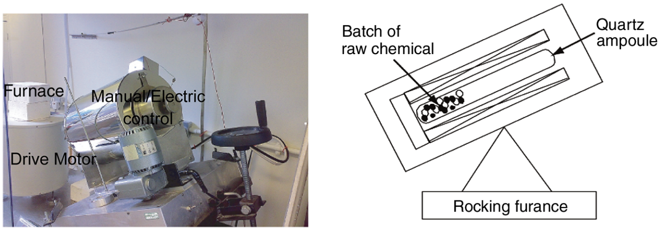

(a) (b)

Figure 3.10 *(a) Photograph and (b) schematic of a rocking furnace used for the fabrication of chalcogenide glasses [32]. Source: X. Jiang 2009. (See colour plate section.)*

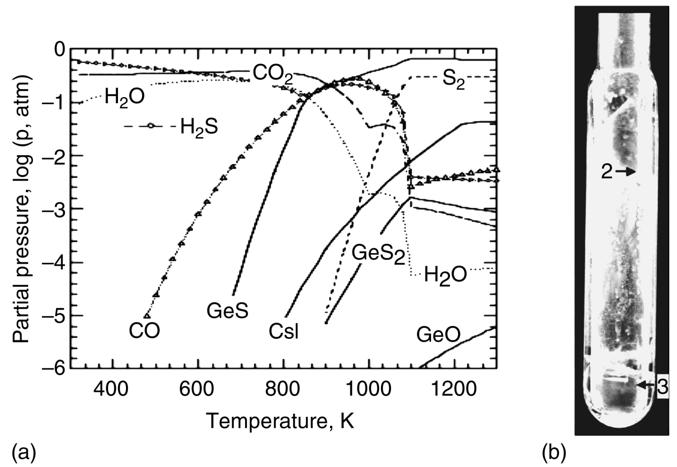

Figure 3.11 (a) Plot of computed partial pressures of various gases formed during melting of a GeS_2-Ga_2S_3-CsI glass inside a carbon coated silica ampoule. (b) Photograph of an ampoule containing GeS_2-Ga_2S_3-CsI glass (3) and condensed droplets (2), which is evidence that the gas phase circulation inside a sealed ampoule may be playing important role in determining the final composition and residual impurities in the quenched glass [27,28]. Reproduced with permission from Cambridge University Press.

carbon crucible inside a glove box to prevent ingression of moisture [32–35]. The melting of sulfide mixtures was carried out at 1150 °C for 23 h inside a silica-lined furnace placed inside a glove box, filled with dry nitrogen gas. The low viscosity of the glass-forming liquid aids homogenization of refractory La_2S_3 and oxygen-bearing sulfides. Using the melting and quenching technique developed by Brady [32], glass rods and tubes with diameters greater than 10 mm were cast with insignificant S-H absorption, although OH absorption was limited due to the residual concentrations of oxygen in the glass, required for its stability.

3.6 Need for Annealing Glass after Casting

As explained in Figure 1.1 in Chapter 1, the quenching of a glass-forming liquid from a temperature above liquidus (at which first crystalline phase may nucleate under equilibrium cooling condition) to room temperature causes non-uniform thermal stress to accumulate. The origin of this thermal stress is the molar volume fluctuation during quenching, which is frozen in. From molar free volume theory, the thermal expansion coefficient of a glass is directly and inversely proportional to the molar volume (V_m) and the glass transition temperature, T_g (see Equation 2.23 in Chapter 2) of a glass; the quenching process creates a gradient of molar volume, with the outside surface of a glass quenching faster than the inside. As a consequence of this molar volume gradient, the molar refractive index also changes proportionately across the dimension, causing significant distortion in images in lenses and telescopic devices.

The accumulated thermal stress (e.g. in the x-direction, σ_x) and strain (ε_x) are directly proportional to the thermal expansion coefficient (α) [36], as shown in Equations 3.18a and

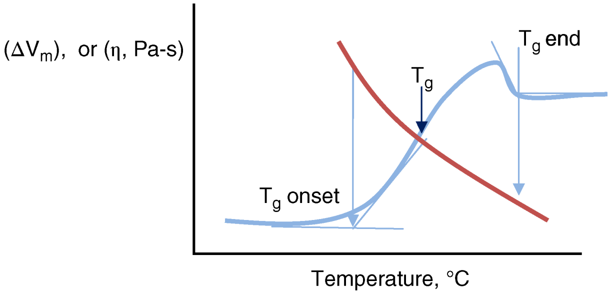

Figure 3.12 Schematic diagram of glass transition showing the transformation range for annealing a quenched glass, after melting and homogenization. The drop in the viscosity of transformed glass is shown schematically in the transformation range.

3.18b, respectively:

$$\sigma_x = -E\alpha(T) \tag{3.18a}$$

and:

$$\varepsilon_x = \frac{\left[\left(\sigma_x - \nu(\sigma_y + \sigma_z)\right]\right.}{E} + \alpha T \tag{3.18b}$$

In these equations, E is the elastic constant and ν is the Poisson's ratio. The thermal stress may be released by annealing the quenched glass at a temperature across the transformation range, i.e. between the onset of T_g and where the transition terminates (T_g end). Due to material flow in this temperature range (T_g end – T_g onset), shown in Figure 3.12, the quenched state inhomogeneity progressively diminishes with annealing time, which depends on the accumulated stress. The relaxation of thermal stress may be explained by the Williams–Landel–Ferry model [37]; using this model it is also possible to explain the relationship between the quenched state T_g and the apparent coefficient of thermal expansion. Alternatively, the relationship between temperature and viscosity using the Vogel–Fulcher equation [36] may be used to ascertain the annealing condition for a glass, as shown in Figure 3.12 in which the viscosity curve is superimposed onto the transformation range. The T_g onset roughly corresponds to the strain point whereas the T_g end is a point where the glass has transformed into a viscoelastic material, depicting creep flow that might be characterized using Fulcher equation.

Table 3.5 lists, for selected glass compositions, the strain ($\eta = 10^{13.5}$ Pa.s), annealing ($\eta = 10^{12}$ Pa.s), softening ($\eta = 10^{6.5}$ Pa.s) and working ($\eta = 10^{3}$ Pa.s) [35], which may be used for annealing and glass shaping and sub-liquidus forming, e.g. via extrusion and drawing.

3.7 Fabrication of Transparent Glass Ceramics

Before explaining the fabrication of transparent glass-ceramic materials, it is important to distinguish between a glass-ceramic and a transparent glass-ceramic. In transparent glass-ceramics, two different types of crystallites may be engineered. In the first approach the crystallite size range is much smaller in dimensions than the wavelength of light, which

Table 3.5 *Strain, annealing, softening and working points for selected glass compositions.*

Glass compositions	Thermal coefficient, ×10^7	Temperatures (°C) at iso-viscosity points			
		η (Pa.s)			
		$10^{13.5}$	10^{12}	$10^{7.5}$	10^3
Fused silica [38]	5.5	1070	1140	1667	2020
96 mol.% Silica glass [28]	8.0	820	910	1500	1960
Soda-lime sheet glass [28]	85	505	548	730	~1000
Aluminosilicate [28]	42	670	715	915	~1200
High lead silicate [28]	91	390	430	580	~1000
Low expansion borosilicate [28]	32	520	565	820	~1230
Phosphate glass [7,8]	70–82	618–685			
Germanium oxide [11,28]	100–110	380–450	415	450	545
Tungsten tellurite [11]	122–153	435	440	490	520
Sodium zinc tellurite [11]	155–185	310			
ZBLA (fluoride glass) [16]	190–220	305	315	345	400
GeS_2 glass [39]		370			
Gallium lanthanum sulfide [33]		520			

minimizes the scattering loss. The second approach may be to engineer glass-ceramics by forming crystallites that are identical or almost similar in molar refractive index so that the scattering factor (Q), arising as a result of the difference between the refractive indices of the glass matrix and nucleating crystals, is negligible. Both approaches require in-depth understanding of phase transformation processes, e.g. the crystal nucleation and growth kinetics and their temperature dependence for constructing a time–temperature–transformation curve, which permits control of crystalline phase volume. These aspects are examined in detail in Chapter 2. At present not many transparent glass-ceramics have been identified for commercial use, despite the potential applications in harmonic generation, photorefractive, acousto-optic, and laser devices.

In a glass-ceramic, two main types of crystallites may be formed and these are via congruent and incongruent process. In a congruent (also known as an isomorphous) phase transformation, the composition difference between the crystallites formed and matrix is negligible. Such congruent crystals nucleate and grow as a result of the relative thermodynamic stability of the crystalline phase with respect to the metastable glass. By contrast, an incongruent transformation is controlled by both the thermodynamics and kinetics of the decomposition of parent glass resulting in formation of multiple phases. The sub-liquidus viscous flow controls both nucleation and growth, as discussed in Chapter 2.

For fabrication of a glass-ceramic, it is essential to follow a set standard procedure that exploits the metastable character of a glass. For nucleation and growth of crystals, a heat treatment schedule is necessary, which is summarized in a diagrammatic illustration in Figure 3.13, and should be analysed in the realm of thermal relaxation of a glass. For this purpose, a differential scanning calorimetric scan is shown with glass transition (T_g), onset (T_x) and peak (T_p) of crystallization or devitrification and melting temperatures.

Several examples of fabrication conditions for binary and ternary silicate glass-ceramics are described in detail by James [40]; however, these examples do not include the size

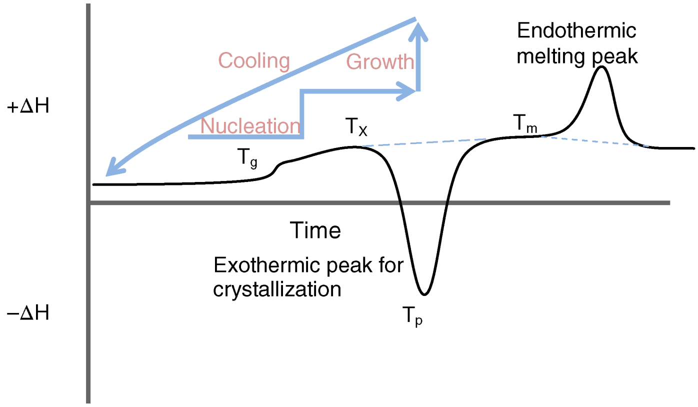

Figure 3.13 *Schematic DSC scan (solid line) showing characteristic thermal events during structural relaxation of a glass. The heat treatment cycle for glass-ceramic fabrication includes nucleation and growth, followed by cooling down to room temperature.*

distribution of nucleated crystals. A classic example of engineering glass-ceramic is Corning's Vycor glass composition (mol.%) $8Na_2O$, $20B_2O_3$ and $72SiO_2$, which is heat treated between 500 and 800 °C, below the liquidus temperature at 1100 °C. The composition suffers from extensive phase separation yielding silica-rich and boric oxide rich phases, which demonstrate a differing solubility in water, especially above room temperature. The boric oxide rich phase, when leached in water above room temperature, dissolves away leaving a silica rich phase intact. The residual concentration of Na_2O and its large internal surface area makes the silica-rich matrix more workable for shape forming at much lower temperature (1200 °C) than 2000 °C. The residual porosity in the Vycor matrix enables its use for infiltration with optically active dyes, rare-earth ions (e.g. Nd^{3+}, Yb^{3+}, Eu^{3+}) and noble metals. Despite such opportunity for engineering applications, little application of Vycor as optically active and photonic materials has been found.

Significant examples of transparent glass-ceramic fabrication are summarized in Table 3.6, in which the proposed applications are also briefly described with the measured dielectric and/or ferroelectric properties.

Other references for glass-ceramic fabrication and applications may be found elsewhere [48–50], which supplement the articles discussed in Table 3.6. The fabrication procedures described therein are applicable to numerous inorganic ferroelectric, piezoelectric and ferroelastic materials, which may be derived from glassy phase. For such materials the poling may also be applied to enhance the second harmonic generation, photorefractive, and ferroelastic and piezoelectric properties.

3.8 Sol–Gel Technique for Glass Formation

3.8.1 Background Theory

Formation of glass using the *sol–gel* technique differs significantly from the melting process, involving high-temperature chemical reactions, mixing and homogenization and quenching.

Table 3.6 *Summary of selected oxide glass-ceramic materials for ferroelectric based photonic device applications. Refractive indices were characterized using Sellmeier parameters:* $n^2(\lambda) = 1 + A + \left[B\lambda^2/\left(\lambda^2 - C\right)\right]$.

Materials system	Fabrication condition	Properties measured	References
Nickel- and silver-containing $BaTiO_3$, silver-containing Pb (Zr,Ti)O_3	Sol–gel mixing for oxide glass followed heat treatment at 300–700 °C in air, depending on oxide mixture. Followed by hydrogen reduction for precipitating nickel or silver, ranging from 3 to 20 nm in size	Dielectric properties as a function of temperature (ε) for $BaTiO_3$ without Ni (100–900), with Ni (400–1000), and Ag (560–1300). Pb(Zr,Ti)O_3 with Ag (550–2550)	[41] Dan *et al.*
Lithium niobate in $30Li_2O$, $10Nb_2O_5$, $15B_2O_3$, $45SiO_2$	Glass melting was carried out in air at ~1227 °C, followed by casting and heat treatment in the range 550–680 °C. Ion exchange at 400 °C in silver nitrate, followed by poling at 20 V at 10^{-3} torr for 1 h	Volume fraction of $LiNbO_3$ 0.02. Dielectric constant 5700	[42] Mukherjee *et al.*
Photorefractive crystals of bismuth germanium oxide $Bi_{12}GeO_{20}$ and lead germanate $Pb_5Ge_3O_{11}$	Note that these compositions form glass, too, which have not been explored thoroughly. Photorefractive crystals were grown via the Czochralski technique	Refractive index measured in the 450–700 nm range using minimum deviation. At 20 °C, for $Bi_{12}GeO_{20}$: $A = 2.165$, $B = 2.655$, $C = 7.891 \times 10^{-14}\,m^2$ and for $Pb_5Ge_3O_{11}$ the ordinary (n_o) and extraordinary (n_e) indices Sellmeier constants are: $A_o = 1.358$, $B_o = 1.929$, $C_o = 5.78 \times 10^{-14}\,m^2$, $A_e = 1.470$, $B_e = 1.687$, $C_e = 6.146 \times 10^{-14}\,m^2$.	[43] M Simon *et al.*
SrO-B_2O_3-TiO_2 with CoO for $SrTiO_3$ crystals	Melting $SrCO_3$, H_3BO_3, SiO_2, TiO_2 and CoO in air at 1100 °C. Dielectric characterization 110 Hz to 1 MHz	DTA was studied; followed dielectric properties in the 300–425 K range (150–325)	[44] Thakur and co-workers
Review of several ferroelectric glass-ceramic system containing $LiNbO_3$, $LaBGeO_5$, $BaTiO_3$, $PbTiO_3$, $LiTiO_3$	Crystallization of ferroelectric phases are described in detail by reviewing literature	For poled materials, the angular dependence of second harmonic generation measured	[45] Jain, [46]Gupta *et al.*
Ferroelastic and second order harmonic generation in glass-ceramic via $Ba_2TiGe_2O_8$ crystals	In a $30BaO$-$15TiO_2$-$55GeO_2$ glass, the $BaTiGe_3O_9$ crystalline phase forms for subsequent nucleation of the ferroelectric $Ba_2TiGe_2O_8$ crystalline phase	In powdered form the SH intensity of $Ba_2TiGe_2O_8$ crystals is about 130 times larger than that of pulverized α-quartz	[47] Takahashi *et al.*

In a sol–gel process, as the name suggests, two distinct steps are involved. A "*sol*" defines a solvent liquid medium in which colloid or polymeric species are present. The molecular assemblages that form the colloid may be amorphous or nano-crystalline, exhibiting a large surface that may not be in equilibrium. The "sol" formation then leads to a structural change in the condensed matter state, called the "*gel*"; during its production a further polymerization or new bond formation occurs by increasing the local order by forming a three-dimensional continuous network of colloidal suspension.

The physical chemistry of sol–gel process is briefly discussed to appreciate the accompanying structural changes from free-flowing liquid-like behaviour to a viscous gel that only flows under the influence of load. The gel-like behaviour is essential for engineering applications of sol–gel products. In sols, the cationic (metal-ion) and polyanionic species are brought into a solution medium in such a way that at a particular pH value the colloidal suspension or polymeric complex with like charge forms. As a result of the surface charge the polymeric clusters appear to be coulombically suspended. The positive surface charge based electric double layer model is a good approximation for characterization of the energy and flow behaviour of sols and gels. In an electric double layer, the surface charge distribution may be defined by using the Stern model [51], according to which the negative charge distribution away from the surface positive charge may vary. Adjacent to the positive charge layer, a more densely packed layer of negative charge exists, which forms the Stern layer, across which the potential (ψ) drops linearly in a manner approximated by the Debye–Hückel theory, which is only true for the following condition for net surface positive (n^+) and negative (n^-) charge distribution (ρ):

$$\rho = ze(n^+ - n^-) = -2n_o ze \sinh \left[\frac{ze\psi}{\kappa_B T}\right] \tag{3.19}$$

where:

$$n^- = n_o \exp \left[\frac{ze\psi}{\kappa_B T}\right] \tag{3.20a}$$

and:

$$n^+ = n_o \exp \left[-\frac{ze\psi}{\kappa_B T}\right] \tag{3.20b}$$

In the above equations, z and e are the magnitude of charge and electronic charge, respectively, T is the temperature on absolute scale, κ_B is the Boltzmann constant ($1.38 \times 10^{-23}\ \mathrm{J\,K^{-1}}$) and n_o is a pre-exponent.

If $ze\psi/\kappa_B T << 1$, then from the Poisson–Boltzmann equation for the divergence of the gradient of electrical potential at a given point (r) in space with dielectric constant (ε) the equation reduces to:

$$\nabla^2\psi = \frac{\left(8\pi n_o z^2 e^2\right)}{\varepsilon \kappa_B T}.\psi = K^2.\psi \tag{3.21}$$

The solution for Equation 3.21 [41] for potential of an ion at a distance r is:

$$\psi(r) = \frac{z.e}{\varepsilon.r}.\exp(-Kr) = \psi_o.\exp(-Kr) \tag{3.22}$$

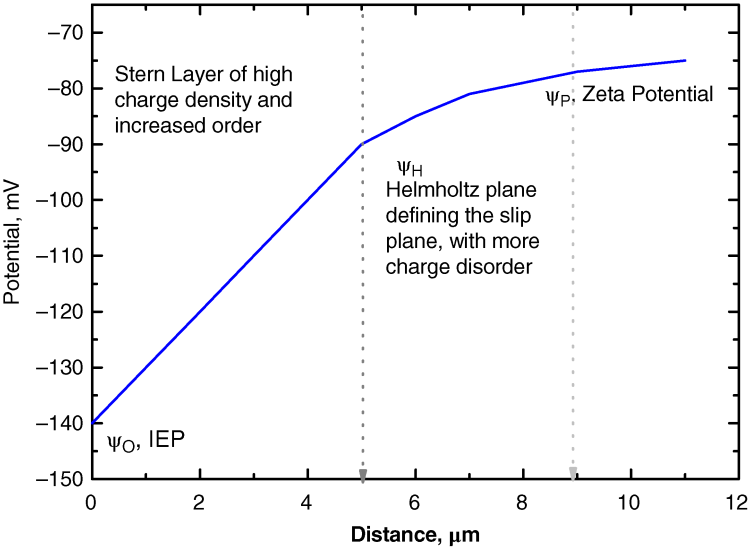

Figure 3.14 Potential versus distance diagram for electric double layer, which has structure characterized in terms of potential gradient between ψ_o, ψ_H and ψ_P.

Equation 3.22 explains the screened coulombic potential, which is inversely proportional to the distance in an electrolyte medium. The reciprocal of K is the length scale for charge screening, which is called the Debye length.

The generic Equation 3.22 for electric potential is fundamental in developing the model for sol–gel energetics that underpins the gel formation and stability. The Gibbs–Thomson model [41] determines the surface concentrations of adsorbed ions, based on the spatial distribution of potential, described in Equation 3.22.

The schematic diagram in Figure 3.14 shows the charge potential diagram, defining a Stern layer with a strong dependence of electrostatic potential, followed by the Helmholtz (ψ_H) plane where the linear relationship defined by the Debye–Hückel model is no longer applicable. The position of the slip plane defines the potential called the zeta (ψ_P) potential, the magnitude of which defines the stability of a colloid. The value of ψ at pH 0 defines the isoelectric potential (ψ_o, IEP). It should be stressed, however, that the isoelectric point is not the surface point of zero charge (PZC) [41].

Following a brief description of the potential energy model for colloids, it is essential to consider examples in the context of silica glass materials in order to make a comparison with materials derived from, say, chemical vapour deposition and melting techniques.

Figure 3.15 shows the relationship between the ψ_o for metals and their corresponding metal oxides, which is relevant for understanding the gelation process. The values of ψ_o obtained for metals are plotted against the ψ_o values of the metal oxide/hydroxide. Clearly, this is a linear relationship, assuming that ($\psi_o^{\text{metal}} = \psi_o^{\text{metal oxide}}$). In the measurements carried out by Kallay and co-workers [52], the isoelectric potentials for metal surfaces were obtained using positively and negatively latex particles, which were then compared with the literature data for corresponding oxides and hydroxides.

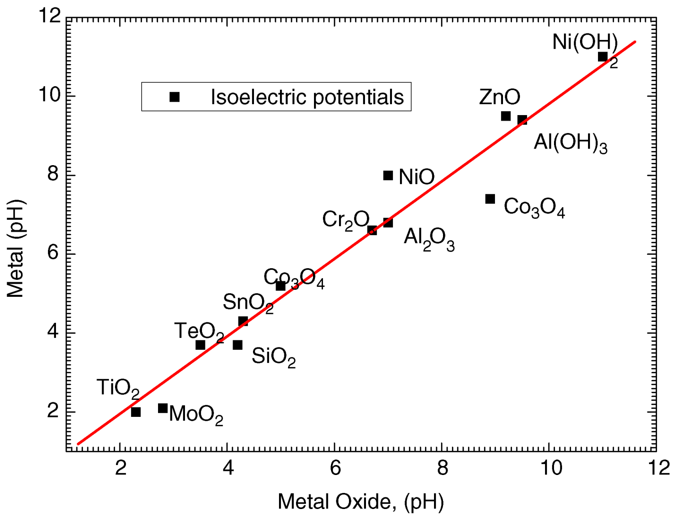

Figure 3.15 *Relationship between the pH for isoelectric potentials of metals and metal oxides. The line shows the relationship for two pH values for metal oxides being equal.*

Figures 3.14 and 3.15 show that the double layer around the particle and the isoelectric points are important for colloidal sol and gel stability. Since the surface of a new phase forming from sol reactions is in local equilibrium with the ionic groups, which characterizes the surface potential defined by Equation 3.22, the opposite charge in the medium will cover the surface away from another phase cluster in the vicinity. Considering a metal hydroxide (M-OH), the surface potential will be pH dependent as explained via Equations 3.23 and 3.24:

$$\text{M-OH} + \text{H}^+ \rightarrow \text{M-OH}_2^+ \tag{3.23}$$

$$\text{M-OH} + \text{OH}^- \rightarrow \text{M-O}^- + \text{H}_2\text{O} \tag{3.24}$$

The pH value at which surface charge neutrality is achieved is called the "point of zero charge (PZC)", which means that when the pH value is larger than pH at PZC the net charge is negative. Alternatively, when the pH is less than the PZC the surface charge is positive, which may be ascertained by using data in Figure 3.15.

3.8.2 Examples of Materials Chemistry and Sol–Gel Forming Techniques

Hench and West [53] wrote a major review in which they describe the history of sol–gel, dating back to the nineteenth century when Ebelman's [54,55] and Graham's [56] curiosity-driven scientific work in the sol–gel area created the embryonic understanding for processing inorganic glass and ceramic materials. The very first material explored then was silica sol–gel (SiO_2 gel) which was derived via the hydrolysis of tetraethyl orthosilicate, $Si(OC_2H_5)_4$ (TEOS) under acidic conditions. At that time, few material characterization techniques were available, including optical microscopy (after Robert Hook and Isaac Newton); it must have proven extremely difficult to understand the physical properties of such sol–gel materials. The sol–gel materials derived were very slow to dry, which meant that the fragility of these materials cannot be controlled for fibre drawing for engineering applications. The sol–gel route for precipitating materials also drew the attention of both Ostwald and Lord Rayleigh, who were intrigued by the formation of Liesegang rings and the growth of crystals.

Much later, in the middle of twentieth century, Roy and co-workers [57] utilized the sol–gel techniques to increase the homogeneity of ceramic materials on a molecular scale, something that was impossible to achieve via mechanical mixing techniques. Through sustained understanding of chemistry, it became apparent that the technique is capable of providing materials with very large surface areas (>100–$400\,\mathrm{m}^2\,\mathrm{g}^{-1}$), leading to the engineering of structures on the sub-micrometre to nanometre scale. The accompanying large surface area of the material, which acts against forming nuclei for crystal growth, is a major engineering issue in making large bulk materials derived from such materials due to poor fracture properties.

In this section we will concentrate on the sol–gel synthesis of silica and silica materials. The use of the silica gel technique for the fabrication of ultra-dry AllWave™ and zero-water optical fibres, which are now widely used in the modern optical fibre communication networks, is described in Chapter 4. Below, the steps involved in silica gel glass formation are described briefly using two different techniques, low pH and high pH techniques. Hench and West [53] summarized a seven-step process for making silica monoliths. Step 1 is mixing, in which sol (or colloid) is formed by mixing a precursor (e.g. alkoxide of silicon, ≡Si-OR) in water at a pH that may prevent precipitation of oxides/hydroxides:

$$\equiv \text{Si-OR} + \text{H}_2\text{O} \rightarrow \equiv \text{Si-OH} + \text{ROH} \tag{3.25}$$

Equation 3.25 is called the hydrolysis reaction. Following the hydrolysis, the condensation reactions shown in Equations 3.26a and 3.26b promote the first stage of polymerization of ≡Si–O groups, leading to the formation of ≡Si–O–Si≡, which is similar to linking of two silicon atoms via a bridging oxygen in a three-dimensional network of SiO_4^{4-} tetrahedra:

$$\equiv \text{Si-OR} + \text{Si-OH} \rightarrow \equiv \text{Si-O-Si} \equiv +\text{ROH} \tag{3.26a}$$

$$\equiv \text{Si-OH} + \equiv \text{Si-OH} \rightarrow \equiv \text{Si-O-Si} \equiv +\text{H}_2\text{O} \tag{3.26b}$$

Especially via Equation 3.26b, multi-member ring structures of (SiO_4) can start forming uniformly and the sol formation begins at a pH which may be close to IEP; this condition may also be structurally characterized by the ratio, $\Gamma = (\text{H}_2\text{O})/(\text{SiOR})_4$. Several examples of kinetics of hydrolysis and polycondensation reactions have been cited in the literature, and compared in the review by Hench and West [53]. Once the sol has formed, in step 2 the low viscosity suspension is cast into a suitable mould, where the gelation (step 3) begins slowly via further polymerization in accordance with Equation 3.26b. As a result the viscosity rapidly increases, providing a required shape of a cast gel. After gelation, in step 4 the ageing of gel (also known as the syneresis) begins, which retains the shape of gelled structure in the liquid during which the polycondensation continues alongside the residual reprecipitation of the gelled network. At this stage the bonding between the gelled mass begins by forming necking regions amongst clusters and as a result the aged materials gains a strength that is higher than that of a gel. Slow ageing is therefore essential for maintaining gel strength.

In step 5 the gel is dried carefully by preventing cracking. This is first step in which the residual liquid is carefully separated from the aged materials. By controlling drying, aero- and xero-gels are formed, which have much lower densities than the gels that are dried slowly. The control of drying conditions, for which the partial pressure difference may be characterized by the average capillary diameter of the aged gels, is essential for making high density materials [58]. After drying there follows the dehydration (step 6), during which the removal of surface silanol (Si–OH) bonds from the porous network is essential for achieving optical transparency of silica glass materials. The porous silanol depleted materials are also suitable for creating a randomly scattered medium into which another refractive index media, namely dyes, low-temperature nonlinear polymer, and fluorophores, may be infiltrated for specific optical functions.

In step 7 the material is densified by heating the porous silanol-depleted gel to a high temperature, e.g. above 900 °C, under controlled heating conditions without causing any structural failure in the material. The high-temperature heat treatment promotes both surface and bulk diffusion, leading to sintering of nano- and meso-scale pores. Alkoxide gels were densified well below the glass transition temperature of silica, which is around 1250 °C [59]. A thoroughly dried gel using chlorine to rid the material of remaining silanol when densified yields very high purity glass, compared to a conventionally melted silica glass. Such materials are not melted and homogenized and yet yield exceptionally high purity material for optical devices. For details on sol–gel processed materials it is recommended that the following references may be consulted: C. J. Brinker and G. W. Scherer [49] and the *Handbook on of Sol–Gel Science and Technology*, Volume 3, edited by S. Saka [60]. The mechanism of gel formation and its relationship with the sol has been investigated under acid and base conditions using Raman spectroscopy [61] and ^{29}Si MAS-NMR [62]. These investigations point out that both characterization techniques are extremely useful in determining the onset of polymerization in sols leading to structural stabilization via the completion of condensation and gelation steps. One way to quantify the ≡Si-O-Si≡ bond formation via bridging oxygen is to adopt Yoldas' model [63] for gelation time in acid (pH range 1–3) and base (pH range 6–9) [51].

Further examples of the sol–gel technique for optical fibre preform and waveguide fabrication are discussed in the context of AllWave ZWP Fibers™ at the website and patents filed by OFS [64].

3.9 Conclusions

In this chapter, the physical chemistry of the preparatory steps for raw and precursor materials for glass making are explained by considering thermodynamic equilibrium conditions. The processing conditions for the main families of inorganic glasses are explained. Supplementary references are given to expand the knowledge base for material preparation. The glass ceramic and sol–gel techniques are also discussed briefly in this chapter.

References

1. S. Sudo (1997) *Optical Fibre Amplifiers: Materials, Devices, and Applications*, Aretch House Incorporated, Norwood MA, ch 2 and 4.
2. S.D. Jackson (2012) Towards high power mid-IR emission from a fibre laser, *Nature Photonics*, **6**, 423–431.
3. R. Nogueira, L. Birlo, N. Alberto, H Lima, and J.L. Pinto (2012) Optical fibre sensors, in *Optical, Acoustic, Magnetic, and Mechanical Sensors Technologies* (ed. K Iniewski), CRC Press, Taylor and Francis Group, Boca Raton, FL, ch. 1.

4. P.S.J. Russell (2006) Photonic-crystal fibers, *Journal of Lightwave Technology*, **24** (12), 4729–4749.
5. F. Yu, W.J. Wadsworth, and J.C. Knight (2012) Low loss silica hollow core fibers for 3–4 μm spectral region. *Optics Express*, **20**, 11153–11158.
6. J.H. Campbell, T.I. Suratwala, C.B. Thorsness, J.S. Hayden, A.J. Thorne, J.M. Cimino, A.J. Marker III, K. Takeuchi, M. Smolley, and G.F. Ficini-Dorn (2000) Continuous melting of phosphate laser glasses. *Journal of Non-Crystalline Solids*, **263 & 264**, 342–357.
7. G. Karlsson, F. Laurell, J. Tellefsen, B. Denker, B. Galagan, V. Osiko, S. Sverchkov (2002) Development and characterization of Yb-Er laser glass for high average power laser diode pumping. *Applied Physics B (Lasers & Optics)*, **75**, 41–46.
8. Y. Mimura and T. Nakai (1991) Optical fibre loss mechanism, in *Fluoride Glass Fibre Optics (eds I.D Aggarwal and G. Lu)*, Academic Press Inc., San Diego, ch 6. pp. 261–270.
9. S. Shen and A. Jha (2004) The influence of F^--ion doping on the fluorescence $^4I_{13/2} \rightarrow {}^4I_{15/2}$ line shape broadening in Er^{3+}-doped oxyfluoride silicate glasses. *Optical Materials*, **25**, 321–333.
10. A.K. Varsheneya (2006) *Fundamentals of Inorganic Glasses*, 2nd edn, Society of Glass Technology, Sheffield, pp. 583–587.
11. X. Jiang, J. Lousteau, B. Richards, and A. Jha (2009) Investigation on germanium oxide-based glasses for infrared optical fibre development. *Optical Materials*, **31**, 1701–1706.
12. A. Jha, B.D.O. Richards, G. Jose, T. Toney Fernandez, C.J. Hill, J Lousteau, and P. Joshi (2012) Review on structural, thermal, optical and spectroscopic properties of tellurium oxide based glasses for fibre optic and waveguide applications. *International Materials Reviews*, **57**, 357–382.
13. A. Jha, B. Richards, G. Jose, T. Teddy-Fernandez, P. Joshi, X. Jiang, and J. Lousteau (2012) Rare-earth ion doped TeO_2 and GeO_2 glasses as laser materials. *Progress in Materials Science*, **57**, 1426–1491.
14. X. Jiang, J. Lousteau, S. Shen, and A. Jha (2009) Fluorogermanate glasses with reduced content of OH-groups for IR fibre optics. *Journal of Non-Crystalline Solids*, **355**, 2015–2019.
15. M.D. O'Donnell, C.A. Miller, D. Furniss, V.K. Tikhomirov, and A.B. Seddon (2003) Fluorotellurite glasses with improved mid-infrared transmission. *Journal of Non-Crystalline Solids*, **331** (1–3), 48–57.
16. P.W. France (1990) Extrinsic absorption, in *Fluoride Glass Optical Fibres* (eds P.W. France, M.G. Drexhage, J.M. Parker, M.W. Moore, S.F. Carter, and J.V. Wright), Blackie and Sons Ltd, Glasgow and London, ch. 6, pp. 136–142.
17. A. Jha (1993) Formation of scattering centres in fluoride glass preforms and fibres. *Journal of Non-Crystalline Solids*, **161**, 41–44.
18. I. Barin and O. Knacke (1977) *Thermo-chemical Properties of Inorganic Substances*, Springer, Berlin, p. 724.
19. ET. Turkdogan (1980) *Physical Chemistry of High Temperature Technology*, Academic Press, London, pp. 18–25.
20. J. Savage (1982) Optical properties of chalcogenide glasses. *Journal of Non-Crystalline Solids*, **47** 101–115.
21. P.N. Kumta and S.H. Risbud (1994) Review: Rare-earth chalcogenides – an emerging class of optical materials. *Journal of Materials Science*, **29** 1135–1158.

22. J.S. Sanghera, J. Heo, and J.D. McKenzie (1988) Chalcohalide glasses. *Journal of Non-Crystalline Solids*, **103**, 155–178.
23. D.R. Simons, A.J. Faber, and H. de Waal (1995) Pr^{3+} doped glasses for fibre amplifiers at 1.3 μm, *Optics Letters*, **20**, 468–470.
24. D. Marchese, G. Kakaranztas, A. Jha, B.N. Samson, and J. Wang (1996) Spectroscopic and thermal properties of GeS_2-based chalcogenide glasses. *Journal of Modern Optics*, **43**, 963–970
25. A.K. Varsheneya (2006) *Fundamentals of Inorganic Glasses*, 2nd edn, Society of Glass Technology, Sheffield, pp. 587–589.
26. A. Roine (2002) *HSC Chemistry® for Windows, Chemical Reaction and Equilibrium Software with Extensive Thermochemical Database, Version 5.1*, Outokumpu Research Oy, Pori, Finland.
27. D. Marchese, G. Kakarantzas, and A. Jha (1996) $^1G_4$ lifetimes, optical and thermal characteristics of Pr^{3+}-doped GeS_2 chalcohalide glasses. *Journal of Non-Crystalline Solids*, **196**, 314–319.
28. X. Liu, V. Tikhomirov, and A. Jha (2000) Influence of vapour-phase reactions on the reduction of OH^- and S-H bands in GeS_2 based glasses for infrared optics. *Journal of Materials Research*, **15**, 2864–2874.
29. D. Marchese and A. Jha (1997) The structural aspects of the solubility of Pr^{3+} ions in GeS_2 based glasses. *Journal of Non-Crystalline Solids*, **213&214**, 381–387.
30. X. Liu, S. Shen, and A. Jha (2005) Investigation on the kinetics of devitrification of GeS_2-based glasses. *Journal of Materials Research*, **20** 856–863.
31. X. Liu, M. Naftaly, and A. Jha (2002) Spectroscopic evidence for oxide dopant sites in GeS_2 based glasses using visible photoluminescence in Pr^{3+} probe ions. *Journal of Luminescence*, **96**, 227–232.
32. X. Jiang (2009) Engineering of Novel Single- and Multi-mode Infrared Optical Fibres for Device Applications, PhD Thesis, University of Leeds, ch 3, p. 147.
33. D. Brady (2000) Gallium-Lanthanum Sulphide Glasses for mid-IR optical fibres, PhD thesis, University of Southampton, ch 3, pp. 59–60.
34. Y.D. West, T. Schweizer, D.J. Brady, and D.W. Hewak (2000) Gallium lanthanum sulphide fibers for infrared transmission. *Fibres and Integrated Optics*, **19**, 229–250.
35. H. Takebe, D.J. Brady, D.W. Hewak, and K. Morinaga (1999) Thermal properties of Ga_2S_3-based glass and their consideration during fibre drawing. *Journal of Non-Crystalline Solids*, **258**, 239–243.
36. C.T. Moynihan (1993) *Journal of the American Ceramic. Society*, **76**, 1081.
37. M.L. Williams, R.F. Landel, and J.D. Ferry (1955) *Journal of the American Chemical Society*, **77**, 3701–3707.
38. A. Paul (1990) *Chemistry of Glasses*, 2nd edn, Chapman & Hall, London, pp. 110–117.
39. X. Liu (2003) Fabrication and Non-linear Properties of GeS_2 Based Chalcogenide Glasses, PhD thesis, University of Leeds, Leeds.
40. P.F. James (1989) Volume nucleation in silicate glasses, in *Glasses and Glass-Ceramics* (ed. M. H. Lewis), Chapman & Hall, London, ch 3, pp. 59–105.
41. A. Dan, T.K. Kundu, B. Satpati, P.V. Satyam, and D. Chakraborty (2004) Glass-ceramic metal nanocomposites containing ferroelectric phase. *Ferroelectrics*, **306**, 95–109.
42. P. Mukherjee and K.B.R. Varma (2004) Crystallization and physical properties of $LiTaO_3$ in a reactive glass matrix ($LiBO_2$-Ta_2O_5), *Ferroelectrics*, **306**, 129–143.

43. M. Simon *et al.* (1997) Refractive indices of photorefractive BIT, BCT, BGO, and PGO. *Physica Status Solidi (A)*, **159**, 559–562.
44. O.P. Thakur, D. Kumar, and O. Parkash (2004) Influence of CoO addition on structural and dielectric properties of strontium titanate glass ceramics. *Ferroelectrics*, **306**, 145–152.
45. H. Jain (2004) Transparent ferroelectric glass ceramics. *Ferroelectrics*, **306**, 111–127.
46. P. Gupta, H. Jain, D.B. Williams, J. Toulouse, and I. Veltchev (2006) Creation of tailored features by laser heating of $Nd_{0.2}La_{0.8}BGeO_5$ glass. *Optical Materials*, **29** 355–359.
47. Y. Takahashi, Y. Benino, T. Fujiwara, and T. Komatsu (2003) Formation mechanism of ferroelastic $Ba_2TiGe_2O_8$ and second order optical non-linearity in transparent crystallized glasses. *Journal of Non-Crystalline Solids*, **316**, 320–330.
48. V.N. Sigaev, S. Yu. Stefanovich, P.D. Sarkisov, and E.V. Lopatina (1995) Stillwellite glass-ceramics with ferroelectric properties. *Materials Science & Engineering*, **B32**, 17–23.
49. P. Gupta, H. Jain, D.B. Williams, O. Kanert, and R. Kuechler (2004) Structural evolution of $LaBGeO_5$ transparent ferroelectric nano-composites. *Journal of Non-Crystalline Solids*, **349**, 291–298.
50. V.N. Sigaev, E.V. Lopatina, P.D. Sarkisov, A. Marotta, and P. Pernice (1996) Non-isothermal crystallization of La_2O_3-B_2O_3.$2GeO_2$ glasses. *Thermochimica Acta*, **286**, 25–31.
51. A.W. Adamson and A.P. Gast (1997) Electrical aspects of surface chemistry, in *Physical Chemistry of Surfaces*, 6th edn, John Wiley & Sons, Inc., New York, ch V, pp. 169–201.
52. N. Kallay, Z. Torbic, M. Golic, and E. Matijevic (1995) Determination of the isoelectric points of several metals by adhesion method. *Journal of Physical Chemistry*, **95**, 7028–7032.
53. L.L. Hench and J.K. West (1990) The sol–gel process. *Chemical Reviews*, **90**, 33–72.
54. M. Ebelmen (1846) Recherches sur les combinaisons des acides borique et silicique avec les éthers. *Annales de Chimie et de Physique*, **16**, 129.
55. M. Ebelman (1847) Sur l'hyalite artificielle et l'hydrphane. *Comptes rendus de l'académie des Sciences*, **25**, 854–856.
56. T. Graham (1864) On the properties of silicic acid and other analogous colloidal substances. *Journal of the Chemical Society London*, **17**, 318–327.
57. D.M. Roy and R. Roy (1954) An experimental study of the formation and properties of synthetic serpentines and related layer silicate minerals. *American Mineralogist*, **39**, 957–975.
58. C.J. Brinker and G.W. Scherer (1990) *The Physics and Chemistry of Sol-Gel Processing*, 1st edn, Academic Press, London and San Diego.
59. L.C. Klein, T.A. Gallo and G.J. Garvey (1984) Densification of monolithic silica sol–gels below 1000°C. *Journal of Non-Crystalline Solids*, **63**, 23.
60. S Sakka (ed.) (2005) *Handbook of Sol–Gel Science and Technology, Volume III: Applications of Sol–Gel Technology*, Springer.
61. T.W. Zerda, I. Artaki and J. Jonas (1986) Study of polymerization process in acid and base catalyzed silica sol–gels. *Journal of Non-Crystalline Solids*, **81**, 365–379.
62. L.L. Hench and G.J. Orcel (1986) Physical-chemical and biochemical factors in silica sol–gels. *Journal of Non-Crystalline Solids*, **82**, 1.
63. B.E. Yoldas (1982) Introduction and effect of structural variations in inorganic polymers and glass networks. *Journal of Non-Crystalline Solids*, **51**, 105.
64. http://fiber-optic-catalog.ofsoptics.com/Asset/AllWave-117-web.pdf.

4

Optical Fibre Design, Engineering, Fabrication and Characterization

4.1 Introduction to Geometrical Optics of Fibres: Geometrical Optics of Fibres and Waveguides (Propagation, Critical and Acceptance Angles, Numerical Aperture)

Before the dawn of the electromagnetic theory of light, proposed by James Clerk Maxwell in 1864, the properties of light were described by Newton's experiments on dispersion and also in the realm of the experimental observations of Thomas Young in 1801, Fresnel in 1815 and Fraunhofer on interference, near field and far field diffractions of light, respectively. These experiments helped the then physicist to visualize light as a wave, with wave fronts when interacting and yielding maxima and minima of intensities, as shown in schematic diagrams in Figure 4.1. From these observations it was apparent that the concepts of plane and spherical waves were emerging, leading to complex forms of far and near forms of diffraction patterns, respectively.

Considering light as a wave helps in understanding how it propagates. Before Maxwell's electrodynamics for the propagation of light in optical fibres is considered, it is important to analyse the fundamentals of a geometrical optics approach, based on the reflection of waves. In the two pictures shown (Young's interference and Fresnel/Fraunhofer diffraction of light waves), it is natural to consider the sine or cosine waves functions for defining the wavelength (λ) and the phase (ϕ). In Figures 4.1a and 4.1b, a wave front is characterized by three important features, the phase (ϕ), its amplitude (I), which is defined by its displacement along the perpendicular axis with respect to the direction of propagation, and finally wavelength (λ, nm or μm). The wavelength is measured as the distance between the two peaks (maxima at $+\pi/2$ or minima at $-\pi/2$) or where the amplitude is zero (i.e. between 0 and π radian) and is always defined by the position of distance along the direction of propagation. The wave propagation is also defined by plotting the amplitude variation with time and, in this way of representation of amplitude, variation on a time scale between the two maxima or minima defines the time period (t, s) of a wave. The reciprocal of time period (t) is defined as the frequency ($1/t = \upsilon$, s^{-1}).

Inorganic Glasses for Photonics – Fundamentals, Engineering and Applications, First Edition. Animesh Jha.
© 2016 John Wiley & Sons, Ltd. Published 2016 by John Wiley & Sons, Ltd.

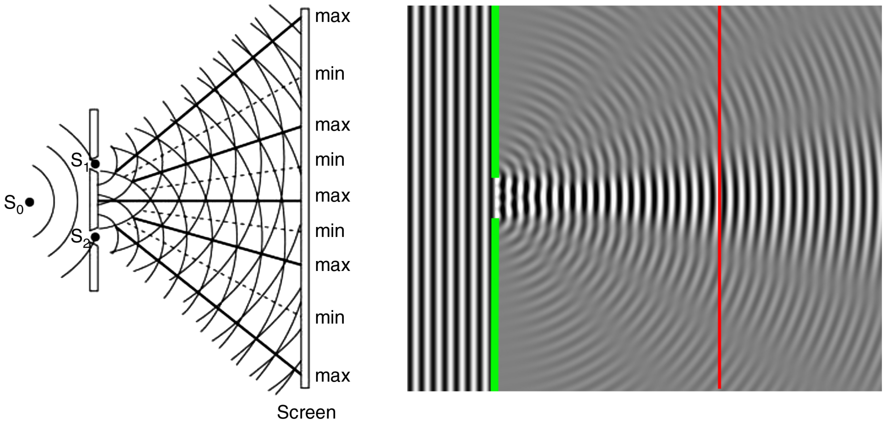
max
min
max
min
max
min
max
min
max
S_0
S_1
S_2
Screen

Figure 4.1 *(a) Young's double slit interference experiment [1] and (b) example of single slit diffraction [2].*

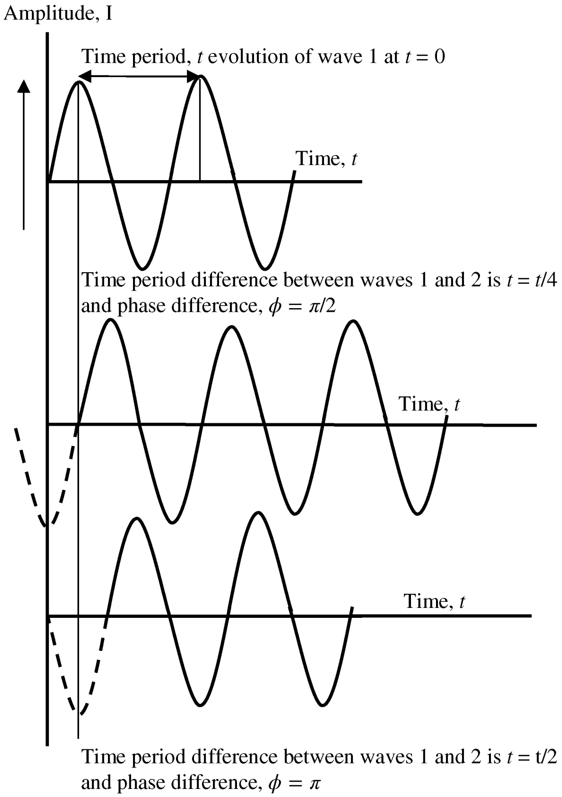
Amplitude, I
Time period, t evolution of wave 1 at $t = 0$
Time, t
Time period difference between waves 1 and 2 is $t = t/4$ and phase difference, $\phi = \pi/2$
Time, t
Time, t
Time period difference between waves 1 and 2 is $t = t/2$ and phase difference, $\phi = \pi$

Figure 4.2 *A temporal (t) illustration of wave propagation showing phase (ϕ) differences [3]. Source: Mynbaev 2001. Reproduced with permission from Prentice Hall.*

Figure 4.2 explains the origin of difference in phase ($\Delta\phi$) between the wave fronts 1 and 2 in relation to the time period. By considering the condition of superimposition, the addition or subtraction of amplitude of moving wave fronts may be analysed using vector analysis, yielding the net energy envelope of a resulting wave front. This is quite important when considering fibre or waveguide engineering. In the context of a propagating electromagnetic wave, the velocity of light (c) is expressed as a product of wavelength (λ, m) and frequency (υ, s^{-1}), i.e. $c = \lambda\upsilon$.

For considering the wave propagation inside optical fibre geometry, we will analyse briefly the condition for sustaining propagation of light inside a medium. When light travels through a homogeneous medium, a part of it may undergo reflection or scattering from the medium surface, while the remaining energy of light may transmit through the medium unattenuated, which is unlikely to happen, because of the interaction of electromagnetic waves with the medium. Invariably some of the incident energy is always absorbed. These three processes, reflection, transmission and absorption, may be explained by using the optical properties of materials, namely the reflectance (R), transmittance (T) and absorbance (A), respectively. The absorbance is explained below using the intrinsic and extrinsic properties of a dielectric medium. However, the reflectance and transmittance may be explained on the basis of the laws of reflection and refraction, respectively. If the incident intensity of light before entering a medium is (I_o), then the total intensity distribution as a result of the interaction with the medium may be attributed to the sum of three fractional or component intensities, I_A, I_T and I_R shown in Equation 4.1:

$$\begin{aligned} I_o &= I_A + I_T + I_R \\ &\qquad\qquad \text{or,} \\ 1 &= A + T + R \end{aligned} \tag{4.1}$$

By dividing both sides with I_o, the fractional representation of overall intensity I_o yields an equation that is sum of the absorbance (A), transmittance (T) and reflectance (R) terms. The absorbance (A) of a medium is characterized by the linear absorption, which is dependent on the path length (ℓ, cm) and the absorption coefficient (α_A), which is expressed mathematically by the Lambert–Beer law:

$$A = \frac{I_A}{I_o} = \exp(-\alpha_A \ell) \tag{4.2}$$

where the absorption coefficient (α_A, cm^{-1}) is also dependent on the molar extinction coefficient (ε_A) of the absorbant and its concentration (c, mol l^{-1}) in a given volume (litre, l), implying that the absorbance (A) may be redefined using the following equations [4]:

$$\alpha_A = \frac{\left[10\ell og_{10}\left(\frac{I_A}{I_o}\right)\right]}{\ell} = \frac{10A}{\ell}, \text{and } \varepsilon_A = \frac{\alpha_A(\text{cm}^{-1})}{c(\text{mol l}^{-1})} \tag{4.3}$$

in which the units of α_A and ε_A are in dB km^{-1} and $\text{dB km}^{-1}(\text{ppm})^{-1}$, respectively. Alternatively, the units of α_A, C (ppm) and ε_A are also expressed in cm^{-1}, mol cm^{-1}, and $\text{l mol}^{-1}\,\text{cm}^{-1}$, respectively. In some text books the term $-\ell og_{10}(I_A/I_o)$ is referred to as the optical density. Note that 1 cm^{-1} is equal to 10^6 dB km^{-1}. One more practical unit conversion is necessary to understand the absorption in a medium, and this is shown in Equation 4.4, in which the concentration, $c = (C\rho/1000M)$ in mol l^{-1}, and density (ρ_d, g.cm^{-3}) of the medium are considered for expressing the molar absorptivity unit (ε_M, l mol^{-1} cm^{-1}):

$$\varepsilon_\mathrm{M} = \frac{\varepsilon 10^{-3} M}{\rho_\mathrm{d}} \tag{4.4}$$

where 1 l mol^{-1} cm^{-1} is equal to $10^3\rho_\mathrm{d}/M$ in dB km^{-1} (ppm)$^{-1}$. Here M is the molecular weight of the medium. These units are useful in representing the density of absorption centres expressed in practical units such dB km^{-1}.(ppm)$^{-1}$.

Having analysed the absorbance of a medium, the reflectance (R) can be expressed in terms of the refractive indices of the boundary and the medium in which light enters, e.g. an air–glass or glass–water interface. The glass medium may be absorbing, which means that the absorbance (α_A) may be significant and may vary with the wavelength. This means that we should define the absorption factor (k_A):

$$k_\mathrm{A} = \frac{\alpha_\mathrm{A}}{4\pi}\lambda \tag{4.5}$$

leading to a redefining of the linear refractive index, $n = n' + ik_\mathrm{A}$. Here n' is the real part of the refractive index and the term ik_A determines the imaginary part. In a high refractive index medium (n'_2), the magnitude of reflectance may be quite large as a result, with respect to a boundary, having a refractive index $n'_1 < n'_2$. In this case a general formula may be written for the normal incidence condition [6]:

$$R = \frac{\left(n'_2 - n'_1\right)^2 + (k_{1\mathrm{A}} - k_{2\mathrm{A}})^2}{\left(n'_2 + n'_1\right)^2 + (k_{1\mathrm{A}} + k_{2\mathrm{A}})^2} \tag{4.6}$$

which for air or vacuum as a boundary medium reduces to Equation 4.7 because the k terms in numerator and denominator are negligible:

$$R = \left[\frac{(n'_2 - n'_1)}{(n'_2 + n'_1)}\right]^2. \tag{4.7}$$

In this analysis, no angular dependence of reflectance was considered, nor have we examined the angular dependence of the polarization of light (i.e. transverse electric (s-) and magnetic (p-) polarizations). The details of angular and polarization dependence of reflectance may be found in References [5] and [7]. For multiple surface reflection, the total reflectance (R_m) loss may be expressed by Equation 4.8:

$$R_\mathrm{m} = 1 - \left[1 - \left\{\frac{(n'_2 - n'_1)}{(n'_2 + n'_1)}\right\}^2\right]^m \tag{4.8}$$

As an example, if we now consider ($\Delta n = n'_2 - n'_1$) equal to 0.001 and $(n'_2 + n'_1) = 3$, then, say, after $m = 1000$ reflections the percentage value of R_m is 0.012%, which will increase to 0.125% when $\Delta n = 0.01$. The dependence of Δn on R_m is quite an important point to consider in optics because the reflection loss increases with the value of Δn, as we will further analyse to recognize its importance in optical fibre splicing and laser cavity engineering.

The residual energy of incident light after absorption inside the medium and reflected from the boundary of the medium is the energy of transmitted light. To analyse the transmittance,

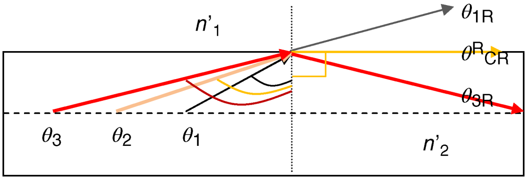

Figure 4.3 *Schematic representation of light guiding under the condition of total internal reflection (angle, θ_3-θ_{3R}). The angle θ^R_{CR} is called the critical angle, which has a corresponding incidence angle, θ_2. At angle θ_1 the light transmits through the medium. (See colour plate section.)*

let us consider the following schematic diagram in which both the reflected and refracted beam paths are shown as a function of the angular dependence of the incident beam. For reflection, the incidence angle (θ_i) is equal to the reflected angle (θ_{1R}) and for refraction Snell's law holds which means: $n'_1.\sin\ \theta_1 = n'_2.\sin\ \theta_2$. Figure 4.3 shows three different conditions of refraction between a denser medium with refractive index n'_2 and an adjacent rarer medium n'_1. The incident angle θ_1 corresponds to a normal refraction when the transmitted light exits the n'_2 medium at an angle of θ_{1R}. On increasing the angle from θ_1 to θ_2, the angle of refraction is equal to 90°, at which condition the light propagates along the interface, defining the minimum incidence angle or *critical angle* at which the incident light may be guided along the medium. At θ_3, which is the larger than θ_2 ($= \theta_{\text{Critical}}$), the light suffers total internal reflection, providing the condition of propagation of light inside the denser medium, n'_2.

For the critical angle condition, the angle of refraction is 90° and by using Snell's law the value of:

$$\theta_{\text{Critical}} = \sin^{-1}\left(\frac{n'_1}{n'_2}\right) \tag{4.9}$$

may be found, which must be satisfied to sustain propagation. Besides the condition for the critical incidence angle, Mynbaev and Scheiner [3] explain the importance of critical propagation and the acceptance angles, which are also essential for geometrical optics of light propagation. Accordingly:

> "a ray diagram is illustrated in Figure 4.4 by showing the critical propagation angle as the angle which a ray of light makes with the imaginary central axis of the fibre, and hits the boundary of the core glass at the critical angle."

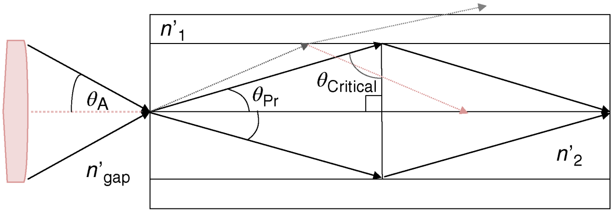

Figure 4.4 *Schematic representation of core and clad glass with propagation θ_{Pr} and critical $\theta_{Critical}$ angles, for a given acceptance angle (θ_A) from a diode laser. The condition for refractive indices of air, cladding and core glasses, respectively, are n'_{gap}(air) $< n'_1 < n'_2$. (See colour plate section.)*

Based on the geometry of propagation condition, the critical angle (θ_{Critical}) supplements the propagation angle (θ_{Pr}) within the triangle, which means it may be expressed using the properties of a triangle and is equal to:

$$\theta_{\text{Pr}} = 90^\circ - \theta_{\text{Critical}} \tag{4.10}$$

and on re-arranging, by moving θ_{Critical} on the left-hand side and using the sine function on both sides, we find that:

$$\sin(\theta_{\text{Critical}}) = \frac{n'_1}{n'_2} = \cos(\theta_{\text{Pr}}) \tag{4.11}$$

Finally, from Snell's law we can also establish that for air ($n'_{\text{gap}} = 1.0003$) as a medium between the source (e.g. a laser diode) and optical waveguide the acceptance angle (θ_{A}) may be calculated using Equation 4.12:

$$n'_{\text{gap}} \sin\theta_{\text{A}} = n'_2 \sin\theta_{\text{Pr}} \tag{4.12}$$

For analysing the geometry of a waveguide, the numerical aperture (NA) is given by:

$$\text{NA} = \left(n'^2_2 - n'^2_1\right)^{\frac{1}{2}} = \sin\theta_{\text{Pr}} \tag{4.13}$$

The numerical aperture defines the capturing capacity of light and is dependent on the refractive indices of the two core–clad media.

4.2 Solutions for Dielectric Waveguides using Maxwell's Equation

For waveguiding in a dielectric medium, such as silica or any inorganic glass, it is important to emphasize the solutions obtained from Maxwell's equation, the derivations for which are available in any textbook on optics and photonics [5,7]. For our purpose it is essential to consider both the geometrical constrains and the refractive index of the guided region. It is possible to characterize the single-mode properties of a waveguide, which means that the total energy of propagating photon in a waveguide with diameter "a" is confined into one packet (TE mode etc.), then for a given NA of the waveguide the cut-off wavelength λ (μm) may be found from the following equation for single-mode condition, where the V parameter is defined:

$$V \le 2.405 = \frac{2\pi a}{\lambda}\text{NA} \tag{4.14}$$

The cut-off wavelength is dependent on the minimum wavelength for the specified geometry and numerical aperture of a waveguide. The difference between single mode and multimode can be understood either by increasing the diameter and numerical aperture or by decreasing the wavelength. By setting these conditions the value of V exceeds more than 2.405, for which the value of number of modes (M) can be found from the acceptance angle, $\theta_{\text{A}} = \pi(\text{NA})^2$, leading to:

$$M = \frac{2A}{\lambda^2}\theta_{\text{A}} = \frac{2\pi^2 a^2}{\lambda^2}(\text{NA})^2 = \frac{V^2}{2} \tag{4.15}$$

Since the single or multimode mode condition in a step index fibre is dependent on Equation 4.14 (or its corollary in Equation 4.15), the modal distribution of total power P between the core (P_{core}) and cladding (P_{clad}) may be determined by the following equation [5]:

$$\frac{P_{\text{clad}}}{P} = 1 - \frac{P_{\text{core}}}{P} = \frac{4}{3}(M)^{-\frac{1}{2}} \tag{4.16}$$

For single mode fibre engineering using a combination of core and cladding glasses the numerical aperture is fixed so that the V value is kept below 2.4 for a given wavelength and core diameter. The approach is especially useful when engineering silica fibres with the chemical vapour deposition technique, the chemical principles of which are explained in Chapter 3 (also see later in this chapter). Controlling the geometry so as to fix the value of V below 2.4 is a means to overcome the inevitable small compositional fluctuations during the deposition of core glass and its diameter in order to minimize the modal dispersion.

4.2.1 Analysis of Mode Field Diameter in Single Mode Fibres [3–5]

In a single mode fibre when a beam of light either from an LED or a laser diode propagates and is imaged at the end of the fibre using a far field screen, the intensity distribution $E(r)$ in the far field may appear as shown in Figure 4.5. The beam profile can be characterized by the footprint of cross-sectional radius of a Gaussian curve [5]:

$$E(r) = E(0)\exp\left(-\frac{2r^2}{w^2}\right) \tag{4.17}$$

The mathematical representation of intensity variation E as a function of radius of the core is a reasonable approximation of the distribution of amplitude of the electric field. Because of the Gaussian nature of the intensity distribution in Equation 4.17, the limiting condition for the spread of intensity might stretch up to infinity, having a maximum, $E(r) = E(0)$. For this reason the mode field diameter is defined as "$2w_o$" for the fundamental LP_{01} mode in a single mode step-index fibre. The term $2w_o$ is defined by the e^{-2} value of the optical power, which for an LP_{01} mode is the equal to [5]:

$$2w_o = 2\left[\frac{2\int_0^\infty r^3E^2(r)\mathrm{d}r}{\int_0^\infty rE^2(r)\mathrm{d}r}\right]^{\frac{1}{2}}, \tag{4.18}$$

where $E(r)$ is the optical field distribution of LP_{01}, which is of course dependent on any microscopic variation in the refractive. By substituting $r = w_o$ into Equation 4.17,

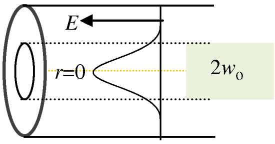

Figure 4.5 *Radial spread of intensity a Gaussian beam from which the mode field diameter ($2w_o$) is defined. Note that the intensity maximum is at $r = 0$ [5].*

we find that:

$$E(r) = \frac{E(0)}{e^2} = 0.135E(0) \tag{4.19}$$

which is where the $2w_o$ is defined, i.e. at the value of r where $E(0)$ reaches its [1/7.4]th value. In conclusion, the definition of mode field diameter is based on a Gaussian model of oscillating electric field component of a single mode light through a medium with effective refractive index, n_{eff}, determined by the component indices of core and cladding glasses.

Now we consider an ideal fibre with perfect rotation symmetry in which the two orthogonal polarization (x and y for electric and magnetic components, respectively) distributions will have a propagation constant of $\kappa_x = \kappa_y$ leading to equal effective index, $n_x = n_y$. This condition implies that from the point of launch into the fibre the two polarization states will remain in phase. However, in an optical fibre this ideal condition is rarely satisfied due to a stochastic variation in the composition, stress and micro-bend arising from fibre preform and fibre fabrication. Such variation yields a condition, $n_x \neq n_y$, which then gives rise to a small difference in phase velocity of the two modes [5]. This phase velocity differential is characterized as fibre or waveguide birefringence (B_f) and may also be written as a propagation constant differential, β:

$$B_f = n_y - n_x \tag{4.20a}$$

which leads to:

$$\beta = k_o\left(n_y - n_x\right) = k_o B_f \tag{4.20b}$$

Here $k_o = 2\pi/\lambda$ is called the free space propagation constant. Due to the presence of inevitable differential in phase velocity, the signal launched into a fibre will suffer from a small delay in phase relative to the fast axis, whereby the apparent difference of 2π will arise in the phase velocity after a critical length, L_{beat} (metres), which is called the beat length and is equal to:

$$L_{\text{Beat}} = \frac{2\pi}{\beta} \tag{4.20c}$$

Keiser [5] explains the difference in the modal properties of single-mode step and graded index fibres by using mathematical representation with boundary conditions ($0 \leq r \leq a$), as shown in Equation 4.21. In a graded index fibre, the index decreases in a parabolic gradient of concentration profile from the centre of a core to the edge of core–clad, after which the cladding index remains constant. The radial dependence of the refractive index is then:

$$n_1'(r) = n_1'\left[1 - 2\Delta\left(\frac{r}{a}\right)^{\alpha}\right]^{\frac{1}{2}} \tag{4.21a}$$

and for:

$$\begin{gathered} r \geq a \\ n_1'(r) = n_2' = n_1'(1 - 2\Delta)^{\frac{1}{2}} \end{gathered} \tag{4.21b}$$

Here $r < a$ is the radial distance from the fibre axis, a is the core radius, n_1' and n_2' are the refractive indices of core and cladding, respectively, and α is defined as a dimensionless parameter that characterizes the refractive index profile. Since the refractive index in a graded index fibre is continually gradient, then the refractive index difference is given by:

$$\Delta = \frac{\left(n_1'^2 - n_2'^2\right)}{2n_1'^2} \approx \frac{\left(n_1' - n_2'\right)}{n_1'} \tag{4.22}$$

In such fibres the numerical aperture NA may be expressed as a radial distribution for boundary conditions $r < a$:

$$\mathrm{NA}(r) = \mathrm{NA}(r = 0)\sqrt{1 - \left(\frac{r}{a}\right)^2} \text{ where } \mathrm{NA}(r = 0) \approx n_1'\sqrt{2\Delta} \tag{4.23a}$$

and for $r > a$:

$$\mathrm{NA}(r) = 0 \tag{4.23b}$$

For graded index fibres, all bound modes in the fibre must satisfy the condition $\beta \geq k_o n_2'$ for trapping the propagating modes within the core. The maximum number of trapped modes (M) can be found by:

$$\beta = k_o n_2' = k_o n_1'(1 - \Delta) \tag{4.24a}$$

and the total number of bound modes (M):

$$M = \frac{\alpha}{\alpha + 2} a(k_o n_1)^2 \Delta \tag{4.24b}$$

in a graded index fibre with refractive index profile given by Equation 4.21a.

4.3 Materials Properties Affecting Degradation of Signal in Optical Waveguides

Preservation of phase (ϕ), temporal (τ) and amplitude characteristics of waves in signal processing is essential for optical and data communication. In a single mode optical fibre, all three characteristics of propagating signal are affected adversely due to the interaction of electromagnetic waves with the medium. For this reason it is essential to analyse the mechanisms of signal degradation in optical fibres, so that necessary remedial steps for the recovery of original signal may be implemented by amplification so as to enhance amplitude, reshaping and reclocking the pulse train via dispersion control and management.

4.3.1 Total Intrinsic Loss

Conduction of photons in a dielectric medium, for example, in a silica optical fibre experiences a loss that may be comparable with the resistance in electronic conduction due to the scattering of electrons with atoms in the lattice structure of a conductor. The main intrinsic sources of loss of energy of propagating photons in light waveguides are the *electronic and molecular absorption processes and Rayleigh scattering*. These three factors add up and determine the theoretical limit of intrinsic loss of propagating photons, which they encounter at the boundary between the high-index core and low-index cladding glass structure in a standard waveguide.

4.3.2 Electronic Absorption

The electronic absorption of photons is determined by the electronic band gap (E_g, eV) of the dielectric medium. At $E_g = h\nu_g$, the energy of a photon is resonant with the band gap, and as a result it is lost in promoting the available valence band electronic states to higher energy states in the conduction band. For this reason, at short wavelengths, the transmission range of a medium is determined by the band gap absorption and the wavelength at which the electronic absorption begins to dominate is called the "*electronic cut-off edge*" of a dielectric medium. By comparison the metals and wide band gap elemental and compound semiconductors (e.g. Si, Ge, GaAs, InGaAs) are essentially opaque in the near-infrared part of the electromagnetic spectrum due to this resonant and above resonant absorption of photon energy. The short wavelength absorption loss (α_{el}, cm^{-1}) due to electronic band gap is expressed in Equation 4.25 in which A and a_o are the materials constant:

$$\alpha_{el} = A \exp\left(\frac{a_o}{\lambda}\right) \tag{4.25}$$

For characterization of electronic absorption in dielectric materials, the most common technique is to use a UV-visible-NIR spectrophotometer, in which a polished dielectric material is placed along the beam path, as shown in Figure 4.6, for measuring the absorption. The measured absorption clearly shows a smooth exponential function, which is possible to characterize by Equation 4.25. However, the overall electronic absorption is quite complex and has three main contributions (Figure 4.6). The Tauc region (A) at the highest energy state ($10^4 < E_o < 10^6$ cm^{-1}) is followed by the Urbach edge (B) in the intermediate energy band ($E_{el} < 10^4$ cm^{-1}). The lowest energy states (C) defines the defect states, which are at the tail end of the energy states [8–11].

In crystalline materials, region C is much more well defined than in amorphous and disordered materials due to the presence of broken or dangling bonds which create imperfections in the electronic states. In the high-photon energy-absorption region A, the absorption (α_{Tauc}) is due to the interband transition in which the valence band states with E energy are excited by the photon ($h\vartheta$, eV) for the combined density of states at E and ($E + h\vartheta$), which on integration yields a parabolic distribution of density of states, given by Equation 4.26 [8,12,13]:

$$\alpha_{Tauc} = C\left(\hbar\omega - E_{Opt}\right)^2 \tag{4.26}$$

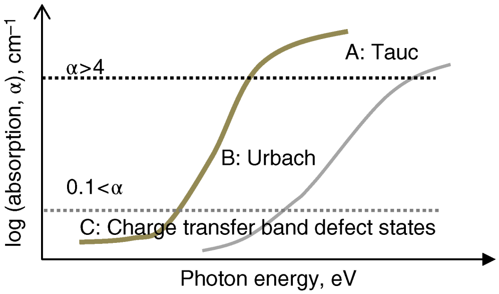

Figure 4.6 *Two different shapes of electronic absorption curves in chalcogenide materials in the UV-visible region. Regions A, B and C are identified in this figure with corresponding values of α [8].*

Table 4.1 *Calculated optical energy (E_{Opt}) gaps, energy tails (E_{tail}) and electronic band gap (E_g) for a range of tellurite and chalcogenide glasses [8–13]. Data from [8, 9, 10, 12, 13].*

Glass compositions (mol.%)	Electronic state energies (eV)			C (cm^{-1} eV^{-1})[a]
	E_{Opt} (eV)	E_{tail} (eV)	E_g (eV)	
$65TeO_2$-$25WO_3$-$10CaO$	3.15	1.34	3.85	NA
$90TeO_2$-$10WO_3$	3.43	0.13	3.80	NA
$90TeO_2$-$10BaO$	3.85	0.134	3.75	NA
$50.14TeO_2$-$35.71P_2O_5$-$14.15Bi_2O_3$	2.63	0.21		NA
As_2S_3	2.30		1.1 at room temp. At 77 K 2.15 amorphous 2.89 crystalline	4.0–7.5×10^5
As_2Se_3	1.76		0.8 at room temp 1.72 amorphous 1.94 crystalline	8.3×10^5
As_2Te_3	0.80		0.4	
Si			1.1	
Ge	0.89			6×10^5
GeS_2			2.88	

[a] NA: not available.

where C is constant and is nearly equal to:

$$\left(\frac{e^2}{nch^2 m_e^*}\right)(2\mu^*)^{\frac{3}{2}}$$

where μ^* is the reduced effective mass of electron and hole, n is the refractive index and E_{Opt} is the direct (smallest) band gap ($E_{cond} - E_{Valence}$) in the iso-wavevector (k) space. The Tauc region has been verified experimentally for many semiconductor crystalline and amorphous materials [9] and these are also applicable to high index oxide glasses and crystalline materials. Mott and Davis [9] pointed out that in Equation 4.26, the exponent on the right-hand side is equal to ⅓ or ½, depending on whether the transition is allowed or forbidden. Hogarth and Assadzadeh-Kashani [10] developed the following equation which was tested for validating the model using a range of calcium-tungsten tellurite (65 mol.% TeO_2, $(35 - x)$ mol.% CaO, x mol.% WO_3) bulk glasses and thin films. Calculated optical energy gaps and energy tails in calcium-tungsten tellurite glasses were reported and explained in detail by El-Mallawany [11]. The data for a range of tellurite glasses are reported in Table 4.1. In this table the energy tails of tellurite glasses are also reported:

$$\alpha(\omega) = \left(\frac{4\pi\sigma_o}{cn}\right)\left[\frac{\left(\hbar\omega - E_{Opt}\right)^2}{\hbar\omega.\Delta E}\right] = C_{Opt}\left[\frac{\left(\hbar\omega - E_{Opt}\right)^2}{\hbar\omega.\Delta E}\right] \tag{4.27}$$

El-Mallawany [11] in his *Tellurite Glasses Handbook* has compiled E_{opt}, E_g and relevant spectroscopic data for a large number of binary and ternary tellurite glasses, which may be relevant in the understanding of the nature electronic states. Mott and Davis [12] wrote a comprehensive review on optical and electronic properties of chalcogenide materials. In

Table 4.1, the electronic band gap (E_g) is approximated at the cut-off edge from a UV-visible absorption plot such as in Figure 4.6; it is the intersection point of the extrapolated linear part of the Urbach edge and the extended electronic absorption tail. The wavelength (λ_g, µm) at this point of intersection is called the cut-off edge and from this value of λ_g, the band gap energy E_g ($\hbar\omega_g$) in eV is given by $1.24/\lambda_g$(µm).

Lower in the energy scale as shown in Figure 4.6 is the Urbach edge, which is below the optical band gap region and defines the energy onset of the optical transition for an absorption coefficient less than $10^4\,\text{cm}^{-1}$. The Urbach edge in crystalline semiconductors is comparatively more sharply defined than in amorphous or glassy semiconductors, oxides and chalcogenides, in which the lack of three-dimensional periodicity creates a spread of electronic states, which may be empirically represented by Equation 4.28 [8]:

$$\alpha_{\text{Urbach}} = \alpha_o.\exp\left[(\hbar\omega - E_{\text{el}})\beta'\right] \tag{4.28}$$

Here β' is equal to 10–25 eV^{-1} and is a constant at room temperature, and E_{el} may be comparable with the lower range of the values of E_o. Besides crystalline semiconductors and oxide and chalcogenide glasses, the Urbach edge relationship is also followed in alkali halides, in which the value of β' is approximated by the temperature dependent factor $0.8/(\kappa_B T)$, where κ_B is the Boltzmann constant. Below room temperature, β' is found to be temperature independent. Elliott [8] explains the nature of Urbach edge in detail, in conclusion stating: "the Urbach behaviour even in crystalline solids is not well understood," which implies that in amorphous and glassy materials, due to the lack of periodicity, the Urbach edge remains more unclear than that in crystalline solids. In general, the Urbach edge, whether due to the intrinsic electronic structure or due to the external factors such as temperature, pressure and external field, can be characterized by:

$$\alpha_{\text{elec}} = \alpha_o.\exp\left(\frac{E - E_g}{\Delta E}\right) \tag{4.29}$$

in which the ΔE is approximated as the energy gap. Besides the temperature dependence of the Urbach edge, it can also change with pressure and application of electric field. With increasing pressure the edge shifts towards lower values, with a parallel shift of the edge in a few amorphous semiconductors. The application of an external electric field causes a shift in the Urbach edge, which is called the electro-absorption and is small in magnitude. For chalcogenide glasses and crystals, the data on electro-absorption process is not so clearly understood in the realm of current theoretical understanding [8]. With increasing field the edge becomes steeper and shifts to lower photon energy.

The optical absorption by intrinsic electronic defects differs from that of the extrinsic defects, such as the transition metals and rare-earth ions and quantum dots. In both cases the energy of defect states is broad, depending on the nature of defects and the electron–phonon coupling. Such states lie well below the optical (E_{Opt}) and electronic (E_{el}) energy gaps. Some materials, however, do exhibit sub-gap energy states which may lie within the band gap, and are observed in lead and bismuth based glasses and crystals. Typically these defect states range between sub-eV to less than 10 eV. Besides these defects, the charge transfer band states (α_{defect}) also contribute to the overall absorption, which may be estimated by:

$$\alpha_{\text{defect}} \cong \exp\left[\frac{\hbar\omega}{E_d}\right]\text{cm}^{-1}$$

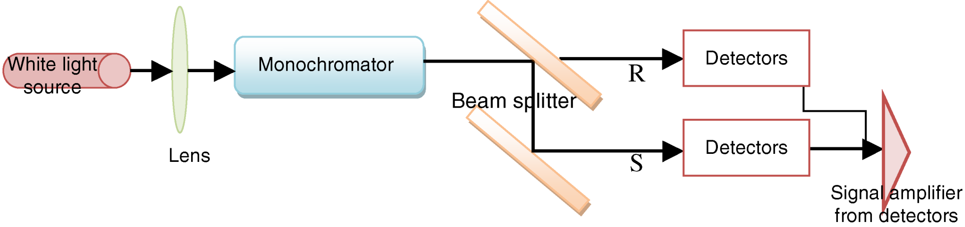

Figure 4.7 *Schematic drawing of a UV-visible spectrometer showing the light path for analysed sample (S) and reference (R).*

In the charge transfer band the oxidation states of defects play an important role, which can change the colour of the dielectric medium. Several transition metal ions due to open 3d–4s electronic transitions manifest such defects and these are well known in the literature as the solarization process. Photo-induced defects and absorptivity fall under this category.

4.3.3 Experimental Aspects of Determining the Short Wavelength Absorption

Absorption in the ultraviolet (UV) and visible (Vis) range may be characterized using a UV-VIS spectrophotometer, which may be able to scan between 180 nm (~6.9 eV) and 800 nm (1 eV). Modern spectrophotometers cover much larger range on the long wavelength part, and provide absorption data up to 3200 nm (~0.39 eV).

As can be seen in Figure 4.7, a white light bulb is used as a broadband source, from which the light travels through a monochromator and bandpass filter, allowing only a narrow line of overall photon spectrum to pass through. Inside the monochromator geometry the incoming light is divided into two beams by a beam splitter: one beam travels along the path of the sample and then reaches the detector whereas the other beam passes the free space in the spectrometer unattenuated and reaches the same detector. The difference in the absorption intensity, e.g. see Figure 4.6 (and also Figure 4.12) below, is plotted as a function of wavelength, since the optomechanical design inside a spectrophotometer and monochromator continuously allows scanning of absorption over a range of wavelength. In one of the light paths the analyte sample (S) is placed so that the other beam is used as a reference (R). When the absorption value reaches several decades, as happens at the electronic edge, the signal-to-noise ratio decreases dramatically, and this appears as sharp spikes in the high absorption part of the recorded data.

4.3.4 Scattering

The origin of light scattering in a dielectric medium is due to intrinsic electronic and molecular structure, which determines the scattering property. The scattering of light may be analysed in two main categories: *elastic* and *inelastic* scattering. During elastic scattering, energy is not lost which means that the scattered light from a medium is at the same wavelength (frequency) as that of the incident photon; this implies that the net change in momentum of incoming and scattered photons is conserved. As a result, the polarization direction (i.e. the circularity or planeness) of a wave front of the electromagnetic wave does not change, as if the oscillating dipoles (e.g. red colour billiards ball) collide elastically with the incoming electromagnetic wave fronts (white colour ball) and scatter the radiation (white ones) into a new direction. This is an elastic analogue of collision of dipoles with electromagnetic waves.

By contrast, in case of the inelastic scattering, the total energy is conserved by altering the frequency of the scattered light, after it has interacted with the medium. For example, in Raman scattering the energy (ω_o, frequency) of a monochromatic source of light after interacting with the quantum mechanically favoured phonons changes into two parts: the high-frequency (anti-Stokes, $\omega_o + \Delta\omega$) and low energy (Stokes, $\omega_o - \Delta\omega$) parts, representing the additive forward direction of scattering and deductive back-scattered processes, respectively. By adopting the billiard ball concept and adding the directionality of the wave vectors, the entire envelope of additive energy represents those billiards balls moving in the forward direction with higher energy than their original energy before interaction with the wave fronts of photons. The deductive ones, therefore, are the backscattered quantum of energy, when compared with the original energy of pump photons.

Since in Raman scattering the electronic polarizability of ionic (or atomic) positions and the selection rule allowed dipole moments contributing to the electronic polarizability are the major factors in determining the intensity of scattering, then it is possible to explain the billiard ball collision concept on the basis of vibronic (electron–phonon coupling) excitation in the presence of electromagnetic field. Using Figure 4.8 it is possible to explain the Stokes and anti-Stokes emissions of photons. The ground state in a molecular structure has a Bose–Einstein distribution at ambient temperature. When a pump laser is incident, selected Raman active vibronic states are excited to a virtual energy by creating the Stokes ($\omega_o - \Delta\omega$) and anti-Stokes ($\omega_o + \Delta\omega$) states.

The relaxation down to the ground state occurs via emission of scattered photons, as shown in the corresponding frequency spectrum. Since these two distributions of energies are quantized, it means that in a Raman spectrum with respect to the pump photon frequency the anti-Stokes (high energy or frequency) and Stokes (low energy or frequency) appear to

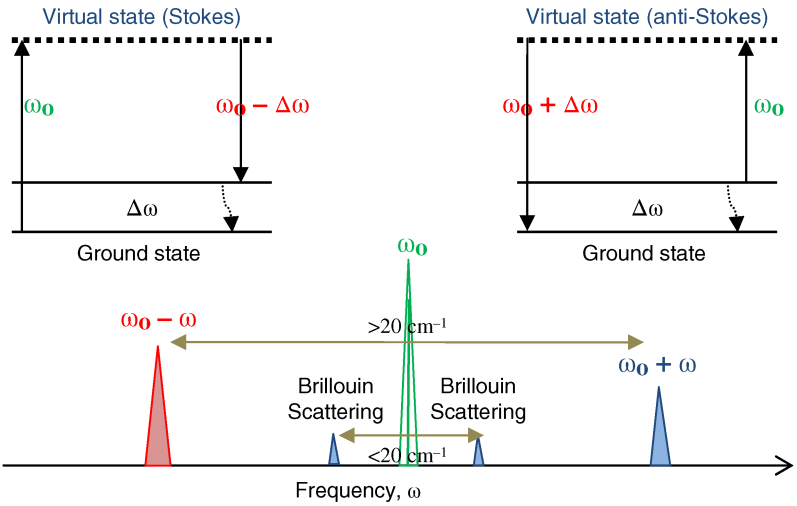

Figure 4.8 *Energy level diagrams for Stokes ($\omega - \Delta\omega_o$) and anti-Stokes ($\omega + \Delta\omega_o$) processes using the pump frequency (ω_o) and Brillouin scattering [7]. Source: Harman 1996. (See colour plate section.)*

the right and left of the spectrum, respectively as shown in Figure 4.8. The probability of the Stokes part is 10^4 to 10^5 less than that for elastic scattering processes. The probability of anti-Stokes is 100 times less than that of Stoke scattering, which is manifested in the magnitude of the spectrum. The frequency shifts compared with respect to the pump photons (ω_o) are characterized as follows: when the shifts are larger than $10\,\text{cm}^{-1}$, these are classed as the Raman scattering dominated by the optical phonons. The scattering with less than $10\,\text{cm}^{-1}$ is classed as the Brillouin shifts corresponding to acoustic phonons, which predominantly carry sound and heat waves in materials. Applications of inelastic scattering will be discussed in Chapter 7.

In comparison with Raman and Brillouin scattering, Rayleigh scattering is elastic scattering and is explained below for the characterization of the intrinsic loss of a dielectric medium.

4.3.4.1 Rayleigh Scattering

In considering Rayleigh scattering [7,14] in a dielectric medium it is important to assume that the mean free path, for example, of a monochromatic light is long, implying that the scattering centres are few and far between to yield a bundle of incoherent (out of phase) electromagnetic waves of energies in the forward direction. The resulting scattering intensity is the summation of all the intensities from all the scattering centres present in a medium.

By considering a monochromatic incident radiation with frequency $\omega = 2\pi c/\lambda$, the scattered intensity (I_s) may be explained in terms of the polarizability (α_o) of the medium under the influence of the maximum electric field strength (E_o), so that the dipole moment (p_d) may be expressed as $p_d \equiv \alpha_o E_o$. Within a sphere of radius r, the scattered intensity (I_s) envelop in the forward direction of ($\theta = 0$ to $\pi/2$) quadrant of a sphere is:

$$I_s(r,\theta) = \frac{\omega^4}{32\pi^2 c^3} \cdot \frac{(\alpha E_o)^2}{\varepsilon_o r} \sin^2\theta = \frac{(\pi\alpha E_o)^2}{\lambda^4} \frac{c}{\varepsilon_o r} \sin^2\theta \tag{4.30}$$

which explains why for Rayleigh scattering the intensity drop (I_s) is proportional to λ^{-4}, where λ is the wavelength of light. Equation 4.30 is useful, as we will employ it later in this chapter for characterization of extrinsic scattering in a dielectric medium. However, for the characterization of total intrinsic loss in a material, the Rayleigh scattering intensity (I_s) may be conveniently represented as a loss of energy (α_s) which is expressed as [14]:

$$\alpha_s = \frac{8\pi^3 p^2 \kappa_B T_f \beta_\alpha}{3} \left(\frac{n^2}{\lambda}\right)^4 = \frac{C_s}{\lambda^4} \left(\text{dB km}^{-1}\right) \tag{4.31}$$

In Equation 4.31, the Rayleigh scattering loss is expressed in terms of the physical properties of materials, namely the photo-elastic constants (p), a phase transition temperature such as melting (T_f), β_α is the isothermal compressibility, and n is the refractive index of medium. With increasing value of n, the value of α_s increases by the eighth power. Notably, the refractive index is dependent on the wavelength (see section below), which means at longer wavelength the value of n is less than that at shorter wavelengths, which is why the magnitude of scattering is much larger at short wavelengths than that at long wavelengths in IR. At a low intensity of monochromatic light, e.g. the transmitted milli-watt level of powers in optical fibres, the Rayleigh scattering is much larger in magnitude than the inelastic Raman and Brillouin scattering.

Table 4.2 *Properties of IR transmitting inorganic and semiconductor materials.*

Materials	Melting or transition temperature (K)	Refractive index at 633 nm	C_s (μm^4 dB km^{-1})	
			Measured	Estimated
Silica (SiO_2)	1995	1.45	0.47	0.02
BeF_2	825	1.37	0.065	0.12
GeO_2	1389	1.7	0.79	1.16
$90TeO_2$-$10Na_2O$	983	2.01	—	6.7
TiO_2 (rutile)	2144	2.84	—	84.7
$ZnCl_2$	591	1.7	—	1.4
$BaF_2.2ZrF_4$	873	1.51	—	0.54
GeS_2	1113	2.01	—	5.32
As_2S_3	585	2.38@1.6 μm	—	20.6
As_2Se_3	650	2.80@1.6 μm	—	75.6
Si	1683	3.44@2.554 μm	—	392
Ge	1213	4.06@2.554 μm	—	1476

Based on the known materials properties, Lines [15] compared the values of C_s (μm^4 dB km^{-1}) for different dielectric and semiconducting glasses, which are summarized in Table 4.2. With large refractive index of material the scattering factor by $(n)^8$, which is why materials such as silica are ideal for optical communication fibres. Notably, the refractive index of BeF_2 at 1.37 is lower than that of silica at 1.45, which at any wavelength within the optical communication window will reduce scattering by nearly 1.6 times. However, BeF_2 is not used in fibre engineering because of its high toxicity and hygroscopic nature, both of which make the fibre engineering and fabrication extremely challenging. In this table the ionic materials such as $ZnCl_2$ and $BaF_2.2ZrF_4$ have much lower refractive indices and transition temperatures than chalcogenide materials with sulfur, selenium and tellurium. The chalcogenide elements have a lone pair of electrons that occupy valence band state and are delocalized, compared with localized electrons in ionic crystals, e.g. halides. The refractive index TiO_2 (rutile) is 2.84 and is attributed to the metallic characteristic of titanium, which when oxidized forms a large band gap oxide with electronic defects. It is apparent from this table that the large refractive index materials in general have a small band gap energy. Silicon and germanium, which also exist in amorphous form and yet demonstrate semiconductor properties, have exceptionally large scattering factors, due to their large refractive indices.

Using Lines' approach, the values of C_s may be estimated by considering the two most dominant factors: $(n)^8$ and the temperature T_f(K), which may be possible by using the following approximation in eq.4.31 for different materials from the corresponding refractive indices and transition temperature (K) data in Table 4.2.

4.3.5 Infrared Absorption

The infrared absorption in dielectric media is determined by resonant dipole (cation–anion or positive–negative pair) interaction with photons. In a classical model when a dipole is induced (e.g. by external field) for inducing oscillation it may partially dissipate its energy by

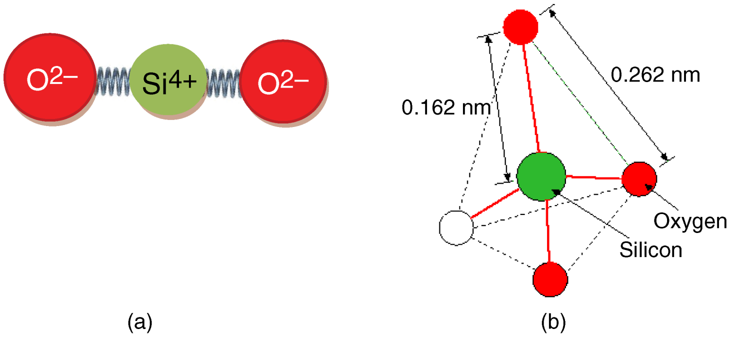

Figure 4.9 (a) Schematic representation of dipole–quadrupole linear harmonic oscillator based on the $(SiO_4)^{4-}$ tetrahedron (b) which is the building block of silica glass network. Note that the Coulombic spring constant is κ_d which is holding the two O^{2-} with Si^{4+} ions. (See colour plate section.)

emitting photons and via release of heat (lattice vibration). Not all dipole motions are energetically favourable in generating photons, as we will see in Chapters 6 and 7; however, the lattice vibration being energetically more favourable occurs more frequently than the photon emission. We consider this lattice vibration model for the analysis of IR absorption with relevant examples in the engineering of IR transmitting fibre and waveguide structures.

Let us consider the molecular structure of silica, which is constituted of cations (Si^{4+}) and anions (O^{2-}) defining the O^{2-}-Si^{4+}-O^{2-} phonons which determine the three-dimensional $[SiO_4]^{4-}$ tetrahedron structure. The cation–anion pair is, therefore, equivalent to two unlike poles, which is a dipole–quadrupole pair since in a dipole both the cation and anion have equal charge. In a Si—O bond, a Si^{4+}-charge is coupled with two O^{2-} anions, which when induced by incident photon under resonant condition performs linear harmonic motion at its mean position, ($x = 0$). The restoring force is equal to the Coulombic spring constant (κ_d) multiplied by distance (x) from the mean position. This force ($-\kappa_d.x$) on the reduced mass of cation–anion pair (μ_m) allows linear harmonic at the mean position of each cation–anion pair in the model tetrahedron structure (Figure 4.9). The equation of motion for such an oscillating dipole–quadrupole pair is:

$$\mu_m \frac{d^2x}{dt^2} + \kappa_d x = 0 \tag{4.32}$$

The solution of this oscillatory motion of dipole–quadrupole pair is:

$$x = x_o \exp(-i\omega_o t) \tag{4.33}$$

The fundamental oscillation angular frequency (ω_o) of the dipole–quadrupole pair is:

$$\omega_o = 2\pi\upsilon_o = \sqrt{\left(\frac{\kappa_d}{\mu_m}\right)}$$

$$\upsilon_o = \frac{1}{2\pi}\cdot\sqrt{\kappa_d/\mu_m}; \tag{4.34}$$

where

$$\mu_m = \frac{m_{Si}m_o}{m_{Si} + m_o}$$

Note that the fundamental frequency of vibration, υ_o in cm^{-1} is dependent on the reduced mass and the restoring force constant (κ_d) of the cation–anion charge pair forming a linear harmonic dipole–quadrupole pair, which is dependent on the Coulombic force acting between the pair. Assuming a linear harmonic oscillator between the cation–anion pair, the fundamental frequency is expected to decrease linearly with value of $\sqrt{\kappa_d}$ in a known family of hosts, e.g. in (SiO_2, GeO_2, SnO_2), (ZrF_4, HfF_4), (AlF_3, GaF_3), (ZnO, ZnS, ZnSe, ZnTe), and alkali and alkaline-earth halides families because of the cation–anion size effects which increase the value of x, leading to a decrease in the value of κ_d. As a result the material becomes more transparent in IR. Note that within a family of compounds, the Coulombic force falls quadratically with the ionic distance between the ion-pair, leading to increased IR transparency. A corollary of this statement is that the fundamental vibration frequency also decreases inversely with the square root of reduced mass in a chosen family of materials. In all such comparisons, the central assumption is that the chemical co-ordination environment is either identical or comparable but not dissimilar, in a given family of glass.

To analyse the extended IR transparency in materials, it is imperative to develop tools that provide insight into the complex vibrational structures of IR transmitting glasses and glass ceramics. Below, two important techniques—Fourier transformed infrared and Raman spectroscopic techniques—are described for inorganic photonic glasses and glass ceramic hosts.

4.3.6 Characterization of Vibrational Structures using Raman and IR Spectroscopy

Raman spectroscopy is an important structural analytical technique for characterization of the vibrational structure of condensed and gaseous states of matter. It is a supplementary technique, especially for material in which the second co-ordination shell ion–ion distances becomes difficult to characterize in disordered solid using the neutron or X-ray diffraction, X-ray photo-electron spectroscopic, EXAFS and nuclear magnetic resonance techniques. The vibration spectroscopic data may also supplement the inelastic neutron scattering which is different from the standard neutron diffraction.

From the selection rule for Raman spectroscopy, the vibration modes associated with the polarizability of molecular structure are probed, which are centrosymmetric (CS) and anti-centrosymmetric (ACS), unlike the asymmetric (A) IR modes (dipole active modes). The symmetric and anti-symmetric vibrations may be understood in terms of a reference ion in the centre, e.g. the Si^{4+} cation in the centre of $(SiO_4)^{4-}$ tetrahedra (Figure 4.9). In crystalline and partially crystalline materials, both types of vibrational modes (polarizability and dipole active) are more discrete due to strong quantization of vibrational density of states, which by contrast in glass and amorphous materials are diffused and broadened. As a result of the broadening (less defined) of vibrational states, it is essential in the analysis of glassy structure to use both the IR and Raman techniques and make comparisons with a reference crystalline sample. For example, comparing the Raman spectroscopic data of crystalline quartz and tridymite with silica and silicate glasses to ascertain a range of possible vibrational modes is quite helpful. By using selected reference crystalline materials, reliable vibrational analysis may be possible for sol–gel, amorphous, nano-crystalline and semi-crystalline materials. Such an approach may be adopted for systematic analysis of a wide range of materials, for example, crystalline, semi-crystalline and amorphous glass, polymers, carbon and semiconductor materials.

4.3.7 Experimental Aspects of Raman Spectroscopic Technique

The power of a scattered beam per unit solid angle in a medium may be expressed as [7]:

$$P_{\mathrm{Raman}} = N\left(\frac{\mathrm{d}s}{\mathrm{d}\Omega}\right).I_{\mathrm{o}}.V_{\mathrm{s}}.\left(\frac{\omega_{\mathrm{s}}}{\omega_{\mathrm{o}}}\right) = N\left(\frac{\mathrm{d}s}{\mathrm{d}\Omega}\right).P_{\mathrm{o}}.l_{\mathrm{s}}.\left(\frac{\omega_{\mathrm{s}}}{\omega_{\mathrm{o}}}\right) \tag{4.35}$$

Here N is number density of Raman active states (Stokes or anti-Stokes), ($\mathrm{d}s/\mathrm{d}\Omega$) is the differential scattering cross-section for photons, I_{o} and P_{o} are the incident intensity and power, respectively, V_{s} is the scattering volume and l_{s} is the length of the laser beam over which the scattered light was collected. For a detector that is used for sampling the Raman signal, then the above equation may be multiplied with the detector efficiency to determine the Raman signal on the detector:

$$P_{\mathrm{Raman}} = N\left(\frac{\mathrm{d}s}{\mathrm{d}\Omega}\right).I_{\mathrm{o}}.V_{\mathrm{D}}.\left(\frac{\omega_{\mathrm{s}}}{\omega_{\mathrm{o}}}\right)\Delta\Omega_{\mathrm{eff}}.\eta_{\mathrm{o}} \tag{4.36}$$

where V_{D}, $\Delta\Omega_{\mathrm{eff}}$ and η_{o} are the volume of the sample which a detector is sampling (it is less than the value of V_{s}), effective solid angle and optical collection efficiency, respectively.

A Renishaw inVia Raman microscope (shown schematically in Figure 4.10) may be equipped with several lasers. One of the commonest lasers for exciting molecular structures is the 514 nm Ar-ion laser, which is widely used for organic materials. The instrument consists of a Raman spectrometer and a modified optical microscope; the latter is especially useful for sampling small regions of less than 10 μm across and a few micrometres in depth. The image obtained is two-dimensional and is reconstructed using the Raman scattered light. It is important that before any measurement a calibration procedure is followed by using a standard for applying any corrections. The readings are taken after the machine is calibrated; the sample for vibration spectroscopic is then placed under the microscope objective and focused until the highest magnification is reached using a visible green laser. For this reason it is important to polish the surface of the sample and the focal power at the surface must be adjusted to reduce photo-induced damage which is often the case with lead oxide containing

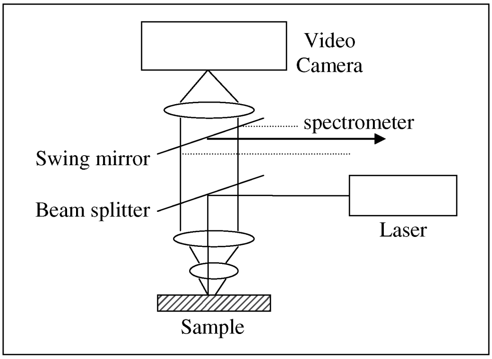

Figure 4.10 *Schematic representation of a Renishaw inVia Raman microscope.*

oxide and chalcogenide glasses. To reduce the photo-induced damage in the structure, it is necessary to adjust the focus power and the number of scans per sample.From experience it was established that less than 5 mW power through the objective lens is sufficient for acquiring data for chalcogenide and other photosensitive glasses. For collecting data for Raman spectroscopic analysis of a chalcogenide glass, each sample is scanned only for few times per sample in order to constitute a spectrum. By comparison, a photo-insensitive glass may be scanned many times under such incident power at 514 nm. Note that for rare-earth ion doped glasses (e.g. Er, Pr, Ho) the 514 nm laser is not suitable, because a significant amount of fluorescence is produced during analysis, which overwhelms the vibration signature from the glass structure.

4.3.8 Fourier Transform Infrared (FTIR) spectroscopy

Infrared spectroscopy is also a vibrational spectroscopic tool for the analysis of materials structure and optical transmission properties of a glass [8]. This spectral range is divided into three regions when compared with the visible range spectrum (0.4–0.75 μm): the near- (0.8–2.0 μm), mid- (2.0–25 μm) and far-infrared (25–1000 μm). The far-infrared region is adjacent to the THz region, and has low energy signifying rotational spectroscopy, whereas the high energy in the near-infrared region reflects the overtones or harmonic vibrational bonds. Between these two regions lies the mid-infrared region, which is typically designated as the region of fundamental vibrations and associated rotational–vibrational structures [16]. There is a difference between a standard IR spectroscopy and an FTIR. In a normal IR spectrometer two beam paths are used, one through the sample and the other blank. The resultant spectrum is the absorption spectrum obtained from the difference of the absorption in the two beam paths. In FTIR, a Michelson interferometer improves the instrument design and data quality.

There are several commercial suppliers of FTIR spectrophotometers in the market place. In one of the types of spectrophotometer, absorption, transmission and reflection measurements may be carried out. A spectrometer consists of a broad band IR source (glow bar) that provides light to pass through a Michelson interferometer, see Figure 4.11, operating over the near- and mid-IR wavelengths. A DTGS (deuterated triglycine sulfate) detector with a KBr window is used to cover the spectral range 4444–400 cm^{-1} (2.25–25 cm^{-1}). The beam splitter used consists of a germanium semiconductor on a potassium bromide KBr substrate

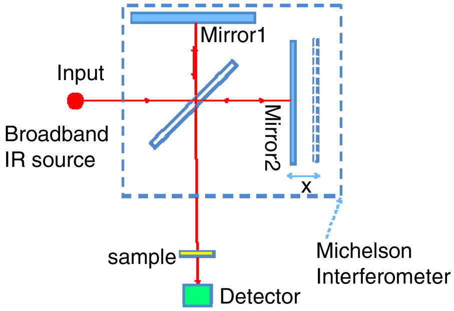

Figure 4.11 Optical path diagram for an FTIR instrument for measuring absorption bands and edges.

operating between 10 000 and 400 cm^{-1} (1–25 cm^{-1}). For measurements it is important to polish sample surface to a reasonably high optical quality with no apparent surface scratch. The light entering and exiting surfaces should be parallel on using a 5 to 10 μm polishing cloth.

The Michelson interferometer in an FTIR consists of two mirrors (1 and 2) and a beam splitter. In an FTIR, mirror 1 is fixed and mirror 2 is moved. One arm of the interferometer is fixed and the other has a moving mirror which allows the path length difference to be changed with time. The output beam from the interferometer passes through the sample and onto a detector. The moving mirror produces a signal at the detector which changes in the time domain; this signal can be converted into the frequency domain by fast Fourier transformation leading to a complete spectrum for the sample.

The difference in distance between the two mirrors and the beam splitter at any time is x. The optical path difference for light traversing to and from the beam splitter to the mirrors is twice (2×) as long for constructive interference to take place, for which the following relationship must hold for a monochromatic light:

$$2x = n\lambda, \text{ or } 2x = \frac{n}{\omega}2\text{x}, \text{ where } \omega = \frac{1}{\lambda} \tag{4.37}$$

Here n is an integer, λ the wavelength in μm and ω the wave number in cm^{-1}. With monochromatic light moving mirror 2 will produce a set of sharp intensity peaks. Broad band illumination will produce a more complex pattern that is dependent upon the exact spectral feature of the white light source. Since the intensity is a function of wave number (ω) and path difference (x) in Equation 4.38, the spectrum to be determined is $I(x, \omega)$ [17]:

$$I(x,\omega) = I(\omega)[1 + \cos(2\pi\omega x)] \tag{4.38}$$

The total intensity at the detector is given by:

$$I(x) = \int_0^\infty I(x,\omega)\mathrm{d}x = \int_0^\infty I(\omega)[1 + \cos(2\pi\omega x)\mathrm{d}x \tag{4.39}$$

Equation 4.39 is a Fourier cosine transform. The inverse of this function may be computed to yield an $I(\omega)$ spectrum of the sample being measured. In practice the mirror is moved over a small range and requires the use of an apodizing function to prevent ringing on peaks due to an abruptly terminated Fourier transform. In general the FTIR instrument has much better signal-to-noise ratio than a dispersive spectrometer. Since all frequencies are sampled simultaneously, the measurements remain unaffected by the intensity fluctuations in IR source, which is a glow bar. An FTIR is also equipped with a laser input, together with a broadband source, which is used to continuously calibrate the instrument, and this leads to extremely accurate wave number measurement.

Once the sample thickness is known or measured, the raw absorption data from the spectrophotometer is then divided by the sample thickness to yield the absorption coefficient or the absorbance (A) in cm^{-1} or % transmission. The principle of IR absorption can be simply explained using the Lambert–Beer law (see Equation 4.2 and 4.3 above) for a given path length (ℓ, cm). A beam of light propagating through this medium will be absorbed, reflected and the remaining will exit the medium, as explained in Equation 4.1. In the case of IR absorption, the photons are absorbed by the dominating molecular vibrations in the

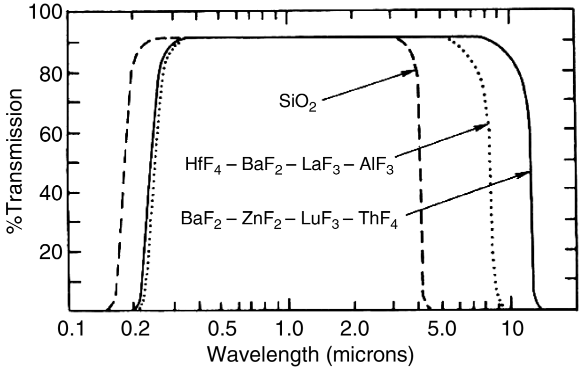

Figure 4.12 *Example of the measured percentage transmission as a function of wavelength for oxide and fluoride glasses [18]. Source: Parker 1989. Reproduced with permission from Springer.*

near-IR and mid-IR regions. The measured absorbance (α_{IR}) is then plotted against wavelength, as shown below in Figure 4.12, for a given sample thickness. In this figure the short-wavelength part of electronic edge absorption, measured using a UV-visible spectrometer, is added with the infrared absorption, yielding a complete transmission spectrum for each type of glass therein.

4.3.9 Examples of the Analysis of Raman and IR spectra

The analysis of vibrational structure using FTIR provides the IR absorption bands and cut-off edge which is the cumulative effect of all possible molecular vibration modes. The FTIR absorption may also be supplemented by Raman spectroscopic data for the symmetric and anti-symmetric (AS) vibrations and IR reflection for asymmetric and symmetric vibrations. Selected examples of vibrational structure of inorganic glasses are discussed in detail by Wong and Angell [19]. Using FTIR and Raman spectroscopy, the transverse optical (TO) and longitudinal optical (LO) phonon structures may be characterized in a glass.

4.3.9.1 Borate Glasses

The spectroscopic analysis of unary B_2O_3 glass using IR transmission [20] and reflectance [21] techniques shows that there exists an intense band at 1260 cm^{-1} followed by a high frequency shoulder at 1420 cm^{-1} and a weak band at 720 cm^{-1}. The presence of boric acid groups at room temperature is apparent from the bands at 3241, 1542 and 1184 cm^{-1}, all of which diminish with increasing temperature and become less apparent at 170 °C. However, on increasing the temperature to 1000 °C the bands at 1316 and 720 cm^{-1} remain dominant.

The Raman spectroscopic data of B_2O_3 glass differs significantly from IR spectroscopic data by depicting two broad weak bands in the regions of 400–750 and 1250–1550 cm^{-1} with a strong peak at 807 cm^{-1}. By comparison the low frequency Boson regime at room temperature shows a peak at 24 cm^{-1}. In the proposed model of B_2O_3 glass, the structural units, consisting of five-atom cells (B_2O_5), are considered to have one bridging oxygen between each pair of boron atoms (Figure 4.13).

More details on the Raman spectroscopy of borate glasses may also be found elsewhere [22,23]. The infrared reflectance and transmission spectra of binary sodium borate

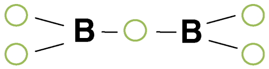

Figure 4.13 *Molecular structure of boron oxide glass showing the $[(BO)_3]^{3-}$ structural units [19].*

(0–33 mol.%) were analysed by Borelli and Su [24] and the main conclusion from the analysis of borate structure was that the molar concentrations of Na_2O affect the threefold boron to fourfold boron ratio, i.e. the (BO_3) to (BO_4) ratio. From the point of view of engineering rare-earth and transition metal ion doped glasses, the co-ordination environment of dopants determines the effective electron–phonon coupling, which is not only important in terms of controlling the spectral broadening due to the electronic transitions in rare-earth or transition metal ion but also the overall phonon-mediated decay rate for the design of lasers and amplifiers. With reference to the borate structure, an example is given in the engineering of Er^{3+}-ion doped boron oxide modified tellurite glass, in which the prevalent boroxyl rings BO_3 dominate, as there was little evidence for BO_4 tetrahedra in the glass [25].

4.3.9.2 *Silicate Glass*

Raman spectroscopic analysis of vitreous silica shows strong optical phonon bands at 470 cm^{-1} and weak high phonon peak at 1120 cm^{-1}. In the IR reflectivity spectrum, due to the selection rule, both peaks at 1120 and 500 cm^{-1} (470 cm^{-1}) appear more intense and are attributed to υ_3 and υ_4 (Type F) asymmetric vibration peaks of SiO_4 units [26]. By contrast, in the Raman spectra the symmetric stretch (υ_1) and double degenerate (υ_2) peaks, assigned as Type A (1065 cm^{-1}) and E (790 and 443 cm^{-1}), are dominant. Wong and Angell [19] compared the Raman spectroscopic data [27] for natural diopside, $(Ca_{0.5}Mg_{0.5})O.SiO_2$, crystals, an example of a chain meta-silicate structure. In this composition range, a glass of identical composition was made and their Raman spectroscopic data were compared with the natural crystals. It was reported that amongst the 30 fundamental oscillations active in Raman, 20 ($10A_g + 10B_g$) modes correspond to the internal vibrations of SiO_4 chains. The external modes are divided between the translation ($2A_g + B_g$) and rotation (B_g) motions of the chains, relative to each other and vibrations of Ca^{2+} and Mg^{2+} ($2A_g + B_g$). When comparing Raman spectra of diopside crystal with glass, which has an equal number of non-bridging and bridging oxygen, the dominant peaks in glass are at 1000 and 625 cm^{-1} and these are redshifted with respect to vitreous silica peaks at 1120 and 790–800 cm^{-1} and correspond to sharp crystalline modes at 1015, 860 and 668 cm^{-1}. The identified vibration frequencies are assigned to a combination of vibrations of Si—O bonds and deformation of O—Si—O bond angles. Since two different cations (Ca^{2+}/Mg^{2+}) are involved in the structure of diopside, the breadth of optical phonon spectrum in glass with respect to Ca and Mg ion doped diopside crystals is large for accommodating a multitude of distribution of bond angles around bridging and non-bridging oxygen ions. The vibrations of cations in an undefined cage of O^{2-} ions are attributed to exist around 340 cm^{-1} in both the crystal and glass. Finally, the bending modes of the Si—O—Si chain are observed around 90 cm^{-1} in both crystals and glass.

Another important aspect of Raman spectroscopic analysis of strong covalent network forming glass, such as silica, is to analyse the extent of interconnectivity of the network, which may be ascertained by characterization of the depolarization ratio ($\rho_{\text{HV-HH}}$). This ratio is a measure of lack of symmetry in the dipole moments of the structural units for which there may be no corresponding change in the polarizability. An example of interaction of silicate with phosphate networks may be explained using the depolarization characterization, since the centre of symmetry in phosphate differs from that of silicate. Effects of a change in the dipole interaction may also be characterized. Galeener [28,29] characterized silica glass and pointed out that the peak near 435 cm^{-1} involves a symmetric stretching (SS) motion of all the bridging oxygen species along the bisectors of the Si—O—Si inter-tetrahedral angles θ, about fixed silicon atoms. The frequency (ω_{ss}) of this vibration, in terms of the central force network model, is given by:

$$\omega_{SS} = \left[\frac{\kappa}{m_o}(1 - \cos\ \theta)\right]^{\frac{1}{2}} \tag{4.40}$$

where k is the same stretching force constant of Equation 2.2. The relatively weak and partially polarized (HV/HH > 0) band near 800 cm^{-1} is due to the same weakly IR-active vibrational mode of Fig. 7-(a). The weak depolarized Raman bands near 1050 and 1200 cm^{-1} correspond to the AS mode, exhibiting a significant TO-LO splitting. In addition, there are also two weak and sharp peaks at 495 and 605 cm^{-1}, which Galeener [26] has attributed to vibrations of planar rings with four and three Si atoms, respectively.

For modified silicates or other oxide glasses, major changes are observed in the Raman spectra, related to the occurrence of strong polarized high frequency or intermediate frequency peaks due to vibrations of non-bridging oxygen (NBO) species.

4.3.9.3 Beryllium Fluoride

The vibrational structure of beryllium fluoride (BeF_2) glass has a surprising similarity with that of a fused silica, except that the high optical phonon energy bands due to υ_4 and υ_3 vibrations of $(BeF_4)^{2-}$ tetrahedron are at 420 and 770 cm^{-1}, respectively [30–32]. When compared with $(SiO_4)^{4-}$, where the υ_3 band is at around 1120–1050 cm^{-1}, the shift in $(BeF_4)^{2-}$ is observed at 770 cm^{-1} and it is attributed to the weaker electrostatic dipole strength of (Be^{2+}-F^-), compared with the Si^{4+}-O^{2-} dipoles.

In view of the reduced mass (μ_m) Equation 4.34, discussed above, it is apparent that in spite of Be atom being lighter than Si, the effect of centre of mass on vibration frequency of the fundamental absorption is much smaller in BeF_2 than in SiO_2. Furthermore, it is the weaker electrostatic force in the cation–anion charge pair (Be^{2+}-F^-) in BeF_2, compared to a stronger Si^{4+}-O^{2-} pair in silica which dominates the force constant and reduced mass effect.

4.3.9.4 Phosphate Glass

The phosphate $(PO_4)^{3-}$ tetrahedron structural unit differs from $(SiO_4)^{4-}$ (compare Figure 4.9 with the structures in Figure 4.14) and $(BeF_4)^{2-}$ and is characterized by the presence of a double bond (P═O) and three single P—O bonds. As in $(SiO_4)^{4-}$ and $(BeF_4)^{2-}$, the bridging P—O bonds in phosphate determine the network continuity whereas the double bonded oxygen becomes a terminating site. This apparent difference in the structures of phosphate, silica and BeF_2 glass structure uniquely defines the viscosity and related flow, thermal and mechanical properties. An example of apparent difference in a phosphate glass from that of binary phosphate–silicate glass structures is discussed below. The vibrational structure of a unary phosphate glass has five well-defined Raman-active bands at 1370, 1170, 700, 500 and

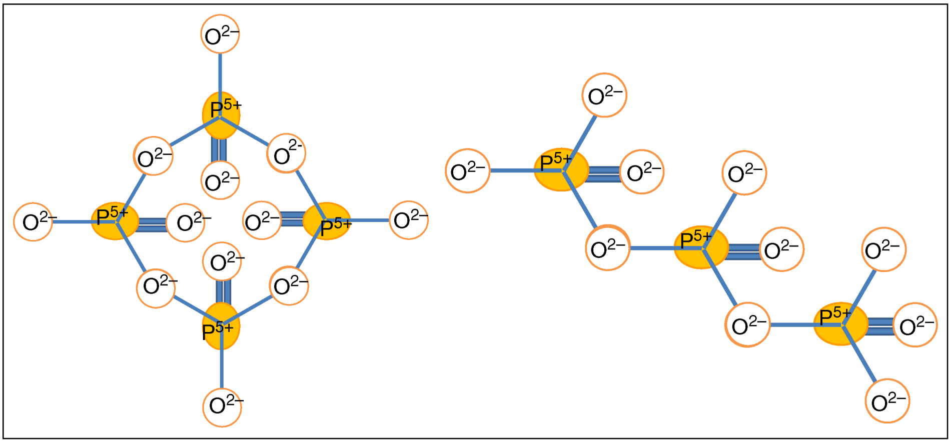

Figure 4.14 Structures of phosphate ring and chain structures may occur, depending on the glass composition [35]. (See colour plate section.)

320 cm^{-1} [19]. Comparison of phosphate glass with silicate requires the doping of silica with phosphate. In the films of phosphate–silica, the P═O vibration band appear at 1310 cm^{-1}. With increasing P_2O_5 concentration in phosphate, from 12.5 to 30 mol.%, the strongest peak of silica at 1120 cm^{-1} (υ_3) overlaps with that of phosphate. With increasing phosphate concentrations beyond 30 mol.%, all of the above phosphate bands appear to share a network bridging role with $(SiO_4)^{4-}$ and the resulting vibration band appears dominant at 1285, 1150, 950 and 400 cm^{-1}. The band at 650 cm^{-1}(υ_4) is redshifted and weakened significantly with respect to the vitreous silica and pure phosphate glasses [33,34].

The polymerization tendency of phosphate polyanions in liquids and glasses with different cations is described in detail by Richardson [35], using the thermodynamic principles, and is compared with the Flory (ideal) distribution model. For example for the reaction:

$$2(P_nO_{3n+1})^{-n-2} = (P_{n+1}O_{3n+4})^{-n-3} + (P_{n-1}O_{3n-2})^{-n-1}; \qquad (4.41a)$$

the equilibrium constant is:

$$K_n = \frac{(P_{n+1})(P_{n-1})}{(P_n)^2} \qquad (4.41b)$$

which can be applied for the polymeric reaction:

$$2(P_3O_{10})^{5-} = (P_4O_{13})^{6-} + (P_2O_7)^{4-} \qquad (4.42a)$$

The equilibrium constant, K_3 may be then written as:

$$K_3 = \frac{(P_4).(P_2)}{(P_3)^2} \qquad (4.42b)$$

using which a relationship between the average chain length ($\hat{n}$), the intensity ratio of bending mode vibrations from Raman and bridging oxygen per $(PO_4)^{3-}$ unit ($Q_1 \ldots Q_3$) for different cations may be established. Richardson pointed out that the average chain length ($\hat{n}$) depends on the ratio of metal oxide and P_2O_5. Examples of different types of polymeric phosphate groups are shown below, with the corresponding vibrational wavenumbers.

4.3.9.5 Tellurium Oxide Glasses

Amongst various oxide glass formers, the family of tellurium oxide glasses have intriguing structural variations which are distinguishable from the strong network forming silicates, phosphates and borates. As an example in Figure 4.15 the normalized intensities of Raman spectra of a set of TeO_2-BaO-Bi_2O_3 glasses are compared in the range 300–850 cm^{-1}. All spectra were normalized with respect to the intensity of peak D and deconvoluted into five symmetrical Gaussian fitted peaks at around 450, 585, 660, 750 and 780 cm^{-1} [36], which were identified from the results reported by Sekiya [36–40] and Himei [41,42] and these were based on the crystallographic data for α-TeO_2 and TeO_2 crystallographic complexes [43,44]. Based on Sekiya's vibrational analysis model [40], the structure of tellurite glasses is comparable with that of α-TeO_2, which has a three-dimensional network of TeO_4 trigonal bipyramid (tbp) forming chains linked by shared vertices. The following main conclusions for the tellurite glass vibrational structure may be drawn based on the Sekiya's model:

i) The peak position A (~450 cm^{-1}) is attributed to symmetric stretching and bending vibration of Te—O—Te linkages. These are formed by shared vertices in TeO_4 (tbps), $TeO_{3+\delta}$ polyhedra and TeO_3 (tps). Depending upon the network modifiers and polyanions used for glass formation, the bridging mode symmetric vibrations may have a bandwidth of 100 cm^{-1} with a variation in peak position of 30 cm^{-1}.

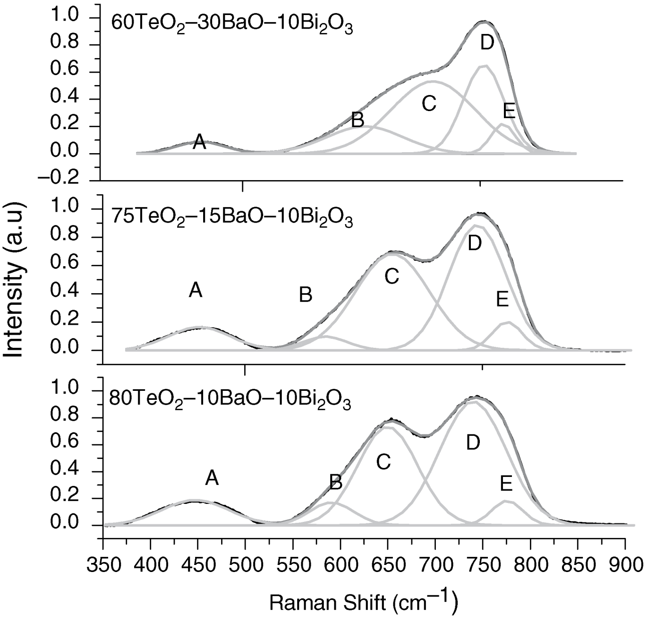

Figure 4.15 *Comparison of the normalized and deconvoluted Gaussian fitted Raman spectra for several TeO_2-BaO-Bi_2O_3 glasses. Note that the relative intensities of peaks A, B and C increase with TeO_2 concentrations and decrease with increasing BaO concentrations in three glass-forming compositions [45]. Source: Hill 2007. Reproduced with permission from Elsevier.*

ii) The peak position B may range between 580 and 630 cm^{-1} and is assigned to the vibration of the continuous network consisting of TeO_4 tbps. From the relative strength of intensities of peaks A and B, the network connectivity of a TeO_2 glass may be defined.
iii) The peak C (~630–660 cm^{-1}) is assigned to the antisymmetric vibrations of Te—O—Te in $TeO_{3+\delta}$, TeO_4, TeO_3 and TeO_4 network.
iv) The stretching vibrations between tellurium and non-bridging oxygen (NBO) atoms have energies of ~750 cm^{-1} and are assigned as peak D. The presence of network modifiers, such as the oxides of alkali and alkaline earth increase the intensity of this band. As a result the overall non-bridging oxygen links decrease, which can be ascertained by comparing with the intensities of peaks A, B and C.
v) Peak E (780 cm^{-1}) is attributed to a continuous network vibration of TeO_4 tbps and a TeO stretching vibration of $TeO_{3+\delta}$ polyhedra or TeO_3 trigonal pyramids.

An example of the Raman spectra of TeO_2 glasses modified with BaO and Bi_2O_3 is shown in Figure 4.15 with the contributing vibration modes identified [45].

4.3.9.6 Phosphate and other Polyanionic Modified Tellurite Glasses

Having examined the vibrational structures of binary and ternary tellurium oxide glasses, it is important to examine the influence of mixing two glass forming networks, namely tellurium oxide and phosphate, on the resulting vibrational structure, which are shown in Figure 4.15. It is evident from the literature on the vibrational structures of binary and ternary TeO_2 glasses [36–40] that alkali and alkaline-earth oxides when incorporated into the tellurium oxide liquids yield more non-bridging high-energy trigonal pyramid structural units and hence non-bridging sites than when a glass former such as phosphate is added [46]. In the FTIR spectra in Figure 4.16 for selected phosphate modified tellurite glasses, the maximum

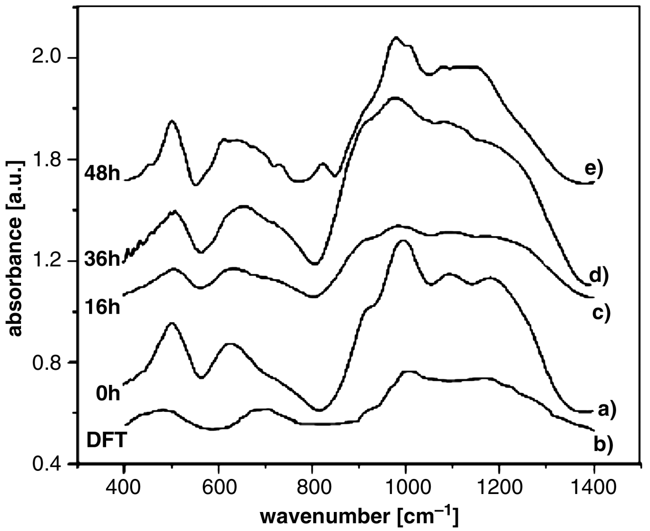

Figure 4.16 Comparison of the FTIR spectra of a $7TeO_2$-$3P_2O_5$ glass and glass ceramic materials obtained after heat treatment. The DFT predicted spectrum (b) is also compared. The time (hour, h) of heat treatment at 500°C in air is also shown [46]. Source: Rada 2009. Reproduced with permission from Springer.

phonon energy at 1200 cm^{-1} is due to the phosphate $(PO_4)^{3-}$ structural units, explained above, which in pure phosphate appears at 1170 cm^{-1}. In this figure the Raman bands between the dominant peaks of TeO_2 glasses (610 cm^{-1} due to bipyramid and 720 cm^{-1} due trigonal prism) and phosphate bands at 1200 cm^{-1} are the intermediate peaks which are attributed to the formation P_2O_5 and TeO_2 structures. In this respect both the trigonal pyramid and bipyramid are likely to couple with the $(PO_4)^{3-}$ tetrahedron structure via bridging oxygen bonds which appear near ~1000 cm^{-1}. This band is broad because of the multitude of coupling interactions between the $(PO_4)^{3-}$ and trigonal pyramids (TeO_3) and bipyramids (TeO_4).

(a) Rada *et al.* [46] examined in detail the FTIR spectra of a gadolinium doped phosphate-tellurite glass with composition ($7TeO_2$-$3P_2O_5$), which was also compared using the density functional theory (DFT). The following are the assignments for the FTIR bands (Figure 4.16). The absorption band at 530 cm^{-1} is assigned to the deformation modes of P—O bonds in the $(PO_4)^{3-}$ tetrahedron, which is consistent with the bulk unary phosphate glass, discussed above.
(b) The band at 625 cm^{-1} is due to the symmetric and anti-symmetric vibrations of TeO_4 bipyramid structure, also observed in the Raman spectrum.
(c) The absorption band at around 720 cm^{-1} also appears in the Raman band (Figure 4.16) and is assigned to the breathing modes of trigonal pyramid (TeO_3).
(d) Depending upon the linear chains present, the vibration bands of meta- and orthophosphates occur at 1100 and 990 cm^{-1}, respectively, depicting the degree of connectivity with the tellurite network. In the phosphate modified tellurite glass the bending mode vibration between the bipyramids and trigonal pyramids is significantly reduced, even though in the glass 7 parts of the overall constituent is TeO_2.
(e) The band centred at about 1175 cm^{-1} is assigned to the PO_2 symmetric stretching modes and the P—O—P of [PO_4] tetrahedral sharing corners. The shoulder near ~900 cm^{-1} is assigned to the asymmetric stretching modes.

It was concluded [46] that:

> "the experimental FT-IR spectrum of the $7TeO_2{\cdot}3P_2O_5$ glass shows that the glass structure is made up mainly of trigonal bipyramidal [TeO_4] groups with a lone pair of electrons, the tetrahedral phosphate anion $[PO_4]^{3-}$, and a small content of tetrahedral [TeO_3] units".

The DFT simulation method used provided a satisfactory model depicting the phosphate and tellurite network structures with rings and cages of fourfold coordinated Te atoms (trigonal bipyramids [TeO_4] in which all the Te—O bonds may be able to form bridging links with the neighbours, namely the threefold coordinated trigonal [TeO_3] pyramids in which a lone pair electron (LPE) is a non-bridging site and the second one forms an oxygen double bond. The LPE in a bipyramid is also a non-bridging site available for coupling with the polyhedron cations. The links with phosphate tetrahedron is predominantly via the remaining available two oxygen sites. The analysis of FTIR data was found to be consistent with recent findings on a range of phosphate modified tellurite glasses [47] used for waveguide fabrication.

Raman spectroscopic analysis of tellurite glasses with polyanionic modifiers (e.g. molybdenum oxy ion, tungstate and niobate/tantalates) were also reported by Jose and co-workers [48] and Murugan *et al.* [49] in which the models for distorted tungstate and molybdates were reported for compensating the structural strain the network.

Joshi and co-workers [25] analysed the Raman spectroscopic data for boron oxide (B_2O_3) modified sodium zinc tellurite glasses, from which the following conclusions may be drawn. The incorporation of B_2O_3 as a glass network former largely keeps the tellurite glass network unchanged, as observed in the case of sodium-zinc tellurite glass compositions, except that the BO_3 symmetric vibrations at around 805 cm^{-1} dominate the high energy optical phonon spectrum. The bridging mode vibrations amongst TeO_3, TeO_4 and BO_3 below 500 cm^{-1} broaden and their intensity increases due to the presence of a BO_3 trigonal prism structure. No evidence for the presence of (BO_4) structural units was confirmed.

4.3.9.7 Germanium Oxide Glasses

For comparing the vibrational structure of GeO_2 based glasses, it is relevant to examine the crystalline forms of GeO_2, which exists in two modifications: tetragonal GeO_2 and an isomorph of the rutile structure. In rutile each titanium (Ti^{4+}) ion is octahedrally co-ordinated with six oxygen ions. The hexagonal form of GeO_2 has an α-quartz structure, and Ge^{4+} is tetrahedrally co-ordinated with four oxygen ions. The optical phonon spectrum of tetrahedrally Ge^{4+} in oxide glass has intense band peaking at 880 cm^{-1}, which is comparable with the phonon vibration structure of hexagonal GeO_2 (α-quartz). By comparison, the maximum phonon vibration band in the rutile polymorph of crystalline GeO_2 is at around 700 cm^{-1}. Table 4.3 summarizes the data for unary GeO_2 with hexagonal and rutile forms of crystalline GeO_2.

The high-energy Raman peak at ~820 cm^{-1} is due to the asymmetric stretching vibrations of O—Ge—O in GeO_4 tetrahedral structural units [51]. The peak D at ~760 cm^{-1} is assigned to the Ge—O- asymmetric stretching vibrations with non-bridging oxygen ions (NBOs) [48]. The peaks at 506 cm^{-1} and C (563 cm^{-1}) are due to the stretching mode contributions from the bending mode vibrations Ge—O—Ge bridging oxygen (BO) vibrations. Peak A (~330 cm^{-1}) is ascribed to the anti-symmetric vibration of Ge—O—Pb bonds. The intensities of these peaks are directly related to the proportion of each bonding vibration reflected in the glass structure. It was reported Figure 4.17 that the intensities of peaks B (506 cm^{-1}) and C (563 cm^{-1}) increase as GeO_2 concentration increases, suggesting that the continuity of GeO_4

Table 4.3 *Raman and IR active vibration modes in germanium oxide glasses [19] [50].*

Hexagonal GeO_2		Vitreous unary GeO_2		Tetragonal GeO_2		70GeO_2-30PbO mol.%, glass	
Raman	IR	Raman 170	IR	Raman 170	IR	Raman reported	Observed
326	333	268	295			330	323
372	343	340	315, 334		300		
385		373–461			370		
440		412			455		
519	515	540	564			506	510
583	551	600				563	569
595	587			680	635		
857		820–860	878	702		760	751
880	872			870		820	807
949	955	987	966				

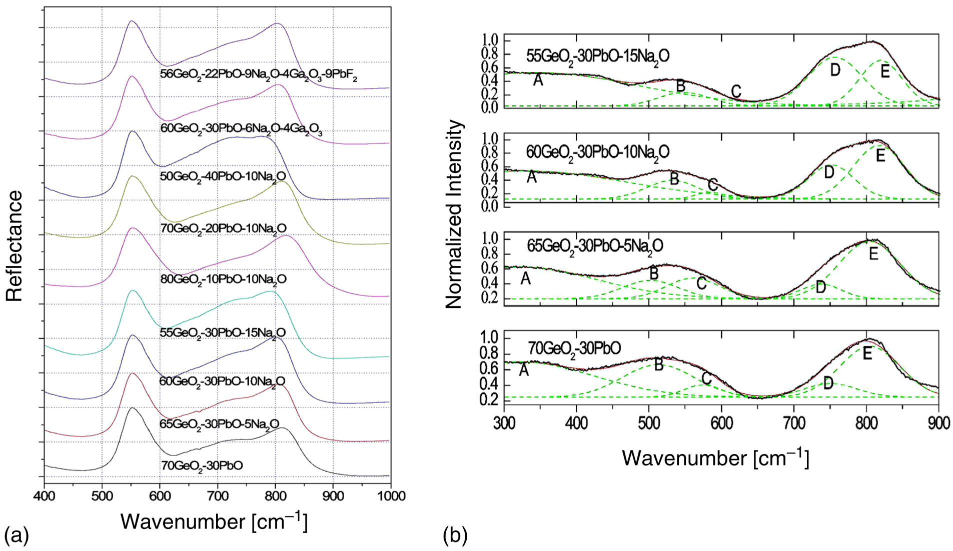

Figure 4.17 *(a) Comparison of the FTIR reflectance spectra for a range of binary and multi-component GeO_2 glasses. Source: Jiang 2009. Reproduced with permission from Elsevier Limited. (b) Raman spectroscopic data for selected GeO_2 glasses in (a). [50,52]. Source: Jiang 2010. Reproduced with permission from Elsevier Limited.*

network increases with increased Ge—O—Ge linkages. By decreasing the composition of GeO_2 in the binary and multicomponent glasses, the proportion of non-bridging oxygen glass network increases. In such compositions of glass the peak at 820 cm^{-1} also diminishes with decreasing GeO_2 concentrations.

In Figure 4.17a and b, the IR reflectance and Raman spectroscopic data for a range of binary and multicomponent GeO_2 glasses are compared, from which the following structural conclusions may be drawn:

1. The increase in concentrations of Na_2O leads to a significant rise in the fractions of non-bridging Ge—O groups, which can be quantified from the intensity analysis of the Raman active band at 760 cm^{-1}.
2. The high frequency band at 810 cm^{-1} in the Raman spectra is due to the asymmetric stretching vibrations in the tetrahedral GeO_4 units. The intensity of this band reduces significantly with lower concentrations of GeO_2.
3. The Raman spectra of binary and ternary GeO_2 glasses (70GeO_2-30PbO, 70GeO_2-21PbO-9Ga_2O_3) do not show any evidence for the presence of octahedral GeO_6 vibrational in the glasses, which was reported at 688 cm^{-1} [19].
4. The intensity of the Raman active bands at 563 and 506 cm^{-1}, which were assigned to the vibrations of Ge—O—Ge with bridging oxygens, increase with the increasing GeO_2 concentrations. The presence of Ga_2O_3 in a ternary composition aids the formation of bridging oxygen sites, which may be identified by comparing the intensities of peaks at 506 and 563 cm^{-1} in Raman spectra.
5. In both binary lead germanate and lead-gallium-germanate, the co-ordination of Pb^{2+} cations is dependent on the concentrations of PbO, which may act as a network contributor at lower concentrations. However, at higher than 30 mol.% of PbO, the role may change to a modifier.

4.3.9.8 Vibrational Spectroscopic Analysis of Selected Fluoride Glasses

The main interest in the optical and spectroscopic properties of fluoride glasses started in the late 1970s when the first tetravalent ZrF_4 and BaF_2 was synthesized serendipitously while making a complex fluoride ceramic which on heating yielded a ZrF_4-BaF_2 glass with near equimolar composition [53]. Since then interest in the structural analysis not only in research on the original ZrF_4-BaF_2 glasses began, but also on the possibility of forming other types of higher valency glasses, based on GaF_3, InF_3 and AlF_3.

The structural analysis of fluorozirconate glasses was only possible by forming a stable glass using NaF and BaF_2 [54], which thermodynamically stabilizes the liquid phase to lower temperatures, as discussed in Chapter 1 under the section on thermodynamic properties of glass forming liquids. The structural analysis of ZrF_4 based glasses revealed that the co-ordination number of central cation (Zr^{4+}) in the network is not similar to strongly covalent glass forming networks, as explained in the realm of the Zachariasen rule. In such glasses, the minimum co-ordination number of a cation is six with octahedral symmetry which may increase up to eight in a complex cationic environment of modifier ions. The dominant vibrational structure is due to the octahedron-preponderance of symmetrical and asymmetrical contributions in the ZrF_n polyhedra.

Furthermore, in the light of the Zachariasen rule, the interatomic and inter-structural forces in the ZrF_n polyhedra are not similar to the corresponding crystalline form, which makes the analysis of co-ordination number in ZrF_n difficult. In such polyanionic structure the co-ordination is expected to vary due to long- and short-bonds, inherent in the structure and, as a result, the co-ordination number cannot be expected to be fixed. Poulain [53,54] proposed that fluorozirconates contain a network of polyhedra with coordination numbers from six to eight, joined together by shared corners, with the network broken down by modifying Ba^{2+} ions. Based on the analysis of possible structure of such ionic glasses, a detailed model was proposed [55]. The IR and Raman analysis showed that the structure of these glasses perhaps consists of zigzag chains of ZrF_6 octahedra, crosslinked by Ba—F bonds. Gonçalves and Almeida [56] proposed a network structure of fluorozirconate glasses built up from linear chains of edge- and corner-sharing [ZrF_7] polyhedra, crosslinked by Ba—F and Na—F ionic bonds (Figure 4.18). A relatively short length of the chains was inferred from the low viscosity of the glass forming fluoride liquids, which may be a characteristic of such ionic bond dominated liquids. However, the origin of cross-linking via F- ions in Figure 4.18 is unclear in a ZBLAN glass.

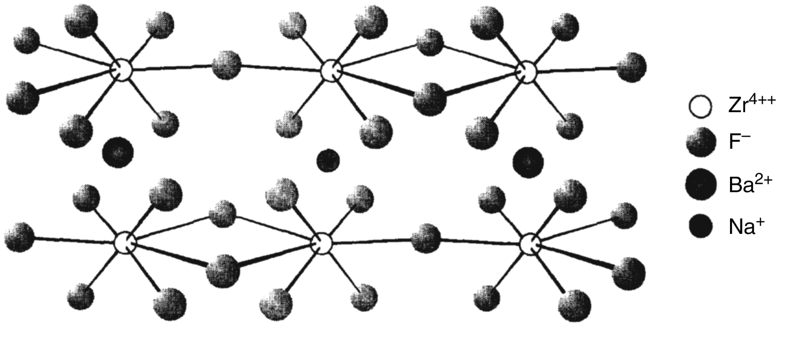

Figure 4.18 *Proposed structure of a ZBLAN glass [56]. Source: Gonçalves 1996. Reproduced with permission from Elsevier.*

The Raman and IR reflectivity data for fluorozirconate glasses were reported by Banerjee [57] and Bendow [58]. In the Raman spectra of fluorozirconate and fluorohafnate glasses, the dominant peak is the polarized VV peak near 580 cm^{-1}, corresponding to (Zr, Hf) F_4 units. The co-ordination number of Zr/Hf were found to be sensitive to the presence of bridging cation (Pb^{2+}, Ba^{2+}). By comparison in a ThF_4-YbF_3-BaF_2-ZnF_2 glass [58] the optical phonon spectrum peaks at 400 cm^{-1} and is much broader than the VV peaks observed at 580 cm^{-1} in fluorozirconate glasses.

From the FTIR reflection and polarized Raman spectroscopic analysis of fluorozirconate glasses, it is apparent that there is little comparison between the phonon structures of a BeF_2 and fluorozirconate glass. The vibrational structure of ZrF_4 based glasses and liquids is not comparable with the glasses and liquids based on $ZnCl_2$ (with $(ZnCl_4)^{2-}$ and $CdCl_2$ (with $CdCl_4)^{2-}$ halide glasses, discussed briefly in Chapter 1.

Amongst the fluoride glasses, the other important family is the trivalent fluoride glasses, based on AlF_3, GaF_3 and InF_3, which were studied for understanding the solubility of rare-earth ions and their photoluminescence [59],[60],[61],[62]. The phonon energy spectra of AlF_3, GaF_3 and InF_3 glasses are dominated by the sixfold co-ordinated $(MF_6)^{3-}$ octahedron, where M designates Al, Ga and In. The peak phonon energy, depending on the strength of M^{3+}–F^- interaction, varies between 500 and 650 cm^{-1}. In AlF_3 based glasses, which is modelled on two different families of compositions, namely the alkali AlF_3-(Ca,Ba,Sr,Mg)F_2-NaF and lanthanide AlF_3-(La,Y)F_3-(Mg,Ca,Sr,Ba)F_2 ternaries, the co-ordination number and hence the phonon energy may vary from four in $(AlF_4)^-$ to six in $(AlF_6)^{3-}$. The predominant co-ordination in an alkali rich environment is six for octahedra, which reduces to five and four, respectively, in bipyramid and tetrahedron structures [62]. As a result of this change in the co-ordination, the AlF_3 based glasses have a much wider distribution of phonon energy, from 650 to 520 cm^{-1}. When fluoride ions are partially replaced by O^{2-}, the cationic-anionic force constant increases and the resulting phonon spectrum shifts to higher energies than 650 cm^{-1}. Note that since the anionic size difference between a fluoride and oxide is small, it is the magnitude of the O^{2-} anion that determines the limit of maximum phonon energy in oxide-fluoride mixtures of trivalent cations, e.g. Al^{3+}. Notably, aluminium fluoride glasses may also be formed by incorporating phosphates that the Hoya Glass Company developed in the 1980s [63].

4.3.9.9 Vibration Spectroscopy of Chalcogenide Glasses

As explained in Chapter 1, the main constituents of chalcogenide glasses are based on sulfur (S), selenium (Se) and tellurium (Te), each of which may combine with more electropositive elements from groups III, IV and V and make chalcogenide glasses, the composition and properties of which are reported in detail by Sanghera and co-workers [64] and Savage [65]. Kumta and Risbud [66] have also reviewed the properties of IR transmitting chalcogenide crystals and glasses. As can be explained from Equation 4.34, the heavier mass of chalcogenide elements shifts the molecular vibrations into the infrared region. As a result, most phonon frequencies are well below 450 cm^{-1}. Besides heavier elemental mass, the chalcogenide elements carry lone-pair electrons. The strongly covalent nature of chemical bonds also allows them to interact and form complex vibrational bonds, which have been a subject of extensive interest in chemistry, physics and optical materials. The vastness of this subject area may not be covered in this text book, which is why only a limited number of

Table 4.4 Comparison of the phonon energies of inorganic glasses, based on FTIR and Raman data.

Composition of glass	Maximum phonon energy range (cm^{-1})	Structural units determining the phonon energy
Silica and silicates	1065–1120	$(SiO_4)^{4-}$
Phosphate	1170–1310	$(PO_4)^{3-}$
Beryllium fluoride	700	$(BeF_4)^{2-}$
Germanium oxide	870–980	$(GeO_4)^{4-}$
Tellurium oxide	610–780	$(TeO_3)^{2-}$, $(TeO_4)^{4-}$,
Zirconium fluoride	580–600	$(ZrF_6)^{2-}$
Aluminium fluoride	610–630	$(AlF_4)^{-}$, $(AlF_5)^{2-}$, $(AlF_6)^{3-}$
Germanium sulfide	350–380	$(GeS_4)^{4-}$
Gallium-lanthanum sulfide	350–380	$(GaS_4)^{5-}$, $(GaS_3)^{3-}$

examples are included for comparing the molecular vibrational properties (Raman and IR) in this section. Sanghera *et al.* [64,67] also included examples of chalcogenide glasses that were modified by incorporating halogen elements, namely chloride, bromide and iodide ions. Only heavier halide ions may be incorporated because of a large size difference between chalcogenide and fluoride ions. Sulfide glasses based on Ga_2S_3-La_2S_3 compositions may also be modified by incorporating oxygen, which might then provide additional thermal stability against devitrification [68]. By comparison, although the presence of oxygen in GeS_2 glasses increases stability the rare-earth solubility decreases and can only be increased in the presence of iodide, e.g. CsI [69]. Such structural changes due to oxygen associated interactions in chalcogenide glasses are apparent in both the molecular vibration structures and via the spectroscopic analysis of dopant rare-earth ion–host interactions. In the context of molecular vibration spectroscopy, the "molecular model" proposed by Lucovsky and Martin [70] for the vibrational analysis of chalcogenide glasses of the type As_2X_3 ($X = S$, Se, Te) is useful in building a concept for glass structure. For example, the IR and Raman spectra of vitreous chalcogenides such as GeS_2 or As_2S_3, as opposed to those of most oxide glasses, tend to exhibit sharp, molecular-like spectral features and a more pronounced mutual exclusion between IR and Raman active bands. Table 4.4 summarizes the measured maximum phonon energy of dominant structural vibration modes of selected inorganic glasses, used for IR application. In this table the infrared cut-off edge for each glass is also compared.

4.4 Fabrication of Core–Clad Structures of Glass Preforms and Fibres and their Properties

As explained above, the total intrinsic loss (α_T) in a dielectric medium is governed by the three main contributing factors [71,72], namely Rayleigh scattering and the short and long wavelength cut-off edges in UV and IR, respectively; the latter two are the resonant absorption edges due to the electronic and molecular absorptions, respectively, whereas the scattering has a λ^{-4} dependence, as explained above in Equation 4.31. The Rayleigh scattering is dependent on the microscopic scale temperature and composition fluctuations in the structure. These fluctuations are affected by the refractive index and related physical and optical properties:

$$\alpha_{\mathrm{Total}} = \alpha_{\mathrm{electronic}} + \alpha_{\mathrm{molecular}} + \alpha_{\mathrm{Rayleigh}} = A_{\mathrm{o}} \exp\left(\frac{a}{\lambda}\right) + B_{\mathrm{o}} \exp\left(\frac{b}{\lambda}\right) + \frac{C}{\lambda^4} \tag{4.43}$$

In Equation 4.43 A_0, a, B_0, b and C_{o} are material constants. The UV and IR absorption spectra of selected oxide, sulfide and fluoride glasses are shown below in Figures 4.19a–d for commercial silica optical fibres [73,78], tellurite glasses [45], fluoride glass [15,18,74] and

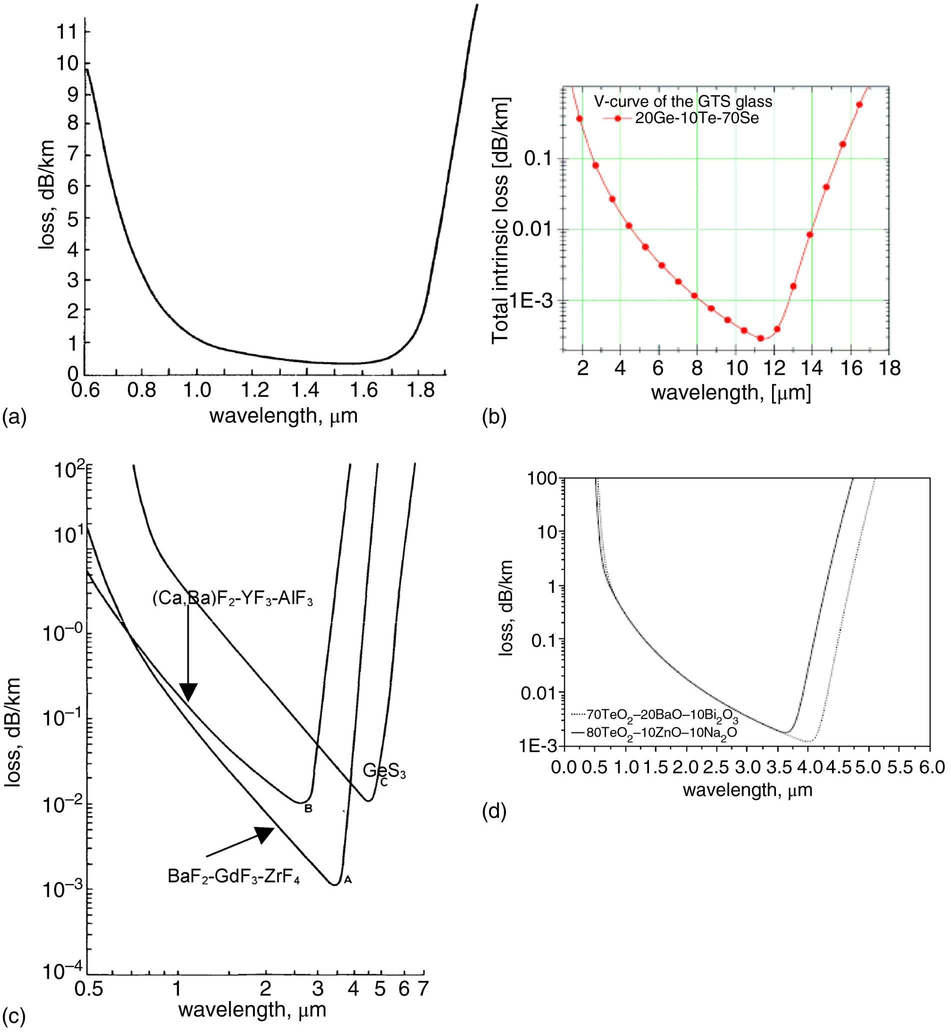

Figure 4.19 Comparison of computed intrinsic loss curves for (a) silica [73,78], (b) chalcogenide [74], (c) ZrF_4 and AlF_3 based (curves A and B) and GeS_3 (curve C) [73], and (d) tellurite glasses [45]. See also References [78–81]. Source (a): Moriyama 1980. Reproduced with permission from Elsevier. (b): Jiang 2014 [74]. Reproduced with permission from Elsevier. (c): Shibata 1981 [73]. Reproduced with permission from Electronics Letters (IET, London). (d): Hill 2007 [45]. Reproduced with permission from Elsevier.

chalcogenide [75] family of fibres, shown respectively. From this comparison, it is evident that the UV edge shifts to shorter wavelengths with the increasing band gap of the materials from sulfide, tellurite to oxides and fluorides. However, the apparent shift in the IR absorption edge to longer wavelengths in tellurite and chalcogenide glasses is consistent with the weaker molecular vibrations in these materials. Note that the Rayleigh scattering, however, in chalcogenide glasses dominates due to an exceptionally high refractive index, which is discussed below in the context of dispersion in optical fibres.

4.4.1 Comparison of Fabrication Techniques for Silica Optical Fibres with Non-silica Optical Fibres

4.4.1.1 Silica Fibre Fabrication

From the shape of intrinsic loss curves discussed in Figure 4.19a–d, the lowest loss window for a medium may be identified for determining the device applications. On this basis, the silica optical fibres as a transparent medium seems most appropriate for optical fibre engineering for long haul applications, a conclusion that was reached more than four decades ago in 1966 by Charles Kao and George Hockham [76]. Kao and Hockham earned celebrity reputation by explaining the light propagation properties of dielectric materials, which led to the Nobel Prize in Physics for Charles Kao in 2009. The dawn of optical communication engineering had started in which physics, chemistry, materials science and communication engineering were brought together for developing the fibre optic cable systems.

The development of optical fibres was spurred by the availability of natural silica. This unique gift from nature to mankind led to the growth of this field. From the discussion on the structural, thermal and processing properties of silica in previous chapters, it is evident that glasses based on silica are much easier to process and control than any other types of glasses discussed in these chapters. From the practical point of view, therefore, silica as fibre optic material has remained the top choice for system engineers for optical fibre communication.

From the intrinsic loss curve, a minimum attenuation of 0.11 dB km^{-1} is possible for silica at around 1500 nm for optical signal transmission. The technology for optical fibre fabrication rapidly grew from the knowledge of synthetic quartz fabrication that existed prior to the discovery of propagating light using waveguides. During and in the post-World War II periods, synthetic quartz was in demand for optics and the technology for making high-purity silica [82] was known to the then chemists worldwide. One of the techniques for synthetic silica and quartz based glass was based on the vapour phase transport of silicon tetrachloride (see Chapter 3, Section 3.2.1) in which high purity $SiCl_4$ liquid is evaporated above room temperature and then combusted in an atmosphere of purified oxygen gas (O_2) to give a silicon dioxide (SiO_2) soot inside a hollow surface of pure silica glass cylindrical mandrel (see Figure 3.1). Based on this principle of vapour phase transport, several techniques for silica glass preform were developed, which are compared elsewhere [78]. Corning Glass Works in New York state (USA) developed the commercial optical fibres using the "outside vapour phase oxidation" (OVPO) technology [73], [83]. In this process, the ceramic or graphite rod mandrel (Figure 4.20a) is used to deposit the silica soot with its other refractive index modifying constituents for forming step or graded index glass preforms. Once the deposition of oxide soot mixture is complete, the mandrel is removed and the porous tube of soot of oxide mixtures is then collapsed, homogenized and vitrified at 1400 °C to an optically clear glass preform. A lot of precise control is required to maintain the homogeneity and control of impurities that are essential in maintaining the optical quality of the fabricated

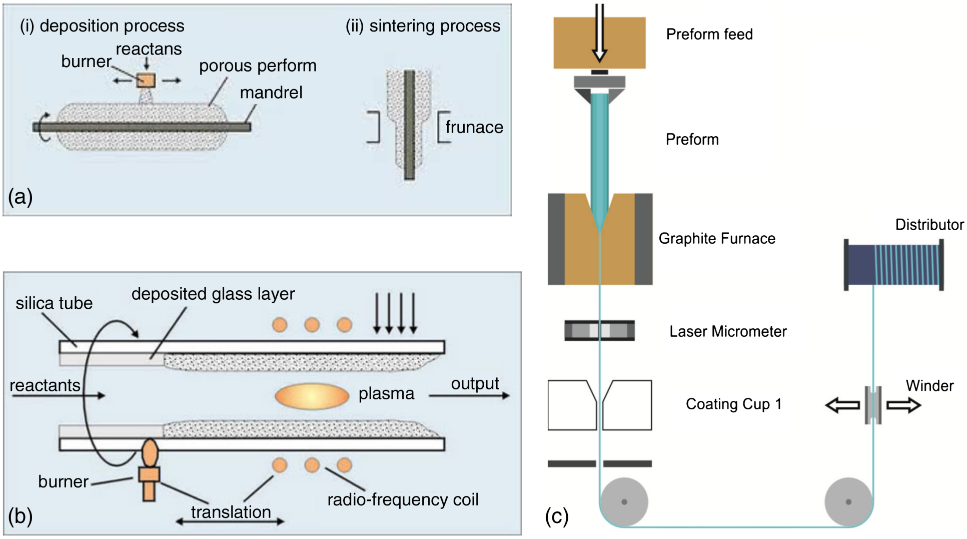
(i) deposition process
reactans
burner
porous perform
mandrel
(ii) sintering process
frunace
(a)
silica tube
deposited glass layer
reactants
plasma
output
burner
translation
radio-frequency coil
(b)
Preform feed
Preform
Graphite Furnace
Distributor
Laser Micrometer
Coating Cup 1
Winder
(c)

Figure 4.20 *Sketches of (a) outside vapour phase oxidation process (csrg.ch.pw.edu.pl); (b) plasma assisted chemical vapour deposition (binoybnair.blogspot.com); (c) fibre drawing tower (www.mpl.mpg.de). See also references [73,77,78,84–87] for other techniques. (See colour plate section.)*

preforms. From these high quality step or graded index preforms the optical fibres are drawn in the draw tower. A commercial silica fibre draw tower is typically 10 m tall. The height is important for achieving the polymer coating and curing at room temperature onto the outer surface of drawn fibres for enhanced fibre strength (Figure 4.20a). The height of the draw tower is also important for maintaining tension and draw speed which controls the inner cladding and core diameters, for minimal variations along the hundreds of kilometres of length of optical fibres. For long haul signal transmission, maintaining the core-to-clad ratio is extremely important for controlling micro-bend loss and overall dispersion.

The first commercial grade optical fibres, fabricated by Corning Glass Works, had at a total attenuation of 20 dB km^{-1} loss [73,78]. This was a landmark achievement over a short space of commercialization of a theoretical concept. Subsequently, in Japan came the vapor phase axial deposition (VAD) process in which the soot of silica with its constituents was seeded onto a vertically moving mandrel. The upward moving mandrel with continuously deposited soot moves out from the deposition chamber into the drying chamber and fusion zone, where the glass preform is consolidated. The advantage of VAD was that it yields a very dry glass preform, leading to low-loss fibres [84,85].

Although the competition for developing the technology for ultralow-loss fibres had begun after the first commercial fibres by Corning, subsequent development in process technology continued with breakthroughs in VAD at Fujikura and NTT in Japan and modified chemical vapour deposition (MCVD) technology at Bell Labs [86,87] for ultralow-loss graded index fibres. In MCVD, the hollow tube high-purity silica was used as a cladding, inside which the core materials were deposited as above in the OVPO and VAD processes. With the implementation of chlorine drying, fabrication of low-loss fibres with less than 0.5 dB km^{-1} loss became a possibility. In Europe at the Philips Research Lab in Eindhoven [80] came a microwave assisted plasma produced decomposition of $SiCl_4$ into oxidation product silica that deposited as glass inside a high purity silica tube. Unlike OVPO, VAD and MCVD, in the plasma-assisted deposition there is no soot formation. Later in the mid-1990s when the demand for broadband communication had begun, AT&T Bell Labs (now OFS) announced the AllWave™ fibres [88] in which the loss floor at 0.18 dB km^{-1} is comparable with the intrinsic loss of pure silica fibres at 1550 nm, leading to another breakthrough for using the optical transmission window (1265–1625 nm) without any OH^- ion absorption. The total loss measured in such fibres was below 0.4 dB km^{-1}.

The essence of success in controlling low loss in silica fibres was the analysis and understanding of process chemistry and control for preform fabrication which, for example for the VAD process, was extensively investigated by the Japanese researchers. A comprehensive chapter with more than 130 pages of discussion on the process and impurity control during the soot formation of silica has been published elsewhere [60]. This reference may further be supplemented by additional preceding literature in this area by French and co-workers [89]. These original references may benefit the readers.

Based on the characterizations of silica optical fibres, by comparing with Equation 4.43, the overall loss spectrum was empirically determined as a function of the wavelength dependence of losses at short-wavelength (α_{UV} and multiphonon edge (α_{IR}) and due to Rayleigh scattering ($\alpha_{\mathrm{Rayleigh}}$) [5]:

$$\alpha_{\mathrm{Total}} = \frac{4.3}{\lambda^4} + \left(\frac{154.2x}{(46.6x + 60)}\right) \times 10^{-2}.\exp\left(\frac{4.63}{\lambda}\right) + (7.81 \times 10^{11}.\exp\left[-\frac{48.48}{\lambda}\right] \text{ dB cm}^{-1} \tag{4.44}$$

Figure 4.21 summarizes the chronological progress in reducing the overall attenuation in silica fibre, showing the key steps that were made to overcome the technological barriers for preform and fibre fabrications.

4.4.1.2 Fluoride Glass Optical Fibres

The discovery of fluoride glass in the late 1970s commenced worldwide research, with major efforts in the USA, Japan and Europe. In this section the methods of preform and fibre fabrication are briefly discussed. For details the original references by France [90], Lu and Aggarwal [91], K. Fujiura, T. Kanamori and S. Sudo [60] may be consulted to gain in-depth understanding of processes involved and their control. The main focus of fibre development in the fluoride glasses concentrated on the family of fluorozirconate based glasses, in which the theoretical aspects of signal attenuation were predicted to supersede that of the performance of already installed silica terrestrial fibres. Although the potential for technology disruption was significant, the materials limitations, however, hindered the realization of this critical goal of the development of fluoride fibres for long haul optical communication application.

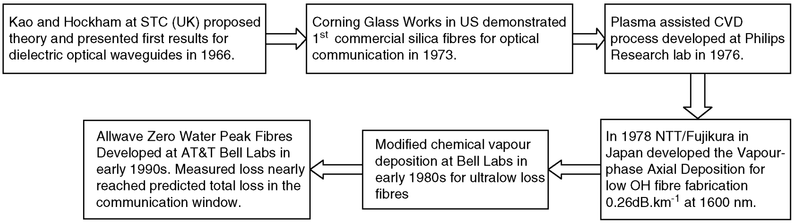

Kao and Hockham at STC (UK) proposed theory and presented first results for dielectric optical waveguides in 1966.

Corning Glass Works in US demonstrated 1st commercial silica fibres for optical communication in 1973.

Plasma assisted CVD process developed at Philips Research lab in 1976.

In 1978 NTT/Fujikura in Japan developed the Vapour-phase Axial Deposition for low OH fibre fabrication 0.26dB.km^{-1} at 1600 nm.

Modified chemical vapour deposition at Bell Labs in early 1980s for ultralow loss fibres

Allwave Zero Water Peak Fibres Developed at AT&T Bell Labs in early 1990s. Measured loss nearly reached predicted total loss in the communication window.

Figure 4.21 *Chronological order of achievements in the reduction of fibre attenuation.*

As explained in Chapters 1 and 2 in structural and thermal properties sections, respectively, the fluoride glasses are predominantly ionic glasses, unlike covalently bonded silica. This fundamental change in the structural property has a major consequence on the design and fabrication of core–clad glass preforms and fibre fabrication. The processing of raw materials also requires stringent control of impurities and their methods of removal. The main features are summarized below [4,60,90–92]:

(a) The fluoride materials, namely ZrF_4, BaF_2, AlF_3, LaF_3, (Li, Na, K)F, and PbF_2, are hygroscopic and require extensive drying using one or more fluorine bearing gases (SF_6, NF_3 and ammonium bifluoride) before melting. The main reactions for the removal of hydroxyl, free and adsorbed water molecules are discussed in Section 3.3.

(b) As explained in Section 3.3, during melting an oxygen-rich atmosphere with halogen is essential for preventing the steady ingress of moisture in the melting chamber, due to a concentration gradient between the melting atmosphere and the gas flow system. This is why the glove box and its piping should be all metal and not made of a polymer or rubber.

(c) Provided the glove box atmosphere is controlled as specified, then the next most important step to control the impurities is the melting chamber where the residual impurities after drying must be removed. These may be a combination of hydroxyl, bicarbonates, carbonates, sulfates and nitrates. When using trivalent rare-earth metals the likelihood of carbonate and sulfate impurities increases because of the processing techniques involved in the manufacturing of such materials.

(d) Most detrimental impurities in any optical fibres and waveguide devices are transition metals, especially iron (Fe^{3+}), nickel (Ni^{2+}), copper (Cu^{2+}, Cu^{+}) and many others, for each of which the method of characterization, dopant–host interaction and their method of reduction and analysis are extensively discussed in References [4,79]. For this reason, readers may find the original references very useful.

(e) OVOP, VAD, MCVD and plasma-based MCVD have not yet been proven suitable for fluoride glass preform fabrication, which implies that the only solution for fluoride glass materials may be to adopt melting and casting, as described below briefly.

(f) The preform fabrication processes for fluoride glasses differ significantly from that of silica, because of a large difference in the viscosity of glass-forming liquid and the softened glass at the fibre drawing temperature, as explained below in the fibre drawing section. Figure 4.22 shows the steps involved in rotational casting.

In step 1 (Figure 4.22), using a preheated metallic mould which is rotated on a lathe, the melted, homogenized and fined cladding glass composition in liquid state is poured into a mould while it is rotated at speeds greater than 1000 rpm. The rpm depends on the thermal mass of the mould, and the core diameter required. It is necessary to optimize the heat transfer during casting, so that an over-chilled glass does not suffer from thermal shock and crack prematurely before the liquid with core glass composition is poured inside the rotating mould in step 2. During casting the thermal stability of a glass is critical as each composition in contact with the mould encounters a temperature excursion, promoting the quenched glass structure into a critical thermal regime where crystal nucleation and growth may begin to dominate. For this region, the pouring temperature of a melted, homogenized and fined core glass is carefully controlled after the cladding glass being already frozen inside the mould, so that the nucleation of crystals and growth during slow cooling does not commence at the core–clad interface. After step 2, the mould is continuously rotated for an additional 1–2 min

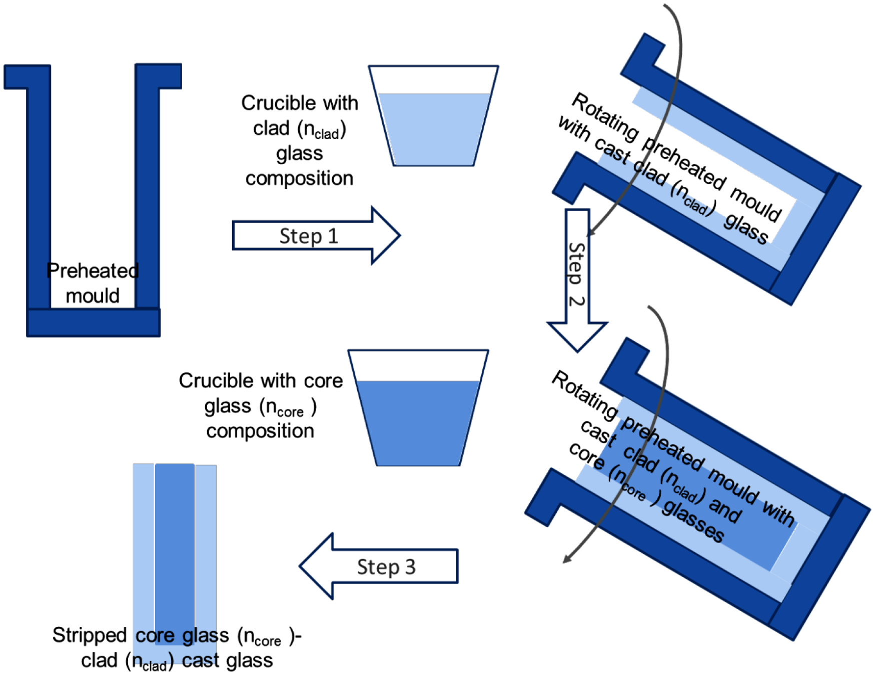
Preheated mould
Crucible with clad (n_{clad}) glass composition
Step 1
Rotating preheated mould with cast clad (n_{clad}) glass
Step 2
Crucible with core glass (n_{core}) composition
Rotating preheated mould with cast clad (n_{clad}) and core (n_{core}) glasses
Step 3
Stripped core glass (n_{core})-clad (n_{clad}) cast glass

Figure 4.22 *Schematic representation of step-wise process of fabrication of a glass preform using a core and clad glass composition, having refractive indices* n_{core} *and* $n_{cladding}$, *respectively [60].*

after pouring core glass, so that a steady state of heat transfer is attained. This step allows the core glass to freeze with minimal interfacial defects and inhomogeneity.

For this reason, to minimize bubble formation at the core–clad interface, the glass-forming core and clad liquids are placed inside a modest vacuum chamber to remove the bubbles as a part of overall fining, before casting. The duration of vacuum treatment depends on the glass composition and may be limited to 30–60 s for low viscosity liquids such as fluorides.

In step 3, the core–clad is stripped out of the mould after annealing for several hours near T_g, at which temperature the glass relaxes by releasing the quenched thermal stress. The annealing of quenched preform is essential in reducing the risk of premature thermal induced cracking. For making optical fibres, a jacket tube with cladding composition is cast into a tube shape for stretching the core–clad/jacket structure inside an extrusion mould. The extrusion may be carried out either outside or inside the tower. The steps are shown in Figure 4.23.

Once the jacketing tube is assembled and stretched into a glass cane by drawing down the preform from, say a 15 mm diameter to less than 2.5 mm diameter, the fibre drawing of canes is then carried out in a draw tower that is shorter in height than a standard silica fibre drawing tower. This is because the drawing temperature of low-glass transition temperature glasses is well below 500 °C. The temperature requirement of the fibre drawing condition for softer glasses such as fluoride is discussed elsewhere [79] using the thermal analysis data and temperature dependence of viscosity of the core–clad glass pair.

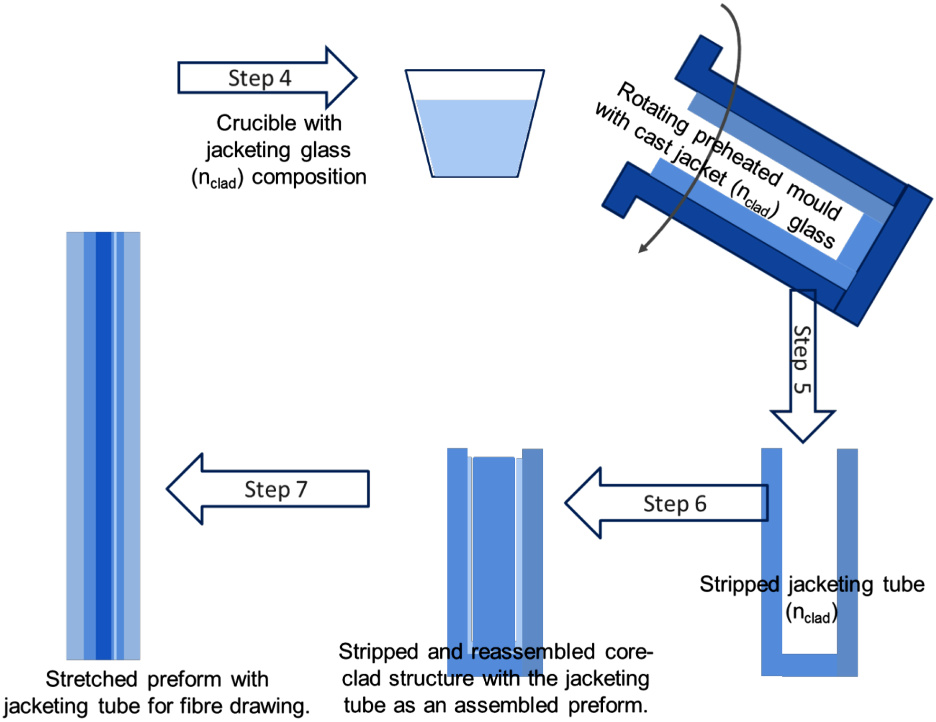
Step 4
Crucible with jacketing glass (n_{clad}) composition
Rotating preheated mould with cast jacket (n_{clad}) glass
Step 5
Stripped jacketing tube (n_{clad})
Step 6
Stripped and reassembled core-clad structure with the jacketing tube as an assembled preform.
Step 7
Stretched preform with jacketing tube for fibre drawing.

Figure 4.23 *Fabrication of jacketed core–clad glass preform using rotational casting [60].*

4.4.1.3 Tellurite and Germanium Oxide Glass Fibres

The requirement for the purification of precursor oxide materials for germanium and tellurium oxide glass preform fabrication is as important as the steps discussed above for fluoride glasses. More specifically, the details of chemical reactions involved in the purification of precursor chemicals are discussed in Chapter 3 (Section 3.2).

For engineering of TeO_2 and GeO_2 based glasses, the major concern is the presence of OH^- ion impurities, which obscure the spectral range between 2.7 and 5.0 μm. The concentration of OH^- ions may be reduced by drying in the presence of a halogen gas or a compound, as has been shown for the silica and silicate glasses. Although the use of thionyl chloride ($SOCl_2$) has successfully been demonstrated [84,93] for silica and fluoride preforms, in case of tellurite and germanium oxide glasses the presence of thionyl chloride with ZnO, PbO, alkali and alkaline earth oxides may not be ideal. This is because the presence of chlorine and S—O bonds in thionyl chloride encourages the formation of chlorides and sulfates, e.g. of zinc and sodium, respectively in a tellurite glass, which further enhance OH^- ion sensitivity. It is for this reason that the consideration of chemical equilibrium is essential prior to designing a suitable drying and melting process.

Despite the differing structural and viscosity behaviour of fluoride and low melt viscosity of tellurite glass-forming liquids, several preform fabrication techniques were developed by exploiting the low-viscosity properties of such glass forming compositions. This is explained with the help of a superimposed differential thermal analysis data for core–clad germanium oxide glasses with the corresponding viscosity data. The temperature regime where the fibre

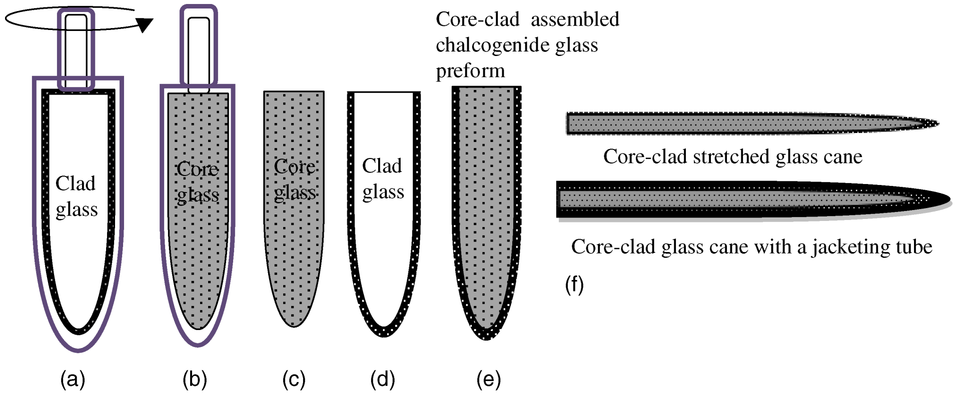
Core-clad assembled chalcogenide glass preform
Clad glass
Core glass
Core glass
Clad glass
Core-clad stretched glass cane
Core-clad glass cane with a jacketing tube
(f)
(a)
(b)
(c)
(d)
(e)

Figure 4.24 *Schematic representation of steps involved in the fabrication of a chalcogenide glass preform and glass cane before fibre drawing. From left to right: (a) spin or rotational casting of vacuum-sealed silica ampoule with cladding chalcogenide glass, (b) air and water quenched core and cladding glass, (c) core and cladding glasses stripped from the silica ampoule, (d) assembled core–clad chalcogenide preform, and (e) the stretched caned structure, needed for (f) fibre drawing with a jacketing tube [60].*

drawing is achieved neither overlaps nor exceeds the crystallization region. This comparison implies that a glass with minimal crystallization is ideal for drawing fibres [50]. The literature points to the possible techniques such as the built-in casting and modified built-in casting, suction casting, rotational casting, extrusion, vacuum casting and rod-in-tube that may be adopted for preform fabrication [60].

In the suction casting technique, the preform fabrication relies on the length pipe formation due to solidification shrinkage of the lower refractive index cladding glass. The length of shrinkage pipe depends on the thermal mass of the mould, casting temperature and the coefficient of volume expansion of the freezing glass-forming liquid. The mould must have a large thermal mass for rapid extraction of heat in a unidirectional manner, to allow the pipe to grow along the axis of a cylindrical mould. The shape of the pipe is often conical and can best be controlled with modelling and experiments, or by trial and error. However, the process suffers from a limitation of core diameter control which is determined by the short (2–3 cm) pipe length. For this reason the technique is only suitable for short lengths of fibres where the modal distribution and dispersion control are not critical.

Many researchers around the world have adopted rotational casting for tube fabrication and extrusion for drawing the core–clad structures [80]. A corollary of rotational casting for tube making is vacuum casting. Such vacuum casting is not ideal for high-vapour pressure containing liquids, and especially in tellurium oxide glass-forming liquids the technique appears to contribute to colour centre formation, which appears as a faint blue/turquoise blue hue in the preform due to electronic defects. This defect also affects the overall loss in the fibre. Such defects are easy to characterize by illuminating a polished glass with an Ar-ion laser at 480 nm excitation wavelength. Weak and broad fluorescence may be observed at red–near IR in tellurite glasses with GeO_2, Bi_2O_3 and PbO.

The techniques for fibre and preform fabrication developed for fluoride fibres were applied by adapting the thermal and viscosity conditions for a range of tellurite, germanium oxide and chalcogenide glass standard preform and photonic crystal and band gap preforms [94,95].

Table 4.5 *Intrinsic loss equations and loss minima at the lowest loss window for various glass-based optical fibre materials.*

For silica fibres, Equation 4.46 should be used [78]
Barium-bismuth-tellurite glass [45]:
$\alpha_{\text{Total}} = \frac{0.80}{\lambda^4} + 4.7 \times 10^{-15}.\exp\left(\frac{12.98}{\lambda}\right) + 2.53 \times 10^{18}.\exp\left(-\frac{263.03}{\lambda}\right)$;
$\lambda_{\text{min}} = 4.1\ \mu\text{m}$, $\alpha_{\text{min}} = 1.2 \times 10^{-3}\ \text{dB km}^{-1}$
Sodium-zinc tellurite glass [45]:
$\alpha_{\text{Total}} = \frac{0.75}{\lambda^4} + 2.967 \times 10^{-16}.\exp\left(\frac{13.55}{\lambda}\right) + 2.79 \times 10^{15}.\exp\left(-\frac{212}{\lambda}\right)$;
$\lambda_{\text{min}} = 3.6\ \mu\text{m}$, $\alpha_{\text{min}} = 2 \times 10^{-3}\ \text{dB km}^{-1}$
AlF_3-BaF_2-CaF_2-YF_3 glass [74]:
$\alpha_{\text{Total}} = \frac{0.106}{\lambda^4} + 1.82 \times 10^{-3}.\exp\left(\frac{3.85}{\lambda}\right) + 1.04 \times 10^{13}.\exp\left(-\frac{99.6}{\lambda}\right)$;
$\lambda_{\text{min}} = 2.65\ \mu\text{m}$, $\alpha_{\text{min}} = 1 \times 10^{-2}\ \text{dB km}^{-1}$
ZrF_4-BaF_2-GdF_3 glass [74]:
$\alpha_{\text{Total}} = \frac{0.112}{\lambda^4} + 2.56 \times 10^{-5}.\exp\left(\frac{6.76}{\lambda}\right) + 2.82 \times 10^{16}.\exp\left(-\frac{163}{\lambda}\right)$;
$\lambda_{\text{min}} = 3.44\ \mu\text{m}$, $\alpha_{\text{min}} = 1.1 \times 10^{-3}\ \text{dB km}^{-1}$
GeS_3 glass [74]:
$\alpha_{\text{Total}} = \frac{3.97}{\lambda^4} + 5.26 \times 10^{-8}.\exp\left(\frac{15.2}{\lambda}\right) + 5.63 \times 10^{12}.\exp\left(-\frac{164}{\lambda}\right)$;
$\lambda_{\text{min}} = 4.54\ \mu\text{m}$, $\alpha_{\text{min}} = 1.1 \times 10^{-2}\ \text{dB km}^{-1}$;
weak absorption tails (α_{tail}, dB km^{-1}): (i) 66.exp $\left(\frac{3.2}{\lambda}\right)$; I (ii) 16.exp $\left(\frac{3.2}{\lambda}\right)$
$As_{40}S_{60}$ glass:
$\alpha_{\text{Total}} = \frac{15.34}{\lambda^4} + 1.6 \times 10^{-11}.\exp\left(\frac{23}{\lambda}\right) + 1.8 \times 10^{9}.\exp\left(-\frac{95}{\lambda}\right)$;
weak absorption tails (α_{tail}, dB km^{-1}): 5.9 exp $\left(\frac{4.4}{\lambda}\right)$
$As_{38}Ge_5Se_{57}$ glass:
$\alpha_{\text{Total}} = \frac{200}{\lambda^4} + 9.3 \times 10^{-8}.\exp\left(\frac{25}{\lambda}\right) + 4.7 \times 10^{8}.\exp\left(-\frac{124}{\lambda}\right)$;
weak absorption tails (α_{tail}, dB km^{-1}): 5.7 exp $\left(\frac{6.4}{\lambda}\right)$

For details on tellurite and germanium oxide glass preform and fibre fabrication, recent research articles [80,94] may be useful, from which the values of intrinsic loss parameters are compiled in Table 4.5.

4.4.1.4 Chalcogenide Glasses

Chalcogenide glass fibre fabrication techniques differ significantly from those of oxide and fluoride glasses, discussed above. This is because of the high vapour pressure and toxic nature of the elements present in the glass. Although chalcogenide glasses are processed under reduced pressure inside the sealed silica ampoule, as described in Chapter 3, there are techniques for preform and fibre fabrication, which rely on the liquidus viscosity of this glass. Fujiura and co-workers [60,96] have described two different techniques:

i) the melt-quenching for forming glass rod and tubes inside the sealed silica tubes (steps shown in Figures 4.24);
ii) the double crucible technique (Figure 4.25).

To minimize the risks of ampoule explosion due to a high vapour pressure of constituent elements during melt spinning, which may be released due to spinning, most fibre fabrication for chalcogenide glasses is carried out at sub-liquidus regime, below the melting

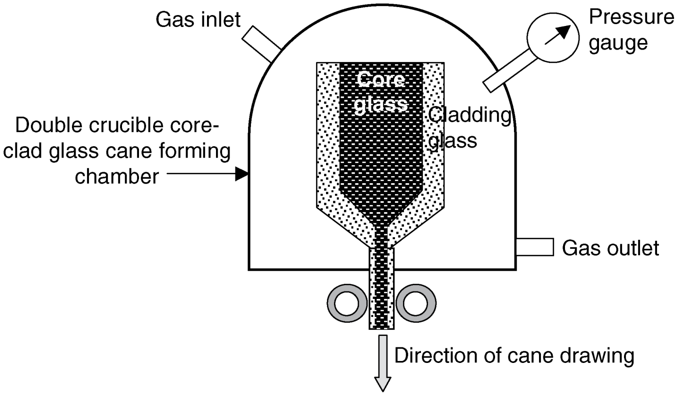
Gas inlet
Pressure gauge
Core glass
Cladding glass
Double crucible core-clad glass cane forming chamber
Gas outlet
Direction of cane drawing

Figure 4.25 *Schematic diagram of the double crucible method of core–clad glass cane drawing under gas pressure and with the assistance of cane pulling rolls in the downward direction [60].*

temperatures. This implies that the extrusion and drawing of glass for preform fabrication is carried out below the crystallization temperature in a mould, as shown in steps in Figure 4.24 in which the core glass is quenched into a rod-shape, followed by spin casting of cladding tube inside the sealed ampoule, which yields a thin and uniform tube for making preforms and stretched core–clad glass cane.

In the double crucible technique the core and clad glasses are contained inside two conical shape crucibles, which are concentrically aligned (Figure 4.25). These two crucibles are placed inside a pressure chamber. The chamber pressure is increased steadily whilst the melt temperature is controlled for the viscosities of two compositions so that the concentric flow of two glasses may be maintained in the non-Arrhenius region of the viscosity–temperature curve. In this regime the viscosity of two glasses may vary in the range 10^2–10^3 Pa.s. Selection of the overpressure gas in the double crucible method is critical because solubility of the gas in core and clad glass may lead to nucleation of bubbles at the interface between the core and cladding glass. In conventional fibre drawing the formation of bubbles at the interface of core–clad is minimized by the application of vacuum. This is impractical, though, for the double crucible method. Note that the technique is only suitable for glass-forming liquids that manifest high viscosity ($>10^3$ Pa.s) at the liquidus temperature.

4.4.2 Fibre Fabrication using Non-silica Glass Core–Clad Structures

For non-silica fibre drawing, as explained the tower height is less than 5 m as there is no requirement for rapid cooling of fibres, which are drawn below 1000 °C. The fibre drawing tower used for non-silica glass is similar to that shown in Figure 4.20c, having a preform feeder, resistive or induction coil furnace, diameter monitor controller, coating cup, UV curing furnace, fibre tension control and winding drum. The drawing temperature for a soft glass fibre must be controlled precisely throughout the drawing process, as exemplified in Figure 4.24. Once the steady state in fibre drawing process is attained via diameter control feedback, the fibre is then fed into a UV-curable polymer acrylate coating cup after which it is spontaneously hardened with a UV light source. The application of polymer coating increases fibre strength and enhances resistance against moisture absorption on the surface.

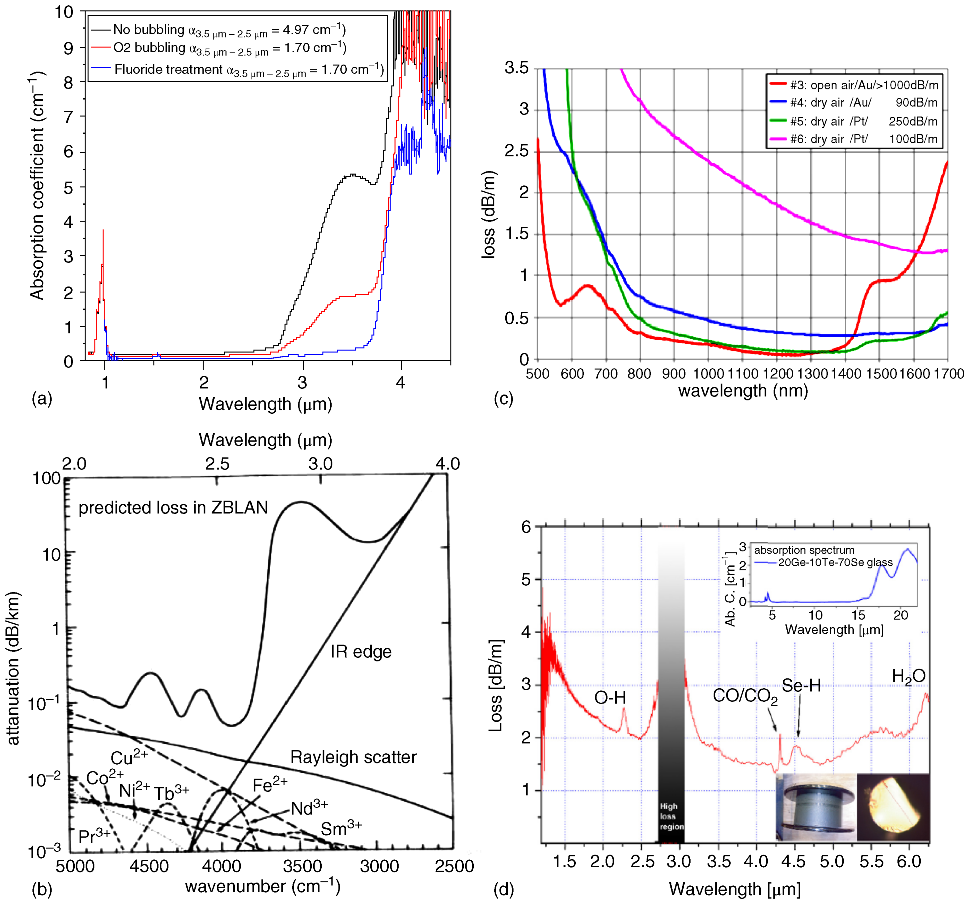

Figure 4.26 *(a) OH$^-$ absorption band in a phosphate glass on the tail of IR absorption edge. The absorption spectra demonstrate the influence of oxygen with halogen (e.g. Cl$_2$) gas purging into the melt, which is essential for reducing OH$^-$ ions. (b) An example of absorption bands due transition and rare-earth metal ions in ZBLAN fluoride glasses. Source: Blackie 1989. Reproduced with permission from Springer. (c) tellurium oxide glasses loss curve. Comparison of loss curves for: (a) phosphate glass absorption curve, (c) ZBLAN fluoride glasses loss curve [97,98], (d) chalcogenide glass loss curve [74]. (See colour plate section.)*

The coated fibre passes through a tension unit, capstan and is finally attached to a winding drum. In standard long-haul telecom fibres the diameter is controlled precisely with a variation in the range of sub 20 nm. Otherwise, a control of less than ±0.1 μm is acceptable for many applications in fibre laser and sensor device engineering.

In Figure 4.26a–d, the loss curves of selected core–clad structured fluoride, tellurite and chalcogenide glass fibres are compared with the intrinsic loss data, from which it is also possible to make comparisons between two and more types of optical fibres for overall loss performance. The overall loss includes the extrinsic loss factors, such as impurities and imperfections which originate in the materials used and during processing, respectively.

4.4.3 Loss Characterization of Fibres

The characterization of total fibre loss includes the propagation loss and end-face reflection loss. The main contributions for propagation loss are the extrinsic and intrinsic factors; the latter is determined by the materials properties, as discussed above. The extrinsic factors arise from the presence of impurities and processing conditions. Examples are given below for each type of fibres known in the literature. The end-face loss is estimated by reflectance Equation 4.7 which for a high refractive index medium must be corrected for absorbance. The fibre cut-back [99,100] is a destructive technique whereas on using FTIR and loss calorimetry [101] the total attenuation may be characterized for entire length of fibre. Using the absorption data from FTIR, the Lambert–Beer law equation may be employed for the characterization of total loss including the analysis of individual absorption peaks for ascertaining their contribution to the total loss. An example of this approach is shown in Figure 4.26b for a ZBLAN based fluoride glass, in which the extrinsic absorptions for OH^- ion, transition metal ions as colour centres, are included for determining the shape of overall loss, which lies above the intrinsic loss curve.

By comparison, in the cut-back technique [100] each length of fibre is measured with identical launch and experimental conditions, and from the difference of launched and transmitted power the loss is determined. From the y-axis intercept of the plot of loss (dB) against the length of the fibre sections the coupling efficiency may also be determined.

On the basis of overall attenuation in a fibre or waveguide medium, the cumulative effect of extrinsic factors may be categorized into two broad classes of loss contributing factors:

(a) extrinsic absorption
(b) extrinsic scattering.

4.4.3.1 Extrinsic Absorption

For extrinsic absorption, the main contributors are the colour centres, for example transition metal and rare-earth ions in the visible and near-IR in most inorganic glasses, as exemplified in Figure 4.26b. The oscillator strength of colour centres determines the strength of the absorption, which is discussed in Chapter 6. In general, notably, the peak and the shape of an absorption band is strongly dependent on the host glass, because of the local electrostatic field and the refractive index affects the line width and intensity. For example, most optical absorption bands for Nd^{3+} in fluoride glasses lie at shorter wavelengths than those observed in silicate glasses.

The absorption centres also arise from the molecular vibration bands and their harmonics and overtones. The most commonly observed molecular absorption bands are due to OH^- ions and CO_2 dissolved in the glass matrix. For chalcogenide glasses used for extended IR transmission the critical molecular absorption bands are S—H, Se—H, oxides which are in addition to the OH^- and carbon dioxide absorption bands as noted by Sanghera and Aggarwal [67].

Besides the molecular and colour centre absorption bands in inorganic glasses, a specific type of absorption, as explained above, is dominant and this is due to the tail of the electronic edge. The materials' fabrication may change the overall stoichiometry with respect to chalcogenide to a semiconductor/sub-metallic element ratio, which may lead to a much

Table 4.6 *List of dominant absorption band strengths (dB km^{-1} ppm^{-1}) due to the presence of transition metal ions as colour centres in inorganic glasses; 1 l mol^{-1} cm^{-1} = $10^3(\rho/M)$ dB km^{-1} ppm^{-1}, where ρ and M are the density and molecular weight of the glass matrix, respectively [4,102].*

Transition metal ion states in equilibrium	Optical transitions	Strengths of dominant absorption peaks measured in dB km^{-1} ppm^{-1}				Strengths, peaks (nm), absorbed in TeO_2 glasses
		Energy (cm^{-1}), λ_{peak} (nm) in fluoride glass	Strength	Energy (cm^{-1}), λ_{peak} (nm) in oxide glass	Strength	
Fe^{3+}	d^5 shell filling is a spin-forbidden transition					
Ti^{3+}	$^2T_{2g}(D) \rightarrow {}^2E_g(D)$	19230, 520	150	20830,	600	
V^{3+}	$^3T_{1g}(D) \rightarrow {}^3A_{2g}(F)$	30268, 330	—	—	—	
Cr^{3+}	$^4A_{2g}(F) \rightarrow {}^4T_{1g}(F)$	22470, 445	860	22300, 448	850	52,~470
	$^4A_{2g}(F) \rightarrow {}^2T_{1g}(G)$	15380, 650	—	15750, 635	200	150,~655
	$^4A_{2g}(F) \rightarrow {}^4T_{2g}(F)$	14710, 680	600	15250, 656	850	130,~675
Cr^{2+}	$^5E_g(D) \rightarrow {}^5T_{2g}(D)$	11900, 840	1190	13200,758	1320	
Fe^{2+}	$^5T_{2g}(D) \rightarrow {}^5E_g(D)$	8930, 1120	120	9100, 1100	130	
Co^{2+}	$^4T_{1g}(F) \rightarrow {}^4T_{1g}(P)$	18520, 540	700	19500, 513	1600	26,~550
Ni^{2+}	$^3T_{2g}(F) \rightarrow {}^3T_{1g}(P)$			24390, 410	1120	28,~410
Cu^{2+}	$^2T_g(D) \rightarrow {}^2T_{2g}(D)$	12500, 500	125			35,~800

extended tail of electronic absorption in the mid-IR. This absorption becomes significant when dealing with the optical transitions in rare-earth (RE^{3+}) and transition metal ion dopants (Cr^{2+}, Co^{2+}, Fe^{2+}). These sub-bandgap transitions might contribute to resonant energy transfer and deplete the population of lasing states. Sanghera and Aggarwal [67] have discussed the characterization of absorption tail in extended IR GeAsS/GeAsSe fibres.

Table 4.6 presents a summary of dominant absorption bands due to the colour centres along with the peaks of absorption wavelength and strengths. Table 4.7 lists dominant molecular absorption bands in known inorganic glasses.

Table 4.7 *Comparison of peak of absorption bands of OH$^-$ fundamental vibration and the molar extinction coefficient (ε, l mol^{-1} cm^{-1}) in various inorganic glasses.*

Glass type	Molar extinction coefficient (ε) (l mol^{-1} cm^{-1})	λ_{peak} (μm)
Silica (SiO_2) [102,103]	90	2.7
SiO_2-Al_2O_3-ZnO-K_2O-Na_2O [103]	33	2.87
B_2O_3 [104]	70	2.8
49ZrF_4-22BaF_2-3LaF_3-3YF_3-3AlF_3-20LiF (ZBLYALi) [105]	8	2.9
79GeS_2-15Ga_2S-6CsI (mol.%) [106]	14	2.9
43AlF_3-25BaF_2-16CaF_2-16YF_3 (ABCY) [107]	37	2.9
60.5ZrF_4-31.7BaF_2-3.8GdF_3-4.0AlF_3 [105,107]	13	2.9
80TeO_2-10ZnO-10Na_2O [80]	Not known	3.3

Relevant absorption due to the rare-earth ions is discussed in Chapter 6 in the context of device spectroscopic properties. However, a significant point to note here is that the transition metal ions, discussed above, have open shell structure for (3d → 4s) transitions, which allows strong electron–phonon coupling with the host electrons in the valence band. This coupling, depending on the electronic structure of the host, then determines the overall line shape of electronic transitions, which is the main focus in Chapter 6. The strength of the coupling consequently determines the absorption strength, yielding high optical density or, in other words, manifests a deep colour in such metal ion doped glasses.

In Table 4.7, the OH^- absorption in different inorganic glasses and other significant molecular absorption are discussed. However, for most commonly used oxide glasses (silica, silicates and non-silicates), the overall contribution for the OH^- absorption in glass hosts in the mid-IR is due to the presence of different molecular vibrations, contributing to the overall broadening. The components of the absorption bands assigned for OH^- and free water in silicate matrices were reported by Bartholomew *et al.* [103] and are summarized as follows:

i) The band at $1630\,cm^{-1}$ (6.13 μm) is due to H—O—H bending, which has a molar extinction coefficient of $16\,l\,mol^{-1}\,cm^{-1}$. The molar absorptivity strongly depends on composition and in alkali containing silicates (e.g. Na_2O-K_2O-ZnO-Al_2O_3-SiO_2) it was found to rise to $28 \pm 5\,l\,mol^{-1}\,cm^{-1}$.
ii) The ≡Si—OH hydrogen bonding may have a broad range of modes with energies spread across $2380–2780\,cm^{-1}$ (4.2–3.6 μm). This band is therefore classed as vibrations due to strongly hydrogen bonded hydroxyl groups ($2650\,cm^{-1}$) and a very strongly bonded OH^- group at $2300\,cm^{-1}$.
iii) The Si—OH and H—O—H stretching with $80\,l\,mol^{-1}\,cm^{-1}$ extinction coefficient is also composition dependent and has a much narrow energy distribution, lying between 3770 and $3500\,cm^{-1}$.
iv) The combination of stretching and bending bands of ≡Si—OH with molar extinction ($1.75\,l\,mol^{-1}\,cm^{-1}$) appears at $4545\,cm^{-1}$.
v) Less significant combination and stretching bands are due to H_2O and X—OH and these lie at $5235\,cm^{-1}$ (1.91 μm) and (7.14) μm, respectively.

In Table 4.7 the molar extinction coefficient of OH^{-1} and the peak of absorption wavelength for different types of glass hosts are summarized. Evidently, the chemical environment of OH^- ions determines the magnitude of extinction coefficient and peak position.

As explained above, the harmonics and overtones of the OH^- fundamental band also increase the background attenuation in all types of optical fibres below 2.0 μm; the overall attenuation across the spectral range, from near-IR to mid-IR may also be affected by the hydrogen bond of chalcogenide element (S—H, Se—H), oxide bonds (Ge—O, As—O, Se—O, Te—O) bonds, dissolved gases in the glass (CO, CO_2, SO_2, H_2S) and sulfate, carbonate and phosphate peaks, each of which has a strong molecular signature in the mid-IR. These data are compiled in Table 4.8 from the literature for comparison with the OH^- ions.

In fluoride and other types of oxide glasses (e.g. TeO_2-WO_3-La_2O_3 or LaF_3), the rare-earth ions are often associated with the lanthanum oxide or fluoride present in the glass. For passive applications where rare-earth ions as dopant are not required, the ground state absorption bands contribute to the overall loss, as exemplified in Figure 4.26b for a ZBLAN glass. Figure 4.26a presents the absorption loss curve for a high-quality calcium-

Table 4.8 *List of molecular absorbers in glass hosts with characteristic wavelength bands and determined extinction coefficients [4,18,50,60,67,75,91,93,108]. Source: Blackie 1989.*

Glass host	Species	Absorption band (cm^{-1})	Absorptivity and dissolved concentrations
Silica & silicates	CO_3^2, CO_2 and CO gases are not reported due to the IR cut-off edge below 2.5 μm		
Phosphate	Not reported as the phosphates have cut-off edge below 4 μm (Figure 4.26a). The dominant band is OH^{-1} which merges with the IR cut-off edge which is reduced to 0.27 cm^{-1} via a reactive melting and stirring procedure, compared with 6 cm^{-1} in untreated glass-forming liquid formed during melting.		
Fluoride glass (e.g. a ZBLAN[a] glass)	CO_2	2350, 3604, 3738 4.255, 2.775, 2.675 μm	At 4.25 μm, 9×10^4 dB km^{-1} ppm^{-1} (0.4 ppmw)
	CO	2100 (4.762 μm)	at 4.762 μm, 2.7×10^4 dB km^{-1} $ppmw^{-1}$, 1.5 ppmw
Tellurite	CO, CO_2	Not observed	Not reported
Sulfide	CO, CO_2, S-H, SO_2, oxides	4.35 μm (CO_2), ~4.0 μm (S—H) 7.69 μm oxides	Not reported
Selenide	CO, CO_2, Se-H, SO_2, oxides	4.35 μm (CO_2), ~4.5 μm (Se—H)	Not reported

[a] A ZBLAN glass has a nominal composition (mol.%) of $50ZrF_4$-$20BaF_2$-20NaF-$6AlF_3$-$4LaF_3$ [90].

barium oxide containing phosphate bulk glass, in which the overall absorption near the OH band is less than 0.3 cm^{-1}. What is apparent from the comparison is that the absorption coefficient of OH^- below 3 μm (3300 cm^{-1}) in much dried phosphate glass is 0.27 cm^{-1} is more than 10^6 times larger than the loss reported in the AllWave fibres. This apparent difference in loss characterizes the properties of phosphate glass, which is an excellent host for rare-earth ions. Due to high OH^- absorption the phosphate glass is limited to bulk glass use, where the overall laser cavity path lengths are limited to less than 10 cm. Some of the characteristic absorption bands which might arise as a result of glass purification steps are residual absorption due to $(NH_4)^-$ (at 2.96 and 3.04 μm) from ammonium bifluoride drying of fluoride precursor materials, phosphate $(PO_4)^{3-}$ (at 4.7 μm) from zirconium and lanthanum fluoride, sulfates $(SO_4)^{2-}$ (at 4.25 and 4.7 μm) from alkali and barium fluorides and from thionyl chloride ($SOCl_2$) treatment of glass-forming oxide and fluoride liquids, respectively.

In emerging tellurite and germanate glass fibres, which are proving useful for mid-IR applications, typical values of the measured losses in single mode fibres varied from 1.5 to 5 dB m^{-1} [50,72,80] and are much higher than those reported elsewhere [109–111]; ultra-low loss tellurite fibres with 0.02 dB m^{-1} loss fibres have been fabricated. Such low-loss tellurite fibres may be obtained by controlling the transition metal impurities (Co, Cu, Fe), discussed above.

Extensive research on chalcogenide fibres revealed that the absorption bands of transition metal impurities, as discussed above, are relevant not only in the near-IR but also in the mid-IR (Cr^{2+}, Fe^{2+}) [18,90]. Sanghera and Aggarwal [67] and Schweizer *et al.* [68] also showed that the oxides of As, Ge and Se contribute to the absorption near the tail of absorption edge; however, the most dominant absorption bands are due to the As—H, Se—H, S—H bands.

More recently, using the vacuum distillation extended window up to 16 μm, chalcogenide glasses with high T_g were reported and, in these fibres, the oxide and Se—H absorption bands were significantly reduced [75], [112,113]. The overall loss in multimode fibres is of the order of a few dB m^{-1}, making them useful for sensor engineering.

4.4.3.2 Extrinsic Scattering

The materials processing steps during glass preform fabrication and fibre drawing, if not controlled, may contribute to a plethora of extrinsic defects that are comparable with the wavelength of light. The extrinsic scattering may be classed into *three different types:* in the Rayleigh regime, the size (a_{Ry}) of scattering centres is below the wavelength of light (λ). Such scattering centres demonstrate a strong power dependence on wavelength (λ^{-4}) and refractive index (n^8). The microscopic density fluctuation and segregation arising from melting and crystal growth in glass and ceramic single crystals may be classed as Rayleigh scattering centres, as discussed below.

Mie scattering also originates from the heterogeneous defects in the medium due to processing, except in this case the size of the defect is larger than that of Rayleigh scattering such that $a_{\mathrm{Ry}} < a_{\mathrm{Mi}} \approx \lambda$. As a result the wavelength dependence of scattering drops to λ^{-2}. Amongst the scattering centres most detrimental are those that are the wavelength independent which are larger than the Mie scattering centres. In brief, the scattering coefficient, $\varepsilon_{\mathrm{Sc}}$ in cm^{-1} or α_{Sc} (dB km^{-1}), can be quantified by using the following equation proposed by van Hulst [4,114]:

$$\varepsilon_{\mathrm{Sc}} = \frac{Q\pi a_{\mathrm{s}}^2 N_{\mathrm{S}}}{L} \tag{4.45}$$

$$\alpha_{\mathrm{Sc}} = 10 \log_{10} \varepsilon_{\mathrm{Sc}} \tag{4.46}$$

$$Q = \frac{8}{3} x^4 \left[\frac{m^2 - 1}{m^2 + 1}\right]^2 \text{for } x = \frac{2a_{\mathrm{s}} n_{\mathrm{o}}}{\lambda} \ll 1 \tag{4.47}$$

Here a_s is defined as the average size of scattering centres with refractive index n_{Sc}, which are present in a surrounding dielectric medium (n_m). The ratio of two indices is $m = n_{\mathrm{Sc}}/n_m$. The term N_{S} is the total number of scattering in the medium. In the above mathematical formulation, Q is true for the scatterers that have a moderately high index above the isotropic index of the surrounding medium. However, as the index of the scattering centre increases:

$$\left[\frac{m^2 - 1}{m^2 + 1}\right]^2 \rightarrow 1$$

As expected, materials such as platinum, gold and semiconductors have a large index, and $x \ll 1$ and $m \rightarrow \infty$, then:

$$Q = \frac{8}{3} x^4 \tag{4.48}$$

Characterization of scattering centres with different parametric conditions is explained elsewhere [4,60] [114] in the context of fluoride glass optical fibre engineering. Nonetheless the scattering conditions, described therein, are general in approach and are applicable to

Table 4.9 *List of scattering centres for various types of glasses [4,60]. Source: Blackie 1989.*

Scattering centre	Refractive index ($n = n_o - i\kappa$)	Origin	Glass host/refractive index
Platinum	At 590 nm, $n = 2.23–3.92i$ At 1130 nm, $n = 3.86–6.24i$ At 2250 nm, $n = 4.58–7.14i$ At 4130 nm, $n = 3.92–16.16i$	Melting crucibles	Silicates/(1.48–1.55) Phosphate/(1.52) Fluoride/(1.53–1.58) Tellurite/(1.97–2.25)
Gold	At 508 nm, $n = 0.908–2.075i$ At 1000 nm, $n = 0.194–5.57i$ At 2000 nm, $n = 0.564–15.4i$ At 3140 nm, $n = 0.800–18.9i$ At 4830 nm, $n = 1.83–33.0i$	Melting crucible	Tellurite glass (1.97–2.1) for low T_g glass melting
LaF_3 ZrO_2 β-$BaZrF_6$ ZrF_{4-x} crystal	$n = 1.6–1.067i$ $n = 2.18–1.453i$ $n = 1.515–1.01i$	Quenching and crystallization Fluorine loss	During fluoride glass melting and quenching, LaF_3, ZrO_2 and $BaZrF_6$ may form. In fluoride glass hosts
$LaPO_4$ (Xenotime)		Crystallization	Forms in phosphates only
Sub-oxides of tellurite	Not known	Oxygen deficiency. Light blue colour	Only in tellurite glasses when processed in oxygen deficient environment
Alumina silicate		Melting crucible	Tellurite glass (1.97–2.1) when using low-T_g glass
Gas bubbles	$n = 1.000$		All types of glasses
Carbon particles		Vitreous carbon	Chalcogenide melting inside the glove box

glass and transparent crystalline media. To conclude on the theoretical aspects of quantifying overall extrinsic scattering in a dielectric media, a general equation may be written as follows:

$$Q_{\text{Total}} = \frac{Q_{\text{Rayleigh}}}{\lambda^{-4}} + \frac{Q_{\text{Mie}}}{\lambda^{-2}} + Q_{\text{Independent}} \tag{4.49}$$

in which the Q_i define the scattering efficiency by including the average size and refractive index of a type of scattering centre. In summarizing this section, it is useful to list typical scattering centres as shown in Table 4.9, where the potential source of scattering centre is also identified during processing steps.

4.5 Refractive Indices and Dispersion Characteristics of Inorganic Glasses

From Maxwell's equation it is apparent that a propagating electromagnetic wave interacts with the medium, which slows down the moving wave. The phase velocity (V_1) of an incoming electromagnetic wave decreases with respect to the velocity of the electromagnetic wave in vacuum ($c \approx 3 \times 10^8\,\mathrm{m\,s^{-1}}$) by the magnitude of the refractive index (n) of the dielectric medium:

$$V_1 = \frac{c}{n} \tag{4.50}$$

Away from the resonance or absorption bands (e.g. the electronic band gap) of a material, the phase velocity is inversely proportional to the refractive index, and is dependent on the wavelength. On examining the electromagnetic interaction of dielectric medium on a microscopic scale, the oscillating electric field creates a disturbance in the materials by interacting with the valence band electrons. This disturbance is proportional to the permittivity of the medium. In the direction of propagation of radiation, the electric dipole thus oscillates slightly out of phase with the incoming electromagnetic radiation, and therefore the resulting emitted radiation, although at the same frequency (wavelength), encounters a phase delay. The electromagnetic wave may be then characterized with a "group" velocity V_g, as in Equation 4.51 with its group velocity index, n_g for the medium. Here the group defines a specific colour or wavelength. To rationalize the electromagnetic interaction, it is essential to distinguish between the group and phase velocities, in which n_g [3,6,78,115] is called the group velocity index which is mathematically expressed in terms of the wavelength dependence of the refractive index, as shown in Equation 4.51 where λ is the wavelength:

$$n_g = n_1 - \lambda . \frac{\mathrm{d}n_1}{\mathrm{d}\lambda} \tag{4.51}$$

Since the first derivative of the refractive index with wavelength in Equation 4.51 is negative, the value of n_g for a given wavelength is larger than the leading wave, and therefore depicts a slower group velocity. Consequently, the group velocity may be expressed as:

$$V_g = \frac{c}{n_g} = \frac{c}{\left[n_1 - \lambda \frac{\mathrm{d}n_1}{\mathrm{d}\lambda} \right]} = \frac{\mathrm{d}\omega}{\mathrm{d}k} \tag{4.52}$$

Here ω and k represent the frequency and wave vector, often used in the wave mechanics treatment of electromagnetic waves. From the Heisenberg uncertainty principle, there is always expected to be uncertainty, $\Delta\phi$, in the phase of a so-called monochromatic wave, which means that there is likely to be distribution of group velocities over the narrow bandwidth ($\Delta\lambda$) of a given laser source. In a single mode step-index fibre medium with a core refractive index n_1, there will be a spread of group velocities because of the group velocity index, n_g, which is related to n_1. Since the fibre is single mode, each wave within $\Delta\lambda$ spread will take the shortest path along the axis to reach the other end after travelling L kilometres. This distribution of velocities will cause a pulse to broaden after travelling, say, L kilometres in fibre, which is characterized as the materials dispersion, D_m. From the expression below in Equation 4.53, D_m is measured in ps km^{-1} nm^{-1} (ps = picosecond):

$$D_m = \frac{\Delta t}{L.\Delta\lambda} \approx -\frac{\lambda}{c} . \frac{d^2 n}{d\lambda^2} \tag{4.53}$$

The delay due to the group velocity index between the leading and trailing wavelengths becomes more apparent when dealing with a fibre which is not single mode. In such a case the zero-order mode (with n'_2 and n'_1 as the cladding and core indices of glass, respectively) propagates along the central axis with velocity (V_o) for a point-to-point length of L km; the propagation time t_o is:

$$t_o = \frac{L}{V_o}. \tag{4.54}$$

By comparison the highest order mode may be propagating with velocity $V_o \cos \alpha_c$ which is less than V_o, and yields signal arrival time (t_H):

$$t_H = \frac{L}{V_o \cos\ \alpha_c} = \frac{Ln'_1}{V_o n'_2}. \tag{4.55}$$

The time differential in the interval of arrival of the zero and highest order modes is called the "link or point-to-point" delay time ($\Delta t_{0\text{-H}}$) [3]:

$$\Delta t_{\text{H-0}} = \frac{L}{V_0}\left[\frac{n'_1}{n'_2} - 1\right] = \frac{Ln'_1}{c}\left[\frac{\Delta n}{n'_2}\right] \tag{4.56}$$

By multiplying denominator and numerator in Equation 4.56 with ($n'_1 + n'_2$), the delay time ($\Delta t_{\text{H-0}}$) may be approximated by considering that $n'_1 \approx n'_2$:

$$\Delta t_{\text{H-0}} = \frac{L}{2n'_1 c}[\text{NA}]^2 \tag{4.57}$$

The physical existence of a signal delay time therefore characterizes the role of dispersion in a dielectric medium.

As apparent from the intrinsic loss mechanisms discussed above, the electromagnetic waves interact strongly with a medium with high refractive index because of the absorption, κ, explained in Equation 4.5, which constitutes the complex part of the refractive index. The absorption κ becomes dominant at the resonant wavelength in the dispersion spectrum of the refractive index of dielectric materials. At the absorption edge, the index of refraction changes asymptotically, which may be explained schematically in Figure 4.27 using the Kramers–Kronig relationship:

$$\Delta n(\omega') = \frac{c}{\pi}\int_0^{\infty} \frac{\Delta\alpha(\omega)\text{d}\omega}{(\omega^2 - \omega'^2)} \tag{4.58}$$

To explain the dispersion of light a simplified empirical approach is to characterize and determine the Abbe number, using the following equation where n_D, n_F and n_C designate the refractive indices of a glass at the Fraunhofer wavelengths, (the D-, F- and C- spectral lines at 589.2, 486.1 and 656.3 nm, respectively). The Abbe number is, for example, for silica 65, whereas for highly dispersive tellurite glasses the value drops to between 14 and 28, as listed in Table 4.10 and Figure 4.28 for selected families of glasses, including silica, commercial silicates, fluoride and tellurite glasses [119]:

$$v_D = \frac{n_D - 1}{n_F - n_C} \tag{4.59}$$

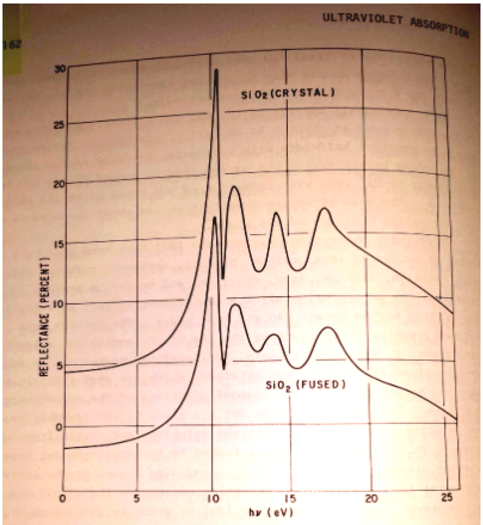

Figure 4.27 *Plot of the reflectance of fused and crystalline silica across the electronic band edge, an example of change in the refractive index of silica glass across the absorption edges [19]. Source: Wong 1976. Reproduced with permission from Marcel Dekker.*

Clearly, from the data in Table 4.10, a large number of commercial bulk optical materials are not as dispersive as tellurite, with the values of Abbe number varying between 14 and 23. Such a low value of Abbe number is due to the presence of a molecular constituent, namely Nb_2O_5, Tl_2O, WO_3, Bi_2O_3, etc. By contrast BeF_2 glasses are the least dispersive, with an Abbe number larger than 106. In general in ionic glasses, namely BeF_2 and ZBLAN, the

Table 4.10 *Comparison of Abbe number (ν_D) of a range of glasses used for optical applications.*

Glass and crystals	n_D at $\lambda_D = 587.6$ nm	ν_D
BeF_2 glass	1.37	106.8
CaF_2 crystal	1.434	95.10
Fused silica	1.458	67.70
Schott Borofloat	1.472	65.7
Schott N-BK7	1.517	64.2
ZBLAN glass	1.515	70
$40TeO_2$-$10Li_2O$-$50WO_3$	2.046	20
$15TeO_2$-$30Li_2O$-$55WO_3$	1.971	22
$20TeO_2$-$25Li_2O$-$55WO_3$	1.932	23
$88.33TeO_2$-$10.67BaO$-$6.0CdO$	2.077	19.06
$88.33TeO_2$-$13.67BaO$-$3.0Ga_2O_3$	2.048	20.02
$88.33TeO_2$-$13.67BaO$-$3.0Y_2O_3$	2.051	18.51
$79.34TeO_2$-$4.6BaO$-$15.88WO_3$	2.174	17.0
$68.6TeO_2$-$6.54Tl_2O$-$14.21WO_3$	2.197	15.1
$68.6TeO_2$-$6.54BaO$-$24.86WO_3$	2.180	16.2
$47.55TeO_2$-$17.07BaO$-$35.38WO_3$	2.301	14.4

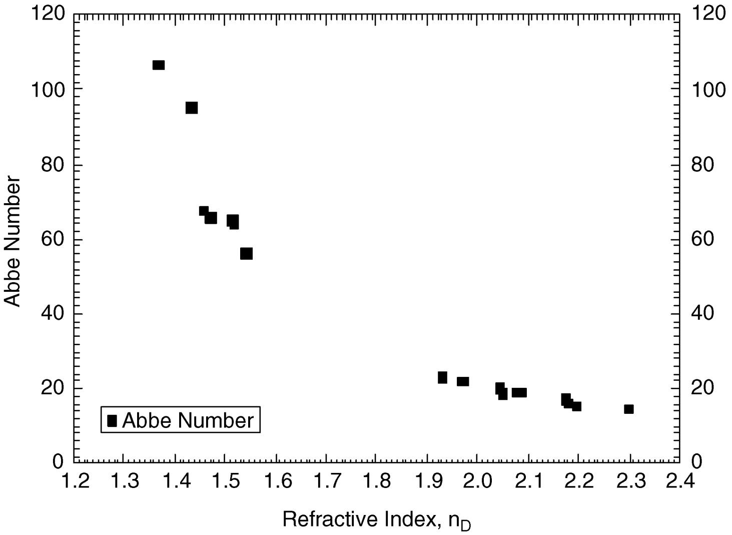

Figure 4.28 *Plot of the Abbe number as a measure of dispersion of a range of optical glass.*

presence of F^- ions reduces the refractive index due to the large electronegativity of fluorine atoms, which implies the presence of a strong electric dipole strength.

From Figure 4.28 it is evident that the relationship between the Abbe number and wavelength is not linear across the spectrum of oxide and fluoride glasses. Limited sets of data in the literature [80,116–118] are available within a family of glasses; however, they point out that the dispersion relationship between Abbe number and n_D may be assumed to be linear for all practical purposes.

The wavelength dependence of the refractive index, known as the materials dispersion (D_m) of a glass, defines another type of dispersion besides the "modal dispersion" (D_M), waveguide (D_w), and polarization (D_P) dispersions. The importance of different types of dispersive effects due to the modal distribution, materials and geometrical constrains are discussed in detail in Chapter 7 in the context of fibre geometries and overall dispersion properties for characterization of signal propagation in long- and short-haul optical communication and speeds. Together with the measured extrinsic loss, the dispersion penalty must be taken into account for determining the wavelength bandwidth of an optical fibre communication system. Overall dispersion is also important in nonlinear and quantum optics and signal processing. Below, examples of wavelength dependence of refractive indices are characterized for selected oxide and chalcogenide glasses (Figure 4.29a and b), from which it is clear that between the visible and IR region the shape of the wavelength dependence of refractive index is not linear. The slope of the n versus λ relationship implies that in order to characterize the zero dispersion it is essential to examine both the first ($dn/d\lambda$) and second ($d^2n/d\lambda^2$) derivatives.

Although there are various models for dispersion, the energy form of the Cauchy equation is one of the models that is used for characterization of the wavelength distribution of the refractive index of dielectric and optoelectronic materials:

$$n = n_-(h\upsilon)^{-2} + n_o + n_+(h\upsilon)^2 + n_{++}(h\upsilon)^4 \tag{4.60}$$

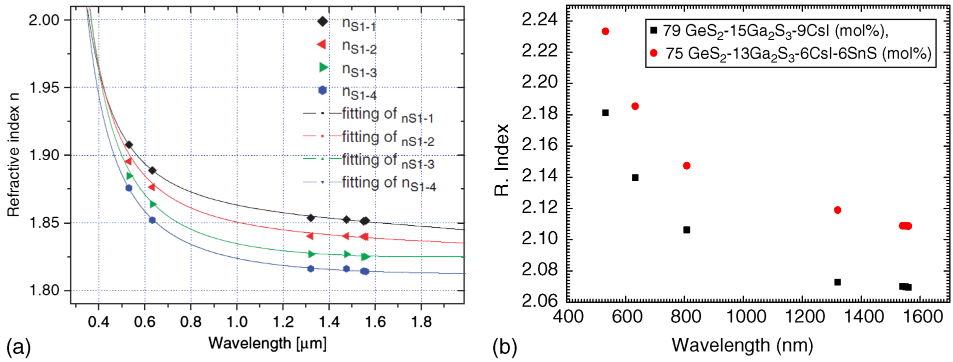

Figure 4.29 *Comparison of the refractive indices of (a) selected germanium oxide [50] and (b) chalcogenide glasses. Source (a): Jiang 2009. Reproduced with permission from Elsevier Limited.*

Here ($h\nu$) represents the photon energy and subscripts of n_i represent constants. The equation is valid for a wide range of photon energies ($h\nu$). For silica optical fibre based and bulk glassy materials the Sellmeier equation 4.61 is useful for characterizing the shape of a refractive index curve as a function of wavelength:

$$n^2(\lambda) = 1 + \sum_j \frac{A_j}{\left(1 - \frac{\lambda_j^2}{\lambda^2}\right)} \tag{4.61a}$$

$$n^2(\lambda) = A + \frac{B}{\left[1 - \frac{C}{\lambda^2}\right]} + \frac{D}{\left[1 - \frac{E}{\lambda^2}\right]} \tag{4.61b}$$

Wetenkamp [119] *et al.*, Ghosh [120], El-Mallawany [121], Takebe *et al.* [122] and Jiang and co-workers [50] have between them reported the refractive index properties of fluoride, a range of tellurite, and selected germanate and chalcogenide glasses. Different polynomial forms of Sellmeier equations are reported in the literature with comprehensive databases on optical glasses, e.g. by Hoya Glass Company in Japan [117], Edmund Optics [116] and SCHOTT Glass Company in the EU and USA [123]. Using the two-pole Sellmeier equation 4.61a, proposed by Ghosh [120], the chromatic dispersion properties were determined with sufficient accuracy. Here A_j, and λ_j are constants which are obtained from curve fitting. The first two terms in Equation 4.61b represent the higher-energy and lower-energy band gaps of electronic absorption, whereas the last term is for the resonant lattice vibration modes. The analysis of the materials dispersion (D_m, ps km^{-1} nm^{-1}) in tellurite glasses can then be carried out using equation (17) and has been found to be zero near 2.0 µm which is comparable with the values of GeO_2 glasses determined by Jiang *et al.* [50,52]. In Figure 4.30b, the dispersion curve for As_2S_3 glass is shown with zero dispersion points in the mid-IR spectrum.

4.5.1 Experimental Procedure for Measuring Refractive Index of a Glass or Thin Film

The refractive index of bulk glass and thin film materials is characterized by M-line spectroscopy, a technique in which the index of a glass or crystal may be measured at

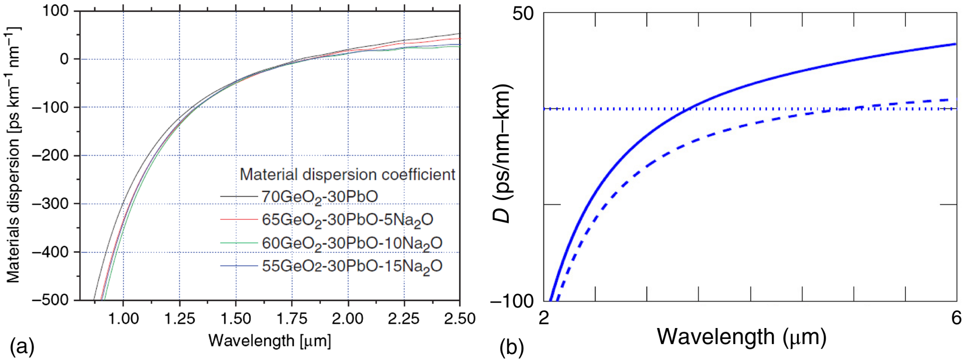

Figure 4.30 Dispersion curves for (a) germanium oxide [50] and (b) chalcogenide glasses [118,124]. Source (a): Jiang 2009. Reproduced with permission from Elsevier Limited. (b): Hu 2010. Reproduced with permission from Springer.

several wavelengths using prism coupling. For example, in a Metricon 2010 prism coupler, wavelengths of 532, 633, 808, 980, 1321, 1476, 1523, 1550 and 1560 nm may be used for determining the shape of the dispersion curve. The accuracy of this technique is 0.001 and this is a reliable technique for refractive index measurements in dielectric materials.

Figure 4.31a shows a schematic diagram of a prism coupler in which the dielectric medium (bulk glass or a film with a refractive index, n_G) is placed in contact with the prism having a refractive index n_P. The close contact is maintained for light coupling by means of a pneumatically operating coupling head shown in this figure. Since the refractive index of a material depends on the wavelength (λ) of the electromagnetic radiation, a laser source fixed at its position with respect to the prism is used. The laser light enters prism face at an angle θ, the intensity of which is measured by a detector on the opposite face of the prism. A computer drives the rotating table by varying the incident angle of the laser and at a certain angle together with the recording of the intensity as a function of angle which is shown schematically in Figure 4.31b. At a critical angle (θ_C) the laser encounters total internal

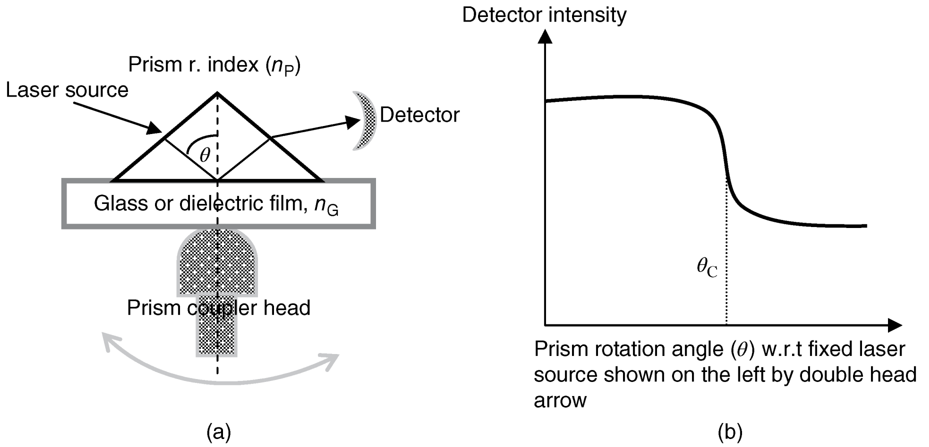
Prism r. index (n_P)
Laser source
Detector
θ
Glass or dielectric film, n_G
Prism coupler head
(a)
Detector intensity
θ_C
Prism rotation angle (θ) w.r.t fixed laser source shown on the left by double head arrow
(b)

Figure 4.31 Principle of refractive index measurement of bulk sample using a prism coupler (a); the critical angle (θ_c) (b).

reflection and travels along the interface, at which point the detector intensity reduces significantly, indicated by a sharp dip in Figure 4.31b of intensity against scanning angle (θ). This angle is the critical angle, which then allows determination of the material index from Snell's law:

$$\sin \theta_C = \frac{n_G}{n_P}$$

In a film of given thickness, the number of modes supported within the modal volume may also be characterized, which is useful, and from each of the modal indices the variation in the average refractive index may be estimated. The technique is also useful for determining the stress accumulated in thin films by measuring the refractive indices using two orthogonal directions of a laser source, yielding values of ordinary and extraordinary modal indices. With a set of materials with known refractive indices, the range of accuracy may be below 0.001, otherwise it is relatively easy to differentiate the index difference within ±0.001. Another important point to note here is that the index of the prism determines the highest index of the medium that can be measured, e.g. the condition $n_G < n_P$ must be maintained for Snell's law. Table 4.11 summarizes the Sellmeier constants for a range of optical glass used in bulk and waveguide optics.

Table 4.11 *Sellmeier constants for several optical glasses used for fibre optics applications.*

Fused silica:

$$n^2 = 1 + \left[\frac{A_1}{1-\left(\frac{\lambda_1}{\lambda}\right)^2}\right] + \left[\frac{B_1}{1-\left(\frac{\lambda_2}{\lambda}\right)^2}\right]\left[\frac{C_1}{1-\left(\frac{\lambda_3}{\lambda}\right)^2}\right]$$

$A_1 = 0.696749$, $B_1 = 0.408218$, $C_1 = 0.890815$, $\lambda_1(\mu m) = 0.0690660$, $\lambda_2(\mu m) = 0.115662$, $\lambda_3(\mu m) = 9.900559$

86.7SiO$_2$-13.3GeO$_2$: same equation as in fused silica. $A_1 = 0.711040$, $B_1 = 0.451885$, $C_1 = 0.704048$, $\lambda_1(\mu m) = 0.06427$, $\lambda_2(\mu m) = 0.129408$, $\lambda_3(\mu m) = 9.425478$

100% GeO$_2$: $A_1 = 0.80686642$. $B_1 = 0.71815848$, $C_1 = 0.85416831$, $\lambda_1(\mu m) = 0.068972606$, $\lambda_2(\mu m) = 0.15396656$, $\lambda_3(\mu m) = 11.841931$

Using **Equation 4.61b**:

$$n^2(\lambda) = A + \frac{B}{\left[1 - \frac{C}{\lambda^2}\right]} + \frac{D}{\left[1 - \frac{E}{\lambda^2}\right]};$$

Glass composition **80TeO$_2$-10ZnO-10Na$_2$O (mol.%):**
$A = 2.16708$, $B = 1.66815$, $C = 0.0481$, $D = 1.35618$, $E = 225$

Glass composition **55 GeO$_2$-30PbO-11Na$_2$O-4Ga$_2$O$_3$**:

$A = 1.74110$, $B = 1.49745$, $C = 0.04289$, $D = -0.85250$, $E = 121$
Glass composition **80TeO$_2$-10P$_2$O$_5$-10Na$_2$O**:

$A = 2.0057$, $B = 1.80594$, $C = 0.04131$, $D = 0.92190$, $E = 80$
Cauchy equation for **As$_2$Se$_3$** glass:

$$n^2(\lambda) = \frac{7.8605 \times 10^{-13}}{\lambda^2} + 7.1308 \text{ [127]}$$

4.5.2 Dependence of Density on Temperature and Relationship with Refractive Index

Characterization of the density of an inorganic glass helps in understanding the molar volume (V_M) and related structural properties. The molar volume depends on density and molar mass. The material density can be measured accurately using the Archimedes Principle adopted for specific gravity and mercury pycnometry. It is important to measure density at an isotherm using suitable calibration with known materials which can then yield data with three significant decimal place accuracy.

As explained, density is a structure sensitive property and changes with compositions. Since the refractive index of a glass depends on composition, it is reasonable to express the materials refraction properties in terms of density or molar volume, called the molar refractive index. In this respect, the original model was proposed by Berthelot in 1856 [125]. It is based on defining the specific refraction (R_m) which is a refractive index term multiplied by molar volume, as shown below where M defines the molecular weight:

$$R_m = \frac{M}{\rho} \cdot \left[\frac{n^2 - 1}{n^2 + 2} \right] \tag{4.62}$$

Since the density of a material defines the packing density of atoms or molecules within the material structure, the overlapping structural discussion on molar volume (V_M) and refractive index becomes even more necessary. The packing density in a material depends on the co-ordination number of cations, which then determines the surrounding number of anions, and therefore the effective electronic structure, which is responsible for molecular configuration. It is the link with electronic configuration in molecular bonds that defines the polarizability (α_M). Based on the relationship between the molar volume and molecular polarizability, the characterization of refractive index with temperature is essential for several engineering applications.

The density and refractive indices of selected tellurium oxide glasses are listed in the data in Table 4.12, to show the relationship between the packing density and refractive index of a medium.

The molecular polarizability and molar volume increase with temperature; each of these has an opposing influence on the refractive index as a result of change in the packing density. By combining the temperature coefficient of molecular polarizability (ϕ_M) and molar volume (β), the temperature coefficient of the refractive index (dn/dT) may be written as follows [117,126]:

$$\frac{dn}{dT} = \frac{(n^2 - 1)(n^2 + 2)}{6n} (\varphi_M - \beta_M) \tag{4.63}$$

Table 4.12 Density (ρ, gm cm^{-3} or kg m^{-3}) and refractive indices of selected glasses.

Glass composition (mol.%)	Density (g cm^{-3})	n	R_M
$65TeO_2$-$35Li_2O$	4.511	1.931	12.06
$84TeO_2$-$16P_2O_5$	4.785	1.993	16.31
$65TeO_2$-$35Nb_2O_5$	5.159	2.211	21.53
$70TeO_2$-$30WO_3$	5.953	2.191	17.01

where:

$$\phi_M = \frac{dR_M}{R_M}\frac{1}{dT} = \frac{d}{dT}\left(\log_e R_M\right) \text{ and } \beta_M = \frac{dV_m}{V_m}\cdot\frac{1}{dT} = \frac{d}{dT}\left(\log_e V_M\right) \tag{4.64}$$

Since the molar or specific index of refraction (R_M) is directly dependent on the molar polarizability (α_M), it may also be used in the above equation to express (ϕ_M).

Based on the expression for dn/dT, three different conditions emerge [126–128] which may be used for describing the temperature coefficient of refractive index of a family of glasses. Such a comparison may be useful for differentiating these properties of glasses by considering data such as α_M, density, β_M, etc.

The *first condition* refers to $\beta_M > \phi_M$, which means that with the temperature rise the refractive index decreases because the ($\phi_M - \beta_M$) differential is a negative quantity, which means that dn/dT is negative with rising temperature. Numerous inorganic oxide glasses, namely phosphate, borate, germanium oxide, tellurite and fluoride glasses, fall into this category.

The *second condition* refers to $\beta_M \approx \phi_M$, in which case the temperature coefficients of ϕ_M and β_M become coincident, at which point dn/dT may be then assumed to be nearly zero, since from this point of inflexion the direction of positive and negative values of dn/dT may be ascertained for given glass composition. In borosilicate and BK7 glass compositions (Figure 4.32) Fanderlik [124] showed that the refractive index increases with temperature between room temperature and 500 °C.

The glass materials that fall into the *third condition*, $\beta_M < \phi_M$, are predominantly silica and quartz based material system. In this family of glasses the molar polarizability increases with temperature faster than the increase in the molar volume. Furthermore, in silica, quartz and silicates the temperature coefficient of molar volume change is much smaller (between 10 to 100 times) than in other types of oxide and fluoride glasses. The temperature dependence of

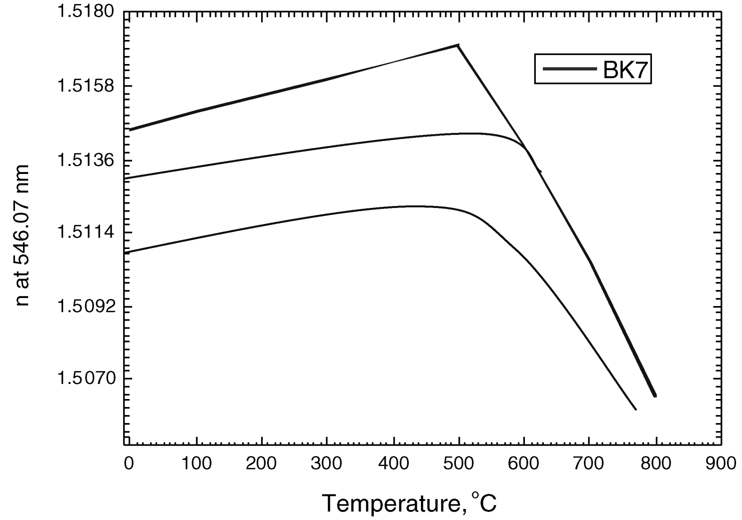

Figure 4.32 *Schematic plot of the temperature dependence of refractive index and molar volume in quenched and annealed glasses. Source: Fanderlik 1983 [124]. Reproduced with permission from Elsevier.*

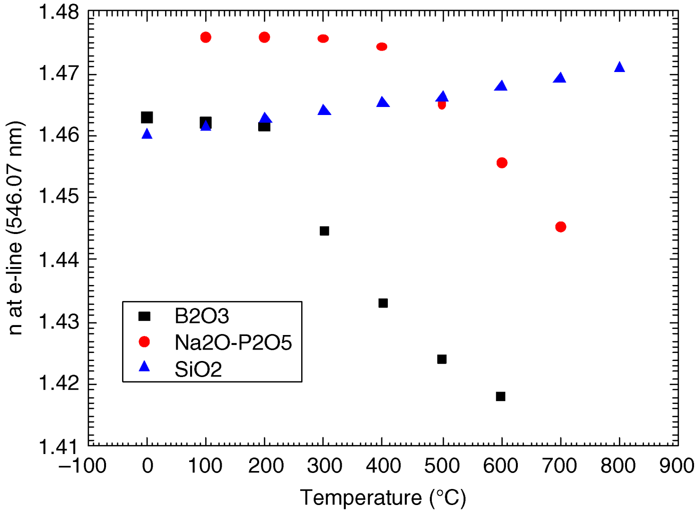

Figure 4.33 *Plot of the refractive indices of three different types of oxide glasses as a function of temperature between −100 and 800 °C; the light source used was at 546.07 nm, which is known as the e-line [123].*

refractive indices (n at the e-line (546.07 nm)) of unconventional oxide glasses namely B_2O_3 and sodium phosphate are plotted in Figure 4.33.

In Figure 4.33, the changes in molar volume and refractive index of a BK7 glass is plotted to demonstrate the effect of quenching rate on the apparent refractive index which represents a metastable state of the glass due to quenched molar volume. In Table 4.13 below, the temperature coefficient of the refractive indices of selected oxide glasses are collected from various references [117,123].

For calculating the absolute temperature coefficient of refractive index, SCHOTT glass has produced a comprehensive database [123] which is helpful for users of the information. For example, Equation 4.65 yields the absolute value of $(dn/dT)_{ab}$ at a given temperature and wavelength which is valid between −100 to +140 °C and covers the wavelength range 365–1014 nm. Notably, the term within the square bracket is the dispersion equation which

Table 4.13 *Refractive indices and temperature coefficients of refractive indices for selected optical materials. See also SCHOTT and CRYSTRAN in References [123,129]. Source: Van Popta 2002.*

Composition of glass and crystals	Refractive index at λ (nm)	dn/dT (°C)$^{-1}$
Fused silica	1.47 at 1060 nm	11.9×10^{-6}
Sapphire crystal	1.74663 at 1060 nm	13.1×10^{-6} at 546 nm
CaF_2 crystals	1.39908 at 5000 nm	10.6×10^{-6}
Borosilicate glass (N-BK7)	1.51680 at 587 nm	See SCHOTT [126]
$75TeO_2$-20ZnO-$5Na_2O$	2.03 at 633 nm	$-23.3 \times 10^{-6}\ K^{-1}$ [130]
Germanium oxide	1.83 at 633 nm	See Reference [130]
Si	3.425 at 25 °C	3.96×10^{-4}

accounts for wavelength and temperature variation. In this respect the dispersive effect under isothermal conditions due to the group velocity dispersion may be considered equivalent to the spread of the group velocities under rising temperature conditions for a monochromatic light. Consideration of these two equivalences in dispersion in optical and high-power laser design is quite critical. Parameters of calculating the absolute value of $(\mathrm{d}n/\mathrm{d}T)_{\mathrm{ab}}$ are:

$$\left(\frac{\mathrm{d}n}{\mathrm{d}T}\right)_{\mathrm{ab}} = \left(\frac{n^2(\lambda, T_{\mathrm{o}}) - 1}{2n(\lambda, T_{\mathrm{o}})}\right) \cdot \left[D_{\mathrm{o}} + 2D_1.\Delta T + 3D_2.\Delta T^2 + \left(\frac{E_{\mathrm{o}} + 2E_1.\Delta T}{\lambda^2 - \lambda_{\mathrm{TK}}^2}\right)\right] \tag{4.65}$$

4.5.3 Effect of Residual Stress on Refractive Index of a Medium and its Effect

When using large pieces of optical glass for camera, telescope in astronomical observatories, and windows for laser cavity, the accumulated stress in the glass determines the refractive index and the path length of the propagating light. Depending on the quenching rate, the thermal stress in the glass, which is dependent on molar volume as explained above, determines the refractive index. In the quenched state the residual molar volume of a bulk glass may reach near equilibrium molar volume, which is why such large pieces of optical components must be annealed for prolonged periods, lasting up to several months. The reduction in overall stress is essential for improving the image quality using bulk mirrors and lenses, when subjected to different environmental conditions. The optical path length $(\ell_{\mathrm{O,T}})$ depends on effective index (n) and coefficient of linear thermal expansion (α_{ℓ}) of bulk glass materials, which is then expressed as follows [123]:

$$\frac{\mathrm{d}\ell_{\mathrm{O,T}}}{\mathrm{d}T} = (n - 1)\alpha + \frac{\mathrm{d}n}{\mathrm{d}T} \tag{4.66}$$

A vast majority of ordinary glasses have a large positive value of the temperature coefficient of path length $(\mathrm{d}\ell_{\mathrm{O,T}}/\mathrm{d}T)$ because the corresponding value of $\mathrm{d}n/\mathrm{d}T$ for such glasses is positive, which in image analysis may contribute to wave front distortion leading to degradation in image quality. Glasses with zero or near zero $\mathrm{d}n/\mathrm{d}T$ are known as athermal glass. Such athermal glasses are also required for controlling the performance of a laser gain medium where the temperature rise may distort the coupling of various modes within the cavity and change beam focussing parameters by creating hot and cold spots instead of maintaining a uniform temperature.

Related to $(\mathrm{d}\ell_{\mathrm{O,T}}/\mathrm{d}T)$ and $\mathrm{d}n/\mathrm{d}T$ is another property which is called the *stress optical coefficient* or *birefringence* (B_{s}) which manifests in optical components in the presence of external stress; for example, in telescopes due to their mammoth size the structural load is directional leading to a directional change in the refractive index. The intrinsic aspect of stress birefringence is the retained molar volume in the quenched glass. The molar volume together with the vectorial nature of stress in large bulk optical materials must be analysed for minimizing the directional change in refractive index, which then also affects the optical path length of propagating light (ℓ_{S}, nm) due to stress:

$$\ell_{\mathrm{S}} = B_{\mathrm{S}}\sigma_{\mathrm{S}}d \tag{4.67}$$

The value of ℓ_{S} (nm) is proportional to B_{s} ($10^{-12}\,\mathrm{Pa}^{-1}$), residual stress ($\sigma_{\mathrm{s}}$, $10^5\,\mathrm{Pa}$) and thickness, d (cm). The value of B_{s} is determined by measuring the optical path difference caused at the centre of a glass disk, using a He-Ne laser light when a bulk glass disk is under compressive stress.

Table 4.14 *Parameters for SCHOTT optical glasses for determining the values of* $(dn/dT)_{ab}$.

SCHOTT glass	D_0, ×10^{-6}	D_1, ×10^{-8}	D_2, ×10^{-12}	E_o, ×10^{-7}	E_1, ×10^{-10}	λ_{TK} (μm)
N-FK5	−7.24	1.58	−9.51	3.51	4.61	0.156
N-BK7	1.86	1.31	−1.37	4.34	6.27	0.170
N-BK10	3.32	1.72	−2.05	3.57	3.90	0.169
N-ZK7	11.5	1.73	−8.06	4.32	7.05	0.179

In concluding this section it is relevant that to note that the displacement at the microscopic scale seen in optical components may also be characterized in terms of the elastic properties, namely the Young's, shear and bulk moduli and Poisson ratio. If the modulus properties are known, the strain component of a large optical structure may be ascertained using Hooke's law provided the applied stress is known. From the measured strain the dimensional changes leading to structural variation in ℓ_s (nm) may also be analysed indirectly.

In considering the fabrication of large pieces of glass based optical components, the heat transfer properties (thermal conductivity and specific heat capacity) are quite relevant. Since glass is classed as condensed matter, the dominant mode of heat transport is conduction not only through phonon vibration but also through radiation conduction (photon propagation at high temperature). The heat transport characteristics of a glass will therefore determine the cooling rate and hence the accumulated stress which might contribute to an overall change in optical path length. For this reason, for a range of commercially available optical glass, the key properties (optical, thermal and mechanical) properties are summarized in Table 4.13.

The values of the constants for selected SCHOTT optical glass are given in Table 4.14 for calculating the value of $(dn/dT)_{ab}$.

Details of physical, thermo-optic, mechanical and spectroscopic properties of optical materials are available in SCHOTT, CRISTRAN and HOYA references, discussed above.

4.6 Conclusion

Consideration for the design of optical fibres using the principles of geometrical optics and Maxwell's electrodynamics model is used in the explanation of propagation of light in a fibre or planar waveguide. The role of materials properties in determining the intrinsic and the measured losses in silica and non-silica fibres is discussed in detail and supplementary references are included. The fabrication techniques for different types of fibres are discussed in the context of processing materials, which relate to the discussions in Chapters 1–3. The temperature, wavelength and stress dependence of refractive indices are discussed and the importance of these properties in controlling dispersion is also explained.

References

1. Anon (19 October 2011) Young's Experiment. http://andrew1615.edublogs.org/2011/10/19/youngs-experiment/.
2. e-VLBI, Diffraction or why a point source isn't one. http://services.jive.nl/evlbi/diffraction.html (accessed June 2014).

3. Mynbaev, D.K. and L.L. Scheiner (2001) *Fibre Optics Communications Technology*, Prentice Hall, Upper Saddle River, NJ (USA).
4. France, P.W. (1989) *Fluoride Glass Optical Fibers*. Blackie, pp. (a) 32–71; (b) 100–121; (c) 132–185.
5. Keiser, G. (1993) *Optical Fibre Communications*, 2nd edn. McGraw Hill International, Singapore, pp. 30–75.
6. Syms, R.R.A. and J.R. Cozens (1992) *Optical Guided Waves and Devices*, McGraw-Hill Publishing Company, London, pp. 179–276.
7. Harman, I.P. (1996) *Optical Diagnostics for Thin Solid Film Processing*, Academic Press, San Diego, CA, pp. 559–563.
8. Elliott, S.R. (1983) *Physics of Amorphous Materials*, Longman, London, pp. 191, 234–237.
9. Mott, N.F. and E.A. Davis (1979) *Electronic Processes in Non-crystalline Materials*, Oxford University Press, Oxford.
10. Hogarth, C.A. and E. Assadzadeh-Kashani (1983) Some studies of the optical properties of tungsten-calcium-tellurite glasses. *Journal of Materials Science*, **18** (4), 1255–1263.
11. El-Mallawany, R.A.H. (2002) *Tellurite Glass Handbook - Physical Properties and Data*. 2002, CRC Press, Boca Raton, FL.
12. Davis, E. and N. Mott (1970) Conduction in non-crystalline systems V. Conductivity, optical absorption and photoconductivity in amorphous semiconductors. *Philosophical Magazine*, **22** (179), 0903–0922.
13. Zakery, A. and S. Elliott (2003) Optical properties and applications of chalcogenide glasses: a review. *Journal of Non-Crystalline Solids*, **330** (1), 1–12.
14. Pinnow, D.A. *et al.* (1973) Fundamental optical attenuation limits in the liquid and glassy state with application to fiber optical waveguide materials. *Applied Physics Letters*, **22** (10), 3.
15. Lines, M.E. (1984) Scattering losses in optic fiber materials- I. A new parametrization. *Journal of Applied Physics*, **55** (11), 4502.
16. Willard, H.H., L.L. MErritt, and J.A. Dean (1965) *Instrumental Methods of Analysis*. 4th edn, D Van Nostrand Company Ltd., Princeton.
17. Hecht, E. and A. Zaiac (1977) *Optics*, 3rd edn, Addison Wesley.
18. Parker, J. and P. France (1989) Optical properties of halide glasses, in *Glasses and Glass-Ceramics*. Springer, pp. 156–202.
19. Wong, J. and C.A. Angell (1976) *Structure of Glass by Spectroscopy*, Marcel Dekker, New York, pp. (a) 429–436 and 517-519; (b) 438–451; (c) 461–467 and 523–526; (d) 451–459.
20. Grove, F.J. and P.E. Jellyman (1955) The infra-red transmission of glass in the range room temperature to 1400°. *Journal of the Society of Glass Technology*, **39**, 3–15.
21. Sodorov, T.A. and N.N. Sobolev (1957) *Optics and Spectroscopy (English Translation)*, **3**, 560.
22. Konijnendijk, W.L. and J.M. Stevels (1975) The structure of borate glasses studied by Raman scattering. *Journal of Non-Crystalline Solids*, **18** (3), 307–331.
23. Konijnendijk, W.L. (1975) Structure of Borosilicate Glasses, Philips Research Reports.
24. Borelli, N.F. and G.J. Su (1963) Structure of sodium borate glasses. *Physics and Chemistry of Glasses*, **4**, 206.

25. Joshi, P., S. Shen, and A. Jha (2008) Er^{3+}-doped boro-tellurite glass for optical amplification in the 1530-1580 nm. *Journal of Applied Physics*, **103** (8), 3543.
26. Sigel, G.H. (1977) Glass I: interaction with electromagentic radiation, in *Treatise on Materials Science and Technology* (ed. M.T.a.R.H. Doremus), Academic Press, New York, pp. 5–89.
27. J. Ecthpare (1970) *Amorphous Material*, (ed. R.W.D.a.B. Ellis), Wiley-Interscience: London, p. P.337.
28. Galeener, F.L. and G. Lucovsky (1976) Longitudinal optical vibrations in glasses: GeO_2 and SiO_2. *Physical Review Letters*, **37** (22), 1474.
29. Galeener, F.L., G. Lucovsky, and R.H. Geil (1978) The Raman and infrared spectra of vitreous BeF_2. *Solid State Communications*, **25**, 405–408.
30. Baldwin, C.M., R.M. Almeida, and J.D. Mackenzie (1981) Halide glasses. *Journal of Non-Crystalline Solids*, **43** (3), 309–344.
31. Baldwin, C.M. and J.D. Mackenzie (1979) Preparation and properties of water-free vitreous beryllium fluoride. *Journal of Non-Crystalline Solids*, **31** (3), p. 5.
32. Baldwin, C.M. and J.D. Mackenzie (1980) Ionic transport and defect structure of vitreous beryllium fluoride. *Journal of Non-Crystalline Solids*, 1980. **40**, 135–148.
33. Milberg, M.E. and M.C. Daly (1963) Structure of oriented sodium metaphosphate glass fibers. *Journal of Chemical Physics*, **39** (11), 2966–2973.
34. Exarhos, G.J. and Risen, W.M. Jr. (1971) Vibrational motion of cations in ionic glasses. *Chemical Physics Letters*, **10** (4), 484–486.
35. Richardson, F.D. (1974) *Physical Chemistry of Melts in Metallurgy*, Vol. 1, Academic Press, London, pp. 87–92.
36. Sekiya, T., *et al.* (1992) Raman-spectra of $MO_{1/2}$-TeO_2 (M = Li, Na, K, Rb, Cs and Tl) glasses. *Journal of Non-Crystalline Solids*, **144** (2–3), 128–144.
37. Sekiya, T., N. Mochida, and S. Ogawa (1995) Structural study of MOO_3-TeO_2 glasses. *Journal of Non-Crystalline Solids*, **185** (1–2), 135–144.
38. Sekiya, T., N. Mochida, and S. Ogawa (1994) Structural study of WO_3-TeO_2 glasses. *Journal of Non-Crystalline Solids*, **176** (2–3), 105–115.
39. Sekiya, T., N. Mochida, and A. Ohtsuka (1994) Raman-spectra of MO-TeO_2 (M = Mg, Sr, Ba and Zn) glasses. *Journal of Non-Crystalline Solids*, **168** (1–2), 106–114.
40. Sekiya, T., N. Mochida, and A. Soejima (1995) Raman-spectra of binary tellurite glasses containing tri-valent or tetra-valent cations. *Journal of Non-Crystalline Solids*, **191** (1–2), 115–123.
41. Himei, Y., *et al.* (1997) X-ray photoelectron spectroscopy of alkali tellurite glasses. *Journal of Non-Crystalline Solids*, **211** (1–2), 64–71.
42. Himei, Y., *et al.* (1994) Coordination change of Te atoms in binary tellurite glasses. *Journal of Non-Crystalline Solids*, **177**, 164–169.
43. S.L. Tagg, J.C. Huffman, and J.W. Zwanziger (1994) Crystal-structure and sodium environments in sodium tetratellurite, $Na_2Te_4O_9$, and sodium tellurite, Na_2TeO_3, by X-ray crystallography and Na-23 NMR. *Chemistry of Materials*, **6** (10), 1884–1889.
44. Tagg, S.L., R.E. Youngman, and J.W. Zwanziger (1995) The structure of sodium tellurite glasses - sodium-cation environments from ^{23}Na NMR. *Journal of Physical Chemistry*, **99** (14), 5111–5116.

45. Hill, C.J. and A. Jha (2007) Development of novel ternary tellurite glasses for high temperature fiber optic mid-IR chemical sensing. *Journal of Non-Crystalline Solids*, **353** (13–15), 1372–1376.
46. Rada, S., *et al.*, (2009) Structural and electronic properties of tellurite glasses. *Journal Materials Science*, **44** (12), 3235–3240.
47. Irannejad, M., *et al.* (2010) A parametric study of Er^{3+}-ions doped Phospho-tellurite glass thin films by pulsed laser deposition. *Optical Materials*, **33** (2), 215–219.
48. Jose, R., *et al.* (2008) Tailoring of Raman gain bandwidth of tellurite glasses for designing gain-flattened fiber Raman amplifiers. *Journal of the Optical Society of America B - Optical Physics*, **25** (3), 373–382.
49. Murugan, G.S., T. Suzuki, and Y. Ohishi (2006) Raman characteristics and nonlinear optical properties of tellurite and phosphotellurite glasses containing heavy metal oxides with ultrabroad Raman bands. *Journal of Applied Physics*, **100**, 023107.
50. Jiang, X., *et al.* (2009) Investigation on germanium oxide-based glasses for infrared optical fibre development. *Optical Materials*, **31** (11), 1701–1706.
51. Jiang, X., J. Lousteau, and A. Jha (2010) The structural, thermal, and optical analyses of multicomponent germanium oxide glasses for engineering mid-infrared fiber chemical sensing. *Journal of the American Ceramic Society*, **93** (10), 3259–3266.
52. Jiang, X. (September 2009) Engineering of Novel Single- and Multi-mode Infrared Optical Fibres for Device Applications, PhD Thesis, University of Leeds, p. 177.
53. Poulain, M. (1981) Glass formation in ionic systems. *Nature*, **293**, 279–280.
54. Poulain, M. and J. Lucas (1978) Une nouvelle classe de materiaux: les verres fluores au tetrafluorure de zirconium. *Verres Refract*, **32** (4), 505–513.
55. Almeida, R.M. and J.D. Mackenzie (1981) Vibrational spectra and structure of fluorozirconate glasses. *Journal of Chemical Physics*, **74** (11), 5954–5961.
56. Gonçalves, M.C. and R.M. Almeida (1996) Incorporation of OH species in fluorozirconate glasses: nature and influence on physical properties. *Journal of Non-Crystalline Solids*, **194** (1), 180–190.
57. Bendow, B., *et al.* (1985) Polarized Raman scattering in rare-earth fluoride glasses. *Journal of the American Ceramic Society*, **68** (4) C-92–C-95.
58. Bendow, B., *et al.* (1981) Vibrational spectra of fluorohafnate glass. *Solid State Communications*, **37** (6), 485–489.
59. Iqbal, T., M.R. Shahriari, and G.H.S. Jr. (1991) A new glass forming ability criterion for multicomponent halide glasses. *Materials Science Forum*, **67–68**, 225–232.
60. Fujiura, K., T. Kanamori, and S. Sudo (1997) Fiber materials and fabrications, in *Optical Fiber Amplifiers - Materials, Devices and Applications.*, (ed. S. Sudo), Artech House Inc., Norwood, MA, pp. 193–403.
61. Cardoso, A.V. and A.B. Seddon (1991) Penetration viscometry using a thermal mechanical analyser. *Glass Technology*, **32** (5), 174–176.
62. Santos, L.F., *et al.* (2001) Raman spectra and structure of fluoroaluminophosphate glasses. *Journal of Non-Crystalline Solids*, **284** (1), 43–48.
63. Toratani, H., X. Zou, and Y. Matsumoto (1996) Fluoride glasses for 193 nm optics. *Japanese Journal of Applied Physics*, **35** (12B), 6351–6355.
64. Sanghera, J.S., J. Heo, and J.D. Mackenzie (1988) Chalcohalide glasses. *Journal of Non-Crystalline Solids*, **103** (2), 155–178.

65. Savage, J.A. and S. Nielsen (1965) Chalcogenide glasses transmitting in the infrared between 1 and 20 μ – A state of the art review. *Infrared Physics*, **5** (4), 195–204.
66. Kumta, P.N. and S.H. Risbud (1994) Rare-earth chalcogenides—an emerging class of optical materials. *Journal of Materials Science*, **29** (5), 1135–1158.
67. Sanghera, J.S. and I.D. Aggarwal (1999) Active and passive chalcogenide glass optical fibers for IR applications: a review. *Journal of Non-Crystalline Solids*, **256**, 6–16.
68. Schweizer, T., D.J. Brady, and D.W. Hewak (1997) Fabrication and spectroscopy of erbium doped gallium lanthanum sulphide glass fibres for mid-infrared laser applications. *Optics Express*, **1** (4), 102–107.
69. Marchese, D. and A. Jha (1997) The structural aspects of the solubility of Pr $^{3+}$ ions in GeS_2-based glasses. *Journal of Non-Crystalline Solids*, **213**, 381–387.
70. Lucovsky, G. and R.M. Martin (1972) A molecular model for the vibrational modes in chalcogenide glasses. *Journal of Non-Crystalline Solids*, **8**, 185–190.
71. Shen, S., *et al.* (2002) Compositional effects and spectroscopy of rare earths (Er^{3+}, Tm^{3+}, and Nd^{3+}) in tellurite glasses. *Comptes Rendus Chimie*, **5** (12), 921–938.
72. Keck, D.B., R.D. Maurer, and P. Schultz (1973) On the ultimate lower limit of attenuation in glass optical waveguides. *Applied Physics Letters*, **22** (7), 307–309.
73. Shibata, S., *et al.* (1981) Prediction of Loss Minima in Infrared Optical fibres. *Electronics Letters*, **17** (21), 775–777. T Kanamori, Y Terunuma, S Takahashi and T Miyashita (1984) Chalcogenide glass fibers for mid-infrared transmission, *Journal of Lightwave Technology, V.* **LT-2**, (5), 607–613.
74. Jiang, X. and A. Jha (2014) Engineering of a Ge-Te-Se glass fibre evanescent wave spectroscopic (FEWS) mid-IR chemical sensor for the analysis of food and pharmaceutical products. *Sensors and Actuators B: Chemical*, **206**, 159–169.
75. Kao, K.C. and G.A. Hockham (1966) Dielectric-fibre surface waveguides for optical frequencies. *Proceedings of the Institution Electrical Engeering*, **113** (7), 1151–1158.
76. Moriyama, T., *et al.* (1980) Ultimately low OH content VAD optical fibres. *Electronics Letters*, **16** (18), 698–699.
77. Keiser, G. (1991) *Optical Fibre Communications*, McGraw Hill International, Singapore, pp. 86–122.
78. Jha, A., *et al.* (2012) Review on structural, thermal, optical and spectroscopic properties of tellurium oxide based glasses for fibre optic and waveguide applications. *International Materials Reviews*, **57** (6), 357–382.
79. Hill, C.J., L. Huang, and A. Jha (2009) High-Tg GeS2 based glasses for chemical sensing applications. *Journal of Materials Science: Materials in Electronics*, **20** (1), 202–206.
80. Gitter, A.J. (1985) Silicon Dioxide for advanced engineering and ceramics, in *Raw Materials for Advanced Engineering Ceramics*, John Wiley & Sons, Inc., New York.
81. Kapron, F.P., D.B. Keck, and R.D. Maurer (1970) Radiation losses in glass optical waveguides. *Applied Physics Letters*, **17** (10), 423–425.
82. Sudo, S., *et al.* (1978) Low-OH-content optical fiber fabricated by vapor-phase axial-deposition method. *Electronics Letters*, **14** (17), 534–535.
83. T. Izawa and N. Inagaki (1980) Materials and processes for fiber preform fabrication—Vapor-phase axial deposition. *Proceedings of the IEEE*, **68** (10), 1184–1187.

84. Geittner, P., D. Küppers, and H. Lydtin (1976) Low-loss optical fibers prepared by plasma-activated chemical vapor deposition (CVD). *Applied Physics Letters*, **28** (11), 645–646.
85. Glass, A.M., *et al.* (1976) Advances in fiber optics. *Bell Labs Technical Journal*, **5** (1), 168–187.
86. OFS (May 2014) AllWave® ZWP Fiber. http://fiber-optic-catalog.ofsoptics.com/Asset/AllWave-117-web.pdf.
87. W G French, *et al.* (1974) Optical waveguides with very low losses. *Bell System Technical Journal*, **53** (5), 951–954.
88. Aggarwal, I.D. and G. Lu (1991) *Fluoride Glass Fiber Optics*. Academic Press Inc., Boston, pp. 141–233.
89. Fujiura, K., *et al.* (1995) Reliability of fluoride fibers for use in fiber amplifiers. *Technical Digest Series-Optical Society of America*, **18**, 104.
90. Edahiro, T., *et al.* (1979) OH-ion reduction in VAD optical fibers. *Electronics Letters*, **15** (16), 482–483.
91. Monro, T.M. and H. Ebendorff-Heidepriem (2006) Progress in microstructured optical fibers. *Annual Review of Material Research*, **36**, 467–495.
92. Liao, M., *et al.* (2009) Tellurite microstructure fibers with small hexagonal core for supercontinuum generation. *Optics Express*, **17** (14), 12174–12182.
93. Y Ohishi, *et al.* (1994) Fabrication of praseodymium-doped arsenic sulfide chalcogenide fiber for 1.3-μm fiber amplifiers. *Applied Physics Letters*, **65** (1), 13–15.
94. Ebendorff-Heidepriem, H. and T.M. Monro (2007) Extrusion of complex preforms for microstructured optical fibers. *Optics Express*, **15** (23), 15086–15092.
95. Oermann, M.R., *et al.* (2009) Index matching between passive and active tellurite glasses for use in microstructured fiber lasers: Erbium doped lanthanum-tellurite glass. *Optics Express*, **17** (18), 15578–15584.
96. Fujiura, K., *et al.* (1995) Fabrication of low-loss and high-Δn single-mode fluoride fiber for 1.3 μm praseodymium-doped fiber amplifiers. *Applied Physics Letters*, **67** (21), 3063–3065.
97. Ohishi, Y., *et al.* (1985) Measurement of the angular distribution of scattered light from ZrF_4-based fluoride fiber. *Applied Optics*, **24** (19), 3227–3230.
98. France, P., *et al.* (1986) Ultimate realistic losses of ZrF_4 based Ir fibres. Presented at *OE/LASE'86 Symposium (January 1986, Los Angeles)*, International Society for Optics and Photonics.
99. Thomas, G.A., *et al.* (2000) Towards the clarity limit in optical fibres. *Nature*, **404**, 262–264.
100. Bartholomew, R.F., *et al.* (1980) Infrared spectra of a water-containing glass. *Journal of the American Ceramic Society*, **63** (9–10), 481–485.
101. Pasteur, G.A. (1973) Optical absorption determination of OH in B_2O_3 glass. *Journal of American Ceramic Society*, **56** (10), 548.
102. Mitachi, S., G. Fonteneau, and J. Lucas (1987) Relationship between the intensity of the molar extinction coefficient of OH in fluoride glasses and glass matrix properties. *Journal of Non-Crystalline Solids*, **95**, 633–640.
103. Liu, X., *et al.*, (1999) Reduction of OH^--related photoluminescence quenching in Pr^{3+}-doped GeS_2-based glasses by means of purification. *Journal of Non-Crystalline Solids*, **256**, 294–298.

104. Mitachi, S. and P.A. Tick (1991) OH absorption in CLAP glass systems. *Journal of Non-Crystalline Solids*, **135** (2), 189–197.
105. Tofield, B.C., *et al.* (1974) On the growth of neodymium pentaphosphate crystals for laser action. *Materials Research Bulletin*, **9** (4), 435–447.
106. Liao, M., *et al.* (2009) Fabrication and characterization of a chalcogenide-tellurite composite microstructure fiber with high nonlinearity. *Optics Express*, **17** (24), 21608–21614.
107. Mori, A., Y. Ohishi, and S. Sudo (1997) Erbium-doped tellurite glass fibre laser and amplifier. *Electronics Letters*, **33** (10), 863–864.
108. Mori, A., *et al.* (1997) 1.5 mm broadband amplification by tellurite-based EDFAs. Optical Fiber Communications Conference, Dallas, Texas, 16 February 1997, OSA Technical Digest Series, paper PD1.
109. Kubat, I., *et al.* (2014) Mid-infrared supercontinuum generation to 12.5 μm in large NA chalcogenide step-index fibres pumped at 4.5 μm. *Optics Express*, **22** (16), 19169–19182.
110. Petersen, C.R., *et al.*, (2014) Mid-infrared supercontinuum covering the 1.4–13.3 μm molecular fingerprint region using ultra-high NA chalcogenide step-index fibre. *Nature Photonics*, **8** (11), 830–834.
111. van Hulst, H.V.D. (1957) *Light Scattering by Small Particles*, Courier Dover Publications.
112. Syms, R.R.A. and J.R. Cozens (1992) *Optical Guided Waves and Devices*, McGraw-Hill Publishing Co., pp. 31–35.
113. Heavens, O.S. and R.W. Ditchburn (1991) *Insight Into Optics*, John Wiley & Sons Ltd, Chichester, pp. 53–55.
114. Mynbaev, D.K. and L.L. Scheiner (2001) *Fibre Optics Communications Technology*, Prentice Hall, Upper Saddle River, NJ, pp. 42–63.
115. Keiser, G. (1991) *Optical Fibre Communications*. McGraw Hill International: New York. pp. 118–120.
116. Edmund Optics (2014) Optical Glass. http://www.edmundoptics.com/technical-resources-center/optics/optical-glass.
117. Hoya Corporation, Optical Glass http://www.hoyaoptics.com/pdf/OpticalGlass.pdf (accessed 5 January 2016).
118. Hu, J., *et al.* (2010) Maximizing the bandwidth of supercontinuum generation in As_2Se_3 chalcogenide fibers. *Optics Express*, **18** (7), 6722–6739.
119. Wetenkamp, L., *et al.* (1991) The effect of small composition changes on the refractive index and material dispersion in ZBLAN heavy-metal fluoride glass. *Materials Science Forum*, 471–476.
120. Ghosh, G. (1995) Sellmeier coefficients and chromatic dispersions for some tellurite glasses. *Journal of the American Ceramic Society*, **78** (10), 2828–2830.
121. El-Mallawany, R.A.H. (2002) *Tellurite Glass Handbook: Physical Properties and Data*, CRC Press.
122. Takebe, H., S. Fujino, and K. Morinaga (1994) Refractive-index dispersion of tellurite glasses in the region from 0.40 to 1.71 μm. *Journal of the American Ceramic Society*, **77** (9), 2455–2457.
123. Schott (2014) Optical Glass 2014: Description of Properties. http://www.schott.com/advanced_optics/english/download/schott-optical-glass-pocket-catalog-january-2014-row.pdf.

124. Fanderlik, I. (1983) *Optical Properties of Glass*, Elsevier Publishing Company, Maryland Heights, pp. 82–89.
125. Van Popta, A., *et al.* (2002) Photoinduced refractive index change in As2Se3 by 633nm illumination, *Optics Express*, **10** (15), 639–644.
126. Paul, A. (1982) *Chemistry of Glasses*. Chapman & Hall.
127. Izumitani, T. and H. Toratani (1980) Temperature coefficient of electronic polarizability in optical glasses. *Journal of Non-Crystalline Solids*, **40** (1), 611–619.
128. Ghosh, G. (ed.) (1998) *Handbook of Optical Constants of Solids: Handbook of Thermo-Optic Coefficients of Optical Materials With Applications*, Academic Press.
129. Crystran (2012) Silica Glass (SiO_2). http://www.crystran.co.uk/optical-materials/silica-glass-sio2.
130. Li, H., *et al.* (2007) Thermal sensitivity of tellurite and germanate optical fibers. *Optics Express*, **15** (14), 8857–8863.

5

Thin-film Fabrication and Characterization

5.1 Introduction

Techniques for the deposition of thin films, many of which have been developed for the fabrication of magnetic and semiconductor devices and optical coatings, can also be applied to grow thick films (1–5 μm) for the fabrication of optical waveguides. For photonic devices, the planar waveguide must have low attenuation, as discussed in Chapter 4, both in the propagating media and at the interconnects [1]. As explained in detail in Chapter 4, the attenuation properties of a dielectric waveguide device depends on the intrinsic and extrinsic losses. The total intrinsic loss is dependent on the sum of electronic and multiphonon absorptions, and Rayleigh scattering [1,2a], whereas the total loss is the sum of extrinsic and intrinsic losses and may be dominated by extrinsic factors [2b]. In thin/thick films the fabrication technique can affect the total waveguide loss, because of the way the film is produced and its density is controlled [3]. By altering the processing conditions, the total loss may either be increased or decreased. The characterization techniques of thin films is discussed in Chapter 2.

The main focus in this chapter is on the principles and processing techniques for thin films, with examples of materials and processing parameters. Basic materials science, physics, and chemistry of a process are also emphasized for appreciating the potential factors that might contribute to attenuation eventually in a waveguide structure. Besides the deposition techniques and examples of thick and thin films, general aspects of photolithography, pattern formation, masking and etching techniques are not discussed here, which are detailed in a chapter dedicated to the waveguide device engineering.

The deposition of materials on a substrate may be classified into two main types—physical vapour deposition (PVD) and chemical vapour deposition (CVD) techniques.

Inorganic Glasses for Photonics – Fundamentals, Engineering and Applications, First Edition. Animesh Jha.
© 2016 John Wiley & Sons, Ltd. Published 2016 by John Wiley & Sons, Ltd.

5.2 Physical Techniques for Thick and Thin Film Deposition

Amongst PVD, the techniques developed so far are *evaporation, sputtering, plasma beam, laser ablation, and ion implantation*. Each technique is discussed in some detail with selected text book and key references. Most plasma generating techniques are incorporated with main deposition techniques e.g. plasma-assisted sputtering, CVD, and molecular beam epitaxy.

5.3 Evaporation

5.3.1 General Description

For evaporation of materials, a solid material is heated under vacuum to form a vapour which then condenses onto a chosen substrate. The evaporation–condensation process is carried out without melting the evaporant. This means that there is a temperature dependence of the solid/liquid/vapour transformation process and a pressure–temperature relationship is essential for identifying the triple, boiling and sublimation points. For maintaining the stoichiometry and composition of evaporant before and after deposition, a solid $[AB]_{solid}$ must evaporate as a gaseous specie $(AB)_{gas}$ which is classed as a congruent evaporation. If the solid AB on evaporation decomposes to a mixture of species, constituted of A and B atoms, e.g. $A_{1-x}B_y$, A_xB_{1-y}, etc. then the evaporation is classed as an incongruent evaporation. Most pure elements evaporate congruently as expected, and in general most congruently melting compounds (i.e. those solids that melt without decomposition) also tend vaporize congruently. A classic example of congruent evaporation is ZnO and stannic oxide (SnO_2) in oxygen rich pressure, diamond, CaF_2. By contrast the high temperature evaporation of alumina in the absence of oxygen occurs incongruently, because of the large thermodynamic stabilities of Al_2O, Al_2O_2 and AlO species above 1500 °C. From these two types of comparison, it is evident that during incongruent evaporation, there is likely to be a large variation in the stoichiometry of material formed on a substrate. By maintaining a positive pressure of oxygen in the deposition chamber, it may be possible to minimize the non-stoichiometry in materials.

5.3.2 Technique, Materials and Process Control

The evaporant is placed inside a water-cooled metal crucible and is bombarded either with a high-energy electron beam (7 to 8 kV at 1 A) or simply resistively or inductively heated to a very high temperature (Figure 5.1). The vapour deposits on a cold substrate and the rate of thickness deposited is proportional to the flux of materials in the vapour phase, which is determined by the equilibrium pressure at the chosen temperature inside the chamber. The mass transport is enhanced via the application of an electric field [3,4]. The uniformity of film thickness on the substrate is maintained by providing a twin-axial circular motion—one fast other slow. Details of the evaporation chamber and its design can be found in the literature [3].

Metal oxides, e.g. SiO_2, Al_2O_3, indium-tin oxide (ITO) and its variants, and perovskites [3], when evaporated lose their oxygen in vacuum and in an inert atmosphere. The lost oxygen must be maintained by injecting oxygen in the evaporation chamber. Occasionally the injected oxygen is also activated by passing it through an electric discharge [3]. Metal halides, e.g. MgF_2, CaF_2 and KI, have been used for antireflection coatings [3,4]. Materials such PbTe, CdS, CdSe and ZnSe [5,6] exhibit more complex behaviour, because these

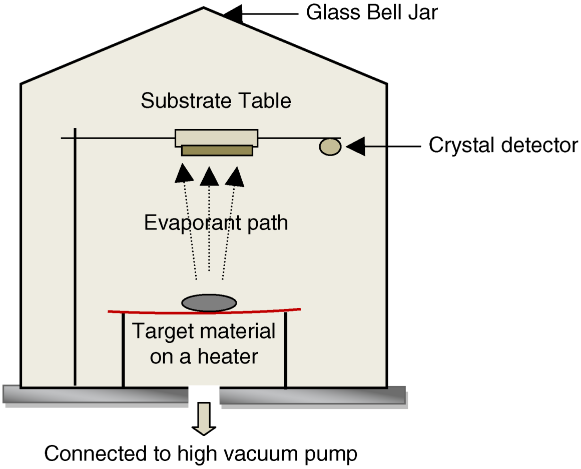

Figure 5.1 *Schematic diagram of the evaporation chamber for dielectric materials as a target which is electrically heated for depositing on a substrate inside an evacuated bell jar. The growth of the deposited layer is monitored with a crystal detector.*

compounds tend to decompose to their elemental states in the vapour form. Controlling the chemistry of evaporant therefore becomes more complex, since high vapour pressures of both metals (Cd, Pb, Zn) and non-metals (S, Se, Te) prevent maintaining the stoichiometry. Consequently, the non-stoichiometry of the deposited materials introduces electronic defects and corresponding band gap or sub-gap absorption peaks. Some of these defects in non-stoichiometric oxides and their films are discussed in detail elsewhere [7].

The following improvements in control of the process can be made.

- Impurities in the evaporant can only be removed by purifying the material to the desired purity level. Such impurities are also likely to introduce absorption bands, depending upon their nature, in the electronic spectra or in the molecular spectra.
- Temperature control is essential. It is carried out using either an optical pyrometer or a thermocouple. An optical pyrometer is much better for temperatures above 1200 °C at which point the radiative heat transfer becomes dominant.
- Changing to a Knudsen cell design with the application of accelerating voltage to increase the deposition rate and the uniformity of deposition is essential for high-quality optical films. Sometimes a supersonic nozzle is introduced to improve deposition [3]

In addition:

- Flux monitoring may be achieved by simultaneously depositing onto a vibrating quartz wafer adjacent to the substrate;
- by monitoring the change in the optical reflection intensity or phase for the film itself with increasing thickness;
- monitoring the periodicity in the reflection high-energy electron diffraction (RHEED) signal for epitaxial growth only. RHEED has not been used for thick films.

There are no significant examples of transparent dielectric thick and thin films and waveguides using thermal evaporation.

5.4 Sputtering

5.4.1 Principle of Sputtering

Sputtering is a physical vapour deposition process involving the removal of materials from a solid cathode surface. This is accomplished by bombarding the cathode with positive ions emitted from a rare-earth gas discharge. When ions with high kinetic energy are incident on the cathode, the subsequent collisions may knock surface atoms and produce a stream of sputter atoms from the target material. The process of transferring momentum from impacting ions to surface atoms forms the basis of sputter coating.

The momentum transfer from the positively charged ions causes surface erosion. It is claimed that the momentum of in-coming ions is transferred to the cathode substrate by volatilizing the materials stoichiometrically [3]. The energy distribution of incoming positively charged ions falls in the same energy regime as the energy required for the displacement of surface atoms. Consequently, sub-surface damage does not take place. During sputtering part of the sputtered material is re-sputtered, and this yields an improved surface quality of the film. Re-sputtering also provides a compressive stress in the deposited layer [3].

There are two main techniques of sputtering employed for the production of metallic and dielectric films. Because of the conducting nature of metallic materials, they are much more easily deposited in a diode sputter source than onto a dielectric material [3]. In a diode sputter source, the plasma or ionized gas is created uniformly between the cathode and anode, leading to a uniform consumption of the target material. Diode sources and target holders are quite cheap, and large size production scale units can be assembled easily (Figure 5.2). However, the sputtering process also produces high-velocity electrons, which often cause major irradiation damage to the deposited layer and, therefore, introduce the loss-contributing colour centres in the optical films and waveguides. The other disadvantage is that the rate of deposition is quite low.

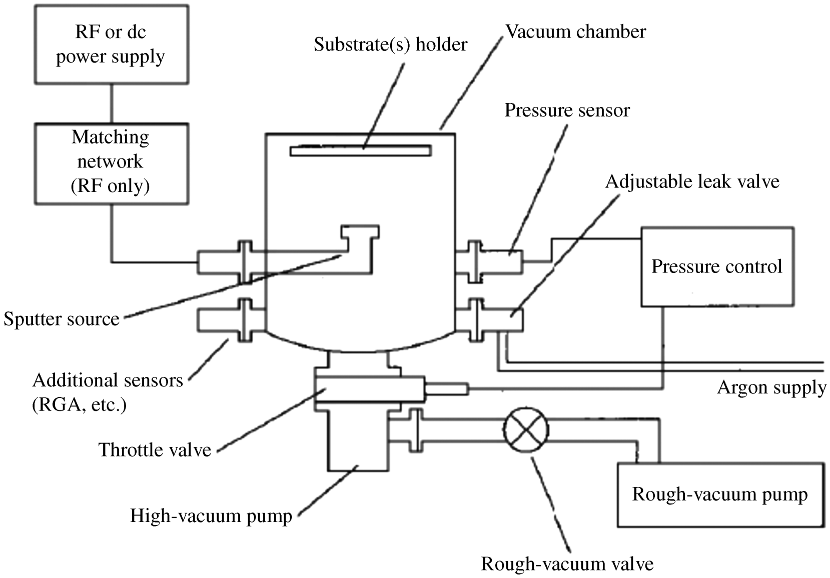
RF or dc power supply
Substrate(s) holder
Vacuum chamber
Matching network (RF only)
Pressure sensor
Adjustable leak valve
Pressure control
Sputter source
Additional sensors (RGA, etc.)
Argon supply
Throttle valve
Rough-vacuum pump
High-vacuum pump
Rough-vacuum valve

Figure 5.2 Sketch diagram of sputtering apparatus with its essential accessories [3]. Source: ElShabini-Riad 1998. Reproduced with permission from McGraw Hill.

The problem of high-energy electron irradiation of substrate and low deposition rate during sputtering can be overcome by using magnetron sputtering, in which the density of plasma is increased by employing magnetic focussing. The magnetic focussing of plasma also overcomes the electron irradiation, because:

$$r = \frac{mv_\perp}{qB}$$

where q is the charge, B the applied magnetic field, r the radius of the helix of charged particles with mass m and $\nu_\perp$. Evidently, low mass-electrons are highly affected by the applied magnetic field, and they are reused in generating more plasma rather than defects in the substrate. The main problems with the magnetron plasma sources are the complex geometry and uneven consumption of target materials; however, commercial devices with RF plasma sources are available. The following process parameters are used for controlling the sputtering process [3].

Threshold energy:

$$E_o = \frac{\Delta H_s}{(1-\gamma_m)\gamma_m} = 8\Delta H_s\left(\frac{M_i}{M_t}\right)^{0.4} \tag{5.1}$$

Sputtering yield:

$$Y_s = \frac{4.2\alpha S_n}{\Delta H_S} \tag{5.2}$$

where α depends on the value of M_i/M_t.

Deposition rate:

$$Q_s\left(\text{atom s}^{-1}\right) = \frac{Y_s I_i}{q_e} \tag{5.3}$$

where q_e is the electronic charge

In the above equations, ΔH_s is the enthalpy of sublimation, S_n is the sputtering cross-section, $\gamma_m < 1$ is a probability function, M_i and M_t are the initial and total molar masses:

$$I_i = \frac{P(\text{power})}{V(\text{voltage})} \tag{5.4}$$

where P represents total power and V is the voltage drop across target and the substrate.

For dielectric oxide materials, oxygen gas is also introduced into the sputtering chamber to replenish the oxygen lost during the process. Similarly, nitrogen or ammonia, and methane or a mixture of carbon monoxide and hydrogen, may be used to maintain the stoichiometry of nitrides and carbides, respectively. Such a sputtering process, which uses a gas atmosphere for replenishing elements in the film, is called "reactive sputtering".

By comparison, in the ion-beam sputtering process, a separate chamber, which is small in size, is used inside the large main chamber for generating a discharge. A neutralized beam of ions is then extracted to perform the sputtering. The neutral discharge in the small chamber is better controlled and is used for the production of high-quality mirrors.

Examples of functional films, which have been sputtered on an industrial scale, are [3] metallized circuits and electronic package, diffusion barriers, optical coatings of ITO and $MgIn_2O_4/ZnIn_2O_4$ solid-solution and superconducting films. The fabrication of channel waveguides and parameters that reduce linear loss in channel waveguides has been investigated using the sputtering of silica [8,9]. An Er^{3+}-doped Al/P silica planar waveguide amplifier was designed and fabricated via radio-frequency sputtering onto a silica substrate, showing 5 dB of signal gain at 1546 nm for signal at −20 dBm power. The pump source was a 980 nm diode laser for the waveguide containing 0.77 wt% of Er_2O_3 [10]. The RF sputtering of Er^{3+}-doped in a SiO_2/TiO_2 waveguide was studied, in which the concentration of Er^{3+}-ions was varied between 0.14 and 1.63 atom%. The waveguide was characterized for linear loss, refractive index, and thickness, using the M-line technique, while the structure of the film was characterized by Raman spectroscopy. By optimizing the phonon energy, the green-to-blue upconversion and 1.5 μm emissions were investigated [11]. Effects of annealing in an oxygen atmosphere on the refractive index and defect structure evolution during sputtering were studied. Using the oxygen annealing of the waveguide structure, the linear loss was reduced to 0.1 dB cm^{-1} at 1550 nm [12]. Yttrium oxide/alumina (Y_2O_3/Al_2O_3) thin films were deposited via sputtering, and the measured total loss in the waveguide was between 10 and 20 dB cm^{-1} [13]. $PbTiO_3$ thin films were sputtered on the (100) plane of $SrTiO_3$ crystals via radio-frequency technique. The propagation loss in the waveguide was around 2.2 ± 0.2 dB cm^{-1} and the refractive index at 632.8 nm was 2.61 [14]. Er^{3+}-doped multicomponent phosphate glass thin films were deposited by radio-frequency (RF) sputtering, in which the dopant concentration was of the order of 5.3×10^{20} cm^{-3}. The waveguide device was pumped with a 21 mW source at 980 nm, yielding a signal gain of 4.1 dB at 1535 nm [15]. A ridge waveguide based on Er^{3+}-doped glass was formed via the collimated sputter deposition technique. The 1.7 cm long waveguide was pumped with a 40 mW source at 980 nm and a gain of 15.4 dB at 1550 nm was recorded. In this investigation, by considering the Er^{3+}-absorption cross-section and the waveguide loss, the net gain was 7.2 dB [16]. Besides, Er^{3+}-doped waveguides other types of passive waveguides, fabricated via sputtering, include:

(a) SiO_2 based waveguides with smooth side walls formed via RF-bias sputtering [17].
(b) A 5-output optical power divider based on multi-channel coupled waveguide structure was designed using the RF sputtering of silica. Experimental observation of the output power distribution at a wavelength of 1310 nm indicated a port-to-port variation of less than 10% of the designed specification [18].
(c) Nd^{3+}:doped YAG and YGG have been produced via RF sputtering [19].
(d) Fluoride crystals and glasses in particular yield rather poor quality films, often with fluorine defects producing colour centres.

5.5 Pulsed Laser Deposition

5.5.1 Introduction and Principle

In the pulsed laser deposition (PLD) technique, a high-energy coherent photon source (excimer laser which is an ultraviolet (UV) laser, e.g. KrF at $\lambda = 248$ nm or ArF at $\lambda = 193$ nm) is used to ablate the materials and redeposit them onto a hot or cold surface inside a vacuum chamber. The process of laser ablation can be explained by the energy–time uncertainty principle, which may explain a significant number of features of PLD that stand out in comparison with the standard physical and chemical deposition techniques. The energy–time uncertainty principle, $\Delta E . \Delta\tau \geq (\hbar/2)$, characterizes not only the laser–matter interaction before ablation but also the spectral distribution of energies of post-ablation matter. Besides the uncertainty principle, it is also important to consider the repetition rate of the incident laser beam, which is explained using Planck's law: $E = n.(h\nu)$ where E defines the total energy of a laser cavity that is a product of the repetition rate of the laser (n) and the photon packet ($h\nu$). This implies that for fixed cavity energy (E), the number (n) of photon packets per second will drop if the photon packet size ($h\nu$) increases, and vice versa. Since the excimer lasers are inherently slow, the repetition rate can only be manipulated between a few Hertz (Hz) to tens of Hz, which implies the photon energy packet size is large, compared with the condition when the repetition rate is large, ranging from kHz to MHz or even GHz, which is possible with solid-state lasers. The second aspect of the uncertainty principle appears in the interaction of lasers with the target. Since the dwell time ($\Delta\tau$) of the excimer laser is sub-nano to 10 ns with each pulse having an energy between sub-joule to a few joules, the incident energy density (J cm^{-2}) on the target is extremely large, causing not only the electrons to exceed their energy beyond conduction band into vacuum but also the atoms to be released as ions. As a result of such intense photon bombardment, electrons, holes and ionic species are produced, forming a plasma; the visible colour appearance of the plasma characterizes the materials used for target, as explained below briefly, and is a subject for ongoing research on laser-induced plasma. In the context of PLD, however, the delivery 0.1 to 1 J pulses, for example, of 15–45 ns duration is commonly used with 1–100 Hz repetition rates to yield deposition rates of 0.1–100 nm s^{-1} [20a]. By scanning the laser beam across the target, the materials absorb excimer radiation via electrons in the valence and conduction bands, resulting in rapid ionization of ablated materials in the gas phase with the generation of plasma [20a]. The generated plasma with constituent ions in the plume is propelled towards the target. In the first few hundred picoseconds the plasma, being highly energetic, decays rapidly via electron–hole recombination, and the energy released is transferred to the remaining ions and atomic species, which are reformed in the ambient gas phase. This phenomenon of plasma relaxation imparts large kinetic energy to the atomic and molecular species which then travel at very high velocity (e.g. 1.5×10^3 m s^{-1} for chalcogenide films see ref. 20b) towards the target. The post-plasma relaxation process is dominated by the molecular reconstitution regime, during which there may be opportunity to manipulate the materials which are likely to be deposited onto a substrate. Unlike a standard chemical reaction, which confronts an activation energy barrier, the down-hill energy pathway from plasma to atomic and molecular states occurs naturally, following the laws of energy minimization and conservation.

In the "atomic/molecular" (pico- to nanosecond) regime, there may be opportunity to redesign materials by maintaining the residual pressure of reactive gases. This may be essential for maintaining the stoichiometry of the materials, because the atomic and molecular species are at the top or may even be above the activation energy barrier, allowing rapid reaction leading to heat dissipation. For example, oxides of Si may be formed by introducing oxygen gas into the chamber during deposition. The reactive gaseous species may therefore prevent decomposition of oxide compounds, e.g. during the deposition of oxides of elements, namely tin, lead, zinc and germanium.

5.5.2 Process

The excimer laser based PLD is more popular these days and the technique has been adopted for studying thin films of a range of materials, oxide ceramics and glasses [21–46], sulfide/chalcogenides, rare-earth doped materials and carbon. In Figure 5.3a, the deposition chamber

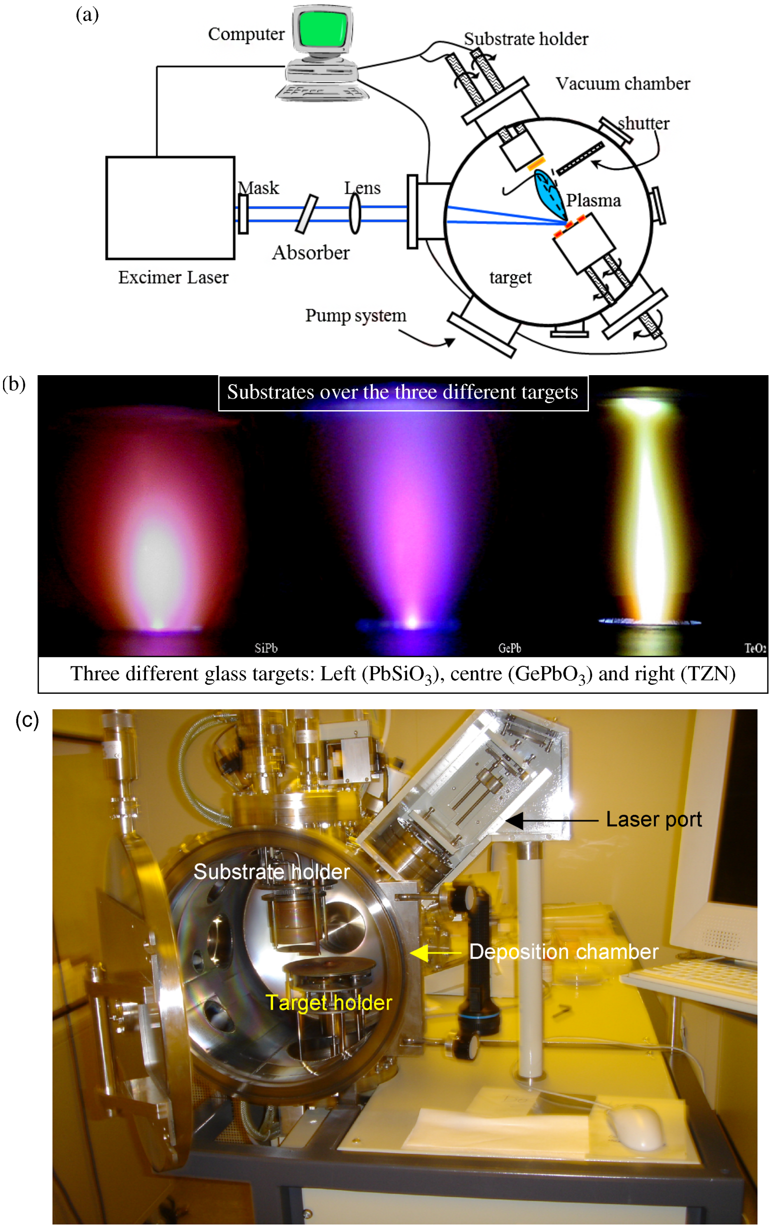
(a)
Computer
Substrate holder
Vacuum chamber
shutter
Mask
Lens
Plasma
Absorber
Excimer Laser
target
Pump system
(b)
Substrates over the three different targets
SiPb
GePb
TeO2
Three different glass targets: Left (PbSiO3), centre (GePbO3) and right (TZN)
(c)
Laser port
Substrate holder
Deposition chamber
Target holder

Figure 5.3 *(a) Schematic diagram of pulsed laser deposition system, showing accessories. (b) Visible colour plumes of plasma generated as a result of excimer (193 nm) laser ablation with three different targets shown in the figure. (c) Photograph of target holder and substrate inside a pressure controlled deposition chamber. (See colour plate section.)*

and the accompanying schematic diagram show the layout for excimer laser, target and substrate. The plasma plume shown in Figure 5.3b emanates from the target surface and directs the ablated materials towards the substrate.

Inside the deposition chamber (Figure 5.3c), rotation of the substrate and rastering of the laser over the eccentrically moving target produces thin films of uniform thickness for waveguide fabrication.

In the laser ablation process, an external laser is positioned to provide high-energy laser pulses directed towards a dielectric target (glass, ceramic, polymer), resulting in a plume of ablated materials from the target that consists of various molecular species, representative of the target materials. A CO_2 laser source or a resistive heating source is often used for heating the substrate to promote the following process, depending upon the type of materials used for deposition:

- Surface diffusion in amorphous and polycrystalline materials for promoting stress relaxation and adhesion at the interface, thereby reducing the Rayleigh and Mie scattering contributions to the overall attenuation in the film.
- Grain growth in polycrystalline materials, which may be controlled by manipulating the substrate temperature to promote a preferred crystallographic texture, e.g. in magnets the application of external field and temperature (below Curie temperature), can lead to highly anisotropic film. Columnar grain growth and preferential texture may reduce Rayleigh and Mie scattering in an anisotropic medium.
- If the substrate temperature is raised above a critical temperature, e.g. in the case of a glass above its glass transition temperature, significant above-T_g structural relaxation will occur and the deposited glassy film may then be rendered into a more homogeneous composition than without annealing. If, however, the temperature of the substrate is higher than the crystallization temperature, the amorphous thin film layer may transform, depending upon the kinetics, into a partially crystalline glass-ceramic or a fully crystalline material.

5.5.3 Key Features of PLD process

- The ns-pulsed laser ablation, by virtue of its nature, produces reproducible films, i.e. the stoichiometry of materials does not change due to ablation. However, it may change due to the application of vacuum, as has been observed in the case of titanate, tantalate, [24,25] and niobate [26] films. The low vacuum is essential for deposition of films in general; however, if required the low pressure may be replaced by the positive pressure of oxygen for the deposition of oxygen-deficient materials, e.g. in tellurium and germanium oxide based glass [44]. On the other hand, when cation deficiency arises, e.g. in $KbNO_3$, it has been remedied by ablating with KNO_3, since the NO_3^- dissociates and produces elemental species and leaves the solid phase [42].
- Laser ablation operates on a nanosecond time-scale determined by the pulse duration of excimer. If, however, pulses of UV lasers shorter than nanoseconds can be employed the substrate can be ablated beyond the regime of chemical reaction, as the pulses will be shorter than the time-scale for chemical reaction kinetics. This is possible because from the reaction rate theory:

$$\mathfrak{R} = \frac{\kappa T}{h}.\exp\left(\frac{-Q}{\kappa T}\right)$$

at the temperature near ablation condition, the activation barrier Q is negligibly small, leading to a condition at which the reaction rate approaches the maximum value of $\kappa T/h \approx 0.2 \times 10^{-10}\ T$ seconds. High-energy laser pulses with shorter pulse duration than nanoseconds can therefore transcend the kinetics and preserve the chemical stoichiometry of the ablated materials.

- Nanosecond pulses of laser also provide rapid quenching, which means a crystalline material can be laser ablated and transformed into an amorphous material by overcoming and bypassing the kinetic energy barrier for crystal formation.
- The pulse repetition rate for ablation for each target can be controlled to sub-nanometre thickness of materials. This has a tremendous potential for engineering a unique combination of materials for integrated optics by suitably designing the plume controlling technique. We know that plume control is possible by mounting multiple targets, which can be periodically ablated using software control for the deposition process. Such a deposition technique can then lead to fabrication of:
  - Unique RE-doped waveguides can be made in which the rare-earth ion layers can be separated by more than a nanometre to reduce the overall ion–ion cross-relaxation by limiting it to be effective only along the RE-ion deposited layer. The cross-relaxation along each layer can be controlled by choosing a suitable host material, which may offer better ion–ion separation. An example is discussed below.
  - Surface plasmon waveguides formed by depositing angstrom thickness of metals, e.g. gold, silver or platinum. Plume dynamics may be controlled to make a low concentration of metals in each layer. Surface plasmon waveguides may be one of the ways to achieve large third order nonlinearity in micro- and nanometre scale waveguides.
  - Deposition of widely varying materials can be made to achieve a refractive index contrast larger than 1.4. This would mean that the photonic band-gap effects can be designed by controlling the deposition rate. Omni directional mirrors can also be designed in this way.
  - Finally there may be opportunity for engineering low-loss photonic band gap and photonic crystal structures in amorphous dielectric media, which have not been investigated at all.
  - By combining the photonic band gap structure with stimulated emission, it may be possible to design high power laser devices with substrate-integrated semiconductor pump sources. The opportunity for engineering dissimilar materials, e.g. a RE-ion doped glass waveguide over GaAs active semiconductor pump layer, has been possible, and this is discussed in another chapter on integrated optics below.

5.5.4 Controlling Parameters and Materials Investigated

The main parameters in a pulsed laser deposition process, which must be controlled for engineering thin films of optical quality, suitable for subsequent waveguide formation are the laser wavelength (λ) (e.g. at 193 nm for ArF^- or KrF^- at 248 nm) and laser fluence, which is energy density, e.g. a typical value of $2\,J\,m^{-2}$ may be used for ablation oxide material. Besides the wavelength and fluence, the solid angle of the laser beam on the target, pulse duration (ns to sub-ns) and laser pulse repetition rate (1–100 Hz), target-to-substrate distance and the residual gas pressure in the deposition chamber are also quite important parameters. The importance of controlling these parameters is illustrated in a short review on pulsed laser deposition of tellurium oxide glass [44], which readers may find useful for enhancing their background knowledge in this area.

Plentiful literature is available in the areas of pulsed laser deposited waveguides and devices based on dielectric, superconducting, ferroelectric and electro-optical materials. The following is a summary of the featured articles in the literature.

PLD of $BaTiO_3$ and $LiNbO_3$ onto buffer layers of MgO with (001) and (111) oriented GaAs wafers were formed, respectively [29].

PLD has been successfully used to grow various dielectric and ferroelectric oxides directly onto insulating substrates for optoelectronic applications, e.g., the films of $LiNbO_3$ and $LiTaO_3$ on sapphire, $BaTiO_3$ on (100) of MgO, (110) of $SrTiO_3$, and (100) of LiF, Bi_2GeO_{20} on (100) of ZrO_2, $KTa_{0.67}Nb_{0.33}O_3$ on $SrTiO_3$, $KNbO_3$ thin films on MgO, and a range of electro-optic materials [29–31].

Several waveguide laser and passive planar devices have been demonstrated using PLD, and are based on Nd^{3+}-doped $Gd_3Ga_5O_{12}$ (gallium-gadolinium garnet) thin film optical waveguides with low-loss (0.5–1.5 dB cm^{-1}) and having laser operation at 1.06 and 0.940 μm [28,34]. A Ti^{3+}:sapphire planar waveguide laser was fabricated by PLD [24,27,28]. Low-loss waveguides of Nd:GGG and Ti-Sapphires deposited by PLD techniques have been reported [24,27,28,32–34]. The loss contributing factors are the density of the film, which is dependent on the substrate temperature, reactivity of substrate, substrate motion and the atmosphere of deposition. All of these parameters are known to affect the total loss in ferroelectric and electro-optic waveguide structures. The demonstration of low-loss (0.5 dB cm^{-1}) waveguides in Nd^{3+}-doped GGG has been achieved by controlling the crystallographic orientation and the crystal structure of the substrate. Some researchers [22] have reported the use of field-assisted deposition of films of electro-optic materials. Since the electro-optic materials are anisotropic in nature, the crystal growth also takes place in the direction of the electro-optic axis.

Among the family of amorphous films, a large number of rare-earth doped glass thin films have been demonstrated over the past ten years, including fluoride-ion modified silicates, chalcogenides, tellurite, and lead germanium oxide glass films on silica substrates [41,42,44]. Most PLD research in the area of glasses is dominated by Er^{3+}-doped phosphate glass and sapphire crystals [26]. Characterization of dopant studies and dopant spectra were carried out for Er^{3+}-doped $KTiPO_4$, phosphates, and alumina. No device experiments have yet been reported using these candidate materials. Amongst the glassy interface a major loss contributing factor has been the interfacial defects between the thin films and the substrate, which primarily contribute to the Rayleigh and Mie scatterer in the waveguide structure.

More recently carbon-based materials [45] as saturable absorbers have become relevant for ultrafast laser engineering. However, a large majority of the data are for the formation of diamond-like carbon films [46].

5.5.5 Fabrication of Thin Film Structures using PLD and Molecular Beam Epitaxy

The emergence of high-power pulsed excimer sources has inspired new approaches in materials synthesis and device engineering which is otherwise impossible by utilizing the conventional approach. In this section, recent advances in materials synthesis and interface engineering are discussed that set a precedence for future work.

Combinatorial materials synthesis using PLD was proposed by researchers in Japan [47]. Takeuchi [48] has captured the essential features of combinatorial materials synthesis, following interesting reports in *Science* [49] and *Nature Materials* [50]. The three main features of combinatorial material synthesis using PLD are:

1. Multiple target holders in the PLD chamber allows any combination of materials to be formed via sequential deposition via pre-programming the laser beam.
2. During deposition a combination of masks may be used for creating patterns across the whole substrate, which may be pre-heated for rapid sintering and annealing the deposited film materials. An example of the synthesis of (Ba,Sr)TiO_3 using BaF_2, SrF_2 and TiO_2 target materials and their post-annealing in air has been illustrated by Takeuchi (Figure 5.4) [51].

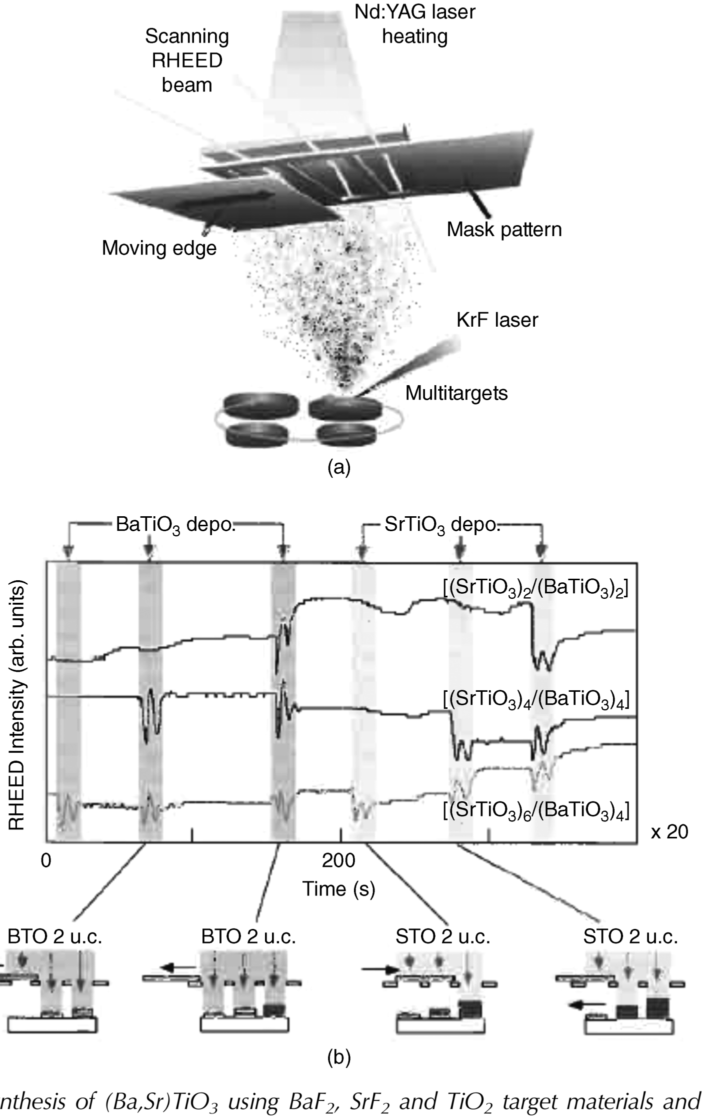
Nd:YAG laser heating
Scanning RHEED beam
Mask pattern
Moving edge
KrF laser
Multitargets
(a)
BaTiO3 depo.
SrTiO3 depo.
RHEED Intensity (arb. units)
[(SrTiO3)2/(BaTiO3)2]
[(SrTiO3)4/(BaTiO3)4]
[(SrTiO3)6/(BaTiO3)4]
x 20
0
200
Time (s)
BTO 2 u.c.
BTO 2 u.c.
STO 2 u.c.
STO 2 u.c.
(b)

Figure 5.4 *Synthesis of (Ba,Sr)TiO_3 using BaF_2, SrF_2 and TiO_2 target materials and their post annealing in air [51]. Source: Takeuchi 2007. Reproduced with permission of John Wiley and Sons.*

3. The deposited films on a substrate can be then transferred via laser lift-off onto a suitable substrate, e.g. a semiconductor.

The success of combinatorial materials synthesis using multiple targets depends also on the *in situ* technique for film thickness and composition monitoring using a RHEED, ellipsometer and a mass spectrometer. Such a combination of diagnostics may then allow control of the individual deposited layer as desired, leading to unusual material combinations.

A PLD system with such an array of diagnostics has been exploited for growing epitaxial layers of $BaTiO_3$ and $SrTiO_3$, using a method called combinatorial laser molecular-beam-epitaxy (CLMBE) [52,53].

Other techniques for growing complex structures of crystalline ceramics are discussed elsewhere [51]. As an example of combinatorial materials engineering, the formation of glass-polymer nanocomposite using 193 nm excimer laser is explained below [54]. Optical quality polymeric materials, e.g. polydimethylsiloxane (PDMS), despite their excellent near-IR transparency [55] between 700 and 1500 nm exhibit very poor solubility of rare-earth ions, e.g. Er^{3+}-ions. Extensive like-ion (Er^{3+}-Er^{3+}) clustering quenches the photoluminescence [56] and makes an inefficient material for planar waveguide amplifier application. This implies that for back-plane circuitry of personal computers the quenching of photoluminescence must be minimized. Since the demand for data is rising year-on-year, a 10 Gb Ethernet system demands high data speed which means that the electronics will no longer be the viable means of data transport, because the long-haul, metro and local area networks use optical carriers. At a PC terminus, at present the optical data is converted into electronic format for electronic compatibility, which slows the data processing. In addition, any conversion of signal format demands energy, which is why it is advantageous to retain the all-optical signal format. With these concepts in mind, research was undertaken to design a PDMS-Er^{3+}-ion doped glass nanocomposite, the processing of which is discussed below.

In order to minimize the like-ion quenching in PDMS, a nanometre-scale sequential deposition of PDMS and Er^{3+}-ion doped phosphate glass, modified with tellurium oxide was adopted [54]. This approach was aimed for engineering a superlattice structure of two amorphous materials, formed via pulsed laser deposition. Er^{3+} ions were chosen as the primary dopant element in the inorganic tellurite-phosphate (PT) glass, which was also co-doped with the Ce^{3+} and Yb^{3+} ions. The ${}^4I_{13/2} \rightarrow {}^4I_{15/2}$, transition in the Er^{3+}-ion is widely used for signal amplification in the 1520–1570 nm wavelength band in optical communications [54]. To grow a superlattice thin-film structure it was necessary to control the laser fluence to $1\,\mathrm{J\,cm^{-2}}$, as reported by Okoshi *et al.* [55], to maintain the chemical stability of the PDMS during ablation.

Figures 5.5a and 5.5b are low and high magnification images, respectively, of the cross-section of the superlattice acquired using bright field TEM, from which it is apparent that the interface between the layers of two dissimilar materials is well defined on a nanometre scale. The superlattice structure, with total thickness of 960 nm, is amorphous, as was confirmed by selected area electron diffraction (SAED) (Figure 5.5a, inset). The thickness of each glass and PDMS interlayer was approximately 7 nm and 4 nm, respectively. In Figure 5.5a a significant number of polymer particulates were produced at $1\,\mathrm{J\,cm^{-2}}$ fluence energy. These impinging particles perturb the flatness of the growing superlattice structure. By reducing the incident fluence to $0.54\,\mathrm{J\,cm^{-2}}$, it was possible to demonstrate a much flatter and thinner superlattice structure (Figure 5.6a), which was verified by the X-ray reflectometry (XRR) in Figure 5.6b

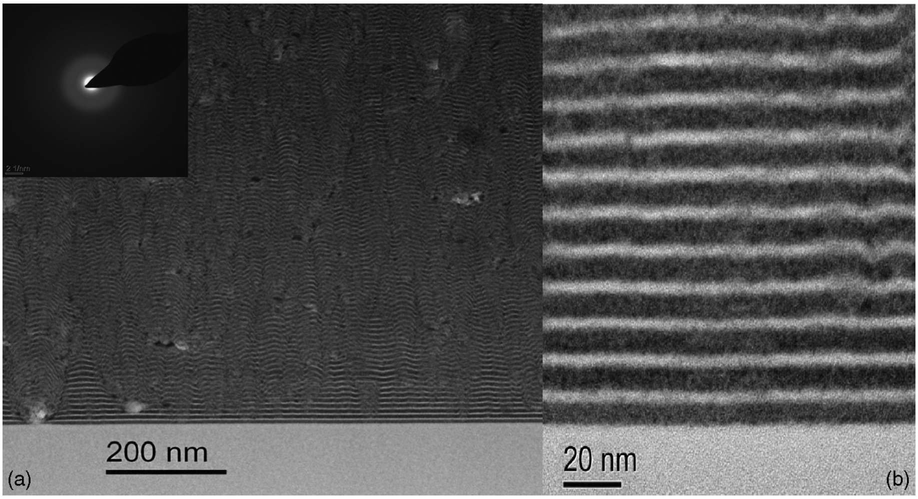

Figure 5.5 TEM images of a cross-section of the superlattice thin film: (a) low magnification image with inset showing SAED; (b) high magnification image of a defect-free region. The laser fluence employed for the deposition of this film was 0.4 J cm^{-2} (other deposition conditions are detailed in the methods) [56]. Source: Z. Zhao 2012. Reproduced with permission from IoP Publishing.

with simulations on interlayer, yielding an estimated average thicknesses of glass and PDMS layers of 16 nm and 5 nm, respectively. Figure 5.6a shows it was possible to control the growth of PDMS to the 2 nm and 4 nm range. From XRR, the estimated average density of the superlattice was 3.5 g cm^{-3}. Since the PDMS polymer is constituted of SiO$_2$ in a polymer matrix, the energy dispersive spectrum in Figure 5.6c characterizes the chemistry on the nanoscale, using *in situ* energy dispersive X-ray analysis for silicon element, which is characteristically absent in the inorganic glass layer. The superlattice thin film was subsequently machined using a femtosecond Ti-sapphire laser for structuring a waveguide for 1.5 μm photoluminescence characterization [56].

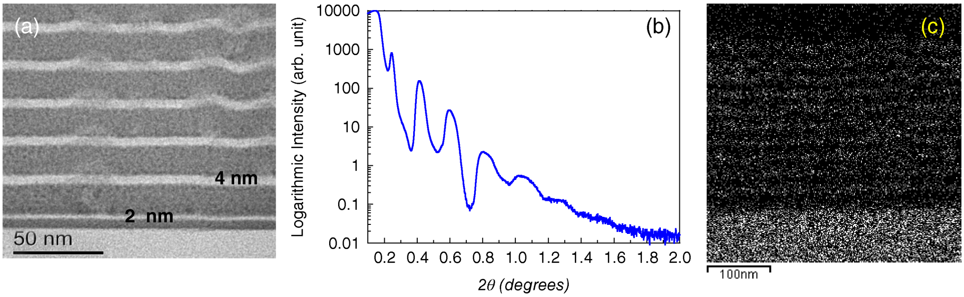

Figure 5.6 (a) TEM image of the cross-section of the superlattice used for X-ray reflectivity (XRR) studies. (b) The XRR curve of the superlattice thin film shows the interference fringes. (c) Si-element map of the cross-section with bright regions representing PDMS layers, the thick layer at the bottom is the silica substrate. Due to electron beam irradiation damage of the superlattice there is an apparent overlap of X-ray signals in the layers [56]. Source: Z. Zhao 2012. Reproduced with permission from IoP Publishing.

This example of a superlattice characterizes the potential for materials engineering using a combinatorial approach, which Takeuchi [51] proposed originally. The glass–PDMS thin film structure also demonstrates how novel interfaces on the nanoscale may be engineered.

5.6 Ion Implantation

5.6.1 Introduction

Energetic ions (100 eV to MeV) interact with solids and bring about consequential changes in the material structure. Based on the energy of the incoming ions, the following types of interactions with the substrate may take place [57–59]:

- In the low energy range (a few eV to 100 eV) the interaction is manifested by electronic absorption. The outer most electrons are affected at low eV dose. On the other hand, as the energy quanta increases to several tens of eV dose, the inner-most electrons begin interacting strongly.
- When the incident energy increases to hundreds of eV, the screened Coulombic collisions between the incoming ions and the substrate nuclei start playing a role in decelerating the incoming ions. The nuclear interactions become important at incoming energies in the range of a few keV to a few hundreds of keV. At higher energies, the interaction between the electrons of the displaced ions from solid surface becomes important in determining the resultant change.
- When the incident energy is of the order of a few MeV, the interaction between the incoming particle and the substrate nuclei once again occurs by Coulombic repulsion. In this regime, screening of the nucleus by electrons can be neglected. This is the case of Rutherford backscattering in the MeV range by α particles, i.e. He^{2+} ions [57–59].

5.6.2 Technique and Structural Changes

For ion implantation studies of materials, it is the few keV to 100 keV regime that is important for effecting structural changes in solids. The mass of ions relative to substrate also plays a critical role in determining the likely interaction, discussed above. With incoming ions that are lighter with respect to the substrate atoms, electronic stopping at lower energies become dominant. For example, for boron penetration in silicon, electronic stopping is operative even at 10 keV, whereas for phosphorus and arsenic the nuclear collision mechanism dominates up to 130 to 700 keV, respectively [58,59].

As the distance between the moving ions and substrate increases, the energy transfer from the incident beam to the target atoms decreases rapidly. The proximity of target nuclei to the ion source can therefore determine a range of the first two types of interactions described above.

When a substrate material is bombarded with high-energy ions, the energy of the incoming ions is lost, as explained above, via the interaction with the substrate nuclei and the electrons. The trajectory of penetrating ions changes several times prior to attenuation of incoming ionic flux. The profile of the ions trajectory changes due to the scattering associated with nuclear and electronic interactions. Besides the main ionic flux and its trajectory, ionic trajectories are also produced by the scattered ions after first collision, and this may lead to a cascade of smaller collisions with ions at the surface, resulting in an array of random displacement ions and atoms from equilibrium position, which then leads to amorphization in most solid crystalline materials.

The penetration of incoming ions and the resultant displacement of the periodic array of atoms and ions from their equilibrium positions produces a spectrum of structural defects, which are broadly described below for crystalline materials. They are the generation of vacancies and interstitial defects, formation of amorphous regions due to recoil and displacement of substrate nuclei, and increase in the dislocation density and hence the residual stress in the waveguides derived from crystalline materials.

In amorphous materials, however, depending upon the thermal history of target material, i.e. the annealing and corresponding glass transition temperature, the molar volume may decrease due to the impact energy, resulting in formation of a high-refractive index region. The differential restructuring of a glass network, especially strong and covalently bonded glasses, may arise due to incident ion bombardment which may force cations and anions to remain trapped in a metastable dense structure, the local density of which may fall between fully annealed and quenched glass. Due to nuclear interaction and recoil encountered by the target atoms, the electronic and point defects such F′-centres and non-bridging hole centre in amorphous hosts form. Metastable bonds are also produced, which are not likely to form via any other chemical and physical techniques, e.g. Si—H bonds in SiO_2 glass after H-implantation [60].

5.6.3 Governing Parameters for Ion Implantation

As explained above, the interaction of incident energy with materials is quite complex. For designing waveguides, the ion implantation must yield a change in the refractive index; it is essential to model the interaction range and penetration depth for a given distribution of energy. For a monochromatic radiation beam, the incident energy produces a concentration profile and the corresponding depth distribution can be approximated by a Gaussian relationship [57,58]:

$$n(x) = N_{\max} \exp\left[\frac{-(x - R_p)^2}{2\Delta R_p}\right] \tag{5.5}$$

where *n(x)* is the concentration of ions as a function of depth x measured in a direction perpendicular to the substrate surface and $N_{\max}$ is the maximum concentration at $x = R_p$. The term R_p is the projected range, and ΔR_p is the projected straggle, which is the standard deviation of the Gaussian distribution (in the incoming direction of the ion).

If ϕ is the integral value of energy dose over a given period of time:

$$\phi = \int_{-\infty}^{+\infty} n(x)\,dx \tag{5.6}$$

and:

$$N_{\max} = \frac{\phi}{\sqrt{2\pi}}\frac{1}{\Delta R_p} = \frac{0.4\phi}{\Delta R_p} \tag{5.7}$$

and the total or integral dose can be then determined using:

$$\phi = \frac{Q}{sqA} \text{ions cm}^{-2} \tag{5.8}$$

where sq is the total charge on ions (e.g. s is 1 for single ions and 2 for doubly charged ions, and q is the electronic charge); A is the ion implanted surface area, and Q is the total integrated charge deposited in the substrate; Q is measured by measuring the current, I which is given by:

$$Q = \int_0^t I\, \mathrm{d}t = It \tag{5.9}$$

where t is the time for which the implantation was carried out. These equations are also now-a-days available as SRIM code simulation which is widely used in the field of radiation damage.

5.6.4 Materials Systems Investigated

GaInAs/InP devices for 1 and 1.55 μm were fabricated using an ion-implantation technique. Band gap shifts of more than 65 meV were reached in a GaInAs/P quantum film structure, which simplifies the integration of non-absorbing waveguide sections with laser, modulators and detectors [58,59]. Fused silica and SiO_2-on-Si were implanted with C, Ge and Si at energy 5 MeV. The structure of silica was found to compact at such high-energy dosage and the structural changes were studied using the EXAFS technique to determine the changes in the nearest neighbour bond length [60].

PL activity observed in Nd^{3+}-doped As_2S_3 planar waveguide at 1083 nm was reported. Nd^{3+}-ions were incorporated in the chalcogenide matrix via ion-implantation. This was intentionally chosen since the solubility of RE-ions in most chalcogenide matrices is extremely small. The dopant distribution in the glass matrix was predicted using the molecular dynamic (MD) simulation which was subsequently confirmed by Rutherford backscattering. It was proposed by the investigators that the RE-ion doped devices could be formed using such techniques [61].

Silicon implant in a-Si and hydrogenated amorphous silicon (a-Si) have also been reported. Er^{3+}-ion implantation into a soda-lime silicate glasses and hydrogenated a-Si have been reported. The Er^{3+}-ion implantation in a-Si and glass matrices led to demonstration of near-infrared photoluminescence around 1530 nm when such materials were excited with a 980 nm laser source. It was proposed that such materials may have potential attraction for development as amplifiers [62,63].

Rare-earth ions (Nd^{3+}, Er^{3+}) were incorporated in the amorphous silica/silicate matrices for designing devices, yielding a net gain of ~2.3 dB at 1.53 μm in an Al_2O_3-doped silica host [64–74]. Barium fluoride crystals were implanted for making a waveguide [70]. Nd^{3+}-doped $LiNbO_3$ on MgO substrate waveguide was fabricated via ion-implantation of Nd^{3+} in the $LiNbO_3$ waveguide [71,72]. In addition, Ti^{n+}-doped $LiNbO_3$ waveguides were also designed [73]. Ion-implantation as a means for either lowering or raising the index of dielectric media was discussed by Townsend and co-workers [68, 69, 73, 75].

5.7 Chemical Techniques

Deposition of glassy thin films using chemical methods differs significantly from the physical methods discussed above. In chemical methods, as expected, one or more chemical reactions are involved and, based on the chemical equilibrium, the techniques widely used are chemical vapour deposition (CVD) including plasma-assisted CVD and molecular beam epitaxy (MBE), ion exchange and sol-gel techniques [76]. In a CVD process, chemical reactions with vapour species are involved. Current CVD techniques include flame hydrolysis or oxidation, plasma assisted CVD and MBE methods. Various chemical techniques adopted for the fabrication of waveguides are discussed below with examples of techniques, controls required, and materials investigated.

5.7.1 Characteristics of Chemical Vapour Deposition Processes

In a CVD process, the main principle employed for forming a thick or thin film is to use a precursor gas phase, in which the molecular species are invariably present and form a solid phase after reaction. Typical examples for dielectric and semiconductor materials are:

$$SiCl_4(g) + 2H_2(g) = Si(c) + 4HCl(g) \tag{5.10a}$$

$$SiCl_4(g) + 2H_2O(g) = SiO_2(c) + 4HCl(g) \tag{5.10b}$$

$$SiCl_4(g) + O_2(g) = SiO_2(c) + 2Cl_2(g) \tag{5.10c}$$

These reactions describe the reduction (first reaction) and oxidation of $SiCl_4$ gas for the formation of Si and SiO_2. In these reactions, we find the total molar volume change for gaseous species is +2 in the forward direction for Reactions 5.10a and 5.10b, and +1 for Reaction 5.10c. The positive molar volume change implies that the HCl gas must be continuously removed to maintain equilibrium in the forward direction. To maintain the equilibrium condition, modelling is adopted to determine the coupled gas flow dynamics, i.e. the flow of reactant and product gases, and chemical kinetics. These two aspects are extensively discussed in the literature [57,77]. Computational methods and software are available to predict the equilibrium gas compositions [78]. To analyse the adsorption characteristics of the condensate on a substrate there are also approaches developed using chemical and quantum-chemical calculations [79]. The latter is quite important for maintaining the defect-free growth of the epitaxial layer. The model approach is supplemented by analytical tools such as LEED (low energy electron diffraction). Applications of CVD for the growth of silica, silicon oxynitride and semiconductor materials (Si and III–V compound semiconductors) using the precursor gases have been extensively studied for commercial systems and dedicated text books are available in this area.

Reactions 5.10b and 5.10c have formed the basis for silica based planar technology, which was adopted widely for passive component fabrication. The CVD reaction carried out at atmospheric pressure is commonly known as a "atmospheric pressure chemical vapour reaction", which differs from the low pressure (LPCVD) and plasma enhanced chemical vapour deposition (PECVD) [57,77].

The Reynolds number (R_e) and Rayleigh number (R_a) strongly determine the flux of the condensate in a CVD reactor, respectively. These two transport numbers R_e and R_a vary linearly and quadratically with the density of vapour. As a result substantial advantages in the control of gas flow condition are achieved by reducing the pressure from 760 to 1 torr. Under the conditions of LPCVD, the linear flow velocity is generally higher than in APCVD [57,77]. However, in terms of the mass flow, the increase in the velocity, as expected from the Bernoulli equation, is compensated by the corresponding reduction in the density leading to a much reduced thermal convection. Consequently, in an LPCVD, a much improved uniformity of films is expected than in the APCVD. The application of low pressure also shifts the equilibrium temperature to a lower value, compared to an APCVD. LPCVD has been employed effectively for the growth of epitaxial layers of crystalline Si and a-Si (hydrogenated) semiconductors.

In an LPCVD process, for which the patterns are generated by photolithography prior to deposition, the epitaxially grown patterns are transferred with smaller distortion than those generated under APCVD. The differential in distortions between APCVD and LPCVD patterns increases with decreasing deposition temperature. The deposition rate in an LPCVD process is much smaller than in APCVD.

A variant of LPCVD is the remote plasma-enhanced CVD (RPECVD) process [77,80], which has the advantage over LPCVD in terms of film density and enhanced gas flow-rate. The technique has been successfully employed for the growth of silicon, and dielectric materials. The plasma in RPECVD can be generated by inductive or microwave techniques.

5.7.2 Materials System Studied and Applications

In an RPECVD, SiO_2-on-Si has been formed, using silane (SiH_4) and O_2 gas mixtures, with a nitrogen or argon carrier gas. RPECVD also lowers the temperature for the formation and deposition of SiO_2 on Si, compared with LPCVD and APCVD. The gas phase chemistry of the plasma is essential for controlling the structural defects, which are likely to form during the deposition process. Some of these defects have been analysed in detail [80]. Process optimization was adopted to fabricate low-loss waveguide structures using silica and silicon oxynitride [80,81]. Several RE-ion doped glasses have also been investigated [82–85]. Using RPECVD, complex glass compositions may be possible to design by mixing gases containing $AlCl_3$, $POCl_3$, BCl_3 and HF, as in conventional optical fibre fabrication, for designing silicate-, phosphate- and borate-rich glass thin and thick films, with as good control of refractive index as during the fabrication of core–clad silica glass preforms. Fluoride and chlorine rich gases may be used to maintain a dry atmosphere during deposition.

Using the CVD technique, both germanium oxide and tellurium oxide glasses may also be deposited as thin and thick films for waveguide engineering. Besides metal oxides, metals sulfides may also be processed for thin film devices and planar waveguide applications [86].

As discussed in the case of PLD, the deposition of epitaxial layer as well as thick crystalline materials is possible. Field-assisted RPECVD can also be employed to grow epitaxial and thick-film layers of ferroelectric and electro-optic materials. Unlike PLD, RPECVD is primarily a chemical process and, therefore, it may be strongly dependent on chemical kinetic barriers for material deposition. Techniques to generate various types of plasmas, e.g. the arc, magnetron, and microwave, and their chemistries and gas phase kinetics can be found in the literature [57,77,80,87–90].

5.7.3 Molecular Beam Epitaxy (MBE)

MBE is a unique thin film deposition process. It combines the features of chemical vapour deposition (CVD) with vacuum technology. It is the only chemical method that is capable of providing growth conditions of a single crystal layer on sub-nanometre scale. An epitaxy is a special type of film deposition characterized by a continuation of crystal structure from the substrate to the film. This type of film is usually single-crystalline, and it can be grown one monolayer (i.e. a single atom layer) at a time. Highly ordered crystalline films can be prepared in this way, which have been widely used in electronic devices. By contrast, non-epitaxial films are amorphous or polycrystalline, in which the crystalline lattices in substrate and film are mismatched. As a result such a film is not often suited for manufacturing electronic devices.

MBE is a highly developed technique used for the epitaxial growth of II–IV and III–V semiconductors to high-temperature superconductors. The technique has undergone a major refinement from the thermal or electron-beam evaporation of molecules for substrate. Instead elements from precursor vapours are precisely controlled on a substrate to form compounds, e.g. GaAs, InSb, etc., with high stoichiometry. During the deposition process, the atomic flux of materials can be rapidly tuned to achieve a gradient of materials. Substrate is heated to provide a high degree of surface mobility for incident species; consequently, the condensate atoms form a crystalline film on a monolayer scale at a time. The high surface mobility and defect-free structure necessitate the maintenance of ultra-low impurity levels, which cannot be ensured without a vacuum of the order of 10^{-10} to 5×10^{-11} torr.

In the molecular flow region for a mean free path ℓ of atoms or molecules in the source vapours that is very large compound to the diameter d_o of the beam defining orifice, the flux f_i of the source labelled i out of the orifice is related to the partial pressure p_i inside the cell as [57,77]:

$$f_i = \frac{\pi}{4} \frac{(d_o)^2 p_i}{\sqrt{2\pi m_i \kappa_B T}} \tag{5.11}$$

where m_i is the mass of the effusing species i. However, under the conditions of MBE, the desire to establish high fluxes usually requires a relatively large opening in the cells so that the output differs from that predicted by Equation 5.11. The flux at the substrate location scales as d_o^2/L^2, where L is the distance from the source. An example of GaAs MBE is: temperatures $T_{Ga} = 1080\,°C$, $T_{As4} \approx 330\,°C$, which correspond to flux values of Ga atoms and As_4 molecules of $10^{15}\,cm^{-2}\,s^{-1}$. In an MBE, as is known, point defects in the epitaxial layer can be introduced by controlling the flux of dopants to make tailor-made band gap materials with epitaxial layers of $Al_xGa_{1-x}As$ and GaP_yAs_{1-y}.

The main control features of MBE are: an ultrahigh vacuum chamber containing Knudsen cells for establishing the required source beam, with the individual Knudsen cells controlled for materials evaporation. A substrate heating and manipulation stage controls the adhesion of epitaxy and its growth. An Auger spectrometer is used *in situ* to examine the surface composition, supplemented by a mass spectrometer. An RHEED spectrometer is used to determine epitaxial crystallographic direction of the film.

For glassy thin films the MBE has not been so successful, primarily because of the cost of operation. By contrast, semiconductor materials for device engineering require controlled growth conditions to minimize interfacial defects which quench photoluminescence.

5.8 Ion-Exchange Technique

The principle of ion exchange in a glass matrix is based on the apparent ionic conductivity of cations, which are much smaller than the anions in a glassy structure. For example, as discussed in Chapter 1, sites between the non-bridging oxygen sites in silica, phosphate, germanium oxide, borate and tellurium oxide glasses are occupied by cations. At such terminal points the oxygen anions (O^{2-}) are coulombically bonded with the core of network forming cations, namely Si^{4+}, for example, in a sodium trisilicate ($Na_2O.3SiO_2$) glass, in which the ionic conductivity of Na^+ ions is of the order of $10^{-11}\,S\,cm^{-1}$ at 300 °C (corresponding to $65\,kJ\,mol^{-1}$ activation energy). Let us assume that in such a glass the alkali (Na^+) ions are exchanged with K^+. The counter cation exchange flux (J^+_{Na}) is based on the standard Fick's diffusion model (Equation 5.12) [91,92] for Na^+ or K^+, in which the additional diffusion flux contribution also arises from the local ionic transport:

$$J_{Na^+} = -D_{Na^+}\left[\frac{dX_{Na^+}}{dx} + X_{Na^+}\frac{F}{RT}\cdot\frac{\partial V}{\partial x}\right] \tag{5.12}$$

where D^+_{Na} is the ionic diffusion coefficient of Na^+ in the glass, F ($96500\,J\,volt^{-1}\,mol^{-1}$) is the Faraday constant, R ($8.314\,J\,mol^{-1}\,K^{-1}$) is the universal gas constant, $\partial V/\partial x$ is the local cationic potential gradient and X^+_{Na} is the ion fraction such that for an exchange $X^+_{Na} + X^+_K = 1$; T is the temperature on the absolute scale. During cationic exchange the electrical charge is conserved by maintaining the inward and outward flow of cations. This implies that $J^+_{Na} + J^+_K = 0$, which then yields an easily tractable equation that is much simpler to utilize for verifying the transport mechanism. By rearranging Equation 5.12 with the net flux equation, the cation transport equation can be rewritten as shown in Equation 5.13:

$$J_{Na^+} = -\tilde{D}\left[\frac{dX_{Na^+}}{dx}\right] \tag{5.13}$$

where $\tilde{D}$ is called the interdiffusivity of cations and is expressed in terms of mole fraction of ions and component diffusivity, as shown in Equation 5.14:

$$\tilde{D} = \frac{D_{Na^+}D_{K^+}}{D_{Na^+}X_{Na^+} + X_{K^+}D_{K^+}} \tag{5.14}$$

For ion exchange, traditionally the molten salt bath is used as a reservoir for exchange cation, into which the glass surface to be modified is dipped for several hours for ion diffusion. It was not until 1972 that Izawa and Nakagome [93] first demonstrated the exchange of monovalent ions in Na^+ and K^+ containing silicate glass. Since then a large number of monovalent cations (Tl^+, Ag^+, Li^+, Rb^+, and Cs^+) have been identified for cation exchange. These monovalent ions have a much smaller local field (V) compared to di- and trivalent cations. The apparatus for an ion-diffusion bath and the results of diffusion with and without the presence of an external field are shown in Figure 5.7a–c [94–97]. Clearly, the apparatus for ion diffusion is simple and easy to design and fabricate. Caution, however, must be taken in drying the hygroscopic salts which otherwise will induce OH^- ion impurities in the ion-exchange layer. Table 5.1 summarizes the ionic radius, polarizability, salt-bath medium and index change achieved after exchange in oxide glass.

From Table 5.1 it is possible to ascertain the scale of parameters that may be varied to achieve refractive index change. The ion-diffusion profile in glass follows the error function shape (from Equation 5.15), as a result of which the index profile cannot be manipulated to

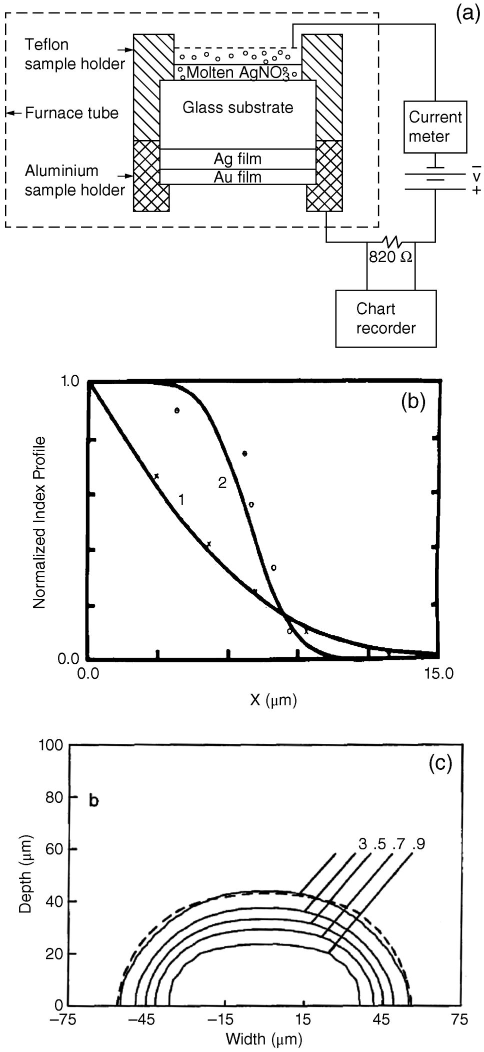
(a)
Teflon sample holder
Furnace tube
Aluminium sample holder
Molten AgNO3
Glass substrate
Ag film
Au film
Current meter
−
V
+
820 Ω
Chart recorder
(b)
1.0
0.0
Normalized Index Profile
1
2
0.0
15.0
X (μm)
(c)
100
80
60
40
20
0
Depth (μm)
b
3 .5 .7 .9
−75
−45
−15
15
45
75
Width (μm)

Figure 5.7 (a) Schematic diagram of the apparatus showing the Na^+–Ag^+ ion-exchange in a glass using molten silver nitrate solution [95]. Source: Najafi 1986. Reproduced with permission of IEEE. The ion exchange takes place is under the application of an external DC field. In (b) the ion diffusion profiles are compared with (2) and without (1) applied DC potential during silver–sodium cation exchange in a glass [96]. In (c) the computed (solid lines) diffusion contours of ions are compared with experimental data (---lines) [97]. Source: J. Albert 1990. Reproduced with permission from OSA Publishing.

larger depths, predominately due to the Fickian nature of ion diffusion. However, a much deeper flat-hat diffusion profile can be obtained by the application of an external field above room temperature, a technique that was explained by Najafi [94b]. Detailed investigations of parameters for ion diffusion profiles were made above ambient temperature in the absence and the presence of an external electromotive force (emf) [94b]. The error function

Table 5.1 *Monovalent ionic radius (Å), polarizability ($\alpha_{p,}$ (Å)^3), glass host, salt bath and melting temperature (°C), and refractive index change (Δn) recorded [94]. Source: Najafi 1986. [94,95].*

Cation radius (Å)	α_p (Å)^3	Glass host	Salt bath composition (melting temperature (°C))	Δn
Li^+ (0.65)	0.03	Soda-lime	Li_2SO_4-K_2SO_4 (520–620)	0.012
K^+ (1.33)	1.33	Soda-lime	KNO_3 (365)	0.008
Ag^+ (1.26)	2.4	Aluminosilicate	$AgNO_3$ (225–270)	0.13
Rb^+ (1.49)	1.98	Soda-lime	$RbNO_3$ (520)	0.015
Cs^+ (1.65)	3.34	Soda-lime	$CsNO_3$	0.03
Cs^+ (1.65)	3.34	BGG21	$CsNO_3$-CsCl	0.043
Tl^+ (1.49)	5.2	Borosilicate	$TlNO_3$	0.1

Equation 5.15 can be simplified by using a Taylor series expansion and ignoring the higher order terms, which then yields a much simpler equation for determining the diffusion profile, which might be estimated from Equation 5.16:

$$X_{\mathrm{Na}^+}(x,t) = X_{\mathrm{Na}^+}(0)\mathrm{erfc}\left(\frac{x}{2\sqrt{D_{\mathrm{Na}^+}t}}\right) \tag{5.15}$$

$$X_{\mathrm{Na}^+}(x,t) = X_{\mathrm{Na}^+}(0)\left(1-\frac{x}{2\sqrt{D_{\mathrm{Na}^+}t\pi}}\right) \tag{5.16}$$

The term $2\sqrt{Dt}$ is called the diffusion distance, which may be estimated if the ion diffusion coefficient is known. Table 5.2 summarizes the properties of RE-ion doped ion-exchange thin films. The details of optical and modal characterizations of ion-diffused layer are discussed elsewhere by Najafi [94]. Using electric field poling for ion diffusion to create a poled glass waveguide is discussed in Chapter 7 (section 7.4.6) in the context of second harmonic generation.

5.9 Chemical Solution or Sol–Gel Deposition (CSD)

5.9.1 Introduction

CSD deposition has a great deal of similarity with the sol–gel technique, discussed in Chapter 3, and it is for this reason this section is described concisely with reference to fabrication of thin films. A chemical-solution based deposition refers to any process in which a film is deposited by coating the substrate with a solution, which contains the constituent ions of the required film. Excess solvent is removed by controlled drying, leaving a precursor film, which is then heat treated to remove volatile groups (pyrolysis) and promote nucleation and growth of the required crystalline phase. The technique is also often referred to as "sol–gel" deposition, as in several examples the process involves the crosslinking of metallo-organic species, with an increase in solution viscosity, and providing a single molecular precursor containing all the relevant elements.

Table 5.2 *Summary of ion-exchanged RE-ion doped glasses and their optical properties [97–100].*

Rare-earth doped glass	Salt bath condition for ion exchange	Refractive index change (Δn)	Loss (dB cm^{-1})	Reference
1.65 wt% Er_2O_3-22 wt% Yb_2O_3 phosphate glass	KNO_3 bath in vacuum then raised to 400 °C, 20 min exchange	n at 1535 nm was 1.521	0.2 (at 1300 nm)	[96]
Nd^{3+} doped BK7 (borosilicate glass) containing 1.5 wt% Nd_2O_3	KNO_3 melt at 395 °C for 12 h	n at 1060 nm was 1.5. After exchange, TM($\Delta n = 0.008$), $\Delta n = 0.0092$ (TE)	0.2 (at signal 1050 nm)	[97]
SiO_2-67.7, Na_2O-12.5, K_2O-3.53, BaO-4.08, Yb_2O_3-12 wt%	KNO_3 salt bath at 418 °C for 20 min	$n_{eff} = 1.5174$ at 632.8 nm $n_{eff} = 1.5039$ at 1300 nm	1.3	[98]
Borosilicate glass with 1 wt% Er_2O_3 and 5 wt% Yb_2O_3	Unknown ion exchange technique		0.2–0.26	[99]
ZrF_4-57,BaF_2-34, 5–$x$$LaF_3$,4$AlF_3$, x REF_3 mol.%	OH^- and OD^- ion exchanged in fluoride glass at 280 °C for 72 h for D_2O exchange with F^- ions in glass	$\Delta n = 0.022$	10 ± 1	[100]

Compared to other methods of deposition, CSD has the advantages of a low entry cost (i.e. capital expenditure is low) and flexibility in being applicable to a wide range of materials, with exact control of cation stoichiometry. On the other hand, it is not perceived as being compatible with other forms of high volume device processes (e.g. standard CMOS) and suffers several drawbacks in device fabrication (e.g. poor step coverage) compared to vacuum and physical deposition methods.

5.9.2 CSD Technique and Materials Deposited

Salts, or organometallic compounds, of the requisite cations (assuming an oxide film) are dissolved in a suitable mutual solvent. These may be simple nitrates in an aqueous system, but more frequently organic salts (e.g. acetates or citrates) may be dissolved in acetic acid along with metal alkoxides in an alcohol. Once a suitable precursor liquid (or sol) has been prepared, the solution is coated on the substrate. This can be by dip-coating, but spin-coating is preferred. Just as in the deposition of photo-resist layers, the thickness and uniformity of the film are controlled by matching the viscosity of the solution and the rotation speed of the substrate. Evaporation of solvent during the spin-coating process effectively results in a solid layer of precursor. Further drying and initial pyrolysis can be carried out on a hot plate up to temperatures of 400 °C. The annealing of coated and dried films is dependent on the application. A low temperature drying may be followed either by using rapid thermal annealing furnace or isothermally at a specified temperature, depending upon the nature of the film.

Films as thin as 10 nm can be deposited by CSD techniques; however, 100 nm is more normal with a single deposition. Whilst it has been known for films as thick as 4 μm to be deposited with a single-step, it is more common for films to be built up by the sequential deposition and annealing of 100 nm layers. This avoids the cracking often associated with the pyrolysis of thick precursor layers.

A wide range of materials have been deposited by CSD, but perhaps the largest number of publications are to be found concerning the ferroelectric oxides, such as barium titanate, lithium niobate, barium strontium titanate, PZT, PLZT and strontium bismuth tantalate. Many applications for these materials in planar form have been demonstrated using ink jet printing: non-volatile memory devices, high permittivity gate oxides, uncooled IR detectors, piezoelectric sensors, MEMS actuators, tuneable microwave filters and electro-optic devices [101–106]. The area in greatest need of improvement in CSD is microstructure control. As deposition is on a cold substrate, crystal nucleation during thermal treatment is poorly controlled. Most films are therefore polycrystalline; however, varying degrees of texture or crystallographic orientation can be engendered in certain cases. For example, in the formation of barium titanate from precursor films, barium carbonate inevitably forms as an intermediate, which does not decompose until the material is well above the threshold temperature for crystallization of the perovskite (e.g. >700 °C). Nucleation is therefore homogeneous and rapid, resulting in a very fine randomly oriented grain structure. On the other hand, pyrolysis of common PZT precursors does not result in the formation of stable intermediates and crystallization can take place as low as 460 °C. At such a low temperature, nucleation takes place preferentially at the interface with the substrate and, in the case of [111] oriented Pt electrodes [111], oriented polycrystalline films of PZT can result; a Pb_3Pt intermetallic is thought to play a role in this process. Columnar growth of successive layers results in films with no grain boundaries parallel to the substrate.

The above examples show that several factors can play a role in controlling microstructure: choice of precursors and substrate, use of seed layers to promote heterogeneous nucleation and the thermal profile. For any given deposition condition, the parameters must be optimized to provide the desired properties in thin films.

5.10 Conclusion

Various methods of deposition of thin films are discussed in this chapter by explaining the fundamental differences in the processes involved. A special feature in the context of thin-film fabrication is the emerging pulsed laser deposition (PLD) technique, which is ideally suited for optical quality film deposition. For each technique examples are included and the relevant properties are discussed.

References

1. R. Syms and J. Cozens (1992) *Optical Guided Waves and Devices*, McGraw Hill, London.
2. P.W. France (ed.) (1990) *Fluoride Glass Optical Fibres*, 1st edn, Blackie, London, (a) pp. 122–131; (b) pp. 133–185.
3. Aicha A.R. Elshabini-Riad and Fred D. Barlow III (1998) *Thin-film Technology Handbook*, *Series Advisor C. M. Harper*, McGraw-Hill, New York, pp. 1–24.
4. D.L. Smith (1995) *Thin-film Deposition: Principles & Practice*, McGraw-Hill, New York.
5. Y. Sripathi, L.K. Malhotra, and G.B. Reddy (1995) GaGeTe films as phase change optical recording media. *Thin Solid Films*, **270**, 60–64.
6. T. Sakaguchi *et al.* (1995) MgO/SiO_2 dielectric multi-layer reflectors for GaN-based UV surface emitting lasers, Conference Proceeding Lasers and Electro-Optic Society Annual Meeting, 1995, vol. 2, IEEE, Piscataway, NJ, No. 95CH35739 pp. 102–103.
7. R A Swalin (1972) *Thermodynamics of Solids*, 2nd edn, John Wiley & Sons, Inc., New York.
8. Z.M. Qi, K. Itoh, M. Murabayashi and C.R. Lavers (2000) Characterisation and application of a channel-planar composite waveguide. *Optics Letters*, **25** (No: 19), 1427–1429.
9. S. Kashimura, M. Takeuchi, K. Maru, and H. Okano (2000) Loss reduction of GeO_2-doped silica waveguide with high refractive index difference by high-temperature annealing. *Japanese Journal of Applied Physics Part 2-Letters*, **39** (No: 6A), L521–L523.
10. Y. B. Choi, S. H. Cho, and D.C. Moon (2000) Er-Al-co-doped silicate planar light waveguide-type amplifier fabricated by radio-frequency sputtering. *Optics Letters*, **25** (No. 4), 263–265.
11. C. Tosello *et al.* (1999) Optical properties and structural characterisation of Er-activated SiO_2-TiO_2 planar waveguides prepared by rf sputtering. *Philosophical Magazine B*, **79** (No. 11–12), 2103–2112.
12. S. Kashimura *et al.* (1999) Refractive-index adjustment of SiO_2-GeO_2 films deposited by RF magentron sputtering, *Applied Surface Science*, **142** (No. 1–4), 58–62.

13. B.J.H. Stadler and M. Oliver (1998) Sputter-deposited yttria-alumina thin films for optical waveguiding. *Journal of Applied Physics*, **84** (No. 1), 93–99.
14. E. Dogheche, B. Jaber, and D. Remiens (1998) Optical waveguiding in epitaxial $PbTiO_3$ thin films. *Applied Optics*, **37** (No. 19), 4245–4248.
15. Y.C. Yan, A.J. Faber, H. de Waal, P. G. Kik, and A. Polman (1997) Erbium-doped phosphate glass waveguide on silicon with 4.1 dB/cm gain at 1535 nm. *Applied Physics Letters* **71** (No. 20), 2922–2924.
16. C.C. Li, H. K. Kim, and M. Migliuolo (1997) Er-doped glass ridge waveguide amplifiers fabricated with a collimated sputter deposition technique. *IEEE Photonics Technology Letters*, **9** (No. 9), 1223–1225.
17. K. Akiba, N. Takegata, S. Kawakami, K. Shiraishi (1995) Fabrication of silica-based optical waveguides with smooth side walls by RF-Bias sputtering. Electron Communications JPN II, **78** (No. 5), 31–39.
18. M. Hafidz, R. Wigayatri, M. O. Tjia, and M. Barmawi (1993) 5-output optical power divider based on multichannel coupled waveguide structure. *Electron Letters*, **29** (No. 13), 1168–1170.
19. M. Yamaga and Y. Miyazaki (1984) RF sputtering crystal-growth and spectroscopy of Nd doped $Y_3Ga_5O_{12}$ thin film waveguide on $Y_3Al_5O_{12}$ substrate for optical amplifiers. *Japanese Journal of Applied Physics Part 1* **23** (No. 3), 312–316.
20. E.G. Gamaly, A.V. Rode, and B. Luther-Davies (2007) *Ultrafast Laser Ablation and Film Deposition, in Pulsed Laser Deposition of Thin Films* (ed R. Eason), Wiley-Interscience, Hoboken, New Jersey, (a) p. 105 and (b) pp. 122–123.
21. E.D. Eugenieva and P.A. Atanasov (2000) Waveguide properties of optical thin films grown by pulsed laser deposition. *Material Science Semiconductor Process*, **3**, (No. 5–6) 575–579.
22. R.I. Tomov, *et al.* (2000) $LiNbO_3$ Optical Waveguides Deposited on Sapphire by electric-field assisted PLD. *Vacuum*, **58** (No. 2–3) 396–403.
23. P. A. Atansov *et al.* (2000) Growth of Nd: potassium Gd-tungstate thin-film waveguides by PLD. *Applied Physics Letters*, **76** (No. 18) 2490–2492.
24. H. Uetsuhara *et al.* (1999) Fabrication of a T: sapphire planar waveguide by PLD. *Applied Physics A – Material Science & Processing*, **69**, S719–722.
25. J. Yin *et al.* (1998) PLD of $SrBi_2Ta_2O_9$ films on fused silica in waveguide form. *Journal of Physics D: Applied Physics*, **31** (No. 22), 3185–3187.
26. K. M. Wang *et al.* (1998) Waveguide laser film in Er-doped $KTiOPO_4$ by PLD. *Applied Physics Letters* **73** (No. 8) 1020–1022.
27. M. Jelinek *et al.* (1998) Waveguiding pulsed laser deposited Ti: sapphire layer on quartz, *Thin Solid Films*, **322** (No. 1–2) 259–262.
28. M.A. Vainos *et al.* (1998) Planar laser waveguides of Ti: sapphire, Nd: GGG, and Nd: YAG grown by PLD. *Applied Surface Science*, **129**, 514–519.
29. M. Jelinek *et al.* (1998) Planar waveguide lasers and structures created by laser ablation –An overview, *Czechoslovak Journal of Physics*, **48** (No. 5), 577–597.
30. J.S. Yeo and L. Hesselink (1998) Synthesis and properties of ferroelectric niobate thin-films prepared by PLD for optical waveguide application. *Journal of the Korean Physical Society*, **32**, S1369–S1371.
31. S.B. Xiong *et al.* (1998) $Sr_xBa_{1-x}Nb_2O_9$ Optical Waveguiding thin films on SiO_2 coated Si(100) substrates. *Journal of the Korean Physical Society*, **32**, S1611–S1614.

32. A.A. Anderson *et al.* (1997) Low-loss (0.5 dB/cm) Nd:$Gd_3Ga_5O_{12}$ waveguide lasers grown by PLD. *Optics Communications*, **144** (No. 4–6) 183–186.
33. A.A. Anderson *et al.* (1997) Ti:sapphire planar waveguide laser grown by PLD. *Optics Letters*, **22** (No. 20), 1556–1558.
34. C.L. Bonner *et al.* (1997) Performance of low-loss PLD Nd:GG Garnet waveguide laser at 1060 nm and 940 nm, *Opt. Lett.* **22** (13), 988–990.
35. W.S. Hu *et al.* (1997) Optical properties of PLD ZnO thin films. *Journal of Physics and Chemistry of Solids*, **58** (No. 6), 853–857.
36. R. Serna, C.N. Afonso, J.M. Ballesteros, and A. Zschocke (1997) *Applied Surface Science*, **110**, 524–527.
37. M. Ezaki, M. Obara, H. Kumagai, and K. Toyada (1996) Characterisation of Nd:YAG thin films grown on various substrate by PLD. *Applied Physics Letters*, **69** (No. 20), 2977–2979.
38. W.S. Hu, Z.G. Liu, Y.Q. Lu, S.N. Zhu, and D. Feng (1996) PLD and Optical Properties of completely (001) textured optical waveguiding $LiNbO_3$ films upon SiO_2/Si substrates. *Optics. Letters*, **21** (No. 13), 946–948.
39. D.S. Gill, A.A. Anderson, R.W. Eason, T.J. Warburton, and D.P. Shepherd (1996) Laser operation of an Nd:GG Garnet thin-film optical waveguide fabricated by PLD. *Applied Physics Letters*, **69** (1), 10–12.
40. S.B. Xiong, X.L. Guo, Z.G. Liu, T. Yu, X.Y. Chen, and X.K. Meng (1996) Optical waveguiding properties of highly [100] textured PLT thin films prepared by PLD. *Materials Letters*, **27** (3), 81–84.
41. K.E. Youden *et al.* (1993) PLD of Ga-La-S Chalcogenide Glass Thin Film Optical waveguides, *Applied Physics Letters*, **63** (No. 12), 1601–1603.
42. C. Zaldo *et al.* (1994) Growth of $KNbO_3$ thin films on MgO by PLD. *Applied Physics Letters*, **65** (No. 4), 502–504.
43. D.S. Gill *et al.* (1995) Characterisation of GLS glass thin film optical waveguides fabricated by PLD. *Journal of Non-Crystalline Solids*, **191**, 321–326.
44. M. Irannejad, Z. Zhao, G. Jose, D.P. Steenson, and A. Jha (2010) A short-review on pulsed laser deposition on Er^{3+}ion doped oxide glass films for integrated optics. *Transactions of the Indian Ceramic Society*, **69**, 207–221.
45. A.V. Rode, B. Luther-Davies, and E.G. Gamaly (1999) Ultrafast ablation with high-pulsed-rate lasers – part I - theoretical considerations. *Journal of Applied Physics*, **85**, 4222–4230.
46. R.J. Narayan (2007) Diamond-like carbon: medical and mechanical applications, in *Pulsed laser Deposition of Thin Films* (ed R. Eason), Wiley-Interscience, Hoboken, New Jersey, ch 15, pp. 333–361.
47. I. Takeuchi, R.B. van Dover, and H. Koinuma (2003) Combinatorial synthesis and evaluation of functional inorganic materials using thin-film techniques. *Materials Research Bulletin*, **27**, 301–308.
48. H. Koinuma and I. Takeuchi (2004) Combinatorial Solid-state chemistry of inorganic materials. *Nature Materials*, **3**, 429–438.
49. X.D. Xiang, X.D. Sun, G. Briceno, Y. Lou, K.A. Chang, W.G. Wallace-Freedman, S.W. Chen, and P.G. Schultz (1995) A combinatorial approach to materials discovery. *Science*, **268**, 1738–1740.
50. I. Takeuchi, O.O. Famodu, J.C. Read, M.A. Aronova, K.S. Chang, C. Craciunescu, S.E. Lofland, M. Wuttig, F.C. Wellstood, L. Knauss, and A. Orozco (2003)

Identification of novel compositions of ferromagnetic shape-memory alloys using composition spreads. *Nature Materials*, **2**, 180–184.

51. I. Takeuchi, (2007) Combinatorial pulsed laser deposition, in *Pulsed laser Deposition of Thin Films* (ed R. Eason), Wiley-Interscience, Hoboken, New Jersey, ch 7, pp. 161–175.
52. H. Minami, K. Itaka, H. Kawaji, Q.J. Wang, and H. Koinuma (2002) Rapid synthesis and characterization of $(Ca_{1-x}Bax)_3Co_4O_9$ thin films using combinatorial methods. *Applied Surface Science*, **197–198**, 442–447.
53. K. Hasegawa, P. Ahmet, N. Okazaki, T. Hasegawa, K. Fujimoto, M. Watanabe, T. Chikyow, and H. Koinuma (2004) Amorphous stability of HfO2 based ternary and binary composition spread oxide films as alternative gate dielectrics. *Applied Surface Science*, **223**, 229–232.
54. Z. Zhao, G. Jose, T.T. Fernandez, T.P. Comyn, M. Irannejad, P. Steenson, J.P. Harrington, M. Ward, N. Bamiedakis, R.V. Penty, I.H. White, and A. Jha (2012) Active glass-polymer superlattice structure for photonic integration. *Nanotechnology*, **23**, 225302.
55. M. Okoshi, M. Kuramatsu, and I. Narumi (2002) Pulsed laser deposition of SiO_2 thin films with dimethylpolysiloxane targets. *Japanese Journal of Applied Physics*, **41**, 1395–1399.
56. R.S. Quimby (1991) Active phenomena in doped halide glasses, in *Fluoride Glass Fibre Optics* (ed I. D. Aggarwal and G. Lu), Academic Press, ch 9, p. 378.
57. S.P. Murarka and M.C. Peckerar (1989) *Electronic Materials Science and Technology*, Academic Press, San Diego.
58. P.D. Townsend (1998) *Development of ion implantation for optical applications*, **Vacuum**, **51** (No. 2), 301–304.
59. H. Konig *et al.* (1998) Focussed ion beam implantation for opto- and microelectronic devices. *Journal of Vacuum Science and Technology B*, **16** (No. 4), 2562–2566.
60. C.M. Johnson, T.D. Thompson, M.C. Ridgeway, and V. Gurarie (1998) Implantation-induced structural and surface modification of silica. *Nuclear Instrumentation and Method Physics Research B*, **141** (No. 1–4) 629–633.
61. C. Meneghini *et al.* (1998) Luminescence from Nd-ion-implanted As_2S_3 waveguides. *Journal of the Optical. Society of America B-Optical Physics*, **15** (No. 4), 1305–1308.
62. W.F. van der Weg, A.J.M. Bernstein, F.W. Saris, and A. Polman (1996) Ion Implantation into amorphous solids. *Material Chemistry and Physics*, **46** (No. 2–3), 140–146.
63. C.M. Johnson, M.C. Ridgeway, and P.W. Leech (1996) Thermal annealing of implantation-induced compaction for improved silica waveguide performance. *Applied Physics Letters*, **69** (No. 7), 984–986.
64. G.N. van den Hoven *et al.* (1996) Net optical gain at 1530 nm in Er-doped Al_2O_3 waveguides on silicon. *Applied Physics Letters*, **68** (No. 14), 1886–1888.
65. C. Wyon and B. Ferrand (1995) Compact planar waveguide lasers. *Annales de Chimie Science des Materiaux*, **20** (No. 5), 273–279.
66. B. Herreros, G. Lifante, F. Cusso, P.D. Townsend, and P.J. Chandler (1995) Luminescence spectroscopy of Nd^{3+}in ion-implanted $LiNbO_3$-Nd-MgO planar waveguides. *Journal of Physics D-Applied Physics*, **28** (No. 8), 1687–1692.
67. C. Buchal (1995) Ion-implantation for optical applications. *Nuclear Instrumentation and Method Physics Research B*, **96** (No. 1–2), 370–373.
68. P.D. Townsend (1994) Ion-Implanted waveguide lasers in insulators. *Nuclear Instrumentation and Method Physics Research B*, **89** (No. 1–4), 270–276.

69. P.J. Chandler and P.D. Townsend (1993) Waveguides and waveguide lasers fabricated by ion-implantation. *Nuclear Instrumentation and Method Physics Research B*, **80** (1), 1135–1142.
70. N. Hamelin, P.J. Chandler, and P.D. Townend (1992) Characterisation of Ion-implanted waveguides in barium fluoride. *Physica Status Solidi A-Applied Research*, **134** (No. 2), 557–566.
71. C. Buchal (1992) Ion-implantation of optical devices. *Nuclear Instrumentation and Method Physics Research B*, **68** (No. 1–4), 355–360.
72. P.D. Townsend (1992) Ion-Implanted waveguide and waveguide lasers. *Nuclear Instrumentation and Method Physics Research B*, **65** (No. 1–4), 243–250.
73. A. Niehof, S. Renner, C. Buchal, and W. Heiland (1991) Optical channel waveguides produced with high-dose Ti^+-implantation. *Nuclear Instrumentation and Method Physics Research B*, **59**, 1355–1357.
74. S.J. Field *et al.* (1991) Ion-implanted Nd^{3+}-YAG waveguide laser. *IEEE Journal of Quantum Electronics*, **27** (No. 3), 428–433.
75. P.D. Townsend (1983) Optical waveguide formation by ion-implantation. *Radiation Physics & Chemistry*, **22** (No. 6), 1049–1059.
76. F. Ladoouceur and J.D. Love (1996) *Silica-based Buried Channel Waveguides and Devices*, Optical and Quantum Electronics Series (Series ed G. Parry and R. Baets), Chapman & Hall, London.
77. K.J. Bachmann (1995) *The Materials Science of Microelectronics*, VCH Publishers Inc., New York.
78. NPL, $F^*A^*C^*T$ Computer Software, MTDATA NPL Thermodynamic Database.
79. J.C. Slater (1974) *Quantum Theory of Molecules and Solids*, vol. 4, McGraw Hill, New York.
80. T. Hattori, S. Semura, and N. Akasaka (1999) Inductively coupled plasma-enhanced CVD of SiO_2 and GeO_2-SiO_2 films for optical waveguides using TEOS and TMGe. *Japanese Journal of Applied Physics Part 1*, **38** (No. 5A), 2775–2778.
81. R.M. de Ridder *et al.* (1998) Silicon oxynitride planar waveguiding structures for applications in optical communications. *IEEE Journal of Selected Topics in Quantum Electronics*, **4** (No. 6), 930–937.
82. B. Wu and P.L. Chu (1995) Fabrication of high concentration of RE-doped silica based waveguide by MCVD method. *IEEE Photonics Technology Letters*, **7** (No. 6), 655–657.
83. Y.P. Li and C.H. Henry (1996) Silica-based optical integrated circuits. *IEE Proceedings – Optoelectronics*, **143** (No. 5), 263–280.
84. K. Hattori *et al.* (1998) Optical and structural properties of Er^{3+}-doped P_2O_5-SiO_2 and Al_2O_3-SiO_2 planar waveguides. *Material Science Engineering*, **B54**, 15–17.
85. J.R. Bonar and J.S. Aitchison (1996) Co-doping effects in RE-doped planar waveguides. *IEE Proceedings – Optoelectronics*, **143** (No. 5), 293–297.
86. A.V. Rode, A. Zakery, M. Samoc, E.G. Gamaly, and B. Luther-Davies (2002) Laser-deposited As_2S_3 chalcogenide films for waveguide applications. *Applied Surface Science*, **197/198**, 481–485.
87. O.P. Agnihotri, R. Tyagi, I. Kato (1997) Silicon oxynitride waveguides for opto-electronic integrated circuits. *Japanese Journal of Applied Physics Part 1* **36** (11), 6711–6713.

88. H. Sato (1994) Preparation of a BaF_2/CaF_2 slab optical waveguide by CVD. *Japanese Journal of Applied Physics Part 2*, **33** (No. 3A), L368–L370.
89. K. Imoto and A. Hori (1993) High-refractive index difference and low-loss optical waveguide fabricated by low-temperature processes. *Electronic Letters*, **29** (No. 12), 1123–1124.
90. K. Imoto and A. Hori (1992) New technology for reduction in cost and size of silica guided-wave component. *Electronic Letters*, **28** (No. 17), 1665–1667.
91. A.K. Varsheneya (2006) *Fundamentals of Inorganic Glasses*, 2nd edn, The Society of Glass Technology, Sheffield, pp. 397–402.
92. P. G. Shewmon (1989) Diffusion in non-metals, in *Diffusion in Solids*, 2nd edn, TMS Publisher, Warrendale, PA, ch 5, pp 151–168.
93. T. Izawa and H. Nakagome (1972) Optical waveguide formed by electrically induced migration of ions in glass plates. *Applied Physics Letters*, **21** 584–586.
94. S.I. Najafi (1992) *Introduction to Integrated Optics*, Artec House Inc. Norwood, MA, (a) pp.17–21; (b) pp. 29–31.
95. S.I Najafi, P.G. Suchoski, Jr. and R.V. Ramaswamy (1986) Silver film diffused glass waveguides: Diffusion process and optical properties. *IEEE Journal of Quantum Electronics*, **QE-22**, 2213–2218.
96. R.V. Ramaswamy and R. Srivastava (1988) Ion exchange glass waveguides: a review. *Journal of Lightwave Technology*, **6**, 984–1002.
97. J. Albert and J.W.Y Lit (1990) Full modelling of field-assisted ion exchange for graded index buried channel optical waveguides. *Applied Optics*, **29**, 2798–2804.
98. P. Fournier, P. Meshkinfann, M.A. Fardad, M.P. Anderson, and S.I. Najafi (1997) Potassium ion exchanged Er-Yb doped phosphate glass amplifiers. *Electronic Letters*, **33**, 293–294.
99. S.J. Hettrick, J.I. Mckenzie, R.D. Harris, J.S. Wilkinson, and D.P. Shepherd (2000) Ion-exchanged tapered waveguide laser in Nd-doped BK7 glass. *Optics Letters*, **25**, 1433–1435.
100. S. Florea and K.A. Winick (1999) Yb-doped glass waveguide laser fabricated by ion exchange. *Journal of Lightwave Technology*, **17**, 1593–1601.
101. J. Roman, P. Camy, M. Hempstead, W.S. Brockelsby, S. Nouh, A. Beguin, C. Lerminiaux, J.S. Wilkinson (1995) Ion exchanged Er-Yb waveguide lasers at 1.5 μm pumped by a diode laser. *Electron Letters*, **31**, 1345–1346.
102. E. Josse, J.E. Broquin, G. Fonteneau, R. Rimet, J. Lucas (1997) Planar and channel waveguides on fluoride glasses, *Journal of Non-Crystalline Solids*, **213 & 214**, 152–157.
103. J. Fick (2000) Fabrication of erbium doped channel waveguides by a combination of ion-exchange and sol-gel techniques. *Journal of Sol-Gel Science Technology*, **19**, 573–576.
104. J.P. Rainho, M. Pillinger, L.D. Carlos, S.J.L. Ribeiro, R.M. Almeida, and J. Rocha (2002) Local erbium (III) environment in luminescent titanosilicate prepared from microporous precursors. *Journal of Materials Chemistry*, **12**, 1162–1168.
105. S. Ono and S. Hirano (1997) Patterning of lithium niobate thin films derived from aqueous solution. *Journal of the American Ceramic Society*, **80**, 2533–2540.
106. B.E. Yoldas (1998) Design of sol-gel coating media for ink jet printing. *Journal of Sol-Gel Science Technology*, **13**, 147–152.

6

Spectroscopic Properties of Lanthanide (Ln^{3+}) and Transition Metal (M^{3+})-Ion Doped Glasses

6.1 Introduction

In this chapter the aim is to discuss the spectroscopic, lasing and amplification properties of rare-earth (RE)-ion and transition metal (TM)-ion doped inorganic glasses and glass ceramics for engineering light amplification devices. In this regard, the radiative properties of light-generating excitonic systems in inorganic materials are considered in explaining the decay process and line broadening of optical transitions. For this purpose the standard models for radiation emission, available in the literature, e.g. Silfvast [1], Koechner and Bass [2] and Fox [3], have been readapted in this chapter in the context of inorganic lasing hosts with examples, wherever possible. The influence of crystal or ligand field on dopants is also used to explain the transition probabilities in RE-ion and TM-ion doped systems, by making a distinction between the dipole coupling properties. Key examples for device applications are taken to illustrate the importance and growth of this field which is now more than 110 years old, having begun when Einstein [4] first published his seminal paper on the photoelectric effect in 1905. To help readers, attempts have been made to not create new mathematical notations so that a universal uniformity of symbols amongst the key references is maintained.

6.2 Theory of Radiative Transition

In a radiative transition, the electronic, atomic or molecular states absorb energy, e.g. photons having energies at least as large as the band gap, $\Delta E = (E_2 - E_1) = \hbar\omega = 2\pi h\upsilon$. By considering the absorption of monochromatic or broadband wavelength (e.g. from super-luminescent diodes) of light at the ground state 1 which corresponds to ΔE (the difference in energy), then the ground states will gain energy to reach excited state 2. In this situation the rate of change in the population of ground state may be written as a product of a probability

---

Inorganic Glasses for Photonics – Fundamentals, Engineering and Applications, First Edition. Animesh Jha.
© 2016 John Wiley & Sons, Ltd. Published 2016 by John Wiley & Sons, Ltd.

function or inversion probability, $B_{12}.\rho(\upsilon)$ at a given pump photon frequency, υ:

$$\frac{\mathrm{d}N_1}{\mathrm{d}t} = -B_{12}\rho(\upsilon)N_1 \tag{6.1}$$

As shown in Figure 6.1, the quantum theory of light emission is based on excitation of "electronic" or "atomic" or "molecular" states to a higher energy metastable level E_2, which is above the ground state energy level E_1, from which the decay may occur *spontaneously*. The energy difference ($\Delta E = (E_2 - E_1) = \hbar\omega = 2\pi h\upsilon$) then defines the energy of the emitted photons. Although the lowering of energy to the ground state energetically occurs *spontaneously*, a special case of this type of photon emission is via *stimulated emission*, as originally proposed by Einstein's model [4]. In the de-excitation of states it is assumed here that the occupied states are relatively isolated from the host environment and that no external effects perturb their occupancy either at the ground or excited levels. This is an ideal situation that never occurs in reality. However, for understanding, this assumption at this point is quite important.

If we now adopt the same form of equation as in Equation 6.1 to characterize the rate of decay using the Einstein coefficient (A_{21}) for the optical transitions between levels 2 and 1, then the rate of photon emission may be expressed as:

$$\begin{gathered}\frac{\mathrm{d}N_2}{\mathrm{d}t} = -A_{21}N_2, \quad \text{or :}\\ \frac{\mathrm{d}N_2}{N_2} = -A_{21}\,\mathrm{d}t\end{gathered} \tag{6.2}$$

The solution for Equation 6.2 is:

$$N_2(t) = N_2(0)\exp\left(-A_{21}\cdot t\right) = N_2(0)\exp\left({}^{-t}/_{\tau_{21}}\right) \tag{6.3}$$

in which the $\tau_{21} = (1/A_{21}) = [A_{21}]^{-1}$ (s); this is called the radiative lifetime measured in time units of the states at the excited level 2. This decay rate is dependent on the magnitude of the decay coefficient and is governed by the oscillator strength, discussed below.

The most important characteristic of spontaneous emission is that the emitted photons are not coherent and, therefore, bear no phase correlation which is manifested in the spectral range of energy of emitted photons. The condition of coherence is important to understand. Although during the excited state the pump photon may be a laser source, for stimulated emission the decay must occur in the presence of an external electromagnetic field of magnitude, ΔE, which flips all the occupied electronic states in the same polarization direction.

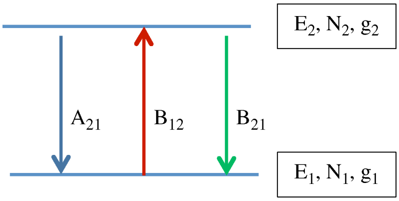

Figure 6.1 *Two energy levels, E_1 (ground) and E_2 (next higher) levels, having g_1 and g_2 degeneracies with N_1 and N_2 populations, respectively. A_{21}, B_{12} and B_{21} are the Einstein constants for spontaneous emission from E_2 to E_1, absorption from E_1 to E_2 and stimulated emission from E_2 to E_1.*

To help the reader understand the condition of coherence, it may be useful to make a comparison with the magnetization process in which all the spin states are randomly oriented before magnetization and fully aligned and parallel with the applied magnetic field at the end of magnetization. Thermodynamically, to minimize the entropic disorder of spin states of excitons, the energy must be invested in maximizing the coherence condition. In our comparison with magnetism, the stimulated photon emission is "induced from an external source" and the resulting equation is comparable with Equation 6.1, except that the absorption of photon from external source for causing decay is taking place at level 2:

$$\frac{\mathrm{d}N_2}{\mathrm{d}t} = -B_{21}\rho(\upsilon)N_2 \tag{6.4}$$

where B_{21} is another Einstein constant and the product $B_{21}\rho(\upsilon)$ is a probability function that is not equal to $B_{12}\rho(\upsilon)$ in Equation 6.1. The negative sign in Equations 6.1, 6.2 and 6.4 designate the decrease in the population of states. In describing stimulated emission, Einstein assumed that a *radiation cavity* is a blackbody. Inside the blackbody box, N number of atoms are at temperature T which do not interact with each other but only participate in the black body radiation absorption ($E_1 \rightarrow E_2$) and emission via either spontaneous or stimulated ($\mathrm{E}_2 \rightarrow \mathrm{E}_1$) (Figure 6.1).

Under thermal equilibrium inside the blackbody cavity, a steady state condition is reached and the resulting population balance equation may be written as a two-level system ($E_2 - \mathrm{E}_1 = \Delta E$). This implies that $N_2 + N_1 =$ constant, which yields:

$$\frac{\mathrm{d}N_2}{\mathrm{d}t} + \frac{\mathrm{d}N_1}{\mathrm{d}t} = 0 \tag{6.5}$$

implying that the rate of change of population at the ground state (E_1) is equal and opposite in sign to that of the rate of change in inversion at level 2 with energy E_2. Equation 6.5 defines the steady state condition for thermal equilibrium for the cavity. For steady state this condition is:

$$B_{12}\,\rho(\upsilon)\,N_1 = A_{21}N_2 + B_{21}\,\rho(\upsilon)N_2 \tag{6.6}$$

in which the left- and right-hand sides describe the absorption and the sum of spontaneous and stimulated emission processes. By dividing both sides of Equation 6.6 with N_1 and solving with the following steps:

$$\frac{N_2}{N_1}A_{21} + \frac{N_2}{N_1}B_{21}\rho(\upsilon) = A_{12}\rho(\upsilon) \tag{6.7}$$

from which the intensity of emitted radiation may be rewritten as:

$$\rho(\upsilon) = \frac{\left(A_{21}\dfrac{N_2}{N_1}\right)}{\left[A_{12} - \left(\dfrac{N_2}{N_1}\right)B_{21}\right]} \tag{6.8}$$

In addition, using the Boltzmann equation for thermal equilibrium of inversion of the electronic states, the inversion ratio may be given as:

$$\frac{N_2}{N_1} = \frac{g_2}{g_1}\exp\left(\frac{-h\upsilon}{\kappa_\mathrm{B}T}\right) \tag{6.9}$$

In Equation 6.9 g_1 and g_2 are degeneracies of levels 1 and 2, respectively. Since we are dealing with the blackbody radiation inside the cavity, then the radiation intensity may be expressed as:

$$\rho(\upsilon) = \frac{\left({A_{21}}\big/{B_{21}}\right)}{\left({g_1}/{g_2}\right)\left({B_{12}}\big/{B_{21}}\right)\left[\exp\left(\frac{h\upsilon}{\kappa_B T}\right) - 1\right]} \tag{6.10}$$

In Equation 6.10:

$$A_{21}\big/B_{21} = \frac{8\pi\upsilon^2 h\upsilon}{(c)^3} \text{ and } B_{21} = \frac{g_1}{g_2}B_{12}$$

Here c is the velocity of light in the medium. In an oversimplified case it is reasonable to assume that $g_1 = g_2$, i.e. the extent of degeneracy of both levels is similar in magnitude, which then leads to $B_{12} = B_{21}$, i.e. the stimulated emission is equal to that of the excited state. In the vast majority of known systems, the condition $B_{12} \neq B_{21}$ is more prevalent.

Since in lasing transition many more levels are active and present inside the cavity, then a much more general form of rate equation may be considered:

$$N_{i\to j}(t) = N_{i\to j}(0)\cdot\exp\left[\left(-\sum A_{ij}\cdot t\right)\right] \tag{6.11}$$

and the decay constant:

$$\tau_i = \frac{1}{\sum A_i} \tag{6.12}$$

Having generalized the mathematical form of the radiative decay for a multiple system, further analysis of radiative process is now analysed in the context of interference from the environment of the host, e.g. the multiplet excitonic interaction and influence of lattice vibrations. All these influence the line shape of emission.

6.3 Classical Model for Dipoles and Decay Process

When a rare earth ion or a transition metal ion is doped in a matrix of glass or a crystalline material, the chemical environment of dopants is influenced by the host. Below, a classical approach is taken to explain the dopant–host interaction. In adopting this approach we consider that an ensemble of charge (e.g. electrons) in a high energy state may decay to the ground state by emitting photons. However, the mechanistic aspects of photon emission from the decay of an exciton (electron or atom) may be dependent on the host–ion interaction, which is fundamental in ascertaining the quantum efficiency of light emission.

In Chapter 4 a linear harmonic oscillator (Equation 4.32) is discussed in the context of lattice vibration. In the case of an excited state electron, a dipole may be considered for which the equation of motion has two components—the inertial motion defined by the Newton's law:

$$\left[m_d \frac{d^2x}{dt^2}\right]$$

and the corresponding restoring component, which is equal to $-\kappa_d x$. These two terms then yield the equation of a linear harmonic oscillator [1]:

$$\left[m_d \frac{d^2x}{dt^2} + \kappa_d x = 0\right] \tag{6.13a}$$

for which the solution for displacement is well known:

$$x = x_o \exp(-i\omega_o t) \tag{6.13b}$$

where:

$$\omega_o = 2\pi\upsilon_o = \left(\frac{\kappa_d}{m}\right)^{\frac{1}{2}}$$

and $\kappa_d = 4\pi^2\upsilon_o^2 m_d$ is the spring constant and m_d is the mass of a dipole.

In the above classical approach an electric charge in motion dissipates energy continuously, which implies that there is a loss of kinetic energy arising from photon emission, leading to damping of dipole motion. From this view point we may be able to define the loss of total energy (E_T) of a dipole by considering the equilibrium point in its steady state of oscillating motion (Figure 6.2).

In considering the oscillatory motion it is implied that the dipole after being displaced from the position at $x = 0$ reaches a maximum distance $x = x_m$, at which point the centre of mass tries exerts a restoring force by bringing the end mass of dipole towards the centre. Consequently, at $x = x_m$, the dipole motion momentarily becomes zero leading to a condition that allows us to quantify the total energy at this point (Equation 6.14a):

$$E_T = \tfrac{1}{2}\kappa_d (x_m)^2 = 2(\pi\upsilon_o x_m)^2 m_d \tag{6.14a}$$

From this condition the energy dissipated per unit time (power) may be derived using the Poynting vector concept from electricity and magnetism, which yields the radiative power

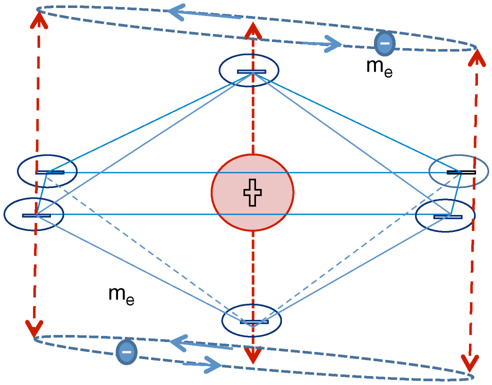

Figure 6.2 *Schematic representation of two symmetrically positioned (4f) electrons in a rare-earth cation in an octahedral co-ordination shell of crystal or glass. The central positive charge represents the rare-earth ions, the oblate negative charge represents each oxygen anion, forming the octahedral cage; m_e represents a 4f-electron (dipole) bound within the shell structure and performing a linear harmonic motion. (See colour plate section.)*

(P_d) of a dipole:

$$-\frac{\mathrm{d}E_\mathrm{T}}{\mathrm{d}t} = P_\mathrm{d} = \frac{16\pi^3 \upsilon_o^4 (ex_\mathrm{o})^2}{3c^3 \varepsilon_\mathrm{o}} = \frac{\omega_o^4 (ex_\mathrm{o})^4}{3\pi \varepsilon_\mathrm{o} c^3} \tag{6.14b}$$

By combining Equations 6.14a and 6.14b, the solution for energy decay may be written as shown in Equation 6.14c:

$$E_\mathrm{T}(t) = E_\mathrm{T}(t=0)\exp\left(-\frac{t}{\tau_\mathrm{o}}\right) = E_\mathrm{T}(t=0)\exp\left(-t\gamma_\mathrm{o}\right) \tag{6.14c}$$

where $\tau_\mathrm{o} = (1/\gamma_\mathrm{o}) = (A_\mathrm{o})^{-1}$ is the radiative rate quantified in s^{-1}.

By including the damping factor (γ_o) into the original Equation 6.13a for the dipole motion, a much more general form of equation of dipole motion may be written that includes not only the restoring force term but also the damping factor, as shown below in Equation 6.15a. The solution for Equation 6.15 is given in Equation 6.15b:

$$\left[m_\mathrm{d}\frac{\mathrm{d}^2x}{\mathrm{d}t^2} + m_\mathrm{d}\gamma_\mathrm{o}\cdot\frac{\mathrm{d}x}{\mathrm{d}t} + \kappa_\mathrm{d}x = 0\right] \tag{6.15a}$$

$$E_\mathrm{T}(t) = E_\mathrm{o}\cdot\exp\left[-\left(\mathrm{i}\omega_\mathrm{o} + \frac{\gamma_\mathrm{o}}{2}\right)t\right] \tag{6.15b}$$

Note that the overall form of Equation 6.15b is same as in Equation 6.13b. This equation is valid for all $t \geq 0$ and $E_\mathrm{T}(t) = 0$ for $t < 0$. This implies that the dipole begins emitting photons at $t \geq 0$ and then decays exponentially. Since we know the form of the energy equation, it is then possible to define the intensity by taking the modulus of the square of $E(t)$, i.e. $|E(t)|^2$, which yields the intensity of photons, $I(t)$:

$$\begin{aligned} I(t) &= I_\mathrm{o}\cdot\exp\left[-(\gamma_\mathrm{o} + 2\mathrm{i}\omega_\mathrm{o})t\right] \\ I(t) &= 0 \end{aligned} \tag{6.16}$$

The above two conditions are valid for $t \geq 0$ and $t < 0$, respectively. In this mathematical analysis, the coherence of emitting photons is not considered. Using Equation 6.16, the population inversion of the electronic states may be redefined by considering the damping factor, which then amends Equation 6.11a to give a new form shown in Equation 6.17:

$$N_{i\to j}(t) = N_{i\to j}(0)\exp\left[\left(-\sum \gamma_\mathrm{o}^{i\to j}\cdot t\right)\right] \tag{6.17}$$

Equation 6.17 is a general form defining the damping factor for individual transitions in a multi-excitonic system.

6.4 Factors Influencing the Line Shape Broadening of Optical Transitions

For analysis of line shape of optical transitions, a simplified two-level (1 → 2) system, as shown in Figure 6.1, may be considered. If the total number of excited states at level 2 is N_2 then the overall distribution of frequencies (υ) for all possible transitions between these two levels may be represented by $g(\upsilon,\upsilon_o)$, then the spectral distribution of states may be mathematically expressed as:

$$\int_0^{\infty} N(\upsilon)\,\mathrm{d}\upsilon = N_2 \int_0^{\infty} g(\upsilon,\upsilon_\mathrm{o})\,\mathrm{d}\upsilon = N_2 \tag{6.18a}$$

from which it is implied that:

$$\int_0^{\infty} g(\upsilon,\upsilon_o)\,\mathrm{d}\upsilon = 1 \tag{6.18b}$$

Rewriting Equation 6.18a in a derivative form:

$$N(\upsilon)\,\mathrm{d}\upsilon = g(\upsilon,\upsilon_\mathrm{o})\,\mathrm{d}\upsilon \cdot N_2 \tag{6.18c}$$

where the term $g(\upsilon,\upsilon_o)$, as explained in the Einstein model, is the probability of an optical transition at a given frequency, υ. The corresponding energy gap of the optical transition is then between $h\upsilon$ and $h(\upsilon + d\upsilon)$. If we consider a frequency representation of either an emission spectrum or an absorption spectrum as a continuum over a frequency range υ and $(\upsilon + d\upsilon)$, then the overall line shape of the absorption and emission curves represent the cumulative probability, which is equal to unity for all possible optical transition frequencies between $\upsilon = 0$ and $\upsilon = \infty$. For this condition if we then review Equation 6.2, the spontaneous emission rate for the above frequency range may be then written as in Equation 6.19:

$$-\frac{\mathrm{d}N_2}{\mathrm{d}t} = A_{21} N_2 g(\upsilon,\upsilon_o)\,\mathrm{d}\upsilon \tag{6.19}$$

In terms of the intensity or the electric field distribution of overall energy, it is possible to use Equation 6.16 and define the maximum intensity I_o as:

$$I_\mathrm{o} = \int_0^{\infty} I(\omega)\,\mathrm{d}\omega \tag{6.20a}$$

from which we may be able to define the full-width of half-maximum (FWHM) in Figure 6.3 using the damping factor (γ_o) in Equation 6.20b:

$$I(\omega)_\mathrm{FWHM} = \frac{I_\mathrm{o}}{\pi\gamma_\mathrm{o}} \tag{6.20b}$$

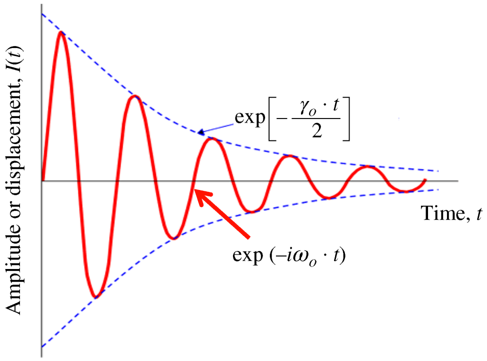

Figure 6.3 *Schematic representation of time dependent decay of intensity* I(t) *of electric field or emission of photons with time, owing to the loss of energy due to a damping factor, which may be of a forced nature.*

where:

$$\Delta\omega_{\mathrm{FWHM}} = 2(\omega - \omega_{\mathrm{o}}) = \gamma_{\mathrm{o}} = \frac{1}{\tau} = 2\pi\Delta\upsilon_{\mathrm{FWHM}} \tag{6.20c}$$

Our main question at this point is to determine the "intrinsic line width of an optical transition". Let us consider an optical transition in which the energy spread of the ground state is ΔE_{gr} and that of the excited state ΔE_{ex}. If we now aim to ascertain the uncertainty in the energy spread of both these states we can then use the quantum mechanical principle for energy and time, i.e.:

$$\Delta E\,\Delta t \geq \frac{h}{2\pi} \tag{6.21a}$$

where Δt is the minimum uncertainty in determining the spread of energy by determining the lifetime τ_{ex}, which then means:

$$\Delta E_{\mathrm{ex}} = \frac{\hbar}{\tau_{\mathrm{ex}}} = \hbar\sum_{i}^{j}(\tau_{\mathrm{ex}})^{-1} \tag{6.21b}$$

For the ground state the energy spread may be then written as in Equation 6.21b:

$$\Delta E_{\mathrm{ex}} = \frac{\hbar}{\tau_{\mathrm{gr}}} = \hbar\sum_{i}^{j}\left(\tau_{\mathrm{gr}}\right)^{-1} \tag{6.21c}$$

By adding Equations 6.21b and 6.21c, the total uncertainty in the spread of energy may be given by the cumulative sum of radiative rates as shown in Equation 6.21d. This spread of energy we designate is as the "*total intrinsic broadening*" ($\Delta E_{\mathrm{T}}^{\mathrm{in}}$) and is also referred as the "lifetime broadening":

$$\Delta E_{\mathrm{T}}^{\mathrm{in}} = \Delta E_{\mathrm{ex}} + \Delta E_{\mathrm{gr}} = \hbar\left[\sum \tau_{\mathrm{ex}}^{-1} + \sum \tau_{\mathrm{gr}}^{-1}\right] \tag{6.21d}$$

Using Planck's law $\left(\Delta E_{\mathrm{T}}^{\mathrm{in}} = \hbar\Delta\omega_{\mathrm{Total}} = h\Delta\upsilon_{\mathrm{Total}}\right)$ yields:

$$\Delta\upsilon_{\mathrm{T}}^{\mathrm{in}} = \frac{\left[\sum \tau_{\mathrm{ex}}^{-1} + \sum \tau_{\mathrm{gr}}^{-1}\right]}{2\pi} \tag{6.21e}$$

The transition from excited to ground states may also be represented by the damping constant (γ) such that:

$$\Delta E_{\mathrm{T}}^{\mathrm{in}} = \hbar\gamma_{\mathrm{T}}^{\mathrm{in}} = \hbar\left[\sum \gamma_{\mathrm{ex}} + \sum \gamma_{\mathrm{gr}}\right] \tag{6.21f}$$

In considering the *additional emission broadening mechanism* we consider that the radiation emission is a "many-photon" process involving "many-body excitonic states", possibly interacting with other states in a complex manner, which may involve the lattice structure (host), in which the excitonic states are physicochemically bound (like a tenant in a rental accommodation). The external sources of interference or energy exchanges may change the "intrinsic characteristics" by adding their own feature which characterizes the perturbation. Let us designate such factors as "*extrinsic broadening*".

The first type of line broadening is via the non-radiative process. The origin of the non-radiative process is the chemical environment of excitons in which the neighbouring states exchange energy via collisional process arising from the lattice vibrations. Since the excitonic states are the result of radiation absorption, in this process the dipole motion, which is the cause of radiation emission, becomes tethered due to the excitonic–lattice interaction. The tethering of excitons is manifested as non-radiative emission (mostly as heat) through lattice vibration. Using Equations 6.14c and 6.21f, the overall damping effect for all levels involved may be redefined as:

$$\hbar\gamma_{\mathrm{T}}^{\mathrm{in}} + \hbar\gamma_{\mathrm{Coll}} = h(\Delta\upsilon)_{\mathrm{T+Coll}} \tag{6.22a}$$

which then yields:

$$\Delta\upsilon_{\mathrm{T}} = \Delta\upsilon_{\mathrm{T}}^{\mathrm{in}} + \frac{\left[\sum \tau_{\mathrm{Coll}}^{-1}\right]}{2\pi} \tag{6.22b}$$

In Equations 6.22a and 6.22b the collisional part includes the contributions from the ground and excited states. An example of collisional interaction may be due to the concentration effects in which two neighbouring excitons interact by allowing the other to relax to the ground state. Such a process may not lead to photon emission. A corollary of concentration quenching is impurity induced quenching where an impurity ion or species irreversibly absorbs energy from the excitonic states and transforms it into heat through molecular vibrations. A well-known example of this effect is the exchange of energy between OH^- and Er^{3+} ions. Since most non-radiative processes are statistically determined, the shape of line broadening is "homogeneous" and mathematically may be described by using a Lorentzian function (Figure 6.4a). In conclusion, the collisional broadening is dependent on the environment of the dipole.

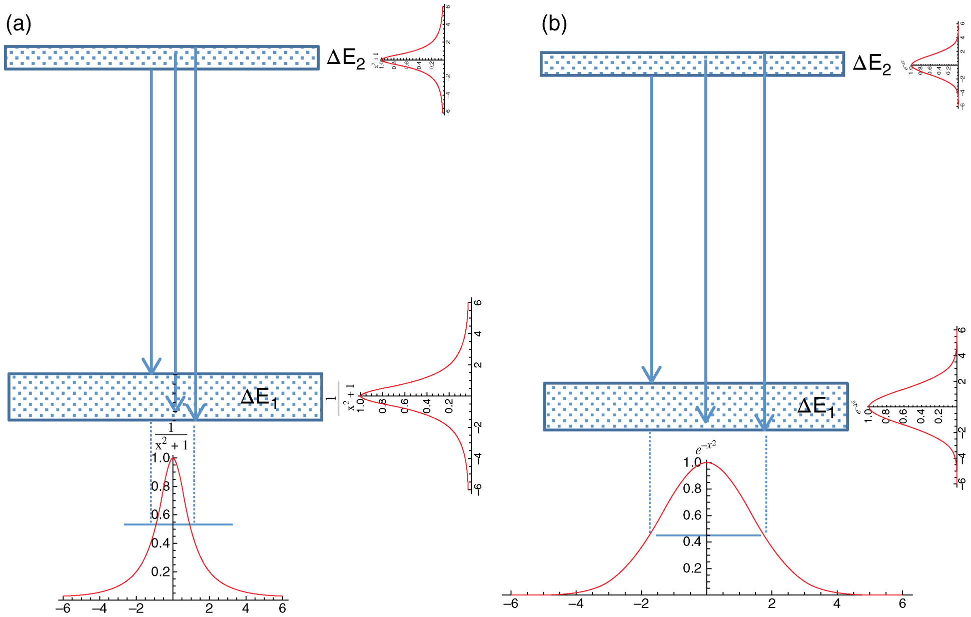

Figure 6.4 *Comparison of (a) Lorentzian and (b) Gaussian spectral shapes representing homogeneous and inhomogeneous broadening, respectively of optical transitions in a hypothetical two-level system. Note that the FWHM in a Lorentzian is smaller than that in a Gaussian which may be inhomogeneously broadened due to host–ion interaction.*

In another type of collisional broadening the effect is more subtle as it involves dipole interaction in which the phase of the moving dipole is perturbed. In this process of phase interruption, the broadening is homogeneous with a broadening mechanism which may be described by a Lorentzian function. A graphical example of phase interruption riding underneath the decay curve is shown in Figure 6.4b. In this case the effect of dephasing may arise due to interaction with unlike electric or magnetic dipoles in the host. Since the phase interruption is observed within the envelope of a sinusoidal function, the dephasing lifetime is much shorter, which may then be explained using Fourier analysis [1]. The observed dephasing lifetime is also known as the T_2 lifetime. By including the dephasing term in the overall broadening, Equation 6.22b changes to:

$$\Delta\upsilon_{\mathrm{T}} = \Delta\upsilon_{\mathrm{T}}^{\mathrm{in}} + \frac{\left[\sum \tau_{\mathrm{Coll}}^{-1}\right]}{2\pi} + 2\left[\tau_{\mathrm{DPh}}^{-1}\right] \tag{6.22c}$$

A number of these homogeneous broadening mechanisms are mathematically discussed in detail by Fox [3] and Silfvast [1]. The equation for a normalized homogeneous broadening is given in Equation 6.23a in which υ_o is the centre frequency:

$$I(\upsilon) = I_o \left[\frac{\gamma_{\mathrm{T}}^{\mathrm{in+Col}} \Big/ 4\pi^2}{\left\{ (\upsilon - \upsilon_o)^2 + \left(\frac{\gamma_{\mathrm{T}}^{\mathrm{in+Col}}}{4\pi} \right)^2 \right\}} \right] \tag{6.23a}$$

The maximum then in the frequency spectrum occurs at $2/(\pi\Delta\upsilon)$.

The inhomogeneous broadening is the collective effect of all the states in a medium. This is quite apparent in dielectric materials doped with either transition metal or rare-earth ions. Because the chemical environment of ions changes rather differently in crystalline and glassy hosts, the inhomogeneous broadening represents the cumulative effect of site dependencies of the dopant ions. Examples of inhomogeneous broadening are considered later, in the example sections later in this chapter. This type of broadening also includes Doppler broadening (as in Doppler shift) which is a result of an apparent shift in the central frequency $\left(= \upsilon_o\left[1 \pm (v/c)\right]\right)$ of moving dipoles with a phase velocity v with respect to a reference point. The overall effect of a Doppler shift is a Gaussian curve, as is the case also with crystal based inhomogeneous broadening. The line shape of an inhomogeneously broadened Gaussian [2] is then given by Equation 6.23b:

$$g(\upsilon) = \frac{2}{\Delta\upsilon} \cdot \left(\ln 2 \Big/ \pi \right)^{0.5} \exp\left[-\ln 2 \left\{ \frac{2(\upsilon - \upsilon_o)}{\Delta\upsilon} \right\}^2 \right] \tag{6.23b}$$

and the peak at:

$$g(\upsilon_o) = \frac{2}{\Delta\upsilon} \left(\ln 2 \Big/ \pi \right)^{0.5} \tag{6.23c}$$

6.5 Characteristics of Dipole and Multi-Poles and Selection Rules for Optical Transitions:

In this chapter we will focus on several inorganic glass hosts whose structural and optical properties have been discussed in previous chapters. Two different types of dopant ions, namely the trivalent lanthanide rare-earth metal (Ln^{3+}) and selected transition metals, will be discussed as examples. We will only focus on glasses with selected rare-earth ions as dopant in this chapter in terms of characterizing the light emitting spectroscopic. The spectroscopic properties of selected transition metals (e.g. bismuth ion) with other device properties are discussed in Chapter 7 briefly.

6.5.1 Analysis of Dipole Transitions Based on Fermi's Golden Rule

To analyse the radiative rate in a multi-electron system in solids, e.g. in a rare-earth or transition metal ion doped glass, we need to determine Einstein coefficients. In this respect, we will follow an elegant approach which Fox [3] has explained in *Quantum Optics: An Introduction*. The quantum mechanical analysis of radiative transition rates is based on time-dependent perturbation theory, in which the transition probabilities for spontaneous photon emission may be calculated using *Fermi's golden rule* defining the transition rate between the active energy levels:

$$W_{2\to 1} = \frac{2\pi}{\hbar} |M_{21}|^2 g(\hbar\omega) \tag{6.24a}$$

Here $g((\hbar\omega)$ represents the number density of states lying between $E + \mathrm{d}E$ and $E = \hbar\omega$, in a given volume. The description of Equation 6.24a if examined closely is comparable with Fermi's model for electron density of states. The term $|M_{21}|$ is the matrix element which from perturbation theory designates the quantum mechanical elements of light–matter interaction. In this approach to characterizing the matrix element, the active ions as dopants or electronic defects are treated as quantum defects whereas the photons are treated in a classical way as a part of dipole motion. In this semi-classical approach the matrix element $M_{2\to 1}$ may be defined as a matrix element of H', representing the perturbation caused by the external electromagnetic field:

$$M_{12} = \langle 2|H'|1\rangle = \int \psi_2^*(r) H'(r) \psi_1(r)\, \mathrm{d}^3 r \tag{6.24b}$$

Here $\psi_1(r)$ and $\psi_2^*(r)$ are the initial and final wave function states, respectively. Let us consider what H' signifies in terms of external perturbation, assuming that the ions or defects are active electric dipoles. If the amplitude of incident electric field (electromagnetic field) is $\vec{E}$, and $\vec{p}_\mathrm{e}$ represents the electric dipole moment then the perturbation Hamiltonian is a scalar product:

$$H' = -\vec{p}_\mathrm{e} \cdot \vec{E} \tag{6.24c}$$

Since $\vec{p}_\mathrm{e}$ is the dipole moment we can express it in terms of electronic charge (e) and $\vec{r}$ (the radial distance vector in the direction the dipole moment is active) as $\vec{p}_\mathrm{e} = -e\vec{r}$. Usually for all three directions, H' may be expressed as:

$$H' = e\left(r_x E_x + r_y E_y + r_z E_z\right) \tag{6.25a}$$

An important assumption here is whether there is likely to be a spatial distribution of electric field around the dipole. Since the ionic and electronic defects are dimensionally much smaller than the wavelength of photons, the spatial distribution of amplitude of the electric field around a defect is insignificant. This implies that the overall potential energy is uniformly small around a defect or dopant, which means that each of the matrix elements for three directions of polarizations can be written in a general form:

$$M_{1\to 2}^{(x,y,z)} = eE^{(x,y,z)} \int \psi_2^*(r)(x,y,z)\psi_1(r)\,\mathrm{d}^3\vec{r} \tag{6.25b}$$

By using the vectorial properties of dipoles and their respective wave functions:

$$M_{1\to 2} = -\vec{\varphi}_{12}\cdot\vec{E}_{\mathrm{o}} \tag{6.26a}$$

where:

$$\vec{\varphi}_{12} = -e\left(2|x|1\hat{i} + 2|y|1\hat{j} + 2|z|1\hat{k}\right) \tag{6.26b}$$

In Equation 6.26b each directional matrix element for dipole moment is represented with a respective unit vector, $\hat{i}, \hat{j}, \hat{k}$. In other words, the uniaxial (e.g. x direction) vector representation of a dipole moment is:

$$\varphi_{12} = -e\langle 2|x|1\rangle \equiv -e\int \psi_2^*(r)x\psi_1(r)\,\mathrm{d}^3\vec{r} \tag{6.26c}$$

which is the most important parameter in controlling the probability of optical transitions. Using Equation 6.24a, defined above, it is now possible to calculate the transition probabilities for each state in a degenerate energy level for radiation absorption and emission at angular frequency ω_{ij} by estimating or determining the respective Einstein coefficients ($B_{i\to j}$) and ($A_{j\to i}$). By including additional quantum numbers m_i and m_j, the radiative transition probabilities may be expressed as follows for g_j values of the degenerate upper states:

$$A_{ji} = \frac{e^2}{3\pi\varepsilon_{\mathrm{o}}\hbar}\left(\frac{\omega_{ji}}{c}\right)^3 \frac{1}{g_j}\sum_{m_j,m_i} |\langle j,m_j|r|i,m_i\rangle|^2 \tag{6.27a}$$

and the corresponding oscillator strength (f_{ij}) is then directly related with the dipole moment of the transition:

$$f_{ij} = \frac{2m\omega_{ji}}{3\hbar}|\langle j|r^{\rightarrow}|\rangle i|^2 \equiv \frac{2m\omega_{ji}}{3\hbar e^2}|\phi_{ij}|^2 \tag{6.27b}$$

When $\phi_{12} = 0$, neither photon absorption nor light emission will occur. Therefore, whether we deal with a classical or quantum mechanical approach for radiation emission, quantifying the dipole moment and emerging oscillator strength is essential.

However, the quantum mechanical concept also further limits the optical transition by imposing *selection rules* [1,3]. For inorganic crystals and glasses with dopants or quantum defects, the selection rule for a multi-electron system is important to consider because the selection rules for a "hydrogen-atom" system with one electron is not valid. Briefly the "general multi-electron selection rules" are:

1. The wave functions $\psi*(r)$ and $\psi(r)$ must have opposite parity [↓↑] for the non-zero value of integrand in the perturbation model equation (e.g. Equation 6.26c). Note that the states with *odd orbital angular momentum* quantum numbers (L) possess *odd parity*. By contrast *the momenta with even quantum numbers have even parity.*
2. For even numbers of odd-parity electrons the energy level has odd parity, and if there are odd numbers of odd-parity electrons, the energy level is odd parity, which means it is necessary to determine how many of the subshells are unfilled with odd parity. This is because filled shells have even numbers of odd-parity electrons. In summary, $\Delta\ell = \pm 1$ for changing electrons.

Table 6.1 *Comparison of range of values of Einstein coefficient (A) and radiative lifetimes for multipoles in the visible frequencies, which are shown as an estimate only. Complex calculations may be required using a suitable model, wherever necessary. Note that the radiative lifetimes equal to the inverse of A [3]. Source: Fox (2006). Reproduced with permission from Oxford University Press.*

Transitions and notations	Einstein coefficient, A (s^{-1})	Radiative lifetimes (n: nano, m: milli)	Parity change
Electric dipole (E1)	10^7–10^9	1–100 ns	Yes
Magnetic dipole (M1)	10^3–10^5	0.01–1 ms	No
Electric quadrupole (E2)	10^3–10^5	0.01–1 ms	No
Magnetic quadrupole (M2)	0.1–10	0.1–10 s	Yes
Electric octupole (E3)	0.1–10	0.1–10 s	Yes

3. $\Delta L = 0, \pm 1$; however, $\Delta L = 0 \to 0$ is a forbidden transition.
4. Similarly, the J momenta rule defines $\Delta J = 0, \pm 1$ and $\Delta J = 0 \to 0$ is a forbidden transition. Rules 3 and 4 arise from the fact that the angular momentum of photons is unity.
5. Finally, $\Delta S = 0$ means that the photons do not interact with the spin states.

The above selection rules applies to simple dipole transitions; however, in higher order magnetic dipole and electric quadrupoles, the wave functions become more complex and demonstrate $|\vec{r}|^2$ dependency in the integral containing opposite parity wave functions. The lifetimes of such interactions are much longer, as summarized below in tables. This is definitely the case when dealing with the rare-earth ions in glasses and crystals because of a large number of (4f) electrons involved, as discussed below. The analytical situation for selection rules is more complex in transition metals because of strong interaction of 3d → 4 s transition shells with the host. Fox [3] summarizes the relaxation rates for different types of multipolar pairs in Table 6.1.

Note that in Table 6.1 the transition lifetimes of complex multipoles are longer because these may have limited pathways for relaxation to the ground state. Note that the multipoles are the consequence of space-charge, and therefore the symmetry elements are inherent in their structure due to the distribution of electronic density of states. These will become much clearer when we consider electronic configurations below in rare-earth and transition metal ions.

6.5.2 Electronic Structure and Some Important Properties of Lanthanides [1,5–7]

The "lanthanide" series, as the name suggests, starts with lanthanum (La) in Table 6.2 with its electronic structure is [Xe]$5d6s^2$, where [Xe] designates the electronic structure of xenon, an inert gas element, with complete electronic shells [$1s^2$ . . . $4d^{10}5s^25p^6$] in lanthanide elements. It should be noted that the elemental electronic structure of each lanthanide differs from the corresponding ionic state.

For lanthanum, the energy difference in 5d and 4f is in favour of the 5d level occupancy, meaning that the (4f)-shell in lanthanum is vacant. However, lutetium (Lu), the last member of the lanthanide series, has a complete (4f) shell with electronic structure: [Xe]$(4f)^{14}5d^o6s^2$. The second member of lanthanide series is cerium (Ce) and it stands out from the remaining lanthanides, because of its peculiar electronic states, [Xe]$4f^15d^16s^2$. Cerium has both 4+ and 3+ valance states as a result, which are stable because of 4f-5d transition. In the series from praseodymium (Pr) to europium (Eu), there are no 5d shells, instead the 4f shell continues

Table 6.2 *Electronic structures of lanthanide atoms and ions and co-ordination numbers. Note that the rare earth ions Nd^{3+}, Tm^{2+}, and Yb^{3+} have also odd-number co-ordination shells.*

Rare-earth elements electronic structure		RE ions, electronic structures and ground state energy levels			Ionic radius (Å)		Co-ordination shell [7]
					Reference [6]	Reference [5]	
La	$[Xe]5d^1 6S^2$	La^{3+}	$[Xe]$	$^1S_0$	1.17	1.03	6
						1.16	8
						1.27	10
						1.36	12
Ce	$[Xe]4f^1 5d^1 6S^2$	Ce^{4+}	$[Xe]4f^0$	$^1S_0$	1.15	0.87	6
		Ce^{3+}	$[Xe]4f^1$	$^2F_{5/2}$		0.97	8
						1.07	10
						1.14	12
						1.01	6
						1.14	8
						1.25	10
						1.34	12
Pr	$[Xe]4f^3 6S^2$	Pr^{4+}	$[Xe]4f^1$	$^2F_{5/2}$	1.13	0.85	6
		Pr^{3+}	$[Xe]4f^2$	$^3H_4$		0.96	8
						0.99	6
						1.13	8
Nd	$[Xe]4f^4 6S^2$	Nd^{4+}	$[Xe]4f^2$	$^4I_{9/2}$	NA	NA	NA
		Nd^{3+}	$[Xe]4f^3$		1.12	0.98	6
						1.12	8
						1.16	**9**
						1.27	12
Pm	$[Xe]4f^5 6S^2$	Pm^{3+}	$[Xe]4f^4$	$^5I_4$	1.11	0.97	6
						1..09	8
Sm	$[Xe]4f^6 6S^2$	Sm^{3+}	$[Xe]4f^5$	$^6H_{5/2}$	1.10	0.96	6
		Sm^{2+}	$[Xe]4f^5 6S^1$	$^7F_0$	1.32	1.08	8
						1.24	12
						1.19	6
						1.27	8
Eu	$[Xe]4f^7 6S^2$	Eu^{3+}	$[Xe]4f^6$	$^7F_0$	1.09	0.95	6
		Eu^{2+}	$[Xe]4f^6 6S^1$	$^8S_{7/2}$	1.31	1.07	8
						1.17	6
						1.25	8
						1.35	10
Gd	$[Xe]4f^7 5d^1 6S^2$	Gd^{3+}	$[Xe]4f^7$	$^8S_{7/2}$	1.08	0.94	6
						1.05	8
Tb	$[Xe]4f^9 6S^2$	Tb^{4+}	$[Xe]4f^7$	$^8S_{7/2}$	1.06	0.76	6
		Tb^{3+}	$[Xe]4f^8$	$^7F_6$		0.88	8
						0.92	6
						1.04	8
Dy	$[Xe]4f^{10} 6S^2$	Dy^{3+}	$[Xe]4f^9$	$^6H_{15/2}$	1.05	0.91	6
		Dy^{2+}	$[Xe]4f^9 6S^1$	$^5I_8$		1.03	8
						1.07	6
						1.19	8
Ho	$[Xe]4f^{11} 6S^2$	Ho^{3+}	$[Xe]4f^{10}$	$^5I_8$	1.04		
Er	$[Xe]4f^{12} 6S^2$	Er^{3+}	$[Xe]4f^{11}$	$^4I_{15/2}$	1.03	0.89	6
						1.00	8
Tm	$[Xe]4f^{13} 6S^2$	Tm^{3+}	$[Xe]4f^{12}$	$^3H_6$	1.02	0.88	6
		Tm^{2+}	$[Xe]4f^{12} 6S^1$			0.99	8
						1.01	6
						1.09	**7**
Yb	$[Xe]4f^{14} 6S^2$	Yb^{3+}	$[Xe]4f^{13}$	$^2F_{7/2}$	1.01	0.99	8
		Yb^{2+}	$[Xe]4f^{13} 6S^1$		1.16	**1.04**	**9**
						1.02	6
						1.14	8
Lu	$[Xe]4f^{14} 5d^1 6S^2$	Lu^{3+}	$[Xe]4f^{14}$	$^1S_0$	1.00	0.86	6
						0.97	8

to fill in Pr [Xe]$(4f^3)6s^2$ until Eu with [Xe]$(4f)^7 6s^2$. In this process of shell filling, all seven 4f-shells of lanthanide elements starting from Ce until Eu are partially filled with one electron in each shell. Gadolinium is the eighth element in the series and its structure is [Xe] $(4f)^7 5d^1 6s^2$. At this mid-point in electron filling, the states again follow a similar trend as observed between Pr and Eu. Terbium (Tb) is the ninth lanthanide element with structure [Xe]$(4f^9)6s^2$, showing that the 5d-shells are unoccupied. The terbium trend in electronic shell configuration continues from dysprosium (Dy) [Xe]$(4f)^{10} 6s^2$ to ytterbium (Yb) [Xe] $(4f)^{14} 6s^2$. The elemental electronic structure configuration then implies that for ionic structure, e.g. for La^{3+}, the configuration is [Xe] and that for Lu^{3+} is [Xe]$4f^{14}$. In Table 6.2 selected properties of rare-earth elements, ions and compounds are compared.

The lanthanide elements form stable oxides, phosphates, sulfide/oxysulfides and halides and surprisingly a range of other compounds such as carbonates and fluorocarbonates, the latter occurring in the natural environment. Besides Ce^{4+}, both Tb^{4+} and Pr^{4+} are commonly reported in mixed oxide forms e.g. Tb_4O_7 and Pr_5O_9 in which both 4+ and 3+ states exist as Magnelli phases, which are quite common in the TiO_2 (rutile) group of oxides. However, the 4+ states in terbium and praseodymium are less stable and they readily decompose at elevated temperatures by releasing molecular oxygen:

$$Tb_4O_7 \rightarrow 2Tb_2O_3 + 0.5O_2(g)$$

The oxides in the middle of the lanthanide series, e.g. Eu and Sm, also form divalent oxides which are metastable and form under partially reducing condition for:

$$Eu_2O_3 + H_2(g) \rightarrow 2EuO + H_2O(g)$$

at elevated temperatures.

The cationic radius of a Ln^{3+} ion decreases with increasing atomic mass and number of electrons in the shell (Table 6.2). In this table wherever possible the ionic radii are also compared for different co-ordination environment, from which it is clear that the ionic radius is directly proportional to the co-ordination cage, i.e. the larger the co-ordination number the bigger is the ionic radius. The data from Cotton and Wilkinson [5] when compared with that from the *Handbook of Physics and Chemistry* [6] suggest a good agreement for $CN = 8$. Note that in this table CN values of 7 and 9 are also reported for Nd, Tm and Yb ionic states. The odd value CNs implies that the symmetry elements for these RE-ligands is not uniform in a 3D-space, which also suggests that the multipolar motions may be non-symmetrical, thereby adding complexity in the analysis of accompanying wave functions.

By considering $CN = 8$ for rare-earth ions, the ionic radius of lanthanide (Ln^{3+}) ions decreases monotonically from 1.17 Å for La^{3+} to 1.00 Å for Lu^{3+} due to the lanthanide contraction of the nucleus, which then affects the strong coulombic interaction for electrons, too. The size factor may therefore affect the solubility of trivalent rare-earth ions in a given glass matrix, which we will discuss below by making comparisons of rare-earth oxide solubility in different types of inorganic glasses.

The rare earth elements also demonstrate paramagnetic properties due to the spin state of the (4f) electrons. In Figure 6.5 the elemental or molecular paramagnetic susceptibility (χ, $cm^3\ mol^{-1}$ or g-atom^{-1}) increases with the atomic number until the $(4f + 5d)$ electron number is 8 for gadolinium, after which the paramagnetic susceptibility drops monotonically towards lutetium. Note that this increase in paramagnetism in gadolinium reaches a maximum due to the presence of $7 + 1$ unpaired electrons; in comparison lanthanum has

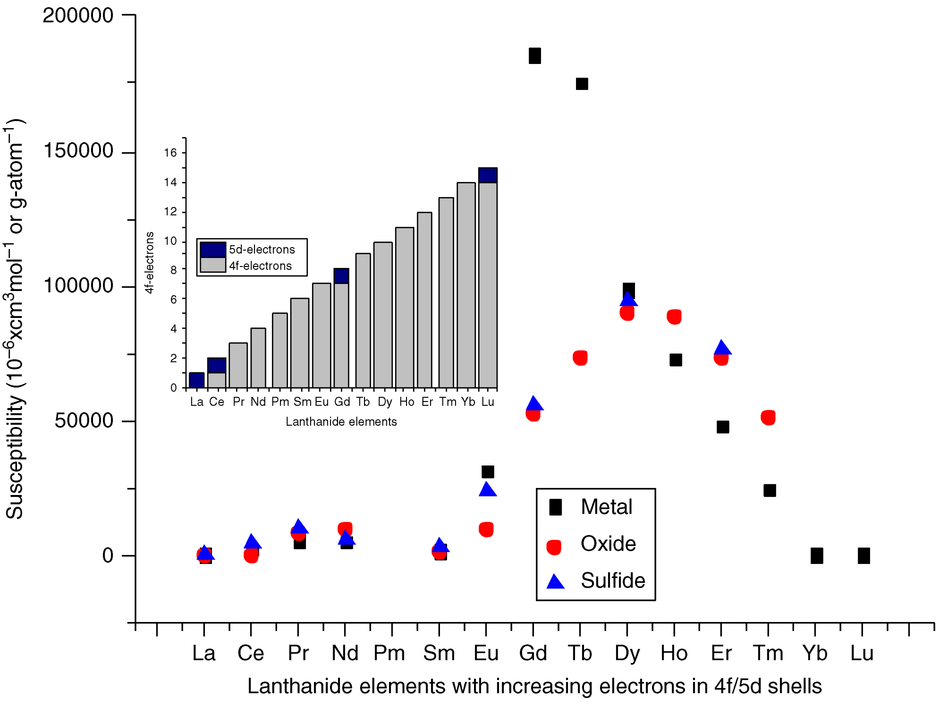

Figure 6.5 *Plot of atomic and molecular susceptibility of lanthanide elements/oxides/sulfides with increasing atomic number of elements. Inset: total number of occupied 4f and 5d electrons [6].*

only one 5d electron. At the end of lanthanide series ytterbium has 14 paired electrons and lutetium has 14 (4f) and one unpaired 5d electrons. The examples in Figure 6.5 and Table 6.2 may help in characterizing complex dipole or multipole structures in trivalent rare-earth ions, complex dipoles and multipoles, responsible for light absorption and emission processes in dielectric hosts.

6.5.3 Laporte Selection Rules for Rare-Earth and Transition Metal Ions

In accordance with the *Laporte selection rules*, the following transition are allowed and forbidden, which then perhaps sets the genesis of optical absorption and emission by taking into the consideration the symmetry elements of electronic configurations in inorganic solids [7]. Based on this approach the electronic transitions giving rise to absorption spectra are those in which:

(a) The electronic transitions are confined to the atomic or ionic geometry.

(b) The exchange of states occur between atoms or ion pairs.

These two types of generalized transition approaches are summarized in Figure 6.6a–c and are commonly known as the *Laporte allowed and forbidden optical transitions*, respectively.

(c) The transitions between s → p and f → d are *Laporte allowed* due to parity change. These are classed as *intershell* transitions.

(d) The *Laporte forbidden* transitions are between d → s, f → f and d → d which are inter- and *intrashell* transitions, respectively.

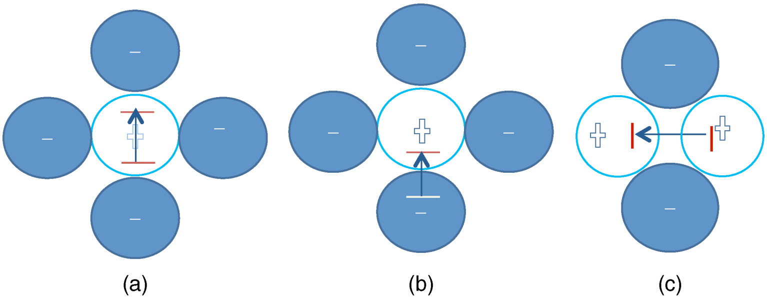

Figure 6.6 *Schematic representation of oscillator models based on electronic transitions, based on Laporte rules: (a) a generic intrashell and (b) and (c) intershell transitions [7]. Source: Duffy 1990. Reproduced with permission from Longman. (See colour plate section.)*

Duffy [7] classed the above transitions as *Type 1*, occurring in the most generic ionic or atomic topological situation. In his schematic illustrations in Figure 6.6a–c, *Type 2* transitions represent many-body atomic or ionic systems in which complex electronic interactions may arise. Amongst Type 2 transitions are:

(a) discrete molecular orbitals in crystals and glasses in which the anions and metallic cation may be involved in excitonic exchange;
(b) charge transfer band type process, in which anions from valence band and metallic cation with empty conduction band state may be active; the charge transfer may also arise between valence band and unperturbed orbital of a metal ion;
(c) the third and final type of electronic exchange may arise between like cations residing in adjoining co-ordination shells.

From the oscillator strength discussion above, the absorption spectra are related to the strength of the oscillator. In this respect, all Type 2 (a)–(c) are *Laporte allowed intershell transitions*. Considering the quantum mechanical nature of the matrix in the oscillator strength equations, the extinction coefficients of absorption bands are 2–3 orders of magnitude stronger than the *Laporte forbidden transitions*, which are significantly weaker. The strength of a *Laporte forbidden transition* is further weakened if it is spin forbidden.

The electronic structure of transition metal ions is based on the 3d-4 s transition showing a range of variable valencies. Unlike the shielded $(4f)^n$ shells in lanthanides, the ionic states in transition metals have open shell structures, which means that the ligand field interaction of these ions with the host is much stronger via the overlapping of the electronic wave functions in the top of valence bands of host ions with the 3d–4 s shells of the dopant. For transition metals, perturbation model based analysis, described in Equations 6.24a–6.27b, may be in general applicable. However, for considering dipolar or multipolar interaction in transition elements, the electronic configurations of d-shells and their symmetry elements must be considered. The strength of overlapping wave functions makes the selection rules more complex and these are manifested in the inhomogeneously broadened absorption and emission spectra of transition metal dopants, as summarized below after the Laporte selection rule. The evidence of line shapes in the literature for transition metals clearly suggests that line broadening mechanisms are also complex due to a range of homogeneous and inhomogeneous mechanisms, which may be affected by both intrinsic and extrinsic factors, discussed above.

These rules in the Laporte model deviate from the original definition because of the complex wave functions and symmetry elements of the electronic configurations which are not identical for every dopant, whether they be a trivalent rare-earth ion or a transition metal ion. Besides the electronic structure of ions themselves, the presence of electronic configurations of valence band of a host also perturbs the wave functions and yields non-zero integrals or oscillator strengths. Such effects are called “vibronic” transitions, which is a combinatorial effect of collisional (vibration) and non-collisional (intrinsic) effects. The rules for “spin-forbidden” transitions may be relaxed due to spin–orbit coupling in transition metal ions. Examples of f-f and vibronic transitions are explained later in this chapter.

A summary of the ground states for all trivalent state of lanthanide elements is listed in Table 6.2; they are based on the Russell–Saunders notations, ${}^{2S+1}$L notations. Here L and J are the total orbital angular momentum and total angular momentum quantum numbers, respectively. L is defined by the letters S, P, D, F, G, H, I . . . , corresponding to $L = 0, 1, 2, 3, 4, 5, 6$ . . . respectively. Since the rare-earth ions, being so large in size, represent a multi-electron system the L and S are not clearly distinguishable quantum numbers for representing the electronic states, because the magnitude of spin–orbit interaction is comparable with the non-central component of electron–electron interaction. By comparison, J is a unique quantum number for such states and each one is $(2J + 1)$-fold degenerate. As an instance, if we then deal with examples of ground state transitions in Table 6.2, the ${}^1S_0$ transitions for Ce^{4+} and Lu^{3+} are classed as singlet level with zero splitting of the ligand field and occur in the UV at 50 900 cm^{-1} (6.311 eV). These transitions are therefore unaffected by phonon interactions and other extrinsic factors. Other examples of above ground state singlet transitions in Pr^{3+}, shown in Figure 6.7, are ${}^1G_4$ (10 000 cm^{-1} = 1.24 eV), ${}^1D_2$ (16 600 cm^{-1}

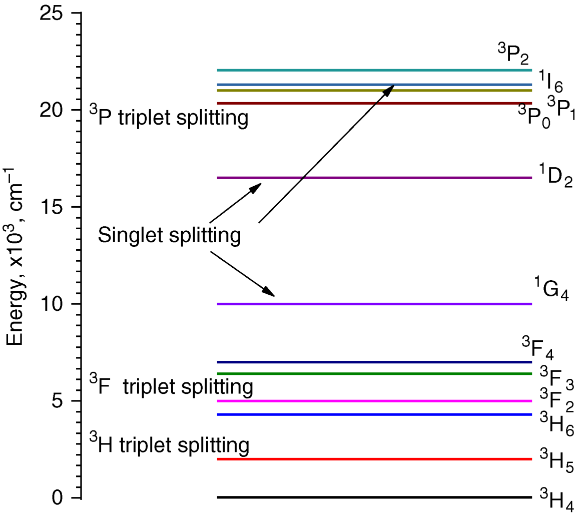

Figure 6.7 *Examples of singlet and triplet splitting of states in the* Pr^{3+}*-ion. Note the juxtaposition of triplet states in comparison with the singlet states which are separated by several thousands of wavenumbers. The third singlet state,* ${}^1S_0$ *in* Pr^{3+} *is at 50 000 cm*$^{-1}$ *(not shown here) in* Pr^{3+}*-doped crystals and glasses. The* ${}^1D_2$ *and* ${}^3P_2$ *have the strongest intensities amongst singlet and triplet states, respectively.*

= 2.05 eV). Detailed analysis of energy levels and the influence of chemical environment of host may be carried out by studying the ground state absorption spectra to see how f-f and f-d states mix, depending on the site symmetry and strength of oscillators, which appears to be true for all lanthanide trivalent states. In trivalent rare-earth ions the effect of host interaction therefore produces a range of distribution of energy states, which may not remain identical. It is for these reasons that the optical transitions in crystals differ greatly from that in a glassy state, lacking in three-dimensional crystalline periodicity. The absence of periodicity in glass creates a wide range of dopant site symmetry due to variations in the local electro-static field. In a nutshell, the site symmetry and coordination field of dopant ions are critical in the analysis of both absorption and emission spectra of both types of ions, rare earth and transition metals.

Based on ligand field theory, the optical transitions in transition metal ions may be analysed with the help of widely known Tanabe–Sugano diagrams and Racah parameters—methods of calculating these are discussed by Duffy [7] and by Imbusch and Kopelman [8]. Besides the dipole model discussed above, the *configurational co-ordinate model* (CCM) is particularly relevant for transition metal ion dopants. In this model, the *configurational co-ordinate* diagram is constructed by showing individual ground and excited states of a dopant in a crystalline host, for example. Using the matrix element analysis for dipoles in the ground and excited states, the optical transitions are determined by plotting the wavelength versus intensity curve, which is basically the line shape profile of all possible transitions. In considering the optical transitions, the model also considers the creation and annihilation of phonons. The details of CCM may be found elsewhere [8] with an example of ruby laser host material.

For transition metal dopant ions the crystal field or ligand field strength is determined by the value of Δ or $10D_q$ and the corresponding Racah parameters, A, B and C, have also been reported for a range of transition metals in oxide, fluoride and sulfide hosts. These are summarized in Table 6.3.

Next we will discuss briefly the theories and characterization of radiative and non-radiative processes that determine the apparent lifetimes of the excited states in key trivalent rare-earth ions for which the devices are extensively used commercially. In this respect, we briefly discuss the analysis of radiative, multiphonon decay, radiation quenching and energy transfer rate processes for their significance in the overall process of device design. Although recent developments in Bi-ion doped glasses [9] and laser and amplifier devices are highly significant, the spectroscopic processes involved in achieving light amplification are discussed in Chapter 7 together with device engineering.

6.6 Comparison of Oscillator Strength Parameters, Optical Transition Probabilities and Overall Lifetimes of Excited States

The host dependence of radiative rates for optical transitions is explained by the magnitudes of the Judd–Ofelt parameters, Ω_2, Ω_4 and Ω_6, which are calculated from measurements of the absorption coefficient for various transitions, refractive index and density of a given host [10–12]. The values of the omega Judd–Ofelt parameter determines the magnitude of oscillator strength, and therefore the radiative rate (W_R (s^{-1})).

In rare-earth ion doped glasses the electric field of neighbouring ions (e.g. in a zinc sodium phosphate glass, the multipolar ion pairs, namely the P^{5+}-O^{2-}, Na^{+}-O^{2-} and Zn^{2+}-O^{2-})

Table 6.3 Optical transitions in transition metal ions and their corresponding absorption strengths in various co-ordination fields.

Absorption energies (cm^{-1}) for **Cr^{3+}** -ions in an octahedral co-ordination field					
Optical transitions	Cr_2O_3	Cr^{3+} in Al_2O_3(ruby)	Cr^{3+} in MgO	Cr^{3+} in oxide glass	Cr^{3+} in fluoride glass
${}^4A_{2g}(F) \rightarrow {}^4T_{1g}(P)$	29 500	39 100	29 700	33 700	33 900
${}^4A_{2g}(F) \rightarrow {}^4T_{1g}(F)$	21 700	25 700	27 700	22 300	22 470
${}^4A_{2g}(F) \rightarrow {}^2T_{1g}(G)$	14 200	14 430	16 200	15 750	15 380
${}^4A_{2g}(F) \rightarrow {}^4T_{2g}(F)$	16 600	18 100	—	15 250	14 710
${}^4A_{2g}(F) \rightarrow {}^2E_g(P)$	—	—	—	14 600	—
10Dq (cm^{-1})	16 600	18 000	—	15 330	14 720
$B/B_{free\text{-}ion}$, $B_{free\text{-}ion} = 918\ cm^{-1}$	0.52	0.71	—	0.80	0.87
Absorption energies (cm^{-1}) for **Cr^{2+}** -ions in an octahedral co-ordination field					
${}^5E_g(D) \rightarrow {}^5T_{2g}(D)$	—	—	—	13 200	11 900
10Dq, cm^{-1}	—	—	—	13 200	11 900
$B/B_{free\text{-}ion}$, $B_{free\text{-}ion} = 810\ cm^{-1}$	—	—	—	Not known	Not known
Absorption energies (cm^{-1}) for **Mn^{2+}** -ions in an octahedral co-ordination field				**Mn^{2+}** in ZnS structure at a tetrahedral site	
	MnF_2	MnO	MnS		
${}^6A_{1g} \rightarrow {}^4T_{1g}(G)$	19 400	16 400	16 700	18 900	
${}^6A_{1g} \rightarrow {}^4T_{1g}(G)$	23 500	20 800	19 800	20 100	
${}^6A_{1g} \rightarrow {}^4T_{1g}(G)$	25 200	23 800	22 200	21 600	
${}^6A_{1g} \rightarrow {}^4T_{1g}(G)$	25 300				
10Dq	7800	9400	7100		
B/B_{free}, $B_{free} = 860\ cm^{-1}$	0.94	0.88	0.89		

Absorption energies (cm^{-1}) for **Co^{2+}** -ions in *cubic* in CaF_2 and *octahedral* co-ordination fields in MgO, oxide (Ox) and fluoride (F) glass					Absorption energies (cm^{-1}) for Co^{2+}-ions in a tetrahedral co-ordination field			
Transitions	CaF_2	Co^{2+}-MgO	Ox-Glass	F-Glass	Transitions	Co^{2+}-ZnO	Co^{2+}-ZnS	Co^{2+}-CdS
$^4T_{1g} \rightarrow {}^4T_{2g}(P)$	3200, 3500	8500	7500	6620	$^4A_2 \rightarrow {}^4T_1(F)$	6100, 7000, 7500	6600	5200, 6500
$^4T_{1g} \rightarrow {}^4T_{2g}(F)$	5900, 6600	17 200		11240	$^4A_2 \rightarrow {}^4T_1(P)$	15 300, 16 400, 17 600	14 400	13 600, 14 100, 14 500
$^4T_{1g} \rightarrow {}^4T_{2g}(P)$	17 800, 18 500, 19 200	19 600	19 500	18 520	10Dq	3800	3850	—
10Dq, $B/B_{f,f} = 971$	3400, 0.96	9600, 0.84	8590, 0.90	6500, 0.95	$B_f = 971\ cm^{-1}$, B/B_f	0.78	0.64	

	Optical transitions		ZrF$_4$ glass		Oxide glass		GLS glass	
Ti^{3+} in an octahedral field	$^2T_{2g}(D) \rightarrow {}^2E_g(D)$		19 230		20 830			
V^{3+} in an octahedral field	$^3T_{1g}(F) \rightarrow {}^3T_{2g}(F)$		23 260		23 500			
	10Dq V^{3+}	B/B_f (V^{3+})	1578	0.82	1675	0.76		

interact with the dopant ions and cause inhomogeneous splitting of the energy levels [11,13,14] when compared with the dopant ions in a free-space with minimal extrinsic coulombic interference. Similarly, the magnetic components of a local field (i.e. a magnetic dipole) also affect the structure of energy levels; however, the magnetic dipoles for a state are typically 10^{-6} times weaker than an electric dipole. As discussed above, the 4f electrons in trivalent rare-earth ions are shielded by outer shells of electrons in the $(Xe)4f^n5s^25p^66s^2$ structure; the energy distribution and sharpness of absorption and emission spectra of a rare-earth ion is manifested by the magnitude of host and dopant ion interaction. The consequence of electronic screening in 4f-electrons narrows the number of available states in comparison with the broad 3d-electronic transitions in transition metal ions. The energy distributions of absorption and emission spectra in rare-earth ions are much narrower than that in a transition metal ion, which is consistent with Heisenberg uncertainty principle means $\Delta E \cdot \Delta\tau \geq \hbar/2$. This uncertainty condition implies that the metastable lifetime ($\Delta\tau$) of the occupied states is much longer in rare-earth ions than that in transition metal ions in a given glass or crystalline host.

The method of Judd–Ofelt analysis is extensively discussed in Reference [11] and for this reason this aspect will not be covered in this textbook. The aperiodic structure of inorganic glass offers a range of chemical environments for dopant ions of transition and rare-earth ion series, many of which are discussed quite extensively in textbooks and the literature. The aperiodicity of the three-dimensional structure in glass may contribute to the multi-variant co-ordination environment which is not as precisely defined as in a periodic structure. For example, because most oxide glass formers have either three- or fourfold cations around oxygen atoms, as discussed in Chapter 1, the consequential structural arrangement may depend on the concentrations of intermediate and modifier ions, which then reconfigure the network forming structures thereby allowing the overall structure to accommodate dopant ions. As an example, Figure 6.8 shows the sevenfold co-ordination of Er^{3+}-ions in a xenotime ($LnPO_4$: Ln designates rare-earth elements) crystal, from which it is evident that the Er^{3+}–Er^{3+}ion distance is more than the Er^{3+}–O^2 distance. The xenotime structure approximation may be quite realistic for considering the co-ordination environment in most phosphate and rare-earth oxide containing glasses, including silica fibres in which both of these oxides are incorporated for active optical fibre engineering. Consideration of co-ordination shell

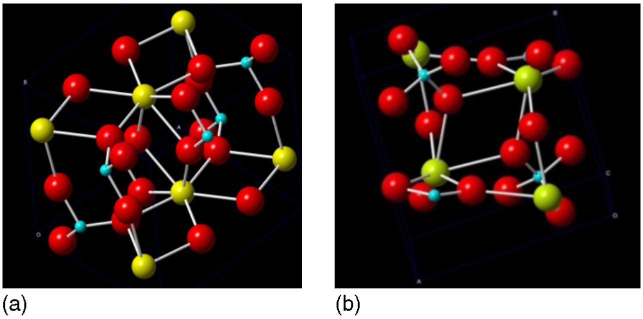
(a) (b)

Figure 6.8 *Crystal structures of (a) xenotime ($YbPO_4$) and (b) monazite ($CePO_4$) using the American Mineralogy Crystal Database. Red, yellow/green and cyan spheres designate oxygen, rare-earth and phosphorus, respectively. Note that the coordination of rare-earth ions with oxygen in xenotime (YPO_4) is seven compared with four in monazite ($CePO_4$) [15]. Source: Ni 1995. Reproduced with permission of Mineralogical Society of America. (See colour plate section.)*

structure is also essential in the analysis of like-ion (e.g. Er^{3+}–Er^{3+}) interaction during the energy exchange processes.

The apparent optical transition rate ($W_{i\rightarrow j}$ (s^{-1})) between the ground state (i) and adjoining and higher metastable upper manifolds, j, is a complex process in a multi-electron system. It involves not only the radiative rate $(W_R)_{j\rightarrow i}$ term but also the non-radiative $(W_{NR})_{i\rightarrow j}$, ($s^{-1}$)) and energy transfer $(W_x)_{p\rightarrow q}$ rates, which may be defined as the sum of these three rate terms, as shown below [16]:

$$(W)^{i\to j}\left(s^{-1}\right) = \sum_j \left(W_i^j\right)_{\mathrm{NR}} + (W_x) + \left(W_i^j\right)_{\mathrm{R}} = \frac{1}{\tau_{\mathrm{NR}}} + \frac{1}{\tau_x} + \frac{1}{\tau_{\mathrm{R}}} \tag{6.28}$$

Here τ_{NR}, τ_x and τ_R are the single-ion non-radiative, inverse of the effective energy transfer and radiative lifetimes of the transitions, respectively, from the metastable manifold j to the ground state. In considering the rate equation (Equation 6.28), the sub-Stark multiplets may be considered for including all possible transitions by utilizing the notations, discussed above. As explained in the previous section on the collisional model, when the dopant concentrations in a host is below a certain value, the energy transfer rate between the ions does not dominate. Its effect may be neglected for concentrations below 2000 ppm weight; however, once a threshold level is reached the effective energy transfer rate (W_x) must be considered by including the bidirectional rates, i.e. the forward and reverse transfer rates arising due to the increasing competition amongst the states at the metastable level, j. A corollary of energy transfer is also the exchange of energy between the activator and donor ions when these two states are resonant. This process may be quite dominant in certain dopants, e.g. in Cr^{3+} co-doped Er^{3+}-phosphate glass laser gain media, Yb^{3+}-ion sensitized Er^{3+}-ion doped and Tm^{3+}-Ho^{3+} co-doped devices.

6.6.1 Radiative and Non-Radiative Rate Equation

Below we have readapted the Einstein equation (6.27a) and that for the oscillator strength (6.27b) for ease of understanding and utilizing the absorption and emission cross-sections in the equations for determining the respective oscillator strengths. The oscillator strength (f) of absorption from a given ground state i to a higher-lying j multiplet, from which the optical transitions may occur, depends upon the corresponding integrated absorption (σ_{ab}) and stimulated emission (σ_{St}) cross-sections over the frequency spectrum ($\int \nu \, d\nu$); the two equations are shown below [10]:

$$f_{\mathrm{ab}} = [4\pi\varepsilon_{\mathrm{o}}]\frac{mc}{\pi e^2}\int \sigma_{\mathrm{ab}}(\nu)\,\mathrm{d}\nu \tag{6.29a}$$

$$f_{\mathrm{em}} = [4\pi\varepsilon_{\mathrm{o}}]\frac{mc}{\pi e^2}\int \sigma_{\mathrm{St}}(\nu)\,\mathrm{d}\nu \tag{6.29b}$$

Here $[4\pi\varepsilon_o]$ designates the permittivity in electrostatic units and m and e are the mass and charge of an electron, respectively. For stimulated emission from j multiplet to the ground state i, the f_{ab} and f_{em} are related and determine the radiative rate (W_R) [1,10,11,13]:

$$f_{\mathrm{em}} = \frac{g_i}{g_j} f_{\mathrm{ab}} \tag{6.30a}$$

$$W_{\mathrm{R}} = \frac{8(\pi e n)^2}{[4\pi\varepsilon_{\mathrm{o}}]mc^3\lambda_{j\to i}{}^2}\cdot\left(\frac{g_i}{g_j}\right) f_{\mathrm{ab}} \tag{6.30b}$$

where $\lambda_{j \to I}$ is the emission or lasing wavelength. From Equation 6.30b we can establish that the radiative rate is proportional to f_{ab}, g_i/g_j: the degeneracy ratio, and the materials refractive index, n. As discussed in the section on dipole moments above and in Chapter 4, the refractive index n depends on the dielectric constant (ε) and permittivity (ξ) of a medium. Note that these two physical properties are structurally dependent on the electronic states in the host material and the band gap. In general, in a large refractive index medium such as the tellurite and chalcogenide families of glasses, in which the values of n may be much larger than 2, the radiative rates will be proportionately larger than that in a standard silicate glass with an index ranging between 1.44 and 1.55.

The overall rate, as explained above in Equation 6.28, is also dependent on the non-radiative components, such as the multiphonon decay rate and the non-radiative energy transfer. The occupied states above ground level j may relax radiatively or non-radiatively back to the ground state i, depending on the magnitude of ΔE, the energy gap. Non-radiative relaxation to the ground state occurs via collisional interaction of excitons with the coupled phonons which then tether the dipole motions by damping down to the ground state. The energy released is in the form of heat. The process effectively shortens the lifetimes of the upper state. Multiphonon decay may also be triggered by the presence of impurities whose spectral width of absorption band may be resonant with the line width of energy gap, ΔE. The coupled phonons (host or impurity) around the dopant ions participate by creating a phonon bridge that then reduces the energy of occupied states. Formation of a phonon bridge is a quantum mechanical process, which requires several phonons to come together as a staircase to initiate the relaxation of electronic states (Figure 6.9). This is an efficient way of depleting pump energy without generating light and should be minimized in engineering laser and amplifier gain media. From the point of view of relaxation then the coupling constant parameter, α_{ep}, and the vicinal phonon energy, $\hbar\omega$, determine the rate of multi-phonon decay, as explained in Equation 6.31a [10–13]:

$$W_{\text{NR}} = W_{\text{MP}}(T) = A_1 \exp\left(-\alpha_{\text{ep}} \Delta E\right)[1+n]^p \tag{6.31a}$$

$$n = \left[e^{\frac{\hbar\omega}{\kappa T}} - 1\right]^{-1} \tag{6.31b}$$

and the coupling constant is expressed using the Reisfeld–Jørgensen model, shown below [12]:

$$\alpha_{\text{ep}} = (\hbar\omega)^{-1}\left[\ln \frac{p}{q(n+1)} - 1\right] = -(\hbar\omega)^{-1} \ln \varepsilon_{\text{ep}} \tag{6.31c}$$

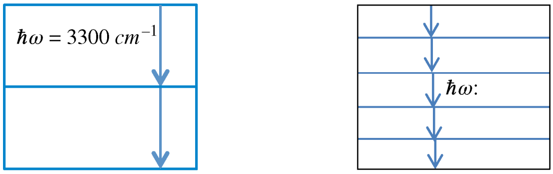

Figure 6.9 The phonon staircase for relaxation of electronic states from level j to the ground state, I, e.g. in Er^{3+} : ${}^4I_{13/2} \to {}^4I_{15/2}$. Considering ΔE is 6600 cm^{-1}, two 3300 cm^{-1} phonons from OH^- and approximately five 1300 cm^{-1} phonons from a phosphate glass are required to bridge the gap. The latter is quantum mechanically less probable than that with OH^- ions.

Table 6.4 *Comparison of parameters for multiphonon decay rates, $W_{mp}(T)$ (cf. Equation 6.31a–c) in different hosts, recompiled from Reference [18] and expanded. Source: Miniscalco 1993. Reproduced with permission from Marcel Dekker.*

Host glass type	A_1 (s^{-1})	$\alpha_{ep} \times 10^{-3}$ (cm)	$\hbar\omega$ (cm^{-1})
Borate	2.9×10^{12}	3.8	1400
Phosphate	5.4×10^{12}	4.7	1200–1300
Silicate	1.4×10^{12}	4.7	1100
Germanate	3.4×10^{10}	4.9	880
Tellurite	6.3×10^{10}	4.7	700–780
Fluorozirconate	1.59×10^{10}	5.19	500–600
GaF_3-PbF_2	10^7	7.4	450
Cd(F,C)	10^7	9.94	300–450
LaF_3	6.6×10^8	5.6	350
Sulfide	$\sim 10^6$	2.9	340–460

where $W_{MP}(T)$ is the multiphonon relaxation rate at a temperature T, and p is the number of phonons required to bridge the ΔE gap, and is equal to $p = \Delta E/(\hbar\omega)$ (see Table 6.4).

The above equations imply that if ΔE is small the simultaneous probability of participating phonons, p, for forming a required staircase will be large. This then helps in explaining the decay process using the combination of the Bose–Einstein equation (6.31b) and Equation 6.31c—the overall multiphonon rate will decrease exponentially. The term q is related with the electron–phonon coupling constant. As the energy gap ΔE increases, the staircase mechanism becomes probabilistically less likely with smaller phonon energy as a collection of steps. The metastable lifetimes of excited states therefore may either be prolonged or shortened, depending on the magnitudes of phonon energy structure ($\hbar\omega$), coupling constant (α_{ep}) and ΔE. When comparing the rare-earth doped glasses with transition metals, the analytical approach to non-radiative rate analysis is far more complex because of the open 3d-4 s electronic shell, which allows the transition states to couple strongly with the host's electronic states. Consequently, the lifetimes of the excited states are much shorter, e.g. the lifetime of emission (800–1050 nm) in Ti^{3+}-doped sapphire is less than 10 μs, compared to emission in, say, Yb^{3+}-doped glass at 1020–1100 nm with nearly 100 times longer lifetimes. Mathematically, the analysis is more complex and requires calculations of the shape and the depth of potential energies of transition states using, for example, the Huang–Rhys model [17].

A characteristic feature of the overall radiative and non-radiative model is the presence of a zero-phonon line in rare-earth and transition metal dopants. Amongst the rare-earth ions, only Yb^{3+} : $^2F_{7/2} \rightarrow {}^2F_{5/2}$ has a sharp zero-phonon line, compared with optical transitions in, say, Cr^{3+} and Cr^{4+} doped crystals and glasses. The zero-phonon line has a narrow linewidth, as expected, due to virtually no interaction with the host phonons [8].

6.6.2 Energy Transfer and Related Non-Radiative Processes

In a rare-earth ion doped glass, the collisional contribution may also manifest in the form of energy exchange, which may lead to loss of emitted radiation via energy exchange. Quimby explains how the rate of population loss due to energy transfer (W_x) can be determined at low and high concentrations using Equation 6.28 [10]. To simplify the analysis, the multiphonon and other non-radiative energy processes are neglected. At low concentrations W_x is negligible. At higher concentrations the difference between the measured lifetimes and that in lower concentrations in Equation 6.28 without radiative and non-radiative contributions yields the representative value of W_x. The energy transfer is also temperature dependent, as explained by Tanimura and co-workers [19], and is shown in Equation 6.32 which is a Maxwell–Boltzmann function:

$$W_x(T) = W_x(\infty)\cdot\exp\left[-\frac{\Delta E}{\kappa_B T}\right] \tag{6.32}$$

where $W_x(\infty)$ is the transfer rate at an elevated temperature, κ_B is Boltzmann's constant and T is the absolute temperature. In the above equation, if the acceptor level energy is at a lower value than the donor level, then the forward transfer rate is classed as the Stoke energy transfer. By comparison, the backward rate from the acceptor (low) to donor (high) then becomes an anti-Stoke process. The probability of an anti-Stoke process is less than that of a Stoke and depends on the magnitude of ΔE. Quimby [11] reviewed the transfer rates in fluoride hosts for different ions and made sound comparisons for different hosts and dopants. A detailed analysis of Er^{3+}-doped zinc tellurite hosts with different concentrations and temperature was reported [20], in which it was shown that both the temperature (40–310 K) and concentrations (0.2–4 mol.%) affect the transfer processes. The optical transitions studied [20] were $^4S_{3/2} \rightarrow {}^4I_{15/2}$ (554 nm) and $^4F_{9/2} \rightarrow {}^4I_{15/2}$ (663 nm). The observed upconversion process has been explained in terms of enhanced Er^{3+} ion concentrations, in relation with the green upconversion. In this investigation [21], the non-radiative model for energy transfer was also proposed instead of the standard non-radiative rate decay model of Riseberg and Moos [21]. The microscopic mechanism of energy transfer is discussed in detail by Quimby [10] and Ohishi [11], in which the roles of dipole–dipole and dipole–quadrupole interactions are explained. The energy transfer rates for some rare-earth doped tellurite glasses are compared in Table 6.5 with selected fluoride glasses.

Amongst the energy exchange models, the explanation of microscopic processes involved may be classified into two types ions in the vicinity: *the exchange of energy between (i) two like ions* and *(ii) two unlike ions*. This approach may be assumed to be like a pair of donor–acceptor states exchanging energy which in condition (i) occurs between two like ions and in

Table 6.5 *Comparison of energy transfer rate parameters for rare-earth ions in different tellurite and fluoride glass hosts [10,16].*

Glass	Ion	Level	$W_x(\infty)$ (s^{-1})	ΔE (cm^{-1})	N (wt%)	Reference
Fluoride glass	Er^{3+}	$^4I_{13/2}$	78	33	2	Tanimura *et al.* [19]
Fluoride glass	Ho^{3+}	$^5I_7$	150	5	2	Tanimura *et al.* [19]
Fluoride glass	Pr^{3+}	$^1D_2$	1100	4	0.5	Adam & Sibley [22]
Fluoride glass	Pr^{3+}	$^1D_2$	6800	8	1.0	Adam & Sibley [22]
Fluoride glass	Yb^{3+}	$^2F_{5/2}$	5000	55	27	Yeh *et al.* [23,24]
Zinc tellurite	Er^{3+}	$^4S_{3/2}$	1.3×10^{-5}			Jaba *et al.* [20]
Sodium zinc tellurite	Er^{3+}	$^4I_{13/2}$		175		Jha *et al.* [25,26]

(ii) arises between two unlike ions. The most important condition for such *energy exchanges* is that these arise only when the concentrations of donor–acceptor pair is high and/or the oscillator strength between the pair is acceptable. Secondly, the exchange path length for energy migration is important, since the energy needs a medium in which to migrate. In this respect a detailed theoretical approach based on multipolar interaction was developed by Nakazawa and Shionoya [27] using Equation 6.33. The cumulative emission intensity of donors, $I_\mathrm{D}(t)$, decays as a result of multipolar interactions with acceptors:

$$I_\mathrm{D}(t) = \exp\left[-\left(\frac{t}{\tau_\mathrm{o}}\right) - \Gamma\left(1-\frac{3}{s}\right)\left(\frac{C}{C_\mathrm{o}}\right)\left(\frac{t}{\tau_\mathrm{o}}\right)^{\frac{3}{s}}\right] \tag{6.33}$$

In Equation 6.33, C is the acceptor concentration and C_o is called the critical transfer concentrations of acceptor and is given by a simplified geometrical model of reciprocal volume density of a state in Equation 6.34:

$$C_\mathrm{o} = \frac{3}{4\pi}\left(\frac{1}{R_\mathrm{o}}\right)^3 \tag{6.34}$$

In Equation 6.34 R_o is the distance between a donor–acceptor pair, at which the probability of electron transfer from donor to acceptor becomes equal to the probability given as $1/\tau_o$, which defines the cumulative probability of radiative and non-radiative processes of a donor state; τ_o is the decay constant of donor luminescence in the absence of acceptors, and s is a constant with values equal to 6, 8 and 10 for dipole–dipole, dipole–quadrupole and quadrupole–quadrupole interactions, respectively. The intensity of emission from a donor state under continuous excitation may be written as:

$$\frac{I}{I_\mathrm{o}} = \frac{1}{\tau_\mathrm{o}}\int_\mathrm{o}^{\infty} I(t)\,\mathrm{d}t \tag{6.35}$$

where I_o is the intensity in the absence of acceptors. Nakazawa and Shionoya [27] redefined the decay constant for experimental convenience. They then compared the results with a previous model, proposed by Inokuti and Hirayama [28], and reported the new results using the following modifications for critical concentrations, C_o, and by including the overlap integral S:

$$C_\mathrm{o} = kS^{-\left(\frac{3}{s}\right)} \tag{6.36}$$

$$S = \int_0^{\infty} \frac{I(E)\cdot\sigma(E)}{E^{s-2}}\,\mathrm{d}E \tag{6.37a}$$

$$\int I(E)\,\mathrm{d}E = 1 \tag{6.37b}$$

Here $\sigma(E)$ is the absorption spectrum of the acceptor, expressed by cross-section. Using the above approach, proposed in References [27] and [28], the critical distances for donor–acceptor pairs are calculated and compared in Table 6.6.

In a donor–acceptor type model, it is also important to note that for energy exchange the electronic edge of dielectric materials may also play an important role via resonant or non-resonant processes, especially in a waveguide geometry where multiple quanta of single

Table 6.6 *Estimated values of critical transfer distances, R_o (Å) from a range of experimental data and energy levels of resonant transition for Tb^{3+}-$(RE)^{3+}$ and Eu^{3+}-$(RE)^{3+}$ pairs [27] (see original reference for details). Source: Nakazawa 1967. Reproduced with permission from Elsevier.*

Donor–acceptor transition		Estimated values of R_o (Å)		
Donor state	Acceptor state	Emission intensity	Decay time	Overlap integral
$Tb^{3+} : {}^5D_4 \rightarrow {}^7F_6$	$Tb^{3+} : {}^7F_6 \rightarrow {}^5D_4$	—	—	5.3
$Tb^{3+} : {}^5D_4 \rightarrow {}^7F_6$	$Dy^{3+} : {}^6H_{15/2}$	4.6	5.5	4.5
$Tb^{3+} : {}^5D_4 \rightarrow {}^7F_5$	$Eu^{3+} : {}^7F_o \rightarrow {}^5D_1$	6.9	6.9	6.4
$Tb^{3+} : {}^5D_4 \rightarrow {}^7F_6$	$Sm^{3+} : {}^6H_{5/2}$	7.0	6.9	6.4
$Tb^{3+} : {}^5D_4 \rightarrow {}^7F_6$	$Tm^{3+} : {}^3H_6 \rightarrow {}^3F_3$	7.5	7.5	7.3
$Tb^{3+} : {}^5D_4 \rightarrow {}^7F_4$	$Pr^{3+} : {}^3F_4 \rightarrow {}^1D_2$	9.4	8.4	9.5
$Tb^{3+} : {}^5D_4 \rightarrow {}^7F_0$	$Er^{3+} : {}^4I_{13/2} \rightarrow {}^4F_{7/2}$	10.8	10.1	10.3
$Tb^{3+} : {}^5D_4 \rightarrow {}^7F_5$	$Ho^{3+} : {}^5I_8 \rightarrow {}^5S_2$	11.3	10.2	11.6
$Tb^{3+} : {}^5D_4 \rightarrow {}^7F_4$	$Nd^{3+} : {}^4I_{9/2} \rightarrow {}^4G_{5/2}$	12.3	12.3	12.4
	Europium rare-earth energy transfer			
$Eu^{3+} : {}^5D_4 \rightarrow {}^7F_6$	$Yb^{3+} : {}^2F_{7/2} \rightarrow {}^2F_{5/2}$	4.8	5.1	3.3
$Eu^{3+} : {}^5D_0 \rightarrow {}^7F_3$	$Er^{3+} : {}^4I_{15/2} \rightarrow {}^4F_{9/2}$	8.5	8.1	7.9
$Eu^{3+} : {}^5D_0 \rightarrow {}^7F_1$	$Nd^{3+} : {}^4I_{9/2} \rightarrow {}^4G_{5/2}$	12.8	10.5	11.5

frequency photons may yield a "staircase of photons", commonly known as "*multiphoton absorption*", which is intensity dependent. Amongst resonant energy transfer mechanisms the cross-relaxation of states is also quite dominant when the doping concentrations increase. In *cross-relaxation*, the higher-lying states exchange energy with the states at the ground level, and by exchanging the energy the direction flow of states culminates at an intermediate energy level which may be half-way between the ground and higher-lying states. Finally, in *excited state absorption* (ESA), which is comparable with multiphoton absorption except that in this process only one photon is involved, a pair of states exchange energy, as in cross-relaxation, to move in the opposite direction to occupy lower and higher energy states. ESA is quite commonly observed in most rare-earth transitions, especially when the occupied energy-exchange level states has a long lifetime. Some classic examples of such energy exchanges are:

i) An unlike pair energy exchange: $Yb^{3+} : {}^2F_{7/2} \rightarrow {}^2F_{5/2}$ donor–$Er^{3+} : {}^4I_{13/2} \rightarrow {}^4I_{15/2}$ acceptor.
ii) Like pair energy exchange: $Yb^{3+} : {}^2F_{7/2} \rightarrow {}^2F_{5/2}$ donor–$Yb^{3+} : {}^2F_{5/2} \rightarrow {}^2F_{7/2}$ acceptor in a gain medium. The same situation arises in Er^{3+}-based amplifiers where the like-ion energy exchange may create spectral holes during light amplification process: via $Er^{3+} : {}^4I_{13/2} \rightarrow {}^4I_{15/2}$ donor–$Er^{3+} : {}^4I_{15/2} \rightarrow {}^4I_{13/2}$ acceptor.
iii) Charge transfer band energy exchange where the donor states arise from valence to conduction band and then transfer to a neighbouring dopant ion, e.g. in the case of narrow band chalcogenide glass in which the band edge coincides with one of the discrete absorption bands of the dopant. A good example to consider is a Si semiconductor (1.1 eV band gap) implanted with $Yb^{3+} : {}^2F_{5/2} \rightarrow {}^2F_{7/2}$.

iv) The energy exchange may lead to quenching via $Er^{3+}: {}^4I_{13/2} \rightarrow {}^4I_{15/2}$ donor–$(OH)^-$ ion acceptor where the acceptor band is the first harmonic of $(OH)^{-1}$ in the range 1300–1500 cm^{-1}. Alternatively, the resonant band of OH^- at around 3300 cm^{-1} is partially coincident with the $Er^{3+}: {}^4I_{11/2} \rightarrow {}^4I_{13/2}$ transition at 2700 nm (~3700 cm^{-1}).

v) A classic example of ESA is in Er^{3+}-doped glasses and crystals when pumped with a 980 nm source to populate the ${}^4I_{11/2}$ level which has multiple hundreds of microsecond lifetimes, depending on the host glass or crystal. Two-photon ESA occurs at this level, in which one state from ground level (${}^4I_{15/2}$) reaches the ${}^4I_{11/2}$ level via exchanges of energy with a neighbouring state, followed by gain of identical quanta of energy from another photon to reach the ${}^4F_{3/2}$ level.

6.6.3 Upconversion Process

In all of the above light emission processes, the pump photon energy is larger than that of the emitted photons. As a result, such transitions are known as "down conversion". In upconversion, the higher energy states are populated via multiple photon absorption processes, as if it were a combination of excited state absorption (ESA). Examples of such transitions are known in Er^{3+}- and Tm^{3+}-ions, when pumped with, say, a diode laser in the range 780–810 nm. In Figure 6.10, taking the example of Tm^{3+}-ion, several of the energy exchange processes, including upconversion, may be explained using the energy level diagram. In this figure we have used coloured arrows for designating various radiative and

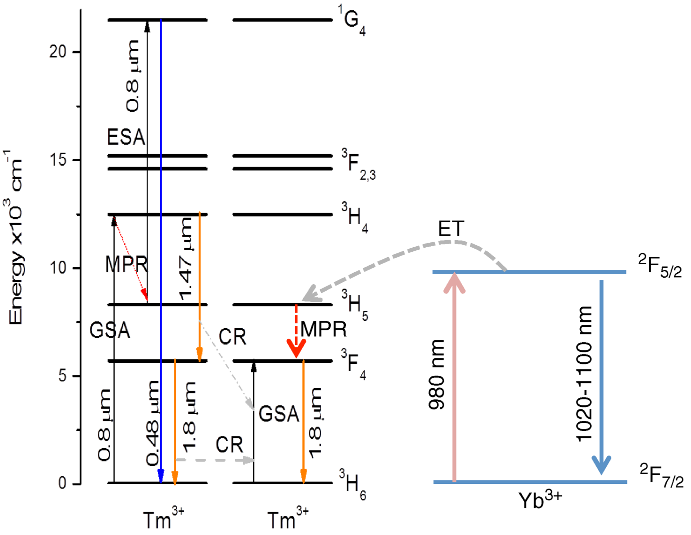

Figure 6.10 *Illustration of cross-relaxation (CR), multiphonon relaxation (MPR), excited state and ground state absorptions (ESA, GSA) in a pair of Tm^{3+} ions, shown with the aid of two energy level diagrams. Using the adjoining Yb^{3+} energy level diagram, energy transfer (ET) takes place between $Yb^{3+}: {}^2F_{5/2}$ and $Tm^{3+}: {}^3H_5$, followed by multi phonon relaxation (MPR) which de-excites the states to ${}^3F_4$, leading to an optical transition at 1.8 μm. The pump ESA at 980 nm also contributes to ESA from a complex co-operation of states between ${}^3F_4$, ${}^3H_5$ and ${}^3H_4$ to ${}^1G_4$, from where the blue upconversion occurs [29]. Source: Richards 2008. University of Leeds Library, PhD thesis.*

Table 6.7 *Comparison of upconversion efficiencies in various glasses doped with* Tm^{3+}*-*Yb^{3+} *and* Er^{3+}*-*Yb^{3+} *at 300 K. Incident light intensity 1 W* cm^{-2}*. BZYTLT glass composition (mol.%):* $19BaF_2$*-*$27ZnF_2$*-*$26YbF_3$*-*$27ThF_4$*-*$0.95LuF_3$*-*$0.05TmF_3$ *[31]. Source: Yeh 1988. Reproduced with permission from American Physical Society (J Applied Physics).*

Host materials	Yb^{3+}, x10^{20} (cm^{-3})	Er^{3+}, x10^{20} (cm^{-3})	Tm^{3+},x10^{20} (cm^{-3})	Efficiency
Fluoride glass	35.7	1.88	—	2×10^{-3}
Fluoride glass	21.4	1.43	—	1×10^{-3}
Silicate glass	9.3	0.31	—	2×10^{-7}
Phosphate glass	12.1	0.04	—	6×10^{-8}
CaF_2 crystals	25.0	2.5	—	2×10^{-3}
BZYTLT glass	48.4	—	1.86	5×10^{-3}
BZYTLT glass	48.4	—	0.093	$1.\times x10^{-2}$

non-radiative processes involved when a diode pumped 800 nm (0.8 μm) source was used to excite the ground states to $^3H_4$ level. The transition from $^1G_4$ to $^3H_6$ at 480 nm is upconversion emission from two-photon absorption at 800 nm (Figure 6.10).

A comprehensive review entitled "Upconversion and anti-Stokes processes with f and d Ions in solids" by Auzel [30] includes ESA, energy transfer, and single, double and co-operative upconversion processes. Readers may be able to benefit from the mechanistic understanding of upconversion given in this review. An example of Tm^{3+}-Yb^{3+} upconversion efficiency is compared in Table 6.7. This example supplements the explanation for the spectroscopic processes in Figure 6.10 in which it is evident that for upconversion to be efficient the multiphonon relaxation rate must be reduced, which is apparent from the efficiency data in Table 6.7.

Before giving examples of selected rare-earth and transition metal ions doped in inorganic glass hosts, the following points may be worth recapitulating for considering the engineering of efficient light emitting devices:

(a) Select and optimize the dopants that demonstrate large radiative rates due to their intrinsic oscillator strength(s) which might be further enhanced via host–ion interactions, e.g. in a large refractive index medium the radiative rate is larger when the same ions dwell in a low refractive index medium.
(b) In all direct band excitation schemes, it is essential to minimize the non-radiative components of overall rate process, described in Equation 6.28. However, if the pumping scheme is indirect, e.g. in Er^{3+} at $^4I_{11/2}$ using a 980 or 940 nm source, the non-radiative rate from $^4I_{11/2}$ to underlying $^4I_{13/2}$ must be large for populating this level.
(c) The energy transfer may be beneficial if the energy is migrating in the forward direction, as exemplified with the Yb^{3+}-Er^{3+} doping scheme. However, all energy depleting and quenching processes are detrimental for device engineering. These may be single- or multi-photon ESA and radiation quenching due to impurities in the host medium.

6.7 Selected Examples of Spectroscopic Processes in Rare-Earth Ion Doped Glasses

In this section we consider only the most commonly used dopant ions in inorganic glass hosts which have been realized as successful commercialized devices. This approach helps in focusing discussions on the spectroscopic features of such doped materials for different types of applications, which is covered in Chapter 7. For this reason the main discussion will be on Er^{3+} and Tm^{3+} ions as dopants in inorganic glasses. The spectroscopic properties of Nd^{3+} and Yb^{3+} in engineering high-power lasers will be covered in Chapter 7, where the spectroscopic properties of transition metal ion, e.g. $Bi^{(2+,1+)}$, doped glasses will be compared.

The popularity of the rare-earth ion doped glasses as a subject area has inspired many authors to write comprehensive reviews on rare-earth doped devices, which may be referred for supplemental knowledge [10,11,13,16,32]. In the examples discussed below attempts have been made to bring out the role of glass structure in determining the spectroscopic properties, which is the main emphasis in this book. For this reason, before examining in detail the spectroscopic properties of Er^{3+} and Tm^{3+} rare-earth ions, equilibrium solubility considerations and crystalline structures are discussed.

6.7.1 Spectroscopic Properties of Trivalent Lanthanide (Ln^{3+})-Doped Inorganic Glasses

In this section we first recapitulate the structures of various inorganic glasses discussed in Chapter 1. It is well known in the literature that silica glass is based on a strong network of $[(SiO)_4]^{4-}$ covalent structure with limited volume space around non-bridging oxygen, which is essential for doping rare-earth ions due to their complex polyhedron coordination shell—the thermodynamic probability of solubilizing and re-accommodating such trivalent ions is extremely small. As a result we see the sub-microscopic phase segregation of rare-earth ions, which then favours adverse spectroscopic features such as concentration quenching by reducing photoluminescence at room temperature. For this reason, it is necessary to modify silica glass structure during preform fabrication with a range of modifying oxides, namely Al_2O_3, P_2O_5 and GeO_2. Incorporation of these oxides during the flame deposition process (Chapter 3) increases the non-bridging oxygen sites where the trivalent rare-earth ions may be easily accommodated. As a result the solubility limits for rare-earth ions in modified silicate are enhanced substantially from less than 200 ppm to more than 2000 ppm by varying the ratios of Al_2O_3 and P_2O_5. The differences in electronegativity factors of these two modifying oxides contribute in enhancing the solubility of rare-earth ions, but also keep the ions dispersed via coulombic interaction, so that the adverse energy exchanges, discussed above, are minimized. The reason for microscopic segregation may be understood from the solubility limit diagram, shown below in Figure 6.11. The rare-earth silicate binary diagrams [34,35] (Figure 6.11a–c) clearly explain the immiscibility conditions, which are thermodynamically determined. The influence of decreasing ion size, from La^{3+} to Yb^{3+}, affords a marginal improvement in the solubility of rare-earth oxides in silicate mixtures, leading to the formation of complex silicates ($2SiO_2.La_2O_3$ etc.), which are not suitable for engineering rare-earth devices. By introducing phosphate into the silicate structure, the dispersion of rare-earth ions in the glass matrix tends to follow the co-ordination environment and site preferences of the parent crystals, such as in xenotime and monazite (Figure 6.8a and b). With the incorporation of phosphate groups into silicates, the larger cations of the lanthanide series preferentially form a monazite-like structure [15,35] whereas the smaller lanthanides tend to form xenotime, as exemplified in the respective crystalline forms in Figure 6.8a and b, from which the rare-earth ion distance(s) may be ascertained and compared with the data obtained in phosphate-incorporated silicate glasses. Note that both xenotime and monazite structures form solid solutions. The crystalline polymorphs of rare-earth phosphates

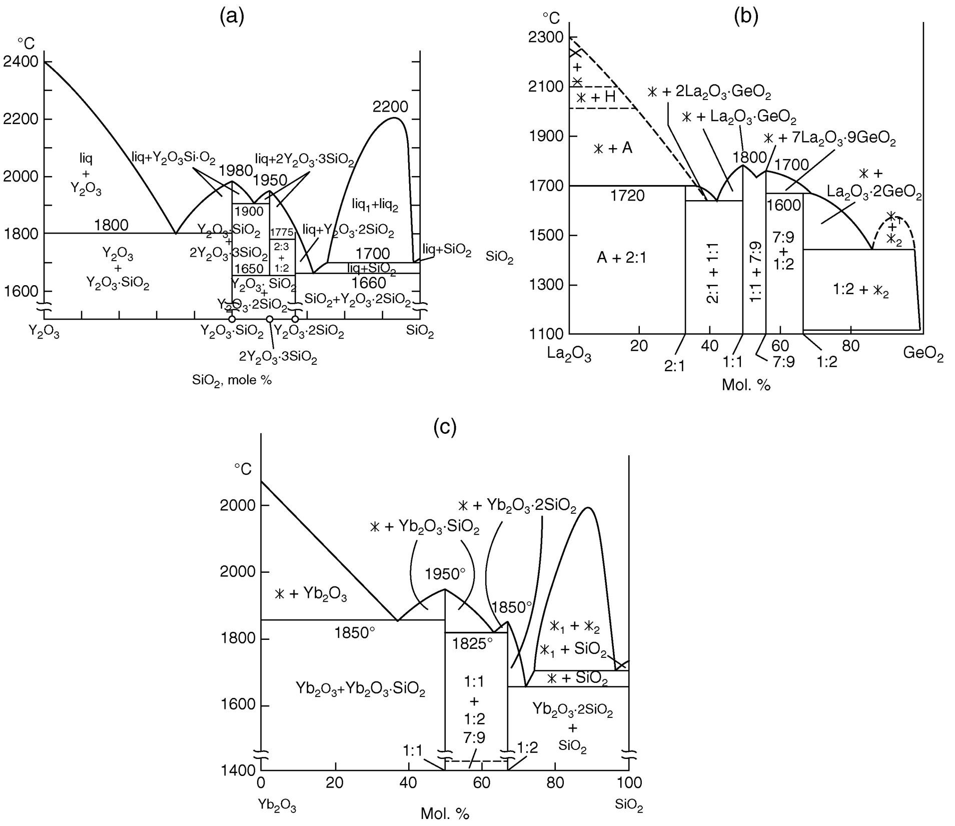

***Figure 6.11** Phase stability diagrams of (a) SiO_2-La_2O_3, (b) SiO_2-Yb_2O_3 and (c) GeO_2-La_2O_3. Note that the liquid–liquid immiscibility region is dominant in the SiO_2 and GeO_2 rich side of the phase stability diagram which implies that the two liquids (silica liquid L_1) and rare-earth oxide rich liquid (L_2) are more stable than a homogeneous single phase liquid from which the glass is made [33,34,36]. *Designates liquid ($L_1 + L_2$) in these figures. Source: Toropov 1961. (a) and (b): Reproduced with permission from Springer. (c): Reproduced with permission from Elsevier.*

occur readily and these are discussed extensively in mineralogy literature [15]. In glasses containing phosphate and alumina, the rare-earth ion co-ordination moieties may be comparable with that of crystalline phosphates, discussed above.

Figure 6.11c shows the solubility line for La_2O_3 in GeO_2-rich liquid, which has a steep solvus line, following from the immiscibility dome which defines a region of two liquids: (a) *GeO_2-rich liquid* and (b) *La_2O_3-rich liquid*. Since the germanium oxide liquid has a great deal of structural similarity with silicates, the behaviour of lanthanide immiscibility is almost similar and, therefore, may be overcome in the same way by incorporating the oxides of group IIIA (Al, Ga, In) with the oxide of a group V (e.g. P_2O_5). We will see how this structure based approach may be applied universally in various inorganic glasses for overcoming the limited solubility of rare-earth oxides.

With the structural aspects of rare-earth ion solubility contextualized for its importance in the spectroscopy of silicate glasses, the energy level and related spectroscopic analysis may be carried out on a comparative basis in various glass hosts.

6.7.2 Brief Comparison of Spectroscopic Properties of Er^{3+}-Doped Glasses

In Figure 6.12 the energy level diagram of Er^{3+}-ions is shown with four different pumping schemes from the ground state $^4I_{15/2}$ level, and these terminate at the $^4I_{13/2}$, $^4I_{11/2}$, $^4I_{9/2}$ and $^2H_{11/2}$ levels. The pumping schemes shown in this figure populate the respective levels; the inversion efficiency of each transition is dependent on the host–ion interactions, which may be analysed by using the standard Judd–Ofelt analysis transitions.

For Er^{3+}-doped silicate, fluorophosphates and fluoride glasses, comprehensive reviews have been written by Miniscalco [38] and by Ohishi [11], in which significant transitions and their spectroscopy are discussed in detail. The discussion in this section on Er^{3+}-doped glasses adds supplementary information, by exemplifying the competing processes, especially in lower phonon energy glasses. Some of these lower phonon energy glasses, although known in the 1990s, were less developed scientifically than specifically for Er^{3+}-doped device applications.

From the energy level diagram in Figure 6.12 and the absorption spectra in Figure 6.13, we find that the largest absorption cross-section is for the transition $^4I_{15/2} \rightarrow {}^4I_{13/2}$ which is between the ground and next upper levels. In Figure 6.14a the Er^{3+} : $^4I_{11/2}$ absorption cross-sections for four different glasses are compared, clearly showing that the Er^{3+}-doped tellurite glass has the largest cross-section. This is also true for other ground state transitions. The significance of a large absorption cross-section becomes apparent in amplifier and laser

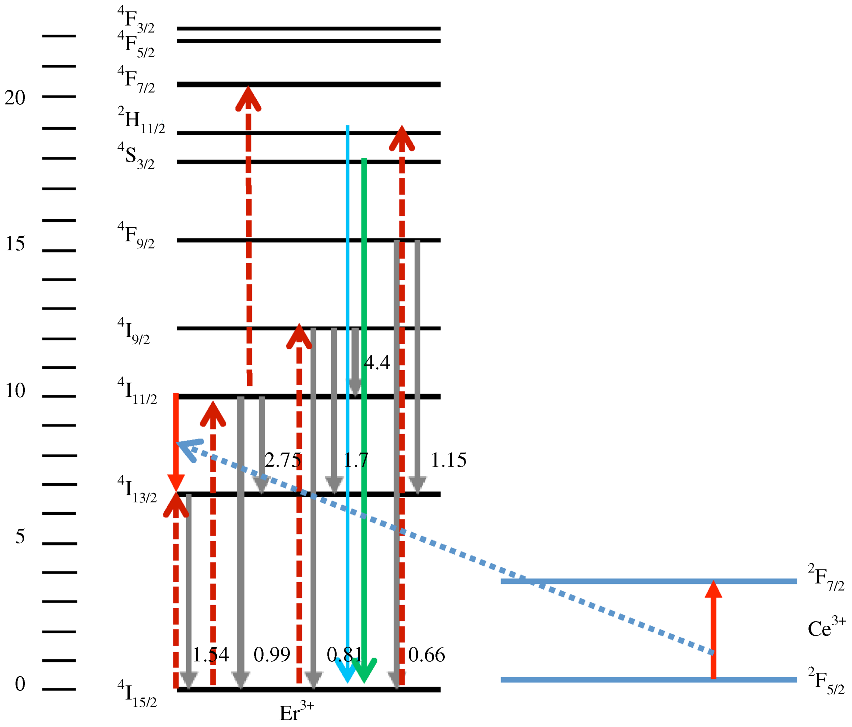

Figure 6.12 *Energy level diagrams for Er^{3+} and Ce^{3+} states in glass hosts, showing pumping schemes, visible cyan, green and red upconversion, and cross-relaxation via Ce^{3+} states (shown by dotted line). The transition wavelengths are shown in micrometers for all downward pointing arrows. The figure has been adapted from Reference [37]. (See colour plate section.)*

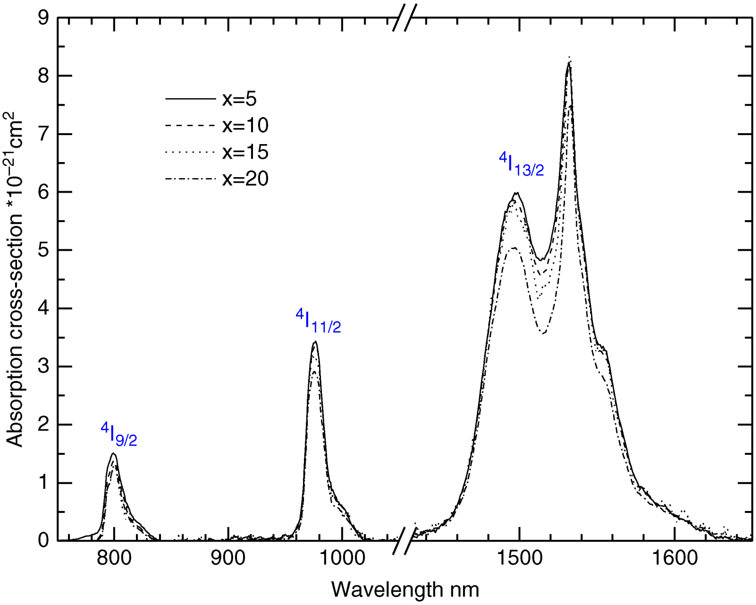

Figure 6.13 *Comparison of three ground state absorption cross-sections in Er^{3+}-doped tellurite glasses at four different doping concentrations. Glass compositions with doping concentrations are (90–x)TeO_2–xNa_2O-9ZnO-1Er_2O_3. (x = 5, 10, 15 and 20 mol.%) glass. The ground state $^4I_{15/2}$ to upper-state transitions at $^4I_{13/2}$, $^4I_{11/2}$ and $^4I_{9/2}$ are designated [14]. Source: Shen 2002. Reproduced with permission from American Ceramic Society.*

design for achieving efficient population inversion, at low pump power. For a vast majority of optical and data communication network amplifiers and lasers, the 980 nm semiconductor laser is a commonly known scheme due to its commercial availability. Once the states occupy the $^4I_{11/2}$ level, depending upon the nature of the glass hosts, the down- and upconversion transitions compete for the pump energy. In all inorganic glasses doped with Er^{3+}-ions, the optical transition leading to photon emission in the range of 1530–1580 nm is the most dominant as explained by comparing the emission cross-sections for silicate, fluoride and tellurite glasses in Figure 6.14a. The quantum efficiency of this transition is nearly 100% in high-phonon energy silicate and phosphate glasses.

By comparison, in lower phonon energy glasses such as in fluoride, tellurite and germanium oxide hosts, the quantum efficiency of this optical transition is greatly reduced due to a strong tendency for two-photon upconversion emission, through which the Er^{3+} : $^4F_{7/2}$ level is populated; this is discussed below.

When pumping Er^{3+}-doped glass with a 980 nm source, the population builds up at $^4I_{11/2}$ readily and, from this level, the two photons at 980 nm promote states to the $^4F_{7/2}$ level from which the non-radiative relaxations to $^4S_{3/2}/^2H_{11/2}$, $^4F_{9/2}$ and $^4I_{9/2}$ occur, leading to dominant optical transitions via emissions at green/cyan (520–550 nm), red (650 nm) and near-IR (~810 nm). The disproportionation of the original pump energy at 980 nm is then manifested via two competing processes: the down conversion leading to Er^{3+} : $^4I_{13/2} \rightarrow {}^4I_{15/2}$ emission in the 1530 nm range and the two-photon upconversion, discussed above. The quantum efficiency of upconversion depends upon the non-radiative relaxation rate from

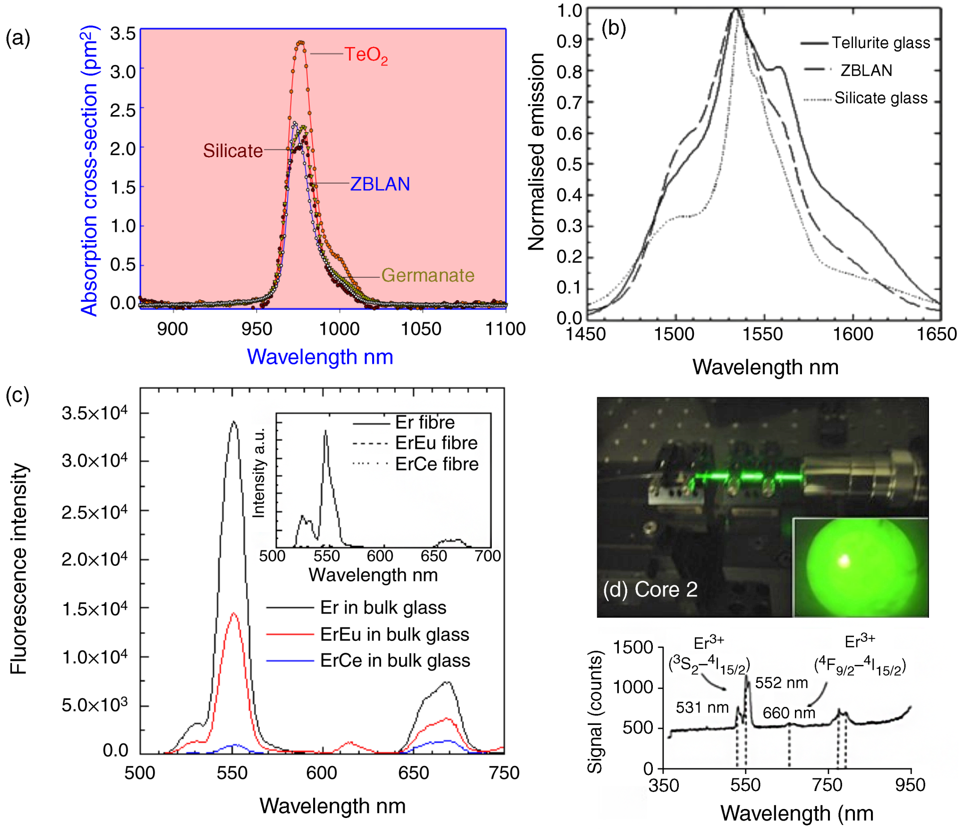

Figure 6.14 *(a) Comparison of pump absorption cross-sections in Er^{3+}-doped silicate, fluoride, germinate and tellurite glasses. Each glass was doped with 1.0 wt% Er$_2$O$_3$ [40]. Source: Bookey 2007. Reproduced with permission from OSA Publishing. (b) Comparison of Er^{3+} : $^4I_{13/2} \rightarrow {}^4I_{15/2}$ emission cross-sections in tellurite, fluoride and silicate glasses with 1 wt% Er$_2$O$_3$. (c) Comparison of the reduction in upconversion emission in Er^{3+}, Er^{3+}-Ce^{3+} and Er^{3+}-Eu^{3+} doped bulk glasses and fibres [39]. (d) Cross-section of multi-core tellurite glass fibre in which one of the cores was doped with Er^{3+}-Yb^{3+} ions and pumped with a 980 nm source [40]. (See colour plate section.)*

$^4I_{11/2}$ to $^4I_{13/2}$, which slows down considerably in low-phonon energy hosts in accordance with Equation 6.13a–c. The magnitude of non-radiative relaxation rate may be quantified either by calculating the rate or via lifetime measurements and radiative rate analysis using Equation 6.28, which then helps in verifying the computed values. The classical upconversion emission spectra in Er^{3+}-doped glass fibres are compared in Figure 6.14c with an accompanying picture in Figure 6.14d for visible transitions. In Figure 6.14d the fibre cross-section is dominated with the green fluorescence from the upconversion emission when clad-pumping a multi-core fibre with a 980 nm laser source. The two-photon upconversion is quite detrimental for engineering lasers and amplifiers utilizing the $^4I_{13/2} \rightarrow {}^4I_{15/2}$ transition, and this upconversion must be controlled to take advantage of the large emission bandwidth in lower phonon energy glasses for applications in broadband amplifiers and tuneable lasers.

One of the most effective means of reducing or controlling the upconversion emission at visible wavelengths is by pumping with a semiconductor laser at 1480 nm, which is also commercially available. The proximity of absorption and emission wavelengths at 1480–1490 and 1530–1535 nm, respectively, yields nearly 95% of Stoke efficiency for laser operation in phosphate glass hosts, for example. The high Stoke efficiency at 95% suggests that the number of potential quantum defects for such a ground state transition is much smaller than when choosing the pump wavelength at 980 and 800 nm (Figure 6.12).

However, when pumping with 1480 nm, the ground state absorption may become significant [41], and this may also affect the gain spectrum, depending on the shapes of GSA and ESA in most inorganic glass fibres. As a result the effective bandwidth for amplification is shortened significantly. An additional adverse feature may also become significant in lower-phonon energy glass fibres, such as in fluorides and chalcogenides, where the ESA may start to dominate via the process of absorption of pump and signal photons, leading to inversion at $^4I_{9/2}$. This type of effect becomes quite apparent in longer lengths of fibres where the modal overlaps of signal and pump photons may arise quite effectively. The ESA in combination with GSA may adversely affect the overall bandwidth of amplifiers. One way to alleviate this problem might be via a co-doping scheme.

The second method of enhancing the non-relaxation rate between $Er^{3+} : {}^4I_{11/2}$ and $^4I_{13/2}$ may be by enhancing the non-radiative relaxation rate, which may be possible by incorporating both B_2O_3 and P_2O_5. Spectroscopic analysis of Er^{3+}-doped boron oxide and phosphorus pentoxide containing tellurite glasses, discussed elsewhere, clearly demonstrates the advantage of high-phonon energy hosts in an intermediate phonon energy glass matrix. The reduction in visible green and red upconversion and 970 nm emission intensities is apparent with boron oxide co-doping in Figure 6.15. The measured lifetimes (shown in the inset in Figure 6.15a) confirms the enhancement in the non-radiative relaxation rate from $^4I_{11/2} \rightarrow {}^4I_{13/2}$ in boron oxide doped TeO_2 glasses [42].

In most Er^{3+}-doped glasses, to enhance the pump inversion efficiency at 980 nm, besides Er^{3+}-doping, the glass is co-doped with Yb^{3+} ions to increase the population inversion via $Yb^{3+} : {}^2F_{5/2} \rightarrow Er^{3+} : {}^4I_{11/2}$ energy exchange. This is because the absorption cross-section of Yb^{3+}-ions at 980 nm is the largest, and it is also resonant with the ground state transition in Er^{3+}-ions ($^4I_{15/2} \rightarrow {}^4I_{11/2}$). Consequently, the Yb^{3+} co-doping scheme with Er^{3+}-ions in glass and crystal hosts is highly beneficial in engineering a large majority of bulk or fibre lasers and fibre and waveguide amplifiers.

However, with increasing concentrations of Er^{3+} and Yb^{3+} dopants, the upconversion becomes significant at high pump power, especially in the fibre and waveguide geometries in which, due to a small core diameter, the modal overlap of pump enhances two-photon pump ESA. If the ESA becomes significant it may lead to wastage of pump photons via upconversion emission and the associated non-radiative processes. For this reason, in such doped materials, the most efficient means to reduce the upconversion emission is to use a third co-dopant, which is Ce^{3+}-ions. The presence of Ce^{3+} in optimal concentrations provides a faster population inversion from $^4I_{11/2} \rightarrow {}^4I_{13/2}$ via a process of cross-relaxation in which a Ce^{3+} state at ground level ($^2F_{5/2}$) occupies the upper lying $^2F_{7/2}$ state (Figure 6.12). The influence of this cross-relaxation in Er^{3+}-doped tellurite glasses and fibres is reported elsewhere, yielding a much higher net gain of 28 dB in a 22 cm short-fibre amplifier and a tuning range of more than 80 nm in a ring lasers [37]. The tuning range and gain may be enhanced further in much longer lengths of fibres or via managing the cross-relaxation.

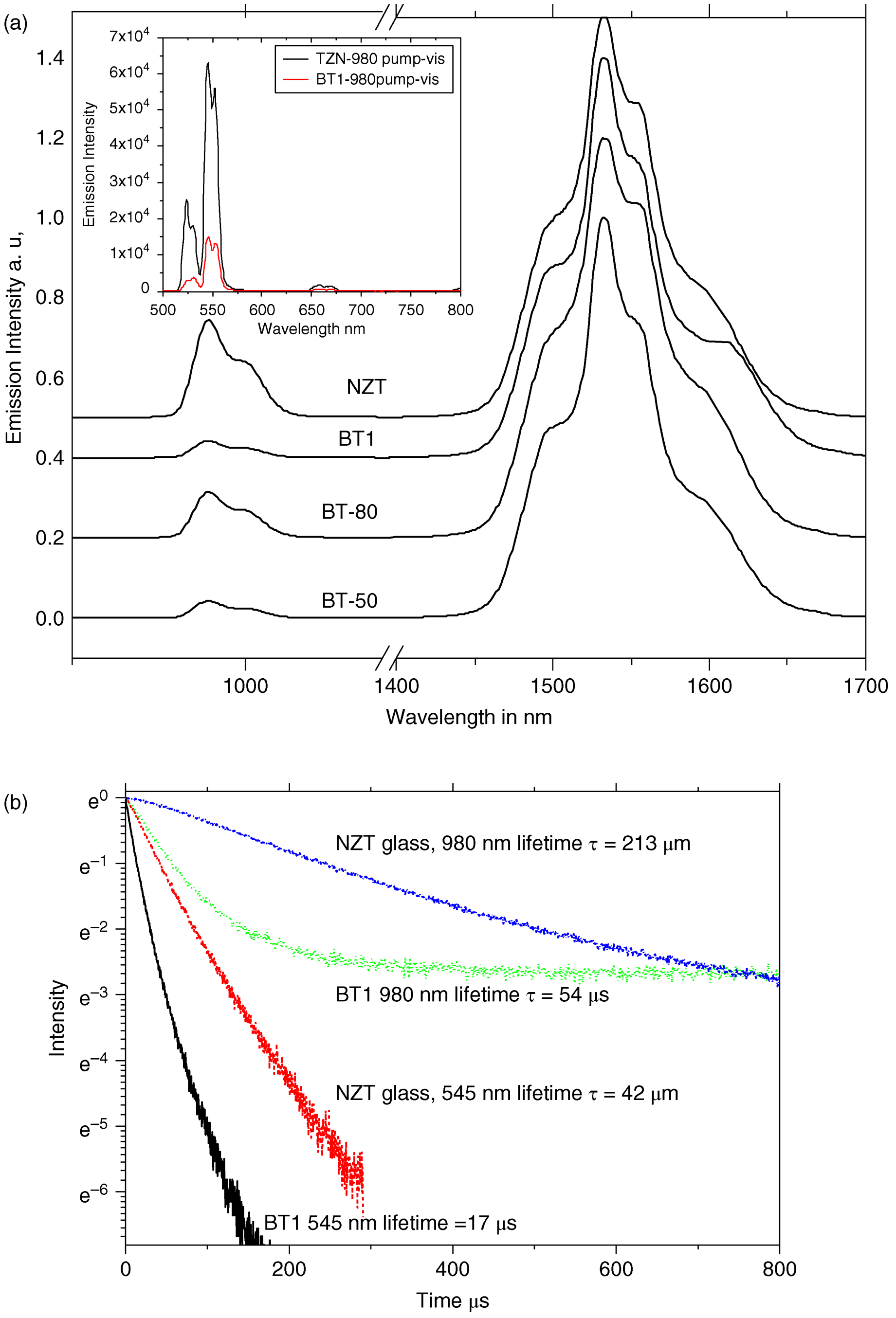

Figure 6.15 *(a) Comparison of emission spectra in NZT and boron oxide modified tellurite glasses (BT), pumped via an Ar^+-ion source at 514 nm. Inset: reduction in the visible upconversion emissions in the BT1 glass, compared to a NZT glass. (b) Comparison of the lifetimes of the $^4I_{11/2}$ and $^4S_{3/2}$ transitions to the ground state in NZT and boron-containing BT1 glass samples [42].*

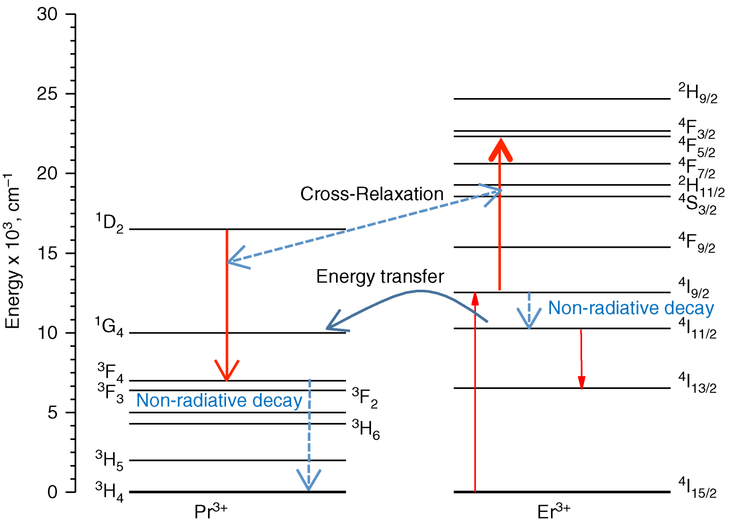

Figure 6.16 *Spectroscopic analysis of* Er^{3+} : $^4I_{11/2} \rightarrow {}^4I_{13/2}$ *transition in the 2690–2780 nm wavelength range in the presence of* Pr^{3+}*-ions in a ZBLAN glass when pumped with a 800 nm source.*

These results compare quite favourably with the original results, reported by Mori *et al.* at the NTT lab in Japan [43,44]. The results in Ce^{3+}-ion co-doping of Er^{3+}/Yb^{3+} doped devices therefore prove that the pump inversion efficiency is significantly improved. The amplification and 80 nm bandwidth [45] observed in tellurite glass fibres may also be compared with the previous results in silica fibre amplifiers. In Figure 6.14c, the effect of Ce^{3+}-Er^{3+} cross-relaxation energy on the reduction of visible upconversion emission intensities is quite dramatic. In this figure the effect of Eu^{3+} ions is also shown; however, the presence of Eu^{3+} ions also shortens the lifetimes of the Er^{3+} : $^4I_{13/2}$ level. Other less preferable ions such as Tb^{3+} and Pr^{3+} have much larger detrimental effect on reducing the lifetimes of Er^{3+} : $^4I_{13/2}$ level than Ce^{3+}, due to a combination of non-radiative and cross-relaxation rates, which is why Tb^{3+} and Pr^{3+} are not used as co-dopants (Figure 6.16). Note that in highly doped phosphate glasses, which contain more than 5 wt% of Yb^{3+}-ions with 0.5 wt% of Er^{3+}-ions, the Ce^{3+}-ion co-doping enhances cross-relaxation rate by building population at Er^{3+} : $^4I_{13/2}$, which is evident from the results reported in this area.

The energy gap for optical transition between Er^{3+} : $^4I_{11/2}$ and $^4I_{13/2}$ is ~3300 cm^{-1} which, as discussed above, is dominated by the non-radiative decay via multiphonon relaxation process. In addition, as this transition is resonant with the OH^- fundamental absorption band in the majority of glasses, the residual presence of OH^- ions may contribute to strong concentration quenching effects. The first ever reported transition at 2.7 μm was observed in a Er^{3+}-doped YAG. It has been used in surgical medicine [46,47] owing to the preponderance of hydroxyl bonds in biological tissues that readily absorb the laser radiation and the resulting minimal collateral damage to surrounding healthier tissues. Until the advent of fluoride glass hosts, no mid-IR fluorescence and lasing was ever reported in glassy hosts, due to the dominance of multiphonon dominated non-radiative decay. Allain *et al.* were first to report the Yb^{3+}-co-doped Er^{3+}-ion 2.73 μm laser in a zirconium fluoride based glass

Table 6.8 *Summary of observed optical transition ($^4I_{13/2} \rightarrow {}^4I_{15/2}$) and the spectroscopic characteristics in Er^{3+}-doped inorganic glasses [41]. This table may also be further supplemented with the references on the Judd–Ofelt parameters and oscillator strengths [11,16,49]. Source: Miniscalco 1991. Reproduced with permission from OSA Publishing.*

Glass	Emission properties			Absorption properties	
	τ (ms)	λ_{peak} (nm)	$\sigma_e \times 10^{-21}$ (cm^2)	λ_{peak} (nm)	$\sigma_a \times 10^{-21}$ (cm^2)
Al/P silica	10.8	1530.8	5.70	1530.1	6.60
Fluorophosphate	8.25	1532.6	7.16	1532.6	6.99
Fluorozirconate	9.4	1530.6	4.95	1530.4	4.98
Ba-Zn-Lu-Th-F glass	—	1530.6	—	1529.4	4.82
Chalcogenide [50]	2.3	1538.5	15.7	1537	14.98
Tellurite	3.5	1535	8.6	1535	

Judd–Ofelt parameters for selected glasses with Er^{3+}-ions ($\times 10^{-20}$ cm^2) [16,49].

Glass host	Ω_2	Ω_4	Ω_6
Fluoride	2.54	1.39	0.96
Oxyfluoride	3.22	1.34	0.61
Borate	3.70	1.36	0.84
Phosphate	6.19	3.70	0.91
$70TeO_2$-$15GeO_2$-$10Nb_2O_5$-$5Li_2O$	7.59	1.88	0.97
$59TeO_2$-$30WO_3$-$10Na_2O$	7.14	1.92	0.82
$85TeO_2$-$15Ga_2O_3$	6.46	1.64	1.47

fibre [48]. This is quite significant because in a fluoride glass, melted under dry fluorine atmosphere, the OH^- ion absorption is minimum and, consequently, the radiative transition probability between Er^{3+} : $^4I_{11/2}$ and $^4I_{13/2}$ increases in fluoride glass hosts due to its lower phonon energy than that in silicates and phosphates. However, if the 980 nm pumping scheme is utilized, the transition terminates at the $^4I_{13/2}$ level due to its long-lived lifetimes which renders this energy level self-terminating. This means, if this level does not empty faster than the rise time of states to occupy the $^4I_{11/2}$ level from the ground $^4I_{15/2}$ level, the lasing operation may cease. It is therefore necessary to engineer a device that may lase at both the wavelengths: 2.73 and 1.55 μm. In Table 6.8, the spectroscopic properties of various optical transitions with oscillator strengths in silicate, phosphate, fluoride and tellurite glasses are summarized for engineering pump efficient devices. In this table the references are also included for lasers and amplifiers operating at optical communication window and other important transitions.

6.7.3 Spectroscopic Properties of Tm^{3+}-Doped Inorganic Glasses

Following on from Figure 6.10 the optical transitions corresponding to the ground state transitions in Tm^{3+} ions are shown in Figure 6.17, which is a UV-visible-near-IR spectrum, obtained at room temperature. In this figure the oscillator strength of transition between the ground state level $^3H_6$ and the next upper level $^3F_4$ is the most dominant; it is utilized in engineering lasers operating in the 1800–1950 nm window, in mid-IR. The optical transition between $^3F_4 \rightarrow {}^3H_6$ is a hypersensitive transition, showing greater inhomogeneous broadening due to host–ion interaction than a normal transition, e.g. Er^{3+} : $^4I_{13/2} \rightarrow {}^4I_{15/2}$ at

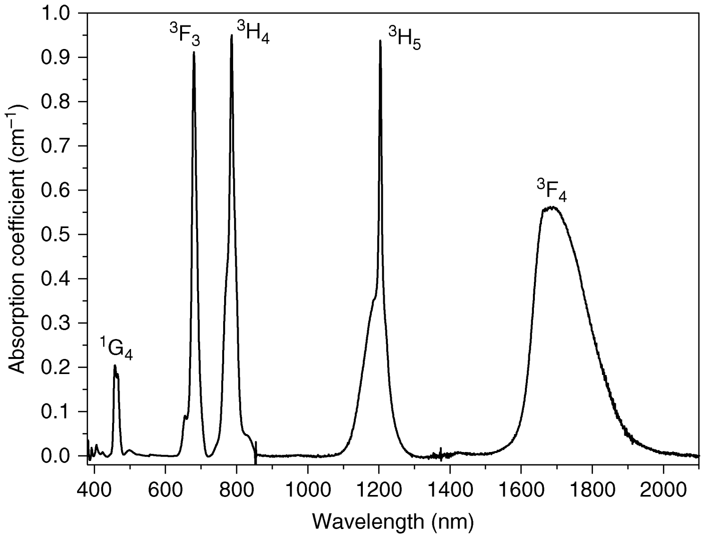

Figure 6.17 *Room-temperature absorption coefficient spectrum of a 1.5 wt% Tm^{3+}-doped tellurite bulk glass sample [51]. Source: Richard 2010. Reproduced with permission from IoP Publishing.*

1530 nm, discussed above. Since the wavelength region 1800–1950 nm is at a longer wavelength than 1530 nm, lasers designed within this spectral range are classed as eye-safe lasers. They are widely used by NASA for wind measurements in the upper atmosphere. The wavelength band is also resonant with the combination IR bands for OH^-, hydrogenated phosphate $(HPO_4)^{2-}$ and bicarbonate $(HCO_3)^-$, all of which are relevant for use in lasers for surgical applications.

The Tm^{3+} : $^3F_4 \rightarrow {}^3H_6$ optical transition has been investigated in most inorganic glasses for its importance in established and emerging mid-IR technologies. The spectroscopic properties for known host–dopant interaction are summarized in Table 6.9 below. Other important transitions in Tm^{3+}-doped glasses may also be understood by examining the absorption spectrum in Figure 6.17 in which the relative strength of each transition is apparent, e.g. in a tellurite glass. Comparable absorption has been reported for silicates, fluoride and gallium-lanthanum sulfide glasses [52–54]. From the known absorption data in Figure 6.17, it is apparent that a Tm^{3+}-doped glass may be pumped with a blue ($^1G_4$: 470 – 490 nm), red ($^3F_{2,3}$: 660 nm), 780–810 nm source resonant with $^3H_4$, and at $^3H_5$: 1200 nm and $^3F_4$: 1600 nm. At present all of these pump sources are commercially available. In the literature all of the above pumping schemes have been reported [39–42], including the $^1G_4$ absorption, which has the smallest absorption cross-section. The existence of a large absorption band facilitates efficient pump induced inversion.

6.7.3.1 Tm^{3+}: $^3F_4 \rightarrow {}^3H_6$ *Transition*

As with Er^{3+}-doped glasses, for a 1.5 μm device engineering the doping with Yb^{3+} ions enhances the pump efficiency, for engineering Tm^{3+} devices. The rare-earth ion pair Tm^{3+}-Ho^{3+} works quite well, offering a large tuning range of wavelength between 1900 and 2100 nm. This spectroscopic feature is exemplified below by investigating the

Table 6.9 *Judd–Ofelt parameters for various Tm^{3+}-doped glass host materials. (GLS = gallium lanthanum sulfide, TZN = zinc sodium tellurite, T = tellurite, LKBBT = lithium potassium barium bismuth tellurite, TZC = zinc chloride tellurite, TZPN = zinc lead niobium tellurite, LT = lithium tellurite, BZT = barium zirconium thorium, ZBLAN = zirconium barium lanthanum aluminium sodium). Refractive index data for each glass is shown within brackets ().*

	Judd–Ofelt parameters ×10^{-20} (cm^2)			
Host glass	Ω_2	Ω_4	Ω_6	Reference
GLS chalcogenide (2.35–2.45)	5.7	1.7	1.4	[54]
Silicate (1.51)	3.26	1.20	0.46	[54]
TZN (2.01)	5.106	1.174	1.082	[67]
T (1.99)	5.04	1.36	1.22	[67]
LKBBT (2.15)	5.40	1.47	1.19	[67]
TZC	2.51	1.71	1.46	[67]
TZN	3.38	2.17	1.17	[67]
TZPN	2.51	1.33	0.95	[67]
LT (1.93)	2.27	1.16	0.11	[67]
BZT fluoride	2.02	1.56	1.10	[68]
Germanate (1.90)	5.55	2.03	1.26	[69]
ZBLAN fluoride (1.52)	2.57	1.90	0.84	[69]
Phosphate (1.51–1.55)	5.63	1.75	1.11	[69]

photoluminescence properties which are dependent on the forward energy transfer from Tm^{3+} : $^3F_4$ to Ho^{3+} : $^5I_7 \rightarrow {}^5I_8$ (Figure 6.18a). As a result, the combination of these two ions offers the broadest fluorescence band for tuning lasers and amplifiers. The Tm^{3+} ion has one of the broadest fluorescence bands amongst rare-earth ions [55] and is centred at around 1.8 μm from the $^3F_4 \rightarrow {}^3H_6$ transition, while Ho^{3+} fluoresces at a slightly longer wavelength of around 2.0 μm from the transition.

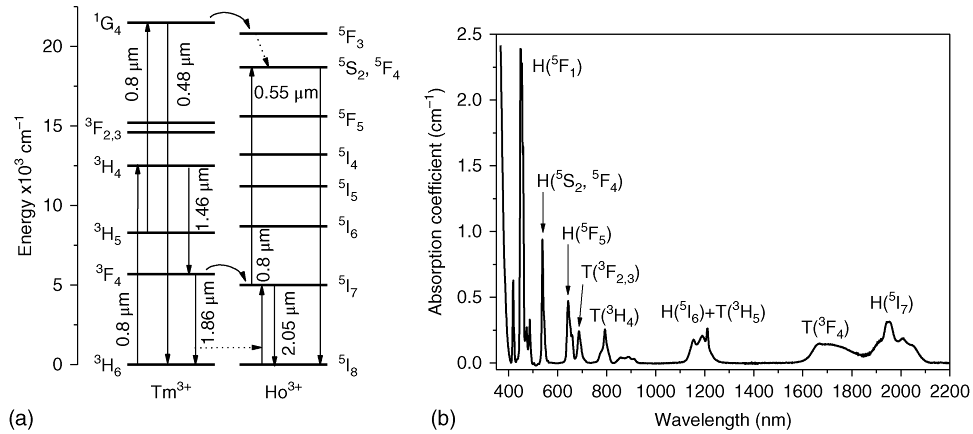

Figure 6.18 *(a) Energy level diagram of Tm^{3+} and Ho^{3+} showing the pumping scheme, energy transfer, radiative transitions and ESA processes. (b) Absorption coefficient spectrum of a 0.5 wt % Tm^{3+}, 1.0 wt% Ho^{3+}-co-doped tellurite bulk glass sample. In this figure T and H represent the Tm^{3+} and Ho^{3+} dopants [51].*

From the energy level diagram shown in Figure 6.18a, both of these rare-earth ions may be pumped with a standard 780–810 nm diode laser and Er^{3+}-doped fibre lasers operating in range 1550–1610 nm. The spectral width of fluorescence in these two dopants defines the ΔE in Figure 6.18b, which in light of the uncertainty principle implies that, if a pulse laser cavity design is considered, it may be possible to generate ultra-short pulses ($\Delta\tau$), which was demonstrated by Fusari *et al.* [56].

The 780–810 nm high-power diode lasers, available commercially in multi-watt to kilowatt output ranges, are suited for pumping bulk glass and crystal gain media doped with Tm^{3+} or Ho^{3+}-ions. At this wavelength the pump absorption cross-section is large, leading to inversion at the $Tm^{3+} : {}^3H_4$ level, from which the quantum cutting effect, shown in Figure 6.18a, for "*each pump state two lasing states*" is possible. This condition theoretically may yield 200% quantum efficiency; however, in practice in germanium oxide and fluoride glass fibres [57–59], the apparent QE was found to be 180% at 1.9 μm, with a slope efficiency of 68%. The apparent difference in QE was due to the loss of pump energy in creating Stoke defects. In Figure 6.18b each peak corresponds to absorption from the Tm^{3+} ground state ${}^3H_6$, or Ho^{3+} ground state ${}^5I_8$, to the identified energy level labelled above each peak. As discussed above, although there is a large absorption band for $Tm^{3+} : {}^3H_4$ for pumping at around 780–810 nm, there are no absorption bands near either 800 or 980 nm for pumping Ho^{3+}-ions, which is why it is common to consider the energy-transfer based on a donor–acceptor mechanism, in which the $Tm^{3+} : {}^3F_4$ states act as donors for the $Ho^{3+} : {}^5I_7$ acceptor level, when using the 800 nm pumping scheme. The internal QE and slope efficiency is known to be 150% and 60%, respectively for such a scheme [60–62]. It is possible, however, to pump Ho^{3+} singly-doped lasers using other pump sources such as Yb^{3+} [63] and Tm^{3+} [64] doped fibre lasers and newly emerging 1.15 μm laser diode sources which are available with powers in the several watts region [65].

In considering most efficient pumping scheme for maximizing the slope efficiency of laser and laser-amplifier using Tm^{3+}- and Tm^{3+}-Ho^{3+}-doped glass hosts, the in-band pumping scheme from the ${}^3H_6$ to ${}^3F_4$ level must be considered for minimizing the quantum defects. For this reason the pump wavelength yielding the highest slope efficiency is the one at which the ratio of absorption and emission cross sections (σ_a/σ_e) at the ${}^3F_4$ level is the highest [66]. This is the feature of most ground state transitions, and for this pump wavelength selection it is especially important for avoiding GSA. Such pumping schemes often redshift the lasing and amplifier operation, in comparison with the pumping scheme that is not in-band. The in-band pumping of $Tm^{3+} : {}^3H_6 \rightarrow {}^3F_4$ is possible by using commercial Er^{3+}-Yb^{3+}-doped fibre lasers.

The fluorescence lifetime decay measurements helps us in the analysis of photoluminescence processes for the spectral region 1.8–2.1 μm, e.g. in Tm^{3+} and Tm^{3+}/Ho^{3+}-doped tellurite glasses. The lifetime analysis may be useful in explaining some important characteristics, especially in explaining the $Tm^{3+} : {}^3H_4 \rightarrow {}^3F_4$ transition which is less efficient in high-phonon energy glasses such as silicates. Using an 808 nm laser diode source, the resulting spectra are shown in Figure 6.19a and 6.19b, respectively, for Tm^{3+}- and Tm^{3+}-Ho^{3+} doped tellurite glasses. In each spectrum the emission peaks at longer wavelengths are compared by normalizing the peak at 1.46 μm due to $Tm^{3+} : {}^3H_4 \rightarrow {}^3F_4$. Optical transitions at $Tm^{3+} : {}^3F_4 \rightarrow {}^3H_6$ and $Ho^{3+} : {}^5I_7 \rightarrow {}^5I_8$ are apparent in these two figures.

Note that the large oscillator strengths of the ground state transitions in $Tm^{3+} : {}^3F_4 \rightarrow {}^3H_6$ and $Ho^{3+} : {}^5I_7 \rightarrow {}^5I_8$ yield strong intensities of fluorescence in comparison with the upper lasing level transition in $Tm^{3+} : {}^3H_4 \rightarrow {}^3F_4$ peaked at 1460 nm. Amongst these three

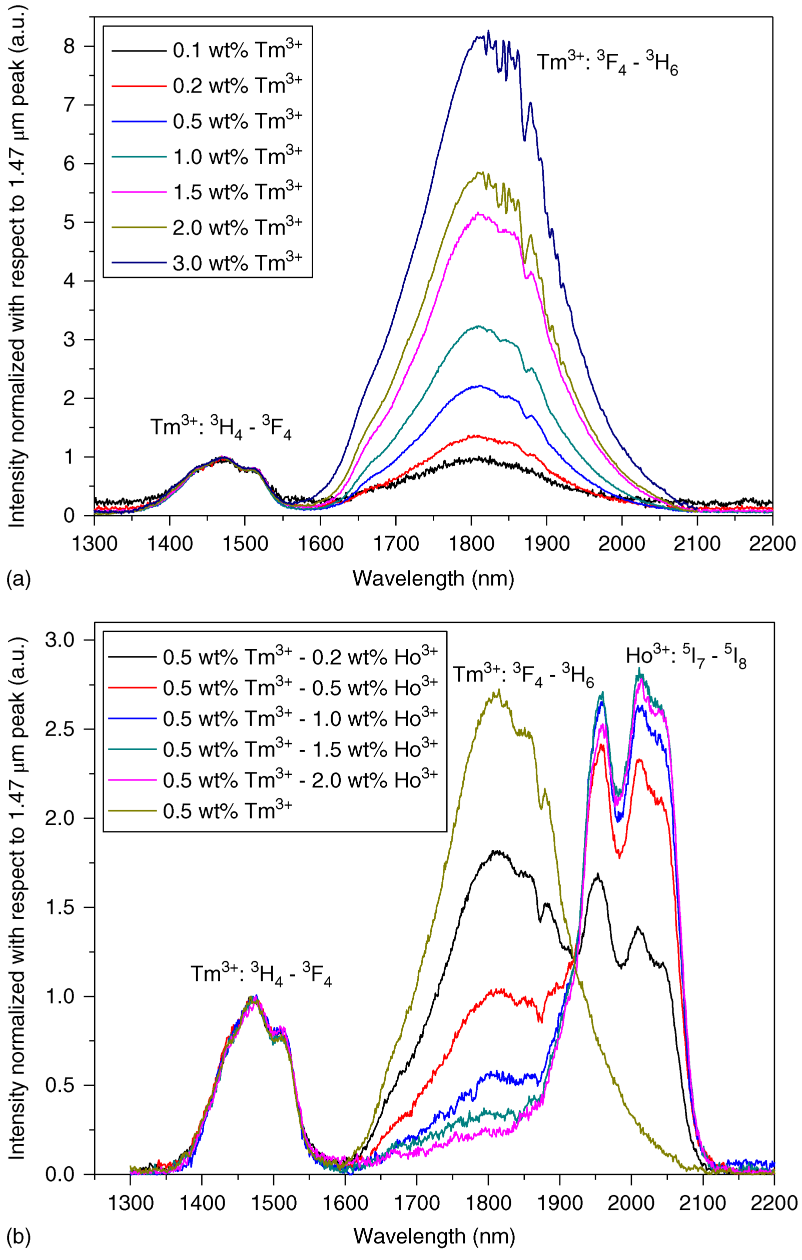

Figure 6.19 *(a) Fluorescence spectra of tellurite bulk glass samples with fixed Tm^{3+} concentration, showing the effect of concentration quenching at room temperature due to ion–ion interaction, and (b) bulk tellurite glass samples with fixed 0.5 wt% Tm^{3+}-ion and varying Ho^{3+} ion concentrations, showing energy transfer from $Tm^{3+} : {}^3F_4 \rightarrow {}^3H_6$ to $Ho^{3+} : {}^5I_7$ level, when excited with an 808 nm laser diode source. Both sets of spectra have been normalised with respect to the peak at 1.47 μm [51]. Source: Richard 2010. Reproduced with permission from OSA Publishing. (See colour plate section.)*

transitions, only the Tm^{3+} : $^3F_4 \rightarrow {}^3H_6$ transition is hypersensitive, as a result it is strongly dependent on the refractive index and dopant-ion site symmetry of the host. The strength of a hypersensitive transition may be estimated by the delocalization of valence band electrons (covalency) in the host and their coupling with dopant ion states. For such estimation, it has been reported that in general the hypersensitivity of the transition increases with an increase in the Ω_2 Judd–Ofelt parameter, where larger Ω_2 values represent a higher degree of covalency of the glass network bonding [54]. Nachimuthu and Jagannathan [49] have shown that for the hypersensitive transitions in Nd^{3+}, Ho^{3+} and Er^{3+} the oscillator strengths increase linearly with the values of the sum of the three Judd–Ofelt parameters ($\Sigma\Omega_\lambda$ ($\lambda = 2, 4, 6$)), while the oscillator strengths of the non-hypersensitive transitions remain unchanged ($\Sigma\Omega_\lambda$). It should be also noted that the magnitude of Ω_2 parameters increases with the refractive index of host material. In Table 6.9 the Judd–Ofelt parameters and refractive indices (shown within brackets) of Tm^{3+}-doped bulk glass samples are compared. Since the ~2.0 μm $^5I_7 \rightarrow I_8$ laser transition of Ho^{3+} is not hypersensitive [67], whereas the Tm^{3+} : $^3F_4 \rightarrow {}^3H_6$ transition is, only the Judd–Ofelt parameters of Tm^{3+}-doped glasses are discussed here. It is apparent that for high refractive index glasses, such as tellurite and chalcogenide glasses, the values of Ω_2 are larger than that for silicate and fluoride glasses. In addition, notably, with the exception of phosphate hosts, the values of Ω_2 parameters in selected high-index glasses are much larger than that in the silicate and fluoride hosts. However, the phosphate hosts have much higher Ω_2 values than any other oxide glass hosts. This unusual enhancement in the Ω_2 parameter in phosphate is due to the strong covalent bonds that form as a result of the hybridisation of electrons in $(PO_4)^{3-}$ and $(Ln)^{3+}$ in xenotime and monazite structures, discussed above. This intrinsic bonding character in phosphate hosts provides them with a unique set of spectroscopic properties, unseen in other glass hosts. From this comparison, evidently, the enhanced hypersensitivity of the Tm^{3+} : $^3F_4$ level might be due to large Ω_2 values in high-index glasses in Table 6.9 which is apparent from increased absorption and emission cross-sections, when compared with Tm^{3+}-doped silica and fluoride glasses.

As shown in Figure 6.19a, the examples of Tm^{3+}-doped glass studied demonstrate that as the Tm^{3+} concentration increases the intensity of the 1.8 μm fluorescence peaks increases proportionately in comparison with the peak at 1.46 μm. This is important evidence for a quantum cutting cross-relaxation process ($^3H_4$, $^3H_6 \rightarrow {}^3F_4$, $^3F_4$) which becomes more probable when the ion–ion distances are reduced at high concentrations. At such concentrations, the probability of energy exchange between the donor and acceptor ion pairs also increases. Consequently, as shown in Figure 6.19b in the Tm^{3+}/Ho^{3+}-co-doped samples, the 1.8 μm Tm^{3+}-ion fluorescence peak reduces in intensity while the Ho^{3+}-ion emission peak at 2.0 μm grows as the Ho^{3+}-concentration increases. For the Tm^{3+}-doped glasses, the 1.8:1.47 μm intensity ratio increases linearly with Tm^{3+} concentration up to 3 wt%. In the Tm^{3+}/Ho^{3+}-co-doped samples the ratio of Ho^{3+} 2.0 μm to Tm^{3+} 1.8 μm fluorescence intensities also increases linearly with increasing Ho^{3+} concentration up to 2.0 wt% Ho^{3+} and fixed Tm^{3+} concentration [29]. From the pumping scheme and energy transfer processes shown in Figure 6.18a, the pump ESA in Tm^{3+} and Ho^{3+} also compete. Consequently, weak visible fluorescence at 480 and 550 nm from the Tm^{3+} : $^1G_4 \rightarrow {}^3H_6$ and Ho^{3+} : $^5S_2$, $^5F_4 \rightarrow {}^5I_8$ transitions, respectively, are apparent. The ESA induced upconversion dominates more in fluoride and chalcogenide glasses because the lifetimes of the lasing levels are significantly longer than those in high- and intermediate phonon energy hosts. It is for this reason that the blue upconversion emission in Tm^{3+}-doped fluoride glasses is more efficient than in oxide glasses. In chalcogenide glasses, the blue upconversion emission is less probable because the energy gap of the upconversion emission is resonant with the electronic band gap (E_g, eV) of the sulfide based chalcogenide glasses which is around 2.5 eV.

Recently [51] the enhanced fluorescence line widths of Tm^{3+} : $^3F_4 \rightarrow {}^3H_6$ transitions in different types of glasses were explained by comparing the structures. In tellurite glasses, the line width is especially broad, which were determined by comparing the full-width of half-maximum (FWHM). From Figure 6.19a for a tellurite glass, the FWHM is typically 200 nm, which may be compared with the values of FWHM of 125 nm in ZBLAN [32] and 150 nm in silica glasses [70]. Based on such a large FWHM in tellurite glasses, the properties of broadly tuneable lasers, Q-switched and mode locked lasers were reported and these are explained in Chapter 7. A comparable spectral broadening in germanium oxide (GeO_2) based glasses was also reported [71–73], and the apparent spectral broadening in TeO_2 and GeO_2 glasses is attributed to the presence of multiple structural units and bond lengths, creating a range of dipole environments for rare-earth ions. By comparison, in silicates and zirconium fluoride based glasses, the apparent multiplicity of dopant sites is limited by the presence of $(SiO_4)^{4-}$ tetrahedral and ZrF_6 octahedra, respectively, which are observed predominantly.

Furthermore, in Tm^{3+}-doped in amorphous silicon, the room temperature photoluminescence spectrum differs significantly from that observed in inorganic glasses. The peak shape for Tm^{3+}-dopant in Si films [74] is shown in Figure 6.20, from which it is evident that the peak of emission is redshifted to longer wavelengths by 180 nm with respect to the peaks observed in inorganic tellurite glasses and GeO_2-based glasses. This apparent shift is

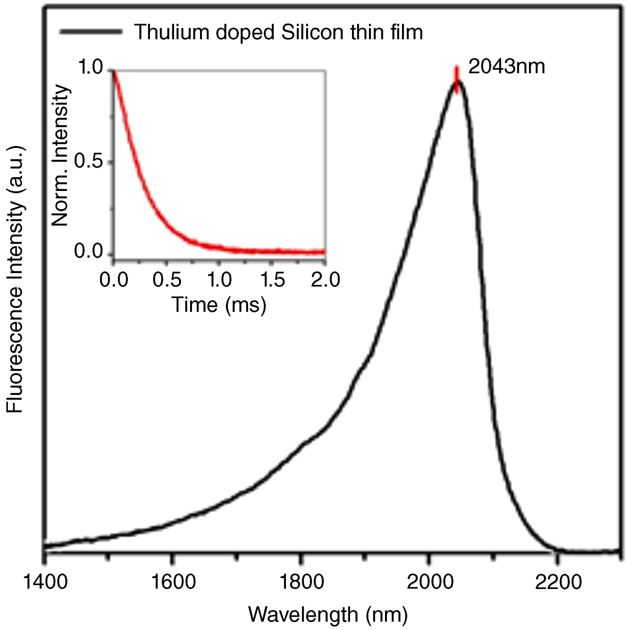

Figure 6.20 *(a) Room temperature fluorescence spectra of Tm^{3+}-doped amorphous Si thin film, deposited via femtosecond pulsed laser deposition onto a silica glass substrate. The excitation wavelength of Tm^{3+}-doped Si film was 808 nm diode laser. Inset: decay lifetime for $^3F_4 \rightarrow {}^3H_6$ transition is 250 μs, compared with 2300 μs in tellurite bulk glass samples [74]. Source: Murray 2012. Reproduced with permission from American Physical Society.*

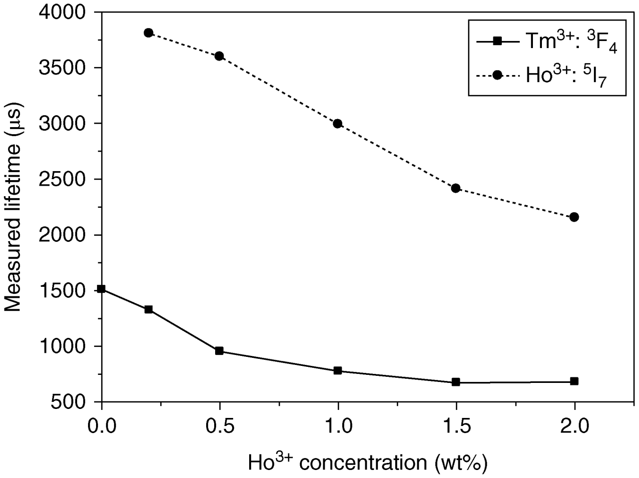

Figure 6.21 *Variation of* Tm^{3+} : $^3F_4$ *and* Ho^{3+} : $^5I_7$ *measured lifetimes with varying* Ho^{3+} *concentration in* Tm^{3+}/Ho^{3+}*-co-doped "TZN" bulk glass samples [29]. Source: Richards (2008). Reproduced with the permission of the University of Leeds Library.*

consistent with the hypersensitivity model for the $^3F_4 \rightarrow {}^3H_6$ transition; however, details of the Ω_j parameters could not be determined because of the limited number of absorption peaks available in Si thin films doped with Tm^{3+}-ions. The inset in Figure 6.20 shows the lifetime decay curve, from which it is apparent that the overall lifetime of Tm^{3+} in Si may be affected by the dipole environment and high concentrations which were reported earlier [74].

Figure 6.19a and 6.19b gives examples of concentration quenching in Tm^{3+}-ion and energy transfer from Tm^{3+} : $^3F_4$ to Ho^{3+} : $^5I_7$; they are discussed in detail elsewhere [51]. In conclusion, the effect of Tm^{3+}–Ho^{3+} ion pair interaction may be explained with the help of lifetime analysis of Tm^{3+} : $^3F_4$ and Ho^{3+} : $^5I_7$ levels which are compared in Figure 6.21. Both ions follow a similar trend; however, due to favourable Stoke energy transfer, the lifetime of the Tm^{3+} level is much shorter, by 33%, compared to Tm^{3+}:doped tellurite glass with no Ho^{3+} ions.

The energy transfer process between Tm^{3+} and Ho^{3+} and Tm^{3+}–Tb^{3+} energy exchange pairs were analysed in tellurite [75] and gallium lanthanum based chalcogenide glasses [54], respectively. It was found that the exchange of energy from Tm^{3+} : $^3F_4$ to Ho^{3+} : $^5I_7$ in tellurite glass was more favourable for enhancing the relative intensity of fluorescence and its lifetimes than the exchange of energy between Tm^{3+} : $^3F_4$ to Tb^{3+} : $^7F_0$. Note that in Tb^{3+} ions in a glass, a cascade of closely spaced energy levels from $^7F_0$ to $^7F_6$ promotes a rapid non-radiative decay and, therefore, quenches the upper lasing level $^3H_4 \rightarrow {}^3F_4$ transition. To make efficient lasers and amplifiers in the S-band of the optical communication window at 1.47 μm it is essential to remove or minimize the bottleneck due to the long-lived Tm^{3+} : $^3F_4$ states and so far the Ho^{3+}-ion as acceptor ion appears to be much better than either Tb^{3+} or Pr^{3+}-ions, both of which promote fast non-radiative decay for the $^3H_4 \rightarrow {}^3F_4$ transition. The bandwidth of the $^3H_4 \rightarrow {}^3F_4$ transition is ~110–120 nm in tellurite glasses, compared to 80 nm in a fluoride host [27], as a result the overlap of emission bands between 1420 and 1530 nm via Tm^{3+} : $^3H_4 \rightarrow {}^3F_4$ and Er^{3+} : $^4I_{13/2} \rightarrow {}^4I_{15/2}$ is much better for a contiguous access of bandwidth [26,76]. Table 6.10 gives the spectroscopic properties of the $^3H_4 \rightarrow {}^3F_4$ and $^3F_4 \rightarrow {}^3H_6$ transitions.

Table 6.10 *Spectroscopic properties of Tm^{3+}-doped inorganic glasses with emphasis on $^3H_4 \rightarrow {}^3F_4$ and $^3F_4 \rightarrow {}^3H_6$ optical transitions. τ_R: Radiative lifetimes (calculated in μs), τ_m: measured lifetimes (μs), σ_e: emission cross-section (m^2), σ_a: absorption cross-section (m^2), β: branching ratio, η: quantum efficiency determined from lifetime measurements; $\Omega_{l,j,k}$ are the Judd–Ofelt parameters in pm^2 [52,55].*

Glass specifications and compositions (mol.%)	Judd–Ofelt parameters (pm^2)			Tm^{3+} : $^3F_4 \rightarrow {}^3H_6$				Tm^{3+} : $^3H_4 \rightarrow {}^3F_4$			
	Ω_2	Ω_4	Ω_6	τ_R (μs)	τ_m (μs)	β	η (%)	τ_R (μs)	τ_m (μs)	β	η (%)
Silicate glass, $\sigma_e = 6.1 \times 10^{-25}$ m^2	3.26	1.20	0.46		200, 500	—	—	—	15–58	—	—
	3.31	1.21	0.48								
$69.5B_2O_3$-$25K_2O$-$5Na_2O$-$0.5Tm_2O_3$, $\sigma_a = 5.85 \times 10^{-25}$ m^2	11.68 ± 1.12	0.65 ± 0.07	1.04 ± 0.12	2850	—	—	—	532	—	—	—
$85TeO_2$-$15CdCl_2$ mol.%	0.131	0.075	0.066	832	84		0.1	2544	455		0.18
$80TeO_2$-10ZnO-$9.0Na_2O$-$1Tm_2O_3$, $\sigma_e = 0.36 \pm 0.06$ pm^2, $\sigma_a = 0.89 \pm 0.01$ pm^2	3.18 ± 0.3	1.8 ± 0.2	1.3 ± 0.1	2365	2200	1.0	93	350	310	0.08	83
$50ZrF_4$-$20BaF_2$-20NaF-$4LaF_3$-$5AlF_3$-$1Tm_2F_3$. $\sigma_a = 0.33 \pm 0.01$, pm^2, $\sigma_e = 0.18 \pm 0.03$ pm^2	2.2 ± 0.2	1.6 ± 0.2	1.3 ± 0.1	—	3600	1.0	100	1310	740	0.08	55
Ga_2S_3-La_2S_3-$0.2Tm_2S_3$ $\sigma_e = 2.16$–2.82 pm^2	5.7	1.7	1.4	—	1160	1.0	—	5708	220	—	—
$70GeO_2$-15BaO-$10Ga_2O_3$-$4La_2O_3$-$1Tm_2O_3$	6.24	0.81	1.41	2909		1.0		516		0.069	

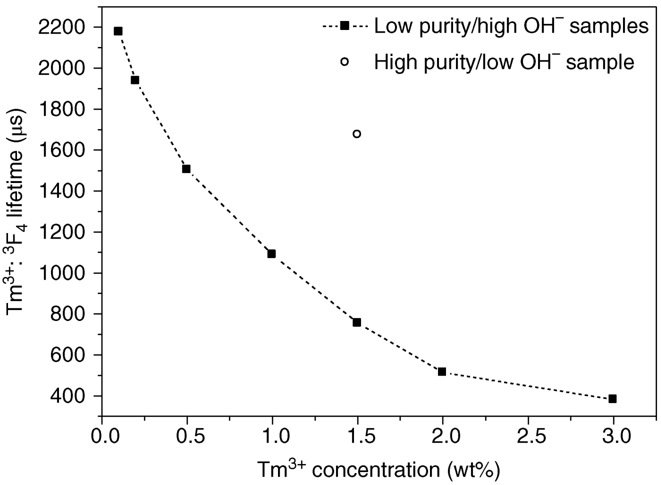

Figure 6.22 *Comparison of the measured* Tm^{3+} : $^3F_4$ *lifetimes at room temperature for varying* Tm^{3+} *concentrations. This figure also compares the lifetime of 1.5 wt%* Tm^{3+} *doped tellurite glass that was purified in a dry* O_2 *and* Cl_2 *gas mixture [29]. Source: Richards (2008). Reproduced with the permission of the University of Leeds Library.*

Before concluding this section, one more spectroscopic feature in Tm^{3+}-doped glass is explained that is essential for amplifier and laser design. In most inorganic glasses, the OH^- and related impurity absorption become more apparent when fibres and waveguides geometries are fabricated, which is due to the increased path length. In rare-earth devices some of the most dominant peaks for optical transition at the Er^{3+} : $^4I_{13/2} \rightarrow {}^4I_{15/2}$, $^4I_{11/2} \rightarrow {}^4I_{13/2}$; Tm^{3+} : $^3H_4 \rightarrow {}^3F_4$, $^3F_4 \rightarrow {}^3H_6$ are resonant with the fundamental, harmonics and overtone bands of OH^{-1} which may be present in the structure of glass host. As a result impurity-induced quenching becomes much more significant than the radiative transition. As an example in a Tm^{3+}-doped glass the effect of impurity induced and ion–ion quenching is shown in Figure 6.22. It is evident from the lifetime measurements of the Tm^{3+} : $^3F_4$ level that a significant concentration quenching effect dominates the decay process, which is apparent from a comparison of the values of measured lifetime at 2.2 ms for 0.1 wt% Tm^{3+}-doped glass, which falls to 0.4 ms in the 3.0 wt% Tm^{3+} sample. However, the apparent concentration quenching effect becomes less dramatic in samples which contained less OH^- ions, a trend that was also apparent in a range of Er^{3+}-doped tellurite glasses [77].

For energy transfer analysis, the metastable lifetimes of the Tm^{3+} : $^3F_4$ and Ho^{3+} : $^5I_7$ levels in the co-doped tellurium oxide glasses were also measured and reported elsewhere in detail [51]. From the measurements, which are summarized in Figure 6.21, it is apparent that with increasing concentrations the lifetimes of Ho^{3+} : $^5I_7$ level decreases from 3.8 ms at 0.2 wt% to 2.2 ms at 2.0 wt%, which is attributed to concentration quenching. Note that the quenching data when compared with Tm^{3+} appears to change less with concentration in Ho^{3+}, which may be due to a co-operative quenching effect caused by OH^- ion overtone–Tm^{3+} ion interaction. For Tm^{3+}-ion as a donor and Ho^{3+}-ion as an acceptor, the Tm^{3+} : $^3F_4$ level lifetime also showed a decrease with increasing Ho^{3+} concentration due to the increased forward energy transfer rate from Tm^{3+} : $^3F_4$ to Ho^{3+} : $^5I_7$.

6.8 Conclusions

In this chapter the Einstein model lays the foundation of the physics of light amplification by differentiating between the amplified spontaneous and stimulated emission processes. For light emission, the classical dipolar/multipolar model based on linear harmonic oscillator is adopted to explain the mechanism of intrinsic and extrinsic spectral broadening. Furthermore, with the help of classical dipole model and Fermi's golden rule the optical transition probabilities are compared. Before explaining the details of radiative, non-radiative and energy-exchange processes, the selection rules including the Laporte selection rule for allowed and disallowed transitions in rare-earth doped hosts are explained. Finally, the examples of radiative, non-radiative, energy transfer and energy quenching processes are explained by considering significant examples of rare-earth ions. These examples of rare-earth ions form the basis for engineering high slope efficiency and quantum efficiency lasers and amplifiers, respectively which are discussed in Chapter 7.

References

1. Silfvast, W.T. (2004) *Laser Fundamentals*, 2nd edn, Cambridge University Press.
2. Koechner, W. and M. Bass (2003) *Solid-State Lasers: A Graduate Text*, Springer Science & Business Media.
3. Fox, M. (2006) *Quantum Optics: An Introduction*, Oxford Master Series in Physics 6, Oxford University Press.
4. Einstein, A. (1906) On the theory of light production and light absorption. *Annalen der Physik*, **20** (Series 4), 199–206.
5. Cotton, F.A. and G. Wilkinson (1988) *Advanced Inorganic Chemistry*. 5th edn., New York, p. 705.
6. Weast, R.C. and M. Astle (eds) (1982) *Handbook of Physics and Chemistry*, 63 edn, CRC Press, Boca Raton, FL.
7. Duffy, J.A. (1990) *Bonding, Energy Levels, and Bands in Inorganic Solids*, Longman.
8. Imbusch, G. and Kopelman (1981) Optical spectroscopy of electronic centeres in solids, *Laser Spectroscopy of Solids* (ed. W.M. Yen and P.M. Selzer), Topics in Applied Physics, vol. 49, Springer, pp 1–37.
9. Meng, X.-g., *et al.* (2005) Near infrared broadband emission of bismuth-doped aluminophosphate glass. *Optics Express*, **13** (5), 1628–1634.
10. Quimby, R. (1991) Active phenomena in doped halide glasses, in *Fluoride Glass Fiber Optics* (ed. I. Aggarwal and G. Lu), Academic Press, Inc., Boston, pp. 351–378.
11. Ohishi, Y. (1997) Rare-earth ions in glasses and transitions for optical amplification, in *Optical Fiber Amplifiers: Materials, Devices, and Applications* (ed. S. Sudo), Artech House, Boston, pp. 149–182.
12. Reisfeld, R. and C.K. Jørgensen (1990) Excited state phenomena in vitreous materials, in *Handbook on the Physics and Chemistry of Rare Earths*, Elsevier, Amsterdam, pp. 1–90.
13. Armitage, J.R. (2000) Introduction to glass fibres and amplifiers, in *Optical Fibre Lasers and Amplifiers* (ed. P. W. France), Blackie & Sons Ltd, London, pp. 14–38.
14. Shen, S., *et al.* (2002) Tellurite glasses for broadband amplifiers and integrated optics. *Journal of the American Ceramic Society*, **85** (6), 1391–1395.

15. Ni, Y., J.M. Hughes, and A.N. Mariano (1995) Crystal chemistry of the monazite and xenotime structures. *American Mineralogist*, **80** (1), 21–26.
16. Jha, A., *et al.* (2012) Rare-earth ion doped TeO_2 and GeO_2 glasses as laser materials. *Progress in Materials Science*, **57** (8), 1426–1491.
17. Moreno, M., M. Barriuso, and J. Aramburu (1992) The Huang-Rhys factor S (a1g) for transition-metal impurities: a microscopic insight. *Journal of Physics: Condensed Matter*, **4** (47), 9481.
18. Miniscalco, W.J. (1993) Optical and electronic properties of rare-earth ions in glasses, in *Rare-Earth Doped Fiber Lasers and Amplifiers* (ed. M.J.F. Digonnet), Marcel Dekker, Inc. pp. 72–105.
19. Tanimura, K., *et al.* (1984) Optical-transitions of Ho^{3+} ions in fluorozirconate glass. *Physical Review B*, **30** (5), 2429–2437.
20. Jaba, N. *et al.* (2000) Infrared to visible up-conversion study for erbium-doped zinc tellurite glasses. *Journal of Physics-Condensed Matter*, **12** (20), 4523–4534.
21. Riseberg, L.A. and H.W. Moos (1968) Multiphonon orbit-lattice relaxation of excited states of rare-earth ions in crystals. *Physical Review*, **174** (2), 429–438.
22. Adam, J. and W. Sibley (1985) Optical transitions of Pr^{3+} ions in fluorozirconate glass. *Journal of Non-Crystalline Solids*, **76** (2), 267–279.
23. Yeh, D. *et al.* (1987) Multiphonon relaxation and infrared-to-visible conversion of Er^{3+} and Yb^{3+} ions in barium-thorium fluoride glass. *Journal of Applied Physics*, **62** (1), 266–275.
24. Yeh, D. *et al.* (1986) Radiation effects and optical transitions in Yb^{3+} doped barium-thorium fluoride glass. *Journal of Non-Crystalline Solids*, **88** (1), 66–82.
25. Huang, L.H., S.X. Shen, and A. Jha (2004) Near infrared spectroscopic investigation of Tm^{3+}-Yb^{3+} co-doped tellurite glasses. *Journal of Non-Crystalline Solids*, **345**, 349–353.
26. Huang, L. *et al.* (2004) Broadband emission in Er^{3+}-Tm^{3+} codoped tellurite fibre. *Optics Express*, **12** (11), 2429–2434.
27. Nakazawa, E. and S. Shionoya (1967) Energy transfer between trivalent rare-earth ions in inorganic solids. *The Journal of Chemical Physics*, **47** (9), 3211–3219.
28. Inokuti, M. and F. Hirayama (1965) Influence of energy transfer by the exchange mechanism on donor luminescence. *The Journal of Chemical Physics*, **43** (6), 1978–1989.
29. Richards, B. (2008) Tellurite Glass Mid-infrared (1.9-2.1 μm) Fibre Lasers, School of Process, Environmental and Materials Engineering - Institute for Materials Research, University of Leeds.
30. Auzel, F. (2004) Upconversion and anti-Stokes processes with f and d ions in solids. *Chemical Reviews*, **104** (1), 139–174.
31. Yeh, D., W. Sibley, and M. Suscavage (1988) Efficient frequency upconversion of Tm^{3+} ions in Yb^{3+} doped barium-thorium fluoride glass. *Journal of Applied Physics*, **63** (9), 4644–4650.
32. Digonnet, M.J.F. (ed.) (2001) *Rare-Earth-Doped Fibre Lasers and Amplifiers*. 2nd edn, Marcel Dekker, Inc.
33. Toropov, N. and I. Bondar (1961) Silicates of the rare earth elements. *Russian Chemical Bulletin*, **10** (4), 502–508.
34. Toropov, N., F.Y. Galakhov, and S. Konovalova (1962) Silicates of the rare earths. *Russian Chemical Bulletin*, **11** (5), 689–693.

35. Deng, H. *et al.* (2005) Controlled hydrothermal synthesis of bismuth oxyhalide nanobelts and nanotubes. *Chemistry-A European Journal*, **11** (22), 6519–6524.
36. Bondar, I. (1982) Rare-earth silicates. *Ceramics International*, **8** (3), 83–89.
37. Dong, J. *et al.* (2011) Dual-pumped tellurite fiber amplifier and tunable laser using Er/Ce codoping scheme. *Photonics Technology Letters, IEEE*, **23** (11), 736–738.
38. Miniscalco, W.J. (1993) Optical and electronic properties of rare-earth ions in glasses. in *Rare-Earth Doped Fiber Lasers and Amplifier* (ed. M. J. Digonnet), Marcel Dekker, Inc., pp. 72–105.
39. Shen, S., B. Richards, and A. Jha (2006) Enhancement in pump inversion efficiency at 980 nm in Er^{3+}, $Er^{3+}/Eu^{3+}+$ and Er^{3+}/Ce^{3+} doped tellurite glass fibers. *Optics Express*, **14** (12), 5050–5054.
40. Bookey, H. *et al.* (2007) Multiple rare earth emissions in a multicore tellurite fiber with a single pump wavelength. *Optics Express*, **15** (26), 17554–17561.
41. Miniscalco, W. (1991) Erbium-doped glasses for fiber amplifiers at 1500 nm. *Journal of Lightwave Technology*, **9** (2), 234–250.
42. Joshi, P., S. Shen, and A. Jha (2008) Er^{3+}-doped boro-tellurite glass for optical amplification in the 1530-1580 nm. *Journal of Applied Physics*, **103** (8), 083543–083543-7.
43. Yamada, M. *et al.* (1998) Gain-flattened tellurite-based EDFA with a flat amplification bandwidth of 76 nm. *Photonics Technology Letters, IEEE*, **10** (9), 1244–1246.
44. Mori, A. *et al.* (2002) 1.58-um Broad-band erbium-doped tellurite fiber amplifier. *Journal of Lightwave Technology*, **20** (5), 794.
45. Sun, Y. *et al.* (1997) 80 nm ultra-wideband erbium-doped silica fibre amplifier. *Electronics Letters*, **33** (23), 1965–1967.
46. Ikesue, A. and Y.L. Aung (2008) Ceramic laser materials. *Nature Photonics*, **2** (12), 721–727.
47. Nair, P. *et al.* (2003) Pulpal response to Er: YAG laser drilling of dentine in healthy human third molars. *Lasers Surgery Medicine*, **32** (3), 203–209.
48. J.Y. Alain, M. Monaire, and H. Poignant (1989) Erbium-doped fluorozirconate single-mode fibre lasing at 2.71um. *Electronics Letters*, **25**, 28–29.
49. Nachimuthu, P. and R. Jagannathan (1999) Judd–Ofelt parameters, hypersensitivity, and emission characteristics of Ln^{3+} (Nd^{3+}, Ho^{3+}, and Er^{3+}) ions doped in PbO-PbF_2 glasses. *Journal of the American Ceramic Society*, **82** (2), 387–392.
50. Ye, C. *et al.* (1996) Spectral properties of Er^{3+}-doped gallium lanthanum sulphide glass. *Journal of Non-Crystalline Solids*, **208** (1), 56–63.
51. Richards, B. *et al.* (2010) Tellurite glass lasers operating close to 2 μm. *Laser Physics Letters*, **7** (3), 177.
52. Jackson, S.D. (2004) Cross relaxation and energy transfer upconversion processes relevant to the functioning of 2 μm Tm 3+-doped silica fibre lasers. *Optics Communications*, **230** (1), 197–203.
53. Jackson, S.D. (2012) Towards high-power mid-infrared emission from a fibre laser. *Nature Photonics*, **6** (7), 423–431.
54. Schweizer, T. *et al.* (1999) Infrared emission and ion-ion interactions in thulium- and terbium-doped gallium lanthanum sulfide glass. *Journal of the Optical Society of America B-Optical Physics*, **16** (2), 308–316.
55. Sorokina, I.T. and K.L. Vodopyanov (2003) *Solid-State Mid-Infrared Laser Sources*, Springer.

56. Fusari, F. *et al.* (2010) Femtosecond mode-locked Tm^{3+} and Tm^{3+}-Ho^{3+} doped 2 μm glass lasers. *Optics Express*, **18** (21), 22090–22098.
57. Wu, J. *et al.* (2007) Highly efficient high-power thulium-doped germanate glass fiber laser. *Optics Letters*, **32** (6), 638–640.
58. Wu, J. *et al.* (2006) Efficient thulium-doped 2-μm germanate fiber laser. *Photonics Technology Letters, IEEE*, **18** (2), 334–336.
59. Percival, R.M. *et al.* (1995) A 1.6-μm pumped 1.9-μm thulium-doped fluoride fiber laser and amplifier of very high-efficiency. *IEEE Journal of Quantum Electronics*, **31** (3), 489–493.
60. Percival, R.M. *et al.* (1992) Thulium sensitized holmium-doped CW fluoride fiber laser of high-efficiency. *Electronics Letters*, **28** (24), 2231–2232.
61. Allain, J.Y., M. Monerie, and H. Poignant (1991) High-efficiency CW thulium-sensitized holmium-doped fluoride fiber laser operating at 2.04 μm. *Electronics Letters*, **27** (17), 1513–1515.
62. Jackson, S.D. *et al.* (2007) High-power 83 W holmium-doped silica fiber laser operating with high beam quality. *Optics Letters*, **2** (3), 241–243.
63. Jackson, S.D. and Y. Li (2004) High-power broadly tunable Ho^{3+}-doped silica fibre laser. *Electronics Letters*, **40** (23), 1474–1475.
64. Jackson, S.D. (2006) Midinfrared holmium fiber lasers. *IEEE J. Quantum Electronics*, **42** (1–2), 187–191.
65. Jackson, S.D., F. Bugge, and G. Erbert (2007) High-power and highly efficient diode-cladding-pumped Ho^{3+}-doped silica fiber lasers. *Optics Letters*, **32** (22), 3349–3351.
66. Tsang, Y.H. and T.A. King (2007) Multi-mode 2 μm Tm-silica fibre lasers with 1.61 μm in-band pumping. *Journal Modern Optics*, **54** (12), 1659–1667.
67. Evans, C.A. *et al.* (2009) Numerical rate equation modeling of a ~2.1-μm - Tm^{3+}/Ho^{3+} co-doped tellurite fiber laser. *Journal Lightwave Technology*, **27** (19), 4280–4288.
68. Yeh, D.C. *et al.* (1989) Energy-transfer between Er^{3+} and Tm^{3+} ions in a barium fluoride-thorium fluoride glass. *Physical Review B*, **39** (1), 80–90.
69. Kermaoui, A. and F. Pelle (2009) Synthesis and infrared spectroscopic properties of Tm^{3+}-doped phosphate glasses. *Journal Alloys Compounds*, **469** (1–2), 601–608.
70. Jackson, S.D. and T.A. King (1999) Theoretical modeling of Tm-doped silica fiber lasers. *Journal Lightwave Technology*, **17** (5), 948–956.
71. Gebavi, H. *et al.* (2011) Novel Tm^{3+}-doped fluorotellurite glasses with enhanced quantum efficiency. *Optical Materials*, **33** (3), 428–437.
72. Fusari, F. *et al.* (2008) Spectroscopic and lasing performance of Tm^{3+}-doped bulk TZN and TZNG tellurite glasses operating around 1.9 μm. *Optics Express*, **16** (23), 19146–19151.
73. Zhou, B., *et al.* (2011) Superbroadband near-infrared emission in Tm-Bi codoped sodium-germanium-gallate glasses. *Optics Express*, **19** (7), 6514–6523.
74. Murray, M., *et al.* (2012) Tm^{3+} doped silicon thin film and waveguides for mid-infrared sources. *Applied Physics Letters*, **101** (14), 141107.
75. Shen, S. *et al.* (2007) Tm^{3+}–Ho^{3+} and Tm^{3+}–Tb^{3+} energy transfer in tellurite glass. *Journal of Luminescence*, **126** (2), 434–440.
76. Naftaly, M., S. Shen, and A. Jha (2000) Tm^{3+}-doped tellurite glass for a broadband amplifier at 1.47 μm. *Applied Optics*, **39** (27), 4979–4984.
77. Jha, A., S. Shen, and M. Naftaly (2000) Structural origin of spectral broadening of 1.5-μm emission in Er^{3+}-doped tellurite glasses. *Physical Review B*, **62** (10), 6215.

7

Applications of Inorganic Photonic Glasses

7.1 Introduction

In this concluding chapter the background knowledge provided in the first six chapters is brought together by reference to key applications which are either part of the state-of-the-art fibre, bulk and waveguide optics or emerging trends that await implementation as technology platforms. For this reasons this chapter is deliberately kept concise because of the vastness of the knowledge developed to date on each application, listed below—each in its own right demands at least a chapter if not a whole book. An attempt has been made to divide this chapter into four sections on *dispersion control and management in optical fibres*, *optical nonlinearity in fibres*, *active fibres and sensor devices*, and *emerging materials and devices and the future*. The culminating section sets the scene for an emerging *roadmap* for future of photonic materials, demanding multifunctional devices forming a part of board-level integrated photonic circuit which may be perhaps connected on a board with incoming and outgoing fibres, as in electronic and optoelectronic circuits where the electron flow is managed in and out of a printed circuit board with copper wires.

7.2 Dispersion in Optical Fibres and its Control and Management

The demonstration of the signal transmission capacity of optical fibres in the early 1970s initiated significant interest in exploiting the technology of guided light in optical communication, influenced by the timely growth of semiconductor diode laser technology and modulation scheme. As stated in earlier chapters, two factors determine the degradation of optical signals and they are the total loss and dispersion. Factors controlling loss have already been discussed in detail in Chapter 4 together with an introduction to materials dispersion in Section 4.5. Looking at a temporal map of signal propagation, say in a single-mode optical fibre, trillions of bits of information carrying signals propagate along the fibre length. Besides propagation loss, these signals may degrade as a result of two dispersion-related factors,

Inorganic Glasses for Photonics – Fundamentals, Engineering and Applications, First Edition. Animesh Jha.
© 2016 John Wiley & Sons, Ltd. Published 2016 by John Wiley & Sons, Ltd.

known as the *intramodal dispersion* and *intermodal delays*, both of which are dependent on the group velocities of guided modes, discussed in Section 4.5 (Chapter 4). If we consider a Gaussian shape pulse, then the leading and trailing ends of this pulse propagate with different velocities because of the energy distribution. At this point readers may wish to recap the quantum mechanical uncertainty principles to appreciate the distribution of energy quanta and their corresponding relaxation time, phase and population distribution. All these classical and quantum mechanical approaches are consistent in defining the dispersion in terms of the group velocity distribution.

7.2.1 Intramodal Dispersion

To appreciate the role of overall dispersion on signal distortion, the characterization of total dispersion (D_{tot}) or total time or group delay $(\Delta t)_{\mathrm{tot}}$ is the best approach. If the group delay t_g is arising as a result of signal propagation over length L, the group velocity, $V_g(\lambda)$, may be represented in Equation 7.1 by the propagation constant β and $k = 2\pi/\lambda$ which is the wave vector [1,2]:

$$\frac{L}{t_g} = V_g(\lambda) = c\left(\frac{\mathrm{d}\beta}{\mathrm{d}k}\right)^{-1} = \left[-\frac{\lambda^2}{2\pi c}\left(\frac{\mathrm{d}\beta}{\mathrm{d}\lambda}\right)\right]^{-1} \tag{7.1}$$

Since $V_g(\lambda)$ is a function of wavelength, each wavelength within the wave envelope propagates with different velocities over fibre length L, which implies that the overall wave envelope has broadened with respect to the starting point at time $t = 0$.

This also means that the modal energy distribution is changing in accordance with the group velocity distribution. This is schematically shown in Figure 7.1, using this schematic

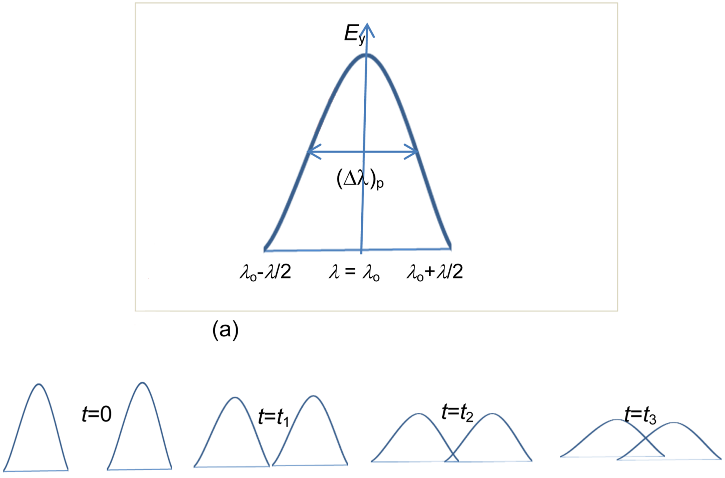

(a)

(b)

Figure 7.1 *Wave properties shown (a). Electric field and spectral width (b) represents a temporal evolution of a propagating electromagnetic wave in the core of an optical fibre with no dispersion management [1]. Source: Keiser 1991. Reproduced with permission from McGraw Hill.*

sketch the time delay (Δt) for each narrow pulse with spectral width $(\Delta\lambda)_p$ along the propagation path length may be defined by Equation 7.2:

$$\Delta t = \frac{dt_g}{d\lambda}(\Delta\lambda)_p \tag{7.2}$$

and the resulting total dispersion in ps (km nm)$^{-1}$ may be expressed as:

$$D_{tot}(\lambda) = \frac{1}{L}\left(\frac{dt_g}{d\lambda}\right) \tag{7.3}$$

and the total pulse spreading (σ_{tot}) is then:

$$\sigma_{tot} = D_{tot}(\lambda).L.(\Delta\lambda)_p \tag{7.4}$$

From Figure 7.1b, it is apparent on temporal scale that the pulse train identity is lost by losing the temporal identity and intensity of electric field, which is again consistent with the Heisenberg uncertainty principle. After sometime $t_3 > t_2 > t_1 > t = 0$, the pulse train identity has been lost significantly. Such a pulse train will require three significant operations in signal processing: reclocking, reshaping and reamplification. The total dispersion (D_{tot}) includes the contributions from the materials and waveguide dispersions. Since the materials dispersion is strongly dependent on the refractive index of a medium, the shape of the wavelength dependence of refractive index may change implying that the total dispersion may also change accordingly. It is important to note that both the waveguide and materials dispersions cannot be treated independent of each other due to complex mathematical relations between wavelength, refractive index and modal distribution. In addition, in a waveguide further complexity arises due to the difference in the refractive indices of core and cladding glasses.

Keiser [1] and Ghatak *et al.* [2] have discussed dispersion in waveguides extensively and argued that a better estimation of each part of overall dispersion can be made by calculating the individual contribution at a time assuming that the other components of dispersion are negligible. By summing the contributory dispersion terms, the *intramodal dispersion* may be estimated with reasonable accuracy.

Let us now analyse the *intramodal dispersion* first in terms of *materials dispersion* which was introduced in Chapter 4 (Section 4.5). In the literature this type of dispersion is also termed *chromatic* or *spectral* dispersion. Using Equation 7.1 for material's dispersion (in ps (km nm)$^{-1}$), the delay time (Δt) for signal arrival between a link of length L (km) was derived:

$$D_{mat} = -\frac{\lambda}{c}.\frac{d^2n}{d\lambda^2}(\times 10^9) = \frac{\Delta t}{(L\Delta\lambda_p)} \tag{7.5}$$

The corresponding magnitude of spectral width of a pulse due to materials dispersion is then:

$$(\sigma_{mat}) = D_{mat}.L.\Delta\lambda_p \tag{7.6}$$

Some examples might help. Due to the wavelength dependence of the refractive index and finite wavelength distribution ($\Delta\lambda$, nm) of a pulse, the spectral broadening will arise after the signal has propagated over L kilometres in a communication fibre. For example, at 1.55 μm, the materials dispersion (D_m) of a silica fibre is positive with a value of 20 ps (nm km)$^{-1}$. If, then, a laser with a pulse width of $\Delta\lambda = 2$ nm at this wavelength is launched, the delay per kilometre of fibre length will be 40 ps due to the materials dispersion. From the materials dispersion curves in Figure 4.30, it is evident that for a given material the dispersion has both positive and negative signs, suggesting that a pulse will spread above the zero materials dispersion wavelength (ZMDW) and, conversely, pulse compression is expected below the ZDW. This is quite fundamental in considering the signal transmission near zero dispersion wavelength with a finite bandwidth of laser light, because the relative flatness of the ZMDW spectral range may help in maintaining the pulse shape of a single frequency laser ($\Delta\lambda$).

The waveguide geometry contributes to the *intramodal dispersion* because of the intensity or energy distribution of a mode in a single mode fibre. Recalling Equation 4.17 (Section 4.2.1), the energy distribution of a Gaussian shape beam has only 80% footprint, as shown in Figure 4.5. As a result, the remaining 20% of energy propagates in the lower refractive index of cladding, in which the phase velocity V_1 of the 20% energy part a signal proportionately increases. In addition, the modal propagation constant (β) in Equation 4.24a depends on the geometrical parameters of a fibre (diameter a). Based on this geometrical constrain of fibre waveguides, the time delay (Δt_w) may be expressed in Equation 7.7 in term of waveguide dispersion (D_w) properties as above for the materials dispersion:

$$\Delta t_w = \frac{L}{c}\left(\frac{d\beta}{dk}\right) = \frac{L}{c}\left[n_{clad} + n_{clad}(\Delta n)\frac{d(Vb)}{dV}\right] \tag{7.7}$$

where:

$$V = ka\left(n_{core}^2 - n_{clad}^2\right)^{\frac{1}{2}}$$

is the parameter defining the mode distribution characteristics, e.g. $V \leq 2.405$ for a single mode fibre. Here $k = 2\pi/\lambda$ and the spectral broadening due to waveguide dispersion (σ_w) is:

$$\sigma_w = \frac{dt_w}{d\lambda}\left(\Delta\lambda_p\right) = (\Delta\lambda)_p D_w(\lambda) L \tag{7.8}$$

Keiser [1] showed that for single mode operation in a fibre the total pulse spread in nm is due to the sum of component parts:

$$\sigma_{tot} = (\sigma_m + \sigma_w) = -\frac{0.023}{Lc}(\Delta\lambda)_p \tag{7.9}$$

In the overall dispersion curve, the material contribution is more dominant at shorter wavelengths, whereas at longer wavelengths in the optical communication window the waveguide dispersion is the dominant factor. The wavelength dependence of D_w, D_M and D_{tot} are shown in Figure 7.2a.

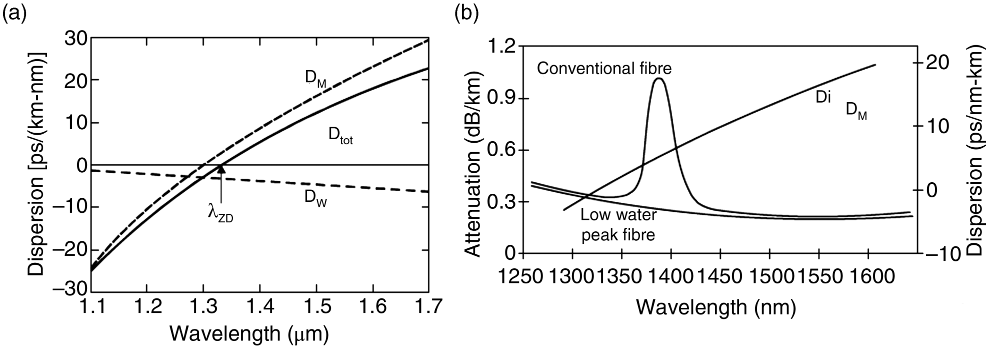

Figure 7.2 *(a) Dispersion properties of a silica fibre is shown with materials (D_M), waveguide (D_w) and total dispersion (D_{tot}). (b) A comparison of materials dispersion and total loss in conventional and low-water peak fibres [3].*

For the intramodal part, from the plot of the three dispersion curves, D_w, D_M and D_{tot}, in Figure 7.2 it is apparent that the total dispersion in ps (km nm)$^{-1}$ is less than the materials dispersion. In addition, the overall shape of the total dispersion curve is controlled by the materials dispersion, and both of these intersect the zero-dispersion wavelength (ZDW) line. The ZDW is usually not a point but a small spectral range in the optical transmission window of silica optical fibres, compared in Figure 7.2b. From these curves it is apparent that below ZDW the values of D_{tot} and D_M are negative, which then becomes positive at longer wavelengths beyond ZDW. This is a significant point from which the ZDW bandwidth for signal transmission may be identified for minimizing pulse broadening.

In Figure 7.2b, the materials or chromatic dispersion of convential silica optical fibre is superimposed with the total loss curves in two types of optical communication fibres—a conventional fibre (also known as legacy fibres) and the zero or ultra-low OH fibres. The conventional fibre shows an attenuation peak due to the first harmonic of OH^- band near 1370 nm which lies above the ZDW, and is a significant contributor to overall degradation of optical signal. By contrast, the signals propagating in the fibre with minimal or no OH^- absorption will only encounter a background loss related penalty near the zero-dispersion wavelength. For this important reason, the International Telecommunication Union (ITU) recommended that the positive dispersion must be minimized at the lowest loss window of the communication fibre, to create larger bandwidth. Consequently, several dispersion management schemes were proposed and implemented for communication fibres. Before embarking on methods of dispersion management in optical fibres, let us consider two other types of dispersions, besides the *materials* and *waveguide* dispersions and they are *intermodal* and *polarization mode* dispersions.

7.2.2 Intermodal Distortion

Based on the concept of group velocity delay ($\Delta t_{\text{H-0}}$) in Section 4.5 in Chapter 4, we may introduce the intermodal delay which arises due to the modal distribution of ray path for individual modes, spread radially across the fibre core. Between the zero-order axial mode (ZoM) and the highest order mode (HoM), several intermediate order modes (e.g. $m = 1, 2$) fill the modal space, leading to a distribution of group velocities which may also be anticipated across the fibre core volume. It is this type of distribution of energy that underpins signal distortion. During propagation, statistical probability of modal interaction increases, resulting in exchange of energy that may then relax the resulting wave into a new temporal domain, with respect to starting time. Based on this understanding, the modal delay (Δt_{MoD}) may be estimated from the following formula:

$$\Delta t_{\text{MoD}} = (t_{\text{HoM}} - t_{\text{ZoM}}) = \frac{(Ln_{\text{core}})}{c(\Delta n)} \tag{7.10}$$

In the fabrication of single-mode fibres, the core–clad structure and the refractive index difference is adjusted in such a way so that it not only supports a single-mode but also minimizes the temporal delays. Note that the modal distribution may also have a different intensity spectrum, by virtue of the degeneracy that is well known from classical electrodynamics. The modal distribution of delay is schematically shown in Figure 7.3. It is for this reason that a multimode fibre is unsuitable for optical and data communication because the modal distribution of energy is difficult to track once it is dispersed.

In optical networks the design parameters for fibre include specifications for reducing intermodal dispersion by defining the refractive index and related geometrical properties. Since in multimode fibres the modal definition cannot be ensured over a large distance of

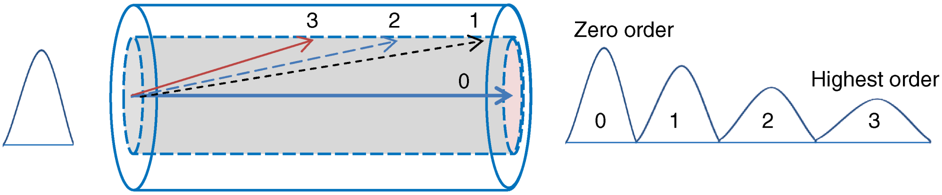

Figure 7.3 *Temporal shapes of zero-order (ZoM) and higher order modes (HoM) (1–3) propagating in the core of an optical fibre [4]. Source: Mynbaev 2001. Adapted with permission from Prentice Hall.*

signal transmission due to the strong overlap of energies from different modes, such fibres are unsuitable for optical communication networks. As we will see below, in the dispersion management section, a single mode graded index fibre may be able to offer better control of modal temporal delay than a standard step index fibre.

7.2.3 Polarization Mode Dispersion (PMD)

The polarization mode dispersion originates from the interaction of angular momentum of a signal photon with the medium. This implies that as a result of propagation the original direction of the momentum relaxes to a new state, which, for example, may be appreciated from the splitting of LP_{01} modes in single-mode fibres. Consider a plane-polarized light with its electric field oscillating in the radial direction and fixed at angle, $\phi = 90°$, so that the azimuthal position remains unchanged. In an idealized fibre with no defects and inhomogeneity along the propagation direction, a plane-polarized wave will propagate without losing its azimuth identity. This means the *angular modal definition* will not change. However, in reality this is far from the truth due to the stochastic nature of accumulated strain and defects in the fibre structure. The strain and complementary refractive index and meso-scale density variation cause perturbation when the single-azimuth photon interacts with the medium, and as a result the original orientation additively changes from each of these stochastic Snell or Rayleigh like interactions, which is why we expect the original polarization direction to be changed, as exemplified schematically in Figure 7.4a and b. Consequently, the time delay due to PMD is given by Equation 7.4:

$$\Delta t_{\mathrm{PMD}} = D_{\mathrm{PMD}}(L)^{0.5} \tag{7.11}$$

Here D_{PMD} is the polarization mode dispersion, with dimensions ps $(\mathrm{km})^{0.5}$. Unlike other types of dispersion and distortion, the PMD is not dependent on wavelength and increases with the square-root of trunk length (L). Amongst the types of dispersion and temporal

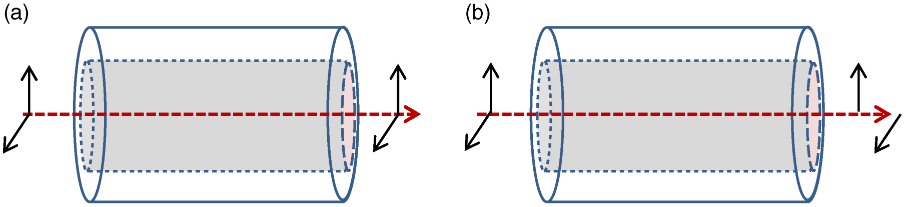

Figure 7.4 *Example of polarization preserving (a) and polarization splitting (b) cores in two different optical fibres. Adapted from [3].*

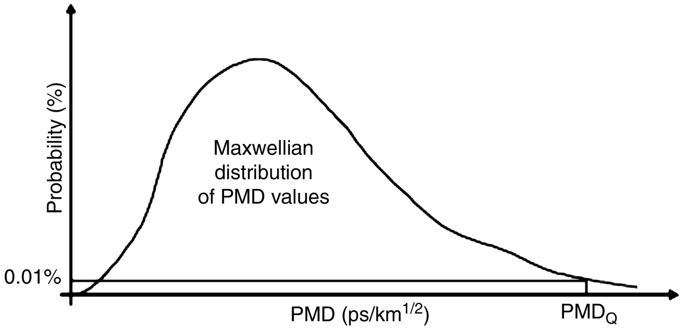

Figure 7.5 Maxwellian distribution of the values of polarization mode distribution; the 0.01% line is the recommended PMD coefficient. Source: Maeda 2010 [3]. Reproduced with permission of International Telecommunication Union.

delays, the PMD is most unpredictable on a microscopic scale, which means for a given length of fibre it has to be measured and included in the overall fibre specification.

In the ITU document [3], the differential group delay resulting from propagation in a given trunk length of L km is characterized and reported as a net effect due to statistical behaviour of PMD. The PMD coefficient is usually specified and it is a value reported as the value normalized to the measurement length. "The ergodic distribution of PMD is normally Maxwellian" (Figure 7.5) [3] and is reported with a single parameter, which is given above in Equation 7.4.

In a fibre the Maxwellian distribution might not arise because of a range of variation in the modal coupling along the length of a cable. Some parts of the fibre might experience much greater bend than the rest of the fibre, which may therefore cause a variation in the point-to-point stress and therefore affect the polarization mode coupling. In a cabled structure of fibres, the PMD is therefore specified as a bundle property rather than the property of an individual fibre. The specification relates to a term called the PMD coefficient, which is a "defined term of small probability" (e.g. 0.01% shown in Figure 7.5).

7.2.4 Methods of Controlling and Managing Dispersion in Fibres

Although the total dispersion in optical fibres, as explained above, depends on materials and waveguide, modal delay and polarization dispersion, the method used to control first three components of dispersion depends primarily on the control of the refractive index profile of a core/clad glass structure, whereas the polarization dispersion is managed by using polarization maintaining fibres to remove the "ergodic distribution" of polarization modes along a network link. These are discussed briefly below.

Index profile engineering for dispersion management and compensation requires re-engineering of the refractive indices of core and cladding glass materials which may be achieved using the following index profiles in Figure 7.6, using both step-index and gradient index profiles. The resulting control of core and clad refractive index is achieved during fabrication by controlling the dopants during the fabrication of silica fibres. To achieve positive refractive indices in the fibre, dopants, namely GeO_2, P_2O_5 and lanthanide oxides, are usually incorporated, whereas to reduce the index B_2O_3 and fluoride ions are incorporated in the radial direction away from the core (Figure 7.6) [1].

The resulting structure may then yield the following types of fibres: (a) *dispersion-shifted fibre* (DSF) to achieve zero dispersion at a different wavelengths when compared with the

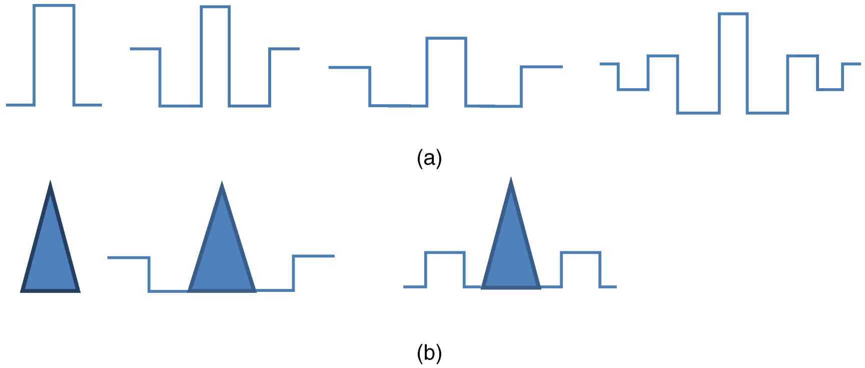

Figure 7.6 *A range of refractive index profiles for dispersion management in step-index (a) and gradient-indexed (b) cores [1,3,4]. Source: Keiser 1991. Adapted with permission from McGraw Hill.*

original dispersion, (b) *dispersion compensation* by flattening the net dispersion profile of a fibre, known as the DCF, and (c) in a *non-zero dispersion shifted fibre* (NZ-DSF), at the wavelength of operation, the net dispersion is adjusted to a negative value, with respect to a dispersion shifted fibre. Case (c) implies that the net dispersion being negative would compress a pulse and that each pulse will regain its temporal profile as it propagates. However, the temporal evolution of a pulse will lead to a power penalty and for this reason the train of pulses encountering temporal reshaping may require reamplification due to the loss of power.

Based on the above three cases, the examples of dispersion curves in standard silica, DSF, and DCF fibres are shown in Figure 7.7, in which the slopes of three different curves and zero-

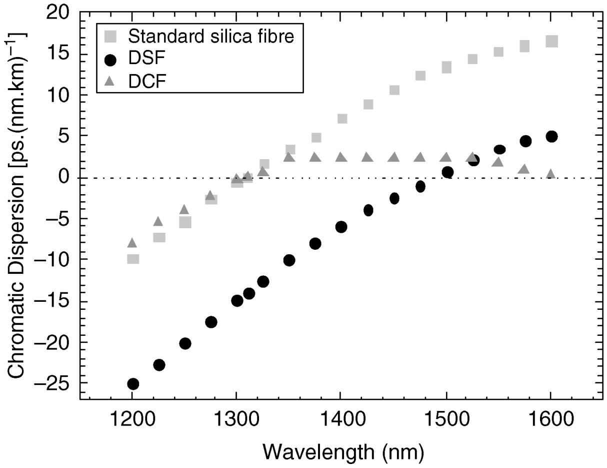

Figure 7.7 *Examples of dispersion profiles in standard, dispersion compensated or flattened (DCF) and dispersion shifted fibres (DSF) as a function of wavelength. Note that the DCF has values closer to zero in the 1300–1600 nm region [3].*

dispersion points are clearly unique, for implementing the management of dispersion in optical fibre networks. From this figure it is evident that the region of near zero dispersion in the standard fibre is near 1310–1320 nm with the zero-dispersion point at 1317.2 nm. The region of near-zero dispersion is determined by ascertaining the zero-dispersion slope (S_o, ps (nm^{-2}) (km^{-1}), from which the dispersion parameter, $D(\lambda)$, may be expressed in terms of wavelength (λ, nm) and the zero-dispersion wavelength point (λ_o, nm):

$$D(\lambda) = \frac{S_o}{4}\left[\lambda - \frac{(\lambda_o)^4}{\lambda^3}\right] \tag{7.12}$$

In this narrow spectral range, the pulse train suffers minimal dispersion related broadening; details may be found in Keiser [1], Mynbaev and Scheiner [4] and ITU-T report [3].

In concluding this section on dispersion and its management, it is important to recognize that the dispersion properties of optical communication fibres determine the "*information carrying capacity*", i.e. the bandwidth (BW), of the fibre which is also measured in terms of bit rate (BR) "bit per second". The fibre bandwidth is measured in frequency (Hz), which in engineering makes sense in representing the "bits per second" since the unit of frequency "Hz" and "bit per second" have time or frequency correspondence. The most commonly used relationship between BR and BW is given in Equation 7.13:

$$\mathrm{BW} = \frac{\mathrm{BR}}{2} \text{ and } \mathrm{BR} < 0.25(\Delta t) \tag{7.13}$$

Here Δt represents the total dispersion related pulse spreading. Since the value of Δt in Equation 7.13 is dependent on the materials and waveguide dispersions in a fibre, the values of BW vary for single-mode, graded-index and multi-mode fibres.

For controlling optical nonlinearity, laser power and long-haul optical signal transmission, dispersion (delay and modal energy distribution) management is one of the most important factors, and its management is expensive because of its intrinsic dissipative nature (such as is viscosity in fluid flow).

7.3 Unconventional Fibre Structures

7.3.1 Fibres with Periodic Defects and Bandgap

The history of PCF and PBG fibres has been in the making since the first optical fibre was developed in 1970s when Kaiser *et al.* at Bell Laboratories [5] demonstrated an air-suspended fibre core supported by a solid jacket using a thin glass membrane. This was the first attempt to incorporate air structure within a glass for guiding light. Unconfirmed reports suggest that there might have been a parallel development in the former Soviet Union as a low-loss light guiding structure. Between 1978 and the end of 1987, Yeh and Yariv [6,7] demonstrated light propagation in periodic defect structures in crystals and glasses, e.g. in periodically poled lithium niobate crystals and in fibre Bragg gratings. John [8,9], and Yablonovitch [10,11] reported confinement of electromagnetic waves in periodic structure. Joannopoulos demonstrated the concept of light guiding in one-, two- and three-dimensional periodic defect photonic crystal in a text book and in an article in *Nature* [12,13]. Subsequently, photonic band gaps in two- and three-dimensional structures were also measured and shown, as discussed below. In addition, an alternative way of viewing the propagation of electromagnetic wave in materials with periodic defects was emerging with a concept of “stop-band” [14]. From a theoretical analysis it was widely recognized that to achieve photonic band gap (PBG), the index ratio was predicted to be 2.2 : 1 in 2D structures, which was confirmed later to be much relaxed to 1.4 : 1 in 3D structures, such as fibre with an invariant direction of propagation, which is along the fibre axis [15]. By recognizing the relaxation of theoretical limit on refractive index for PBG structures, Russell’s group was first to demonstrate the trapping of light inside a photonic crystal fibre (PCF) structure. Silica glass capillaries were assembled in a specially designed hexagonal capillary supporting mould, to create a periodic defect of air-holes in a lattice of silica capillaries, which was then drawn carefully by preserving the original structure, such that the drawn fibre structure replicates the periodicity on the micrometre scale and compares with the wavelength of photons (e.g. in the visible to infrared spectrum). In such structures it was considered that the air-guiding regions may be able to confine the fundamental mode into the core in the same way as in the case of Bragg reflections. Based on this assumption, the electromagnetic wave propagation model, discussed in Chapter 4 (Section 4.1) can be readapted for a cylindrical geometry. Invoking the single-mode propagation solution yields the V value, which for standard step-index fibre is equal to:

$$V \leq 2.405 = \frac{2\pi a}{\lambda}\left(n_{\text{core}}^2 - n_{\text{clad}}^2\right)^{\frac{1}{2}} \tag{7.14}$$

By introducing the periodic defects into a dielectric medium, e.g. silica, the transverse continuum condition for refractive index in the core glass can no longer hold, which means a newly parameterized equation for air-guiding index in PCF is required, which was derived using a scalar approximation of the Maxwell’s equation for periodic defects [11–13,16]. In Equation 7.15, the V value of PCF may be compared with Equation 7.14:

$$V = \Lambda\kappa\left[\left(n_{\text{high}}\right)^2 - \left(n_{\text{low}}\right)^2\right]^{\frac{1}{2}} \tag{7.15}$$

Here Λ is the fill factor for the dielectric and κ is the wave vector. In air-guided PCF, the propagation of fundamental modes dominates in the core glass region by squeezing the higher order modes out or, in another words, these modes are disallowed in the core region. This type of “disallowed mode” guidance by energetically supporting the fundamental mode in the core is a unique characteristic of air-index guiding PCF (also known as microstructured optical fibres (MOFs)). It is not dependent on the total internal reflection at the boundary of core–clad structure, as observed in a standard single mode fibre. The preservation of fundamental mode within the core region then imposes an important condition for air-index guiding, which is based on the “maximum value of refractive index, n_{max}”, along the radial direction of the waveguide for the condition $\kappa\Lambda \rightarrow 0$, i.e. when λ is large. By assuming a non-dispersive glass (g) and air (a), the value of n_{max} may be ascertained using the scalar approximation [15,17] from the following equation:

$$n_{\text{max}} \rightarrow \sqrt{(1-F)n_{\text{g}}^2 - Fn_{\text{a}}^2} \tag{7.16}$$

Here F is the fractional volume of defects in the PCF structure. Unlike in a standard step-index single mode fibre in which the number of modes increases with decreasing wavelength

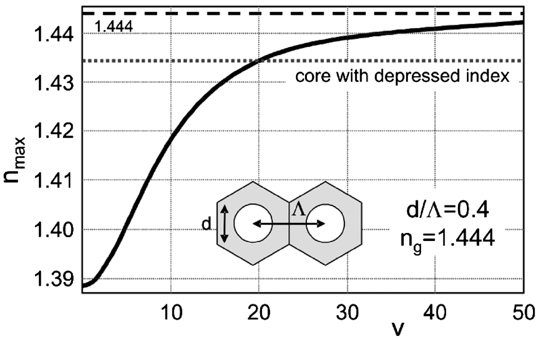

Figure 7.8 *Plot of maximum axial refractive index in the photonic crystal cladding as a function of the normalized frequency parameters* v *for* d/*Λ = 0.4 and* n$_g$ *= 1.444. The filling fraction of air was 14.5%. As* v → *0,* n → *1.388. The horizontal dotted line corresponds to a condition when the core is replaced by glass with a refractive index of 1.435, leading to ceasing of guidance at* v *= 20 [17]. Source: Russell 2006. Reproduced with permission from OSA Publishing.*

(i.e. $\kappa\Lambda \rightarrow \infty$) in the high-index core region, in PCF the modal energies become better defined in the high-index region implying that, with respect of air or vacuum, the glass region becomes the guiding region preventing the escape of modal energy. In Figure 7.8, the maximum axial refractive index in the photonic crystal cladding is plotted against normalized frequency parameter (ν), derived from the scalar approximation in Reference [17]. In this figure for a hexagonal photonic crystal lattice, the interspace distance between two adjacent defect is d, which then yields a geometrical parameter, $d/\Lambda = 0.4$, and $n_g = 1.444$ and $\Lambda = 0.145$, yielding $n_{\max} \approx 1.39$ for $\nu \rightarrow 0$ or $\kappa\Lambda \rightarrow 0$. In Figure 7.8, the dotted line at $n_{\max} = 1.435$ represents a condition when the light is no more guided for $\nu > 20$. As in our discussion on the wavelength dependence of refractive index and vice versa, in the context of PCF, it is important to define the “transverse effective wavelength” (λ_{PCF}), characterizing the structure, which is given in Equation 7.17:

$$\lambda_{\mathrm{PCF}} = \frac{2\pi}{\sqrt{\kappa^2 n_i^2 - \beta^2}} \tag{7.17}$$

Here n_{i} is the effective index along the radius in the PCF. Equating the term in the denominator to zero sets the critical angle condition at which the value of $\lambda_{\mathrm{PCF}} \rightarrow \infty$.

Another model for propagation of electromagnetic waves in defect lattice is to solve Maxwell’s electrodynamic equations with the Schrödinger equation [12,13]. Whether one considers the solutions, discussed above from scalar the approximation of Maxwell’s equation, demonstrated by Russell [17], or from the combined vectorial representation of the Maxwell–Schrödinger equations, the resulting physical picture of photonic crystal structure remains similar in the expression of light guiding. Based on three scalar approach, three different mechanisms are known:

1. the modified form of total internal reflection (TIR) [18];
2. the photonic band gap guidance [19,20];
3. a leaky mechanism based on a low density of photonic states in the cladding [21].

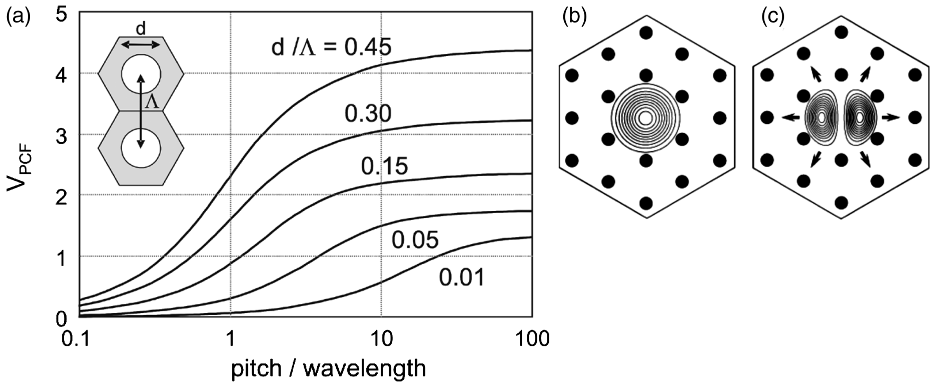

Figure 7.9 *(a) V_{PCF} parameter plot against the reciprocal of wavelength (frequency). (b, c) Modal distribution showing that the fundamental is trapped in the core (b) whereas the higher order modes are leaky (c) [17,18]. Source: Russell 2006. Reproduced with permission from OSA Publishing.*

7.3.2 TIR and Endlessly Single Mode Propagation in PCF with Positive Core–Cladding Difference

Russell [17], in his review on photonic crystal fibres (PCF), based on the above types of guiding mechanisms, summarizes many examples of microstructured fibres. Selected examples are discussed below. Resonance and anti-resonance structure for preserving light in the high-index medium is quite unique, as the light from the high-index core can only escape when modal phase matching states between the high and low index exist. Taking this concept further in the design of positive core–cladding difference yields a unique type of microstructured fibre, known as the "endlessly single mode (ESM)", in which the cladding operates in a regime in which λ_{PCF} in silica tends towards a value that corresponds to the wavelength for that effective index in the vicinal periodic structure. In other words in Equation 7.17 the denominator is tending towards zero, which defines the TIR condition for PCF. The effective V parameter for PCF (V_{PCF}) was computed for different d/Λ ratio (Figure 7.9).

From this figure it is evident that the number of guided modes are almost independent of wavelength when $(V_{\text{PCF}})^2/2$ is levelling off against the reciprocal of wavelength (i.e. at high frequency), confirming that the structure is endlessly single mode due to the geometrical constrains. For $d/\Lambda < 0.43$, no higher order modes can energetically exist in the core, thereby confirming the ESM condition. Such a unique feature is not feasible in standard step-index fibres. In Figure 7.9b and c the fundamental mode is confined in the high index region, from where the higher order modes are squeezed out.

7.3.3 Negative Core–Cladding Refractive Index Difference

For the photonic band gap low-loss waveguiding condition to be realized, the value of β must be less than κn_{high}. In a hollow-core silica–air structure (i.e. $\beta < \kappa$, since $n_{\text{core}} = 1$), as an example, a larger air filling fraction (Λ) and smaller value of d are necessary in a PBG design. The bandgap is quite narrow, in which the modal distribution (N_{PBG}) is expressed by the geometrical optic parameter [17]:

$$N_{\text{PBG}} \approx \frac{(\kappa d_{\text{PBG}})^2}{2}\left(n_{\text{high}}^2 - n_{\text{low}}^2\right) \tag{7.18}$$

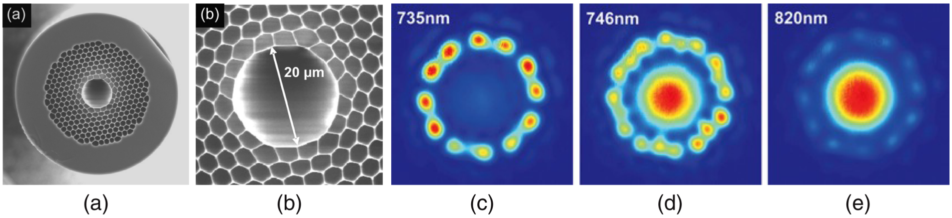

(a) (b) (c) (d) (e)

Figure 7.10 *(a) Low magnification scanning electron microscopic cross-section of an air-guiding PCF, whereas (b) is a high-magnification SEM image showing 20 μm core. (c)–(e) Near-field images of air-guiding core in (b) supporting 735, 746 and 820 nm wavelength propagation, respectively [17]. Source: Russell 2006. Reproduced with permission from OSA Publishing. (See colour plate section.)*

Equation 7.18 necessitates that for PBG to exist it must be large to accommodate the modes, because the square index difference is small, by a few percent, between silica and air. The air guiding condition cannot be achieved in a conventional optical fibre. The first demonstration was realized in 1999 [20], showing a 20.4 μm hollow core structure in which the apparent attenuation at 1550 nm was 1 dB km^{-1}. Modal partitioning (surface versus hollow core mode) was demonstrated by fabricating a PBG for 800 nm wavelength (Figure 7.10).

Furthermore, calculations also showed that if the glass refractive increases, for example by using the tellurite or chalcogenide glasses, the refractive index contrast in Equation 7.18 becomes larger, implying that a proportionately larger number of modes in the hollow core are likely to pile up and confine, say, in chalcogenide glass than in silica. This is quite important in the engineering of such PBG with softer glass, because the mechanical properties are less favourable than silica, and the related processing is more involved in maintaining the larger number of holes, which ultimately affects the robustness of a PBG fibre for optical confinement and mechanical durability of such structures for engineering applications.

7.3.4 Control of Group Velocity Dispersion (GVD)

Recalling the discussions above on various types of dispersion and their dependence on materials and geometrical properties, the total dispersion in a standard fibre is dependent on the group velocity dispersion (GVD, ps (nm km)$^{-1}$) and waveguide dispersion; the latter is strongly dependent on the geometrical factors. In a microstructured optical fibre (MOF), the fill factor (Λ), magnitude of spacing (d) between the two defects, and its diameter are the contributing factors in determining the shape of GVD versus wavelength curve, such as that shown for a silica based MOF in Figure 7.11. The computed GVD for two different values of defect diameters (1 and 0.4 μm) are shown; from these plots the zero-dispersion wavelength (ZDW) in the designed PCF shifts towards the blue wavelengths, with respect to the ZDW point at ~1317.0 nm in a standard single-mode silica fibre. For example, in a PCF with defect diameter of 1.0 μm, the ZDW is nearly at 730 nm. On changing the defect diameter size to 0.4 μm, the ZDW shifts further into the visible region at 560 nm which means that the longer wavelengths in such MOFs may be then transmitted as solitons. In addition, notably, in MOFs with defect diameter of 0.4 μm, there are two ZDW points at 560 nm and at the longer wavelength at around 1300 nm. Between these two wavelengths, the pulse propagation is in the positive dispersion regime. The soliton propagation in such fibres is of significant interest

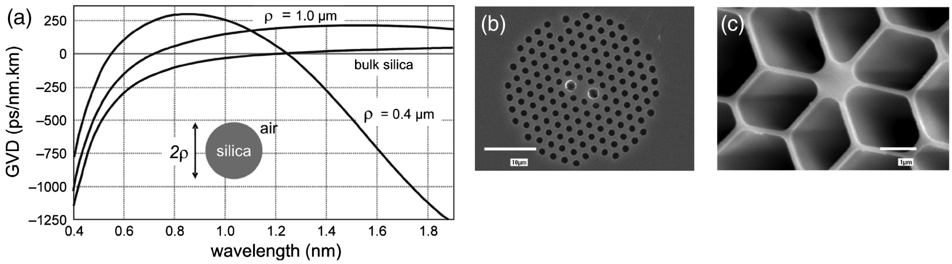

Figure 7.11 *(a) Examples of group velocity dispersion in two different strands of circular silica glass with 0.4 and 1.0 radii, when compared with bulk silica. The 0.4 circular strand shows two zero-dispersion wavelengths. (b) and (c) SEM cross-sections of two different types of PCFs for managing birefringence and with zero GVD at 560 nm [17]. Source: Russell 2006. Reproduced with permission from OSA Publishing.*

in optical communication, especially given that multiple wavelength bands are now potentially possible.

Indeed, the elegance of dispersion managed or perhaps dispersion-free wave propagation is a unique feature of photonic crystal fibre which is not so easily achievable in any standard optical communication fibres discussed above. The flexibility with which the GVD and dispersion slope, which can be managed all across the visible to the long wavelength part of optical communication window, is truly a unique feature of MOF fibres.

7.3.5 Birefringence in Microstructured Optical Fibres

Birefringence arises due to differential coupling of electromagnetic wave with the optically active structures in a material, which was discussed in detail in Chapter 4. In the context of ordinary and extraordinary direction of propagation of electromagnetic waves in standard fibres, the birefringence is quite small and is typically of the order of 10^{-4}. In such fibres, because of very precise control in fibre fabrication and over cladding for fibre protection, the nature of fibre birefringence is largely stochastic. Otherwise, specially designed fibres (e.g. the bow-tie, non-isotropic cores) often introduce birefringence for polarization maintenance.

By contrast, in MOFs the birefringence is inherent in structure because of the biphasic anisotropy introduced in the MOF structure, which naturally attempts to create the birefringence due to geometrical and symmetrical constraints imposed. If an MOF has symmetrical cross-section, the birefringence is usually negligible but otherwise increases much more dramatically. By introducing defects or asymmetry during MOF fabrication, the birefringence may be introduced for controlling the guidance mechanism by introducing asymmetry around the core in index-guiding and photonic band gap fibres. The resulting feature may help in controlling the beat lengths in such fibres, which can be reduced to a few millimetres, e.g. at 1550 nm in a designed MOF. As a result the PMD can be quite effectively controlled using such fibres [17,22]. An example of asymmetry introduced during fibre fabrication may be seen in Figure 7.12.

The beat length (L) in such fibres can be determined from the relationship in Equation 7.19, which shows the dependence on the measured birefringence:

$$L_{\text{Beat}} = \frac{2\pi}{\left(\beta_x - \beta_y\right)} = \frac{\lambda_{\text{Beat}}}{n_x - n_y} = \frac{\lambda}{B} \tag{7.19}$$

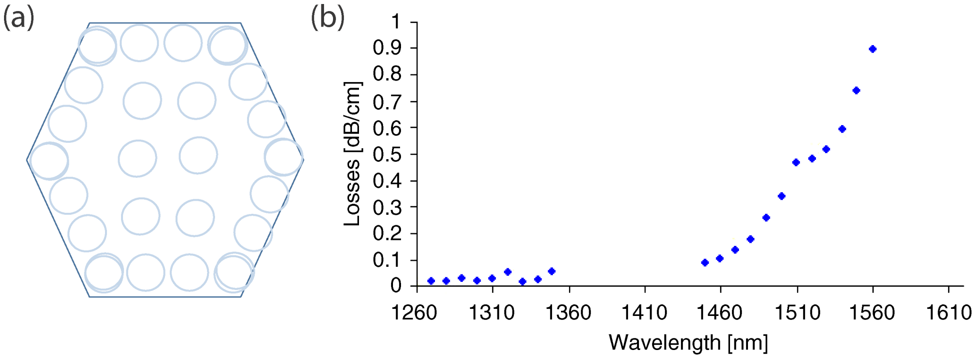

Figure 7.12 *Schematic diagram of birefringent PCF (a). In a silica PCF of comparable periodic structure,* d = *1.16 μm and defect diameter of 0.54 μm has a polarization induced loss above 1500 nm, supporting the modes at these wavelengths (b) [17]. Source: Russell 2006. Reproduced with permission from OSA Publishing.*

Here β_x and β_y are the propagation constants in two orthogonal direction, x and y, along which the refractive indices are n_x and n_y, respectively. Birefringence is quite important in the engineering of temperature and strain based sensors, for which the details may be found elsewhere [2].

7.4 Optical Nonlinearity in Glasses, Glass-Ceramics and Optical Fibres

7.4.1 Theory of Harmonic Generation

In this section two types of optical nonlinearity in inorganic glasses are discussed briefly, to explain their importance in device engineering. From the microscopic model of propagation of an intense light beam of light in a *nonlinear* medium both the spatial and temporal distribution of electric charge present in the medium are affected by the electromagnetic field of the incident wave. As a result of this interaction between the electromagnetic field and the electric charge present in the medium, the force exerted by the electric field perturbs the charge from equilibrium (in space and time); consequently, the induced polarization ($\vec{P}$) is then proportional to the magnitude of electric field ($\vec{E}$). At higher intensities of incident electromagnetic wave, the resulting polarization ($\vec{P}$) is then expressed as a polynomial in Equation 7.20 [23]:

$$\vec{P} = \varepsilon_o\chi^{(1)}\vec{E} + \varepsilon_o\chi^{(2)}\vec{E}\vec{E} + \varepsilon_o\chi^{(3)}\vec{E}\vec{E}\vec{E} + \ldots \tag{7.20}$$

Here ε_o is the permittivity of free space. $\chi^{(1)}$ is the linear susceptibility, which is only valid for the linear response of the material; however, $\chi^{(2)}$ and $\chi^{(3)}$ are the second- and third-order susceptibilities of the material. The microscopic relation of susceptibility with macroscopic polarization is a complex vectorial property that not only depends on the magnitude but also on direction. This is because the susceptibility may be dependent on the active optical axes along which the dipoles may be induced in the presence of electromagnetic field. In general in nonlinear media the first order susceptibility ($\chi^{(1)}$) is much larger than the second- and third-order susceptibilities, $\chi^{(2)}$ and $\chi^{(3)}$, respectively. By considering the anisotropic and directional nature of linear susceptibility, we may be able to express the polarization ($\vec{P}$) in the following scalar form to simplify the discussion below. However, in reality the linear susceptibility has a tensor form:

$$P = \varepsilon_o\left[\chi^{(1)}E + \chi^{(2)}E^2 + \chi^{(3)}E^3 + \ldots\right] \tag{7.21}$$

In linear polarization the scalar form of linear susceptibility is dependent on the linear refractive index, i.e. $\chi^{(1)} = n_o^2 - 1$ and the dielectric constant, $\varepsilon = \varepsilon_o\left(1 + \chi^{(1)}\right)$.

Importantly, Equation 7.21 is a time-dependent equation, representing an instantaneous interaction of electromagnetic wave with a nonlinear medium, which has no dispersion and loss, i.e. it is only under the phase-matched condition that the re-radiation of photons may only arise, which may add to or take away from the incident frequency. Based on the important phase-matching condition, we may be able to further analyse the optical nonlinearity as second and third order effects, in which the apparent polarization may be expressed as:

$$P_2 = \varepsilon_o\chi^{(2)}E^2 \tag{7.22a}$$

$$P_3 = \varepsilon_o\chi^{(3)}E^3 \tag{7.22b}$$

The second order nonlinearity differs from the third order in terms of materials properties. The second order effects are only observable in non-centrosymmetric materials, whereas third order effects are observed in both centrosymmetric and non-centrosymmetric systems. In other words, the presence of strong optical axes in materials, along which the dipoles are excited, is essential for second harmonic generation. This is why even in liquid crystals, which are not like inorganic crystalline solids, the effect of second order nonlinearity is observed. To compare the magnitudes of second and third order susceptibilities, we must chose a reference point with respect to the linear polarization (P_1) when the applied field becomes comparable with the field produced between the electron and proton in a hydrogen atom [23]:

$$E \approx \frac{e}{4\pi\varepsilon_o a_H^2}(\mathrm{V})$$

based on which the magnitudes of second and third order susceptibilities are $\chi^{(2)} \approx 2 \times 10^{-11}\,\mathrm{m\,V^{-1}}$ and $\chi^{(3)} \approx 4 \times 10^{-23}\,\mathrm{m\,V^{-1}}$.

Let us now briefly discuss the effects of second and third order nonlinearity in the context of crystalline and non-crystalline dielectric materials. We will only discuss the main features as these areas are vast and excellent text books are available [23–25]. In second harmonic generation, since the polarization (P_2) in Equation 7.22a has a parabolic dependence on the incident electric field of the electromagnetic wave of frequency (ω), mathematical treatment of the substitution of original electric field, $E = E_o e^{-i\omega t} + E_o^* e^{+i\omega t}$, yields the polarization (P_2) in the following form, which helps in understanding the physical concept of the second harmonic generation. The incident electric field is represented in terms of complex conjugate. For the phase matching condition in second harmonic generation:

$$P_2 = 2\varepsilon_o\chi^{(2)}E^*E + 2\varepsilon_o\chi^{(2)}E^2 e^{-i(2\omega)t} + 2\varepsilon_o\chi^{(2)}(E^*)^2 e^{+i(2\omega)t} \tag{7.23a}$$

A similar type of mathematical treatment also yields the sum and difference frequency generation as a result of field induced polarization P_2 in Equation 7.23b. Note that the components of electric field are E_1 and E_2 and their conjugates have the corresponding frequencies ω_1 and ω_2:

$$P_2 = \varepsilon_0 \chi^{(2)} \begin{bmatrix} E_1^2 e^{-i(2\omega)t} + \left(E_1^*\right)^2 e^{-i(2\omega)t} + E_2^2 e^{-i(2\omega)t} + \left(E_2^*\right)^2 e^{-i(2\omega)t} \\ +2\left(E_1 E_1^* + E_2 E_2^*\right) \\ +2\left\{\left(E_1 E_2 e^{-i(\omega_1+\omega_2)t}\right) + \left(E_1^* E_2^* e^{-i(\omega_1+\omega_2)t}\right)\right\} \\ +2\left\{\left(E_1 E_2 e^{-i(\omega_1-\omega_2)t}\right) + \left(E_1^* E_2^* e^{-i(\omega_1-\omega_2)t}\right)\right\} \end{bmatrix} \tag{7.23b}$$

Figure 7.13 represents the virtual energy level diagram for frequency conversion, from which the additive and subtractive natures of frequency mixing become apparent under the phase matching condition.

The energy levels shown in Figure 7.13 are virtual states, and only are created when an intense electric field is incident in the medium. In Equation 7.23b, the second harmonic terms, $2\omega_1$, $2\omega_2$, are the second harmonic terms, and the additional terms have frequency sum and difference frequency terms: $\omega_3 = \omega_1 + \omega_2$ and $\omega_3 = \omega_1 - \omega_2$, for which the generation mechanisms are shown in Figure 7.13, under the phase matching condition, which means that both the energy and momenta are conserved. In the sum frequency generation schemes, there is parametric amplification of ω_2 at the expense of ω_1 and the generation of a new frequency, ω_3. The creation of a new frequency (ω_3) via the difference frequency scheme similarly conserves momenta and energy, which is why, under the sum and difference frequency schemes, the second harmonics of ω_1 and ω_2 are not favourable under the phase matching condition when these two frequencies are mixed inside a medium.

In a parametric amplification process using a second harmonic or a suitable medium, three wave mixing conditions may be achieved inside a cavity in which the mirror reflects the ω_2 frequency inside and allows mixing with the pump frequency at ω_1, which then yields the amplification of ω_2 signal frequency and an idler at ω_3. Since this process of frequency mixing occurs under phase matching condition, if the idler is reflected back into cavity, one of the ω_2 photons mixes with ω_3 and yields ω_1. Such a scheme of frequency mixing may be simply designed using a Fabry–Perot cavity for parametric amplification.

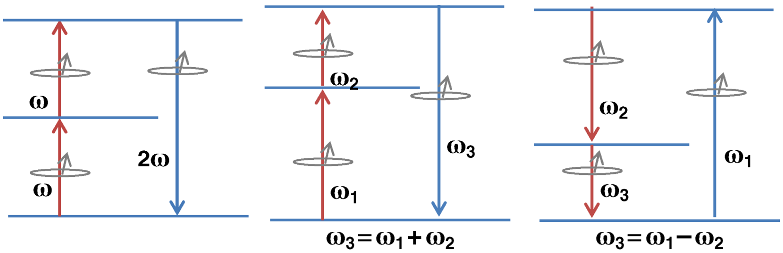

(a) (b) (c)

Figure 7.13 *The circle with an arrow symbolizes the phase-matching condition of different frequencies (ω). (a)–(c) describe three different phase matching conditions in second harmonic, sum frequency and difference frequency generations, respectively. Adapted from [23].*

Having examined the conditions for second harmonic generation using Equation 7.22a, we will focus on the third order nonlinearity, using Equation 7.22b, from which the polarization (P_3) is dependent on the incident oscillating electric field, say $E_1 \cos(\omega_1 t)$:

$$P_3 = \chi^{(3)}\varepsilon_o^3 E_1^3 \cos^3(\omega_1 t) = \chi^{(3)}\varepsilon_o^3 E_1^3\left[\tfrac{1}{4}\cos 3\omega_1 t + \tfrac{3}{4}\cos \omega_1 t\right] \tag{7.24}$$

Evidently, in this equation, the first term represents the third harmonic generation, for which the energy level diagrams are comparable with the second harmonic and sum frequency generation diagrams in Figure 7.14. In third harmonic generation, three ω_1 photons combine at high intensity and yield $3\omega_1$ photons (Figure 7.14b). As in the case of sum frequency generation with second order nonlinearity, in third order nonlinearity one of the processes is four-wave mixing (Figure 7.14a).

As in sum and difference frequency generation, under the phase matching condition two new photons ($\boldsymbol{\omega_4}$, $\boldsymbol{\omega_3}$) are generated from the original frequencies ($\boldsymbol{\omega_1}$, $\boldsymbol{\omega_2}$).

It is quite evident from the diagrams in Figures 7.13 and 7.14 that the intensity of photons required for such nonlinear processes is high, as necessitated by the corresponding Equations 7.22a and 7.22b. In second harmonic and sum and difference frequency generation, two photons are required to be available together in temporal domain and in phase inside the medium. By comparison, for third order nonlinearity the electric field dependence is even larger than in second harmonic generation. Below some examples of intensity dependent optical nonlinear processes are briefly discussed, before describing the materials used and their properties.

When a strong beam of coherent light passes through a nonlinear medium, the index of refraction of material increases at the focus point, making the propagating beam more confined. This is called self-focussing. As a result the apparent refractive index of a material at the incident frequency, ω, may be then described as in Equation 7.25:

$$n(\omega) = n_o(\omega) + n_2(\omega)I(\omega) \tag{7.25}$$

In Equation 7.25, the nonlinear refractive index (n_2) has the units $m^2\ W^{-1}$ so that when the intensity is specified in $W\ m^{-2}$ both terms of Equation 7.25 become dimensionless, as expected for the normal refractive index equation.

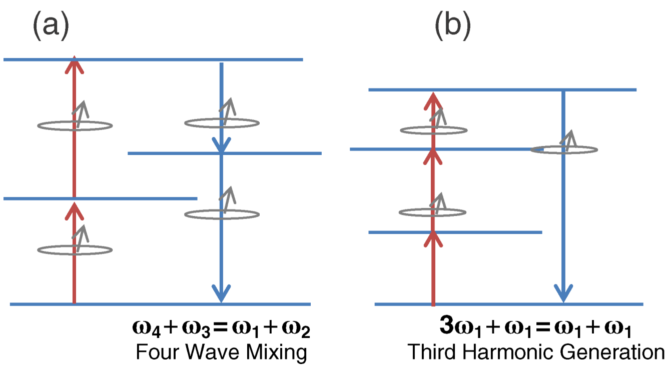

Figure 7.14 As in Figure 7.13, the figure schematically shows the four-wave mixing and third harmonic generation under phase matching conditions, in (a) and (b), respectively. Adapted from [23].

7.4.2 Nonlinear Materials for Harmonic Generations and Parametric Processes

7.4.2.1 Bulk Glass Based Kerr Media

As explained above, third order nonlinearity is observed in both centrosymmetric and non-centrosymmetric materials. Glass based materials are isotropic and have been used for investigating Kerr nonlinearity (n_2) which may be expressed in terms of linear susceptibility $\chi^{(1)}$ and third order susceptibility $\chi^{(3)}$ in electro-static unit, which then makes it easier to compare with Miller's rule:

$$\chi^{(3)}(\text{esu}) = \left[\chi^{(1)}(\text{esu})\right]^4 \times 10^{-10} \tag{7.26a}$$

and:

$$\chi^{(1)} = n_o^2 - 1 \tag{7.26b}$$

yield the following equation:

$$n_2(\text{SI}) = k_{\text{fitting}} \frac{40\pi^2}{cn_o^2} \chi^{(3)} \tag{7.26c}$$

An important unit conversion to note is:

$$n_2\left(\text{m}^2\,\text{W}\right) = \frac{8.4 \times 10^{-7} n_2(\text{esu})}{n_o} \tag{7.26d}$$

In Equation 7.26c, k_{fitting} is a fitting parameter that is determined from the plot of measured data, which are $\chi^{(3)}$ and n_o, and is compared with Miller's rule in Figure 7.15 [26]. A range of glass materials are compared with silica, which has the lowest value of n_2 amongst the glasses compared.

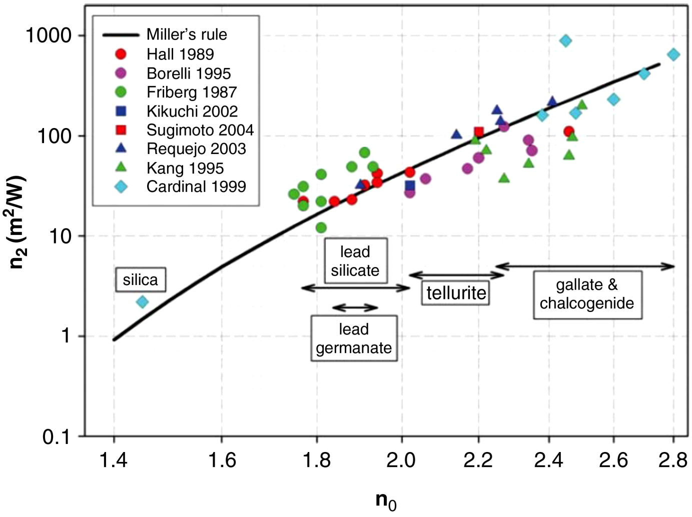

Figure 7.15 Plot of the linear refractive indices (n_o) and n_2 ($m^2\,W^{-1}$) for a range of glasses for engineering photonic crystal fibre based nonlinear media [26]. Source: Monro 2004. Reproduced with permission from Annual Review of Materials Science.

Besides Miller's rule the other method of calculating n_2 is to use Boling's approximation [27] for the long-wavelength (e.g. IR) region by determining the Abbe number:

$$\upsilon = \frac{n_\mathrm{d} - 1}{n_\mathrm{F} - n_\mathrm{c}}$$

and the refractive index at the *d*-line (n_d). Here n_c, n_d and n_F are the measured refractive indices at 656.2725, 587.5618 and 486.1327 nm, respectively. The first two lines are from the hydrogen spectrum and the third one is from the helium spectrum:

$$n_2 = \frac{K'[n_\mathrm{d} - 1]\left[n_\mathrm{d}^2 + 2\right]^2}{n_\mathrm{d}\upsilon_\mathrm{d}\left\{1.52 + \frac{(n_\mathrm{d} + 1)\left(n_\mathrm{d}^2 + 2\right)\upsilon_\mathrm{d}}{6n_\mathrm{d}}\right\}^{\frac{1}{2}}} \tag{7.27}$$

In this equation the value of $K' = 2.8 \times 10^{-18}\,\mathrm{m^2\,W}$.

There is another model, which is based on the band gap and cation–anion distance, which we discuss in the context of the two-photon absorption model. One of the most important applications of Kerr nonlinearity is in all-optical switching, using non-resonant nonlinearity. From the definition of non-resonant nonlinearity, it does not originate from the electronic bandgap effects, but far away from the electronic band edge into the IR region via the virtual states (as shown above in Figures 7.13 and 7.14) that are created due to the intense electric field. The optical switching at non-resonant wavelengths is relevant for attaining high data speed in optical communication systems. The switching speed depends on the apparent relaxation processes in the nonlinear media, for which the figure-of-merit (*F*) is defined as:

$$F \equiv \frac{n_2}{\tau\alpha} \tag{7.28}$$

Here τ is the relaxation time and α is the absorption coefficient. Note that the relaxation time only considers the nonlinear processes, and precludes the thermal effects [28]. Evidently, from Equation 7.28, an ideal Kerr medium must have the following characteristics: (i) a large value of n_2, (*ii*) fast response time and (iii) a small total attenuation, including nonlinear absorption, e.g. the two- or multi-photon absorption, β. The resonant absorption processes have different relaxation time domains, and in a medium may depend on the molecular configuration and vibrations, orientation (e.g. in liquid crystals), dopant's electronic states and defect absorption bands. The time-scale may vary from a few seconds to several femtoseconds, e.g. in surface plasmon resonant relaxation [29,30]. By referring to Equation 7.28 it is, therefore, possible to achieve a large value of transient Δn at the resonance frequencies, which will depend on the relaxation time, discussed above.

Another resonant feature is a complex photon absorption, in which the imaginary part (as in the linear refractive index equation, $n = n_\mathrm{o} + \mathrm{i}k$) contributes to two-photon absorption. The intensity of beam I propagating in the z-direction changes along this direction due to nonlinear absorption:

$$\frac{\mathrm{d}I}{\mathrm{d}z} = \alpha I - \beta I^2 \tag{7.29}$$

Here β is the two-photon absorption ($\mathrm{m\,GW^{-1}}$ or $\mathrm{m\,W^{-1}}$). As stated above, the non-resonant process, depending on the wavelength, may dominate at wavelengths far from the fundamental absorption band and it may be dependent on the sub-gap electronic absorption process. Relaxation from the sub-gap or the virtual states occurs under large optical fields and is usually in the sub-picosecond time-scale. By comparison, the apparent change in index in a resonant process occurs at small optical fields. This distinction between the resonant and non-resonant processes shows that the design requirement for optical switching devices is different. As the interaction length for the resonant nonlinear absorption is large, the device interaction length is significantly smaller than in the non-resonant processes. Consequently, the interaction lengths required for propagating optical field may be 100–10 000 longer than in a resonant process.

Notably, there are also non-Kerr like and quasi-Kerr-like media, in which the intensity modulation effects are also observed; however, in these two types of media, n_2 is not proportional to I or $|E^2|$, for which the details may be found elsewhere [25,31].

Some important examples of electromagnetic phenomena originating from the nonlinear index of refraction are the optical Kerr effect, degenerate four-wave mixing, real-time holography, two-beam coupling, optical bistability, self-focussing and white-light continuum generation. Amongst these applications, recently the generation of white light supercontinuum has becomes the most significant emerging application of waveguide based nonlinear optics. In the context of applications, therefore, it is essential to characterize the nonlinear optical properties which may be carried out using one the following techniques: degenerate four-wave mixing, nearly degenerate three-wave mixing, *Z*-scan, optical Kerr-effect and ellipse rotation, and third harmonic generation [31]. These characterizations must proceed hand-in-hand with the measurements of multiple-photon absorption at the wavelength of interest, which is why one of the most popular characterization techniques is via a *Z*-scan, on using which both the values of n_2 and β may be obtained for optimizing the engineering design of devices needed for optical switching, data storage, volatile memory, solitons, reduction of nonlinearity and cross-talk in lasers and amplifiers [25]. Details of the Z-scan experimental technique may be found in the *Tellurite Glass Handbook* [32], from which one of most important points to note is the sample thickness, which must be less than 1 mm to minimize absorption. The surface finish must be achieved with a better than 1.0 μm polishing cloth.

Along with our discussion of the significance of two- and multi-photon process, in Equations 7.28 and 7.29, another approach for establishing the dependence of n_2 on n_o and electronic band gap energy (E_g) is also known in the literature [33,34] for calculating the values of n_2 and it has been applied, for example, in a family of chalcogenide and tellurite glasses. This approach was originally developed for predicting the dispersion of n_2 in crystalline semiconductors [35,36], which have a wide range of band gap values. The model also appears to work satisfactorily for chalcogenide and tellurite glasses, since these two glasses also exhibit a wide distribution of band gaps, as is evident from the electronic edge data in Reference [34]. According to the model the relationship between n_2 and band-gap energy (E_g, eV) and linear refractive index is shown in Equation 7.30:

$$n_2(w) = 1.7 \times 10^{-14}\left(n_\mathrm{o}^2 + 2\right)^3\left(n_\mathrm{o}^2 - 1\right)\left(\frac{d}{n_\mathrm{o}E_\mathrm{s}}\right)^2 D_\mathrm{NLO}\left(\frac{\hbar\varpi}{E_\mathrm{g}}\right) \tag{7.30}$$

Here, d (in nm) is the mean cation–anion bond length responsible for nonlinear response, E_s (eV) is the Sellmeier gap energy and is approximately equal to 2.5 times the value of E_g, D_NLO is the dispersion of nonlinear refractive index and ($\hbar\varpi$) is the pump energy.

In the context of Kerr nonlinearity related optical switching, we need to then establish the relationship of the apparent phase difference, $\Delta\Phi$, due to the intensity-induced change in the refractive index (Δn) of the medium [37]:

$$\Delta\phi = 2\pi n_2 \frac{IL}{k_o} \tag{7.31}$$

Here k_o is the propagation constant in a vacuum and I is the intensity (W), L is in metres and n_2 is in $m^2\ W^{-1}$. The unit of phase change may be suitably represented in radians or degrees. Thus, using Equation 7.31 for Kerr switching at $\Delta\Phi = \pi$ radian, the critical length (L_c) may be determined for a given value of n_2 and the magnitude of incident intensity (I). Note that in Equation 7.31 the larger the value of n_2 the smaller the required intensity for a known L_c. Alternatively, one can set the design criterion such that as the value of n_2 increases, the intensity required for a π-phase change decreases in a chosen Kerr media. We will examine the effect of nonlinearity in the fibre section below.

In Table 7.1, the nonlinear properties of oxide and non-oxide glasses are compared, from which it is evident that with an increase in the cationic and anionic radii. The value of n_2 also increases, and the gap energy decreases, which implies that the two-photon absorption will increase in such media with large d values. The bond-length approach is also consistent with the structural unit approach, connecting the polarizability of cations, as discussed in References [35,37,38]. Perhaps by far the most significant finding in recent years has been cited in Reference [34], which compares the nonlinear properties of an optimized multi-component arsenic sulfide (As_2S_3), a quaternary germanium sulfide (GeS_2) and a ternary tellurium oxide (TeO_2) glasses [39]. It was reported that the two-photon absorption process in tellurite and multicomponent chalcogenide glasses was negligible, when compared with the arsenic trisulfide, germanium selenide and telluride glasses. In tellurite and GeS_2 based glasses, it was found that only higher than three-photon absorption processes dominated at large irradiance. The two-photon absorption process in selenide and telluride glasses reported in References [33,34,40,41] practically renders these materials unusable at telecommunication wavelengths between 1300 and 1550 nm. A summary of nonlinear properties of relevant oxide and silicate and network-forming glasses is given in Tables 7.1 and 7.2 [37,42–45].

$$\chi^{(3)}\mathrm{esu} = \left(\frac{n_o^2 - 1}{4\pi}\right)^4 \times 10^{-10}; \chi^{(1)}\mathrm{esu} = \frac{n_o^2 - 1}{4\pi}; \quad n_2\left(\mathrm{m^2\ W^{-1}}\right) = \frac{8.4 \times 10^{-7}}{n_o} n_2(\mathrm{esu})$$

$$n_2\left(\mathrm{m^2\ W^{-1}}\right) = \frac{39.58 \times 10^{-7}}{n_o^2} \chi^{(3)}(\mathrm{esu})$$

On the basis of the multi-photon analysis, it was also concluded that, for a π-phase change to occur in a signal pulse, at least 1 metre long polarization preserving TeO_2, GeS_2 and As_2S_3 fibres at peak irradiances of 200, 84 and 42 MW cm^{-2}, respectively are required.

Experimentally the attenuation due to three-photon absorption of the pump beam, at 1550 nm, was found to be less than 1%, and no photo-darkening effect in the tellurite and multi-component germanium oxide glasses were observed at 1300 and 1550 nm.

The empirical model proposed by Boling and co-workers [27] has remained the basis for designing glasses for non-resonant all-optical switching devices. High refractive index

Table 7.1 *Nonlinear optical coefficients for chalcogenide and heavy metal oxide glasses at 1550 nm.* n_2 *(silica) = 2-3 ×* 10^{-20} $m^2 W^{-1}$. β_2 *(cm* W^{-1}*),* β_3 *(cm*^{3} W^{-2}*), and* β_4 *(cm*^{5} W^{-3}*) are the 2-photon, 3-photon, and 4-photon absorptions respectively.*

Sample compositions	Refractive indexn	Bandgap E_geV	n_2x10^{-19} m^2W^{-1}		Multiphoton absorption				
			Expt	Theory	β_2	β_2	β_2	E_g/(w	Refs.
Our As_2S_3-GeS_2-Sb_2S_3	~2.4	2.27	18	28.7	X	2.0	X	2.84	KSB
As_{40}-S_{60}	—	1.41	4	—	0.03	X	X	1.75	Rich
$As_{40}S_{40}Se_{20}$	2.47	1.70	8	—	<0.01	X	X	2.12	—
$As_{24}S_{38}Se_{38}$	2.32	1.67	17.5	—	<0.05	X	X	2.08	—
$As_{37}S_{56}Se_7$	2.43	1.79	3	—	<0.03	X	X	2.23	—
$As_{30}S_{63}Se_4$ Sn_3	2.80	1.28	10	—	0.17	X	X	1.60	—
As_2Se_3	2.78	1.77	170	—	—	—	—	2.21	—
Our GeS_2	~2.15	2.73	9.2	13	—	—	53	3.4	KSB
$Ge_{0.25}Se_{0.75}$	2.40	2.07	40.8	—	—	—	—	1.25	NRL
$Ge_{0.25}Se_{0.65}Te_{0.10}$	2.50	1.73	74.8	—	—	—	—	2.16	—
$Ge_{0.28}Se_{0.60}Sb_{0.12}$	2.61	1.62	122	—	—	—	—	2.02	—
$Ge_{28}Sb_{12}Se_{60}$	—	1.39	8 (1.3 μm)	—	—	—	—	1.73	—
Our TeO_2 glass	~2.05	3.44	3.8	4.3	—	—	21	4.27	KSB
$30Tl_2O$-$50Bi_2O_3$-$20Ga_2O_3$	n_d 2.47	1.89	58.1 (1.25 μm)	—	—	—	—	1.89	
$57.2PbO$-$24.9Bi_2O_3$-$17.8Ga_2O_3$	2.46	2.43	37.9 (1.25 μm)	—	—	—	—	2.43	
$60PbO$-$25TeO_2$-$15SiO_2$	2.27	2.53	18.9 (1.25 μm)	—	—	—	—	2.53	
$64.1PbO$-$14.2Bi_2O_3$-$6.7B_2O_3$-$15.1SiO_2$	2.34	2.63	28.9 (1.25 μm)	—	—	—	—	2.63	
$35La_2S_3$-$65Ga_2S_3$	2.50	2.69	124.7 (1.25 μm)	—	—	—	—	2.69	
$7.5BaS$-$17.5Ga_2S_3$-$70GeS_2$	2.22	2.88	34.7 (1.25 μm)	—	—	—	—	2.88	
$87.3GeS_2$-$12.7Ga_2S_3$	2.19	2.95	42.6 (1.25 μm)	—	—	—	—	2.95	

Table 7.2 *Kerr nonlinearity of selected inorganic glasses including some commercial glasses. Key equations for this table to convert esu units into SI units are shown below.*

Composition (mol.%)	n_o @ 633 nm	n_2 Optical nonlinearity ($m^2\ W^{-1}$) Measured	Calculated	($\chi^{(3)}$, ×10^{-15} (esu)
$8Nb_2O_5$-$10TiO_2$-$20Na_2O$-$60SiO_2$	1.64	1.60×10^{-19}		
$13Nb_2O_5$-$17TiO_2$-$20Na_2O$-$50SiO_2$	1.78	0.75×10^{-19}		
$10Nb_2O_5$-$10TiO_2$-$20Na_2O$-$60SiO_2$	1.70	1.83×10^{-19}		
$15Nb_2O_5$-$15TiO_2$-$20Na_2O$-$50SiO_2$	1.85	2.69×10^{-19}		
$30Nb_2O_5$-$30TiO_2$-$20Na_2O$-$20SiO_2$	1.95	4.03×10^{-19}		
$80TeO_2$-$20Nb_2O_5$	2.26	18.0×10^{-19}		
$75TeO_2$-$25ZnO$	2.13	15.3×10^{-19}		
$85TeO_2$-$15BaO$	2.44	$6.2\pm0.8\times10^{-18}$		
$50TeO_2$-$10Nb_2O_5$-$10Li_2O$	2.17	15×10^{-19}		
GeS_2	2.7		5.4×10^{-17}	
$42Bi_2O_3$-$12Ga_2O_3$-$46PbO$	2.37	1.4×10^{-17}		
Commercial glasses				
Fused silica	1.458	5.47×10^{-20}		0.8
Silicate with 57 mol.% PbO	1.953	1.46×10^{-19}		37
BK7	1.517	6.36×10^{-20}		
Aluminium fluorophosphate	1.492	4.22×10^{-20}		

materials ($n > 1.9$) exhibit a large intensity dependence of change in refractive index, which is a non-resonant process, when pumped at wavelengths 3 to 4 times larger in magnitude than the electronic absorption edge. The general trend, which appears to be consistent with Boling's approach, is that as the value of linear refractive index, n_o, increases the electronic edge shifts to longer wavelengths, and the magnitudes of the real and imaginary parts of third order susceptibility increases, leading to a simultaneous enhancement in the value of n_2 [33,35,46,47]. Nuclear contributions to third order electronic susceptibilities were systematically analysed in gallium lanthanum sulfide, germanium sulfide and heavy-metal oxide glasses [8], and these were found to vary between 1/10th and 1/9th of the electronic susceptibility at 1250 nm. The nuclear component of susceptibility was evaluated to assess its impact on nonlinearity in Raman amplifiers which utilize over 10 km of large NA silica fibres, thereby providing an excessively large interaction length for a 180° phase change. Any nonlinear contribution in optical amplifiers is detrimental to its performance.

Based on the characterization of optical nonlinearity in bulk glasses, discussed above, a number of fibre based results are discussed below briefly in the context of applications of Kerr optical nonlinearity.

7.4.3 Fibre Based Kerr Media and its Application

As we have seen from the basic theory of nonlinear processes, described above, multiple photons at high intensities are required for effecting such quantum processes, needing much higher power in bulk materials, e.g. in optical parametric oscillator (OPO) crystals, such as in garnets, lithium niobate, KDP, etc. than in an optical fibre with small cores, in which the power density can rapidly scale up by thousands of times. In addition, for optical switching, as discussed in Equation 7.31, the critical length (L_c) also helps in reducing the power requirement. For this reason in fibres the effective core-area or the Gaussian modal field diameter becomes important, and on this basis it then helps in defining the "effective nonlinearity" (γ_{eff}) [25,26]:

$$\gamma_{\mathrm{eff}} = \frac{2\pi n_2}{\lambda A_{\mathrm{eff}}} \tag{7.32}$$

Here A_{eff} is the effective mode area of a fibre, which is strongly dependent on the waveguide geometry, as exemplified by comparison of a standard single-mode fibre with a corresponding photonic crystal or band gap fibre. In Equation 7.32, by substitution of the temporal evolution of intensity (I) of a Gaussian beam in the core of a single-mode or photonic crystal fibre [25] [23]:

$$I = I_o \exp\left[-2\left(\frac{t}{t_o}\right)^2\right] \tag{7.33}$$

yields the equation for $\Delta\phi$, *which is:*

$$\Delta\phi = 2\pi n_2 \frac{LI_o}{k_o} exp\left[-2\left(\frac{t}{t_o}\right)^2\right] \tag{7.34}$$

Since the frequency:

$$\omega = \omega_o - \frac{d\phi}{dt}$$

the temporal evolution of phase shift will then yield a frequency chirp which can then lead to spectral broadening. The effect of self-phase modulation for optical switching, for example, becomes more dominant in fibres than in bulk materials. The observation of frequency chirp as a result of SPM is an apparent consequence of optical nonlinearity, which may be detrimental for optical signal communication. However, for parametric gain, the SPM in fibre may be exploited for signal amplification.

Another type of nonlinearity in materials that tends to manifest much better in fibres is the cross-phase modulation (XPM), which arises when more than one beam (optical field) is propagating simultaneously inside a medium, e.g. in a single-mode fibre or PCF. In this situation, each beam as in SPM not only induces the change in polarization due to its own field but also due to mutual interaction of fields, which may be characterized by the equations below by the corresponding intensity modified refractive index equations in (7.35a) and (7.35b):

$$n_{(1)} = n_{o,1} + n_2 I_1 + 2n_2 I_2 \tag{7.35a}$$

$$n_{(2)} = n_{o,2} + n_2.I_2 + 2n_2.I_1 \tag{7.35b}$$

The net effect of cross-phase modulation may be explained using the first two terms in the polarization Equation 7.23b by minimizing the phase matching condition which then gives rise to four-wave mixing. By considering the condition, $n_{0,1} = n_{0,2} = n_0$ for two beams, which may generate new frequencies within the Gaussian envelope, then the temporal evolution of phase, ϕ may then be expressed as [25] [23]:

$$\phi_{\text{total}}(t) = \frac{2\pi L_c n_2}{\lambda}\left[|E_j|^2 + 2|E_{3-j}|^2\right] \tag{7.36}$$

In Equation 7.36, $j = 1$ or 2 which might vary whether the frequencies are degenerate or distinct. Here the first term represents the SPM whereas the second term arises due to XPM, in Equation 7.23b, depending on the frequencies of states participating, i.e. distinct versus degenerate. Evidently, the XPM (second term in Equation 7.36) is twice as large as the first term, representing SPM.

To observe four-wave mixing in fibres, it is essential that the phase-matching conditions are achieved at or near zero-dispersion wavelength (ZDW), otherwise the positive or negative dispersion effects will contribute to pulse broadening, as exemplified in the case of photonic crystal and standard single-mode fibres, discussed below.

One of the earliest results on Kerr nonlinearity in non-silica fibres was demonstrated with arsenic trisulfide fibres produced using the conventional preform fabrication and the double-crucible techniques [48–50]. The measured values of total loss at 1550 nm varied between 0.9 and 3 dB m^{-1}. The switching power required for 180° phase change was 0.4 W for a nonlinear optical loop mirror (NOLM) experiment, and 3 W and 11 W, respectively, for Kerr-gate experiments in 3 and 6 μm core-diameter fibres. The As_2S_3 fibres were also used for error-free all-optical de-multiplexing using a NOLM configuration. The transmission loss of the arsenic sulfide fibre was 0.6 dB m^{-1}, $n_2 = 2.0 \times 10^{-14}$ cm^2 W^{-1} and $n_o = 2.4$ at 1550 nm. The group velocity dispersion was −410 ps km^{-1} nm^{-1}. The peak power required was 1.6 W. A short review on Kerr optical nonlinearity has been published [45].

Ongoing developments in fibre fabrication of chalcogenides have led to attaining low-losses not only in arsenic sulfide fibres but also in a whole range of sulfide, selenide and telluride fibres [51–58]. Some of these fibres have a wide transmission, range from 1 up to 20 μm in the mid-IR region, opening novel opportunities for chemical sensing, imaging and *in situ* spectroscopy. However, due to intrinsic limitations on narrow band gap and enhanced intrinsic and extrinsic scattering, and susceptibility to mechanical failure, such fibres have not yet found their way into device applications for optical communication systems. In the optical communication wavelength region, the observed loss for such fibres are in the dB m^{-1}, which is a major limitation. The higher loss in the selenide and telluride fibres arises due to increased electronic absorption and Rayleigh scattering in the 1300–1550 nm region [53].

Photonic crystal and band gap fibres (PCF, PBG) provide a novel means for confining electromagnetic radiation, as discussed in Section 7.3 [17,59]. Together with the control of dispersion and birefringence, the optical nonlinearity in such fibres is large due to the smaller effective modal area (A_{eff}) than in a SM fibre. By engineering the dispersion properties of silica based PCF and its optical nonlinearity, a white light super continuum [60] spectrum was demonstrated. This demonstration has since generated much interest in this area using a whole host of PCF and near or single-mode fibres with controlled zero-dispersion wavelength. Examples of supercontinuum spectrum are summarized and exemplified in Table 7.3. The modelling of electromagnetic wave propagation also demonstrates that a 180° phase

Table 7.3 *Key results on supercontinuum (SC) generation in optical fibres. The data for pump wavelength (λ_p, nm), fibre mode area (A_{eff}, μm^2), γ (W.km)$^{-1}$, zero-dispersion wavelength (ZDW, nm), dispersion [ps (nm km)$^{-1}$] and SC bandwidth (λ_{SCG}, nm) are included.*

Fibre type	Pump energy, λ_p (nm), *dispersion (D) [ps (nm km)$^{-1}$],* A_{eff}, γ, λ_{SCG}
Silica tapered fibre [62]	3.9 nJ, $\lambda_p = 850$ nm, $D = 122$, 1.8 μm^2, 70 W km^{-1}, 370–1545 nm
Silica PCF [63]	425–739 pJ, $\lambda_p = 1.06$ μm, $D = -110$, 4 μm^2, 400–1650 nm
Silica PCF [64]	24.2 pJ, $\lambda_p = 770$ nm, $D = -110$, 1 μm^2, 500–1600 nm
Lead silicate [65]	100 pJ, $\lambda_p = 1060$ nm, 1 μm^2, 500–1600 nm
Chalcogenide [61]	$n_2 = 177–217 \times 10^{-20}$ m^2 W^{-1}, ZDW = 2 μm, $A_{eff} = 5.5$ μm^2
Chalcogenide step-index fibre [66]	2.3 μJ, $\lambda_p = 1.5–11.7$ μm, $D = +3.24$ ps nm^{-1} km^{-1}, ZDW = 5.83 μm, $\gamma = 0.04$ W km^{-1}
ZBLAN PCF [67]	830 pJ, $\lambda_p = 1.042$ μm, dispersion is flattened near zero 670–1300 nm, $\gamma = 0.04$ W km^{-1}
Tellurite PCF [60]	1.9 nJ, 1550 nm, $D = 0$ at 1380 nm, $\gamma = 586$ W km^{-1}, SCG bandwidth = 4080 nm

change in endlessly single-mode silica PCF structure is possible at an appreciably low pump power than for conventional single-mode fibres [16,18,20]. Modelling of propagation in the gallium-lanthanum sulfide PCF structure has also revealed that the length required for a π-phase switching is less than a centimetre at pump power below 0.5 W [61]. The new design with PCF structure clearly opens up new opportunities for fibre and planar device development.

7.4.4 Resonant Nonlinearity in Doped Glassy Hosts

In this section, the properties of materials with resonant nonlinear properties are briefly reviewed, by including concise details on semiconductor quantum-dots and surface plasmon resonance effects in metal doped glasses. However, notably, so far no tangible devices have emerged from this research leading to any significant applications, which is why the review will be limited. For semiconductor doped glass materials, the review by Vogel and Weber [38] may be referred to. Below, only surface plasmon resonance effects are discussed.

The electromagnetic interaction in glassy-hosts doped with metallic dispersion at a nano-scale is quite unique owing to quantum-dot semiconductor structures. The resonant and off-resonant light-driven plasmon effects in the nano-scale dispersion of metal particles have been investigated [68]. The electric dipole contribution to third order susceptibility is predicted to vary approximately as the reciprocal of radius of the single nanoparticle. The experimental observation of surface-plasmon induced coupling in nano-scale gold particles and silver nano-rods [69] [70] were reported, in which it was shown that the morphology of the particulates largely determine the resonance frequencies. For silver nano-rods with large aspects ratio (100–1000 nm in length, 85 nm by 25 nm in cross-section) the resonance wavelength increases with the length of the nano-rod, varying between 500 and

950 nm. A more detailed electromagnetic interaction was discussed by pointing out two different types of interactions in single-particle clusters and a 2D- or 3D-arrayed ensemble of nanoparticles. In the single particle case, the strength of dielectric fields of the metal and glassy host are important factors for determining the resonance wavelength band. A single-particle plasmon behaves almost independently. By comparison, in the 2D- and 3D-clusters, besides the single-plasmon effects, there also exists plasmon–plasmon interaction. The plasmon–plasmon interaction is divided into near-field and far-field coupling. The near-field coupling is limited to particle–particle interaction, which by contrast is mediated by the scattered light field along the array of dipolar particles. These dipolar fields interfere constructively for confining and trapping the radiation.

The relaxation time-scales in the nano-scale particle 2D array were found to be of the order of 3–5 fs. The 2D grating array of 3 nm diameter particles varied between 350 and 850 nm, for which the array size was found to determine the shape of the resonance band [71].

Fabrication of a 2D array of gold nanoparticles and gratings has been demonstrated by using a non-ionic liquid medium. Amongst the information on fabrication, the most significant results concerned the assembly of 2D and 3D clusters of gold spheres, of 4–8 nm in diameter, that were formed from a non-ionic solution medium. The dielectric properties of the cluster were also modelled as a function of inter-particle spacing [71].

7.4.5 Second Harmonic Generation in Inorganic Glasses

As explained in the background to second harmonic generation, a glass is a centrosymmetric material, which implies that it does not have a preferred optical axis, which in turn implies that in such materials the electric field of a propagating wave cannot couple preferentially to cause any phase and frequency change under the phase matching condition, discussed above. Frequency generation via SHG and sum and difference techniques are is important not only in physics but also in the applications of lasers. In this respect, since the first glass based lasers were developed in the mid-1960s by Koester and Snitzer [72], there has been a continuous interest in the search for a glassy medium for harmonic and sum and difference frequency generation.

Two main principles of generating harmonics in glass concern control of its structure:

(a) micro- and nano-scale crystallization leading to glass-ceramic formation;
(b) electric-field DC poling of a glass at or above ambient using high voltage (in kV) range, or using a source of light (e.g. UV); in this case, sometimes, ultrasound waves are also used for modulating the concentrations of the electro-optic phase; in the case of UV-light, the dynamic field is controlled to achieve poling in a particular direction including in glass.

In the case of controlling the nucleation and growth of the microstructure of an electro-optically active crystalline phase, the principles of phase transformation for surface nucleation and growth must be analysed, as discussed in Chapter 2. So far, little is known in terms of controlling the preferential surface nucleation and growth of electro-optic phase, leading to formation of low-loss waveguide for harmonic generation. Limited examples in silicate and tellurite based glasses with lithium niobate have been reported with limited success on frequency generation, because of the intrinsic stochastic nature of crystallization, in which randomness and uncontrolled crystallization may dominate. Since harmonic generation

Table 7.4 *Properties of selected glass media capable of generating second harmonics in the presence of nucleated and grown crystals with* d_{33} *properties. References are included in the main text [73–76]. Source: Ding 1994. Reproduced with permission from Elsevier Limited.*

Glass (mol.%) composition	Crystalline phase and growth conditions	Linear optical and harmonic generation properties
47.5BaO-47.5B_2O_3-5Al_2O_3	β-BaB_2O_4 grown @ 540 °C, 6–12 h	$d_{33} = 4.9\text{–}5.2\ \mathrm{pV\,m^{-1}}$, $d_{31} = d_{21} = d_{24} = d_{15} = 0.04\text{–}0.2\ \mathrm{pV\,m^{-1}}$
15K_2O-15Nb_2O_5-70TeO_2	Crystalline phase $LiNbO_3$, 380–475 °C	$\chi^{(3)} = 3.3 \times 10^{-13}$ to 1.19×10^{-12} esu
20Li_2O-80TeO_2	Poled glass at 3.2 kV (DC), 250 °C for 30 min	SHG was observed. No values of d_{33} and susceptibility reported

Glass compositions and heat treatment conditions for selected tellurite glasses. Heat treated at 300 °C for 40 min. DC poled at 4 k

Compositions of tellurite glasses (mol.%)	Properties at fundamental and harmonic wavelengths			
	n_{532}	n_{1064}	ℓ_c (μm)	d_{33} (pV m^{-1})
30ZnO-70TeO_2	2.02	1.97	5.3	0.22
10MgO-20ZnO-70TeO_2	1.99	1.94	5.3	0.11
15MgO-15ZnO-70TeO_2	1.98	1.93	5.3	0.13
20B_2O_3-80TeO_2	2.06	2.00	4.4	0.11
25B_2O_3-75TeO_2	2.00	1.94	4.4	0.08

necessitates the presence of a non-centrosymmetric crystalline phase, the nucleation and growth of the electro-optic phase must be controlled with the help of an external field. In this respect, Ding *et al.* [73] reported SHG generation in barium-borate glass (BBO) with an electro-optic phase (β-BaB_2O_4) which was controlled crystallized using ultra-sound. The resulting crystalline phase film thickness and the measured electro-optic properties (second order nonlinear susceptibility) are summarized in Table 7.4. The reason for selecting BBO is that the borate glasses are quite easy to form and barium borate single crystals are known for their electro-optic properties, for which the electro-optic coefficient d_{33} is known to be 4.9–5.2 pm V^{-1}. The corresponding d_{11} in single crystal BBO is 1.6 pm V^{-1}.

7.4.6 Electric-Field Poling and Poled Glass

Since a glass is made up of inorganic compounds in which a range of coulomb forces between the cations and anions determines the distribution of chemical bonds, the resultant average change in the spatial distribution of charge is proportional to the strength of the applied field. This change is manifested as the direction electro-optic properties (second order nonlinear susceptibility and directional change in the refractive index). This may be a simplified concept, based on the potential energy model. However, the metastable change in the ionic and defect position yields an electro-optically active layer of glass, when a field is applied (Figure 7.16). An example of direct-current (DC) field poling of lithium-niobate modified

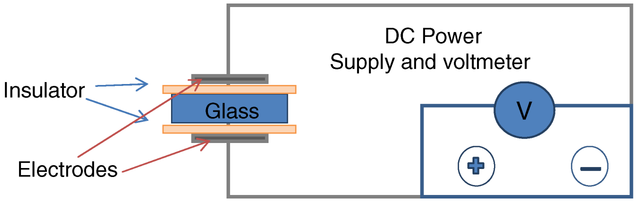

Figure 7.16 Schematic diagram of poling of a glass with a DC supply [75]. Source: Tanaka 1996. Adapted with permission from AIP Publishing.

tellurite glass is described below, which is also the principle used for silicate glasses in the past. As in case of BBO glass, in this case the electro-optic phase is lithium niobate, and when poled along its electro-optic direction this material responds by generating an active layer of higher refractive index, which is orthogonal to the direction of the applied field.

For calibration, Y-cut α-quartz was also measured using $d_{11} = 0.34$ pm V^{-1}. The refractive index for poled tellurite glass was characterized using ellipsometry at the fundamental (1064 nm) and second harmonic (532 nm) wavelengths and was found to be 1.930 and 1.983, respectively. The coherence length for Maker fringe formation at the fundamental wavelength was then determined from Equation 7.37 [75]:

$$\ell_{c,\omega} = \frac{\lambda_\omega}{[4(n_{2\omega} - n_\omega)]} \tag{7.37}$$

The calculated coherence length for the tellurite glass, described above, is 4.87 μm. To date, Maker fringes have been observed in very few glasses and glass ceramics (Figure 7.17), which suggests that much more research may be needed by analysing the role of glass structure, phase separation and crystallization of electro-optic phase for enhancing the SHG efficiency.

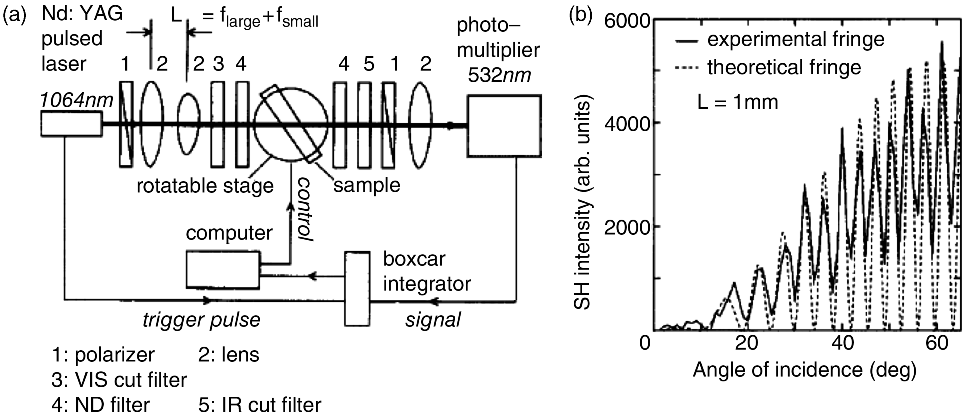

Figure 7.17 (a) Experimental set up for SHG characterization in poled glass; (b) Maker fringe patterns observed in a $15MgO\text{-}15ZnO\text{-}70TeO_2$ glass poled at 280°C. The solid lines are measured Maker fringe, compared with the computed (dotted) fringe using $d_{33} = 0.13$ pm V^{-1}, L = 1 mm, $n_{2\omega} = 1.983$, $n_\omega = 1.930$ [76]. Source: Tanaka 1996. Adapted with permission from Elsevier.

7.4.7 Raman Gain Medium

Among the known nonlinear processes, which are not based on phase-matching conditions, one of the most useful techniques for lasing and new wavelength generation is Raman amplification. Following on from the introductory discussion in Chapter 4 (Section 4.3.9), Raman amplification is an inelastic scattering process in which energy exchange occurs between the "optical phonons" in the medium and the "photon field" propagating in a nonlinear medium [25]. Since Raman gain is based on the "phonon scattering process" in a nonlinear medium, both the Stokes (lower frequency than pump) and anti-Stokes (higher frequency than pump) waves are produced, respectively, after the energy of incident photon is exchanged in both directions (forward and back scattering) by conserving the total energy. As explained earlier in Chapter 4, for spontaneous Raman scattering, the probability of "photon–phonon interaction" leading to new frequency generation is 10^3–10^5 less than a rare-earth ion based dopant process, which then necessitates that only phonons of the right energy distribution participate in the exchange of energy with pump photons, and yield new Stokes or anti-Stokes frequencies. The process of energy exchange for Stokes and anti-Stokes may be understood better from the schematic diagram in Figure 7.18, from which a clearer picture for stimulated Raman scattering may emerge, based on the intrinsic molecular polarizability of the medium. These polarizable molecular states, characterized by a required tensor matrix, therefore participate with the propagating photon field in the medium and create anti-Stokes and Stokes states. Under resonant conditions in the Stokes and anti-Stokes frequency range, if corresponding signal photons are injected into the cavity, stimulated Raman scattering frequencies may then be emitted. From Figure 7.18 it is apparent how the pump photons may gain or lose energy, respectively, from the high and low-energy optical phonons for the emission of corresponding Stokes and anti-Stokes frequencies, respectively. Furthermore, quantum mechanically the Stokes emission is more probable than the anti-Stokes process (as shown in Figure 7.18)—relying on gaining energy not only with the pump but also with the anti-Stokes phonon.

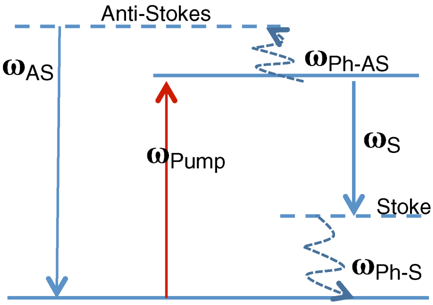

Figure 7.18 *Schematic representation of energy levels for Stokes and anti-Stokes Raman scattering emerging from pump photon and optical phonon interaction in a nonlinear medium. The* ω *symbols here define the photon frequencies at pump (*ω_{Pump}*), Stokes (*ω_S*) and anti-Stokes (*ω_{AS}*), and phonons at anti-Stokes (*$\omega_{Ph\text{-}AS}$*) and Stokes (*$\omega_{Ph\text{-}S}$*). The broken lines are the two virtual states (Stokes and anti-Stokes) with their corresponding phonon arrows.*

The initial growth of the intensity of the Stokes wave may be then described in the z-direction of propagation in an optical fibre by Equation 7.38 [25]:

$$\frac{\mathrm{d}I_Z^{(\mathrm{S})}}{\mathrm{d}z} = g_\mathrm{R} I_\mathrm{P} I^{(\mathrm{S})} \tag{7.38}$$

The threshold power in a nonlinear fibre with effective mode field area, A_eff, may be then expressed as in Equation 7.39a with the help of a complementary Equation 7.39b for critical fibre length, L_eff. Here α_P is the pump loss factor:

$$P_\mathrm{Th}^{(\mathrm{S})} \approx \frac{16A_\mathrm{eff}}{L_\mathrm{eff}\, g_\mathrm{R}} \tag{7.39a}$$

$$L_\mathrm{eff} = \frac{1 - \exp\left(-\alpha_\mathrm{P}\right)}{\alpha_\mathrm{P}} \tag{7.39b}$$

The Raman gain of an amplifying medium may then be calculated using Equation 7.40:

$$G(\mathrm{dB}) = 10.\log\left[\exp\left(\frac{g_\mathrm{R} P_\mathrm{o} L_\mathrm{eff}}{A_\mathrm{eff}} - \alpha_\mathrm{P} L\right)\right] \tag{7.40}$$

From Equation 7.40, it is apparent that by decreasing A_eff the Raman gain may increase exponentially for a given length of fibre. Another consequence of reduction in the value of A_eff may be the length required to achieve Raman gain, which drops dramatically in a PCF structure, when compared with a standard step index silica fibre.

Belardi [22] in 2004 and Lee and his co-workers [77] demonstrated Raman gain in a silica-based holey fibre in the spectral range 1610–1645 nm with signal at −10 dB. The internal gain at 1635 nm was 40 dB, recorded with 6.7 W pump power and the amplifier noise figure was less than 10 dB. The first results on Raman gain in tellurite fibres were demonstrated by engineers at NTT [78] in a seminal paper, which then led to further investigation on studies in bulk glasses. Consequently, exceptionally large (30–40 times that in silica) Raman gain coefficients in niobium and tantalum oxide containing tellurite bulk glasses were reported by Stegeman *et al.* [79]. Observation of an exceptionally large Raman gain [6] prompted more research into fibre structures, namely in tellurite PCF by Ravi Kumar *et al.* [80], and in standard fibres by Jose and co-workers [60,81,82]. The key to the successful demonstration of large Raman gain in tellurite fibres at NTT in Japan was the engineering of low-loss (sub 50 dB km^{-1}) tellurite fibres which is essential for pump efficient Raman gain (15–20 dB) in the optical communication window. Due to exceptionally large optical nonlinearity ($n_2 = 2.5 \times 10^{-19}\,\mathrm{m}^2\,\mathrm{W}^{-1}$, nonlinear coefficient, $\gamma_\mathrm{eff} = 47.8\,\mathrm{km}^{-1}\,\mathrm{W}^{-1}$) and small mode area ($21.2\,\mu\mathrm{m}^2$) in a tellurite PCF with $2.5\,\mathrm{dB\,m}^{-1}$ linear loss, the length requirement for comparable Raman gain is proportionally reduced, as was demonstrated by Ravi Kumar [80]. Such white light sources are much needed for mid-IR chemical sensing. To date, the literature on Raman gain and resonant Raman lasers using bulk glass and waveguides is rather sparse.

7.4.8 Photo-induced Bragg and Long-Period Gratings in Fibres

The principle of Bragg reflection is quite well known; however, its introduction in fibre optics happened serendipitously by Ken Hill in 1978 while using a visible laser in an optical fibre [83]. Later, in 1990 [84], Gerald Meltz [85] demonstrated the formation of a Bragg grating in an optical fibre using transverse holographic inscription in a photo-sensitive optical fibre, in which the UV laser radiation was made incident from the side, causing interference pattern. Meltz's technique was subsequently commercialized using UV excimer lasers, and less successfully with copper-vapour lasers, for engineering grating patterns. As the new applications started emerging with the availability of optical fibres from commercial sources, the opportunities for discovery and engineering new functions using fibres started to soar including the use of fibres for lasers, amplifiers, filters, optical switching and routing, and sensors. In this respect a comprehensive review has been published by Canning [86] which includes the techniques for writing gratings, e.g. *interference, sequential writing, photo-mask and point-by-point*. Several grating patterns and structures have since been reported in the literature and are only captured here briefly, as this is now considered to be a subject area in its own right, and deserves due credit, e.g. in the form of a dedicated book [87]. A number of techniques for writing gratings are discussed, namely apodized, chirped fibre gratings, tilted fibre gratings and long-period gratings [88].

Although the success of a UV-excimer based laser for writing gratings has been widely acknowledged now in industry, with its implementation during fibre drawing of silica based fibres, UV-based laser based writing gratings is not suitable for optical fibres such as the tellurite and chalcogenide glasses, in which the electronic band gap is at a longer wavelength than that of the excimer laser. The excimer laser photosensitizes both the core and cladding glass structures and changes the refractive index locally. In traditional silica Bragg grating inscription, the UV-light penetrates through the cladding layer and reaches the core–clad interface, where the gratings are written. Because of enhanced electronic absorption of UV-lasers in chalcogenide and tellurite glasses, an alternative technique using ultrafast femto-second lasers at IR wavelengths (e.g. 800 nm using Ti-Sapphire) or CO_2 laser lines may be used. Quite recently, using IR-femtosecond lasers (120 fs pulsed at 800 nm with 1 kHz repetition rate), Suo and co-workers [89] demonstrated fibre Bragg and long-period grating inscription on tellurium oxide and germanium oxide fibres, for engineering temperature and strain sensors. The setup is shown in Figure 7.19. For inscription FBG on the core of GeO_2 and tellurite fibres, a custom designed phase mask with a grating period 1697.33 nm was used. The second order FBG inscription from the phase mask in these high refractive index fibre was at around 1500–1800 nm. The output beam, with a radius of 5 mm, was focused in y-axis by a cylindrical lens of 30 mm focal length and through the phase mask to the fibre core.

Due to the high refractive index of the cladding, the laser beam was highly focused. Hence the width of fs-inscribed grating structure along x-axis, as shown in Figure 7.19, is merely $\sim$2 μm. Such a thin-layer of FBG structure would not give a high reflectivity and also in the experiment it was easy to miss the core region. To ensure maximum coverage of fs-inscription in the core region, the incident beam was scanned along the x-axis from -30 to 30 μm with an incremental step of 2 μm for the single-core GeO_2 fibre and from -50 to 50 μm for the three-core tellurite fibres. It was found that the energy of the pulsed laser was critical for FBG inscription; from several tests, it was established between 22 μJ for GeO_2 and 14 μJ for tellurite single and multi-core fibres, respectively.

Once the Bragg inscriptions were written using the set up shown in Figures 7.19a and b for the single and multi-core fibre structures, these structures were analysed for the presence of interference fringes by examining them with an optical microscope. The grating structures are shown in Figure 7.19c and d for the side and top views, respectively, of a three-core tellurite (TeO_2) fibre, proving the efficacy of a novel way of writing gratings using a 800 nm

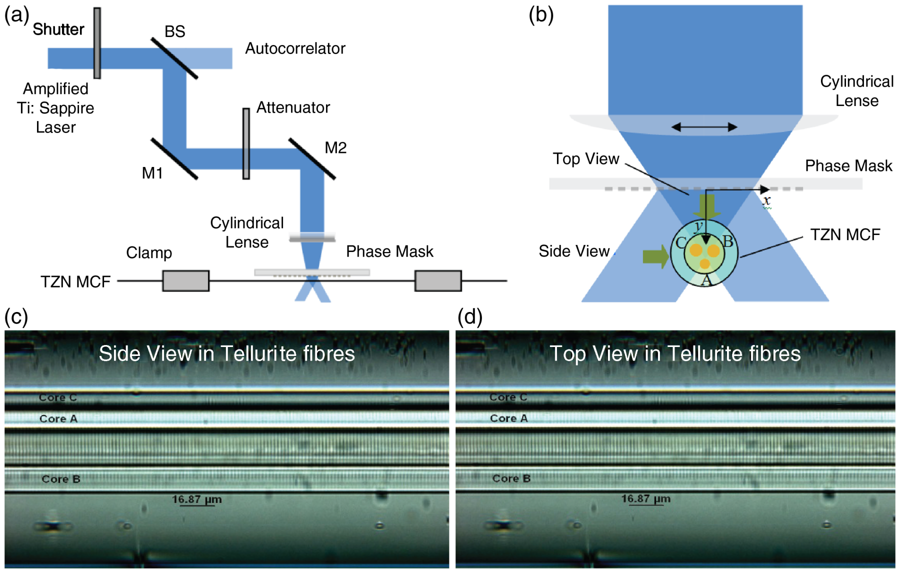
(a)
Shutter
BS
Autocorrelator
Amplified
Ti: Sappire
Laser
Attenuator
M1
M2
Cylindrical
Lense
Clamp
Phase Mask
TZN MCF
(b)
Cylindrical
Lense
Top View
Phase Mask
x
y
Side View
C
B
A
TZN MCF
(c)
Side View in Tellurite fibres
Core C
Core A
Core B
16.87 μm
(d)
Top View in Tellurite fibres
Core C
Core A
Core B
16.87 μm

Figure 7.19 *Schematic diagram of FBG inscription system using fs laser and phase mask with a tellurite multi-core fibre mounted. The x axis in (b) is parallel to the phase mask and perpendicular to the grooves, and the y axis is normal to the phase mask. The TZN glass fibre stands for a glass composed of 80* TeO_2*-10ZnO-10*Na_2O *mol.%. Microscopy images of grating structure from (c) the side view and (d) top view of the TZN passive fibre. In both (c) and (d), the periods of the structures are measured as 1.687 μm [89]. Source: Suo 2009. Reproduced with permission from OSA Publishing.*

fs-laser without causing any damage to the cladding. The transmission properties of single- and triple-core BG structured fibres are explained in detail in the context of sensor design [89]. As an example, only a comparison of the second order FBG transmission spectra is shown in Figure 7.20 for the triple-core tellurite fibres. The sensor related results are reported elsewhere [89].

7.5 Applications of Selected Rare-earth ion and Bi-ion Doped Amplifying Devices

7.5.1 Introduction

Following on from the discussions and examples in Chapter 6, in this section the main emphasis will be on rare-earth ion and Bi-ion doped glass based devices for which significant results have been demonstrated by several research groups worldwide for device and sub-system engineering. Especially, for rare-earth ion doped glass based devices our main emphasis will be on Yb^{3+}, Nd^{3+}, Er^{3+} and Tm^{3+}/Ho^{3+} doped glass, fibres and waveguides. Results from each of these dopants are discussed by taking examples of lasers and amplifiers, which are briefly discussed below.

Before we discuss individual trivalent rare-earth ion based devices, it is important to reiterate the following points, to appreciate the convergence of several important discoveries

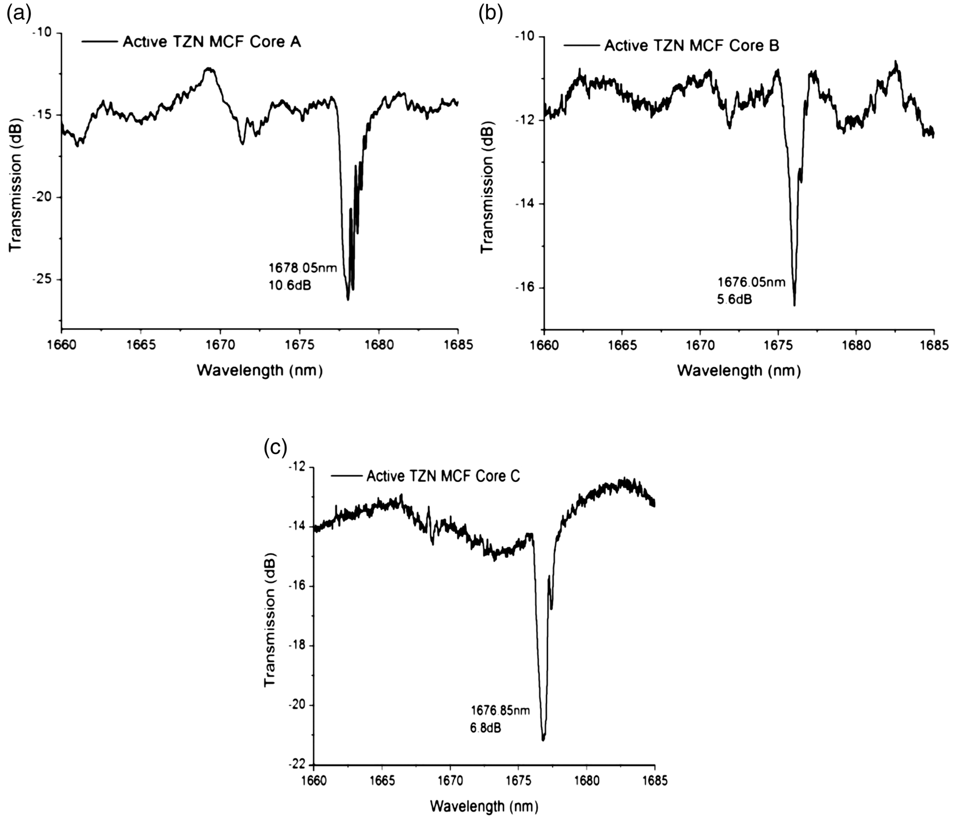

Figure 7.20 *Second order FBG transmission spectra (a)–(c) of cores A–C, respectively, of a tellurium oxide multi-core fibre [89]. Source: Suo 2009. Reproduced with permission from OSA Publishing.*

and engineering inventions which are brought together in realizing modern lasers in fibre and waveguide forms. These are the original theory of spontaneous and stimulated emission by Einstein, and light guiding in a confined medium, discovery of semiconductor pump sources and associated engineering of beam combiners for launching into a laser cavity, polarization control for modes, and Bragg gratings as mirrors and engineering to reduce the thermal load inside the cavity. As exemplified below, these aspects are important controlling factors in the design of light amplification media, e.g. lasers and amplifiers.

From our earlier discussion in Chapter 6 on population inversion theory for stimulated emission, the following two types of pumping schemes are considered for lasing: three(3)-level and four(4)-level systems (Figures 7.21a and 7.21b). For details on the rate equation models for 3-level and 4-level systems, relevant references in Chapter 6 may be useful; however, for a more focused discussion on aspects of glass materials engineering for a laser cavity and heat management therein, the following points must be considered, when comparing with a semiconductor pump laser source. A semiconductor pump source is 3-4 orders of magnitude smaller in dimension than for glass or crystal based lasers, which clearly implies that the population inversion density per unit volume or length in a semiconductor device is much

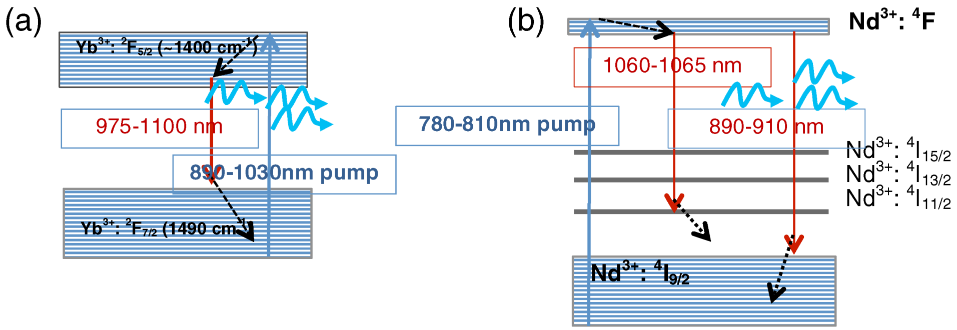

Figure 7.21 Examples of pseudo 3-level, 3-level (a), and 4-level (b) optical transitions in Yb^{3+} and Nd^{3+}-doped glass for lasing actions via $Yb^{3+}: {}^2F_{5/2} \rightarrow {}^2F_{7/2}$ (in the 975–1100 nm region), $Nd^{3+}: {}^4F_{3/2} \rightarrow {}^4I_{9/2}$ (890–910 nm) and $Nd^{3+}: {}^4F_{3/2} \rightarrow {}^4I_{11/2}$ (1060–1065 nm), respectively. The respective pump source wavelengths for Yb^{3+} and Nd^{3+} are in the range 890–1030 and 780–810 nm.

larger than in a rare-earth or transition metal doped crystal or glass. The structural aspects of dopant solubility in various glasses were discussed in Chapter 6 and, from the spectroscopic analysis therein, it is evident that the silica and chalcogenide based (except for gallium-lanthanum-sulfide, GLS) glasses are not the ideal host for rare-earth ions, whereas the phosphate, fluoride and tellurite glasses are at least 10 times, if not 100 times, better than silica and tetrahedron co-ordinated sulfides. Depending on the pumping scheme (3- or 4-level), it may determine the inversion efficiency, depending on the optical energy exchanges and its release, by minimizing the thermal components.

7.5.2 Examples of Three-Level or Pseudo-Three-Level Transitions

The optical transition pathway for a pseudo 3-level system is almost identical with the transition pathways in a 3-level system, in which a pump source excites the ground states to a higher lying state, within which rapid thermalization may lead to population build-up at the lower lying levels of the lasing transition level (e.g. in $Yb^{3+}: {}^2F_{5/2}$ and in $Nd^{3+}: {}^4F_{3/2}$ shown by broken lines in Figure 7.21). In both the pseudo 3-level and 3-level, after the transition the states further thermalize and attain lowest energy state in the ground state. Notably, for lasing transitions to occur in a pseudo-3- and 3-level, the population inversion may be maintained by pumping sufficiently. The inverted population at $Yb^{3+}:{}^2F_{5/2}$ and $Nd^{3+}: {}^4F_{3/2}$ must be around 50% to sustain the lasing action. This condition therefore determines the pump power requirement for a gain medium in which the necessary rapid rise time of the states from ground level and their subsequent thermal relaxation must be facilitated for efficient lasing transition. The pump requirement is therefore high, because of the faster steps involved in a 3-level or pseudo 3-level system. A balanced disproportionation of population of states between the ground and lasing states, in general, is essential for pump efficient lasing. The structure of glass and dopant environment, as discussed in Chapter 6, play critical role in determining the radiative, non-radiative and potential energy-favouring and depleting exchanges in a lasing transition, some of which are exemplified below. Well-known examples of optical transitions, which are classed as the ground-state 3-level or pseudo-level transitions, are in Yb^{3+} (see Figure 7.21a), Nd^{3+} (Figure 7.21b), Er^{3+}

(Figure 6.13) and Tm^{3+} and Ho^{3+} ions (Figure 6.18a). These dopants have been investigated in a wide variety of inorganic glass hosts, namely silicates, non-silicates (phosphate, tellurite and germanium oxide), fluoride and chalcogenide for a range of lasing and amplification experiments, including power scaling in continuous wave (CW), Q-switching and mode-locking operations.

7.5.2.1 Yb^{3+}-Doped Glass Lasers

The example of Yb^{3+}-doped silicate glass for laser transition is a classic instance of a device with the least quantum defects and energy depletion mechanism, e.g. upconversion transition, discussed in Chapter 6. Based on the spectroscopic parameters of Yb^{3+}-doped aluminium oxide and phosphorus pentoxide doped silicate glass fibres, Zervas and Codemard [90] in a recent review summarized the efficiency budget of Yb^{3+}-fibre lasers and pointed out that, depending on the pumping scheme chosen, the output efficiency of a fibre laser may be in the range 60–80%, with 8–12% lost in quantum defects, 5–10% in excess pump loss, 5–10% excess signal loss and 0.5–1% for non-optimized cavity design.

From Figure 7.21a it is evident that in Yb^{3+}-dopant the highest energy level is $^2F_{5/2}$, which is the lasing level and both the ground ($^2F_{7/2}$) and lasing levels are sufficiently Stark-split (~1400 cm^{-1}) due to strong covalent bonding. This means if a fibre or waveguide device can be designed carefully, the in-band pumping (1010–1020 nm) from lasing action may be combined with the external pump source for power scaling to multi-kilowatt (kW) levels of power in fibre geometries, which is necessary for industrial materials manufacturing. This in-band pumping is possible due to the overlap between absorption and emission cross-sections (Figure 7.22). In kilowatt lasers with fibre geometries the power-scaling pushes the threshold power, as a result the probability for multi-photon absorption leading to fibre damage

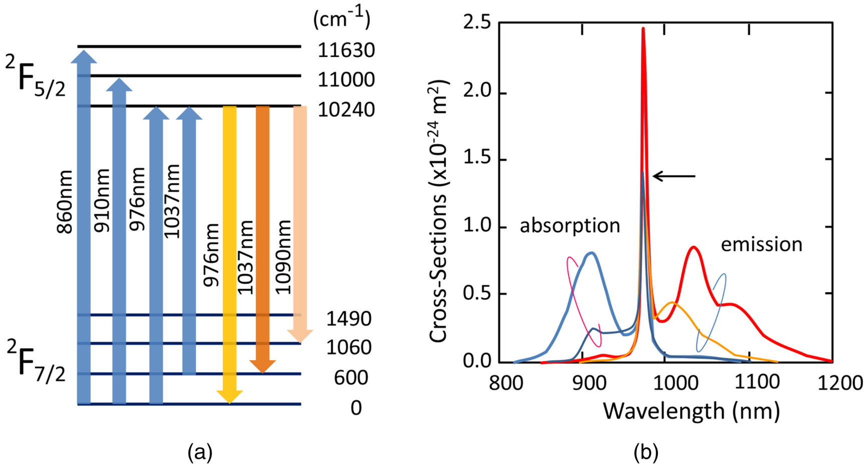

Figure 7.22 *Optical transition wavelengths in Yb^{3+}-doped silicate glass fibres. In (a) the blue arrows show the pump wavelengths. The spontaneous emission transitions are probable wavelengths pointing downward, which are shown in (b). Note that the zero-phonon line emission remains virtually invariant in spectral width in the excited and emission states [90]. Source: Zervas 2014. Reproduced with permission from IEEE Explore. (See colour plate section.)*

increases in Yb^{3+}-doped silicate fibres. Such photo-darkening in core glass may be reduced by controlling UV-desensitization by doping with the oxides of phosphorus, aluminium, and cerium [91–93]. Besides photo-darkening the fibre core may also be damaged by nonlinear effects, e.g. stimulated Brillouin and Raman scattering and photo-avalanche effects [90]. These nonlinear effects in high-power and kilowatt fibre lasers manifest more easily due to long interaction length in fibres than in bulk glass cavities, which is why the softer glasses have not yet found applications in kW-laser application space, because of their redshifted electronic edge, larger nonlinearity than silicates (e.g. in tellurite, germanium oxide and chalcogenides). Non-silicate fibres are much weaker in mechanical strength than the standard silica fibres.

Besides power scaling in the CW mode, laser cavities may be set up to yield Q-switched and mode-locked outputs, the details of which are readily available in standard textbooks on lasers. Very briefly, a Q-switched laser cavity must maintain its quality (Q) factor, which is the ratio of the energy stored per cycle to the loss factor of the cavity. This implies that the higher the Q-factor of a cavity the lower is the loss (intrinsic and extrinsic losses). To achieve a Q-switch operation the following *four conditions* must be satisfied, which are also represented diagrammatically in Figure 7.23 [23].

In a Q-switch cavity the lifetime of the lasing level must be long enough for building the population that will store the extra pump energy by occupying the lasing state for a longer time than in a CW cavity. This condition implies that the lifetime of the lasing level (τ_{up}) must be longer than the stimulated emission lifetime (i.e. $\tau_{st} < \tau_{up}$). The second condition necessitates that the pump rise time (τ_{Pump}, i.e. pumping flux) must be comparable with the lifetime of the upper level (i.e. $\tau_{Pump} \geq \tau_{up}$). The third condition requires that during the pump rise time the initial cavity loss is higher so that the stimulated emission does not occur during the pump cycle rise, allowing the stored energy to grow and reach saturation level before releasing. This means that in the steady state region of rise time of the population the cavity loss dominates the gain due to amplification, as can be seen in Figure 7.23. Finally, when the amplifying or the lasing level saturates, the loss must be reduced quickly, so that the upper occupying states are depopulated rapidly by releasing a giant pulse of energy, called the Q-switched pulse. This implies that, during the pump-on and pump-off, the cavity turns into a high-Q cavity by turning the loss mechanism on and off. The loss mechanism may be of several types in a cavity from an electro-optic or acousto-optic modulator to saturable absorber, which may allow a rapid on–off mechanism for Q-switching [23,94]. To date, hundreds of examples of Q-switched glass, fibre and waveguide lasers based on rare-earth

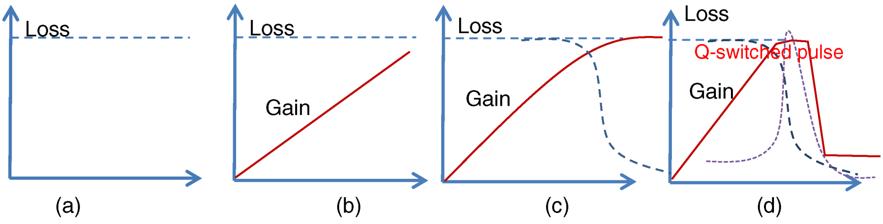

Figure 7.23 *Graphical representation of Q-switched pulse evolution in a cavity: (a) represents a loss in the cavity; (b) shows that the gain is less than loss and in (c) the gain dominates the loss at which point the inversion condition releases the stored energy in a pulsed form as a Q-switched pulse in (d). Source: Silfvast 2004. Reproduced with permission from Cambridge University Press.*

ions as dopant are known. Selected examples will help readers to appreciate the applications of Q-switched lasers. For example, in a Yb^{3+}-Tm^{3+} doped fibre a Q-switched output power of 2.4 W was reported with 140 kHz repetition rate. The maximum pulse energy was 21.8 μJ and minimum pulse duration was 1.1 μs. The tunable wavelength of the cavity was 1055–1090 nm [95]. The output radiation showed a maximum spectral linewidth of 4 GHz. Other examples of Q-switched lasers using silica and non-silica fibres doped with Tm^{3+}, Ho^{3+}, Er^{3+} and Nd^{3+} ions are discussed below briefly.

Before moving on to other important examples of lasers, another mechanism of increasing the output power of a cavity is by mode-locking the longitudinal modes. Inside a cavity due to its geometry, a number of frequencies over a narrow bandwidth of the amplifying medium oscillate. These frequencies may not be in phase, thereby yielding a phase distribution together with the frequency distribution. As a result the total energy of a cavity is dispersed, which must be controlled by adding the phase and amplitudes of each frequency, culminating in a transition from multi-frequency out of phase oscillation to a mode-locked pulsed operation. Such model-locked cavities must have a means to control dispersion and a saturable absorber for pulsed operation, as described in the Q-switched operation. The combination of these two techniques is described widely in the literature and is beyond the scope of this text.

Amongst various mode-locking techniques, the pioneering achievement in the technique called the Kerr-lens mode-locking (KLM) yielded sub-100 femtosecond (fs) pulses [96]. This has led to applications of short pulses for a range of emerging applications [97]. The KLM based mode-locking consequently has now become a common feature in sub-pico- and femtosecond pulsed solid-state lasers, based on bulk glass and crystal, fibre, and waveguide based cavities. In such cavities the gain medium, based on rare-earth ion dopants, exhibits two essential features—a long metastable lifetime of the lasing transition and broad emission bandwidth. A long metastable lifetime is essential for energy storage in the cavity, as is known from the principles of Q-switching; however, the large spectral bandwidth (ΔE) then helps in controlling the temporal width ($\Delta\tau$) of mode-locked pulse. This means that such mode-locked pulses are the purest forms of light sources and represent one of the fastest clocks in the universe for use in investigating other comparable processes. In other words short pulses are like a *new temporal ruler* for measuring and comparing with other phenomena in physics, chemistry and biology. For such a temporal ruler design, the rare-earth or transition metal ion doped glass based host plays an important role as it provides a broadband spectroscopic features ($\Delta E\Delta\tau \geq h/4\pi$) of metal dopant ions (e.g. Tm^{3+}, Ho^{3+}, Cr^{2+}) [98,99] together with the optical nonlinearity for self-starting the mode-locking process. The cavity design of such lasers also allows generation of multi-billions of pulses, as exemplified in the case of Yb^{3+}-doped lasers [100,101]. Examples of generating 1–100 GHz repetition rates per second (10^{11} pulses per second) pulses from bulk and waveguide cavities have been demonstrated, which means that opportunities for transcending chemical barriers in reactions and phase transformation may be possible. These are truly new opportunities in materials science for discovering novel structures and applications.

By discussing the example of Yb^{3+}-doped lasers, it has become easier to summarize the properties of other types of rare-earth ion doped lasers; the design of each is based on the ground-state transitions (Er, Tm, Ho) and their salient features are summarized in Table 7.5 below. We conclude this section by showing the chronology of power-scaling in fibre lasers to the kilowatt level, e.g. see in Figure 7.24 [102].

Table 7.5 *Brief summary of references in selected rare-earth doped and Bi-ion doped lasers and amplifiers.*

Rare-earth doped device	Specification of the device and key remarks
Nd^{3+}-doped fibre lasers and amplifiers	Wavelength operation 1064 nm, high-power industrial lasers for manufacturing [24], NIF operation aims to create 500 TW power in a few picoseconds using Nd^{3+}-doped phosphate glass [104].
Bi-doped lasers and amplifiers	A bismuth-doped fibre laser emitting at wavelengths within the second transparency window of silica fibres has been fabricated. It was shown that Bi-doped aluminium-free phosphate modified GeO_2-SiO_2 fibres pumped in the regions of 800 and 1200 nm have the amplification band at 1275–1375 nm. Fibre laser with 10 W output power was also shown operating in the 1150–1215 nm and frequency doubling at 580 nm [105–107].
Er^{3+}-doped fibre lasers Er^{3+}-doped fibre amplifiers	A range of Er^{3+}-doped glass fibre lasers and amplifiers operating in the 1505–1610 nm range have been reported since the first Er^{3+}-doped fibre laser was demonstrated [108]. Key references are included herein [109,110,103,111,112,113,114]. However, there has been a serious problem in the power scaling of Er^{3+}-doped laser devices because of the large quantum defects and thermal management [90].
Tm^{3+}- and Ho^{3+}-doped fibre lasers and amplifiers	Laser operations in Tm^{3+} and Tm^{3+}-Ho^{3+} doped fibre lasers have been shown with a range of diode and fibre laser pumping schemes. Several watts to kW levels of power have been reported in CW and pulsed laser regimes. Tm^{3+}-doped non-silica (fluoride and tellurite) fibres have been proven to be efficient amplifiers for S-band (1450–1530 nm) window. The amplification characteristics supplement that using Er^{3+}-ions for the lowest loss window. [98,115–120,99,121,122,123,124,125,126–128].

7.5.3 Examples of Four-Level Laser Systems

The credit for the discovery of Nd^{3+}-doped fibre lasers goes to Koester and Snitzer [72] who understood the importance of optical fibres in the engineering of lasers, especially for reducing the threshold power. The optical transition utilizing the seminal work by Snitzer, as shown in Figure 7.21b, was the $^4F_{3/2} \rightarrow {}^4I_{11/2}$ transition, which has the largest branching ratio against three other competing transitions from the lasing level $^4F_{3/2}$. The transition terminating at the ground state, $^4I_{9/2}$ (890–910 nm) is only 60% stronger than that at $^4I_{11/2}$ at 1060–1065 nm. Two other transitions terminating at $^4I_{13/2}$ and $^4I_{15/2}$, respectively at 1310–1360 and ~1870 nm, are much weaker than the two optically strong transitions. Details of spectroscopic features of optical transitions in Nd^{3+}-doped glasses may be found elsewhere [103]. However, without duplicating information in this text book, the following spectroscopic features of Nd^{3+}-ion as a dopant must be noted for engineering devices:

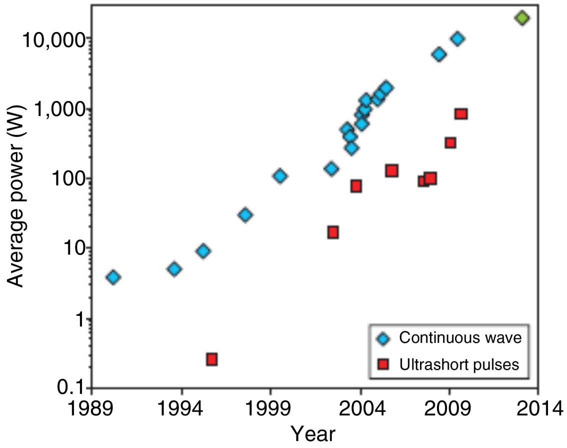

Figure 7.24 *A chronology of power-scaling in solid-state CW and ultrashort pulsed lasers [102]. Source: Jauregui 2013. Reproduced with permission of Nature Publishing Group.*

(a) The pumping wavelength for population inversion at $^4F_{3/2}$ is at 780–810 nm, at which plenty of power (kilo watts) is available at present from commercial sources, and this is very important for power scaling of bulk and fibre lasers, based on Nd^{3+} and Yb^{3+} doped glass based devices.

(b) The optical transitions are strongly dependent on the electric-dipole strength, which implies that the Stark level splitting of energy levels is very much dependent on the refractive index of a medium. In an ionic fluoride glass the Stark splitting is less dominant due to the localization of valence electrons, whereas in silicates, phosphates and tellurite glasses, the Stark splitting is quite dominant. As a result the peak of emission and gain in amplification for the transitions originating from the $^4F_{3/2}$ level shift to longer wavelengths with increasing covalent bonding in the glass. The trend for redshift in the emission and gain peaks with the refractive index is, however, less apparent [103].

(c) The optical transition at 1310–1360 nm has a bottleneck, which is the excited state absorption at emission wavelength. This means that the peak shifts to longer wavelengths, negating any gain in the shorter wavelength part in the 1310 nm region. It is for this reason that the fluoroberyllate (BeF_2), fluorophosphates and AlF_3 based glasses are most useful [103].

(d) As explained above in the section on the 3-level system with an example of Yb^{3+}-laser, the in-band pumping of Yb^{3+}-doped fibre is an important step for realizing power scaling. In this respect, the co-doping of Nd^{3+} with Yb^{3+} facilitates the utilization of excessively high power pump laser diodes, which enable power scaling with novel pump–beam combining techniques, as explained in a review [90].

(e) The availability of kilowatt pump power, advanced manufacturing technology for phosphate glass and passive optics that are able to withstand kilowatt level of power has enabled the design of multi peta- to exa-watt lasers for studying the fusion of hydrogen atoms for energy generation in the USA and Europe. The ambition of achieving sustained fusion for energy generation is a long-term goal of human civilization, for which many more hurdles may need to be overcome in the next few

> decades. However, important point to note in the context of inorganic photonic glasses is that it is the spectroscopic properties of phosphate glass for high power lasers that has enabled the growth of the National Ignition Facility at the Lawrence Livermore Laboratory in the USA. This is a major national campaign from the Department of Energy for the future of energy in the USA, in which advanced rare-earth doped based laser technology will continue to play an important role [104]. The need to secure a supply of clean energy with low carbon footprint is so great that a similar campaign in Europe is also actively pursuing research using ultrafast photon science, based on power-scaling with advanced laser technology.

In the literature there is a wealth of information on lasers and amplifiers which is unnecessary to duplicate here and, for this reason, this section is concluded with a summary (Table 7.5) on other rare-earth ion and bismuth ion doped lasers and amplifiers. In this text the mechanism of photon emission using bismuth-ion doped fibres is not discussed in detail, because the defect state (or states) participating in the photon emission process is unclear. Bismuth is a photosensitive metal ion and has multiple ionic states (Bi^+, Bi^{2+}, Bi^{3+} and Bi^{5+}) on heating [105–107] or with UV-light the oxidation states change. The pentavalent state is the most oxidizing and can only remain stable in glass and crystal matrices. The thermodynamic stabilities of oxides and sulfides of bismuth are more comparable with the oxides and sulfides of metallic lead and cadmium, as shown by comparing the Gibbs energies of individual oxides with the oxides of lead and cadmium. From such a comparison it is evident that during melting and fibre drawing the oxidation states of Bi-ion may change, depending on the ambient oxygen potential. The lack of control in maintaining the concentrations of so-called "photo-emitting states" in bismuth oxide doped glasses is still an unsolved problem, although reasonable modest efficiency devices have been demonstrated. Salient results in this area are captured in Table 7.5.

7.6 Emerging Opportunities for the Future

In today's world connectivity and communication are important, which then pushes demand for more bandwidth for data transmission between the standard fibre optics [129] and non-fibre optics based communications (e.g. microwave and radio waves). In the state-of-the-art handheld devices, the bandwidth is limited and the trend is to have more signal transmission in the optical frequency band through line-of-sight communication. This means in large premises the line-of-sight communication using polymer or silica fibres, the visible-light based optical connection may become feasible and in this respect broader band rare-earth transitions will play a significant role in device engineering. Optical signal processing on a chip will emerge and will be an important part of future handheld devices.

Continuing with the trend in consumer electronics, the handheld device is also beginning to emerge as a personal management device for organizing diaries for social activities and health and physical and mental fitness. In this respect there is an emerging trend to incorporate more sensors and tools (apps etc.) for consumers, which will empower them to connect with the rest of the world. Personalized health monitoring may be enabled via multiple sensors and communication platforms in emerging handheld devices, in which the optical interconnect based on waveguide integration will play an important role. Dissimilar materials integration for creating optical circuits may be necessary, for which earlier attempts with glass and semiconductor and glass and polymer have been made [130,131]. This means that the engineering of active and passive components together for integrated photonics, electronics, and optoelectronics will be a natural trend for industry. Enabling physics, chemistry, biology and materials science may be required for complex integrated circuit design and manufacturing on a large scale.

In relation with information technology, there is need for data storage and retrieval at high-speed. Two types of optical memory materials may be required in future—these may be volatile and read-write (multiple) memory devices. Original work on chalcogenide glasses by Stanford R Ovshinsky [132] on non-volatile phase change memory has laid the foundation for its applications in CD and DVD. Research in a new direction on chalcogenide glasses [133] is emerging, and is based on ultrafast devitrification–revitrification in glass. Volume and holographic data storage are also quite important for the future, as society moves towards a world of virtual and augmented realities.

The science of ultrafast laser–glass interaction has seen more applications since 1995 at the device front, by using a range of glasses for making lasers and amplification devices. However, for the last 20 years no high-speed manufacturing technology has emerged for making this technique a commercial success. More glass research and basic physics of laser–matter interaction may be necessary in future. The current topics are very widely discussed by Hirao and co-authors [134], showing clearly a path for the future.

There is an urgent need to expand the optical bandwidth of fibres into the mid-IR spectral range (2–20 μm), which is an extremely important region for medicine, sensor and imaging technologies, and environment monitoring. Most chemical spectroscopic analysis will be better served by exploiting the fundamental vibration (2.5–8 μm) and finger printing (7–20 μm) regions together, for manufacturing and process control, emerging needs in clinical diagnostics for early detection of chronic and non-communicable diseases, security and military, and above all environment management. For these applications, fibres, waveguides and high quality light sources (lasers and broadband supercontinuum sources) are required [66].

As explained above, the need to conserve energy and resources is the greatest challenge for mankind in this millennium. This has clear implications for solar photovoltaic, solid-state lighting and nuclear fusion. Rare-earth and transition metal ion and quantum-dot based glass technologies are clearly important; however, at present there is no clear winner in terms of which one of these techniques might be adopted for solar PV.

7.7 Conclusions

In this concluding chapter, the major highlights of optical fibre, laser and light amplification techniques are discussed briefly and relevant references are given to supplement the reader's knowledge. The importance of unconventional fibre structures is discussed in the context of controlling the properties of light. The examples of high power lasers are discussed especially for demonstrating the growing need for newer and emerging materials. The nonlinear optical properties of glass based materials are explained for device applications. Emerging photonic devices are also briefly discussed.

References

1. Keiser, G. (1991) *Optical Fibre Communications*, McGraw Hill International, New York. pp. 118–120.
2. Ghatak, A. and K. Thyagarajan (2000) *An Introduction to Fibre Optics*, Cambridge University Press, Cambridge (UK), pp. 84–89.
3. Maeda, Y. and F. Montalti (2010) *Optical Fibres, Cables and Systems - An ITU-T 2009 Manual*, pp. 5–29.
4. Mynbaev, D.K. and L.L. Scheiner (2001) in *Fibre Optics Communications Technology*, Prentice Hall, Upper Saddle River, NJ (USA), pp. 42–63.
5. Kaiser, P. and H. Astle (1974) *The Bell System Technical Journal*, **53** (6), 1021–1039.
6. Yeh, D.C., *et al.* (1989) Energy-transfer between Er^{3+} and Tm^{3+} ions in a barium fluoride-thorium fluoride glass. *Physical Review B*, **39** (1), 80–90.
7. Yeh, P., A. Yariv, and E. Marom (1978) Theory of Bragg fiber. *Journal of the Optical Society of America*, **68** (9), 1196–1201.
8. John, S. (1987) Strong localization of photons in certain disordered dielectric superlattices. *Physical Review Letters*, **58** (23), 2486–2489.
9. John, S. (1984) Electromagnetic absorption in a disordered medium near a photon mobility edge. *Physical Review Letters*, **53** (22), 2169–2172.
10. Yablonovitch, E. (1987) Inhibited spontaneous emission in solid-state physics and electronics. *Physical Review Letters*, **58** (20), 2059–2062.
11. Yablonovitch, E. *et al.* (1991) Donor and acceptor modes in photonic band-structure. *Physical Review Letters*, **67** (24), 3380–3383.
12. Joannopoulos, J.D., R. Meade, and J. Winn (1995) *Photonic Crystals*, Princeton Press, New Jersey.
13. Joannopoulos, J.D., P.R. Villeneuve, and S.H. Fan (1997) Photonic crystals: putting a new twist on light. *Nature*, **386** (6621), 143–149.
14. Bowden, C.M., J.P. Dowling, and H.O. Everitt (1993) Development and applications of materials exhibiting photonic band gaps: introductions. *Journal of the Optical Society of America*, **B**, **10** (2), 218–413.
15. Russell, P.S.J. (2003) Designing photonic crystals, in *Electron and Photon Confinement in Semiconductor Nanostructures* (ed. B. Deveaud, A. Quattropani, and P. Schewndimann) IOS Press, Amsterdam, pp. 79–103.
16. Knight, J.C. *et al.* (1996) All-silica single-mode optical fiber with photonic crystal cladding. *Optics Letters*, **21** (19), 1547–1549.
17. Russell, P.S.J. (2006) Photonic-crystal fibers. *Journal of Lightwave Technology*, **24** (12), 4729–4749.
18. Birks, T.A., J.C. Knight, and P.S. Russell (1997) Endlessly single-mode photonic crystal fiber. *Optics Letters*, **22** (13), 961–963.
19. Knight, J.C., *et al.* (1998) Photonic band gap guidance in optical fibers. *Science*, **282** (5393), 1476–1478.
20. Cregan, R.F. *et al.* (1999) Single-mode photonic band gap guidance of light in air. *Science*, **285** (5433), 1537–1539.
21. Benabid, F., *et al.* (2002) Stimulated Raman scattering in hydrogen-filled hollow-core photonic crystal fiber. *Science*, **298** (5592), 399–402.

22. Belardi, W. (2004) *Holey Optical Fibres for Nonlinear Devices*, PhD Thesis, University of Southampton.
23. Silfvast, W.T. (2004) *Laser Fundamentals*, 2nd edn, Cambridge University Press.
24. Koechner, W. (2013) *Solid-State Laser Engineering*, vol. 1, Springer.
25. Agrawal, G.P. (2007) *Nonlinear Fiber Optics*, Academic Press, pp. 261–270.
26. Monro, T.M. and H. Ebendorff-Heidepriem (2006) Progress in microstructured optical fibers. *Annual Review of Materials Research*, 467–495.
27. Boling, N.L., A.J. Glass, and A. Owyoung (1978) Empirical relationships for predicting nonlinear refractive index changes in optical solids. *IEEE Journal of Quantum Electronics*, **14** (8), 601–608.
28. Vogel, E.M., M.J. Weber, and D.M. Krol (1991) Nonlinear optical phenomena in glass. *Physics and Chemistry of Glasses*, **32** (6), 231–254.
29. Glass, A. *et al.* (1975) Excited state polarization, bulk photovoltaic effect and the photorefractive effect in electrically polarized media. *Journal of Electronic Materials*, **4** (5), 915–943.
30. Cotter, D. *et al.* (1989) Picosecond pump–probe interferometric measurement of optical nonlinearity in semiconductor-doped fibers. *Optics Letters*, **14** (6), 317–319.
31. Sutherland, R.L. (2003) *Handbook of Nonlinear Optics*, CRC Press.
32. El-Mallawany, R.A.H. (2002) *Tellurite Glass Handbook: Physical Properties and Data*, CRC Press.
33. Rangel-Rojo, R. *et al.* (1994) Near-infrared optical nonlinearities in amorphous chalcogenides. *Optics Communications*, **109** (1), 145–150.
34. Bindra, K.S. *et al.* (2001) Nonlinear optical properties of chalcogenide glasses: Observation of multiphoton absorption. *Applied Physics Letters*, **79** (13), 1939–1941.
35. Lines, M. (1991) Oxide glasses for fast photonic switching: A comparative study. *Journal of Applied Physics*, **69** (10), 6876–6884.
36. Hutchings, D. and B. Wherrett (1994) Theory of the dispersion of ultrafast nonlinear refraction in zinc-blende semiconductors below the band edge. *Physical Review B*, **50** (7), 4622.
37. Ainslie, B.J. (1992) Optically non-linear glasses, in *High-Performance Glasses* (eds M. Cable and J.M. Parker), Blackie Press, London, pp. 210–228.
38. Vogel, E., M. Weber, and D. Krol (1991) Nonlinear optical phenomena in glass. *Physics and Chemistry of Glasses*, **32** (6), 231–254.
39. Shen, S.X. *et al.* (2002) Tellurite glasses for broadband amplifiers and integrated optics. *Journal of the American Ceramic Society*, **85** (6), 1391–1395.
40. Lenz, G. *et al.* (2000) Large Kerr effect in bulk Se-based chalcogenide glasses. *Optics Letters*, **25** (4), 254–256.
41. Cerqua-Richardson, K., *et al.* (1998) Comparison of nonlinear optical properties of sulfide glasses in bulk and thin film form. *Optical Materials*, **10** (2), 155–159.
42. Berthereau, A. *et al.* (1994) Nonlinear optical properties of some tellurium (IV) oxide glasses. *Materials Research Bulletin*, **29** (9), 933–941.
43. Vogel, E.M. (1989) Glasses as nonlinear photonic materials. *Journal of the American Ceramic Society*, **72** (5), 719–724.
44. Sabadel, J., *et al.* (1997) Structural and nonlinear optical characterizations of tellurium oxide-based glasses: TeO_2–BaO–TiO_2. *Journal of Solid State Chemistry*, **132** (2), 411–419.

45. Jha, A. *et al.* (2001) Inorganic glasses as Kerr-like media. *Current Opinion in Solid State and Materials Science*, **5** (6), 475–479.
46. Bindra, K. *et al.* (2001) Nonlinear optical properties of chalcogenide glasses: Observation of multiphoton absorption. *Applied Physics Letters*, **79** (13), 1939–1941.
47. Eggleton, B.J., B. Luther-Davies, and K. Richardson (2011) Chalcogenide photonics. *Nature Photonics*, **5** (3), 141–148.
48. Asobe, M. (1997) Nonlinear optical properties of chalcogenide glass fibers and their application to all-optical switching. *Optical Fiber Technology*, **3** (2), 142–148.
49. Asobe, M. *et al.* (1993) Efficient and ultrafast all-optical switching using high Δn, small core chalcogenide glass fibre. *Electronics Letters*, **29** (22), 1966–1968.
50. Asobe, M. *et al.* (1997) All-optical switching by use of cascading of phase-matched sum-frequency-generation and difference-frequency-generation processes in periodically poled $LiNbO_3$. *Optics Letters*, **22** (5), 274–276.
51. Cole, B. *et al.* (1999) Rare-earth doped selenide glasses and fibers for active applications in the near and mid-IR. *Journal of Non-Crystalline Solids*, **256&257**, 253–259.
52. Sanghera, J. and I. Aggarwal (1999) Active and passive chalcogenide glass optical fibers for IR applications: a review. *Journal of Non-Crystalline Solids*, **256**, 6–16.
53. Sanghera, J.S. and I. Aggarwal (1998) *Infrared Fiber Optics*, CRC Press.
54. Sanghera, J.S., L. Brandon Shaw, and I.D. Aggarwal (2002) Applications of chalcogenide glass optical fibers. *Competes Rendus Chimie*, **5**, 873–883.
55. Sanghera, J.S., L.B. Shaw, and I.D. Aggarwal (2009) Chalcogenide glass-fiber-based mid-IR sources and applications. *IEEE Journal of Selected Topics in Quantum Electronics*, **15** (1), 114–119.
56. Troles, J., *et al.* (2010) Low loss microstructured chalcogenide fibers for large non linear effects at 1995 nm. *Optics Express*, **18** (25), 26647–26654.
57. Seddon, A.B. *et al.* (2010) Progress in rare-earth-doped mid-infrared fiber lasers. *Optics Express*, **18** (25), 26704–26719.
58. Kobelke, J. *et al.* (1999) Chalcogenide glass single mode fibres–preparation and properties. *Journal of Non-Crystalline Solids*, **256**, 226–231.
59. Russell, P., (2003) Photonic crystal fibers. *Science*, **299** (5605), 358–362.
60. Domachuk, P. *et al.* (2008) Over 4000 nm bandwidth of mid-IR supercontinuum generation in sub-centimeter segments of highly nonlinear tellurite PCFs. *Optics Express*, **16** (10), 7161–7168.
61. Monro, T.M. *et al.* (2000) Chalcogenide holey fibres. *Electronics Letters*, **36** (24), 1998–2000.
62. Birks, T.A., W.J. Wadsworth, and P.S. Russell (2000) Supercontinuum generation in tapered fibers. *Optics Letters*, **25** (19), 1415–1417.
63. Tse, M.-L.V., *et al.* (2006) Supercontinuum generation at 1.06 μm in holey fibers with dispersion flattened profiles. *Optics Express*, **14** (10), 4445–4451.
64. Ranka, J.K., R.S. Windeler, and A.J. Stentz (2000) Visible continuum generation in air-silica microstructure optical fibers with anomalous dispersion at 800 nm. *Optics Letters*, **25** (1), 25–27.
65. Price, J.H. *et al.* (2006) Non-silica microstructured optical fibers for mid-IR supercontinuum generation from 2 μm-5 μm. in *Lasers and Applications in Science and Engineering*. International Society for Optics and Photonics, Bellingham.

66. Petersen, C.R. *et al.* (2014) Mid-infrared supercontinuum covering the 1.4–13.3 μm molecular fingerprint region using ultra-high NA chalcogenide step-index fibre. *Nature Photonics*, **8** (11), 830–834.
67. Jiang, X. *et al.* (2015) Deep-ultraviolet to mid-infrared supercontinuum generated in solid-core ZBLAN photonic crystal fibre. *Nature Photonics*, **9** (2), 133–139.
68. Lamprecht, B. *et al.* (1999) Resonant and off-resonant light-driven plasmons in metal nanoparticles studied by femtosecond-resolution third-harmonic generation. *Physical Review Letters*, **83** (21), 4421.
69. Lamprecht, B. *et al.* (2000) Metal nanoparticle gratings: influence of dipolar particle interaction on the plasmon resonance. *Physical Review Letters*, **84** (20), 4721.
70. Sönnichsen, C. *et al.* (2000) Spectroscopy of single metallic nanoparticles using total internal reflection microscopy. *Applied Physics Letters*, **77** (19), 2949–2951.
71. Rechberger, W. *et al.* (2003) Optical properties of two interacting gold nanoparticles. *Optics Communications*, **220** (1), 137–141.
72. Koester, C.J. and E. Snitzer (1964) Amplification in a fiber laser. *Applied Optics*, **3** (10), 1182–1186.
73. Ding, Y., A. Osaka, and Y. Miura (1994) Enhanced surface crystallization of β-barium borate on glass due to ultrasonic treatment. *Journal of the American Ceramic Society*, **77** (3), 749–752.
74. Kim, H.G. *et al.* (1996) Transparent tellurite-based glass-ceramics with second harmonic generation. *Journal Non-Crystalline Solids*, **208** (3), 303–307.
75. Tanaka, K. *et al.* (1996) Poling temperature dependence of optical second-harmonic intensity of MgO–ZnO–TeO2 glasses. *Journal of Applied Physics*, **79** (7), 3798–3800.
76. Tanaka, K. *et al.* (1996) Optical second harmonic generation in poled MgO, ZnO, TeO_2 and B_2O_3 TeO_2 glasses. *Journal of Non-Crystalline Solids*, **203**, 49–54.
77. Lee, J. *et al.* (2001) A holey fibre Raman amplifier and all-optical modulator, in *ECOC'01. 27th European Conference on Optical Communication, 30 September to 4 October 2001*, IEEE, Volume 6, pp. 46–47.
78. Mori, A. *et al.* (2001) Ultra-wideband tellurite-based Raman fibre amplifier. *Electronics Letters*, **37** (24), 1442–1443.
79. Stegeman, R. *et al.* (2003) Tellurite glasses with peak absolute Raman gain coefficients up to 30 times that of fused silica. *Optics Letters*, **28** (13), 1126–1128.
80. Kumar, V. V. R. K. *et al.* (2003) Tellurite photonic crystal fiber. *Optics Express*, **11** (20), 2641–2645.
81. Qin, G., R. Jose, and Y. Ohishi (2007) Stimulated Raman scattering in tellurite glasses as a potential system for slow light generation. *Journal Applied Physics*, **101** (9), 093109–093109-5.
82. Feng, X. *et al.* (2008) Single-mode tellurite glass holey fiber with extremely large mode area for infrared nonlinear applications. *Optics Express*, **16** (18), 13651–13656.
83. Hill, K. *et al.* (1978) Photosensitivity in optical fiber waveguides: Application to reflection filter fabrication. *Applied Physics Letters*, **32** (10), 647–649.
84. Morey, W.W., G. Meltz, and W.H. Glenn (1990) Fiber optic Bragg grating sensors. *Proceedings of the SPIE*, **1169**, doi: 10.1117/12.963022.
85. Hill, K.O. and G. Meltz (1997) Fiber Bragg grating technology fundamentals and overview. *Journal of Lightwave Technology*, **15** (8), 1263–1276.

86. Canning, J. (2008) Fibre gratings and devices for sensors and lasers. *Laser & Photonics Reviews*, **2** (4), 275–289.
87. Kashyap, R. (1999) *Fiber Bragg Gratings*. Academic Press.
88. Petermann, I. *et al.* (2002) Fabrication of advanced fiber Bragg gratings by use of sequential writing with a continuous-wave ultraviolet laser source. *Applied Optics*, **41** (6), 1051–1056.
89. Suo, R. *et al.* (2009) Fiber Bragg gratings inscribed using 800nm femtosecond laser and a phase mask in singleand multi-core mid-IR glass fibers. *Optics Express*, **17** (9), 7540–7548.
90. Zervas, M.N. and C.A. Codemard (2014) High power fiber lasers: a review. *IEEE Journal of Selected Topics in Quantum Electronics*, **20** (5), 219–241.
91. Jetschke, S., S. Unger, and J. Kirchhof (2007) Photodarkening in Yb doped fibers: experimental evidence of equilibrium states depending on the pump power. *Optics Express*, **15** (22), 14838–14843.
92. Jetschke, S. *et al.* (2008) Efficient Yb laser fibers with low photodarkening by optimization of the core composition. *Optics Express*, **16** (20), 15540–15545.
93. Engholm, M., L. Norin, and D. Åberg (2007) Strong UV absorption and visible luminescence in ytterbium-doped aluminosilicate glass under UV excitation. *Optics Letters*, **32** (22), 3352–3354.
94. Koechner, W. (1999) *Solid-State Laser Engineering*, 5th edn, Springer.
95. Adel, P. *et al.* (2003) Passive Q-switching by Tm^{3+} co-doping of a Yb^{3+}-fiber laser. *Optics Express*, **11** (21), 2730–2735.
96. Spence, D.E., P.N. Kean, and W. Sibbett (1991) 60-fsec pulse generation from a self-mode-locked Ti: sapphire laser. *Optics Letters*, **16** (1), 42–44.
97. Sibbett, W., A. Lagatsky, and C. Brown (2012) The development and application of femtosecond laser systems. *Optics Express*, **20** (7), 6989–7001.
98. Jackson, S.D. (2012) Towards high-power mid-infrared emission from a fibre laser. *Nature Photonics*, **6** (7), 423–431.
99. Godard, A. (2007) Infrared (2–12 μm) solid-state laser sources: a review. *Comptes Rendus Physique*, **8** (10), 1100–1128.
100. Keller, U. (2003) Recent developments in compact ultrafast lasers. *Nature*, **424** (6950), 831–838.
101. Lagatsky, A.A. *et al.* (2013) Fundamentally mode-locked, femtosecond waveguide oscillators with multi-gigahertz repetition frequencies up to 15 GHz. *Optics Express*, **21** (17), 19608–19614.
102. Jauregui, C., J. Limpert, and A. Tünnermann (2013) High-power fibre lasers. *Nature Photonics*, **7** (11), 861–867.
103. Miniscalco, W.J. (2001) *Rare-Earth-Doped Fibre Lasers and Amplifiers*, 2nd edn (ed. M.J.F. Digonnet), Marcel Dekker, Inc., New York.
104. PhysOrg.com (8 October 2010). General Physics. First successful integrated experiment at National Ignition Facility announced. http://phys.org/news/2010-10-successful-national-ignition-facility.html.
105. Dianov, E.M. *et al.* (2008) Bi-doped fibre lasers and amplifiers emitting in a spectral region of 1.3 μm. *Quantum Electronics*, **38** (7), 615–617.
106. Bufetov, I.A. *et al.* (2008) Bi-doped fiber lasers and amplifiers for a spectral region of 1300–1470 nm. *Optics Letters*, **33** (19), 2227–2229.

107. Dianov, E.M. *et al.* (2007) High-power cw bismuth-fiber lasers. *Journal of the Optical Society of America*, **B**, **24** (8), 1749–1755.
108. Mears, R.J. *et al.* (1987) Low-noise erbium-doped fibre amplifier operating at 1.54 μm. *Electronics Letters*, **23** (19), 1026–1028.
109. Giles, C.R. and E. Desurvire (1991) Modeling erbium-doped fiber amplifiers. *Journal of Lightwave Technology*, **9** (2), 271–283.
110. Miniscalco, W.J. (1991) Erbium-doped glasses for fiber amplifiers at 1500 nm. *Journal of Lightwave Technology*, **9** (2), 234–250.
111. Yamada, M., *et al.* (1998) Gain-flattened tellurite-based EDFA with a flat amplification bandwidth of 76 nm. *IEEE Photonics Technology Letters*, **10** (9), 1244–1246.
112. Mori, A., Y. Ohishi, and S. Sudo (1997) Erbium-doped tellurite glass fibre laser and amplifier. *Electronics Letters*, **33** (10), 863–864.
113. Dong, J., *et al.* (2011) Dual-pumped tellurite fiber amplifier and tunable laser using Er^{3+}/Ce^{3+} codoping scheme. *IEEE Photonics Technology Letters*, **23** (11), 736–738.
114. Sudo, S. (1997) *Optical Fiber Amplifiers: Materials, Devices, and Applications*, Artech House.
115. Jackson, S.D. (2001) 8.8 W diode-cladding-pumped Tm^{3+}, Ho^{3+}-doped fluoride fibre laser. *Electronics Letters*, **37** (13), 821–822.
116. Jackson, S.D. (2004) High power diode-pumped triply doped fibre laser. *Applied Physics B-Lasers and Optics*, **78** (3–4), 269–272.
117. Jackson, S.D. (2006) Midinfrared holmium fiber lasers. *IEEE Journal Of Quantum Electronics*, **42** (1–2), 187–191.
118. Jackson, S.D. and S. Mossman (2003) Diode-cladding-pumped Yb^{3+}, Ho^{3+}-doped silica fiber laser operating at 2.1-μm. *Applied Optics*, **42** (18), 3546–3549.
119. Jackson, S.D. *et al.* (2007) High-power 83 W holmium-doped silica fiber laser operating with high beam quality. *Optics Letters*, **32** (3), 241–243.
120. Jeong, Y. *et al.* (2005) Power scaling of 2 μm ytterbium-sensitised thulium-doped silica fibre laser diode-pumped at 975 nm. *Electronics Letters*, **41** (4), 173–174.
121. Shen, D., J. Sahu, and W. Clarkson (2006) High-power widely tunable Tm: fibre lasers pumped by an Er, Yb co-doped fibre laser at 1.6 μm. *Optics Express*, **14** (13), 6084–6090.
122. Richards, B. (2008) *Tellurite Glass Mid-infrared (1.9-2.1 μm) Fibre Lasers, School of Process, Environmental and Materials Engineering - Institute for Materials Research*, Thesis, University of Leeds.
123. Richards, B. *et al.* (2010) Tellurite glass lasers operating close to 2 μm. *Laser Physics Letters*, **7** (3), 177–193.
124. Shen, S. *et al.* (2005) 980-nm diode-pumped Tm^{3+}/Yb^{3+}-codoped tellurite fiber for S-band amplification. *Optics Letters*, **30** (12), 1437–1439.
125. Imeshev, G. and M. Fermann (2005) 230-kW peak power femtosecond pulses from a high power tunable source based on amplification in Tm-doped fiber. *Optics Express*, **13** (19), 7424–7431.
126. Komukai, T. *et al.* (1995) Upconversion pumped thulium-doped fluoride fiber amplifier and laser operating at 1.47 μm. *IEEE Journal of Quantum Electronics*, **31** (11), 1880–1889.
127. Yamamoto, T., Y. Miyajima, and T. Komukai (1994) 1.9-μm Tm-doped silica fiber laser-pumped at 1.57-μm. *Electronics Letters*, **30** (3), 220–221.

128. Yamamoto, T. *et al.* (1993) 1.9-μm Tm-doped fluoride fiber amplifier and laser-pumped at 1.58-μm. *Electronics Letters*, **29** (11), 986–987.
129. Mijović, J. and J. Wijaya (1990) Review of cure of polymers and composites by microwave energy. *Polymer Composites*, **11** (3), 184–191.
130. Zhao, Z. *et al.* (2012) Active glass–polymer superlattice structure for photonic integration. *Nanotechnology*, **23** (22), 225302.
131. Irannejad, M. *et al.* (2012) Active glass waveguide amplifier on GaAs by UV-pulsed laser deposition and femtosecond laser inscription. *Laser Physics Letters*, **9** (5), 329.
132. Ovshinsky, S.R. (2012) *Disordered Materials: Science and Technology*, Springer Science & Business Media.
133. Wuttig, M. and N. Yamada (2007) Phase-change materials for rewriteable data storage. *Nature Materials*, **6** (11), 824–832.
134. Hirao, K. *et al.* (2001) *Active Glass for Photonic Devices - Photoinduced Structures and their Applications*, Springer Series in Photonics (ed. T. Kamiya, B. Monemar, and H. Venghaus), Springer-Verlag, Berlin.

Supplementary References

CHAPTER 1

1. S.R. Elliott (1990) *Physics of Amorphous Materials*, 2nd edn, Longman, London.
2. A.K. Paul (1990) *Chemistry of Glasses*, 2nd edn, Chapman & Hall, London.
3. A.K. Varsheneya (2006) *Fundamentals of Inorganic Glasses*, 2nd edn, Society of Glass Technology, Sheffield.
4. J. Wong and C.A. Angell (1976) *Glass Structure by Spectroscopy*, 1st edn, Marcel Dekker, New York.
5. A.F. Wells (1945) *Structural Inorganic Chemistry*, 1st edn, Clarendon Press.
6. A.R. West (1984) *Basic Solid State Chemistry*, John Wiley & Sons Ltd, Chichester.
7. Z.U. Borisova (1981) *Glassy Semiconductors* (translated from Russian by J.G. Adhasko), Plenum Press, New York.
8. R.H. Doremus (1973) *Glass Science*, 1st edn, Wiley-Interscience.

CHAPTER 2

1. W.D. Kingrey, H.K. Bowen, and D.R. Uhlmann (1976) *Introduction to Ceramics*, 2nd edn, John Wiley & Sons, Inc., New York.
2. P.W. France (editor) (1990) *Fluoride Glass Optical Fibres*, Blackie & Sons Ltd, London.
3. M.H. Lewis (ed.) (1989) *Glasses and Glass Ceramics*, Chapman & Hall, London.
4. S.A. Brawer (1985) *Relaxation in Viscous Liquids and Glasses: Review of Phenomenology, Molecular Dynamics Simulations, and Theoretical Treatments*, American Ceramic Society.

CHAPTER 3

1. I.D. Aggarwal and G Lu, (eds) (1991) *Fluoride Glass Fibre Optics*, Academic Press, London.
2. S. Sudo (ed.) (1997) *Optical Fibre Amplifiers: Materials, Devices, and Applications*, Artech House, Inc., Norwood, MA.
3. A.K. Varsheneya (2006) *Fundamentals of Inorganic Glasses*, 2nd edn, Society of Glass Technology, Sheffield.

Inorganic Glasses for Photonics – Fundamentals, Engineering and Applications, First Edition. Animesh Jha.
© 2016 John Wiley & Sons, Ltd. Published 2016 by John Wiley & Sons, Ltd.

CHAPTER 4

1. R.A.H. El-Mallawany (2002) *Tellurite Glass Handbook – Physical Properties and Data*, CRC Press, Boca Raton, FL.
2. G. Keiser (1991) *Optical Fiber Communications*, 2nd edn, Electrical & Electronics Engineering Series, McGraw Hill International Editions, New York.
3. D.K. Mynbaev and L.L. Scheiner (2000) *Fiber-Optic Communications Technology*, Prentice Hall, Upper Saddle River, New Jersey.
4. P.W. France (1989) *Fluoride Glass Optical Fibers*, Blackie.
5. F. Ivan (1983) *Optical Properties of Glass*, Elsevier Publishing Company, Maryland Heights, pp. 82–89.
6. R.R.A. Syms and J.R. Cozens (1992) *Optical Guided Waves and Devices. 1992*, McGraw-Hill Publishing Company, London.
7. I.P. Harman (1996) *Optical Diagnostics for Thin Solid Film Processing*, Academic Press, San Diego, pp. 559–563.

CHAPTER 5

1. D.L. Smith (1995) *Thin-film Deposition: Principles & Practice*, McGraw-Hill, New York.
2. R. Syms and J. Cozens (1992) *Optical Guided Waves and Devices*, McGraw Hill, London.
3. P.W. France (ed.) (1990) *Fluoride Glass Optical Fibres*, 1st edn, Blackie, London, pp (a) 122–131; (b) 133–185.
4. A. Elshabini-Riad and F.D. Barlow III (1998) *Thin-film Technology Handbook* (Series advisor C.M. Harper), McGraw-Hill, New York, pp. 1-12–1-24.

CHAPTER 6

1. M. Fox (2006) *Quantum Optics – An Introduction*, Oxford Master Series in Atomic, Optical and Laser Physics, Oxford University Press, Oxford.
2. W. Koechner and M Bass (2003) *Solid-State Lasers: A Graduate Text*, Springer Science & Business Media.
3. W.T. Silfvast (2004) *Laser Fundamentals*, Cambridge University Press, Cambridge, UK.
4. M.J.F. Digonnet (ed.) (1993) *Rare-Earth Doped Fibers Lasers and Amplifiers*, Marcel Dekker, Inc.
5. J.A. Duffy (1990) *Bonding, Energy Levels, and Bands in Inorganic Solids*, Longman.
6. I.D. Aggarwal and G. Lu, (eds) (1991) *Fluoride Glass Fibre Optics*, Academic Press, London.
7. F.A. Cotton and G. Wilkinson (1998) *Advanced Inorganic Chemistry*, 5th edn, Wiley-Interscience, New York.
8. G.F. Imbusch and R. Kopelman (1986) in *Laser Spectroscopy of Solids* (eds W.M. Yen and P. M. Selzer) Topics in Applied Physics, vol. 49, Springer, pp. 1–37.

9. R. Reisfeld and C.K. Jorgensen (1987) Excited state phenomena in vitreous materials, in *Handbook on the Physics and Chemistry of Rare-Earths*, vol. 9, North-Holland, Amsterdam, ch 58, pp. 1–90.

CHAPTER 7

1. G. Keiser (1991) *Optical Fiber Communications*, 2nd edn, Electrical & Electronics Engineering Series, McGraw Hill International Editions, New York.
2. D.K. Mynbaev and L.L. Scheiner (2000) *Fiber-Optic Communications Technology*, Prentice Hall, Upper Saddle River, New Jersey.
3. A. Ghatak and K. Thyagrajan (1998) *An Introduction to Fibre Optics*, Cambridge University Press, Cambridge, UK.
4. J.D. Joannopoulos, R. Meade, and J. Winn (1995) *Photonic Crystals*, Princeton Press, New Jersey.
5. G.P. Agrawal (2007) *Nonlinear Fiber Optics*, Academic Press, pp. 261–270.
6. K. Hirao, T. Mitsuyu, J. Si, and J. Qui (eds) (2001) *Active Glass for Photonic Devices – Photoinduced Structures and their Applications* Springer Series in Photonics, vol. 7 (series ed. T. Kamiya, B. Monemar, and H. Venghaus), Springer-Verlag, Berlin.

Symbols and Notations Used

c	Velocity of light (2.9979×10^9 m s^{-1})
e	Electronic charge (Coulomb) = 1.60218×10^{-19} C
h	Planck's constant (6.6261×10^{-34} J s = 4.1357×10^{-15} eV s),
$\hbar$	$h/2\pi = 1.0546 \times 10^{-34}$ J s = 6.5821×10^{-16} eV s
κ_B	Boltzmann constant (1.3807×10^{-23} J K^{-1})
m_e	Rest mass of an electron, 9.10939×10^{-31} kg
ε_o	Absolute permittivity (8.8542×10^{-12} F m^{-1})
μ_o	Absolute permeability or vacuum permeability ($4\pi \times 10^{-7}$ H m^{-1})
$4\pi\varepsilon_o$	Permittivity in electrostatic unit (esu)
R	Universal gas constant = 8.31457 J mol^{-1} K^{-1} = 1.987 calorie mol^{-1} K^{-1}
1 eV	1.60218×10^{-19} (J in atomic units)
1 eV	96499.3 ≅ 96500 (J in molar units)
N_A	Avogadro's number = 6.0221×10^{23} mol^{-1} = 6.0221×10^{23} (g-atom)$^{-1}$
1 Å	1 Ångström = 100 pm = 0.1 nm = 10^{-4} μm = 10^{-8} cm = 10^{-10} m.
e	Exponent = 2.7183, i.e. ln(2.7183) = ln(e^{1})
p_i	Pressure or partial pressure, atmosphere (atm), 1 atm = 101 308 Pa ≡ 760 mm of Hg (mercury) column
η	Viscosity, Pascal.second (Pa.s). 1 Pa.s = 10 Poise
F	Faraday Constant = 96500 J volt^{-1} mol^{-1}.
D	Diffusion coefficient (cm^2 s^{-1})

Inorganic Glasses for Photonics – Fundamentals, Engineering and Applications, First Edition. Animesh Jha.
© 2016 John Wiley & Sons, Ltd. Published 2016 by John Wiley & Sons, Ltd.

Index

A
Abbe number, 160
absorption, 120
  electronic, 120
  extrinsic, 153
  intrinsic, 120
  molecular, 141
activation energy, 4
AgI-CsI binary phase diagram, 9
amorphous, 23, 119, 120, 124, 126, 127, 187, 188, 190, 193, 194, 197, 253
  state, 1, 5, 23
angles, 109
  acceptance, 113
  critical, 113
  propagation, 113
annealing, 53
  stress, 91
arrhenius equation, 66

B
band gap energy (E_g), *18*
batch preparation, 81
binary phase diagrams, 13
  AgI-CsI, 13
  BaF_2-ZrF_4, 12
  NaF-ZrF_4, 12
bit rate and bandwidth, 269
Boltzmann constant (k_B), *4*
Born-Haber cycle, 7
Bose-Einstein distribution, 122
Bragg gratings, 269
  long-period gratings, 292

C
cation-anion pair ($\psi_{C\text{-}A}$), 14
$CdCl_2$-BaF_2 liquid, 11
chemical reaction, 82
  equilibrium, 82
  melting, 82
chemical vapour, 80
  deposition, 195
  glass formation, 99
  materials system, 196
  reaction, 88
classical theory, 52
coefficient of thermal expansion (α_v), 3, 69
co-ordination, 14
  cuboctahedron, 25
  pentagonal antiprism, 25
  prisms, 25
  rhombo dodecahedron, 25
  square anti-prism, 24
co-ordination number (Z^N), 14
covalent, 26
critical cooling rates, 51
crystal growth
  rate, 59
crystalline state, 4
Curie temperature, 4

D
decahedron, 25
decay parameters, 227
  multiphonon, 232
  radiative, 212
defect states energy, 118
delocalization of valence electrons, 23
dielectric films, 181
  chemical methods, 194
  deposition, 197
  evaporation, 179
  ion implantation, 192
  multi-layer structures, 190

Inorganic Glasses for Photonics – Fundamentals, Engineering and Applications, First Edition. Animesh Jha.
© 2016 John Wiley & Sons, Ltd. Published 2016 by John Wiley & Sons, Ltd.

dielectric films (*Continued*)
  physical methods, 179
  sputtering, 181
dielectric waveguides, 114
differential mechanical, 68
  analyser, 68
  analysis, 62
differential thermal, 62
  analysis, 62
  calorimetry, 62
diffraction, 109
dipole motion, 217
  radiation decay, 217
dispersion, 158, 261
  curves, 164, 265
  intermodal, 265
  intramodal, 263
  materials, 162, 163
  polarization, 267
  total, 269
  waveguide, 269
dispersion management, 267
  flattening, 268
  shifted fibres, 268
  slope, 269
dodecahedron, 25
drying, 88
  ammonium hydrogen bifluoride, 88
  chemicals for glass melting, 81
  chlorine based, 80
  fluorine based, 89
  HF formation, 88
  hydroxyl-chlorine reactions, 105
  process, 90
  purification reactions (GeO_2,TeO_2), 84
  reactions, 83

E
elasticity and elastic behaviour, 1
electronegativity ($\psi_{C\text{-}A}$), 14
electronegativity ($\psi_{C\text{-}A}$)
  Pauling's $(\psi_{C\text{-}A})^P$, 14
  Sanderson$(\psi_{C\text{-}A})^S$, 19
electronic structures, 222
  lanthanide elements, 221
  transition metal elements, 225
electron-phonon coupling, 233
energy, 7
  band gap (E_g), 18
  Gibbs (ΔG), 2
  heteropolar (E_{Hetero}), 21
  homopolar (E_{Homo}), 21
  optical gap (E_{Opt}), 118
  surface, 53
  tail of electronic states, 118
energy transfer (ET), 233
  Europium doped glass, 238
  non-radiative processes, 232
  terbium doped glass, 223
enthalpy
  fusion or melting (ΔH_f), 2
  partial molar, 8
entropy, 8
  configurational, 11
  fusion or melting, ΔS_f, 16
  partial molar, 8
  system and surrounding, 4
  thermal, 11
  universe, 4
equation, 4
  Maxwell's, 114
  nonlinear, 275, 279
equilibrium, metastable, 3
equilibrium, thermodynamic, 3
eutectic, liquid and phase transition, 9
evaporation, 4, 62, 179
  congruent, 179
  incongruent, 179
  materials used, 179, 197

F
fabrication of, 97
  chalcogenide fibres, 156
  chalcogenide glasses, 95
  chemical solution & sol-gel, 200
  fluoride fibres, 145
  fluoride glasses, 87
  heavy-metal oxide fibres, 134
  heavy-metal oxide glasses, 87
  multi-core fibres, 243
  oxide glasses, 80
  silica fibres, 145
  thin films, 200
  transparent glass ceramics, 97–99
fibres, 148
  bandgap, 269
  graded index, 117
  multi-mode, 157

- periodic defects, 269
- photonic crystal, 269
- single mode, 115
- step-index, 115

fictive glass temperature, 3
flame hydrolysis process, 195
- glass preforms, 79
- thin films, 195

G

gibbs energy, 11
- energy barrier, 53

glass, 14
- ceramics, 59
- chalcogenide, 45, 64
- conditional, 29
- fluoride, 65
- heavy-metal oxide, 65
  - Ga_2O_3, 65
  - GeO_2, 65
  - tellurite (TeO_2), 65
- oxide-nitride, 36
- oxycarbide, 26
- sulphide
  - Ga_2S_3-La_2S_3, 16
  - GeS_2, 6

glass and glassy state, 1
glass composition range, 65
- in binary phase diagrams, 65
- in ternary or triangular sections, 65

glass formation, 14
- kinetic theory, 51

glass-forming, 7
- ability, 7
- liquids, 4
- range, 29
- tendency, 7

glass network, 23
- formers, 23
- intermediates, 23
- modifiers, 20
- sol-gel, 26

glass transition, 1
glass transition temperature (Tg), 1

H

harmonic generation, 275
- second harmonic, 276
  - electric-field poled glass
    - maker fringe pattern, 290
- third harmonic, 278

heat (Q), 5
hybridization, 23
- sp, sp^2, sp^3, sp^3d, sp^3d^2, 25

I

ideal, mixtures, 8
infrared absorption (IR), 124
interference, 129
ion exchange, 197
- glass materials, 197
- technique, 195
- waveguide profiles, 200

ionic radius, 44
ion implantation, 192
- materials, 194
- parameters, 193
- techniques, 192

isothermal compressibility (β_T), 3

J

Judd-Ofelt analysis, 230
- omega parameters, 227

K

Kauzmann paradox, 4
kinetics of glass formation, 7

L

Lambert-Beer's law, 129
lasers, 295
- CW, 298
- four-level system, 300
- Nd^{3+}-fibre lasers, 300
- power scaling, 301
- Q-switched, 298
- three-level system, 295
- Yb^{3+}-fibre lasers, 297

lattice energy (U_{Tot}), *14*
- covalent ($U_{Covalent}$), 20
- ionic(U_{Ion}), 20

line shape broadening, 214
- extrinsic broadening, 216
- Gaussian, 217
- intrinsic broadening, 216
- Lorentzian, 218

liquid, multicomponent, 8
- Eutectic, 9

liquidus temperature, 8

loss characterization of
  comparison, 153
  optical fibres, 153

M
melting and fusion techniques, 87
  chalcogenide glasses, 91
  fluoride glasses, 88
  oxide glasses, 87
melting and melting point (T_m), 2
melting reactions, 91
  chalcogenide glass, 91
  fluoride glass, 90
  oxide glass, 81
metastable, 2
mode field diameter, 115
modes, 155
  higher order, 160
  zero-order, 160
molecular beam epitaxy, 196
  chemical vapour deposition, 195
  materials, 196
  with pulsed-laser deposition, 183
  thin films, 188
molecular susceptibility, 224
mole fraction (X_i), 8
Mott's 8-N rule, 18

N
nucleation, 52
  heterogeneous, 55
  homogeneous, 53
  non-steady, 54
  steady, 53
  surface, 55
  volume, 54
nucleation rate, 59
  Li_2O-SiO_2 glass, 57
nucleus, 52
  critical, 53
numerical aperture, 114

O
octahedron, 16
  $(ZrF_6)^{2-}$, 14
optical fibres, 145
  characterization, 145
  engineering, 157
  geometricaloptics, 109
  loss, extrinsic, 161
  loss, intrinsic, 171
optical nonlinearity, 269
  harmonic generation and dipoles, 275
  Kerr media, 285
  materials for harmonic generations, 279
  parametric processes, 279
  resonant, 287
optical transitions, 227
  dipole, 218
  line broadening, 218
  multipole, 221
  transition metal ions, 227
oscillator, 153
  linear harmonic, 125
  non-radiative, 231
  radiative rate, 238
  strength, 227
oxygen, 23
  bridging, 26
  non-bridging, 26

P
partial charge on anions ($-\delta_A$), 19
Pauling's electronegativity, 14
permeability, dielectric, 159
permittivity, dielectric, 159
phase diagrams
  binary, 13
  rare-earth silicate, 239
  ternary composition, 29
Phillips' bond stretching and bending model, 18
  bi-, 31
  pyramids, 10
  trigonal, 24
phonons, 22
phosphate crystals, 230
  monazite, 230
  xenotime, 230
photoelasticity, 123
photo-induced gratings, 292
photonic crystal fibres, 272
  birefringence, 274
  dispersion curves, 268
  microstructured, 272
  optical nonlinearity, 275
  Raman gain, 291
Planck's constant, 4

polarizability, 123
polyanions of, 9
  $(AgI_3)^{2-}$, (Ag_2I_3), 9
  $(AlO_3)^{3-}$, $(AlO_4)^{5-}$, $(AlO_5)^{7-}$, 18
  $(BO_3)^{3-}$, $(BO_4)^{5-}$, 18
  $(PO_4)^{3-}$, 14
  $(SiO_4)^4$, 14
  $(TeO_3)^{2-}$, $(TeO_4)^{4-}$, 18
pulsed laser deposition, 183
  ablation, 186
  chamber, 189
  characterization, 188
  excimer, 184
  materials for thin films, 184
  plasma plume, 186
  superlattice thin films, 190

Q
quenched state, 3
quenched stress, 97
quenching rate (Q_i *and* Q_o), 3

R
radiative transition models, 209
  Einstein, 221
Raman frequency, 126
  anti-stoke, 127
  stoke, 127
Raman gain
  medium, 291
Raman microscope, 127
Raman spectroscopy of, 130
  chalcogenide, 140
  fluoride, 139
  germanium oxide, 137
  phosphate, 156
  silicate, 131
  tellurite, 135
raw materials purification, 88
  chalcogenide glasses, 91
  fluoride glasses, 91
  oxide glasses, 91
reciprocal salt mixture, 10
reflectance, 153
reflection, 109
  total internal reflection, 113
refraction, 166
refractive index, 166
  measurements, 129
  stress dependence, 170
  temperature dependence, 167
  wavelength dependence, 159

S
Sanderson's electronegativity model, 20
scattering, 121
  anti-stoke, 122
  Brillouin, 123
  extrinsic, 123
  intrinsic, 117
  Mie, 157
  Raman, 123
  Rayleigh, 123
  Stoke, 123
selection rules, 218
  Fermi's golden rule, 219
  Laporte, 224
  optical transitions, 218
semiconductor materials, 124
SiALON, 25
silica
  quartz, 167
  tridymite, 126
Si-O non-bridging, 15
Si-O-Si bridging, 105
sol-gel, 5, 26, 53, 62, 79, 80, 99
  coatings, 200
  Coulombic charge, 101
  Debye-Hückel equation, 102
  definitions, 101
  depositions, 80
  electric double layer, 101
  Gibbs-Thomson model, 102
  glass, 99–103
  glass formation, 99–105
  isoelectric point, 102
specific heat, constant pressure (C_p), 3
  change (ΔC_p), 3
specific heat, constant volume (C_v), 3
  change (ΔC_v), 3
spectrophotometry, 118, 121, 128, 129
  IR, 128
  UV-visible, 121
spectroscopic properties, 239
  trivalent lanthanide dopants
    Er^{3+}-doped, 241
    Pr^{3+}-doped, 246
    Tm^{3+}-doped, 247
    Yb^{3+}-doped, 238
spectroscopy, 126

  Fourier transform infrared (FTIR), 128
  Raman spectroscopy, 126
  ultraviolet-visible (UV), 121
sputtering process, 181
  deposition rate, 182
  radio frequency, 183
  threshold energy, 182
  yield, 182
Stark splitting, 231
Stoke-Einstein equation, 53

T
Tauc region, 118
temperatures, 62
  dependence of crystal growth, 59
  dependence of nucleation, 59
  dependence of viscosity, 60
  reduced glass (T_g/T_m), 57
  reduced maximum (T_{max}/T_m), 57
tetrahedra, 14
  $(AlF_4)^{-}$or $(AlO_4)^{5}$, 18
  $(BeF_4)^{2-}$, 31
  $(GeS_4)^{4-}$, 141
  $(GeSe_4)^{4-}$, 38
  $(PO_4)^{3-}$, 14
  $(SiO_4)^{4-}$, 14
  $(ZnX_4)^{2}$, 33
theory
  growth, 58
  kinetic, 51
  nucleation, 52
thermal characterization, 62
  crystal growth, 60
  nucleation, 62
  phase transformation, 59
thermal stress, 96
thermodynamic state, 2, 3, 6
thin films, 179
  glass-polymer, 190
  pulsed laser deposition, 183
  sputtering, 181
  superlattice growth, 190
  waveguides, 181
transition, 2
  first-order, 4
  liquid-to-crystal, 2
  liquid-to-glass, 2
  second-order, 4
  solid-to-liquid, 2
transition rates, 219
  non-radiative, 231
  radiative, 231
  theories, 209
transparent glass ceramics, 297

U
undercooling, 7
universal gas constant *(R)*, 8
upconversion, 237
  fluoride glasses, 241
  phosphate glasses, 242
Urbach edge, 118

V
valency, 39
  anion (Z_A), 8
  cation (Z_c), 8
velocity, 159
  group, 159
  light, 121
  phase, 116
vibrational, 126
  structures of glass, 141
virtual energy states, 122
viscosity (η), 18
viscosity map
  crystal growth-temperature, 59, 62
  for inorganic glasses, 239
  nucleation-temperature, 55, 59
viscosity relationship
  Angell, 75
  Arrhenius, 151
  Cohen-Grest, 72
  Eyring, 72
  Vogel-Fulcher, 72, 97
V-parameters, 114, 273

W
waveguides, 182
  ion-exchanged, 197
  ion-implanted, 194
  sol-gel, 200
waves, 109

X
xenotime, 230
  rare-earth phosphate, 239

Y
yttrium phosphate, 230

Z
Zachariasen model, 15